



universität
wien

DISSERTATION

Titel der Dissertation

„Macroscopic Matter-wave Interferometry“

Verfasser

Dipl.-Phys. Stefan Nimmrichter

angestrebter akademischer Grad

Doktor der Naturwissenschaften (Dr. rer. nat.)

Wien, im Juli 2013

Studienkennzahl lt. Studienblatt: A 091 411

Dissertationsgebiet lt. Studienblatt: Physik

Betreuer: Univ.-Prof. Dr. Markus Arndt



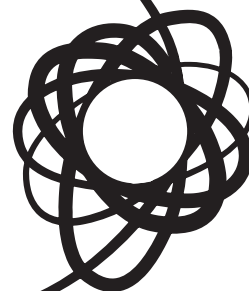
Macroscopic Matter-wave Interferometry

Stefan Nimmrichter

Vienna 2013



Quantum Nanophysics Group



Abstract

In this thesis I develop theoretical methods to facilitate, assess, and interpret macroscopic matter-wave interference experiments with molecules and nanoparticles, as conceived and implemented in the Quantum Nanophysics Group at the University of Vienna. Introducing a theoretical framework to describe the interaction of polarizable particles with light, I first study the feasibility of dissipative slowing and trapping of sub-wavelength molecules and dielectric nanospheres by means of high-finesse cavities and strong laser fields – an essential prerequisite to facilitate matter-wave interferometry with heavy nanoparticles. I proceed with an in-depth analysis of matter-wave near-field interferometry, focusing on the most recent implementation of the Talbot-Lau scheme with pulsed optical gratings. In particular, I assess the feasible mass limits of this scheme, as well as the influence of hypothetical macrorealistic models. Finally, I turn to the question of how to quantify the macroscopicity of mechanical quantum phenomena in general, developing a systematic and observation-based answer. From this I derive a physical measure for the degree of macroscopicity of superposition phenomena, which admits an objective comparison between arbitrary quantum experiments on mechanical systems.

Zusammenfassung

Die vorliegende Arbeit umfasst die theoretischen Grundlagen und Methoden zur Beschreibung makroskopischer Materiewelleninterferenzexperimente, wie sie in der Quantennanophysikgruppe an der Universität Wien mit Molekülen und anderen Nanoteilchen durchgeführt werden. Ich bespreche zunächst die Wechselwirkung von polarisierbaren Teilchen mit Lichtfeldern, um anschließend die dissipative Wirkung von Laserfeldern und optischen Resonatoren auf die Teilchen zu beschreiben. Damit lassen sich die Voraussetzungen für das optische Bremsen und Einfangen großer Nanoteilchen diskutieren, das für Interferenzexperimente mit solch massiven Objekten benötigt wird. Es folgt eine ausführliche theoretische Beschreibung von Nahfeldinterferometrie. Dabei konzentriere ich mich auf das Wiener Talbot-Lau-Interferometer mit gepulsten Lasergittern und diskutiere, welchen Massenbereich man damit prinzipiell erreichen kann. Es zeigt sich, dass gängige makrorealistische Hypothesen zum quanten-klassischen Übergang überprüfbar werden, was mich anschließend zu der Frage führt, was Makroskopizität eigentlich bedeutet. Im letzten Abschnitt der Dissertation entwickle ich eine physikalisch-empirische Interpretation des Makroskopizitätsbegriffs für Quanteneffekte. Daraus lässt sich schließlich ein Maß für den Grad an Makroskopizität ableiten, mit dem man beliebige Superpositionsexperimente in mechanischen Systemen objektiv erfassen und vergleichen kann.

Contents

1. Introduction	1
2. Interaction of polarizable particles with light	5
2.1. Mechanics of polarizable point particles in coherent light fields	5
2.1.1. The linear response of a polarizable point particle to light	6
2.1.2. Absorption, emission and Rayleigh scattering of photons	8
2.1.2.1. Photon absorption	9
2.1.2.2. Photon emission into free space	11
2.1.2.3. Elastic light scattering into free space	13
2.1.3. Classical dynamics of a polarizable point particle coupled to a strongly pumped cavity mode	14
2.1.3.1. Intra-cavity field dynamics	14
2.1.3.2. Coupled cavity-particle dynamics	15
2.1.3.3. Estimated friction force	17
2.1.4. Optical gratings for matter waves	18
2.1.4.1. Coherent grating interaction	20
2.1.4.2. Amplitude modulation by means of optical depletion gratings	22
2.1.4.3. Momentum transfer by absorption and scattering	23
2.2. Quantum mechanics of polarizable point particles in high-finesse cavities	26
2.2.1. Quantum model of a PPP coupled to multiple cavity modes	26
2.2.1.1. Quantum description of a driven cavity mode	28
2.2.1.2. A particle, a driving laser, and a handful of empty cavity modes	30
2.2.2. Eliminating the quantum field dynamics in the weak coupling limit	31
2.2.2.1. The first weak-coupling assumption	31
2.2.2.2. The second weak-coupling assumption	33
2.2.2.3. Effective time evolution of the reduced particle state	35
2.2.3. Semiclassical description of friction and diffusion	37
2.2.3.1. Friction and diffusion terms in the Fokker-Planck equation	38
2.2.3.2. Conditions for cavity-induced slowing	40
2.2.3.3. Case study: A single strongly pumped standing-wave mode	41
2.2.3.4. Multimode enhancement in degenerate resonator configurations	44
2.3. Mechanics of spherical particles in coherent light fields	48
2.3.1. Light extinction and light-induced forces	50
2.3.1.1. The Poynting vector and the extinction power of the sphere	51
2.3.1.2. Maxwell stress tensor and optical forces	53
2.3.2. Optical standing-wave gratings	57
2.3.2.1. Phase modulation effect	57

2.3.2.2.	Amplitude modulation effect	58
2.3.3.	Slowing and trapping of microspheres by a cavity	59
2.3.3.1.	Cavity resonance shift induced by microspheres	60
2.3.3.2.	Classical simulation of slowing and trapping	62
3.	Near-field interference techniques with heavy molecules and nanoclusters	67
3.1.	The Poisson spot interferometer (PSI)	68
3.1.1.	Phase-space description of the ideal effect	71
3.1.1.1.	Ideal diffraction pattern	71
3.1.1.2.	Poisson's spot	73
3.1.1.3.	Classical ideal shadow projection	76
3.1.2.	Modified effect in the presence of interaction	77
3.1.2.1.	Modified diffraction pattern	77
3.1.2.2.	Modified shadow pattern	78
3.1.2.3.	Interaction potential at dielectric discs and spheres	80
3.1.2.4.	Numerical analysis of realistic scenarios	81
3.2.	Talbot-Lau interferometer (TLI) scheme	83
3.2.1.	Generic description of the Talbot-Lau scheme	87
3.2.1.1.	Coherent grating transformation in phase space	88
3.2.1.2.	Step-by-step derivation of the Talbot-Lau fringe pattern	89
3.2.1.3.	Incoherent effects and decoherence events	93
3.2.2.	The Kapitza-Dirac Talbot-Lau interferometer (KDTLI)	95
3.2.2.1.	Coherent description	95
3.2.2.2.	Modification due to the absorption of grating photons	96
3.2.3.	The optical time-domain ionizing Talbot-Lau interferometer (OTITLI)	99
3.2.3.1.	Coherent description and results	99
3.2.3.2.	Incoherent modification due to Rayleigh scattering	103
3.3.	Absolute absorption spectroscopy in the TLI scheme	105
3.3.1.	Experimental setup and theoretical description	105
3.3.1.1.	Theoretical description	106
3.3.1.2.	Quantitative analysis	109
3.3.2.	Dealing with fluorescence	112
3.4.	Mass limits of the OTITLI scheme	114
3.4.1.	Experimental methods and challenges	114
3.4.1.1.	Particle candidates and sources	114
3.4.1.2.	Interferometer design	115
3.4.1.3.	Signal detection	116
3.4.2.	Standard mass limitations	117
3.4.2.1.	Temporal stability and inertial forces	117
3.4.2.2.	Decoherence	118
3.4.2.3.	Particle size effect	121
3.4.3.	Test of spontaneous localization models	123
3.4.3.1.	The CSL master equation	124
3.4.3.2.	Contrast reduction predicted by the model	125

4. Classicalization and the macroscopicity of quantum superposition states	127
4.1. A minimal modification of quantum mechanics	128
4.1.1. The operational framework and the dynamical semigroup assumption . . .	129
4.1.2. Galilean covariance	130
4.1.2.1. The Galilei symmetry group	131
4.1.2.2. The projective unitary representation of Galilean boosts	132
4.1.2.3. Galilean covariance of the modified time evolution	133
4.1.2.4. Implications for the form of the modification	134
4.1.3. The modified time evolution of a single particle	135
4.1.3.1. Covariance with respect to rotations	136
4.1.3.2. Decay of coherence	136
4.1.4. The modified time evolution of a many-particle system	138
4.1.4.1. Basic consistency and scaling requirements	139
4.1.4.2. Center-of-mass translations	140
4.1.4.3. Single-particle translations	141
4.1.4.4. Universality and scale invariance of the modification	143
4.1.4.5. General form of the modification	144
4.1.4.6. Second quantization formulation	144
4.1.5. Center-of-mass motion of rigid compounds	146
4.1.5.1. Case study: The two-particle modification	147
4.1.5.2. Rigid compounds of many particles	149
4.2. Observable consequences of the modification	150
4.2.1. Effects of the single-particle classicalization	150
4.2.1.1. Diffusion and energy increase	151
4.2.1.2. Discussion of the coherence decay effect	152
4.2.2. Explicit solution for harmonic potentials	154
4.2.2.1. Derivation of the explicit solution	154
4.2.2.2. Free propagation in the presence of a constant acceleration . . .	156
4.2.2.3. The description of lower dimensional motion	157
4.2.2.4. Harmonic solution in 1D	157
4.2.3. Classicalization of Bose-Einstein condensates	157
4.2.3.1. Effective single-particle description of BEC interference	158
4.2.3.2. Interference in terms of second order correlation functions . . .	159
4.2.4. Classicalization of Cooper-paired electrons	161
4.2.4.1. Experimental situation	162
4.2.4.2. Theoretical description of the superconducting state	163
4.2.4.3. Classicalization of current superposition states	165
4.3. The measure of macroscopicity	168
4.3.1. Definition of the macroscopicity measure	169
4.3.1.1. The electron as a natural reference point particle	169
4.3.1.2. Minimizing parameter space with a Gaussian distribution	170
4.3.1.3. Parameter limitations on the subatomic scale	170
4.3.1.4. Formal definition of the macroscopicity	170

4.3.2.	Assessing the macroscopicity of quantum experiments	171
4.3.2.1.	De Broglie interference of point-like particles	172
4.3.2.2.	Center-of-mass interference of extended objects	181
4.3.2.3.	Superpositions of micromechanical oscillations	182
4.3.2.4.	Superpositions of persistent loop currents	183
4.3.2.5.	Survey of past and future experiments	184
4.3.3.	Concluding remarks and future directions	186
5.	Conclusion and outlook	189
A.	Light-matter interaction	193
A.1.	Complex field amplitude and quantization	193
A.2.	Gaussian modes	194
A.3.	Phase space representation of states and observables	196
A.4.	Weak-coupling dynamics of N particles in M modes	197
A.5.	Spherical wave expansion	199
A.6.	Mie scattering at spherical dielectrics	202
B.	Matter-wave interferometry	205
B.1.	Ideal Poisson spot diffraction	205
B.2.	Classical Poisson spot of a point source	206
B.3.	Capture range of a spherical obstacle	207
B.4.	General form of the Talbot-Lau fringe pattern	207
B.5.	Decoherence events in the general TLI scheme	209
C.	Classicalization and Macroscopicity	211
C.1.	Decay of persistent current superpositions	211
C.2.	Geometry factors of spheres, cuboids and cylinders	213
C.2.1.	Homogeneous spheres	213
C.2.2.	Homogeneous cuboids	214
C.2.3.	Homogeneous cylinders	215
C.3.	Superpositions of harmonic oscillator states	215
C.3.1.	Superposition of the oscillatory ground and excited state	216
C.3.2.	Coherent state superposition by photon entanglement	217
	Acknowledgements	221
	Bibliography	222

Chapter 1.

Introduction

“The most essential characteristic of scientific technique is that it proceeds from experiment, not from tradition.”

— Bertrand Russell

It goes without saying that quantum mechanics has stood its grounds over the decades as an immensely powerful and successful theory to describe the physics on microscopic scales. Even more so, it has proven to be astonishingly reliable and robust whenever one has tried to push it one step further to the extreme; both into the relativistic subnuclear domain of high-energy physics, and into the meso-to-macroscopic low-energy regime which was originally thought to be ruled by classical physics. In fact, relativistic quantum field theory has led to the standard model of particle physics, which is currently being tested to an unprecedented degree at CERN, while research on standard quantum mechanics has led to the discovery and understanding of large-scale many-body quantum phenomena such as superconductivity, Bose-Einstein condensation, and molecular interference. It is quite remarkable that, even with the continuous growth in system sizes over the years and up to the present day, no sign has appeared whatsoever that would indicate the slightest breakdown of good ol' Schrödinger's equation. Yet, many open questions are still to be answered and the two 'breaking points' of the theory, the measurement problem and the incompatibility to general relativity, have remained unsolved.

Hence, although all previous attempts to falsify quantum mechanics on extreme and originally unintended scales have utterly failed, people do raise serious doubts whether this might still be true for long. Among others, Anthony Leggett was studying this problem intensely with the advent of the first experiments verifying the collective quantum behaviour of billions of Cooper-paired electrons generating currents through superconducting loops [1, 2]. He regarded this as the first truly macroscopic quantum observation and coined the term “macroscopic realism” in his timely article of 2002 [3], suggesting that there should be some kind of breakdown of the superposition principle somewhere along the way from the atom to the feline if we want to reconcile quantum theory with our classical world view (including the concepts of gravity and measurements). At the same time, also matter-wave experiments took one major step beyond the atomic size regime when the first large molecules were interfered at the turn of the millennium [4, 5]. Continued progress towards the macroscopic domain has occurred in various fields ever since, and we may soon witness the first quantum superposition experiments with heavy nanoobjects or even micromechanical oscillators.

The theoretical assessment of macroscopic quantum superposition phenomena is not just counting beans or, to be precise, atomic mass units in superposition. It rather breaks down into several problems which must be tackled separately and by quite different means:

- ★ **Physical understanding of a system of interest** The relevant physical behaviour of a given system must first be understood sufficiently well to be able to devise means to interact with it and control it in the experiment. Molecule interferometry, for instance, requires that we know how to produce, control, diffract and detect large molecules.
- ★ **Conception of feasible macroscopic quantum experiments** We must identify a concrete quantum phenomenon and develop a feasible experimental scheme that can be implemented in the lab. Needless to say, the theory must produce quantitative predictions that would match the experimental data.
- ★ **Theoretical consequences of macroscopic quantum experiments** What can we learn about the system or about possible new physics by measuring a given macroscopic quantum effect systematically? Molecule interference data, for instance, can give us information on the structure and dynamics of the molecules. It also allows us to assess environmental decoherence or possible non-standard modifications of quantum theory.
- ★ **Meaningful definition of the term ‘macroscopic’** This may sound like nitpicking, but it is in fact a fundamental and nontrivial theoretical task. How do we define ‘macroscopicity’ in a universal and objective manner, irrespectively of the concrete physics of an observed effect? What is it that makes a given quantum observation more macroscopic than another one? And what is the best way to improve in macroscopicity in future experiments?

Readers are invited to keep these basic issues in the back of their head when working through the following text. They can be regarded as the common thread connecting all the concrete problems that will be dealt with below.

This thesis covers most of the theoretical and conceptual work I have contributed to the Quantum Nanophysics group of Markus Arndt in Vienna in close collaboration with my experimental colleagues and with Klaus Hornberger, Klemens Hammerer, Helmut Ritsch and Claudiu Genes. The main results have all been published separately [6–14], but they are layed out here in more detail and presented retrospectively in a common theoretical framework. What is to follow will be divided into three main chapters, which can be regarded as three major steps in approaching the macroscopic world and probing Schrödinger’s quantum mechanics by means of matter-wave experiments with large objects.

The first and foremost step is to develop the means to control and manipulate matter waves, and to assess their basic quantum mechanical behaviour under experimental conditions. These methods will be the basis of all that is to follow. In **Chapter Two**, I will focus on coherent optical means, mostly lasers and cavities, to interact with matter waves. I will lay out general theoretical tools to describe the motion of polarizable particles under the influence of coherent light fields, optical high-finesse resonators, or simply the vacuum radiation field. Everything will revolve around the somewhat complementary issues of light-induced dissipation and coherence, ultimately joining a stale punchline: “size matters”. Nevertheless, the inclined reader can expect results less boring than that¹.

¹ In addition, the appendix of this chapter features the longest and ugliest mathematical expressions of this thesis.

I will study how cavities can be employed to dissipatively slow down large polarizable particles, how laser fields can be employed as diffractive elements for the very same particles, and how these effects will scale as the particles approach the dimension of optical wavelengths in size. Such large objects may exhibit low-field seeking behaviour, and they could even be dissipatively captured in Gaussian cavity modes under realistic conditions. After all, optical diffraction and cavity cooling techniques have been studied, perfectionized and routinely implemented with atomic matter waves for decades [15–18], and it is time to take this over from this community and do some ‘big’ business again².

Having all necessary tools at hand, **Chapter Three** will be dedicated to the theory behind modern matter-wave interference techniques with nanoparticles, that is, with large molecules and clusters ranging between several hundred and a billion atomic mass units. Naturally, the Talbot-Lau interferometer (TLI) scheme will be at the center of attention there, as it is not only the top dog in this field holding the mass records of interference to date. In fact, the TLI is the only setup capable of interfering molecules of several thousand mass units at the moment [13,19]. Despite the fact that significant progress has also been made in conventional far-field interference of large molecules [20], and that conceptually different methods to show the wave nature of molecules [9, 21, 22] or large nanospheres [23–25] are currently pursued in various groups, the TLI scheme still offers greatest potential to venture to the highest possible mass regime. And the experiment already works, too!

I will therefore spend most of the time in the third chapter discussing the theoretical description and the mass-limiting factors in Talbot-Lau interferometry. A time-domain implementation using ionizing standing-wave laser pulses will turn out to be most promising for this purpose, and it may facilitate the test of hypothetical modifications of quantum physics in the macroscopic domain. Moreover, I will show that the Talbot-Lau setup can also be employed as a sensitive measurement device for the optical properties of the interfering particles.

In order to avoid the impression that I am truly obsessed with Talbot and Lau, I will actually begin the chapter with an in-depth discussion of another near-field interference phenomenon, which seems to be applicable to large masses as well: Poisson’s spot. At first glance, the observation of a bright spot in the shadow region behind a circular obstacle appears to be a clear signature of quantum interference. But we will find out that this is not true anymore when highly polarizable particles are concerned, which interact dispersively with the walls of real-sized obstacle. On the long run, Poisson’s spot will thus be more strictly limited in mass than the Talbot-Lau scheme, and one should better bet on the latter (hence my obsession).

The detailed discussion of the mass limits of matter-wave interferometry, and of how far we can push quantum wave behaviour towards the classical world of macroscopic objects, ultimately raises the pivotal question: What does it mean to be ‘macroscopic’? People working in molecule interferometry would intuitively argue that it means to be as massive as possible. Obviously, this is how they would try to persuade funding agencies. Then again, there are many physicists working hard to realize superposition states of nanomechanical oscillators of much greater mass in the lab nowadays [26, 27]. Atomic physicists, on the other hand, could argue that it is not only the mass that counts, but also the interference ‘arm separation’ and the time that separates macroscopic from microscopic superpositions, and the men from the boys. To make matters worse, one could also criticize that all the various interferometry experiments merely involve a single motional degree of freedom, whereas truly macroscopic quantum phenomena should be many-body phenomena.

² No offence, if you are an atomic physicist. You’re doing a great job.

Purely formal arguments and intuition fail to give an answer to this very physical question of macroscopicity.

In **Chapter Four** I develop a novel answer based on physical principles, which puts intuition back on the ground of hard empirical facts. For this purpose I will adopt Leggett’s famous common-sense argument of “macroscopic realism” [3]: If we believe in our century-old classical reasoning to describe the physics of the macroscopic everyday world we live in, and if, at the same time, we accept the quantum superposition principle in all its weirdness as we observe it on the microscopic scale, then there should be a breakdown of standard quantum theory somewhere in between³. Macroscopicity can then be defined in an objective and physical manner by the amount to which an observed quantum phenomenon excludes such possible breakdown mechanisms of quantum theory. While this sounds like a fair and straightforward approach to settle the controversy of macroscopicity in mechanical quantum systems, there is no free lunch, of course. Turning this idea into a robust quantitative statement requires a whole lot of tedious and formal reasoning, which will await the bold reader in all its bone-dry glory throughout most of the fourth chapter.

I will show that the mathematical form of reasonable breakdown mechanisms, or ‘classicalizing modifications’ of quantum mechanics, can be pinned down by demanding that fundamental symmetry and consistency principles, such as the invariance under Galilean symmetry transformations, must not be violated. With this we will be able to quantify and compare the macroscopicity of arbitrary quantum experiments with mechanical systems, past and proposed, in a neutral and objective manner. Yet, we will find that molecule interferometry is still ahead by a nose at the moment, even without bias. The pinnacle of my theoretical reasoning will be the description of an ordinary house cat as a 4 kg sphere of water just to prove that a superposition state à la Schrödinger would correspond to a macroscopicity value of something like 57—a value where everything quantum must certainly end, and also this thesis.

I will close with a short conclusion and outlook in the fifth chapter.

³ For the sake of this fundamental argument, environmental decoherence cannot be the breakdown mechanism. Supporters of macrorealistic theories would argue that decoherence does not resolve the core issue of quantum theory, the measurement problem, nor does it exclude macroscopic superpositions by principle.

Chapter 2.

Interaction of polarizable particles with light

“More light!”

— Johann Wolfgang von Goethe (last words)

A proper understanding of the mechanics and susceptibility of nanoparticles under the influence of coherent light fields will be a core ingredient throughout this thesis. It will be required for the description of new matter-wave interferometry schemes and of optical methods to manipulate the motion or measure the optical properties of molecules and clusters. This chapter is dedicated to the light-matter interaction in the presence of coherent laser fields, of high-finesse cavity modes and not least of a (thermally occupied) radiation field. The latter will mainly be useful to describe decoherence processes by the emission, absorption and scattering of photons, whereas the coherent interaction with laser fields and cavity modes is the basis of optical interference gratings and cavity-induced slowing and trapping methods.

I will start by introducing the basic effect of coherent light fields on the center-of-mass motion of small particles in Section 2.1. In the limit of short interaction times this directly leads to the description of optical gratings, as commonly used in matter-wave interferometry. I will proceed with the more complex long-time dynamics of polarizable point particles (PPP) coupled to strong laser fields in Section 2.2, where I will present in detail the influence of high-finesse cavity modes. They can be used to dissipatively slow down single particles, or to cool the motion of a hot ensemble of particles, respectively [8].

In Section 2.3 I eventually take a step beyond the point-particle approximation and study the effect of standing-wave fields on wavelength-sized dielectric spheres using Mie theory [28, 29]. The results derived there will be directly applied in Section 2.3.3 where I discuss the radial slowing and trapping of microspheres in a strongly pumped cavity mode.

2.1. Mechanics of polarizable point particles in coherent light fields

In a first and most elementary approach to the light-matter problem let us study the classical and quantum dynamics of a polarizable point particle (PPP) in the presence of a classical electromagnetic field mode. The point-particle idealization is considered valid in many experimental situations where subwavelength molecules or clusters are coupled to high-intensity light fields of laser beams or strongly pumped cavity modes. Consequences and applications of the basic effect are discussed

here, before the restriction to point particles and classical light fields will successively be lifted in the next sections.

For the moment let us represent the light by a single-mode electric and magnetic field

$$\mathbf{E}(\mathbf{r}, t) = E_0 e^{-i\omega t} \mathbf{u}(\mathbf{r}), \quad \mathbf{H}(\mathbf{r}, t) = \frac{E_0}{i\mu_0\omega} e^{-i\omega t} \nabla \times \mathbf{u}(\mathbf{r}) \quad (2.1)$$

with a harmonic time dependence on the frequency $\omega = ck$. It will be convenient to work with complexified fields and allow for complex mode-polarization functions $\mathbf{u}(\mathbf{r}) \in \mathbb{C}$, as discussed in Appendix A.1. The physical fields are then represented by the real parts $\Re\{\mathbf{E}\}$ and $\Re\{\mathbf{H}\}$. We will mostly deal with the important case of linearly polarized standing or running waves,

$$\mathbf{E}_{\text{sw}}(\mathbf{r}, t) = E_0 e^{-i\omega t} \mathbf{e}_x f(x, y) \cos(kz), \quad \mathbf{H}_{\text{sw}}(\mathbf{r}, t) = \frac{iE_0}{\mu_0 c} e^{-i\omega t} \mathbf{e}_y f(x, y) \sin(kz), \quad (2.2)$$

$$\mathbf{E}_{\text{rw}}(\mathbf{r}, t) = E_0 \mathbf{e}_x f(x, y) \exp(ikz - i\omega t), \quad \mathbf{H}_{\text{rw}}(\mathbf{r}, t) = \frac{E_0}{\mu_0 c} \mathbf{e}_y f(x, y) \exp(ikz - i\omega t), \quad (2.3)$$

with $f(x, y)$ the transverse mode profile. Realistic light fields occupy only a finite region in space, as described by their mode volume $V = \int d^3r |\mathbf{u}(\mathbf{r})|^2$, and we may associate with the field of strength E_0 a complex amplitude $\alpha = \sqrt{\epsilon_0 V / 2\hbar\omega} E_0$ and a mean photon number $|\alpha|^2$. With this the Hamiltonian, that is, the field energy contained in the mode, takes the well-known form

$$H_f = \frac{1}{2} \int_V d^3r [\epsilon_0 \Re\{\mathbf{E}(\mathbf{r}, t)\}^2 + \mu_0 \Re\{\mathbf{H}(\mathbf{r}, t)\}^2] = \frac{\hbar\omega}{2} (\alpha^* \alpha + \alpha \alpha^*) = \hbar\omega |\alpha|^2. \quad (2.4)$$

The amplitude is replaced by the photon annihilation operator a when generalizing to quantum fields. A Gaussian mode¹ is described by two waist parameters w_x, w_y and the transverse mode profile $f(x, y) = \exp(-x^2/w_x^2 - y^2/w_y^2)$.

2.1.1. The linear response of a polarizable point particle to light

In order to model the interaction of a polarizable point particle with harmonic light fields one generally associates to the particle a scalar polarizability $\chi = \chi(\omega)$, which represents its linear response to the electric light field \mathbf{E} . In most cases beyond the level of a single atom, the polarizability is taken to be a phenomenological frequency-dependent parameter². It determines the induced electric dipole moment $\mathbf{d} = \chi \mathbf{E}$ and the associated Lorentz force [32], $\mathbf{F}(\mathbf{r}, t) = (\Re\{\mathbf{d}\} \cdot \nabla) \Re\{\mathbf{E}\} + \mu_0 \Re\{\partial_t \mathbf{d}\} \times \Re\{\mathbf{H}\}$. It involves only real physical quantities. The first term represents the net Coulomb force of the electric field component $\mathbf{E}(\mathbf{r})$ acting on the dipole \mathbf{d} at position \mathbf{r} , whereas

¹ The full mathematical description of Gaussian light fields, as generated by focused laser beams or found in curved-mirror cavities, is a little bit more involved than presented here. I give a detailed formula for symmetric Gaussian mode functions with $w_x = w_y = w$ in Appendix A.2. Strictly speaking, the above representations (2.2) and (2.3) are zeroth order approximations of the Gaussian mode fields in the waist parameter $1/kw$, and additional polarization components must be taken into account for higher orders.

² Note that the light-atom interaction can also be modeled by a complex linear polarizability provided the light is far detuned from any internal electronic transition and the transition is not strongly driven. In the latter case the atom's response saturates at sufficiently high field intensities, as described by the Jaynes-Cummings model [30, 31].

the second term describes the force exerted by the magnetic field component $\mathbf{H}(\mathbf{r}')$ on the associated current density $\mathbf{j}(\mathbf{r}') = \partial_t \mathbf{d}(\mathbf{r} - \mathbf{r}')$. We find that the overall force oscillates rapidly at the given optical frequency, and it is therefore expedient to restrict to the time-averaged expression³

$$\begin{aligned} \langle \mathbf{F}(\mathbf{r}) \rangle_t &= \left\langle \left(\Re \{ \chi \mathbf{E}(\mathbf{r}) e^{-i\omega t} \} \cdot \nabla \right) \Re \{ \mathbf{E}(\mathbf{r}) e^{-i\omega t} \} + \mu_0 \Re \{ -i\omega \chi \mathbf{E}(\mathbf{r}) e^{-i\omega t} \} \times \Re \{ \mathbf{H}(\mathbf{r}) e^{-i\omega t} \} \right\rangle_t \\ &= \frac{1}{2} \Re \{ \chi [\mathbf{E}(\mathbf{r}) \cdot \nabla] \mathbf{E}^*(\mathbf{r}) \} + \frac{1}{2} \Re \{ \chi \mathbf{E}(\mathbf{r}) \times [\nabla \times \mathbf{E}^*(\mathbf{r})] \} \\ &= \frac{\Re \{ \chi \}}{4} \nabla |\mathbf{E}(\mathbf{r})|^2 - \frac{\Im \{ \chi \}}{2} \Im \{ [\nabla \circ \mathbf{E}^*(\mathbf{r})] \mathbf{E}(\mathbf{r}) \}. \end{aligned} \quad (2.5)$$

In the absence of absorption, $\Im \{ \chi \} = 0$, the average force is conservative, and it can be written as the negative gradient of the time-averaged dipole interaction potential,

$$H_{\text{int}}(\mathbf{r}) = -\frac{1}{4} \Re \{ \chi \} |\mathbf{E}(\mathbf{r})|^2. \quad (2.6)$$

The second term in (2.5) represents the non-conservative radiation pressure force related to the net absorption of field momentum per time. It appears only in the case of complex running-wave fields with a directed momentum flux, and it acts only on particles with a nonzero light absorption cross-section $\sigma_{\text{abs}} = \sigma_{\text{abs}}(\omega)$, which determines the imaginary part of the complex polarizability χ . We find the relation $\sigma_{\text{abs}} = k \Im \{ \chi \} / \varepsilon_0$ between both parameters by looking at the average power absorbed by the dipole. It is determined by the average rate of work the field does on the dipole [33, 34],

$$\begin{aligned} P_{\text{abs}}(\mathbf{r}) &= \left\langle \int d^3 r' \Re \{ \mathbf{j}(\mathbf{r}', t) \} \cdot \Re \{ \mathbf{E}(\mathbf{r}', t) \} \right\rangle_t = \frac{1}{2} \Re \{ [\partial_t \mathbf{d}(\mathbf{r})]^* \cdot \mathbf{E}(\mathbf{r}) \} \\ &= \frac{\omega}{2} \Im \{ \chi \} |\mathbf{E}(\mathbf{r})|^2 \equiv \sigma_{\text{abs}} I(\mathbf{r}), \end{aligned} \quad (2.7)$$

with $I(\mathbf{r}) = c \varepsilon_0 |\mathbf{E}(\mathbf{r})|^2 / 2$ the local electric field intensity.

Another contribution to the radiation pressure effect on the particle is due to the Rayleigh scattering of light from the coherent field into free space. The absorption cross-section σ_{abs} is thus complemented by the elastic light scattering cross-section $\sigma_{\text{sca}} = k^4 |\chi|^2 / 6\pi \varepsilon_0^2$, as given by the total radiated power of the oscillating dipole [34],

$$P_{\text{sca}}(\mathbf{r}) = \frac{\omega^4}{12\pi \varepsilon_0 c^3} |\mathbf{d}|^2 = \frac{ck^4 |\chi|^2}{12\pi \varepsilon_0} |\mathbf{E}(\mathbf{r})|^2 \equiv \sigma_{\text{sca}} I(\mathbf{r}). \quad (2.8)$$

The cross-section $\sigma_{\text{ext}} = \sigma_{\text{abs}} + \sigma_{\text{sca}}$ describes the combined extinction of the light by absorption and Rayleigh scattering. The influence of Rayleigh scattering on the force (2.5) can usually be neglected for point-like particles of diameter $a \ll \lambda$. Since their polarizability is roughly determined by the

³ The vector identities [33],

$$\begin{aligned} \nabla(\mathbf{a} \cdot \mathbf{b}) &= \mathbf{a} \times (\nabla \times \mathbf{b}) + \mathbf{b} \times (\nabla \times \mathbf{a}) + (\mathbf{b} \cdot \nabla) \mathbf{a} + (\mathbf{a} \cdot \nabla) \mathbf{b}, \\ (\nabla \circ \mathbf{b}) \mathbf{a} &= \mathbf{a} \times (\nabla \times \mathbf{b}) + (\mathbf{a} \cdot \nabla) \mathbf{b}, \end{aligned}$$

might occasionally be useful here and in the following. The dyadic term $B = \nabla \circ \mathbf{b}$ is defined as the matrix $B_{jk} = \partial b_k / \partial x_j$.

volume, $\chi \sim a^3$, the scattering contribution to the total force is then strongly suppressed by the factor $(ka)^3 \ll 1$.

The conservative part of the interaction generalizes to the case of a quantum particle in a straightforward manner; we simply replace the position \mathbf{r} by the operator \mathbf{r} and add the dipole potential $H_{\text{int}}(\mathbf{r})$ to the Hamiltonian of the free particle,

$$H_{\text{PPP}} = \frac{\mathbf{p}^2}{2m} - \frac{\Re\{\chi\}}{4} |E(\mathbf{r})|^2 = \frac{\mathbf{p}^2}{2m} + \hbar U_0 |\alpha|^2 |\mathbf{u}(\mathbf{r})|^2. \quad (2.9)$$

In the second equation I have introduced the coupling frequency

$$U_0 = -\frac{\omega}{2\varepsilon_0 V} \Re\{\chi\}, \quad (2.10)$$

which represents the single-photon interaction strength or, in the case of a high-finesse cavity field, the cavity resonance shift due to the presence of the particle. A full quantum treatment of both light and matter is obtained by replacing $|\alpha|^2 \rightarrow \mathbf{a}^\dagger \mathbf{a}$ and adding the single-mode Hamiltonian $H_f = \hbar\omega \mathbf{a}^\dagger \mathbf{a}$.

The quantum counterpart of the non-conservative light-matter interaction cannot be obtained by such simple means as it cannot be expressed in terms of the particle's Hamilton operator. We expect that, apart from exerting a net radiation pressure force, it also contributes a diffusion in momentum space as the particle randomly absorbs and scatters single photons from the field mode. That is to say, the full quantum dynamics of the particle must be phrased in terms of a Lindblad-type master equation [35, 36].

2.1.2. Absorption, emission and Rayleigh scattering of photons

A physical derivation of the nonconservative radiation pressure forces, of momentum diffusion and the associated decoherence effects requires a full quantum description of the coupling to both the coherent light field and the free-space mode vacuum. This will be given in Section 2.2. At this point we take a more intuitive, operational approach to arrive at the same results based on a formulation in terms of quantum jumps [36].

The absorption, emission, or scattering of single photons can be understood as a stochastic Poisson process, where the random variable $N(t) \in \mathbb{N}_0$ denotes the number of absorbed, emitted, or scattered photons at each point in time t starting from $N(0) = 0$. Given a mean rate of events Γ the Poisson process is determined by the time evolution of the probability $P(n, t)$ of counting a total of n events until time t ,

$$\frac{d}{dt} P(n, t) = \Gamma [P(n-1, t) - P(n, t)], \quad P(n, 0) = \delta_{n,0}. \quad (2.11)$$

As time evolves, the number of events increases stepwise by the increment $dN(t) = N(t+dt) - N(t) \in \{0, 1\}$ in each coarse-grained time step⁴ dt , with the expectation value $\mathcal{E}[dN(t)] = \Gamma dt$.

⁴ Stochastic differential equations can serve to describe the effective time evolution of open systems in contact with an environment inducing rapid (uncontrollable) state transitions that cannot be examined with the coarse-grained time resolution of observation [35]. The transitions thus show up as random events, or 'jumps'. Using a Poissonian model we assume single infrequent jumps that can be clearly distinguished.

The binary random variable $dN(t) = dN^2(t)$ can now be employed in the stochastic time evolution of the quantum state of motion $|\psi(t)\rangle$ of a particle absorbing, emitting or scattering photons at an average rate Γ . Let us suppose that the system state undergoes the transition $|\psi\rangle \mapsto A|\psi\rangle/\sqrt{\langle\psi|A|\psi\rangle}$ in the case of an event (which would correspond to a momentum kick in our case), while it evolves coherently under the influence of the Hamiltonian H otherwise. The random trajectory of the system state is then described by the stochastic Schrödinger equation [36]

$$d|\psi(t)\rangle = \left(-\frac{i}{\hbar}H + \Gamma \frac{\langle\psi(t)|A^\dagger A|\psi(t)\rangle - A^\dagger A}{2} \right) |\psi(t)\rangle dt + \left(\frac{A}{\sqrt{\langle\psi(t)|A^\dagger A|\psi(t)\rangle}} - 1 \right) |\psi(t)\rangle dN(t), \quad (2.12)$$

where the antihermitian addition to the coherent time evolution in the first line ensures norm conservation. An ensemble average over all random trajectories leads to a master equation for the motional state ρ of the system, which is of the renowned Lindblad form,

$$\partial_t \rho = -\frac{i}{\hbar} [H, \rho] + \Gamma \left(A \rho A^\dagger - \frac{1}{2} \{A^\dagger A, \rho\} \right) \equiv -\frac{i}{\hbar} [H, \rho] + \mathcal{L}(\rho). \quad (2.13)$$

Additional Lindblad superoperators \mathcal{L} appear in the presence of several statistically independent jump processes influencing the system.

We are left with specifying the rate constants Γ and the jump operators A of the Lindblad terms that correspond to photon absorption, emission and scattering at a PPP,

$$\partial_t \rho = -\frac{i}{\hbar} [H_{\text{PPP}}, \rho] + \mathcal{L}_{\text{abs}}(\rho) + \mathcal{L}_{\text{emi}}(\rho) + \mathcal{L}_{\text{sca}}(\rho) \quad (2.14)$$

2.1.2.1. Photon absorption

Complex polarizabilities represent point-like particles that absorb light. Dividing the average absorption power (2.7) by the energy of a single photon yields the rate constant $\Gamma_{\text{abs}} = P_{\text{abs}}/\hbar\omega \equiv \gamma_{\text{abs}}|\alpha|^2$, which can be expressed as a product of the photon number in the field times the *single-photon absorption rate* $\gamma_{\text{abs}} = c\sigma_{\text{abs}}/V = \omega\Im\{\chi\}/\epsilon_0 V$.

Each absorbed photon modifies the particle momentum state according to the mode function $\mathbf{u}(\mathbf{r})$ of the coherent light field. In the simple case of a plane wave, for instance, the absorbed photon shifts the particle by $\hbar\mathbf{k}$ in momentum space, so that the jump operator reads as $A = \exp(i\mathbf{k} \cdot \mathbf{r})$. Different mode structures emerge when plane waves are reflected and transmitted at particular geometries. We restrict our view here to modes with a fixed (linear, circular or elliptic) polarization vector, $\mathbf{u}(\mathbf{r}) = \epsilon u(\mathbf{r})$. The spatial structure of the mode is then contained in the scalar mode function⁵ $u(\mathbf{r})$, which can be decomposed into a Fourier sum of polarized plane-wave components,

⁵ Using a fixed polarization $\epsilon(\mathbf{r}) = \epsilon$ is a good approximation in many practical cases such as Gaussian TEM modes, where position-dependent corrections are negligibly small. A detailed description of modes with a position-dependent polarization vector is more involved and requires a specific physical model of the particle's response during the absorption process. This is because the orientation of the induced dipole moment then contains information about the position of the particle in the field mode, which is traced out when only the center-of-mass state is monitored.

$u(\mathbf{r}) = \sum_{\mathbf{k}} u_{\mathbf{k}} \exp(i\mathbf{k} \cdot \mathbf{r})$. The momentum components $u_{\mathbf{k}}$ being indistinguishable, photon absorption transforms a momentum state $|\mathbf{p}\rangle$ of the particle into the superposition state

$$|\mathbf{p}\rangle \mapsto \sum_{\mathbf{k}} u_{\mathbf{k}} |\mathbf{p} + \hbar\mathbf{k}\rangle = \sum_{\mathbf{k}} u_{\mathbf{k}} e^{i\mathbf{k} \cdot \mathbf{r}} |\mathbf{p}\rangle = u(\mathbf{r}) |\mathbf{p}\rangle, \quad (2.15)$$

accordingly. The jump operator is thus given by $A = u(\mathbf{r})$, and the corresponding Lindblad term of photon absorption reads as

$$\mathcal{L}_{\text{abs}}(\rho) = \gamma_{\text{abs}} |\alpha|^2 \left[u(\mathbf{r}) \rho u^*(\mathbf{r}) - \frac{1}{2} |u(\mathbf{r})|^2 \rho - \frac{1}{2} \rho |u(\mathbf{r})|^2 \right]. \quad (2.16)$$

Note that this form of the superoperator fully accounts for the local intensity distribution of the field. If the particle state is localized, say, at the node of a standing-wave field (2.2), where the mode function vanishes, the Lindblad term will not contribute to the master equation of the particle. In contrast, the particle is most strongly affected in the antinodes.

From the resulting master equation $\partial_t \rho = -i[H_{\text{PPP}}, \rho] / \hbar + \mathcal{L}_{\text{abs}}(\rho)$ we can deduce the mean force acting on the particle by means of the Ehrenfest theorem. The time derivative of the momentum operator expectation value in the Heisenberg picture should correspond to the expected classical force expression (2.5). A straightforward calculation (using the commutator identity $[\mathbf{p}, f(\mathbf{r})] = -i\hbar \nabla f(\mathbf{r})$) reveals that this is indeed the case,

$$\begin{aligned} \partial_t \langle \mathbf{p} \rangle &= \text{tr} \left(-\frac{i}{\hbar} \mathbf{p} [H_{\text{PPP}}, \rho] + \mathbf{p} \mathcal{L}_{\text{abs}}(\rho) \right) \\ &= \frac{i}{\hbar} \langle [H_{\text{int}}(\mathbf{r}), \mathbf{p}] \rangle + \frac{\gamma_{\text{abs}}}{2} |\alpha|^2 \langle [u^*(\mathbf{r}), \mathbf{p}] u(\mathbf{r}) + u^*(\mathbf{r}) [\mathbf{p}, u(\mathbf{r})] \rangle \\ &= -\hbar U_0 |\alpha|^2 \langle \nabla |u(\mathbf{r})|^2 \rangle + \hbar \gamma_{\text{abs}} |\alpha|^2 \langle \Im \{ u^*(\mathbf{r}) \nabla u(\mathbf{r}) \} \rangle \\ &= \frac{\Re \{ \chi \}}{4} \langle \nabla |E(\mathbf{r})|^2 \rangle - \frac{\Im \{ \chi \}}{2} \langle \Im \{ [\nabla \circ E^*(\mathbf{r})] E(\mathbf{r}) \} \rangle, \end{aligned} \quad (2.17)$$

with the electric field $E(\mathbf{r}) = E_0 \epsilon u(\mathbf{r})$. The absorption superoperator (2.16) reproduces the classical radiation pressure force correctly, but it also contributes a diffusion of the particle momentum. The time derivative of the energy expectation value $\partial_t \langle H_{\text{PPP}} \rangle$ becomes non-zero due to the presence of the absorption-induced momentum diffusion⁶,

$$\begin{aligned} \partial_t \langle H_{\text{PPP}} \rangle &= \text{tr} \left(\frac{\mathbf{p}^2}{2m} \mathcal{L}_{\text{abs}}(\rho) \right) = \frac{\gamma_{\text{abs}} |\alpha|^2}{4m} \langle [u^*(\mathbf{r}), \mathbf{p}^2] u(\mathbf{r}) + u^*(\mathbf{r}) [\mathbf{p}^2, u(\mathbf{r})] \rangle \\ &= \frac{\hbar \gamma_{\text{abs}} |\alpha|^2}{m} \langle \Im \{ u^*(\mathbf{r}) \nabla u(\mathbf{r}) \} \cdot \mathbf{p} \rangle + \frac{\hbar^2 \gamma_{\text{abs}} |\alpha|^2}{2m} \langle |\nabla u(\mathbf{r})|^2 \rangle. \end{aligned} \quad (2.18)$$

The first term is related to the radiation pressure force exerted by directed running waves; it vanishes in the case of standing-wave modes $u(\mathbf{r}) \in \mathbb{R}$. The positive second term is always present, it describes the heating of the particle by momentum diffusion, and it represents the main quantum correction to the classical derivation of the non-conservative radiation pressure force.

⁶ Here I have used the identity $[\mathbf{p}^2, f(\mathbf{r})] = -\hbar^2 \Delta f(\mathbf{r}) - 2i\hbar \nabla f(\mathbf{r}) \cdot \mathbf{p} = \hbar^2 \Delta f(\mathbf{r}) - 2i\hbar \mathbf{p} \cdot \nabla f(\mathbf{r})$, as well as the fact that the mode function by construction solves the Helmholtz equation $\Delta u = -k^2 u$.

This raises the question as to whether, or when, the diffusion correction becomes relevant in practice. Given that the mode function solves the Helmholtz equation $\Delta u = -k^2 u$ we can estimate the magnitude of the gradient by $|\nabla u| \sim k$, which leads to an energy increase per time of the order of $\gamma_{\text{abs}} |\alpha|^2 \hbar^2 k^2 / 2m = \Gamma_{\text{abs}} \hbar \omega_r$ due to diffusion. That is, the energy grows at the total absorption rate Γ_{abs} in units of the so-called *recoil energy* $\hbar \omega_r = \hbar^2 k^2 / 2m$, or *recoil frequency* ω_r if units of \hbar are discarded. This diffusion heating must be compared to the rate of change in potential energy $\sim 2\hbar k v U_0 |\alpha|^2$ when the particle is moving at the velocity v . The ratio of non-conservative heating to the conservative change in potential energy $\gamma_{\text{abs}} \omega_r / 2U_0 k v$ then scales as the quotient of recoil frequency over Doppler frequency $\omega_r / k v = \hbar k / 2m v$ —a tiny quantity in many practical cases dealing with fast and large molecules or clusters.

The diffusion effect becomes relevant in the quantum limit of motion, where particles are so slow that their momentum $p = mv$ becomes comparable to the photon momentum $\hbar k$. The minimal kinetic energy a particle can reach in the presence of the photon field is then given by the recoil energy $\hbar \omega_r$. The absorption, emission, or scattering of photons induces a random walk in momentum space and thereby prevents the particle from reaching even lower velocities.

A purely classical treatment of the radiation pressure forces may suffice far above the quantum limit as long as decoherence is of no concern. On the other hand, if the particle is prepared in a nonclassical state of motion, the Lindblad superoperator (2.16) accounts for the coherence loss due to photon absorption.

2.1.2.2. Photon emission into free space

The discussed absorption model eventually runs into constraints once the total absorbed photon energy during the time scale of the experiment reaches a critical level where it significantly modifies or destroys the internal structure of the particle such that the linear response regime breaks down.

On the other hand, an internally hot or excited particle may gradually reduce its internal energy by fluorescence or thermal emission of radiation, which results in a similar diffusion and decoherence effect as in the absorption process. The associated Lindblad term can be modeled as a random unitary process [37]. Each emitted photon with a wave vector \mathbf{k} exerts a momentum kick of $-\hbar \mathbf{k}$ onto the particle, as described by the unitary transformation $U_{\mathbf{k}} = \exp(-i\mathbf{k} \cdot \mathbf{r})$. Given the spectral emission rate $\gamma_{\text{emi}}(\omega)$ and the normalized angular distribution $R(\mathbf{n})$ of the emitted radiation, $\int_{|\mathbf{n}|=1} d^2 n R(\mathbf{n}) = 1$, the Lindblad term reads as

$$\mathcal{L}_{\text{emi}}(\rho) = \int_0^\infty d\omega \gamma_{\text{emi}}(\omega) \left[\int d^2 n R(\mathbf{n}) e^{-i\omega \mathbf{n} \cdot \mathbf{r}/c} \rho e^{i\omega \mathbf{n} \cdot \mathbf{r}/c} - \rho \right]. \quad (2.19)$$

While the details on the radiation spectrum $\gamma_{\text{emi}}(\omega)$ and pattern $R(\mathbf{n})$ depend on the nature of the emission process, we should certainly expect that there is no preferred direction of emission, $\int d^2 n R(\mathbf{n}) \mathbf{n} = 0$. This is fulfilled in the case of an isotropic radiation pattern, $R(\mathbf{n}) = 1/4\pi$. As a consequence, the emission process does not contribute another net force term to (2.17), but it naturally contributes to the momentum diffusion effect,

$$\langle \mathbf{p}^2 \mathcal{L}_{\text{emi}}(\rho) \rangle = \int_0^\infty d\omega \gamma_{\text{emi}}(\omega) \left(\frac{\hbar \omega}{c} \right)^2, \quad (2.20)$$

as well as to decoherence. For instance, nondiagonal elements in the position representation decay like

$$\langle \mathbf{r} | \mathcal{L}_{\text{emi}}(\rho) | \mathbf{r}' \rangle = - \int_0^\infty d\omega \gamma_{\text{emi}}(\omega) \left[1 - \int d^2 n R(\mathbf{n}) \exp\left(-i\omega \mathbf{n} \cdot \frac{\mathbf{r} - \mathbf{r}'}{c}\right) \right] \langle \mathbf{r} | \rho | \mathbf{r}' \rangle \quad (2.21)$$

due to emission. The decay saturates at the maximum rate $\Gamma_{\text{emi}} = \int d\omega \gamma_{\text{emi}}(\omega)$ for nondiagonal elements that are further apart than the spectrum of emitted wavelengths. We can distinguish between three types of emission spectra:

- ★ **Fluorescence** Some species of excited molecules or clusters may get rid of their excess energy by emitting a fluorescence photon, which typically happens within nanoseconds after the excitation [6]. The emission spectrum is expected to be narrow, but it is often red-shifted with respect to the excitation energy due to fast internal relaxation before reemission. In fact, these energy conversion processes may be so efficient that the particle hardly fluoresces at all. One generally observes a low *quantum yield of fluorescence* $P_{\text{flu}} \ll 1$ in a variety of complex organic molecules which may even absorb energies beyond the ionization threshold emitting neither an electron nor a fluorescence photon [38, 39]. Such particles then simply heat up internally and will cool down slowly by thermal radiation.
- ★ **Thermal radiation of a hot particle** Large and hot particles with many internal degrees of freedom can be regarded as a (microcanonical) heat bath of fixed energy [40]. Neglecting small corrections due to the finite number of excited degrees of freedom (finite heat capacitance $C_V < \infty$), we may approximate the particle as a canonical heat bath at a temperature T that is much higher than the temperature T_0 of the environment. The particle can thus freely emit photons into the essentially unoccupied free-space radiation field, at a rate given by the spectral free-space mode density, the frequency-dependent photon absorption (and emission) cross-section $\sigma_{\text{abs}}(\omega)$ and a Boltzmann factor relating the internal density of states before and after the emission of $\hbar\omega$ [41],

$$\gamma_{\text{emi}}(\omega) = \frac{\omega^2 \sigma_{\text{abs}}(\omega)}{\pi^2 c^2} \exp\left(-\frac{\hbar\omega}{k_B T}\right). \quad (2.22)$$

If thermal emission is to be observed over a long period of time the gradual temperature decrease must be taken into account, which may also impact the absorption cross section.

- ★ **Blackbody radiation in thermal equilibrium** The radiation spectrum changes if the particle and the environment are in thermal equilibrium, $T = T_0$. We may then approximate the particle as a blackbody radiator with an aperture given by its photon absorption cross section, and the emission spectrum is of the well-known Planck form

$$\gamma_{\text{emi}}(\omega) = \frac{\omega^2 \sigma_{\text{abs}}(\omega)}{\pi^2 c^2} \left[\exp\left(\frac{\hbar\omega}{k_B T}\right) - 1 \right]^{-1}. \quad (2.23)$$

The particle becomes a colored body if finite-size corrections are taken into account [41].

2.1.2.3. Elastic light scattering into free space

The effect of Rayleigh scattering on the particle can now be understood as a combination of photon absorption from the coherent light field followed by a reemission of the same energy into free space. Hence, the net momentum transfer of a single scattering event is described by applying the mode function operator $u(\mathbf{r})$ times the unitary operator $\exp(-i\mathbf{k} \cdot \mathbf{r})$ on the particle state, with $|\mathbf{k}| = k$ the wave number of the original light mode. Averaging over all possible scattering directions (in the same way as in the emission case (2.19)) yields the Lindblad term

$$\mathcal{L}_{\text{sca}}(\rho) = \gamma_{\text{sca}} |\alpha|^2 \left[\int d^2n R(\mathbf{n}) u(\mathbf{r}) e^{-i\mathbf{k}\mathbf{n}\cdot\mathbf{r}} \rho e^{i\mathbf{k}\mathbf{n}\cdot\mathbf{r}} u^*(\mathbf{r}) - \frac{1}{2} \{ |u(\mathbf{r})|^2, \rho \} \right], \quad (2.24)$$

with the single-photon scattering rate $\gamma_{\text{sca}} = ck^4 |\chi|^2 / 6\pi\epsilon_0^2 V$. The Rayleigh scattering pattern of the PPP is that of a radiating dipole [34], $R(\mathbf{n}) = 3 \sin^2 \theta / 8\pi$, where θ denotes the angle of \mathbf{n} with respect to the polarization direction $\boldsymbol{\epsilon}$ of the electric field (and therefore of the induced dipole).

Rayleigh scattering contributes to both the radiation pressure force and the momentum diffusion effect. The former has the same form as the absorption term in (2.17), as is immediately understood by viewing a scattering event as a subsequent absorption and emission process. The latter does not induce any net force since there is no preferred direction of emission, $\int d^2n R(\mathbf{n}) \mathbf{n} = 0$.

In summery, we find that the total non-conservative radiation-pressure part of the force on a PPP reads as

$$\mathbf{F}_{\text{nc}} = \langle \mathbf{p} [\mathcal{L}_{\text{abs}}(\rho) + \mathcal{L}_{\text{sca}}(\rho)] \rangle = \hbar (\gamma_{\text{abs}} + \gamma_{\text{sca}}) |\alpha|^2 \langle \mathfrak{Im} \{ u^*(\mathbf{r}) \nabla u(\mathbf{r}) \} \rangle. \quad (2.25)$$

It complements the conservative force from the optical potential, $\mathbf{F}_c = -\hbar U_0 |\alpha|^2 \langle \nabla |u(\mathbf{r})|^2 \rangle$. Both the absorption and the reemission part of the scattering process induce momentum diffusion,

$$\langle \mathbf{p}^2 \mathcal{L}_{\text{sca}}(\rho) \rangle = \hbar \gamma_{\text{sca}} |\alpha|^2 \langle 2\mathfrak{Im} \{ u^*(\mathbf{r}) \nabla u(\mathbf{r}) \} \cdot \mathbf{p} + \hbar |\nabla u(\mathbf{r})|^2 + \hbar k^2 |u(\mathbf{r})|^2 \rangle. \quad (2.26)$$

The total increase of kinetic energy due to absorption, emission and elastic light scattering then becomes

$$\begin{aligned} \partial_t \langle H_{\text{PPP}} \rangle &= \frac{\hbar (\gamma_{\text{abs}} + \gamma_{\text{sca}}) |\alpha|^2}{2m} \langle 2\mathfrak{Im} \{ u^*(\mathbf{r}) \nabla u(\mathbf{r}) \} \cdot \mathbf{p} + \hbar |\nabla u(\mathbf{r})|^2 \rangle \\ &\quad + \frac{\hbar^2 k^2 |\alpha|^2}{2m} \gamma_{\text{sca}} \langle |u(\mathbf{r})|^2 \rangle + \int_0^\infty \frac{d\omega}{2m} \gamma_{\text{emi}}(\omega) \left(\frac{\hbar\omega}{c} \right)^2. \end{aligned} \quad (2.27)$$

The emission part can be safely neglected in the presence of strong coherent fields, $|\alpha|^2 \gg 1$, and the scattering part is only relevant if the particle does not absorb considerably at that particular wavelength.

In the course of this work, I will focus on two main types of applications of the developed formalism, corresponding to two distinct interaction regimes between the PPP and the strong coherent light field:

- ★ **Cavity-assisted motion control** The non-conservative nature of the light-matter coupling can be exploited to dissipatively manipulate and slow down the motion of hot and free-flying polarizable particles while they interact with the strong coherent field inside a high-finesse

optical cavity. This requires sufficiently long interaction times, as compared to the time scale of the cavity field dynamics. I will present a basic classical assessment of the general effect in the next Section 2.1.3, before turning to a more rigorous quantum model in Section 2.2, and before I generalize the description to objects beyond the point-particle approximation in Section 2.3.

★ **Diffraction elements for matter-wave interferometry** Coherent light fields act as beam splitters and optical diffraction elements for matter waves of polarizable particles in the limit of short interaction times (i.e. passage times through the field mode). Modern-day interference experiments with molecules and clusters [12] rely on the coherent part of the light-matter interaction to create optical gratings for matter waves, while the non-conservative part of the interaction plays only a minor role in these applications. I will discuss in Section 2.1.4 how light fields can coherently modulate the phase or the amplitude of matter waves of polarizable particles. This effect will be an essential ingredient in the general assessment of matter-wave interferometry in Chapter 3 of this thesis.

2.1.3. Classical dynamics of a polarizable point particle coupled to a strongly pumped cavity mode

Both the conservative and the non-conservative light forces can be employed to dissipate kinetic energy of a PPP when it is coupled to the retarded dynamics of a high-finesse optical resonator. Off-resonant cavity-assisted slowing is a well-studied effect [15, 42, 43] (so far only observed in experiments with atoms [44–47]), whose potential lies in its applicability to arbitrary polarizable particles without the need to address a distinct internal level structure [8, 48].

To begin with, let me present the cavity-assisted slowing effect by the example of a PPP inside an ideal Fabry-Pérot standing-wave cavity. A sketch of the geometry is given in Figure 2.1. For the time being, I shall restrict the view to a classical one-dimensional treatment of the particle motion, assuming that it stays far above the quantum limit of motion (where momentum diffusion would have a strong impact) and that we may neglect weak light forces perpendicular to the standing-wave direction due to the finite-size intensity profile $f(x, y)$ of the cavity mode⁷.

2.1.3.1. Intra-cavity field dynamics

The field dynamics is comprised of the pump laser power P_{in} leaking through the mirrors into the Fabry-Pérot resonator and the power loss P_{out} leaking out. In the steady-state situation when no particle is present, the net power flow must cancel, $P_{\text{in}} = P_{\text{out}}$ (assuming other scattering losses at the mirrors are negligible). The description of the field dynamics is based on the simple differential equation

$$\partial_t \alpha(t) = -i\omega_c \alpha(t) + \eta e^{-i\omega_p t} - \kappa \alpha(t). \quad (2.28)$$

It complements the harmonic oscillation of the intra-cavity field amplitude $\alpha(t)$ at its resonance frequency ω_c by the input term $\eta \exp(-i\omega_p t)$ and the output term $-\kappa \alpha(t)$. The former represents the driving of the amplitude by a strong pump laser at frequency ω_p that leaks into the resonator volume at a rate η . The latter represents the loss of field amplitude due to the finite reflectivity of the

⁷ In this approximation, the intensity profile merely limits the interaction time between the field mode and the PPP traversing the cavity volume.

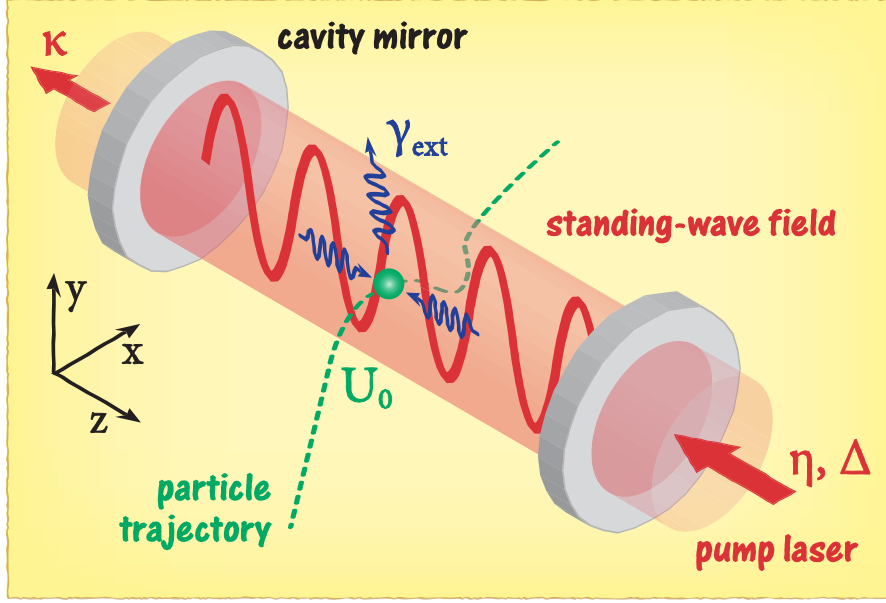


Figure 2.1. Sketch of the experimental situation when a polarizable point particle (PPP) passes a standing-wave Fabry-Pérot cavity pumped by a strong laser field through one of the cavity mirrors. The steady-state amplitude of the cavity is determined by the pump rate η , the cavity decay rate κ , and the detuning Δ between the cavity resonance and the pump laser frequency. The PPP couples coherently to the intra-cavity field through the single-photon coupling frequency U_0 , and it may also scatter or absorb cavity photons at the total extinction rate γ_{ext} .

mirrors. Equation (2.28) describes a harmonically driven damped oscillator, where the steady-state amplitude

$$\alpha_{ss}(t) = \frac{\eta}{\kappa + i\Delta} e^{-i\omega_p t} \quad (2.29)$$

oscillates at the driving frequency ω_p . The steady-state intensity $\propto |\alpha_{ss}|^2 = |\eta|^2 / (\kappa^2 + \Delta^2)$ has a Lorentzian shape as a function of the detuning $\Delta = \omega_c - \omega_p$ between cavity resonance and pump frequency, with κ the cavity linewidth. For far detuned driving frequencies, $|\Delta| \gg \kappa$, the cavity volume inside the Fabry-Pérot mirror geometry is impenetrable, and the pump field is totally reflected on the outside. On resonance, $\Delta = 0$, the cavity becomes perfectly transmissive, and the intra-cavity field energy assumes its maximum $E_f = \hbar\omega_p |\eta|^2 / \kappa^2$. The transmitted power is obtained by decomposing the standing-wave field into two running-wave components; only the forward-directed part can be transmitted. This amounts to 50% of the intra-cavity amplitude, or 25% of the intra-cavity intensity, which leaks out at the rate κ , or 2κ , respectively. The fully transmitted input power thus reads as $P_{\text{in}} = P_{\text{out}} = 2\kappa E_f / 4 = \hbar\omega_p |\eta|^2 / 2\kappa$, which determines the pump rate η up to an arbitrary phase by $|\eta| = \sqrt{2\kappa P_{\text{in}} / \hbar\omega_p}$.

2.1.3.2. Coupled cavity-particle dynamics

Inserting a PPP into the cavity mode volume modifies the steady-state field amplitude by detuning the cavity resonance frequency and by introducing an additional damping channel. The detuning scales with the single-photon coupling frequency U_0 of the particle, and it is accounted for by adding the dipole interaction potential $H_{\text{int}}(\mathbf{r})$ from Equation (2.6) to the field Hamiltonian. The

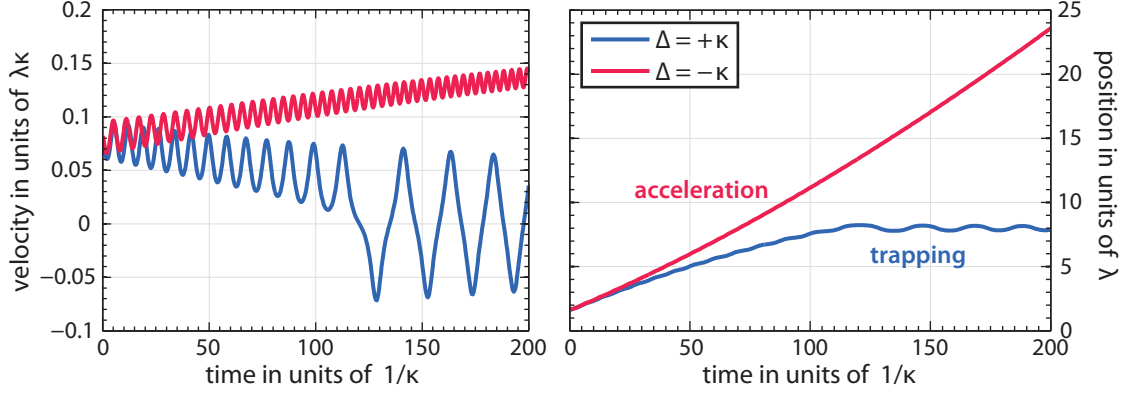


Figure 2.2. Trajectories of a model particle along the standing wave of a Fabry-Pérot cavity for positive (blue, bottom curve) and negative (red, top curve) cavity-pump detuning, $\Delta = \pm\kappa$. The left and the right panel depict the particle's position and velocity, respectively. Natural, cavity-related units are used. The simulation is based on Equations (2.30) and (2.31), using the parameters $\eta = 10^3\kappa$, $U_0 = -0.1\kappa$, $\gamma_{\text{ext}} = 0$, $\omega_r = 10^{-6}\kappa$. We assumed an initial velocity of $kv_z = 0.5\kappa$. While the red trajectory is constantly accelerated, the blue trajectory is slowed until trapping occurs after about 100 cavity lifetimes.

additional damping is given by the combined photon absorption and scattering rate of the particle, $\gamma_{\text{ext}} = \gamma_{\text{abs}} + \gamma_{\text{sca}}$; the field amplitude decays at half this rate. One usually formulates the resulting field evolution equation in a rotating frame, which removes the fast oscillation at the optical pump frequency ω_P from the much slower particle-field dynamics [49],

$$\partial_t \alpha(t) = -(i\Delta + \kappa) \alpha(t) + \eta - \left(iU_0 + \frac{\gamma_{\text{ext}}}{2} \right) \alpha(t) |f(x, y)|^2 \cos^2 kz(t). \quad (2.30)$$

The motion of the particle along the cosine pattern of the standing wave is then governed by the z -component of the dipole force (2.5),

$$\partial_t^2 z(t) = \frac{2\hbar k}{m} U_0 |\alpha(t) f(x, y)|^2 \sin kz(t) \cos kz(t) = \frac{2\omega_r U_0}{k} |\alpha(t) f(x, y)|^2 \sin 2kz(t). \quad (2.31)$$

There is no radiation pressure force in the standing-wave case. The two coupled differential equations (2.30) and (2.31) describe the one-dimensional particle-cavity dynamics in the classical limit if transverse light forces are neglected. For a particle traversing the cavity we can introduce a finite time window of the interaction by setting $x = x_0 + v_x t$ and $y = y_0 + v_y t$.

Figure 2.2 depicts two simulated trajectories of a model particle moving along the central z -axis of a pumped standing-wave cavity ($x = y = 0$). The upper (red) and lower (blue) trajectories correspond to a negative and positive detuning Δ between the cavity and the laser, respectively. In both cases we observe a sinusoidal velocity modulation as the particle moves along the periodic optical potential of the standing-wave cavity field. Indeed, if the cavity field α were not modified by the presence of the particle, Equation (2.31) would describe the oscillatory motion of a mathematical pendulum.

On a time scale larger than the cavity reaction time $1/\kappa$, the trajectories exhibit a gradual decrease (blue, bottom curve) or increase (red, top curve) in velocity, which cannot be explained by the conservative dipole force. In the former case, the particle is eventually trapped in the optical

potential, and its total energy becomes negative. Its velocity then oscillates between negative and positive values as it bounces between the walls of the standing-wave potential.

It is the delayed reaction of the cavity to the particle that is responsible for the effective dissipation (or heating) of the kinetic energy. This effect establishes the basis of potential cavity-induced slowing and trapping methods for molecules, clusters and other polarizable objects. In the following I will study this effect in more detail, including also an assessment of its strength and applicability under realistic conditions.

2.1.3.3. Estimated friction force

The characteristics of the dissipation effect are best studied in a first order approximation of the delayed reaction of the cavity to the moving particle. For this we expand the field amplitude $\alpha(t) = \alpha_0(t) + \alpha_1(t)$ into the modified steady-state term

$$\alpha_0(t) = \frac{\eta}{\kappa + i\Delta + (i\tilde{U}_0 + \tilde{\gamma}_{\text{ext}}/2) \cos^2 kz(t)} \doteq \frac{\eta}{\Omega(t)}, \quad (2.32)$$

which would be the solution if the field adjusted instantaneously to the current position $z(t)$ of the particle, and the term $\alpha_1(t)$ incorporating the corrections due to the finite reaction time scale of the cavity. Here I have absorbed the transverse coordinates into the coupling parameters $\tilde{U}_0 = U_0 |f(x, y)|^2$, $\tilde{\gamma}_{\text{ext}} = \gamma_{\text{ext}} |f(x, y)|^2$. Neglecting again their time dependence, we find that the correction term evolves according to

$$\partial_t \alpha_1(t) = \eta \frac{\partial_t \Omega(t)}{\Omega^2(t)} - \Omega(t) \alpha_1(t), \quad (2.33)$$

which can be formally solved by applying the same expansion procedure iteratively, $\alpha_1(t) = \eta \partial_t \Omega / \Omega^3 + \alpha_2(t)$ etc. Let us, however, stop the iteration at the first order correction term, $\alpha_1(t) \approx \eta \partial_t \Omega(t) / \Omega^3(t)$, neglecting all higher-order delayed reaction contributions. This is valid if the particle does not couple too strongly to the cavity and moves slowly along the standing wave profile so that the field amplitude can keep up. In other words, the approximation holds for coupling frequencies U_0 and Doppler frequencies kv smaller than the parameters κ and Δ which determine the reaction time scale of the cavity. The approximate field amplitude now also depends on the velocity $v(t) = \partial_t z(t)$ of the particle,

$$\alpha(t) \approx \frac{\eta}{\Omega(t)} \left[1 - \frac{kv(t)}{\Omega^2(t)} \left(i\tilde{U}_0 + \frac{\tilde{\gamma}_{\text{ext}}}{2} \right) \sin 2kz(t) \right], \quad (2.34)$$

which results in a velocity-dependent force when inserted into the equation of motion (2.31). Looking only at the friction force term that is linear in velocity, $F_v = m\beta v$, we find as the approximate friction coefficient

$$\beta = -\omega_r \left| \frac{\eta}{\Omega^3} \right|^2 \sin^2 2kz \left[-8\kappa\Delta\tilde{U}_0^2 - 2(\kappa^2 - \Delta^2) \tilde{U}_0\tilde{\gamma}_{\text{ext}} - 2\kappa\tilde{U}_0(\tilde{\gamma}_{\text{ext}}^2 + 4\tilde{U}_0^2) \cos^2 kz - \tilde{U}_0\tilde{\gamma}_{\text{ext}}(\tilde{\gamma}_{\text{ext}}^2 + 2\tilde{U}_0^2) \cos^4 kz \right]. \quad (2.35)$$

Only the first two terms in the square brackets can change their sign by varying the detuning Δ . Given that most polarizable particles in question are high-field seeking, $U_0 < 0$, we observe that

a negative friction coefficient β can only be obtained for positive detuning $\Delta > 0$. That is to say, dissipative slowing requires the pump laser to be red-detuned with respect to the cavity resonance, whereas a blue-detuned laser will always lead to the opposite effect.

The basic physical picture underlying the slowing effect is sketched in Figure 2.3. Suppose the pump laser is red-detuned to the steep flank of the Lorentzian cavity resonance line, $\Delta \sim \kappa$, and the particle moves towards the antinode of the intra-cavity standing-wave field. As it enters the high-intensity region its potential energy decreases immediately, and it speeds up until it reaches the potential minimum at the antinode. At the same time, the particle shifts the cavity resonance towards the laser frequency, thereby effectively decreasing the detuning Δ and increasing the field intensity. This leads to a slightly delayed lowering of the optical potential 'valley', while the particle is already moving out of the minimum and up the potential 'hill', which is now higher than it was when the particle came in. Hence, if the cavity delay matches the particle's velocity, $k v < \kappa$, the latter must on average climb up more than it falls down, gradually losing kinetic energy.

Are the simulated results comparable to a realistic scenario? I list the light coupling parameters of different polarizable particles in Table 2.1. The selection covers a mass range of 9 orders of magnitude between a single lithium atom and a gold nanosphere. The coupling parameters are evaluated for a standing-wave cavity operating at the IR wavelength $\lambda = 1.56 \mu\text{m}$ with $\kappa = 1 \text{ MHz}$ linewidth, which is pumped at the detuning $\Delta = -\kappa$ by a laser of $P_{\text{in}} = 1 \text{ W}$ continuous-wave power. These rather demanding parameters should be feasible using a resonator geometry with 25 mm curved mirrors that are positioned at $L = 1 \text{ mm}$ distance [56]⁸. By pumping a Gaussian TEM_{00} mode with a waist of $w = 40 \mu\text{m}$ it should be possible to achieve a mode volume as small as $V = \pi L w^2 / 4 = 0.0013 \text{ mm}^3$, which trumps our earlier estimates for the light-matter coupling parameters in [8] by orders of magnitude. This leads to considerable friction rates $|\beta|$, as given by the position-averaged expression (2.35). The latter predicts an average dissipation of the z -velocity on a time scale $\sim 1/|\beta|$. Within the boundaries of the above model, the obtained values that can be as small as a few nanoseconds for the heaviest nanoparticles in the table. Being 100 nm large in diameter, these are at the top end of the point particle regime; the description of larger objects will be discussed in Section 2.3. Moreover, a more rigorous quantum treatment of the dissipative slowing effect in the limit of weakly coupling point particles will be discussed in detail in Section 2.2.

2.1.4. Optical gratings for matter waves

Having discussed the classical long-time dynamics of a PPP in the presence of a (classical) strong cavity field I now turn to quite the opposite regime: The short-time effect of strong coherent fields on the propagation of PPP matter waves. Rather than trying to explicitly solve the time evolution in the presence of the field, I am going to adhere to the scattering picture and implement the short presence of the field as a scattering *event* that transforms an incoming matter-wave state ρ to an outgoing, scattered state $\rho' = \mathcal{S}(\rho)$.

The coherent standing-wave (or running-wave) light field in question shall be generated by a strong laser that is (or is not) retroreflected off a mirror (rather than by a driven high-finesse res-

⁸ A cavity linewidth of 1 MHz corresponds to a so-called cavity finesse parameter $F = \pi c / 2\kappa L \approx 5 \times 10^{-5}$. The latter is related to the reflectivity R of both mirrors via the relation $F = \pi\sqrt{R}/(1-R)$ in the absence of additional losses in the resonator [57]. The suggested cavity setup requires $1 - R \approx 7 \times 10^{-6}$.

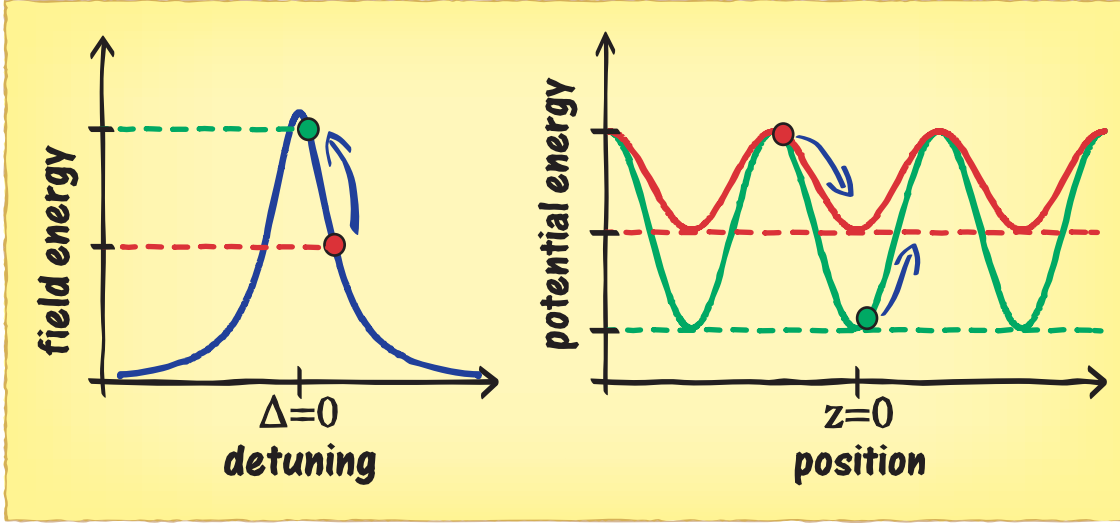


Figure 2.3. Schematic energy diagram of Fabry-Pérot cavity and particle for two different particle positions (red and green circles). The initial detuning of the pump laser to the red side flank of the cavity resonance line ($\Delta = \omega_c - \omega_p > 0$) facilitates a dissipative slowing effect. A high-field seeking particle moving from a node (red circle) to an antinode (green circle) of the standing wave is accelerated due to the change in optical potential. In addition, it tunes the cavity resonance closer to the pump frequency, thereby lowering its own optical potential. As the latter effect lags behind due to the finite reaction time of the cavity, the particle must climb up a steeper potential hill, and gradually loses kinetic energy, when moving towards the next field node.

Table 2.1. Coupling parameters between the standing-wave field of an IR high-finesse cavity ($\lambda = 1.56 \mu\text{m}$, $\kappa = 1 \text{ MHz}$, $V = 0.0013 \text{ mm}^3$) to various polarizable (high-field seeking) particles ranging from a single lithium atom to nanospheres of 50 nm radius. The dielectric functions of bulk lithium ($\epsilon = -50.41 + 7.55i$), gold ($\epsilon = -91.49 + 10.35i$), silicon ($\epsilon = 12.05$) and silica ($\epsilon = 2.1 + 6 \times 10^{-12}i$) are used to estimate the cluster parameters [50, 51]. Their polarizabilities are given by the standard formula [52], $\chi = 4\pi\epsilon_0 R^3 (\epsilon - 1) / (\epsilon + 2)$, with $R = \sqrt[3]{3m/4\pi\rho}$ the sphere radius and ρ the bulk mass density. The polarizability of C_{60} is taken from [53], and the static value per atom is used for the Li atom and the He droplet [54, 55]. We neglect the absorption of the IR-transparent particles. The position-averaged friction coefficient $\bar{\beta}$ is evaluated at the cavity-laser detuning $\Delta = \kappa$.

Particle	m (amu)	ω_r (Hz)	$ U_0 $ (Hz)	γ_{abs} (Hz)	γ_{sca} (Hz)	$ \bar{\beta} $ (Hz)
Li	7	7.4×10^4	0.14	—	3.0×10^{-10}	1.2×10^4
C_{60}	720	715	0.50	2.4×10^{-4}	3.6×10^{-9}	1.4×10^3
He_{1000}	4000	129	1.2	—	2.1×10^{-8}	1.5×10^3
Li_{1000}	7000	74	33	0.59	1.6×10^{-5}	6.4×10^5
$(\text{SiO}_2)_{1000}$	60 000	8.6	18	1.4×10^{-10}	4.4×10^{-6}	2.1×10^4
Au_{1000}	197 000	2.6	25	0.19	9.2×10^{-6}	1.3×10^4
SiO_2 sphere	6.9×10^8	7.4×10^{-4}	2.0×10^5	1.6×10^{-6}	592	2.9×10^8
Si sphere	7.3×10^8	7.1×10^{-4}	5.9×10^5	—	5.1×10^3	3.2×10^9
Au sphere	6.1×10^9	8.5×10^{-5}	7.8×10^5	5.8×10^3	8.8×10^3	6.9×10^8

onator mode, as in the previous section). The laser may either be shortly pulsed⁹ or continuous, in which case we shall assume the particle to be fast in traversing the light mode. This regime provides the means to employ light fields as diffractive elements in matter-wave interferometry, as will be discussed in the following with a focus on the Viennese near-field interference experiments with molecules and clusters [12].

2.1.4.1. Coherent grating interaction

In the absence of photon absorption and Rayleigh scattering the interaction between the laser field and the particle is entirely coherent. That is to say, the impact of the short field presence on the quantum state of motion can be described by a unitary scattering transformation $\mathcal{S}(\rho) = \mathcal{S}\rho\mathcal{S}^\dagger$, $\mathcal{S}^\dagger\mathcal{S} = \mathbb{I}$. An explicit form is obtained in the basis of plane wave states by the renowned eikonal approximation [58–60],

$$\langle \mathbf{r} | \mathbf{p} \rangle \mapsto \langle \mathbf{r} | \mathcal{S} | \mathbf{p} \rangle = \exp \left[-\frac{i}{\hbar} \int_{-\infty}^{\infty} dt H_{\text{int}} \left(\mathbf{r} + \frac{\mathbf{p}t}{m} \right) \right] \langle \mathbf{r} | \mathbf{p} \rangle, \quad (2.36)$$

with $H_{\text{int}}(\mathbf{r}) = -\Re \{ \chi \} |E(\mathbf{r})|^2 / 4$ the optical dipole potential of the particle in the field. The approximation holds in a semiclassical high-energy limit where the classical action associated to the motion of the particle over the course of the short interaction time exceeds by far the eikonal action integral over the optical potential in (2.36) [60]. The transformation describes a coherent phase modulation of incoming matter waves. In the case of a standing-wave field, $E(\mathbf{r}) = E_0 \epsilon f(x, y) \cos kz$, it constitutes a one-dimensional periodic phase grating.

In practice, one can employ an even simpler form of the transformation that acts only on the reduced one-dimensional state of motion along the z -axis, thus omitting the generally weak modulation effect in the x - and y -direction due to the transverse mode profile $f(x, y)$. Moreover, if the velocities v_z constituting the state of motion of the particle are sufficiently small¹⁰, we may take the position distribution on the z -axis to be at rest during interaction time. We arrive at the transformation rule

$$\langle z | \psi \rangle \mapsto \exp(i\phi_0 \cos^2 kz) \langle z | \psi \rangle \quad (2.37)$$

for any state vector $|\psi\rangle$ for the one-dimensional z -motion of the particle that complies with the above constraints. This *longitudinal eikonal approximation* is commonly used to describe thin optical transmission gratings in matter-wave interferometry [7, 18, 61], and it will be presumed throughout the remainder of the manuscript. I refer the reader to [59, 60] for an exhaustive study of semi-classical corrections to the eikonal approximation. The eikonal phase factor ϕ_0 is obtained by integrating the interaction potential over the intensity profile of the laser. We distinguish two implementations regarding the interferometry of large molecules and clusters:

★ **Kapitza-Dirac Talbot-Lau interferometer (KDTLI)** The KDTLI setup is a three-grating near-field interferometer where the interference effect is related to the periodic phase modulation at the central grating, a standing laser wave [7]. A collimated beam of fast molecules traverses

⁹ Since the wavelength of the laser is required to be sufficiently well defined for the present purposes, ultrashort pulses with a broad frequency spectrum are excluded here.

¹⁰ To be more concrete, the travelled distance $v_z \tau$ during the interaction period τ between the particle and the field must be small compared to the laser wavelength, $|v_z \tau| \ll \lambda$. Given the reduced one-dimensional quantum state of motion ρ_z , the condition should cover its entire velocity distribution $\langle mv_z | \rho | mv_z \rangle$.

the three-grating geometry along the x -axis, and it is aligned in such a way that it crosses the laser grating centrally and (almost) perpendicular to the standing-wave z -axis¹¹. This is made possible by using a cylindrical lens system to narrow the laser spot (down to a few tens of microns) in the direction of flight x , while keeping a large waist (of roughly one millimeter) along y . We may thus assume that the collimated molecule beam passes the laser grating in the xz -plane, setting $y \approx 0$. The phase factor (2.37) then reads as

$$\phi_0 = \frac{\Re\{\chi\} |E_0|^2}{4\hbar} \int_{-\infty}^{\infty} \frac{dx}{v} f^2(x, 0), \quad (2.38)$$

assuming a fixed longitudinal velocity v of the molecules¹². Assuming a Gaussian intensity profile $f(x, y) = \exp(-x^2/w_x^2 - y^2/w_y^2)$ with waist parameters $w_{x,y}$ and an input laser power P_L , we find [7]

$$\phi_0 = \frac{4\sqrt{2\pi}\Re\{\chi\} P_L}{hc\epsilon_0 v w_y}. \quad (2.39)$$

Given molecular velocities of the order of 100 m/s and an x -waist of $w_x = 20 \mu\text{m}$ each molecule spends less than a microsecond in the laser grating. It can travel not more than 100 nm along the grating axis during that period, as the molecule beam is typically collimated to a few milliradians opening angle. Hence, the longitudinal eikonal approximation is well justified.

★ **Optical time-domain ionizing Talbot-Lau interferometer (OTITLI)** The OTITLI¹³ is a Talbot-Lau setup in the time domain where the gratings are generated by three short laser pulses, which are retroreflected off a mirror [10]. A small cloud of nanoparticles flying alongside the mirror surface illuminated this way may be ionized in the antinodes of the pulses; they play the role of the thin transmission gratings of a regular Talbot-Lau setup. The phase modulation in each pulse is given by

$$\phi_0 = \frac{4\pi\Re\{\chi\} E_L}{hc\epsilon_0 a_L} \quad (2.40)$$

if we assume that the particle ensemble is always well localized in the center of focus, $f(x, y) \approx f(0, 0) = 1$, when illuminated by grating laser pulses of sufficiently large spot size $a_L = \int dx dy f^2(x, y)$ (or a flat-top shaped spot profile). The pulse energy $E_L = \int_{\tau} dt P_L(t)$ is obtained by integrating the laser power over the temporal pulse shape of length τ . Again, the eikonal expression (2.37) is only valid if the particles are approximately at rest over the pulse duration τ . The present experimental realization of the OTITLI setup in the Vienna group operates with vacuum-ultraviolet (VUV) laser pulses of $\tau \lesssim 10 \text{ ns}$ at a wavelength of $\lambda = 157 \text{ nm}$. The particle velocities therefore must be restricted to below 10 m/s in z -direction by means of collimation, for instance.

¹¹ Note that the direction of the grating is commonly referred to as the x -axis in the interferometry literature, whereas the standing wave is directed along z in the present notation, which is conventionally used in the description of light scattering at spherical particles. I will resort to the x -notation in Chapter 3.

¹² A realistic description of the molecular beam state involves a broad distribution of velocities v , and the resulting ϕ_0 -dependent interferogram must be averaged accordingly.

¹³ Also referred to as OTIMA: optical time-domain ionizing matter-wave interferometer.

The general working principle of Talbot-Lau interferometry will be discussed in detail in Chapter 3. There I will show how the periodic phase modulation at a standing-wave grating leads to matter-wave interferograms. A full assessment of thin optical gratings, however, must also account for non-conservative effects, most prominently, photon absorption.

2.1.4.2. Amplitude modulation by means of optical depletion gratings

The absorption of light from an optical standing-wave grating does not necessarily imply the loss of matter-wave coherence. The latter can be avoided (or suppressed) if the absorption of one or more photons removes the particle from the interfering ensemble present in the experiment. Depending on the internal properties of the particles and the selectivity of the detection scheme with respect to these properties, the removal can in principle be achieved by the ionization, fragmentation, isomerization, excitation, or simply internal heating, that may be triggered by the deposited photon energy. Consequently, the particle ensemble is depleted in the antinodes, whereas nothing happens in the nodes of the standing-wave grating. The resulting periodic modulation of the matter-wave amplitude renders the standing laser wave an optical generalization of a material diffraction mask, with the nodes representing the apertures and the antinodes representing (semi-transmissive) walls of the grating.

Optical depletion gratings of this kind have been used in atom interferometry [62], where the absorption of a single photon induces an internal state transition and the atoms are post-selected according to their energy level in the detector. The experimentalists working on the OTITLI setup in the Vienna lab make use of photon-induced ionization to generate depletion gratings from VUV laser pulses¹⁴, as the energy of a single UV photon exceeds the ionization threshold of most molecular and atomic cluster particles.

Let me now describe the action of an optical depletion grating on the matter waves interacting with the standing-wave field, in analogy to material diffraction masks. An ideally thin one-dimensional diffraction grating, where the slits are periodically arranged along the z -axis, is described by a periodic aperture function $P(z)$, which can only take the values zero (wall) or one (opening). Given an incoming matter-wave state $\psi(z) = \langle z|\psi \rangle$ we find the density distribution of particles behind the grating to be $P(z) |\psi(z)|^2$. That is to say, the grating transformation modulates the matter-wave state by the square root of the transmission probability, $\psi(z) \mapsto \sqrt{P(z)}\psi(z)$, up to a prefactor that accounts for the renormalization of the state vector.

In the case of a thin optical depletion grating, the transmission probability $P(z)$ may take any value between zero and one, depending on the local standing-wave intensity (with $P(z) = 1$ at the nodes of the standing wave). Including also the phase modulation effect (2.37) due to the dipole interaction, as discussed in the preceding section, we can introduce a complex transmission function $t(z)$ to describe the full modulation of the matter-wave state,

$$\langle z|\psi \rangle \mapsto \sqrt{P(z)} \exp(i\phi_0 \cos^2 kz) \langle z|\psi \rangle \equiv t(z) \langle z|\psi \rangle. \quad (2.41)$$

The density operator ρ transforms as $\rho \mapsto t(z) \rho t^*(z)$. Using a Poissonian model for the photon absorption, as discussed in Section 2.1.2, and following the same arguments as for the phase modulation, we can express the transmission probability in terms of the mean number of absorbed

¹⁴ The ionized particles are in practice removed from the ensemble with the help of a constant electric field applied to the interferometer setup.

photons, $\bar{n}(z) = n_0 \cos^2 kz$. In the case of fast particles crossing a stationary thin laser beam of power P_L , the value n_0 at the antinodes reads as

$$n_0 = \frac{8\sigma_{\text{abs}}P_L\lambda}{\sqrt{2\pi\hbar c\nu w_y}}, \quad (2.42)$$

and in the case of illumination by a short laser pulse of energy E_L as

$$n_0 = \frac{4\sigma_{\text{abs}}E_L\lambda}{\hbar c a_L}. \quad (2.43)$$

When a single absorbed photon suffices to remove a particle from the ensemble (e.g. by ionization) the transmission probability can be written as the Poisson probability $p_0(z)$ of zero absorption, $P(z) = p_0(z) = \exp[-\bar{n}(z)]$, and the transmission function becomes

$$t(z) = \exp\left[\left(-\frac{n_0}{2} + i\phi_0\right)\cos^2 kz\right]. \quad (2.44)$$

In the inverted situation, where it is the non-absorbing particles that are removed from the ensemble, we arrive at

$$t_{\text{inv}}(z) = \sqrt{1 - \exp(-n_0 \cos^2 kz)} \exp(i\phi_0 \cos^2 kz). \quad (2.45)$$

More generally, one could also conceive situations where the depletion threshold is reached by absorbing N or more independent photons, in which case the transmission function reads as

$$t_N(z) = \sqrt{\sum_{n=0}^{N-1} \frac{1}{n!} (n_0 \cos^2 kz)^n} \exp\left[\left(-\frac{n_0}{2} + i\phi_0\right)\cos^2 kz\right]. \quad (2.46)$$

Here one must be careful with using the simple Poissonian model of absorption. The latter is only meaningful when subsequent absorption events can be regarded as statistically independent, and it ceases to be valid when the internal state and the absorption cross-section σ_{abs} of the particle are noticeably modified by each absorption. Moreover, one must also take into account the photon momenta transferred to all those particles that did not absorb enough photons to be removed.

2.1.4.3. Momentum transfer by absorption and scattering

Any full description of optical elements, which are not based on single-photon depletion, must include the momentum transfer due to the possible absorption and Rayleigh scattering of laser photons. This generally comes with the loss of matter-wave coherence, an unwanted side-effect in optical gratings. For instance, it would be inexpedient to try interfering strongly absorptive molecules in a KDTLI setup, where the purpose of the laser grating is to modulate coherently the phase of the matter waves. On the other hand, for most polarizable subwavelength particles the inevitable coherence loss due to Rayleigh scattering is usually a negligible effect in the short-time interaction regime relevant for interferometry at optical gratings.

Absorption I presented a model of the absorption-induced momentum transfer in Section 2.1.2.1. In accordance with the longitudinal eikonal approximation for the coherent grating transformation, let me omit any action of the Lindblad term (2.16) on the transverse motion in the field mode. This results in the effective one-dimensional transformation

$$\mathcal{L}_{\text{abs}}(\rho) = \Gamma_{\text{abs}}(t) \left[\cos(kz) \rho \cos(kz) - \frac{1}{2} \{ \cos^2(kz), \rho \} \right] \quad (2.47)$$

of the quantum state ρ of motion along the standing-wave axis z . The time-dependent rate term relates to the mean number of absorbed photons $n_0 = \int dt \Gamma_{\text{abs}}(t)$ through an integration over the transverse laser beam profile in a co-moving frame along the particle trajectory, Eq. (2.42), or over the temporal shape of the laser pulse, Eq. (2.43). The above part of the master equation can be explicitly integrated in the position representation $\langle z|\rho|z' \rangle$, which amounts again to omitting motion during the interaction time,

$$\begin{aligned} \langle z|e^{\mathcal{L}_{\text{abs}}t}\rho|z' \rangle &= \exp \left[-n_0 \left(\frac{\cos^2 kz}{2} + \frac{\cos^2 kz'}{2} - \cos kz \cos kz' \right) \right] \langle z|\rho|z' \rangle \\ &= \exp \left[-2n_0 \sin^2 \left(k \frac{z+z'}{2} \right) \sin^2 \left(k \frac{z-z'}{2} \right) \right] \langle z|\rho|z' \rangle \equiv \mathcal{R}_{\text{abs}}(z, z') \langle z|\rho|z' \rangle. \end{aligned} \quad (2.48)$$

The decohering effect is evident: All nondiagonal matrix elements are damped except for $z-z' = n\lambda$, the strongest effect occurring between nodes and antinodes¹⁵.

In the position representation the transformation simply reduces to a multiplication of the density matrix by the positive decoherence function $0 < \mathcal{R}_{\text{abs}}(z, z') \leq 1$. Recalling that the coherent grating transformation also contributes a mere multiplication by $t(z) t^*(z')$ in this representation, we are allowed to combine both factors to obtain the overall grating transformation $\langle z|\rho|z' \rangle \mapsto t(z) t^*(z') \mathcal{R}_{\text{abs}}(z, z') \langle z|\rho|z' \rangle$.

Scattering The Rayleigh scattering of photons into free-space discussed in Section 2.1.2.3, no matter how weak in practice, can be incorporated in the same manner. Tracing out the transverse part of the motion, the reduced one-dimensional version of the scattering Lindblad term (2.24) reads as

$$\begin{aligned} \mathcal{L}_{\text{sca}}(\rho) &= \Gamma_{\text{sca}}(t) \left[\int d^2n R(\mathbf{n}) \cos(kz) e^{-ikn_z z} \rho \cos(kz) e^{ikn_z z} - \frac{1}{2} \{ \cos^2(kz), \rho \} \right] \\ &= \Gamma_{\text{sca}}(t) \left[\int d\Omega \frac{3 \sin^2 \theta}{8\pi} \cos(kz) e^{-ik \sin \theta \sin \varphi z} \rho \cos(kz) e^{ik \sin \theta \sin \varphi z} - \frac{1}{2} \{ \cos^2(kz), \rho \} \right]. \end{aligned} \quad (2.49)$$

Note that the solid angle integration over the dipole radiation pattern $R(\mathbf{n}) = 3 \sin^2 \theta / 8\pi$ must be performed on a sphere with its poles oriented along the polarization ϵ of the electric light field,

¹⁵ This is intuitively clear since the absorption of a photon reveals the information that the particle is not located at a node. On the other hand, the photon cannot distinguish two positions z and z' , which differ by an integer multiple of the wavelength.

which is perpendicular to the z -axis. The explicit expression for the decoherence function becomes¹⁶,

$$\begin{aligned}\mathcal{R}_{\text{sca}}(z, z') &= \exp \left\{ -n_{\text{sca}} \left[\frac{\cos^2 kz + \cos^2 kz'}{2} - \frac{3 \cos kz \cos kz'}{8\pi} \int d\Omega \sin^2 \theta e^{ik(z'-z) \sin \theta \sin \varphi} \right] \right\} \\ &= \exp \left\{ -n_{\text{sca}} \left[\frac{\cos^2 kz + \cos^2 kz'}{2} - \frac{3 \cos kz \cos kz'}{2} \int_0^{\pi/2} \sin^3 \theta d\theta J_0(k(z'-z) \sin \theta) \right] \right\} \\ &= \exp \left\{ -n_{\text{sca}} \left[\frac{\cos^2 kz + \cos^2 kz'}{2} - 3 \cos kz \cos kz' \frac{\sin k(z'-z) - j_1(k(z'-z))}{2k(z'-z)} \right] \right\}.\end{aligned}\quad (2.50)$$

Here, n_{sca} gives the mean number of scattered photons in the antinodes. It is obtained from the expressions (2.42) and (2.43) by replacing the absorption cross section with σ_{sca} .

A slightly different and somewhat simpler result would be obtained if the particle scattered the light isotropically, a frequently used simplification,

$$\mathcal{R}_{\text{sca,iso}}(z, z') = \exp \left\{ -n_{\text{sca}} \left[\frac{\cos^2 kz + \cos^2 kz'}{2} - \cos kz \cos kz' \text{sinc} k(z'-z) \right] \right\}. \quad (2.51)$$

In most cases relevant for interferometry, however, the mean number of scattered photons is negligibly small, $n_{\text{sca}} \ll 1$, and one may omit the Rayleigh scattering effect altogether.

Taking both the absorption and the scattering effect into account, the overall matter-wave state transformation at an optical standing-wave grating becomes

$$\langle z|\rho|z' \rangle \mapsto t(z) t^*(z) \mathcal{R}_{\text{abs}}(z, z') \mathcal{R}_{\text{sca}}(z, z') \langle z|\rho|z' \rangle. \quad (2.52)$$

We note that the present absorption and scattering transformations are based on an elementary Markovian model where the laser mode is linearly coupled to an initially cold reservoir of free-space vacuum modes (in case of scattering) and of internal degrees of freedom of the particle (in case of absorption). In particular, the model accounts for the correct momentum state of a standing-wave photon, a *superposition* of two counterpropagating plane waves, which is coherently transferred to the particle upon absorption. This improves the probabilistic argument presented in [7], where the absorption of standing-wave photons is implemented as a purely classical binary random walk with 50% chance to be kicked by $+\hbar k$ or $-\hbar k$.

This classical model is indistinguishable from the present treatment in the case of photon absorption from a running-wave field, say, directed into the positive z -direction. The corresponding Lindblad term is then of random unitary type, $\mathcal{L}_{\text{abs}}(\rho) = \Gamma_{\text{abs}} [\exp(ikz) \rho \exp(-ikz) - \rho]$, and the

¹⁶ I made use of the integral representation of the Bessel function $\int_0^{2\pi} d\varphi \exp(i\xi \sin \varphi) = 2\pi J_0(\xi)$, as well as of the integral identity [63]

$$\int_0^{\pi/2} d\theta J_0(\beta \sin \theta) \sin \theta \cos^{2r+1} \theta = 2^r \beta^{-1-r} \Gamma(r+1) J_{r+1}(\beta),$$

with $r = \pm 1/2$ and the Gamma function $\Gamma(3/2) = \sqrt{\pi}/2 = 2\Gamma(1/2)$. The identity leads naturally to spherical Bessel function expressions $j_n(\beta) = \sqrt{\pi/2\beta} J_{n+1/2}(\beta)$, where $j_0(\beta) = \text{sinc}\beta$.

quantum state of motion transforms as

$$\begin{aligned} \langle z|\rho|z'\rangle &\mapsto \exp\left\{-n_0\left[1 - e^{ik(z-z')}\right]\right\} \langle z|\rho|z'\rangle = e^{-n_0} \sum_{n=0}^{\infty} \frac{n_0^n}{n!} \langle z|e^{inkz}\rho e^{-inkz'}|z'\rangle \\ &\equiv \langle z|\sum_{n=0}^{\infty} p_n \mathbf{U}_n \rho \mathbf{U}_n^\dagger|z'\rangle. \end{aligned} \quad (2.53)$$

This expression is a probabilistic sum of unitary momentum kick transformations $\mathbf{U}_n = \exp(inkz)$, which also follows from a classical Poissonian ansatz.

2.2. Quantum mechanics of polarizable point particles in high-finesse cavities

The preceding study of polarizable point particles interacting with coherent light fields has lead to a first assessment of cavity-induced slowing in Section 2.1.3, where both the PPP motion and the field were treated classically, and to the description of optical diffraction gratings of PPP matter waves in Section 2.1.4, where the strong coherent field remained a classical degree of freedom.

Let me now proceed with a full quantum treatment of both the light and the particle, a necessary prerequisite to assess the diffusive and dissipative effects arising from the coupling between a PPP and one or more driven or empty high-finesse cavity modes. A rigorous derivation of the friction and diffusion parameters in the presence of one strongly driven *pump mode* will be given in the weak-coupling limit where the particle-induced field fluctuations are small. This assumption of weak coupling holds true for many subwavelength molecules and clusters, which do not exhibit a distinct internal resonance that could be addressed by the cavity light. Table 2.1 lists several examples where the rate U_0 defined in Equation (2.10), at which the particle may induce field shifts, is by orders of magnitude smaller than realistic decay rates $\kappa \sim 1$ MHz of optical high-finesse cavities.

This does not mean, however, that it is a lost cause to study the dynamics of weakly coupling particles in a cavity. I will show how a large coherent driving field can effectively enhance the coupling to the empty cavity modes by orders of magnitude. The weak coupling model, as presented in the following, will then admit a systematic assessment of the main dissipative effects of the enhanced coupling. In particular, we will find that the cavity-induced friction force increases with each empty cavity mode that is accessible for the pump light—a potential application for confocal resonator geometries with a large spectrum of degenerate modes. The presented results have been published in [8].

2.2.1. Quantum model of a PPP coupled to multiple cavity modes

I start by quantizing the light-matter interaction model of Section 2.1 for the generic configuration of one particle in the presence of M empty cavity modes and one strongly driven pump mode, which provides the necessary field input to enhance the coupling of the PPP with the cavity. In practice, one of the cavity modes can play the role of the pump mode when driven by a strong mode-matched laser. An alternative two-dimensional implementation is sketched in Figure 2.4, where the pump field is generated in a different (free laser or driven cavity) mode oriented perpendicularly to the empty cavity axis. This configuration may be favourable in practice, as it avoids a strong dipole force

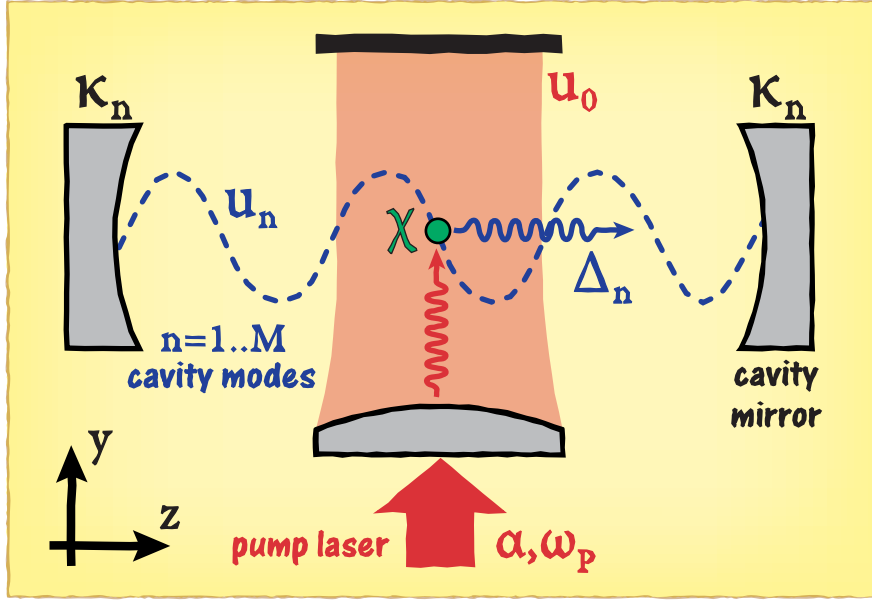


Figure 2.4. Sketch of an exemplary two-dimensional mode configuration with a strongly driven field mode u_0 directed along the y -axis and a multitude of M empty standing-wave cavity modes u_n along the z -axis. In the overlapping region, a particle of polarizability χ redistributes photons between the modes thereby inducing dissipation. Each mode is damped by the rate κ_n and detuned by Δ_n with respect to the driving field. The latter generates a steady-state amplitude α in the absence of the particle.

along the cavity axis as well as the need for selective single-mode driving of a (possibly degenerate) multimode cavity.

The described configuration is characterized by the following parameters:

- ★ The driving field is described by the steady-state pump amplitude α (in the absence of the particle) and by the pump frequency ω_p . The latter serves as the fast reference frequency, and I will switch to the corresponding rotating frame to describe the field dynamics of all other modes.
- ★ The behaviour of each field mode (including the pump) is determined by its detuning $\Delta_n = \omega_n - \omega_p$ with respect to the pump frequency, its decay rate κ_n , its mode function $u_n(\mathbf{r})$, and its mode volume $V_n = \int d^3r |u(\mathbf{r})|^2$, where $n = 0, 1, \dots, M$, and $n = 0$ is representing the pump mode. The field polarization vectors are omitted by assuming the same polarization throughout¹⁷.
- ★ The particle of mass m_p is described by a scalar polarizability χ , which leads to the effective coupling frequencies $U_{mn} = -\sqrt{\omega_n \omega_m / V_n V_m} \Re\{\chi\} / 2\epsilon_0$ between the n th and the m th mode.

¹⁷ The coupling strength between fields of different polarizations through a PPP may vary, most notably if the particle is described by a tensorial polarizability. I omit this additional modulation of the coupling for simplicity.

2.2.1.1. Quantum description of a driven cavity mode

Before introducing the coupling to the particle, I first translate the classical description of a driven high-finesse cavity mode in Section 2.1.3.1 into the quantum picture. Here I make use of the canonical field quantization procedure [64–66] and replace the coherent field amplitude and its complex conjugate by the annihilation and creation operators in the expressions for the physical fields,

$$\mathbf{E}(\mathbf{r}, t) \mapsto \sqrt{\frac{2\hbar\omega_0}{\epsilon_0 V_0}} \mathbf{a}_0 \boldsymbol{\epsilon} u_0(\mathbf{r}), \quad \mathbf{H}(\mathbf{r}, t) \mapsto -ic \sqrt{\frac{2\hbar}{\mu_0 \omega_0 V_0}} \mathbf{a}_0 \nabla \times \boldsymbol{\epsilon} u_0(\mathbf{r}). \quad (2.54)$$

This results in the free field Hamiltonian $H_0 = \hbar\omega_0 (\mathbf{a}_0^\dagger \mathbf{a}_0 + 1/2)$, where the constant term is dropped for convenience. In order to describe a driven cavity mode one must include the driving field leaking into the cavity and the losses leaking out. Both effects are covered by a linear coupling model, where the exchange of field amplitude with an external mode \mathbf{b} is described by a coupling Hamiltonian of the form¹⁸ $\propto \mathbf{a}_0 \mathbf{b}^\dagger + h.c.$ That is, the coupling of the modes can be understood as an exchange of single photons between the field states.

Based on this physical picture we may pin down the loss and driving terms heuristically. The cavity field loss can be seen as a random and uncontrolled elimination of photons as they escape through the cavity mirrors or by scattering into free space at a total rate $2\kappa_0$. In mathematical terms, this is well modelled by a Poisson jump process of the same type as in (2.13), with the jump operator given by the photon annihilator \mathbf{a}_0 , $\mathcal{L}_{\text{loss}}(\rho) = \kappa_0 (2\mathbf{a}_0 \rho \mathbf{a}_0^\dagger - \{\mathbf{a}_0^\dagger \mathbf{a}_0, \rho\})$.

The same linear description can be applied to the driving by the mode \mathbf{b} of a strong laser illuminating the cavity mirror. The quantum representation of a strong coherent laser field is given in terms of coherent states [65]

$$|\beta\rangle = D(\beta) |0\rangle = e^{-|\beta|^2/2} \sum_{n=0}^{\infty} \frac{\beta^n}{\sqrt{n!}} |n\rangle = \exp(\beta \mathbf{b}^\dagger - \beta^* \mathbf{b}) |0\rangle, \quad (2.55)$$

with β the complex field amplitude and $|\beta|^2$ the mean photon number. Coherent states are defined as displaced vacuum states, and they are the eigenvectors of the annihilation operator, $\mathbf{b}|\beta\rangle = \beta|\beta\rangle$. Mimicing the behaviour of classical monochromatic light fields they oscillate harmonically at the laser frequency ω_p , $|\beta(t)\rangle = \exp(-i\omega_p t \mathbf{b}^\dagger \mathbf{b}) |\beta\rangle = |\beta \exp(-i\omega_p t)\rangle$. They can be understood as the vacuum state in a displaced and rotating frame¹⁹. In the classical limit $|\beta| \gg 1$ the vacuum field fluctuations around the displacement amplitude are small compared to $|\beta|$, and we may substitute the laser mode operator \mathbf{b} by $\beta \exp(-i\omega_p t)$ (assuming there is no relevant backaction of the cavity field onto the state of the driving laser). The driving Hamiltonian thus assumes the form $H_{\text{pump}}(t) \propto \beta^* \exp(i\omega_p t) \mathbf{a}_0 + h.c.$ We get rid of the time dependence by switching to a frame

¹⁸ The form is easily obtained by adding the quantized physical fields (2.54) of the modes \mathbf{a}_0 and \mathbf{b} to an overall electric and magnetic field. When the corresponding field energy density is integrated over the volume in (2.4) the cross terms between both modes yield the above linear coupling Hamiltonian. Terms of the form $\mathbf{a}_0 \mathbf{b}$ and $\mathbf{a}_0^\dagger \mathbf{b}$ are omitted in the *rotating wave approximation* [65], since they oscillate rapidly at twice an optical frequency, $\omega_p + \omega_0$, and thus do not affect the actual mode coupling.

¹⁹ A rotating frame is defined through the unitary state transformation $U(t) = \exp(i\omega_p \sum_n \mathbf{a}_n^\dagger \mathbf{a}_n)$, with ω_p the corresponding rotation frequency. Given the quantum state $\rho(t)$ of a system of field modes $\{\mathbf{a}_n\}$ in the Schrödinger picture, the state in the rotating picture reads as $\rho' = U(t) \rho(t) U^\dagger(t)$. Analogously, a displaced frame is defined via the unitary displacement operator, $\rho' = D^\dagger(\beta) \rho D(\beta)$. Field observables are displaced as $D^\dagger(\beta) \mathbf{b} D(\beta) = \mathbf{b} + \beta$.

rotating at the optical pump frequency ω_P , introducing the cavity-pump detuning $\Delta_0 = \omega_0 - \omega_P$ and the effective pump rate η . This leaves us with the master equation for the field state of a driven cavity mode,

$$\partial_t \rho = -i [\Delta_0 \mathbf{a}_0^\dagger \mathbf{a}_0 + i\eta \mathbf{a}_0^\dagger - i\eta^* \mathbf{a}_0, \rho] + \kappa_0 (2\mathbf{a}_0 \rho \mathbf{a}_0^\dagger - \{\mathbf{a}_0^\dagger \mathbf{a}_0, \rho\}). \quad (2.56)$$

The quantum expectation value of the field amplitude evolves in the same way as the classical version (2.28),

$$\partial_t \langle \mathbf{a}_0 \rangle = -(i\Delta_0 + \kappa_0) \langle \mathbf{a}_0 \rangle + \eta. \quad (2.57)$$

It is then straightforward to show that the coherent state $\rho_{ss} = |\alpha\rangle\langle\alpha|$ is the steady-state solution of the above master equation for the same steady-state amplitude $\alpha = \eta / (\kappa_0 + i\Delta_0)$ as in the classical case. An elegant and convenient way to incorporate the driving is to work with quantum states in the displaced frame, $\rho \mapsto \rho_\alpha = \mathbf{D}^\dagger(\alpha) \rho \mathbf{D}(\alpha)$, where the steady-state amplitude shifts the state of the mode from $|\alpha\rangle\langle\alpha|$ to the ground state $\mapsto |0\rangle\langle 0|$. The resulting master equation,

$$\partial_t \rho_\alpha = -i [\Delta_0 \mathbf{a}_0^\dagger \mathbf{a}_0, \rho_\alpha] + \kappa_0 (2\mathbf{a}_0 \rho_\alpha \mathbf{a}_0^\dagger - \{\mathbf{a}_0^\dagger \mathbf{a}_0, \rho_\alpha\}), \quad (2.58)$$

does not contain the explicit driving term anymore, and the field operator \mathbf{a}_0 now represents the quantum field fluctuations on top of the coherent steady state.

Derivation of the loss term Note that the non-Hamiltonian loss term in the master equation (2.56) can also be derived using a standard textbook approach [35, 67]. For this let us couple the cavity mode linearly to a bath of harmonic oscillators, $\mathbf{H}_{\text{env}} = \sum_j \hbar \omega_j \mathbf{b}_j^\dagger \mathbf{b}_j$. It represents the environmental vacuum of modes, which can be populated by a photon escaping the cavity. We shall assume a linear coupling term of the form $\mathbf{H}_{\text{int}} = \sum_j \hbar g_j \mathbf{a}_0 \mathbf{b}_j^\dagger + h.c.$, with g_j the effective photon exchange rates between cavity and environment. The coupled dynamics of the combined state $\rho_{SE}(t)$ of system and environment is most conveniently assessed in the interaction frame, $\rho_{SE,I}(t) = \mathbf{U}(t) \rho_{SE}(t) \mathbf{U}^\dagger(t)$, with $\mathbf{U}(t) = \exp[i(\mathbf{H}_0 + \mathbf{H}_{\text{env}})t/\hbar]$. A formal integration and re-insertion of the von Neumann equation yields the integro-differential equation for the combined state,

$$\partial_t \rho_{SE,I}(t) = -\frac{i}{\hbar} [\mathbf{H}_I(t), \rho_{SE,I}(0)] - \frac{1}{\hbar^2} \int_0^t d\tau [\mathbf{H}_I(t), [\mathbf{H}_I(\tau), \rho_{SE,I}(\tau)]], \quad (2.59)$$

where

$$\mathbf{H}_I(t) = \mathbf{U}(t) \mathbf{H}_{\text{int}} \mathbf{U}^\dagger(t) = \sum_j \hbar g_j e^{i(\omega_j - \omega_0)t} \mathbf{a}_0 \mathbf{b}_j^\dagger + h.c. \quad (2.60)$$

We obtain a closed equation for the reduced cavity state $\rho_I = \text{tr}_E(\rho_{SE,I})$ by tracing out the environment and subsequently applying the so-called Born approximation: The cavity leaves the environment practically unaffected at all times, $\rho_{SE,I}(t) \approx \rho_I(t) \otimes |\text{vac}\rangle\langle\text{vac}|$. Every photon that escapes disperses almost immediately, and the cavity is thus effectively surrounded by vacuum²⁰ on

²⁰ Optical frequencies in the environmental mode spectrum are practically unoccupied even at finite temperatures. I thus use the zero-temperature vacuum state here, since the cavity only couples to modes of similar frequencies.

all relevant time scales. We find

$$\begin{aligned}\partial_t \rho_I(t) &= -\frac{1}{\hbar^2} \int_0^t d\tau \text{tr}_E ([H_I(t), [H_I(t-\tau), \rho_I(t-\tau) \otimes |\text{vac}\rangle\langle\text{vac}|]]) \\ &= \sum_j \int_0^t d\tau |g_j|^2 e^{-i(\omega_j - \omega_0)\tau} \{a_0 \rho_I(t-\tau) a_0^\dagger - a_0^\dagger a_0 \rho_I(t-\tau)\} + h.c.\end{aligned}\quad (2.61)$$

Next we can apply the Markov approximation: The environment shall not memorize the cavity state at earlier times and the time evolution equation shall become time-local. That is to say, we may set $\rho_I(t-\tau) \approx \rho_I(t)$ and integrate up to infinity. This is formally justified if the cavity field couples to a sufficiently broad frequency range such that $\sum_j |g_j|^2 \exp[i(\omega_0 - \omega_j)\tau] \approx \kappa \delta(\tau)$ and

$$\partial_t \rho_I(t) \approx \kappa [2a_0 \rho_I(t) a_0^\dagger - a_0^\dagger a_0 \rho_I(t) - \rho_I(t) a_0^\dagger a_0]. \quad (2.62)$$

The desired master equation (2.56) follows by combining this with the above driving term of a classical coherent laser field.

2.2.1.2. A particle, a driving laser, and a handful of empty cavity modes

With the quantum model of a driven cavity mode at hand we can now collect all ingredients to model the system of a single pump mode, M empty cavity modes and a PPP, as sketched in Figure 2.4. It will be expedient to work in a frame rotating at the optical frequency ω_P of the driving laser, with the pump mode displaced by the steady-state amplitude α . This results in a master equation term of the above form (2.58) for each of the $M+1$ modes.

The presence of a polarizable particle comes with an additional Hamiltonian representing the optical potential, as well as with scattering and absorption contributions, which couple the motion of the particle to the field degrees of freedom. We obtain directly the optical potential term by quantizing the electric field expression $\mathbf{E}(\mathbf{r})$ in the PPP Hamiltonian (2.9). However, we must bear in mind that the electric field is now given by a sum of all M cavity modes plus the displaced pump mode. This results in the total particle Hamiltonian

$$\begin{aligned}H_{\text{PPP}} &= \overbrace{\frac{\mathbf{p}^2}{2m_P}}^{\equiv H_P} + \overbrace{\hbar U_{00} |\alpha u_0(\mathbf{r})|^2 + \sum_{n=0}^M \hbar U_{0n} [\alpha a_n^\dagger u_n^*(\mathbf{r}) u_0(\mathbf{r}) + h.c.]}^{\equiv H_I} + \sum_{k,n=0}^M \hbar U_{kn} a_n^\dagger a_k u_n^*(\mathbf{r}) u_k(\mathbf{r}).\end{aligned}\quad (2.63)$$

The first term H_P describes the particle motion in the steady-state dipole potential, the second term H_I represents the pump-enhanced linear coupling of the particle to the field fluctuations in each cavity mode, and the remainder represents the inter-mode coupling, which also causes the position-dependent resonance shift of the modes.

The above Hamiltonian must be complemented by the field energy term in the displaced and rotating frame, $H_C = \sum_n \hbar \Delta_n a_n^\dagger a_n$. The free fields are thus included via the superoperator

$$\mathcal{L}_C(\rho) = -i \sum_{n=0}^M \Delta_n [a_n^\dagger a_n, \rho] + \sum_{n=0}^M \kappa_n (2a_n \rho a_n^\dagger - \{a_n^\dagger a_n, \rho\}). \quad (2.64)$$

It describes the field evolution in the absence of the particle. In addition, the time evolution of the combined state of cavity and particle contains another two field loss terms \mathcal{L}_{abs} and \mathcal{L}_{sca} due to absorption and scattering,

$$\partial_t \rho = -\frac{i}{\hbar} [\mathbf{H}_{\text{PPP}}, \rho] + \mathcal{L}_C(\rho) + \mathcal{L}_{\text{abs}}(\rho) + \mathcal{L}_{\text{sca}}(\rho). \quad (2.65)$$

Both cause additional coupling between the particle motion and the field fluctuations. The explicit form of these terms is found by combining the original expressions (2.16) and (2.24) for a classical field with the above derivation of the Lindblad term (2.62), which represents the incoherent loss of single field quanta. Keeping the displacement of the pump mode in mind, we arrive at

$$\begin{aligned} \mathcal{L}_{\text{abs}}(\rho) = & \sum_{n=0}^M \frac{c\sigma_{\text{abs}}}{V_n} \left[(\mathbf{a}_n + \alpha\delta_{n0}) u_n(\mathbf{r}) \rho (\mathbf{a}_n + \alpha\delta_{n0})^\dagger u_n^*(\mathbf{r}) \right. \\ & \left. - \frac{1}{2} \left\{ (\mathbf{a}_n + \alpha\delta_{n0})^\dagger (\mathbf{a}_n + \alpha\delta_{n0}) |u_n(\mathbf{r})|^2, \rho \right\} \right], \end{aligned} \quad (2.66)$$

$$\begin{aligned} \mathcal{L}_{\text{sca}}(\rho) = & \sum_{m=0}^M \frac{c\sigma_{\text{sca}}}{V_m} \left[\int d^2n R(\mathbf{n}) (\mathbf{a}_m + \alpha\delta_{m0}) u_m(\mathbf{r}) e^{-ik\mathbf{n}\cdot\mathbf{r}} \rho (\mathbf{a}_m + \alpha\delta_{m0})^\dagger e^{ik\mathbf{n}\cdot\mathbf{r}} u_m^*(\mathbf{r}) \right. \\ & \left. - \frac{1}{2} \left\{ (\mathbf{a}_m + \alpha\delta_{m0})^\dagger (\mathbf{a}_m + \alpha\delta_{m0}) |u_m(\mathbf{r})|^2, \rho \right\} \right]. \end{aligned} \quad (2.67)$$

Thermal or fluorescent photon emission from the particle into free space is neglected, as well as internal heating of the particle due to photon absorption²¹. In the following I will simplify the overall master equation (2.65) to the case of weak coupling.

2.2.2. Eliminating the quantum field dynamics in the weak coupling limit

With the quantum model of the coupled cavity-particle dynamics at hand, I will now assess the general effect of the dynamical quantum field on the motion of the PPP. The goal is to find an effective description of the reduced particle state by eliminating the explicit field dynamics. We should expect that such a separation can formally be achieved only in the limit of weak coupling between the particle and the field. I will therefore introduce two weak coupling assumptions which will facilitate a low-order expansion of the coupling effect. Although the resulting model will be strictly valid under those assumptions only, we might retain its qualitative predictions even beyond the weak coupling limit.

2.2.2.1. The first weak-coupling assumption

I assume that the coupling rates of the polarizable particle to the modes are significantly smaller than the mode damping rates, $|U_{mn}| \ll \kappa_n \forall m, n$. This means that the particle-induced cavity field fluctuations are limited to a few photons, as they typically escape the cavity much faster than they can be redistributed by the particle. The strong pump amplitude $|\alpha| \gg 1$ then represents the only potential source of large photon numbers that may populate empty modes through coherent

²¹ Practical implementations of the present cavity dissipation scheme are restricted to non-absorbing particle species. The typically large pump field intensities might otherwise lead to the destruction of the particle.

scattering at the particle. We may thus omit those coupling terms in the Hamiltonian (2.63) which are of second order in the field fluctuations, $H_{\text{ppp}} \approx H_P + H_I$.

Secondly, if we extend the above weak-coupling assumption for the coherent inter-mode scattering rates to the rates of photon absorption and Rayleigh scattering, we may approximate the Lindblad terms (2.66) and (2.67) as

$$\mathcal{L}_{\text{abs}}(\rho) \approx \gamma_{\text{abs}} |\alpha|^2 \left[u_0(\mathbf{r}) \rho u_0^*(\mathbf{r}) - \frac{1}{2} \{ |u_0(\mathbf{r})|^2, \rho \} \right], \quad (2.68)$$

$$\mathcal{L}_{\text{sca}}(\rho) \approx \gamma_{\text{sca}} |\alpha|^2 \left[\int d^2 n R(\mathbf{n}) u_0(\mathbf{r}) e^{-ik\mathbf{n}\cdot\mathbf{r}} \rho e^{ik\mathbf{n}\cdot\mathbf{r}} u_0^*(\mathbf{r}) - \frac{1}{2} \{ |u_0(\mathbf{r})|^2, \rho \} \right]. \quad (2.69)$$

The terms $\gamma_{\text{abs,sca}} = c\sigma_{\text{abs,sca}}/V_0$ denote the absorption and the Rayleigh scattering rate with respect to the pump mode volume V_0 . According to our assumption, both the absorption and the scattering rate must be small compared to the cavity decay rates, and we can safely neglect their contribution to the particle-cavity dynamics. We are left with the momentum diffusion caused by the absorption and scattering of pump photons in (2.68) and (2.69); the only relevant non-conservative contributions to the model, apart from the cavity damping terms in \mathcal{L}_C .

The first weak-coupling assumption simplifies considerably the quantum description of cavity and particle at almost no costs. In fact, the assumption is very well fulfilled in practice by a wide range of nanoparticles, as can be seen from the exemplary Table 2.1. Using infrared light it remains valid up to a mass of roughly 10^8 amu. The quantum description of the weakly coupling system splits into the two separate superoperators \mathcal{L}_C and $\mathcal{L}_P(\rho) = -i[H_P, \rho]/\hbar + \mathcal{L}_{\text{abs}}(\rho) + \mathcal{L}_{\text{sca}}(\rho)$ acting solely on the cavity and particle subspace, respectively. The coupling of both subsystems is mediated by the effective interaction Hamiltonian

$$H_I = \sum_{n=0}^M \hbar U_{0n} \alpha a_n^\dagger u_n^*(\mathbf{r}) u_0(\mathbf{r}) + h.c. \quad (2.70)$$

It resembles the standard linear coupling Hamiltonian, but with a coupling rate $|U_{0n}\alpha|$ enhanced by the strong pump field α . In principle, this allows a weakly coupling particle to enter the strong coupling regime $|U_{0n}\alpha| \gtrsim \kappa_n$ with the help of a sufficiently strong pump laser. Note that it requires only one driving mode to enhance the coupling of the particle to all the other modes that overlap with the pump field. However, cavity modes with a large detuning Δ_n cannot be addressed in practice, given that their oscillating amplitude a_n averages out in the interaction Hamiltonian. What counts are degenerate or near-degenerate resonator modes with a detuning of the order of the cavity linewidth. Only they contribute to the interaction. I will analyze the benefit of a large degenerate mode spectrum for cavity-induced cooling in Section 2.2.3.4.

While previous weak-coupling approaches towards the cavity-induced slowing of atoms [68] did not yet consider the pump enhancement (because it was not necessary there), it is a practiced technique in the field of optomechanics [26] to reach the strong coupling regime [69, 70]. There, however, the interaction is restricted to a single oscillatory degree of freedom of a rigid system such as a mirror or membrane. It is typically coupled to a single driven cavity mode a_0 , and a low-order expansion of the respective mode function $u_0(\mathbf{r})$ around the equilibrium value of the oscillator yields the standard optomechanical interaction Hamiltonian [71].

The pump enhancement facilitates the strong coupling of a weakly interacting nanoparticle to high-finesse cavity modes. It thus has the potential of inducing a substantial dissipative slowing

effect. We have seen this already in the simple classical model calculation in Section 2.1.3.1, and I will study the strong coupling regime further in Section 2.3.3. On the other hand, an effective master equation for the reduced particle state can only be derived by adiabatically eliminating the cavity degrees of freedom. This requires an even stronger assumption.

2.2.2.2. The second weak-coupling assumption

I now assume in addition that even the pump-enhanced coupling rates are small compared to the decay rates of all relevant cavity modes, $|U_{0n}\alpha| \ll \kappa_n \forall n$. In other words, any excitation of the cavity field will always leak out much faster than it can be built up by the in-mode scattering of pump photons off the particle. As a consequence, the M cavity modes (and the pump mode) will remain empty (relative to the pump displacement) at almost all times, $\langle a_n^\dagger a_n \rangle \ll 1$.

Obviously, the second weak-coupling assumption represents a very restrictive condition, which one should be anxious to violate in actual experiments in order to achieve a significant slowing effect. Still, I make the assumption here to define an effective quantum description of the particle motion under the dissipative influence of the cavity. It will provide us with a clear and rigorous understanding of the origin of cavity-induced friction and diffusion effects. Judging from complementary semiclassical treatments and numerical simulations [17, 68], we should expect the basic features and qualitative behaviour of those effects to remain valid in a strong-coupling regime where our effective quantum model will break down.

In the following I derive the effective master equation for the reduced particle state by employing the projection formalism [72–74]. For this let me define a superoperator \mathcal{P} as the projection of the combined cavity-particle state on the cavity ground state in the displaced frame, $\mathcal{P}\rho = \text{tr}_C(\rho) \otimes |\text{vac}\rangle\langle\text{vac}|$. The complementary projection shall be denoted by $\mathcal{Q} = \text{id} - \mathcal{P}$. As both superoperators represent orthogonal projections in operator space ($\mathcal{P}^2 = \mathcal{P}$, $\mathcal{Q}^2 = \mathcal{Q}$ and $\mathcal{P}\mathcal{Q} = \mathcal{Q}\mathcal{P} = 0$), the master equation $\partial_t \rho = -i[H_I, \rho]/\hbar + \mathcal{L}_C(\rho) + \mathcal{L}_P(\rho)$ can be divided into two coupled equations for $\mathcal{P}\rho$ and $\mathcal{Q}\rho$ with help of the following relations:

- ★ Both superprojectors \mathcal{P} and \mathcal{Q} commute with the master equation term \mathcal{L}_P , that is, $\mathcal{P}\mathcal{L}_P = \mathcal{L}_P\mathcal{P} = \mathcal{P}\mathcal{L}_P\mathcal{P}$ and $\mathcal{Q}\mathcal{L}_P = \mathcal{L}_P\mathcal{Q} = \mathcal{Q}\mathcal{L}_P\mathcal{Q}$. The reason is that the projectors act solely on the field degrees of freedom, whereas \mathcal{L}_P operates on the particle subspace.
- ★ The relation $\mathcal{L}_C\mathcal{P} = 0$ is obviously true since \mathcal{P} singles out the cavity vacuum state.
- ★ The flipped relation $\mathcal{P}\mathcal{L}_C = 0$ holds as well since \mathcal{L}_C is restricted to the cavity subspace and traceless by construction, $\text{tr}(\mathcal{L}_C\rho) = \text{tr}_C(\mathcal{L}_C\rho) = 0$.
- ★ It follows immediately from the previous two points that $\mathcal{Q}\mathcal{L}_C = \mathcal{L}_C\mathcal{Q} = \mathcal{Q}\mathcal{L}_C\mathcal{Q}$.
- ★ The relation $\mathcal{P}\mathcal{L}_I\mathcal{P} = 0$, with $\mathcal{L}_I(\rho) = -i[H_I, \rho]/\hbar$, can easily be verified by plugging in the explicit form of the coupling Hamiltonian (2.70) and noting that $\langle \text{vac} | H_I | \text{vac} \rangle = 0$.

Putting everything together we arrive at the coupled equations

$$\partial_t \mathcal{P}\rho(t) = \mathcal{P}\mathcal{L}_P\mathcal{P}\rho(t) + \mathcal{P}\mathcal{L}_I\mathcal{Q}\rho(t), \quad (2.71)$$

$$\partial_t \mathcal{Q}\rho(t) = \mathcal{Q}(\mathcal{L}_P + \mathcal{L}_C)\mathcal{Q}\rho(t) + \mathcal{Q}\mathcal{L}_I\mathcal{P}\rho(t) + \mathcal{Q}\mathcal{L}_I\mathcal{Q}\rho(t). \quad (2.72)$$

The initial conditions at time $t = 0$ shall be given by the initial state $\rho_P(0)$ of the particle and the steady state of the cavity system, $\mathcal{P}\rho(0) = \rho_P(0) \otimes |\text{vac}\rangle\langle\text{vac}|$ and $\mathcal{Q}\rho(0) = 0$. The second weak-coupling assumption will now form the basis of three steps of approximation that will finally lead to a closed equation for $\mathcal{P}\rho(t)$ and for the reduced particle state $\rho_P(t) = \langle\text{vac}|\mathcal{P}\rho(t)|\text{vac}\rangle$.

Recall that any particle-induced field excitations in the weak-coupling limit are assumed to decay before they can add up or disperse over the system of modes. The state of the cavity is thus well approximated by the vacuum at almost all times, and the component $\mathcal{Q}\rho$ can be regarded as a small correction to the full quantum state $\rho = \mathcal{P}\rho + \mathcal{Q}\rho$. This component will only be occupied at the effective coupling rates $|U_{0n}\alpha|$ via the term $\mathcal{Q}\mathcal{L}_I\mathcal{P}\rho$ in (2.72), while the term $\mathcal{Q}\mathcal{L}_C\mathcal{Q}\rho$ causes it to decay on a much faster time scale of the order of the cavity lifetimes $1/\kappa_n$. The assumption $|U_{0n}\alpha| \ll \kappa_n$ allows us to neglect the ‘second order’ term $\mathcal{Q}\mathcal{L}_I\mathcal{Q}\rho$, which would describe the back-action of persistent field excitations on the particle. The remainder can be formally integrated respecting the initial condition $\mathcal{Q}\rho(0) = 0$,

$$\mathcal{Q}\rho(t) = \int_0^t d\tau \mathcal{Q}e^{(\mathcal{L}_C + \mathcal{L}_P)(t-\tau)} \mathcal{Q}\mathcal{L}_I\mathcal{P}\rho(\tau). \quad (2.73)$$

Inserting this into Equation (2.71), we arrive at a closed integro-differential equation for the vacuum component,

$$\begin{aligned} \partial_t \mathcal{P}\rho(t) &= \mathcal{P}\mathcal{L}_P\mathcal{P}\rho(t) + \int_0^t d\tau \mathcal{P}\mathcal{L}_I\mathcal{Q}e^{(\mathcal{L}_C + \mathcal{L}_P)(t-\tau)} \mathcal{Q}\mathcal{L}_I\mathcal{P}\rho(\tau) \\ &= \mathcal{L}_P\mathcal{P}\rho(t) + \int_0^t d\tau \mathcal{P}\mathcal{L}_Ie^{(\mathcal{L}_C + \mathcal{L}_P)\tau} \mathcal{L}_I\mathcal{P}\rho(t-\tau), \end{aligned} \quad (2.74)$$

which depends on the whole past trajectory of $\mathcal{P}\rho$. The integral represents the small correction to the particle state evolution in the absence of field fluctuations. A standard way of converting the above expression to a time-local differential equation is to expand it as $\mathcal{P}\rho = \mathcal{P}\rho_0 + \mathcal{P}\rho_1 + \dots$ using the following iteration process: First one formally solves the time-local equation in the absence of the integral term to obtain the zeroth order solution $\mathcal{P}\rho_0(t) = \exp[\mathcal{L}_P(t-t_0)]\mathcal{P}\rho_0(t_0)$. This is then plugged into the correction term to obtain an equation for the first-order term $\mathcal{P}\rho_1$, which is again solved in the absence of the next-order correction, and so forth. Here we are only interested in the lowest order, which leaves us with the equation

$$\partial_t \mathcal{P}\rho(t) \approx \mathcal{L}_P\mathcal{P}\rho(t) + \int_0^t d\tau \mathcal{P}\mathcal{L}_Ie^{\mathcal{L}_C\tau}e^{\mathcal{L}_P\tau}\mathcal{L}_Ie^{\mathcal{L}_P(t-\tau-t_0)}\mathcal{P}\rho(t_0), \quad (2.75)$$

with $t_0 > 0$ an arbitrary initial time. I have separated the time evolution under \mathcal{L}_C and \mathcal{L}_P since the superoperators commute as they act on distinct subsystems.

Unfortunately, we are now running into trouble when we try to make this equation time-local by setting $t_0 = t$. Temporal inversion of the particle evolution \mathcal{L}_P is not allowed due to the non-unitary contributions $\mathcal{L}_{\text{abs},\text{sca}}$ of absorption and Rayleigh scattering, which increase the entropy of the particle state by diffusion.

Fortunately, we can generally neglect the non-unitary parts when the weak-coupling conditions hold. This is because the past-trajectory integral in (2.75) involves only time periods τ of the order of the cavity lifetimes $1/\kappa_n$ as the rapid cavity decay term in $\exp(\mathcal{L}_C\tau)$ suppresses the coupling term \mathcal{L}_I . During that period, absorption and scattering events changing the particle momentum in units

of $\hbar k$ occur at the rates $\gamma_{\text{abs,sca}} |\alpha|^2$. We can safely ignore them if they do not modify the particle's momentum $m_P v = \langle |\mathbf{p}| \rangle$ too much,

$$\frac{\gamma_{\text{abs,sca}} |\alpha|^2}{\kappa_n} \left| \frac{2\omega_r}{kv} \right| \ll 1 \quad \forall n. \quad (2.76)$$

As once again illustrated in Table 2.1 typical nanoparticles (in the absence of strong internal resonances close to the laser frequency) exhibit scattering and absorption rates smaller than their respective coupling frequencies. The weak-coupling limit thus implies $\gamma_{\text{abs,sca}} |\alpha| \ll |U_0 \alpha| \ll \kappa_n$. At the same time, the massive molecules and nanoparticles of interest feature sub-kHz recoil frequencies $\omega_r = \hbar k^2 / 2m_P$ when interacting with infrared light. This must be compared to Doppler frequencies of $kv \sim 4 \text{ MHz} \gg \omega_r$ at rather low velocities of $v \sim 1 \text{ m/s}$; such slow particles are still orders of magnitude away from the quantum limit of motion.

Moreover, given that the integral in (2.75) is restricted by the integrand to times $\tau \lesssim 1/\kappa_n$, we can replace the upper integral bound by infinity. This leaves us with the time-local equation

$$\partial_t \mathcal{P} \rho(t) \approx \left[\mathcal{L}_P + \int_0^\infty d\tau \mathcal{P} \mathcal{L}_I e^{\mathcal{L}_C \tau} \mathcal{L}_I(\tau) \right] \mathcal{P} \rho(t), \quad (2.77)$$

where $\mathcal{L}_I(\tau)$ represents the von Neumann commutator with the back-in-time-evolved coupling Hamiltonian

$$\mathbf{H}_I(\tau) = e^{-i\mathbf{H}_P \tau / \hbar} \mathbf{H}_I e^{i\mathbf{H}_P \tau / \hbar} = \sum_{n=0}^M \hbar U_{0n} \alpha \mathbf{a}_n^\dagger u_n^*(\mathbf{r}, \mathbf{p}; \tau) u_0(\mathbf{r}, \mathbf{p}; \tau) + h.c., \quad (2.78)$$

$$u_n(\mathbf{r}, \mathbf{p}; \tau) = u_n \left(\exp \left[-\frac{i\mathbf{p}^2 \tau}{2m_P \hbar} - iU_{00} |\alpha u_0(\mathbf{r})|^2 \tau \right] \mathbf{r} \exp \left[\frac{i\mathbf{p}^2 \tau}{2m_P \hbar} + iU_{00} |\alpha u_0(\mathbf{r})|^2 \tau \right] \right). \quad (2.79)$$

2.2.2.3. Effective time evolution of the reduced particle state

The time-local expression (2.77) is now easily turned into an effective time evolution equation for the reduced particle state $\rho_P(t) = \text{tr}_C[\rho(t)]$,

$$\begin{aligned} \partial_t \rho_P(t) &= \langle \text{vac} | \partial_t \mathcal{P} \rho(t) | \text{vac} \rangle = -\frac{i}{\hbar} [\mathbf{H}_P, \rho_P(t)] \\ &\quad - \frac{1}{\hbar^2} \int_0^\infty d\tau \text{tr}_C \{ [\mathbf{H}_I, e^{\mathcal{L}_C \tau} [\mathbf{H}_I(\tau), \rho_P(t) \otimes |\text{vac}\rangle \langle \text{vac}|]] \}. \end{aligned} \quad (2.80)$$

The free evolution under \mathcal{L}_C and the trace over the cavity subsystem can be performed straightforwardly²²,

$$\partial_t \rho_P(t) = \mathcal{L}_P \rho_P(t) - \sum_{n=0}^M |U_{0n} \alpha|^2 ([u_0^*(\mathbf{r}) u_n(\mathbf{r}), \mathbf{g}_n \rho_P(t)] + h.c.). \quad (2.81)$$

Here I introduce the so-called *memory operators*

$$\mathbf{g}_n = \int_0^\infty d\tau e^{-(\kappa_n + i\Delta_n)\tau} u_n^*(\mathbf{r}, \mathbf{p}; \tau) u_0(\mathbf{r}, \mathbf{p}; \tau). \quad (2.82)$$

²² Applying the interaction Hamiltonian to the vacuum state leads to nondiagonal elements of the form $|1_n\rangle \langle \text{vac}|$, with $|1_n\rangle = \mathbf{a}_n^\dagger |\text{vac}\rangle$ a single-excitation multimode Fock state. One can easily show that these nondiagonals evolve like $\exp(\mathcal{L}_C t) |1_n\rangle \langle \text{vac}| = \exp(-\kappa_n t - i\Delta_n t) |1_n\rangle \langle \text{vac}|$

They collect the particle-induced coupling between the pump field and the cavity modes over a short period of time before the present time t . In other words, they represent the delayed reaction of each cavity mode to the position of the particle that continuously scatters pump light into them. The delay, or memory time scale, is determined by the damping rate κ_n and the detuning Δ_n of each mode.

Once again, we can approximate the past trajectory of sufficiently fast particles by neglecting the influence of the optical potential on short time scales. We may follow the same line of argument as in the case of absorption and Rayleigh scattering. The optical dipole potential of a standing-wave pump mode²³ can be viewed as a coherent backscattering process of pump photons within the mode and at the rate $U_{00} |\alpha|^2$. As each backscattering event transfers $2\hbar k$ of momentum to the particle, we find that the optical potential is negligible in the limit of

$$\left| \frac{U_{00} |\alpha|^2}{\kappa_n} \frac{4\omega_r}{kv} \right| \ll 1 \quad \forall n. \quad (2.83)$$

If this is the case we can explicitly write

$$\mathbf{g}_n \approx \int_0^\infty d\tau e^{-(\kappa_n + i\Delta_n)\tau} u_n^* \left(\mathbf{r} - \frac{\mathbf{p}\tau}{m_P} \right) u_0 \left(\mathbf{r} - \frac{\mathbf{p}\tau}{m_P} \right). \quad (2.84)$$

The memory operators then average the inter-mode coupling over an approximately straight particle trajectory reaching a few mode lifetimes into the past. Note that the above condition (2.83) is only relevant for a standing-wave pump mode directed along the axis of the other cavity modes. In an orthogonal configuration with a running-wave pump field, as depicted in Figure 2.4, the optical dipole force merely scales with the transverse pump laser profile²⁴.

I will discuss in the following section that the delay effect is responsible for cavity-induced friction forces and the potential slowing of the particle. It vanishes in the limit of far-detuned or bad cavity modes, when the field fluctuations can follow the moving particle almost instantaneously. This happens in the limit of $|kv| \ll \kappa_n, |\Delta_n|$, as the Doppler frequency determines the rate at which the particle-induced coupling changes during motion. We may then approximate $\mathbf{g}_n \approx u_n^*(\mathbf{r}) u_0(\mathbf{r}) / (\kappa_n + i\Delta_n)$ leaving us with the completely positive Lindblad-type master equation

$$\begin{aligned} \partial_t \rho_P = & -\frac{i}{\hbar} \left[H_P - \sum_{n=0}^M \frac{\hbar \Delta_n |U_{0n} \alpha|^2}{\kappa_n^2 + \Delta_n^2} |u_0(\mathbf{r}) u_n(\mathbf{r})|^2, \rho_P \right] + \mathcal{L}_{\text{abs}} \rho_P + \mathcal{L}_{\text{sca}} \rho_P \\ & + \sum_{n=0}^M \frac{\kappa_n |U_{0n} \alpha|^2}{\kappa_n^2 + \Delta_n^2} \left[2u_n^*(\mathbf{r}) u_0(\mathbf{r}) \rho_P u_0^*(\mathbf{r}) u_n(\mathbf{r}) - \{|u_0(\mathbf{r}) u_n(\mathbf{r})|^2, \rho_P\} \right]. \end{aligned} \quad (2.85)$$

Apart from the addition to the Hamiltonian, it features a positive Lindblad term, which is form-equivalent to the Rayleigh scattering term (2.69). Bad cavity modes simply act as an additional diffusion channel for the particle. On the other side, even good cavity modes will result in a mere momentum diffusion when the particle is sufficiently slow.

²³ Running-wave modes do not exhibit a wavelength-scale oscillatory intensity pattern. Their influence on the particle through the optical potential is considerably weaker.

²⁴ Condition (2.83) would be alleviated by a factor $kw \ll 1$ in the case of a Gaussian profile with waist w .

2.2.3. Semiclassical description of friction and diffusion

Based on the effective evolution equation (2.81) and the memory operator (2.84) for a particle in the presence of a strongly driven pump and M empty cavity modes, I will formulate the resulting dissipative dynamics using a semiclassical phase-space picture.

To keep things simple and clear let me trace out the particle's xy -motion and resort to a one-dimensional version of the present model along the z -axis of the standing-wave modes of the cavity, $u_n(x, y, z) \mapsto f_n(x, y) u_n(z)$. This is where a moving particle can cause the fastest field modulation and the most delayed reaction by the cavity. Dissipative effects, and indeed any field-induced forces on the particle, are expected to be much weaker in the xy -directions, given that the transverse mode profiles of the cavity $f_n(x, y)$ extend over much more than a wavelength. To be concrete, the delayed cavity-backaction on the transverse motion is negligible for velocities $|v_{x,y}/w_n| \ll \kappa_n, \Delta_n$, with w_n the characteristic transverse width of the n th mode (as given by the waist in case of an xy -symmetric Gaussian mode profile).

We are left with the one-dimensional memory operator

$$\mathbf{g}_n^{(z)} = \int_0^\infty d\tau e^{-(\kappa_n + i\Delta_n)\tau} u_n^* \left(z - \frac{\mathbf{p}\tau}{m_p} \right) u_0 \left(z - \frac{\mathbf{p}\tau}{m_p} \right). \quad (2.86)$$

for the z -state of the particle, at fixed transverse coordinates x and y . The latter can be sufficiently well described by a straight classical trajectory (x_t, y_t) if we assume that the particle is hardly affected in its transverse motion while it passes the high-intensity region of the cavity. This effective parametric time dependence can be incorporated, if necessary, in the coupling frequencies, $\tilde{U}_{mn}(t) = U_{mn} f_m^*(x_t, y_t) f_n(x_t, y_t)$, as already done in the simple classical model of cavity-induced slowing in Section 2.1.3. For the time being I will simply ignore the transverse trajectory when assessing the one-dimensional friction and diffusion effects. Nevertheless, one should take notice of this time dependence when estimating the overall effect in realistic scenarios. The one-dimensional slowing of the z -motion of a particle crossing the cavity, for instance, would have to be averaged over its limited residence time inside the pump mode. In the complementary case of a trapped particle that overlaps with the cavity modes, one could average the slowing effect over each trapping cycle. In such scenarios, the cavity system could well be given by the configuration sketched in Figure 2.4, or by the simpler setup of Figure 2.1, where a single Fabry-Pérot mode is directly pumped by a laser.

The starting point shall now be the master equation for the one-dimensional state of motion ρ , as obtained from (2.85) using the discussed simplifications,

$$\begin{aligned} \partial_t \rho = & -\frac{i}{\hbar} \left[\frac{\mathbf{p}^2}{2m_p} + \hbar \tilde{U}_{00} |\alpha u_0(z)|^2, \rho \right] \\ & - \sum_{n=0}^M |\tilde{U}_{0n} \alpha|^2 \left([u_0^*(z) u_n(z), \mathbf{g}_n^{(z)} \rho] + h.c. \right) \\ & + \tilde{\gamma}_{\text{abs}} |\alpha|^2 \left[u_0(z) \rho u_0^*(z) - \frac{1}{2} \{|u_0(z)|^2, \rho\} \right] \\ & + \tilde{\gamma}_{\text{sca}} |\alpha|^2 \left[\int d^2 n R(\mathbf{n}) u_0(z) e^{-ikn_z z} \rho e^{ikn_z z} u_0^*(z) - \frac{1}{2} \{|u_0(z)|^2, \rho\} \right]. \end{aligned} \quad (2.87)$$

2.2.3.1. Friction and diffusion terms in the Fokker-Planck equation

The effective friction force and diffusion effect can now be extracted in a standard procedure [75] from the phase-space representation of the above master equation (2.87); the resulting partial differential equation can be expanded in orders of \hbar , and the respective friction and diffusion terms can be identified by comparison to the standard form of a Fokker-Planck equation [35, 49, 76].

For this purpose I introduce the Wigner function,

$$w(z, p) = \frac{1}{2\pi\hbar} \int ds e^{ips/\hbar} \left\langle z - \frac{s}{2} | \rho | z + \frac{s}{2} \right\rangle, \quad (2.88)$$

which represents the one-dimensional quantum state of motion ρ in a phase-space picture with position and momentum coordinates $(z, p) \in \mathbb{R}^2$. It is a real-valued and normalized function, $\int dz dp w(z, p) = 1$, and it can be regarded as the natural quantum generalization of the phase-space distribution function $f(z, p) \geq 0$ of a classical particle state [59, 77]. The Wigner function of sufficiently mixed states, such as the thermal state $\rho_{\text{th}} \propto \exp(-\mathbf{p}^2/2m_p k_B T)$, is in fact indistinguishable from its counterpart in a purely classical description, the Maxwell-Boltzmann distribution $w_{\text{th}}(z, p) = f_{\text{th}}(z, p) \propto \exp(-p^2/2m_p k_B T)$. At the same time, the time evolution equation for the Wigner function equals the classical Liouville equation up to second order in Planck's quantum of action \hbar if it is governed by a conservative force field [77]. See Appendix A.3 for detailed expressions. In particular, the time evolution under at most harmonic potentials $V(z) = a + bz + cz^2$ is exactly the same in both the quantum and the classical case.

Using the phase-space translation rules given in Appendix A.3 we can translate the above master equation (2.87) into a partial differential equation for the corresponding Wigner function. If, in addition, we omit any derivatives higher than second order in position and momentum we will arrive at a Fokker-Planck-type equation (FPE) of the generic form [35]

$$\begin{aligned} \partial_t w(z, p) = & -\partial_z [g_z(z, p) w(z, p)] - \partial_p [g_p(z, p) w(z, p)] + \frac{1}{2} \partial_z^2 [D_{zz}(z, p) w(z, p)] \\ & + \frac{1}{2} \partial_p^2 [D_{pp}(z, p) w(z, p)] + \partial_z \partial_p [D_{zp}(z, p) w(z, p)] + \mathcal{O}(\hbar^3). \end{aligned} \quad (2.89)$$

We note that this approximation can also be understood as a semiclassical expansion of the Wigner time evolution up to the second order in \hbar . Each term in the FPE has a clear physical meaning which becomes evident when looking at the time evolution of the position and momentum expectation values as well as their second moments²⁵,

$$\partial_t \langle z \rangle = \int dz dp z \partial_t w(z, p) = \int dz dp g_z(z, p) w(z, p), \quad (2.90)$$

$$\partial_t \langle p \rangle = \int dz dp p \partial_t w(z, p) = \int dz dp g_p(z, p) w(z, p), \quad (2.91)$$

$$\partial_t \langle z^2 \rangle = \int dz dp [2zg_z(z, p) + D_{zz}(z, p)] w(z, p), \quad (2.92)$$

$$\partial_t \langle p^2 \rangle = \int dz dp [2pg_p(z, p) + D_{pp}(z, p)] w(z, p), \quad (2.93)$$

$$\partial_t \langle zp + pz \rangle = 2 \int dz dp [pg_z(z, p) + zg_p(z, p) + D_{zp}(z, p)] w(z, p). \quad (2.94)$$

²⁵ Here I make use of the procedure of integration by parts and of the fact that a well-behaved and normalizable Wigner function should vanish at the infinities.

The term g_z describes the overall drift of the position coordinate, the other drift term g_p represents the force field acting on the ensemble state. The combined diffusion of both the position and the momentum coordinate, which leads to an increase in the occupied phase-space area, is related to the diffusion matrix²⁶ $D_{jk}(z, p)$. An alternative way to describe the semiclassical motion of a particle is to work with a set of stochastic Langevin equations for position and momentum random variables, which reproduces the same ensemble-averaged time evolution as the FPE [49].

Let me split the phase-space representation of the state evolution (2.87) into a coherent part as well as a dissipative and a diffusive part,

$$\partial_t w(z, p) = [\partial_t w(z, p)]_{\text{coh}} + [\partial_t w(z, p)]_{\text{dis}} + [\partial_t w(z, p)]_{\text{dif}}, \quad (2.95)$$

following my notation in [8]. The first part is associated to the first line in (2.87) which describes the conservative motion under the optical potential of the pumped mode. The second part represents the second line and contains the delayed reaction of all cavity modes. The remainder, that is, the momentum diffusion by absorption and elastic light scattering, is contained in the last part. All three parts are Taylor-expanded and brought into the semiclassical FPE form in a tedious but straightforward calculation with help of the tools in the appendix.

The coherent part A second-order expansion of the coherent part yields

$$[\partial_t w(z, p)]_{\text{coh}} = -\frac{p}{m_p} \partial_z w(z, p) + \hbar \tilde{U}_{00} \partial_z |\alpha u_0(z)|^2 \partial_p w(z, p) + \mathcal{O}(\hbar^3). \quad (2.96)$$

This equation describes a deterministic evolution of the system along classical trajectories in the dipole force field the pump mode. The conservative motion does not lead to any diffusion effect. This semiclassical approximation amounts to omitting any diffraction effects and treating the motion through the optical potential in a purely classical manner²⁷. The lowest order quantum corrections originate from the non-conservative parts of the time evolution.

The dissipative part Our main interest lies in the dissipative part of the motion, which contains the cavity-induced friction force. The phase-space representation of the memory operators (2.86),

$$G_n(z, p) = \int_0^\infty d\tau e^{-(\kappa_n + i\Delta_n)\tau} u_n^* \left(z - \frac{p\tau}{m_p} \right) u_0 \left(z - \frac{p\tau}{m_p} \right), \quad (2.97)$$

and several steps of calculation lead to the following additions to the force and to the diffusion:

$$g_p^{(\text{dis})}(z, p) = \sum_{n=0}^M |\tilde{U}_{0n}\alpha|^2 \Re \{ 2i\hbar G_n(z, p) \partial_z u_0^*(z) u_n(z) - \hbar^2 [\partial_p G_n(z, p)] \partial_z^2 u_0^*(z) u_n(z) \}, \quad (2.98)$$

$$D_{pp}^{(\text{dis})}(z, p) = \sum_{n=0}^M 2\hbar^2 |\tilde{U}_{0n}\alpha|^2 \Re \{ [\partial_z G_n(z, p)] \partial_z u_0^*(z) u_n(z) \}, \quad (2.99)$$

$$D_{zp}^{(\text{dis})}(z, p) = -\sum_{n=0}^M \hbar^2 |\tilde{U}_{0n}\alpha|^2 \Re \{ [\partial_p G_n(z, p)] \partial_z u_0^*(z) u_n(z) \}. \quad (2.100)$$

²⁶ The diffusion matrix generally should be positive semidefinite in order to ensure that the occupied phase-space area increases and that the time evolution produces physical states at all times.

²⁷ This would be a bad approximation if the underlying quantum state would be a delocalized matter-wave state that could be diffracted by the standing-wave structure of the pump mode (see Section 2.1.4).

There is no dissipative contribution to the drift and the diffusion of the position coordinate, $g_z^{(\text{dis})} = D_{zz}^{(\text{dis})} = 0$. The memory effect due to the delayed cavity reaction lies in the memory term $G_n(z, p)$. It is responsible for the velocity dependence of the dissipation force which may result in a net friction effect. I will analyze the dissipative contributions in more details for specific cavity configurations below.

The diffusive part The absorption and elastic scattering of pump photons contributes an additional momentum diffusion effect, as we have already seen in Section 2.1.2. It complements the non-conservative influence of the high-finesse cavity by the following terms:

$$g_p^{(\text{dif})}(z, p) = 2\hbar (\gamma_{\text{abs}} + \gamma_{\text{sca}}) |\alpha|^2 \Im \{u_0(z) \partial_z u_0^*(z)\}, \quad (2.101)$$

$$D_{pp}^{(\text{dif})}(z, p) = \hbar^2 |\alpha|^2 [(\gamma_{\text{abs}} + \gamma_{\text{sca}}) |\partial_z u_0(z)|^2 + \gamma_{\text{sca}} k^2 \langle n_z^2 \rangle |u_0(z)|^2]. \quad (2.102)$$

They must be added to Eqs. (2.98) and (2.99), respectively. Scattering and absorption mainly enhance the momentum diffusion by $D_{pp}^{(\text{dif})} \geq 0$. Only for complex running-wave modes u_0 with a directed net momentum flow, there is a radiation-pressure addition $g_p^{(\text{dif})}$ to the dissipative force (2.98). The diffusion effect consists of two parts related to the absorption and to the scattering of pump photons. The latter depends on the angular scattering distribution of the particle, which is given by the dipole pattern $R(\mathbf{n}) = 3[1 - (\mathbf{n} \cdot \boldsymbol{\epsilon})^2]/8\pi$ in the case of a PPP and a pump mode polarization $\boldsymbol{\epsilon}$ perpendicular to the z -axis²⁸. This leaves us with $\langle n_z^2 \rangle = \int d^2 n R(\mathbf{n}) n_z^2 = 2/5$.

2.2.3.2. Conditions for cavity-induced slowing

The velocity-dependent part of the overall force acting on the particle lies solely in the expression (2.98) which is a sum over $M + 1$ single-mode force terms, $g_p^{(\text{dis})}(z, p) = \sum_{n=0}^M g_p^{(n)}(z, p)$. The potential motional damping induced by each mode can be made explicit by a first-order expansion in the limit of low particle velocities,

$$g_p^{(n)}(z, p) = g_p^{(n)}(z, 0) + \beta^{(n)}(z) p + \mathcal{O}(p^2). \quad (2.103)$$

The delayed reaction of the n th cavity mode damps the motion when the respective friction coefficient $\beta^{(n)}(z)$ is negative, otherwise it accelerates the particle. To be concrete, the above low-velocity expansion is valid when the Wigner function of the particle covers mainly those velocities $v = p/m_p$ that correspond to a Doppler shift $|kv| < \kappa_n$. The field fluctuations in the n th mode then lag behind the particle motion only a little and we may expand the memory function (2.97) to

$$G_n(z, p) = \frac{u_n^*(z) u_0(z)}{\kappa_n + i\Delta_n} - \frac{p}{m_p} \frac{\partial_z u_n^*(z) u_0(z)}{(\kappa_n + i\Delta_n)^2} + \frac{p^2}{m_p^2} \frac{\partial_z^2 u_n^*(z) u_0(z)}{(\kappa_n + i\Delta_n)^3} + \mathcal{O}(p^3). \quad (2.104)$$

We arrive at the friction coefficient

$$\beta^{(n)}(z) = -\frac{4\hbar |\tilde{U}_{0n}\alpha|^2 \kappa_n}{m_p (\kappa_n^2 + \Delta_n^2)^2} \left[\Delta_n |\partial_z u_0^*(z) u_n(z)|^2 + \frac{\hbar (\kappa_n^2 - 3\Delta_n^2)}{2m_p (\kappa_n^2 + \Delta_n^2)} |\partial_z^2 u_0^*(z) u_n(z)|^2 \right]. \quad (2.105)$$

²⁸ Rayleigh scattering can be viewed as absorption and immediate reemission of a pump photon into free space. The absorption is responsible for the radiation pressure force, whereas the reemission does not contribute on average because there is no preferred direction of scattering, $\langle n_z \rangle = \int d^2 n R(\mathbf{n}) n_z = 0$.

Note that the z -derivative of the mode function is proportional to $\partial_z \sim k$. Hence, the two terms in the brackets correspond to first and second orders in the recoil frequency $\omega_r = \hbar k^2 / 2m_p$, which is assumed to be small, $\omega_r \ll \kappa_n, |\Delta_n|$. We may thus neglect the second order contribution for all practical purposes (except for the marginal cases where the first order term vanishes) and focus entirely on the first term.

I conclude that damping may only occur for blue-detuned cavity modes, $\Delta_n > 0$, which agrees with the classical model from Section 2.1.3 illustrated in Figure 2.3. Moreover, we find a similar parameter dependence as in the classical expression (2.35), which is was derived with less rigour from a slightly different set of assumptions. The slowing rate (2.105) is modulated by the z -dependence of the mode, but it does not flip sign and accelerate the particle for a given set of cavity parameters. It appears strongest neither at the nodes nor at the antinodes of each cavity mode, but rather in between, at the steepest points of the overlap $u_0^* u_n$. If we average over all z -positions we find that each cavity mode overlapping with the pump mode contributes a mean velocity damping rate of $|\bar{\beta}^{(n)}| \sim 8\omega_r \kappa_n \Delta_n |\tilde{U}_{0n}\alpha|^2 / (\kappa_n^2 + \Delta_n^2)^2$. It is maximized for a detuning of $\Delta_n = \kappa_n / \sqrt{3}$.

2.2.3.3. Case study: A single strongly pumped standing-wave mode

It is instructive to apply the results to the most elementary case of a PPP inside a single driven Fabry-Pérot standing-wave mode, as already discussed earlier and sketched in Figure 2.1. If we set $u_0(z) = \cos kz$ we can compute the memory function explicitly,

$$\begin{aligned} G(z, m_p v) &= \frac{1}{2(\kappa + i\Delta)} + \frac{1}{4} \left[\frac{\exp(2ikz)}{\kappa + i(\Delta + 2k\nu)} + \frac{\exp(-2ikz)}{\kappa + i(\Delta - 2k\nu)} \right] \\ &= \frac{1}{2\nu} + \frac{\nu \cos 2kz + 2k\nu \sin 2kz}{2[\nu^2 + (2k\nu)^2]}, \end{aligned} \quad (2.106)$$

with the complex damping-detuning parameter $\nu = \kappa + i\Delta$. The non-conservative force term becomes

$$\begin{aligned} g_p^{(\text{dis})}(z, m_p v) &= \hbar k |\tilde{U}_{00}\alpha|^2 \left[\Im \left\{ \frac{1}{\nu} + \frac{\nu \cos 2kz + 2k\nu \sin 2kz}{\nu^2 + (2k\nu)^2} \right\} \sin 2kz \right. \\ &\quad \left. + \Re \left\{ \frac{\sin 2kz}{\nu^2 + (2k\nu)^2} - 2k\nu \frac{\nu \cos 2kz + 2k\nu \sin 2kz}{[\nu^2 + (2k\nu)^2]^2} \right\} 4\omega_r \cos 2kz \right]. \end{aligned} \quad (2.107)$$

Once again, we may neglect the second line because of its higher-order dependence on the recoil frequency ω_r . Let us, for the moment, focus on the velocity dependence of the remaining term by averaging over the position in the standing wave,

$$\overline{g_p^{(\text{dis})}(m_p v)} = \frac{-4|\tilde{U}_{00}\alpha|^2 \omega_r \kappa \Delta}{|\nu^2 + (2k\nu)^2|^2} m_p v + \mathcal{O}(\omega_r^2). \quad (2.108)$$

I plot the velocity dependence for different positive detunings, which correspond to a net slowing effect, in Figure 2.5. Given a fixed cavity-pump detuning $\Delta > 0$, we observe that only a limited range of velocities is efficiently slowed. If we increase the detuning, the maximum of the friction

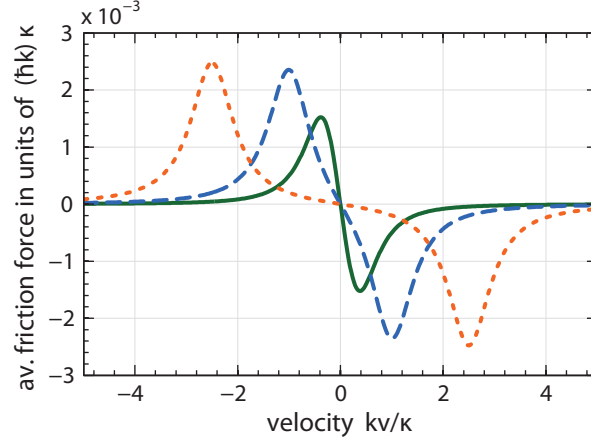


Figure 2.5. Position-averaged friction force (2.108) of a pumped Fabry-Pérot cavity as a function of velocity for different cavity-pump detunings [8]. It is positive on the left and negative on the right of $v = 0$, which means that it slows the particle. I use an effective coupling rate of $|\tilde{U}_0\alpha| = 0.1\kappa$. The solid, the dashed, and the dotted lines correspond to $\Delta = \kappa/\sqrt{3}$, 2κ and 5κ , respectively. Both velocity and force are plotted in natural cavity-related units of κ/k and $(\hbar k)\kappa$.

force shifts to larger velocities, and faster particles are more efficiently slowed at the expense of not capturing already slow ones. In the limit of very large detunings $\Delta \gg \kappa$ the velocity capture range is determined by $kv \approx \Delta$. On the other hand, we observe the strongest damping effect (steepest slope) for small velocities at the detuning $\Delta = \kappa/\sqrt{3}$ (solid line). This is no surprise since we have found one section earlier that this detuning corresponds to an optimal friction coefficient β .

The friction force is accompanied by momentum diffusion, which prevents the cavity from slowing a particle arbitrarily close to zero velocity,

$$D_{pp}^{(\text{dis})}(z, m_p v) = 2(\hbar k)^2 |\tilde{U}_0\alpha|^2 \Re \left\{ \frac{v \sin^2 2kz - 2kv \sin 2kz \cos 2kz}{v^2 + (2kv)^2} \right\}, \quad (2.109)$$

$$\overline{D_{pp}^{(\text{dis})}(m_p v)} = \frac{(\hbar k)^2 \kappa |\tilde{U}_0\alpha|^2}{|v^2 + (2kv)^2|^2} [|v|^2 + (2kv)^2]. \quad (2.110)$$

Although the position-averaged diffusion coefficient is strictly positive, this does not hold everywhere in the standing wave. The diffusion coefficient (2.109) is plotted as a function of z in Figure 2.6 for various particle velocities. In the vicinity of the antinodes of the standing wave the diffusion coefficient assumes negative values at nonzero velocities. The positive regions clearly dominate for slow particles, $|kv| \lesssim \kappa$, where the position-averaged expression (2.110) assumes its maximum. Moreover, the positive and negative parts nearly compensate for faster particles (solid line). Anyway, the overall momentum diffusion effect vanishes in this case, because the cavity dynamics can no more keep up with the moving particle.

Completely positive Lindblad-type master equations must always yield positive semidefinite diffusion matrices $D_{jk}(z, p)$. In the present case, we have a vanishing position diffusion, $D_{zz}^{(\text{dis})} = 0$,

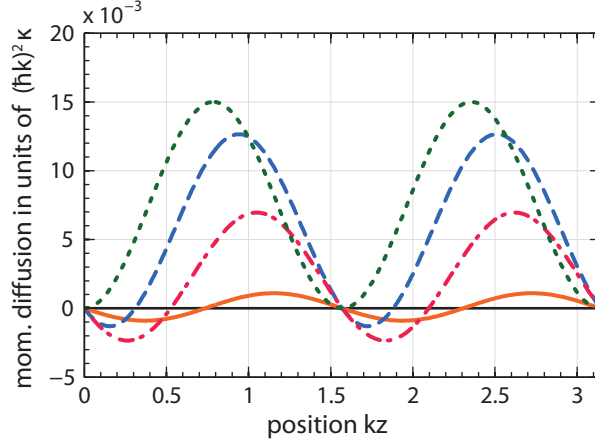


Figure 2.6. Momentum diffusion coefficient (2.109) of a pumped Fabry-Pérot cavity as a function of position for different particle velocities. We use the effective coupling rate $|\tilde{U}_0\alpha| = 0.1\kappa$ and the detuning $\Delta = \kappa/\sqrt{3}$. The solid, dashed, dash-dotted, and dotted line correspond to $kv = 5\kappa, \kappa, 0.5\kappa$, and 0, respectively. The diffusion coefficient and the position are expressed in cavity-related units of $(\hbar k)^2 \kappa$ and $1/k$.

and a non-diagonal element given by

$$D_{zp}^{(\text{dis})}(z, m_P v) = 2\hbar\omega_r |\tilde{U}_0\alpha|^2 \Re \left\{ \frac{4vk v \cos 2kz + [(2kv)^2 - v^2] \sin 2kz}{[v^2 + (2kv)^2]^2} \right\} \sin 2kz. \quad (2.111)$$

The resulting determinant is negative and the diffusion matrix is indefinite. This shows that the underlying master equation (2.87) is non-Markovian and cannot be cast into the completely positive Lindblad form. I attribute this to the memory effect of the cavity [78–80]. Its field does not adjust to the change in particle position instantaneously, but it reacts retardedly to the trajectory that is accumulated over the cavity lifetime $1/\kappa$. The negativity in the diffusion matrix is negligible in most practical cases when the cavity-induced slowing of large polarizable particles is concerned. The diffusion effect hardly affects the motional state of fast particles, which are far above the quantum limit of motion, as I will discuss in the following.

The whole cavity-induced damping-diffusion process can be understood as a random walk induced by the recoil related to the coherent scattering of pump photons between the two running-wave components of the standing-wave cavity mode. A moving particle emits Doppler-shifted light which is blue-detuned in the direction of motion and red-detuned in the opposite direction. By detuning the pump laser to the red side of the cavity resonance, we enhance the coherent scattering of photons into the direction of motion, thereby gradually taking away kinetic energy over many random walk cycles. It is then intuitively clear that the cavity-induced slowing effect cannot decrease the kinetic energy of a particle further than the so-called recoil limit $\hbar\omega_r$. The accompanying momentum diffusion in units of $\hbar k$ simply cannot be overcome.

Is it then, at least in principle, possible to reach the recoil limit after a sufficiently long waiting time? Let me answer this question by estimating the final kinetic energy that can be obtained in the limit of $t \rightarrow \infty$. For this purpose consider again the time evolution equation (2.93) of the second moment in momentum, and ignore the z -modulation by averaging both the force and the diffusion term over the standing-wave profile. This cancels the conservative dipole force and leaves

us with the dissipative terms (in the absence of absorption and Rayleigh scattering). Given the above expressions (2.108) and (2.110) in the limit of small particle velocities, $|k\nu| \ll \kappa$, we find that the average kinetic energy has a fixed point at the value²⁹

$$\left\langle \frac{p^2}{2m_P} \right\rangle_\infty = - \frac{\overline{pD_{pp}^{(\text{dis})}}(p)}{4m_P \overline{g_p^{(\text{dis})}}(p)} \approx \frac{\hbar}{8} \left(\Delta + \frac{\kappa^2}{\Delta} \right). \quad (2.112)$$

Ensembles of initially faster particles are eventually slowed down towards this limiting mean kinetic energy value. It depends on the cavity reaction time scale, and it reads as $\hbar\kappa/2\sqrt{3}$ in the case of the optimal detuning $\Delta = \kappa/\sqrt{3}$. Note that this limit is considerably higher than the fundamental recoil limit since $\omega_r \ll \kappa$. It illustrates that the cavity-induced slowing effect is in practice already limited by the finite cavity lifetime and the associated energy uncertainty. In the presence of absorption and Rayleigh scattering we must take the respective diffusion term (2.102) into account, which leads to the increased slowing limit

$$\left\langle \frac{p^2}{2m_P} \right\rangle_\infty \approx \frac{\hbar}{8} \left[\Delta + \frac{\kappa^2}{\Delta} + \frac{(\kappa^2 + \Delta^2)^2}{2\tilde{U}_0^2 \kappa \Delta} \left(\gamma_{\text{abs}} + \frac{7}{5} \gamma_{\text{sca}} \right) \right]. \quad (2.113)$$

Concerning the interplay between friction and diffusion, I conclude: While the friction force determines the rate at which the kinetic energy of the particle is gradually dissipated through the cavity over many lifetime cycles of its field, the overall diffusion term sets the kinetic energy of the limiting velocity, which cannot be undercut in the present slowing scheme. Current sources for molecules and nanoparticles, which are used in matter-wave interferometry, are typically far above this limit. Assuming a cavity linewidth of $\kappa \sim 1$ MHz, the cavity-slowing limit corresponds to motional temperatures of the order of microkelvins.

2.2.3.4. Multimode enhancement in degenerate resonator configurations

Having studied the generic dissipation effect in the instructive case of a single Fabry-Pérot cavity mode, I now turn to a more practical multimode configuration, as sketched in Figure 2.4. Each of the $M > 1$ empty cavity modes represents a dissipation channel which adds to the overall friction effect along the z -axis of the cavity. The strong pump mode is directed along the y -direction and should overlap with the cavity volume as much as possible to maximize the effective interaction region for each passing particle.

An experimental realization may be feasible in a setup where a large manifold of degenerate modes can be created in a confocal resonator configuration with two circularly symmetric curved mirrors. If the distance d between the mirrors is exactly the same as their radii of curvature, then, in principle, the resonator will support an almost infinite spectrum of higher-order transverse modes that share the same resonance frequency with a given fundamental standing-wave mode. These higher-order modes exhibit a larger effective mode waist, and the mode spectrum is in practice limited to a finite number M due to the finite aperture of real-life mirrors. In addition, if the setup is not precisely confocal, the contribution of higher-order modes to the friction force will decrease with shifting resonance frequency.

²⁹ The expression (2.112) ceases to be valid for large velocities and at $\Delta = 0$, where the first-order friction term (2.108) vanishes.

The controlled optical driving of one of the degenerate modes would require good mode matching, and it would lead to strong conservative dipole forces modulating the motion of particles along the standing wave. Both the mode matching and the dipole force can be avoided by shining a broad running-wave laser mode perpendicular to the cavity axis. It acts as an optical pump mode where it overlaps with the cavity modes, but it does not induce any significant dipole force along the cavity axis. Moreover, the absorption-induced momentum diffusion along the z -axis is also suppressed. This perpendicular pump configuration comes at the price of less available pump power. It could be enhanced by means of another cavity, of course.

In the following I will discuss the enhancement of the cavity-induced friction by the number M of accessible cavity modes. Once again, we restrict our view to the z -motion along the cavity axis, omitting any influence on the transverse motion of the particle. The resulting friction and diffusion terms still depend on the off-axis xy -coordinates of the particle, and we can average them over the trajectory of a particle traversing the cavity for an estimate of their mean effects³⁰.

The modes of a confocal standing-wave resonator [57, 81–83] are characterized by one longitudinal mode index $n \in \mathbb{N}$ and two transverse mode indices $m, \ell \in \mathbb{N}_0$. From the boundary conditions at the curved mirror surfaces follow the respective resonance frequencies [83]

$$\omega_{n,m,\ell} = \frac{\pi c}{d} \left(n + m + \frac{\ell + 1}{2} \right), \quad (2.114)$$

with d the mirror distance (and radius of curvature). A given fundamental mode $(n_0, 0, 0)$ of wavelength $\lambda = 2\pi/k$ shares the same resonance frequency with a huge manifold of transverse modes $(n < n_0, m, \ell)$, since $n_0 = 2d/\lambda$ is typically a large number. We can assign the effective waist parameter $w_{n,m,\ell} = w_0 \sqrt{2m + \ell + 1}$ to each higher-order transverse mode [82, 83]; it describes the growing mode volume with respect to the fundamental mode of waist $w_0 = \sqrt{d\lambda/2\pi}$. If the waist is aperture-limited by $w_{n,m,\ell} \lesssim aw_0$, then both $2m$ and $\ell + 1$ are restricted to values less or equal to a^2 , which leads to a total number of supported modes $M \lesssim a^4/2$. (The quantity a measures the aperture in units of w_0 .)

The field distribution of each mode can be approximated by Laguerre-Gaussian functions³¹ in the case of large-aperture mirrors [82], $a^2 \gg 1$. We obtain the explicit form of the three-dimensional mode function [83] by assuming linear polarization and omitting any off-axis corrections to the field polarization due to the transverse mode profile (see Appendix A.2 for the specific case of a Gaussian mode, $m = \ell = 0$). In cylindrical coordinates the full three-dimensional mode functions $\mathbf{u}_{n,m,\ell}(\mathbf{r}) = \boldsymbol{\epsilon} f_{m,\ell}(r, \phi, z) u_{n,m,\ell}(r, z)$ factorize into the on-axis standing-wave mode functions $u_{n,m,\ell}$, the Laguerre-Gaussian transverse mode profiles $f_{m,\ell}$, and a fixed polarization vector $\boldsymbol{\epsilon}$,

$$u_{n,m,\ell}(r, z) = \begin{Bmatrix} \cos \\ \sin \end{Bmatrix} \left[kz \left(1 + \frac{4r^2}{d^2 \xi^2(z)} \right) - (2m + \ell + 1) \arctan \left(\frac{2z}{d} \right) \right] \vee \begin{Bmatrix} n \text{ odd} \\ n \text{ even} \end{Bmatrix}, \quad (2.115)$$

$$f_{m,\ell}(r, \phi, z) = \frac{\cos(\ell\phi)}{\xi(z)} \left(\frac{\sqrt{2}r}{w_0 \xi(z)} \right)^\ell L_m^\ell \left(\frac{2r^2}{w_0^2 \xi^2(z)} \right) \exp \left(\frac{-r^2}{w_0^2 \xi^2(z)} \right). \quad (2.116)$$

³⁰ This corresponds to the experimental situation when a dilute beam of molecules or nanoparticles crosses the cavity, such that there is on average only one particle inside the cavity at a given time.

³¹ Laguerre-Gaussian modes can only be used if the mirror system exhibits a cylindrical symmetry. This symmetry may be violated in applications with birefringent mirrors. In this case one must use the rectangular Hermite-Gaussian modes instead [82], which yield similar results as presented here.

Here, L_m^ℓ denotes the associated Laguerre polynomial [63] and $\xi(z) = \sqrt{1 + 4z^2/d^2}$. We obtain a simple expression for the mode volume in the case of large apertures,

$$V_{n,m,\ell} = \frac{\pi}{8} w_0^2 d (1 + \delta_{\ell 0}) \frac{(\ell + m)!}{m!}, \quad (2.117)$$

if we approximate the on-axis function in the volume integral by an unmodified standing wave, $\int_{-d/2}^{d/2} dz u_{n,m,\ell}^2(r, z) \approx d/2$.

I now assess the contribution of each mode to the overall slowing effect in terms of its friction coefficient (2.105). To keep things simple, I assume that all contributing modes share the same linewidth κ and the optimal detuning $\Delta = \kappa/\sqrt{3}$, and I confine the analysis to the center of the cavity, $|z| \ll d$, where $\xi(z) \approx 1$. Moreover, we can safely omit the z -derivative of the orthogonally oriented pump mode. This leaves us with the estimate for the friction coefficient,

$$\begin{aligned} \beta^{(n,m,\ell)}(r, \phi, z) \approx & -\frac{3\sqrt{3}m!\omega_r |U_0\alpha|^2}{(\ell + m)! (1 + \delta_{\ell 0}) \kappa^2} |u_0(r, \phi, z) f_{m,\ell}(r, \phi, 0)|^2 \left(1 + \frac{4r^2}{d^2} - \frac{4m + 2\ell + 2}{kd}\right)^2 \\ & \times \begin{cases} \sin^2 \\ \cos^2 \end{cases} \left[kz \left(1 + \frac{4r^2}{d^2} - \frac{4m + 2\ell + 2}{kd}\right) \right] \vee \begin{cases} n \text{ odd} \\ n \text{ even} \end{cases}, \end{aligned} \quad (2.118)$$

to first order in the recoil frequency ω_r and in the parameters³² z/d and $1/kd$. Here, the term U_0 is defined as the coupling rate between the pump mode and the fundamental Gaussian cavity mode $(n_0, 0, 0)$. The pump mode shall be given by a Gaussian running wave of the same waist w_0 , $|u_0(r, \phi, z)|^2 = \exp(-2z^2/w_0^2 - 2r^2 \cos^2 \phi/w_0^2)$.

The total friction coefficient of the cavity is the sum over the terms (2.118) of all degenerate modes that are accessible by the pump laser. The overall cavity-induced slowing rate is amplified by the number of transverse modes supported by the cavity. This is demonstrated in Figure 2.7 for a set of exemplary parameters. There, the friction rate is averaged over the off-axis coordinates³³ and plotted as a function of z close to the center of the resonator. The plot compares the contribution of the fundamental mode (dotted curve) to the collective friction rate of $M = 15$ (dashed) and $M = 55$ (solid) degenerate modes. Notice that, besides the overall multimode enhancement, the standing-wave modulation of the friction rate is also reduced. This is due to the equal contribution of both sine and cosine standing-wave modes in the confocal configuration. Hence, there is a nonzero slowing effect everywhere on the standing-wave axis.

In a real-life experiment the number of supported higher-order modes can be much higher, depending on the quality and aperture of the cavity mirrors. In Figure 2.8 I plot the position-averaged friction rate of the resonator versus the number M of degenerate modes that were taken into account in the computation. The plotted data are normalized to the single-mode value. The rightmost point corresponds to $M = 406$ indicating an amplification of the single-mode friction effect by almost two orders of magnitude. The increase per mode gets diminished with growing mode volume due to the decreased overlap with the pump mode.

³² Second order terms of the form z^2/d^2 , $1/k^2 d^2$ and z/kd^2 are dropped. The inverse tangent is linearized as $\arctan(2z/d) \approx 2z/d$.

³³ The average friction rate depends on the size of the averaging area. A larger area covers more space outside the cavity where the friction effect is zero. Nevertheless, the average value is a meaningful quantity to assess the net slowing of particles that are trapped in or passing the chosen region in a given amount of time.

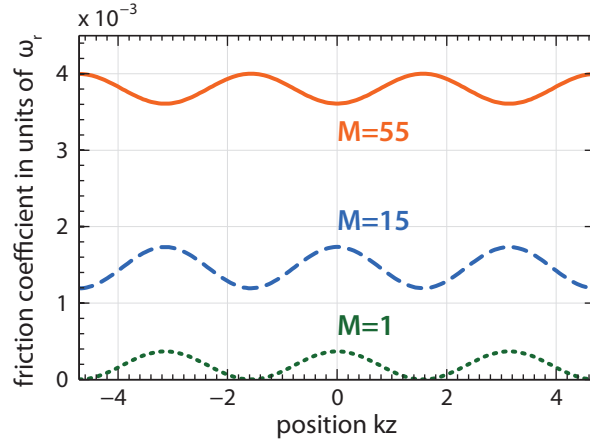


Figure 2.7. Modulus of the overall friction coefficient of M confocal cavity modes in units of the recoil frequency and as a function of the on-axis position kz . The cavity mirrors are $d = 10$ mm apart. The dotted line represents the friction coefficient of the fundamental Gaussian mode (20000, 0, 0) of wavelength $\lambda = 2\pi/k = 1\text{ }\mu\text{m}$ and waist $w_0 = 40\text{ }\mu\text{m}$. It is pumped by a Gaussian wave of the same waist running along the y -axis. I assume an effective coupling of $|U_0\alpha| = 0.1\kappa$ between both modes, and a detuning of $\Delta = \kappa/\sqrt{3}$. The contributions (2.118) of the 14 and 54 closest degenerate transverse modes are added to the fundamental mode for the dashed and the solid lines, respectively. In all cases, the off-axis coordinates x and y are averaged over a circle of radius $5w_0$.

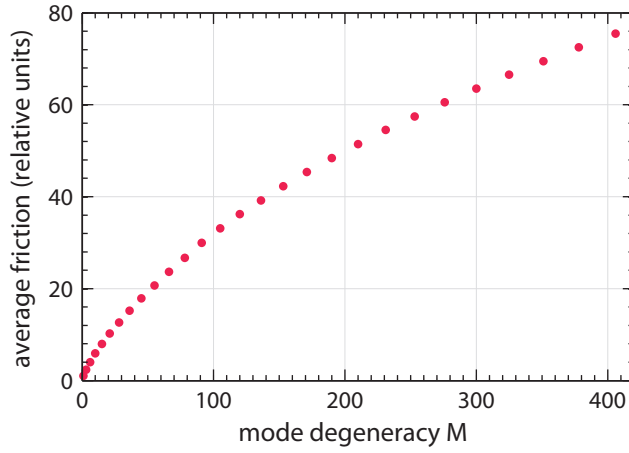


Figure 2.8. Position-averaged friction coefficient of a confocal resonator as a function of the number M of degenerate modes that are taken into account. All the settings of Figure 2.7 are used, and the results are additionally averaged over the range of z -coordinates depicted there. The data points are given in proportion to the average friction rate of the fundamental mode (mean value of the dotted curve in Figure 2.7).

Let me close this section on the cavity-induced slowing of a PPP in the weak coupling regime with a few remarks. I have developed a rigorous quantum description of the dissipative motion of a particle in the presence of pump field and cavity by means of an effective (non-Markovian) master equation. It has led us to the understanding of the emergent friction and diffusion effects using a semiclassical phase-space approach. After studying the basic phenomena in an idealized single-mode configuration, I have provided a detailed assessment of the multimode case. At this point we should note that not only the friction force is enhanced by the presence of many modes, but also the accompanying momentum diffusion effect. While the former determines the effective rate at which the motion of the particle is damped, the latter raises the ultimate cooling limit. In other words, more modes imply a larger limiting kinetic energy value, down to which the particle can be damped by the cavity. Absorption and Rayleigh scattering contribute to this limit as well.

In many potential laboratory applications with molecules and clusters, one must often deal with particle ensembles whose initial temperature is far above this limit. In practice, it would be much more important to boost the effective damping rate from the unsuitably low values, as implied by the parameters listed in Table 2.1, to a feasible regime. This requires one to leave the weak coupling regime by increasing the pump field strength or by using even larger particles, as I will discuss in the next section. Another option is to increase the number of particles that interact with the cavity at the same time. In Appendix A.4 I show how to generalize our quantum treatment and the effective master equation to $N > 1$ particles in M driven or empty modes. There, however, the validity of the resulting friction and diffusion terms is restricted to an even more rigid weak-coupling limit. This is because the individual field fluctuations induced by each particle may add up. By breaking the weak-coupling limit with many particles one may benefit from strong cavity-mediated inter-particle correlations and from collective phenomena such as self-organisation [84, 85].

2.3. Mechanics of spherical particles in coherent light fields

So far I have discussed the (off-resonant) light-matter interaction, and its mechanical action on matter waves, in terms of point-like particles characterized by a scalar complex dipole polarizability χ . Whereas this is a good approximation for many molecules and clusters, which are by orders of magnitude smaller than the wavelength of the light they interact with, it ceases to be valid for nano- and microparticles of the same size as the wavelength or larger. The light scattering properties get more complex as higher-order multipole components take over, and a rigorous quantum description of both the light and the matter degrees of freedom is a difficult task due to several reasons:

- ★ The quantization of the center-of-mass motion of the particle depends on explicit expressions for the force and the optical potential induced by the light field. However, we will see below that the force on extended particles cannot be reduced to a simple analytical expression anymore, but must be evaluated numerically in practice. Moreover, the result contains both the conservative light force and the radiation pressure force due to light absorption and Rayleigh scattering. Consequently, the optical potential cannot be directly deduced. We can avoid these difficulties in the effectively one-dimensional situation of matter-wave diffraction at optical standing-wave gratings in Section 2.3.2.

- ★ If a large particle couples strongly to a high-finesse cavity field, it may change the spatial mode structure of the resonator. This is intuitively clear since the particle becomes a semitransparent mirror for the cavity field if it is large enough. Whereas one may benefit from the strong coupling when trying to observe cavity-induced slowing of large particles, the theoretical modelling requires a proper treatment of the modified boundary conditions. I will present an approximate solution when I discuss the classical slowing of spherical particles in Section 2.3.3.
- ★ A rigorous quantum description of the dynamics of both the light field and the particle requires an elaborate model for light scattering at extended material objects. This is a matter of current research [86], and it has gained interest with the upcoming of proposals to observe the ground-state motion of optically trapped microspheres [23,24]. One possible model treats the extended object as an assembly of point-like scatterers at which single photons can scatter along multiple paths [86]. The resulting master equation gives proper account to the scattering-induced decoherence and diffusion effects, provided that the local fields are correctly described for each scatterer. Another possibility is to model the particle as a dielectric medium, which then requires the canonical quantization of the macroscopic field inside this medium [87]. However, this approach requires one to determine the precise momentum carried by the radiation field inside the dielectric medium when trying to assess the force density acting on the material—an old and controversial issue [32, 88].
- ★ Apart from the center-of-mass effect, an extended dielectric object may also experience elastic stress due to light-induced bending and shearing forces. This may, in turn, deform the particle and modify its response to the light field depending on its stiffness properties [89]. Here, I avoid this additional complication by assuming rigid atomic clusters. Nevertheless, we must keep in mind that this might be an issue when dealing with hot or fluid particles, such as nanodroplets.

In this thesis I focus on generally hot and fast ensembles of particles far above the quantum limit of motion, which interact with strong coherent light fields. In the effective description of such particles, we may therefore avoid many of the aforementioned difficulties by assuming a stationary mode configuration and ignoring the full quantum nature of the photon field dynamics.

Moreover, I restrict the considerations to homogeneous dielectric spheres³⁴, which is a good representation of many heavy clusters consisting of $N \gg 1$ atoms [52]. We can employ the Mie theory of light scattering at spherical objects [28, 29, 34, 90] to understand the light-matter interaction, as outlined in Appendix A.6. The idea is to start with a given light field \mathbf{E}_0 in the absence of the sphere, and to expand it in the basis of spherical vector harmonics, that is, multipole components which respect the spherical symmetry of the problem. The origin of the coordinate system must be shifted to the center of the sphere \mathbf{r}_0 , accordingly. The spherical wave expansion is outlined in Appendix A.5.

Putting the sphere into the game introduces a different field \mathbf{E}_{int} inside the dielectric medium, and it modifies the external field by adding a scattering component, $\mathbf{E}_0 \rightarrow \mathbf{E}_{\text{ext}} = \mathbf{E}_0 + \mathbf{E}_{\text{sca}}$. The

³⁴ Nonspherical particles scatter light in different patterns, that is, the multipole composition of the scattered field deviates from the spherical case. The basic consequences of leaving the subwavelength size regime are similar to the spherical case, with the additional complication of coupling to the rotation of the object.

expansion coefficients of the new field components E_{int} and E_{sca} are obtained from the boundary conditions at the sphere surface. I have done this explicitly for plane running and standing waves, and for Gaussian modes in Appendix A.6. In the following, let me discuss the consequences for the mechanical action of light onto the particle.

2.3.1. Light extinction and light-induced forces

Mie theory provides us with the field configuration when a dielectric sphere of relative permittivity ε is placed into an electromagnetic field $\{E_0, H_0\}$ at the position \mathbf{r}_0 . Following Appendix A.6, the field outside of the sphere is then complemented by the scattering component

$$E_{\text{sca}} = \sum_{\ell=1}^{\infty} \sum_{m=-\ell}^{\ell} \left[\alpha_{\ell} C_{\ell,m}^{(M)} h_{\ell}(kr) X_{\ell,m}(\theta, \phi) + \frac{\beta_{\ell} C_{\ell,m}^{(E)}}{k} \nabla \times h_{\ell}(kr) X_{\ell,m}(\theta, \phi) \right], \quad (2.119)$$

with $h_{\ell} X_{\ell,m}$ and $\nabla \times X_{\ell,m} h_{\ell}$ the partial-wave multipole solutions (see Appendix A.5). The terms $C_{\ell,m}^{(M,E)}$ are the multipole expansion coefficients of the original field E_0 , which depend on the position \mathbf{r}_0 of the sphere. The coordinates $\mathbf{r} = (r, \theta, \phi)$ are defined relative to \mathbf{r}_0 . The scattered field differs from the original field mainly by the scattering coefficients α_{ℓ} and β_{ℓ} . They read as

$$\alpha_{\ell} = \frac{j_{\ell}(\sqrt{\varepsilon}kR) \partial_R [R j_{\ell}(kR)] - j_{\ell}(kR) \partial_R [R j_{\ell}(\sqrt{\varepsilon}kR)]}{h_{\ell}(kR) \partial_R [R j_{\ell}(\sqrt{\varepsilon}kR)] - j_{\ell}(\sqrt{\varepsilon}kR) \partial_R [R h_{\ell}(kR)]}, \quad (2.120)$$

$$\beta_{\ell} = \frac{\varepsilon j_{\ell}(\sqrt{\varepsilon}kR) \partial_R [R j_{\ell}(kR)] - j_{\ell}(kR) \partial_R [R j_{\ell}(\sqrt{\varepsilon}kR)]}{h_{\ell}(kR) \partial_R [R j_{\ell}(\sqrt{\varepsilon}kR)] - \varepsilon j_{\ell}(\sqrt{\varepsilon}kR) \partial_R [R h_{\ell}(kR)]}, \quad (2.121)$$

for a dielectric sphere of radius R , as given in the Appendix. (There I also present the case of a hollow sphere, which leads to more cumbersome expressions.) Note that the coefficients are independent of the chosen mode structure of the light field, as given by the $C_{\ell,m}^{(M,E)}$. They are the same in a running wave as in a standing wave. In the case of a point-like particle, $kR \ll 1$, we find that the lowest-order contribution is given by³⁵ $\beta_1 \approx 2i(kR)^3(\varepsilon - 1)/3(\varepsilon + 2)$. All other coefficients are of higher order in kR and thus negligible. One can convince oneself, using the identities and relations of Appendix A.5, that this yields the scattering field of the induced dipole $\chi E_0(\mathbf{r} = 0)$, with the complex polarizability of a subwavelength sphere [52],

$$\chi \approx 4\pi\varepsilon_0 R^3 \frac{\varepsilon - 1}{\varepsilon + 2} \quad \text{if } kR \ll 1. \quad (2.122)$$

Hence, the point-particle limit is properly reproduced by the Mie expansion. Having the Mie expression (2.119) at hand, we are now able to study the light extinction properties of the sphere, as well as the light-induced force acting on it. I will focus on standing-wave light modes, as opposed to running waves, since they are the basis of the optical diffraction gratings and the two-mirror cavities studied here.

³⁵ I use that the spherical Bessel functions can be approximated by $j_{\ell}(x) \approx x^{\ell}/[1 \cdot 3 \cdot \dots \cdot (2\ell + 1)]$ and $y_{\ell}(x) \approx -[1 \cdot 3 \cdot \dots \cdot (2\ell - 1)]/x^{\ell+1}$ to lowest order in $x \ll 1$, while the spherical Hankel function becomes $h_{\ell}(x) \approx iy_{\ell}(x)$.

2.3.1.1. The Poynting vector and the extinction power of the sphere

Scattering and absorption of light by finite geometries can be treated formally by means of the Poynting vector $\mathbf{S} = \Re\{\mathbf{E}\} \times \Re\{\mathbf{H}\}$. It has the dimension W/m^2 and describes the net energy flux per unit surface $|\mathbf{S}|$ into the direction $\mathbf{S}/|\mathbf{S}|$ in vacuum³⁶ [33, 34, 91]. That is, the time-averaged field energy flowing through a small surface element $dA = r^2 d\Omega$ at position \mathbf{r} into direction \mathbf{n} per unit time is given by $P_n(\mathbf{r}) = \langle \mathbf{n} \cdot \mathbf{S} \rangle_t = -r^2 d\Omega \Re\{\mathbf{E}(\mathbf{r}) \cdot [\mathbf{n} \times \mathbf{H}^*(\mathbf{r})]\} / 2$. From this it is intuitively clear how to obtain the total field energy per time scattered or absorbed by the sphere.

In order to assess the scattered power (2.123) we must take the outward-directed Poynting vector corresponding to the scattering field \mathbf{E}_{sca} and integrate it over the sphere surface [29, 34]. The absorbed power (2.124) is given by the net energy flux into the sphere, that is, by the integrated inward-directed Poynting vector corresponding to the total external field $\mathbf{E}_{\text{ext}} = \mathbf{E}_0 + \mathbf{E}_{\text{sca}}$. The extinction power (2.125) is defined as the sum of both contributions.

$$P_{\text{sca}} = -\frac{R^2}{2} \int d\Omega \Re\{\mathbf{E}_{\text{sca}}(R\mathbf{n}) \cdot [\mathbf{n} \times \mathbf{H}_{\text{sca}}^*(R\mathbf{n})]\} \quad (2.123)$$

$$P_{\text{abs}} = \frac{R^2}{2} \int d\Omega \Re\{\mathbf{E}_{\text{ext}}(R\mathbf{n}) \cdot [\mathbf{n} \times \mathbf{H}_{\text{ext}}^*(R\mathbf{n})]\} \quad (2.124)$$

$$P_{\text{ext}} = P_{\text{sca}} + P_{\text{abs}} = \frac{R^2}{2} \int d\Omega \Re\{\mathbf{E}_0(R\mathbf{n}) \cdot [\mathbf{n} \times \mathbf{H}_{\text{sca}}^*(R\mathbf{n})] + \mathbf{E}_{\text{sca}}(R\mathbf{n}) \cdot [\mathbf{n} \times \mathbf{H}_0^*(R\mathbf{n})]\} \quad (2.125)$$

A straightforward calculation using the orthogonality properties of the multipole expansion given in Appendix A.5 leads to the explicit forms

$$\begin{aligned} P_{\text{sca}} &= \frac{c\epsilon_0}{2k^2} \sum_{\ell,m} \left[|\alpha_\ell C_{\ell,m}^{(M)}|^2 + |\beta_\ell C_{\ell,m}^{(E)}|^2 \right], \\ P_{\text{ext}} &= -\frac{c\epsilon_0}{2k^2} \sum_{\ell,m} \left[\Re\{\alpha_\ell\} |C_{\ell,m}^{(M)}|^2 + \Re\{\beta_\ell\} |C_{\ell,m}^{(E)}|^2 \right], \end{aligned} \quad (2.126)$$

and $P_{\text{abs}} = P_{\text{ext}} - P_{\text{sca}}$. If the medium is non-absorptive, that is, if the refractive index $\sqrt{\epsilon}$ is real, then one can easily check that $P_{\text{abs}} = 0$ and $|\alpha_\ell|^2 = -\Re\{\alpha_\ell\}$, $|\beta_\ell|^2 = -\Re\{\beta_\ell\}$. We observe that the extinction power is a sum over the independent contributions of electric (E) and magnetic (M) multipole components.

The expressions simplify further in the case of a cosine-type standing wave,

$$P_{\text{sca,ext}}(z_0) = \frac{\pi I_0}{k^2} \left[\Pi_{\text{sca,ext}}^{(+)} + \Pi_{\text{sca,ext}}^{(-)} \cos 2kz_0 \right], \quad (2.127)$$

with z_0 the z -coordinate of the sphere center and $I_0 = c\epsilon_0 |E_0|^2 / 2$ the field intensity at the antinodes. The offset factors (+) and the modulation factors (−) read as

$$\begin{aligned} \Pi_{\text{sca}}^{(\pm)} &= \sum_{\ell} (2\ell + 1) (\pm)^\ell \left[|\alpha_\ell|^2 \pm |\beta_\ell|^2 \right], \\ \Pi_{\text{ext}}^{(\pm)} &= -\sum_{\ell} (2\ell + 1) (\pm)^\ell \left[\Re\{\alpha_\ell\} \pm \Re\{\beta_\ell\} \right]. \end{aligned} \quad (2.128)$$

³⁶ All the calculations can be done in the vacuum surrounding the sphere, thus avoiding the discussion [88] which form of the Poynting vector to choose inside the medium.

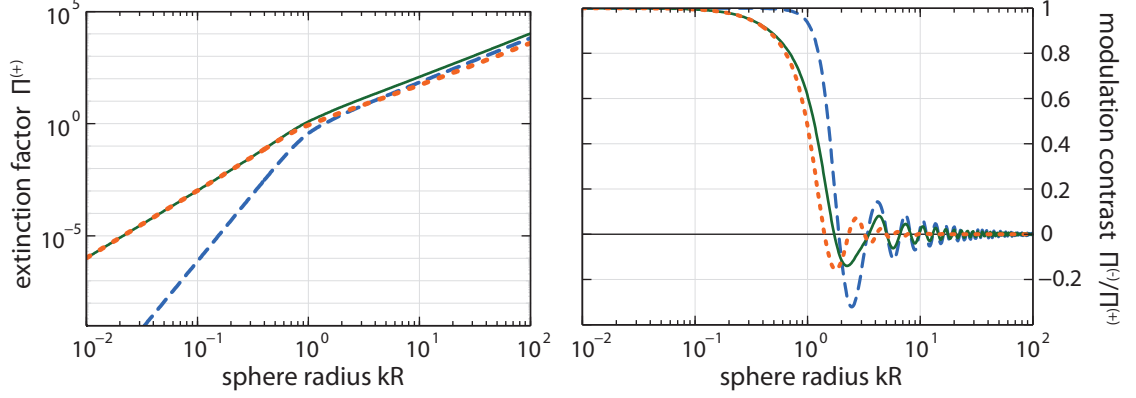


Figure 2.9. Mean value (left) and modulation (right) of the UV light extinction power of gold spheres as a function of the sphere radius. We use the bulk permittivity of gold [50], $\epsilon_{\text{Au}} = 0.9 + 3.2i$ at $\lambda = 157$ nm. The solid, the dashed, and the dotted lines correspond to the extinction, the scattering, and the absorption power, respectively. The mean value on the left diagram is plotted in dimensionless units $\pi I_0/k^2$ relative to the field intensity I_0 , as given by the $\Pi^{(+)}$ -factors in (2.128). The modulation contrast on the right is given by the ratio of the modulation amplitude and the mean value.

It is once again easy to verify that the dipolar values (2.7) and (2.8) for the absorbed and scattered power are assumed in the limit $kR \ll 1$, with the polarizability given by (2.122).

Similar expressions hold in the case of a Gaussian standing-wave mode. The multipole expansion in (2.126) then includes corrections due to the finite Gaussian waist w , as listed in Appendix A.5. In many practical situations, however, one is only interested in the standing-wave modulation of the scattering and absorption power as a function of the on-axis coordinate z_0 . If we neglect corrections of the order of $1/kw$, then formula (2.127) applies also to the Gaussian mode; we must simply append the Gaussian mode profile to the field intensity, $I_0 \rightarrow I(x_0, y_0) = c\epsilon_0 |E_0|^2 \exp[-2(x_0^2 + y_0^2)/w^2]/2$.

Figure 2.9 illustrates the standing-wave light extinction as a function of the radius for gold spheres at the UV wavelength $\lambda = 157$ nm ($\epsilon_{\text{Au}} = 0.9 + 3.2i$ is taken from [50]). The solid line on the left panel represents the offset factor $\Pi_{\text{ext}}^{(+)}$, that is, the z_0 -averaged extinction power (2.127) divided by $\pi I_0/k^2$, as a function of the radius on a logarithmic scale. The dashed and the dotted line represent the offset factors of the scattered power and the absorbed power, respectively. The mean absorption power grows like the volume, in proportion to $(kR)^3$, when the field fully penetrates the sphere in the subwavelength regime, $kR < 1$. The Rayleigh scattering power, which scales like $(kR)^6$, is strongly suppressed in this regime. The scattering contribution slowly takes over for larger radii, where the total extinction scales like the sphere surface, in proportion to $(kR)^2$. Absorption and reflection prevent the light field from entering deeply into the large sphere. The varying power laws in kR are nicely visible in the double-logarithmic plot.

The right panel in Figure 2.9 shows the contrast of the z_0 -modulation, $\Pi^{(-)}/\Pi^{(+)}$, for the extinction power (solid), the scattering power (dashed), and the absorption power (dotted). It starts at unity in the point-particle limit, decreases to smaller values and oscillates finally between positive and negative values. We find that the standing-wave modulation is strongly suppressed once the particle extends over more than a single wavelength. Note that a negative value means that the sphere scatters more light when it is centered at a node of the standing wave. This can be explained

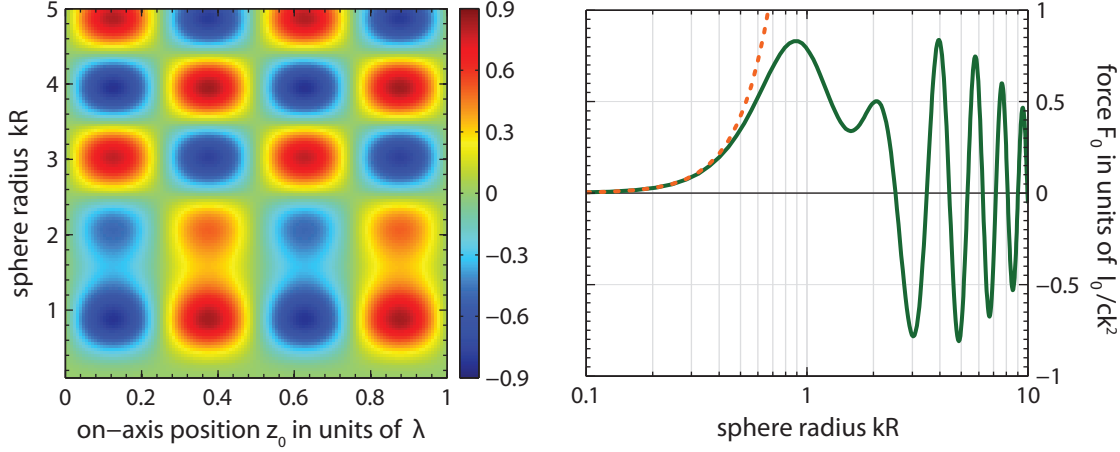


Figure 2.10. On-axis force on finite-size gold spheres in a vacuum-UV standing-wave field ($\lambda = 157$ nm, $\epsilon_{\text{Au}} = 0.9 + 3.2i$), as predicted by the Mie expression (2.130). The left panel is a density plot of the force versus the center position z_0 (in units of λ) and the normalized radius $kR = 2\pi R/\lambda$ of the sphere. The right panel depicts the maximum force with respect to z_0 as a function of the radius. The solid line represents the result of the full Mie calculation, whereas the dotted line corresponds to the point-particle approximation. The force data are plotted in natural units relative to the field intensity, $I_0/c k^2$.

by higher multipole (e.g. the quadrupole) components which are more dominantly addressed at the field nodes.

2.3.1.2. Maxwell stress tensor and optical forces

The light-induced forces acting on a dielectric are related to the Maxwell stress tensor

$$\mathbf{T} = \epsilon_0 \left[\Re \{ \mathbf{E} \} \circ \Re \{ \mathbf{E} \} - \frac{\mathbb{I}}{2} \Re \{ \mathbf{E} \} \cdot \Re \{ \mathbf{E} \} \right] + \mu_0 \left[\Re \{ \mathbf{H} \} \circ \Re \{ \mathbf{H} \} - \frac{\mathbb{I}}{2} \Re \{ \mathbf{H} \} \cdot \Re \{ \mathbf{H} \} \right], \quad (2.129)$$

with $(\mathbf{a} \circ \mathbf{b})_{jk} = a_j b_k$ the dyadic product and \mathbb{I} the three-dimensional identity matrix. In general, the change of the momentum carried by the field inside a finite volume of free space is given by the corresponding surface integral of the stress tensor [34, 91]. This implies that, if we take that the dielectric spheres to be rigid [89], the time-averaged force acting on the center of mass reads as

$$\mathbf{F} = \frac{R^2}{2} \int d\Omega \Re \left\{ \epsilon_0 \left[(\mathbf{n} \cdot \mathbf{E}_{\text{ext}}) \mathbf{E}_{\text{ext}}^* - \frac{\mathbf{n}}{2} |\mathbf{E}_{\text{ext}}|^2 \right] + \mu_0 \left[(\mathbf{n} \cdot \mathbf{H}_{\text{ext}}) \mathbf{H}_{\text{ext}}^* - \frac{\mathbf{n}}{2} |\mathbf{H}_{\text{ext}}|^2 \right] \right\}. \quad (2.130)$$

The external fields in the integral are evaluated on the sphere surface, $\mathbf{r} = R\mathbf{n}$. The force is always proportional to the intensity parameter $I_0 = c\epsilon_0 |\mathbf{E}_0|^2/2$ of the input light mode \mathbf{E}_0 .

In the idealized case of a plane standing or running wave the force must point into the z -direction, and it can only depend on the coordinate z_0 of the sphere. Transverse force components are excluded due to the symmetry under x_0 - and y_0 -translations. The left panel in Figure 2.10 shows a density plot of the standing-wave force F_z on gold spheres as a function of z_0 and of the normalized sphere radius kR . I evaluated the integral (2.130) numerically, using the representation of the scattering field (2.119) and the expansion coefficients of a standing wave given in Appendix A.5. The

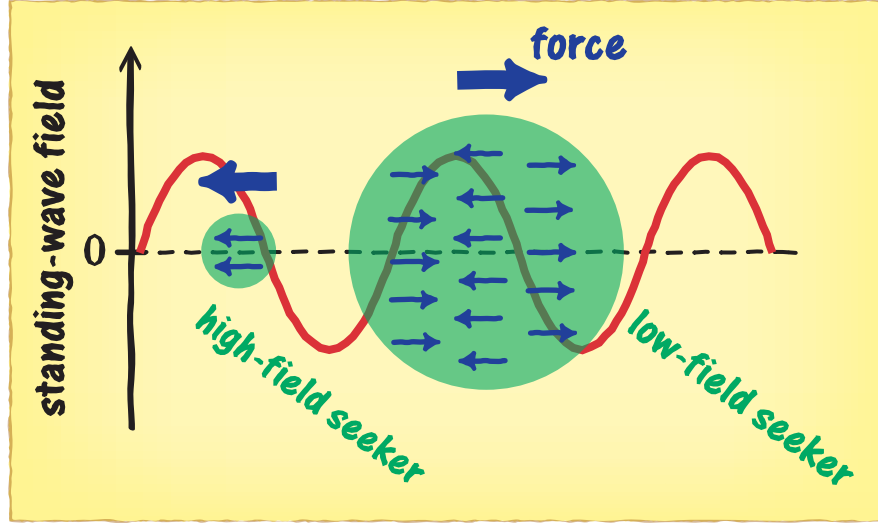


Figure 2.11. Sketch of the optical forces on a small and a large dielectric sphere in a standing-wave field. Both sphere centers are between an antinode and a node of the field. The net force on the small sphere points towards the high field since most of its volume is subject to the same field polarization and dipole force. The large sphere experiences a net force towards the low field. Different parts of the sphere experience are subject to opposite field polarizations and are drawn to opposite directions.

force is given in proportion to the field intensity, that is, in units of $I_0/c\hbar^2$. We observe that the symmetry of the standing wave sets the z_0 -modulation of the force to be $F_z(z_0) = -F_0 \sin 2kz_0$, irrespective of the sphere size. In particular, the force is always zero at the nodes and antinodes of the field. At the same time, the radius R does affect the force amplitude F_0 significantly. The latter even flips its sign for $kR \gtrsim 2$, in clear contradiction to the behaviour of a polarizable point particle.

The disparate behaviour of point particles and extended spheres is more clearly seen on the right panel, where I have plotted the force amplitude $F_0 = F_z(-\lambda/8)$ versus the radius (solid line). I compare it to the maximum PPP force (dashed line), $F_{\text{PPP}} = 2\pi I_0 k R^3 \Re\{(\epsilon - 1)/(\epsilon + 2)\}/c$, which would be obtained if the sphere were approximated by a point-like particle with the polarizability (2.122). This approximation ceases to be valid already for $kR \gtrsim 0.5$. From this point on the force does not grow with the sphere volume any longer. We observe quite a contrary behaviour; the force term oscillates between positive and negative values. In other words, the sphere may become an *effective low-field seeker*. An explanation for this remarkable size effect is illustrated in Figure 2.11 depicting a small and a large sphere placed in between a node and an antinode of the standing-wave field. Suppose that we decompose each sphere into small volume elements, and assume that the individual elements are subject to the local dipole force (We neglect both the modification of the local field and the absorption inside the sphere). We arrive at the total force by adding the individual contributions. This leads to a high-field seeking behaviour of the small sphere because all constituents are drawn to the same antinode of the field. The net force on the large sphere, on the other hand, points to the low field, because different parts are drawn to opposite directions.

Let me now turn to the more realistic case of a Gaussian standing-wave mode with finite waist w . Here we must distinguish between the force F_z along the standing-wave axis and the non-vanishing off-axis forces $F_{x,y}$. Considering the former, we should merely expect small corrections to the ideal

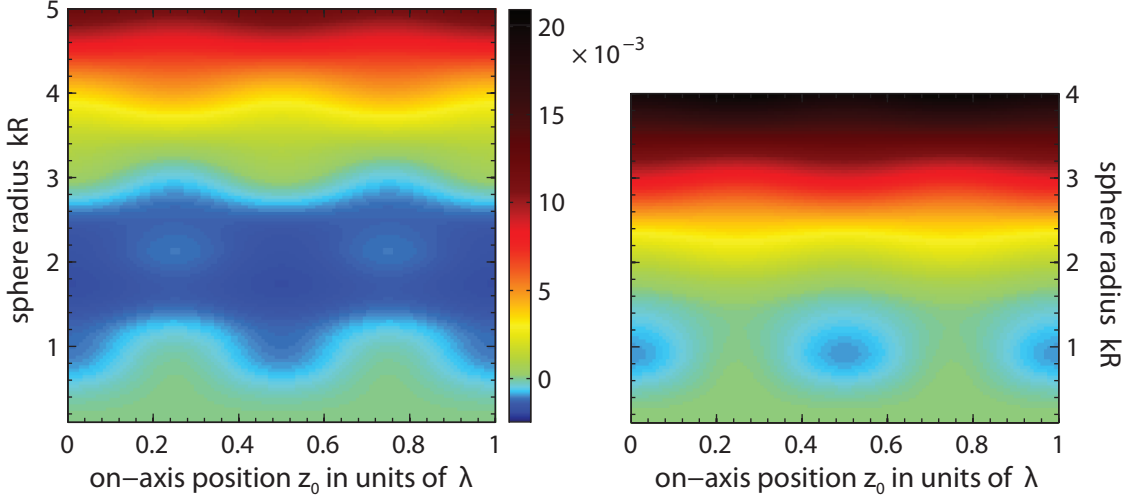


Figure 2.12. Density plot of the transverse forces on gold spheres in a Gaussian standing-wave mode versus the sphere radius and the on-axis position. The left and the right panel correspond to the force components $F_{x,y}$ in the direction of and perpendicular to the electric field polarization, respectively. They are obtained from a Mie-theory calculation ($\lambda = 157$ nm, $\epsilon_{\text{Au}} = 0.9 + 3.2i$) and evaluated in units of $I_0/c k^2$ at the sphere coordinates $x_0 = y_0 = w/2$. I use the same axes and color scaling for better comparison, and so the right panel is restricted to appropriate axis boundaries.

standing-wave modulation studied before. This follows by comparing the multipole expansion of the ideal standing wave with the Gaussian one, as given in Appendix A.5. Corrections to the standing-wave modulation are of the order of the waist parameter $1/kw \ll 1$, and we may neglect them for most practical purposes³⁷. In this case we may again use the standing-wave results after replacing the standing-wave intensity parameter I_0 by the local intensity $I(x_0, y_0)$ in the Gaussian mode.

The same argument does not apply to the off-axis transverse forces $F_{x,y}$ which are by themselves terms of the order of $1/kw$. A numerical evaluation of the transverse forces reveals some peculiar size effects which become evident when we compare the numerical results with the subwavelength approximation based on the polarizability expression (2.122),

$$\begin{aligned} \begin{pmatrix} F_x^{(\text{PPP})}(\mathbf{r}_0) \\ F_y^{(\text{PPP})}(\mathbf{r}_0) \end{pmatrix} &= - \begin{pmatrix} x_0 \\ y_0 \end{pmatrix} \frac{4\pi R^3 I_0}{c w^2} \Re \left\{ \frac{\epsilon - 1}{\epsilon + 2} \right\} e^{-2(x_0^2 + y_0^2)/w^2} (1 + \cos 2kz_0) \\ &= - \frac{2F_{\text{PPP}}}{kw^2} e^{-2(x_0^2 + y_0^2)/w^2} \left[\begin{pmatrix} x_0 \\ y_0 \end{pmatrix} + \begin{pmatrix} x_0 \\ y_0 \end{pmatrix} \cos 2kz_0 \right]. \end{aligned} \quad (2.131)$$

At first one might think that, if one took the average of the transverse force over one period of the standing wave, the point-particle approximation would be still valid for particles that are larger than the wavelength, and yet smaller than the waist. This would be a wrong assertion, as demonstrated in Figure 2.12, once again for the exemplary case of gold spheres in vacuum-UV light. Here I plot the x -force (left) and the y -force (right) at $x_0 = y_0 = w/2$, as obtained from the full Mie calculation,

³⁷ This argument holds as long as the sphere is not too far away from the focus of the Gaussian mode. The reason is that the representation of the Gaussian TEM₀₀ mode given in Appendix A.2 ceases to be valid for far-off center coordinates $|\mathbf{r}_0| \gg w$. This limit should hardly be of relevance in any practical implementation.

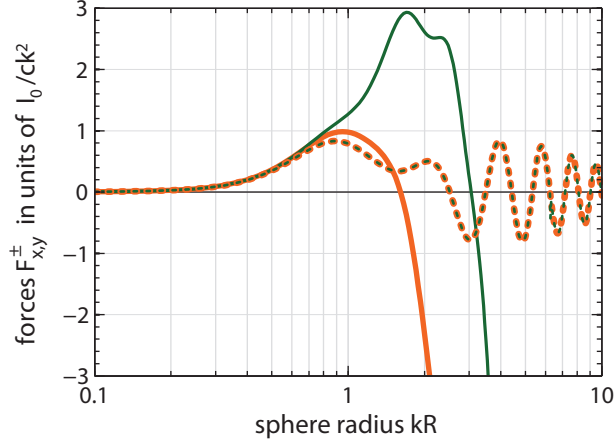


Figure 2.13. Offset factors $F_{x,y}^{(+)}$ (solid lines) and modulation factors $F_{x,y}^{(-)}$ (dotted lines) of the transverse forces (2.132) as a function of the normalized radius kR of gold spheres in a Gaussian standing-wave mode ($\lambda = 157$ nm, $\epsilon_{Au} = 0.9 + 3.2i$). The data were computed with help of the Mie expression (2.130) and plotted in units of $I_0/c k^2$. The dark green curves correspond to the x -direction, which is also the main polarization direction of the electric field. The light orange curves represent the y -direction. The two modulation factors (dashed) are almost identical, except for small numerical uncertainties.

versus the sphere radius R and the on-axis coordinate z_0 . The forces are again plotted in units of $I_0/c k^2$. I have assumed a realistic waist of $w = 100 \lambda$. Judging from an extensive numerical analysis and from the plotted data, I have found a similar functional dependence of the two components $F_{x,y}$ of the Mie force (2.130) on \mathbf{r}_0 as in the point-particle approximation,

$$\begin{pmatrix} F_x(\mathbf{r}_0) \\ F_y(\mathbf{r}_0) \end{pmatrix} = -\frac{2}{kw^2} e^{-2(x_0^2+y_0^2)/w^2} \left[\begin{pmatrix} x_0 F_x^{(+)} \\ y_0 F_y^{(+)} \end{pmatrix} + \begin{pmatrix} x_0 F_x^{(-)} \\ y_0 F_y^{(-)} \end{pmatrix} \cos 2kz_0 \right]. \quad (2.132)$$

Figure 2.12 shows that the force components differ significantly from a point-particle behaviour at sphere radii $kR \gtrsim 1$. At smaller radii, the average force is negative (i.e. pointing inwards the center of the Gaussian mode) and exhibits a pronounced standing-wave modulation. Then, however, the modulation dies off quickly, and we notice a non-recurring inversion of the sign once the sphere diameter approaches the wavelength, $kR \lesssim \pi$. The gold spheres turn into low-field seekers; they are effectively pushed away from the center of the Gaussian mode profile, although their radii are still much smaller than the mode waist. Moreover, we observe that the cylindrical symmetry breaks down, since the x - and the y -components are no longer the same.

We see this more clearly in Figure 2.13, where the four terms $F_{x,y}^{(\pm)}$ extracted from a numerical evaluation of (2.132) are plotted as a function of R . The differences between the two transverse directions indicate the presence of non-conservative forces. If the two transverse components were identical, $F_x^{(\pm)} = F_y^{(\pm)}$, and if the modulation factors matched the on-axis force factor, $F^{(-)} = F_0$, then the force could be written as the gradient of the potential $V(\mathbf{r}_0) = -\exp[-2(x_0^2 + y_0^2)/w^2] (F^{(+)} + F^{(-)} \cos 2kz_0)/2k$. Evidently, no such potential exists for (sufficiently large) gold spheres in the Gaussian mode. The non-conservativity is related to the radiation pressure induced by the absorption and free-space scattering of light, and it leads to notable asymmetries and a low-field seeking behaviour at large radii, as shown in the diagram.

One important practical consequence is the following: One cannot deduce the optical potential of wavelength-sized particles coupled to Gaussian modes from the electromagnetic force alone. We must find a different method to extract the position-dependent coupling energy between such a particle and a high-finesse cavity mode in order to assess cavity-induced dissipation effects. I will deal with this issue in Section 2.3.3. Before that, let me briefly discuss the effect of optical standing-wave gratings on extended spherical particles.

2.3.2. Optical standing-wave gratings

With the extensive discussion of Mie theory in the preceding section at hand, I will now generalize the model of optical standing-wave gratings developed in Section 2.1.4. There I discussed how a coherent standing-wave field can act as a diffraction grating for matter-wave states of polarizable point particles in the limit of short interaction times. Two separate processes can contribute to the diffraction effect: The periodic phase modulation of the matter wave due to the action accumulated in the optical dipole potential and the amplitude modulation that occurs if the absorption of single photons depletes the matter-wave state.

In the following, I will generalize both effects to dielectric spheres of finite radius. We will see that the effective grating modulation becomes less effective with growing particle size. A more detailed analysis of the consequences for matter-wave interferometry will be given in Chapter 3.

Note that the grating modulation acts along the standing-wave axis, and we are only concerned with the reduced one-dimensional z -state of the matter waves. The latter are assumed to interact sufficiently shortly with the light field such that any transverse forces and corrections due to the finite mode waist can be safely omitted. We can therefore reduce our Mie-theory considerations to the case of an ideal standing wave with a Gaussian intensity profile.

2.3.2.1. Phase modulation effect

The phase modulation is described by the eikonal phase factor (2.36) for a point particle. If we neglect any z -motion during interaction time we arrive at the standing-wave expression (2.37). It is equivalent to the transformation rule $\langle z|\psi\rangle \mapsto \exp[i(\phi_0/2)\cos 2kz]\langle z|\psi\rangle$ for a given matter-wave state $|\psi\rangle$ up to a constant global phase. The term ϕ_0 denotes the eikonal phase collected at the antinodes of the standing-wave field.

Fortunately, the transformation rule can be adopted to the case of dielectric spheres of larger radii without further trouble. The reason is that, according to Section 2.3.1.2, the on-axis force on a dielectric sphere is always of the form $F_z(z) = -F_0 \sin 2kz$, if higher-order corrections by the Gaussian mode profile are neglected. Since there are no transverse forces to be considered either, we are left in a one-dimensional situation with no non-conservative corrections. The force can be integrated to obtain an expression for the optical potential (up to an arbitrary constant), $V(z) = -(F_0/2k)\cos 2kz$. The force factor F_0 must be computed by means of the Mie formula (2.130); it will be proportional to the standing-wave intensity $I_0 = c\epsilon_0 |E_0|^2/2$ at the antinodes.

Comparing this to the point-particle model in Section 2.1.4.1, we must simply substitute

$$\Re\{\chi\} \mapsto \frac{4F_0}{k|E_0|^2} \equiv \frac{2c\epsilon_0}{k} f_0 \quad (2.133)$$

in all the eikonal phase terms ϕ_0 to generalize from point particles to finite-size spheres. Here I have removed the field intensity using the convenient notation $F_0 = f_0 I_0$ in terms of the factor f_0 .

2.3.2.2. Amplitude modulation effect

Standing-wave gratings can modulate the amplitude of matter waves by optical depletion if the absorption of one or a few photons ionizes, fragments, or removes a particle by other means from the matter-wave ensemble. I have discussed in Section 2.1.4.2 that the corresponding transmission probability can be obtained in a Poissonian model from the mean number of absorbed photons. For point particles, this quantity can be written as $\bar{n}(z) = (n_0/2)(1 + \cos 2kz)$, where $n_0 \propto \sigma_{\text{abs}} I_0$. The offset factor and the z -modulation factor are the same in this expression, and no photons are absorbed in the field nodes.

This is different in the case of larger spheres. Here we must distinguish between the offset and the standing-wave modulation. We must replace the PPP-absorption power $\sigma_{\text{abs}} I_0$ by the Mie expression $P_{\text{abs}}(z) = P_{\text{ext}}(z) - P_{\text{sca}}(z)$, as obtained from (2.127). We arrive at the form $\bar{n}(z) = n_+ + n_- \cos 2kz$ with two different coefficients n_{\pm} . The transformation $n_0/2 \mapsto n_{\pm}$ from the PPP-expressions given in Section 2.1.4.2 to the generalized form for finite spheres is done by substituting the absorption cross section, $\sigma_{\text{abs}} \mapsto 2\pi\Pi_{\text{abs}}^{(\pm)}/k^2$. The absorption terms $\Pi_{\text{abs}}^{(\pm)} = \Pi_{\text{ext}}^{(\pm)} - \Pi_{\text{sca}}^{(\pm)}$ are determined by the Mie expressions (2.128).

Putting everything together, the following grating modulation parameters must be used for spherical particles passing a thin standing-wave beam of input laser power P_L and waist w_y at the velocity v :

$$\tilde{\phi}_0 = \frac{8f_0 P_L}{\sqrt{2\pi}\hbar k v w_y}, \quad n_{\pm} = \frac{4\sqrt{2\pi}\Pi_{\text{abs}}^{(\pm)} P_L}{\hbar c k^3 v w_y}. \quad (2.134)$$

If the grating is realized by a short laser pulse of energy E_L and spot area a_L , we find

$$\tilde{\phi}_0 = \frac{4f_0 E_L}{\hbar k a_L}, \quad n_{\pm} = \frac{4\pi\Pi_{\text{abs}}^{(\pm)} E_L}{\hbar c k^3 a_L}. \quad (2.135)$$

I will mostly refer to the case of single-photon depletion, where the absorption of one photon already removes the particle from the ensemble. Then the grating transmission function (2.41), which describes the matter-wave state transformation $\langle z|\psi\rangle \mapsto t(z)\langle z|\psi\rangle$, reads as

$$t(z) = \exp\left[-n_+ + \left(i\frac{\tilde{\phi}_0}{2} - n_-\right)\cos 2kz\right]. \quad (2.136)$$

We notice here a general complication for wavelength-sized spheres: While the position-averaged overall transmission probability decreases exponentially with the term n_+ , the modulation contrast between the nodes and the antinodes of the grating depends on n_- . As seen for the exemplary case of gold spheres in vacuum-UV gratings in Figure 2.9, the ratio $n_-/n_+ = \Pi_{\text{abs}}^{(-)}/\Pi_{\text{abs}}^{(+)}$ is strongly suppressed for large spheres. That is to say, a pronounced optical grating mask goes along with a massive loss of matter-wave signal in the case of wavelength-large spheres. This will impose a hard mass limitation of optical matter-wave interferometry, as will be discussed in Chapter 3.

Another limitation might arise from the decoherence associated with the increased scattering³⁸ of photons at large dielectric spheres. This side effect does not generalize in a straightforward manner from the point-particle case discussed in Section 2.1.4.3 to large spheres. The reason is that we cannot adopt the local field coupling model, which describes the momentum transfer by scattering and absorption in terms of Lindblad master equations $\mathcal{L}_{\text{sca,abs}}$, if the coupling extends over a large volume. A proper description of decoherence would, for instance, require a rigorous multipath scattering model of light at an extended dielectric object, as presented in [86]. This goes beyond the scope of the present work. As I will show later, the proposed scheme of high-mass matter-wave interferometry [10, 11] studied in the present work is already more or less confined to the subwavelength regime due to the above mentioned tradeoff between transmission and modulation at optical depletion gratings.

2.3.3. Slowing and trapping of microspheres by a cavity

Let me conclude the present chapter with a final glance at the cavity-induced slowing of polarizable particles. I have started from a classical one-dimensional model of the mechanical action of a driven cavity mode on a polarizable particle in Section 2.1.3. There I could simulate the slowing and trapping of a strongly coupled particle in a high-finesse standing-wave cavity, as plotted in Figure 2.2. Later I reassessed the effect in a more realistic scenario with molecules and nanoclusters, which exhibit a much weaker coupling strength and slowing rate. This led to the rigorous weak-coupling quantum model in Section 2.2.

We are now in a position to be able to reconsider the strong-coupling situation. Mie theory offers us the means to describe the optical properties of realistic particles that are sufficiently extended to couple strongly enough to be eventually trapped by a cavity. Let me show that it is indeed feasible in a realistic setting to trap wavelength-sized dielectric spheres crossing a strongly pumped cavity mode. The corresponding experiments are prepared and conducted in the labs of my group in Vienna and elsewhere [25].

I resort to the exemplary case of silicon spheres ($\rho_{\text{Si}} = 2300 \text{ kg/m}^3$) at the IR telecommunications wavelength $\lambda = 1560 \text{ nm}$. The reason is that the silicon material is highly refractive and almost perfectly transparent at this wavelength. No heating losses or absorption-induced diffusion need to be taken into account. I will estimate the sphere permittivity by the bulk value $\epsilon_{\text{Si}} = 12.1$ [50]. Moreover, I will consider the following demanding but feasible resonator configuration for the cavity [56]: Two 25 mm-curved high-reflectivity mirrors shall be placed at 1 mm distance, constituting a resonator with a narrow linewidth $\kappa = 1 \text{ MHz}$. The TEM_{00} standing-wave resonator mode shall have the waist $w = 40 \mu\text{m}$, which results in the mode volume $V = 0.0013 \text{ mm}^3$. (See Appendix A.2 for details on the Gaussian mode.) It is driven by a laser with several Watts of continuous-wave input power.

For a preliminary assessment of the coupling let us assume that the silicon spheres of radius R are described by the subwavelength polarizability (2.122). Then both the cavity resonance shift and the optical dipole force depend on a single coupling rate parameter, $U_0 = -2\pi\omega (R^3/V) (\epsilon_{\text{Si}} - 1) / (\epsilon_{\text{Si}} + 2)$. A coupling rate of, say, $U_0 = -\kappa$ would correspond to $R = 59 \text{ nm}$. The subwavelength approximation may still seem reasonable in this case, which represents the bottom end of the strong-

³⁸ Decoherence by absorption becomes relevant, too, but only if the optical depletion effect requires more than one photon to be triggered.

coupling regime. Larger spheres should also be taken into consideration. Hence, before we can continue solving the classical cavity-particle equations of motion, we must address a yet omitted issue: The effect of the particle on the cavity field.

2.3.3.1. Cavity resonance shift induced by microspheres

Throughout the preceding sections I applied Mie theory to study the optical forces and the light extinction properties of large spherical particles. The Mie ansatz is based on a stationary scattering situation: One starts from a given field configuration $\{\mathbf{E}_0, \mathbf{H}_0\}$ in the absence of the scatterer, which is, in principle, determined by some asymptotic boundary conditions at infinite distance. Parts of these fields are scattered off the sphere in the form of outgoing multipolar waves $\{\mathbf{E}_{\text{sca}}, \mathbf{H}_{\text{sca}}\}$, which do not involve the asymptotic boundary conditions.

This is where the Mie ansatz runs into problems. By construction, it cannot account for the modified boundary conditions in a finite-size resonator due to the presence of the sphere. On the other hand, we know that small refractive modifications within the resonator configuration amplify to a substantial change of the intra-cavity light that cycles many times between the mirrors. We did not run into these difficulties in the point-particle limit, since the optical dipole potential was there responsible for both the light-induced forces and the cavity resonance shift. In the present case, the optical potential cannot be deduced from the light force anymore.

One way to resolve this issue, at least to a reasonable degree of approximation, is to invoke the principles of cavity perturbation theory [92]. Let us assume that the presence of the dielectric sphere leads to a small shift of the cavity resonance frequency, $|\delta\omega| \ll \omega$, which modifies the Maxwell equations in the resonator volume,

$$\nabla \times \begin{pmatrix} \mathbf{E}_0 \\ \mathbf{H}_0 \end{pmatrix} = i\omega \begin{pmatrix} \mu_0 \mathbf{E}_0 \\ -\varepsilon_0 \mathbf{H}_0 \end{pmatrix} \rightarrow \nabla \times \begin{pmatrix} \mathbf{E} \\ \mathbf{H} \end{pmatrix} = i(\omega + \delta\omega) \begin{pmatrix} \mu_0 \mathbf{E}_0 \\ -\varepsilon(\mathbf{r}) \varepsilon_0 \mathbf{H}_0 \end{pmatrix}. \quad (2.137)$$

Here I denote by $\{\mathbf{E}, \mathbf{H}\}$ the intra-cavity fields in the presence of the sphere. The permittivity $\varepsilon(\mathbf{r})$ is piecewise constant; it assumes ε_{Si} inside the sphere and unity outside. By making use of the vector identity $\nabla \cdot (\mathbf{a} \times \mathbf{b}) = \mathbf{b} \cdot (\nabla \times \mathbf{a}) - \mathbf{a} \cdot (\nabla \times \mathbf{b})$ we can combine the above four equations to obtain the two mixed identities

$$\nabla \cdot (\mathbf{H} \times \mathbf{E}_0^*) = -i(\omega + \delta\omega) \varepsilon(\mathbf{r}) \varepsilon_0 \mathbf{E}_0^* \cdot \mathbf{E} + i\omega \mu_0 \mathbf{H}_0^* \cdot \mathbf{H}, \quad (2.138)$$

$$\nabla \cdot (\mathbf{H}_0^* \times \mathbf{E}) = i\omega \varepsilon_0 \mathbf{E}_0^* \cdot \mathbf{E} - i\omega \mu_0 \mathbf{H}_0^* \cdot \mathbf{H}. \quad (2.139)$$

These, in turn, can be combined to

$$-i\nabla \cdot (\mathbf{H} \times \mathbf{E}_0^* + \mathbf{H}_0^* \times \mathbf{E}) = \omega \varepsilon_0 [1 - \varepsilon(\mathbf{r})] \mathbf{E}_0^* \cdot \mathbf{E} - \delta\omega [\varepsilon(\mathbf{r}) \varepsilon_0 \mathbf{E}_0^* \cdot \mathbf{E} + \mu_0 \mathbf{H}_0^* \cdot \mathbf{H}]. \quad (2.140)$$

At this point we can explicitly use the cavity boundary conditions by integrating the expression over the resonator volume V . It follows from Gauss' theorem that the left hand side must vanish due to the vanishing boundary conditions at the mirror surfaces. We are left with an equation that determines the shift $\delta\omega$ from the fields,

$$\frac{\delta\omega}{\omega} = \frac{-\varepsilon_0 \int_{r < R} d^3r \Re \{ (\varepsilon_{\text{Si}} - 1) \mathbf{E}_{\text{int}} \cdot \mathbf{E}_0^* \}}{\int_V d^3r \Re \{ \varepsilon(\mathbf{r}) \varepsilon_0 \mathbf{E} \cdot \mathbf{E}_0^* + \mu_0 \mathbf{H} \cdot \mathbf{H}_0^* \}}, \quad (2.141)$$

where I have taken the real part to arrive at physical expressions in the end. The integral in the numerator extends merely over the polarization density $\mathbf{P} = \epsilon_0 (\epsilon_{\text{Si}} - 1) \mathbf{E}_{\text{int}}$ inside the sphere. The denominator can be rewritten as

$$\int_V d^3r \Re \{ \epsilon \epsilon_0 \mathbf{E} \cdot \mathbf{E}_0^* + \mu_0 \mathbf{H} \cdot \mathbf{H}_0^* \} = 4H_f + \int_V d^3r \Re \{ \epsilon_0 [\epsilon \mathbf{E} - \mathbf{E}_0] \cdot \mathbf{E}_0^* + \mu_0 [\mathbf{H} - \mathbf{H}_0] \cdot \mathbf{H}_0^* \}, \quad (2.142)$$

with $H_f = \hbar \omega |\alpha|^2$ the free energy of the unmodified cavity field. We are still not able to compute $\delta\omega$ in practice since we must know the exact form of the modified fields $\{\mathbf{E}, \mathbf{H}\}$, which depend on the frequency shift, too. If we regard the sphere as a small perturbation, however, we should not only expect that the relative shift $\delta\omega/\omega$ is small, but also that the fields are hardly modified in most of the resonator volume. We can therefore neglect the addition to the field energy term in the denominator, and we can insert the Mie expression for the internal field \mathbf{E}_{int} from Appendix A.6, to obtain the approximate formula

$$\frac{\delta\omega}{\omega} = -\frac{\epsilon_0}{4H_f} \int_{r < R} d^3r \Re \{ (\epsilon_{\text{Si}} - 1) \mathbf{E}_{\text{int}} \cdot \mathbf{E}_0^* \}. \quad (2.143)$$

A tedious but straightforward calculation using the multipole expansion properties from Appendix A.5, and a few additional integration steps³⁹, yield the expansion

$$\delta\omega = \frac{-\omega}{2k^3 V |E_0|^2} \sum_{\ell, m} \left[\Im \{ \beta_\ell \} \left| C_{\ell, m}^{(\text{E})} \right|^2 + \Im \{ \alpha_\ell \} \left| C_{\ell, m}^{(\text{M})} \right|^2 \right]. \quad (2.144)$$

Here I have used that ϵ_{Si} is real. If we focus again on the standing-wave modulation of the resonance shift, then we can neglect higher-order corrections in the waist w of the Gaussian mode profile. The resonance shift reduces to the simple form

$$\begin{aligned} \delta\omega(\mathbf{r}_0) &= \frac{1}{2} e^{-2(x_0^2 + y_0^2)/w^2} \left[U^{(+)} + U^{(-)} \cos 2kz_0 \right], \\ U^{(\pm)} &= -\frac{\pi\omega}{k^3 V} \sum_{\ell=1}^{\infty} (\pm)^\ell (2\ell + 1) \Im \{ \alpha_\ell \pm \beta_\ell \}, \end{aligned} \quad (2.145)$$

with \mathbf{r}_0 the position of the sphere center. The form is very similar to the expression (2.127) for the extinction power in a standing wave. It is easily checked that the two coupling rates $U^{(\pm)}$ reduce to the point-particle value in the limit of small radii, $U^{(\pm)} \approx U_0 = -2\pi R^3 \omega (\epsilon_{\text{Si}} - 1) / (\epsilon_{\text{Si}} + 2) V$.

Similar effective coupling rates can be defined for the on-axis z -force,

$$F_z(\mathbf{r}_0) = \hbar k U_z |\alpha|^2 \exp \left[-2 \frac{x_0^2 + y_0^2}{w^2} \right] \sin 2kz_0, \quad (2.146)$$

³⁹ The following integral identities for spherical Bessel functions must be used [63]:

$$\begin{aligned} \int_0^X dx x^2 j_\ell(x) j_\ell(nX) &= \frac{X^2}{1-n^2} [j_{\ell+1}(X) j_\ell(nX) - n j_\ell(X) j_{\ell+1}(nX)] \\ \int_0^X dx \{ \ell(\ell+1) j_\ell(x) j_\ell(nX) + [x j_\ell(x)]' [x j_\ell(nX)]' \} &= \frac{X^2}{1-n^2} [n^2 j_{\ell+1}(X) j_\ell(nX) - n j_\ell(X) j_{\ell+1}(nX)] \\ &\quad + (\ell+1) X j_\ell(X) j_\ell(nX) \end{aligned}$$

as well as for the transverse forces $F_{x,y}(\mathbf{r}_0)$. In the latter case, the coupling rates are determined from (2.12) by the terms $F_{x,y}^{(\pm)} = -\hbar k |\alpha|^2 U_{x,y}^{(\pm)}$. All the various coupling rates $U^{(\pm)}$, U_z , $U_{x,y}^{(\pm)}$ reduce to U_0 in the limit $R \rightarrow 0$. Any substantial difference from U_0 indicates a breakdown of the point-particle approximation. I list the coupling rates of various silicon sphere sizes in Table 2.2, which was generated from a Mie calculation based on the given cavity parameters. We observe that the point-particle breakdown occurs already at relatively small radii compared to the wavelength. This is due to the large refractive index of silicon. The table also contains the light extinction rate parameters $\gamma_{\text{ext}}^{(\pm)} = 2\pi c \Pi_{\text{ext}}^{(\pm)} / k^2 V$, as determined by the Mie expressions (2.127) and (2.128).

We notice that the point-particle limit already fails at $R = 60$ nm. At the same time, however, all the offset terms (+) and modulation terms (−) of the coupling rates are practically identical for spheres smaller than $R = 200$ nm; the cylindrical symmetry remains valid. In this quasi-conservative size regime the cavity resonance shift and the mechanical action of the light field on the spheres are fully characterized by the effective optical potential

$$V(\mathbf{r}_0) = \frac{1}{2} \hbar |\alpha|^2 \exp \left[-2 \frac{x_0^2 + y_0^2}{w^2} \right] \left(U^{(+)} + U^{(-)} \cos 2kz_0 \right). \quad (2.147)$$

2.3.3.2. Classical simulation of slowing and trapping

With the relevant parameters at hand we can finally draw our attention to the cavity-induced slowing effect in a realistic strong-coupling scenario with silicon spheres. The effect will be studied in the classical regime, far above the quantum limit of motion. Hence, I will not account for any kind of diffusion or other quantum corrections, and I base my considerations on the coupled classical equations of motion for the center-of-mass $\mathbf{r}_0(t)$ of the particle and the intra-cavity field $\alpha(t)$. I have derived a set of equations for the one-dimensional point-particle case in Section 2.1.3. Using

Table 2.2. Table of light coupling and extinction parameters for silicon spheres of different radii ($\epsilon_{\text{Si}} = 12.1$) in a standing-wave cavity at the IR wavelength $\lambda = 1560$ nm. We assume a Gaussian mode of waist $w = 40$ μm and volume $V = 0.0013$ mm^3 .

Radius	30 nm	60 nm	150 nm	200 nm	250 nm
m in amu	1.57×10^8	1.25×10^9	1.96×10^{10}	4.64×10^{10}	9.07×10^{10}
ω_r in mHz	3.29	0.411	0.0263	0.0111	5.68×10^{-3}
$U^{(+)}$ in MHz	−0.130	−1.09	−23.7	−103	−24.0
$U^{(-)}$ in MHz	−0.128	−1.02	−13.5	10.2	−122
U_z in MHz	−0.128	−1.02	−13.5	12.0	−79.1
$U_x^{(+)}$ in MHz	−0.130	−1.09	−23.7	−105	−75.5
$U_x^{(-)}$ in MHz	−0.128	−1.02	−13.5	12.0	−79.1
$U_y^{(+)}$ in MHz	−0.130	−1.09	−23.8	−101	16.9
$U_y^{(-)}$ in MHz	−0.128	−1.02	−13.5	12.0	−79.1
$\gamma_{\text{ext}}^{(+)}$ in MHz	2.41×10^{-3}	0.0160	5.36	56.1	208
$\gamma_{\text{ext}}^{(-)}$ in MHz	2.41×10^{-3}	0.0160	4.74	−2.18	94.5

the results from Mie theory, the equations (2.30) and (2.31) can be readily generalized to the case of silicon spheres of mass $m = 4\pi\rho_{\text{Si}}R^3/3$ in three dimensions,

$$\partial_t \alpha = \eta - \left\{ i\Delta + \kappa + \frac{g(\sqrt{x_0^2 + y_0^2})}{2} \left[iU^{(+)} + \frac{\gamma_{\text{ext}}^{(+)}}{2} + \left(iU^{(+)} + \frac{\gamma_{\text{ext}}^{(+)}}{2} \right) \cos 2kz_0 \right] \right\} \alpha, \quad (2.148)$$

$$\partial_t^2 \begin{pmatrix} x_0 \\ y_0 \end{pmatrix} = \frac{2\hbar}{mw^2} |\alpha|^2 g(\sqrt{x_0^2 + y_0^2}) \left[\begin{pmatrix} x_0 U_x^{(+)} \\ y_0 U_y^{(+)} \end{pmatrix} + \begin{pmatrix} x_0 U_x^{(-)} \\ y_0 U_y^{(-)} \end{pmatrix} \cos 2kz_0 \right], \quad (2.149)$$

$$\partial_t^2 z_0 = \frac{\hbar k}{m} U_z |\alpha|^2 g(\sqrt{x_0^2 + y_0^2}) \sin 2kz_0. \quad (2.150)$$

Here, the Gaussian profile is denoted by $g(r_0) = \exp(-2r_0^2/w^2)$. Note that the light extinction effect merely adds to the cavity loss channel since I neglect its contribution to momentum diffusion. The driving term $\eta = \sqrt{2\kappa P_{\text{in}}/\hbar\omega}$ is related to the power P_{in} of the driving laser. In the following, I shall fix the cavity-pump detuning to $\Delta = \kappa$, which is where the Lorentzian intra-cavity intensity is most sensitive to the refractive index change induced by the particle.

Table 2.2 shows that the strong-coupling condition is already fulfilled for relatively small spheres. We may restrict our considerations to the quasi-conservative size regime, where the forces are symmetric and the angular momentum $L = x_0 p_y - y_0 p_x$ is conserved. This reduces the equations (2.149) and (2.150) to two equations of motion for the radius $r_0(t)$ and the axial position $z_0(t)$ in cylindrical coordinates, $\mathbf{r}_0 = (r_0, \varphi_0, z_0)$. They evolve under the forces resulting from the effective radial potential

$$V_{\text{eff}}(r_0, z_0) = \frac{\hbar |\alpha|^2}{2} g(r_0) \left(U^{(+)} + U^{(-)} \cos 2kz_0 \right) + \frac{L^2}{2mr_0^2} \quad (2.151)$$

The angular coordinate follows $\partial_t \varphi_0 = L/mr_0^2$. The centrifugal barrier in the effective potential prevents particles from reaching the center of focus if they impinge on the cavity mode with a finite impact parameter. Let us, for the moment, assume that the cavity adjusts instantaneously to the presence of the particle, so that we may set $\alpha = \eta/\Omega(r_0, z_0)$, with Ω the curly-bracketed term in (2.148). We are left with a strictly conservative motion in the adiabatic potential

$$V_{\text{ad}}(r_0, z_0) = \frac{\hbar \eta^2 g(r_0)}{2 |\Omega(r_0, z_0)|^2} \left(U^{(+)} + U^{(-)} \cos 2kz_0 \right) + \frac{L^2}{2mr_0^2}, \quad (2.152)$$

and no dissipation effect can occur. The potential is positive for sufficiently large or small r_0 , where the centrifugal term dominates. In between it may assume a minimum at negative values, depending on the light coupling parameters.

The adiabatic potential proves useful when discussing the conditions for radial slowing and trapping, in addition to the conventional standing-wave slowing of the z_0 -coordinate which we have found in Section 2.1.3. A trapping of both r_0 and z_0 means that the particle is captured in the Gaussian mode and that it orbits around the center of focus $r_0 = 0$ with a constant angular momentum, while it oscillates around a field antinode along the z -direction. If we assume that the z -coordinate is already trapped then the radial coordinate evolves approximately under the one-dimensional potential $V_{\text{ad}}(r_0, 0)$. In the purely conservative case, a particle would be accelerated towards the center, $r_0 = 0$, until it hits the centrifugal barrier and gets reflected. The particle would pass the cavity on a deflected trajectory in the xy -plane.

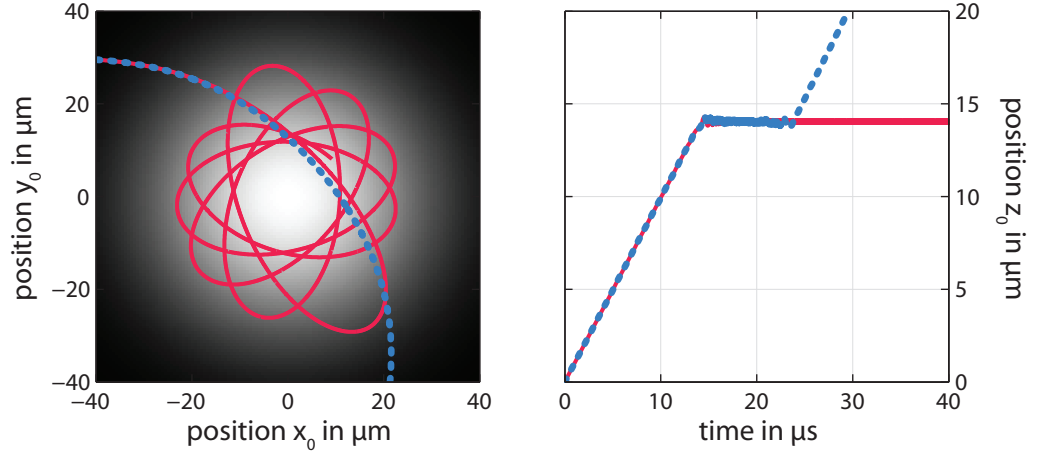


Figure 2.14. Simulated trajectory of a silicon sphere of 60 nm radius that is captured and trapped by a Gaussian standing-wave cavity mode. All parameters are taken from Table 2.2; the initial conditions are given in the text. The xy -projection of the trajectory is plotted on the left, where the background shading indicates the Gaussian intensity profile of the mode. The z -component is plotted on the right versus time. The full simulation based on the coupled cavity-particle dynamics (solid line) is compared with a hypothetical trajectory (dotted line), where the cavity is assumed to react without delay to the particle. The simulation was run up to $t = 50 \mu\text{s}$.

The delayed cavity reaction modifies this adiabatic trajectory and may dissipate kinetic energy from the radial motion. For trapping to occur the parameters must be chosen such that V_{ad} exhibits a pronounced local minimum close to the centrifugal barrier into which the particle could be captured. This happens if the particle has lost enough kinetic energy to remain bounded after it has been reflected at the centrifugal barrier.

In Figure 2.14 I plot a simulated trapping trajectory for the 60 nm silicon sphere from Table 2.2. The particle approaches the cavity with the initial velocity $\mathbf{v}_0(0) = (10, 0, 1) \text{ m/s}$ starting from the point $\mathbf{r}_0(0) = (-200, 30, 0) \mu\text{m}$. The cavity is pumped with an input power of $P_{\text{in}} = 1 \text{ W}$, which amounts to a steady-state number of about 8×10^{12} intra-cavity photons in the absence of the particle. This value is almost doubled as the particle gets trapped and shifts the cavity closer to resonance. The solid line in the left panel of Figure 2.14 represents the xy -projection of the particle trajectory. (The shading of the background mimics the Gaussian intensity profile $g(r_0)$.) We find that the particle is at first deflected and then eventually trapped in a stable orbit precessing around the central cavity axis.

Notice that the centrifugal barrier keeps the particle away from the center, which explains the empty spot in the middle of the bound orbit. For comparison I have also plotted the strictly conservative trajectory (dotted line), which would be obtained if the particle moved under the influence of the adiabatic potential (2.152). No dissipation can occur in this case. The particle is merely deflected on its passage through the cavity. The z -component of both trajectories is plotted as a function of time on the right panel. Also here the trapping effect appears only in the simulated trajectory that includes dissipation (solid line).

The cavity-induced slowing cycles are clearly seen in Figure 2.15. On the right panel, the above trajectory is depicted in an energy diagram. The total energy of the sphere is given by the sum of kinetic and potential energy, $E = m\mathbf{v}_0^2/2 + V_{\text{eff}}(r_0, z_0)$. It is plotted relative to the initial value $E_0 =$

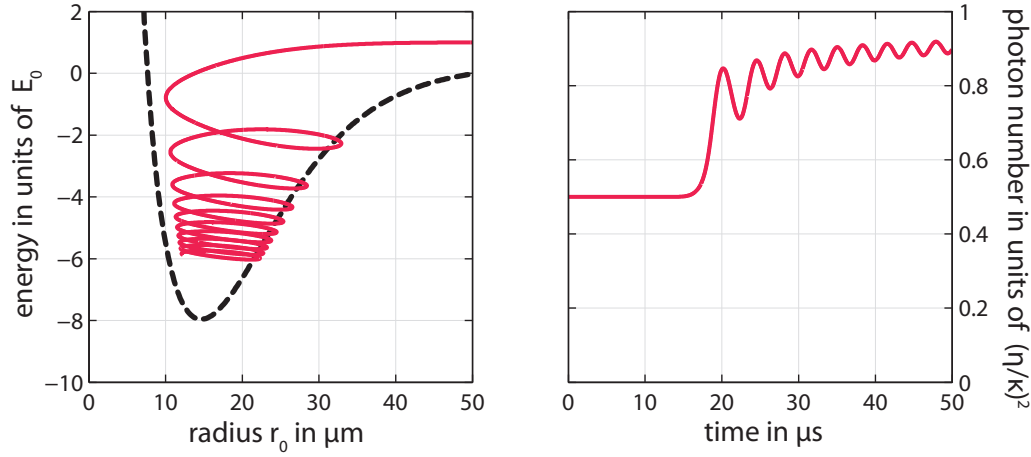


Figure 2.15. Energy and field intensity diagrams for the simulated trajectory of Figure 2.14. In the left panel we plot the total (kinetic plus potential) energy of the particle versus its off-axis distance $r_0 = \sqrt{x_0^2 + y_0^2}$ in units of its initial kinetic energy E_0 . The dashed line represents the adiabatic potential $V_{\text{ad}}(r_0, 0)$, as defined in the text. On the right we plot the intra-cavity photon number $|\alpha|^2$ versus time. It is normalized to the maximum possible value $(\eta/\kappa)^2$ on resonance.

$E(0) = m |\mathbf{v}_0(0)|^2 / 2$ versus the radial coordinate r_0 . We notice that the energy is dissipated over many slowing cycles while the particle orbits around the central cavity axis. The particle gets deeper and deeper trapped in a potential well approximately given by the adiabatic potential $V_{\text{ad}}(r_0, 0)$ (dashed line). At the same time, the cavity is shifted more and more towards resonance, which increases the photon number $|\alpha|^2$ towards the on-resonance value $(\eta/\kappa)^2$. The ratio between the photon number and the on-resonance value is plotted against time in the right panel. It starts at the steady-state value 0.5 corresponding to the initial detuning $\Delta = \kappa$ in the absence of the sphere.

With this I have demonstrated that the strong coupling and radial trapping of subwavelength nanospheres by a standing-wave cavity is feasible in a realistic setup. I should remark, however, that the exemplary trapping behaviour shown here does not necessarily improve when going to even larger particles with coupling rates way beyond the cavity decay rate κ . Coupling rates of the order of 100κ imply that the particle is able to shift the cavity resonance by 100 linewidths, and the initial cavity-pump detuning Δ would have to be adjusted accordingly. Otherwise the particle would simply kick the cavity out of resonance and switch off the field immediately upon entrance. A more serious obstruction is related to the large light extinction rate that comes with the coupling. Recall that the dissipation effect can only be achieved with high-finesse resonator modes, which exhibit a long lifetime on the scale $1/\kappa$ of the intra-cavity field. This prerequisite becomes obsolete, and the cavity will effectively lose finesse, when the particle directly extinguishes the cavity field at a much faster rate. As a result, the particle effectively depletes the cavity by its presence.

Here ends the first part of this thesis, which contains a detailed overview of the principles and consequences of the linear coupling between polarizable objects and light. The possibility to cool and trap dielectric nanoparticles by cavity light represents one of the key results regarding potential applications in the lab. (It is in fact being implemented in the Vienna group as I write these lines.) The other key topic of this chapter, optical diffraction gratings for molecules and nanoparticles, will be applied in the next chapter on high-mass matter-wave interference methods.

Chapter 3.

Near-field interference techniques with heavy molecules and nanoclusters

“Never express yourself more clearly than you are able to think.”
— Niels Bohr

We will now devote our attention to one of the boldest enterprises in the field of matter-wave physics: Single-particle interference experiments with large molecules and clusters far beyond a single atom. This chapter is dedicated to the drudgery of my experimental colleagues down in the gloomy basement vaults of the Quantum Nanophysics Group in Vienna, who are as committed as ever to break their own current mass records and to demonstrate the quantum nature of larger and larger objects.

While atom interferometry has gained tremendously in (phase) sensitivity, stability and precision over the last decade, opening up for numerous applications in metrology [18, 93–95], the experimentalists in Vienna have managed to observe quantum interference of molecules with masses from several hundred to about 10^4 atomic mass units [12, 96]. New and improved interferometer designs may promise a further increase by two orders of magnitude in lab-based experiments over the next decade [10]. Starting from the first far-field diffraction experiments with fullerenes [4] in 1999, the group’s main interest shifted towards the conceptually more difficult near-field interferometry, which turned out to be more suitable for higher masses. Apart from an ongoing branch of diffraction experiments in the conventional far-field geometry [20], the three-grating Talbot-Lau interferometer (TLI) scheme has become the working horse setup in the group’s striving for highest masses. Most of this chapter thus will be dedicated to the TLI scheme and, in particular, to its modern manifestations employing optical standing-wave gratings. (Matter-wave Talbot-Lau interferometry was pioneered by John Clauser using material gratings [97, 98].)

The theoretical description of near-field interference is more involved than the far-field case, and it must be properly distinguished from potential classical shadow effects in order to assure a quantum origin of the observed pattern. This is preferably done in the phase-space representation by means of Wigner functions [77], as it was advocated and worked out elsewhere [7, 40, 59].

Before we will delve into the TLI scheme and its applications, I will first discuss a different near-field interference effect with the help of the phase-space framework: The matter-wave analogue of Poisson’s spot, a diffraction phenomenon originally proposed to demonstrate the wave nature of light [99] by the observation of a bright spot in the shadow region behind a circular aperture. At first one may think that, if the same idea were implemented with particles instead of

light, the appearance of such a bright spot would be a striking demonstration of quantum matter-wave interference. Poisson's spot was in fact observed with electrons and deuterium molecules [21,100,101]. However, I will show that for the cases of large molecules and nanoparticles interacting with the diffractive element during passage the appearance of a spot could also be explained by classical theory [9]; it would not demonstrate the quantum wave nature of the particles.

I will proceed with a detailed theoretical description of the generic TLI effect in Section 3.2, focusing on its current implementations employing one optical phase grating (KDTLI) or three optical ionizing gratings (OTITLI). The KDTLI was first proposed for molecules in [102]; its first demonstration can be found in [103], a detailed assessment in [7]. The OTITLI scheme was first conceived in [104], fully worked out and proposed in [10], and first observed in [13]. Both setups are also suitable for metrological applications. In fact, deflectometric measurements of static molecular polarizabilities are regularly carried out in the Vienna group [105,106]. In Section 3.3 I will describe a method to measure the absorption cross section of interfering particles in the TLI scheme, as we have proposed it in [6].

The chapter closes with an in-depth outlook on future time-domain experiments in the OTITLI setup, which are most suited to reach masses beyond 10^5 amu. There I will start by discussing the technical details and the first measurement results of the present implementation of the OTITLI scheme in the Vienna lab [13]. This sketch of the experimental methods and challenges will then be helpful in the subsequent analysis of all relevant effects that would eventually bound the reachable mass to less than about 10^9 amu in future experiments with the current scheme. Moreover, we will see that macrorealistic modifications to the Schrödinger equation may become testable with the present setup by operating in this high-mass regime [11].

3.1. The Poisson spot interferometer (PSI)

Poisson's spot, or Arago's spot, is an interference phenomenon dating back to the early 19th century, when Fresnel pushed his wave theory of light after a century-old academic dispute. Poisson discovered a peculiar implication of Fresnel's diffraction theory, which was then confirmed experimentally by Arago [99]: If a circular obstacle was illuminated by a (sufficiently collimated) beam of light, a bright spot would appear in the center of the shadow region behind the obstacle—a striking demonstration of the wave nature of light.

So far, Poisson's spot has been demonstrated by means of matter waves only with electrons [100, 101] and deuterium molecules [21]. Similar phenomena, such as the one-dimensional diffraction at thin wires or the two-dimensional diffraction at Fresnel zone plates, were observed with neutrons [107,108] and atoms [109,110]. Recent theoretical works, including our own, study the feasibility of the Poisson spot setup for fullerenes [22] and gold clusters [9].

The generic layout of a Poisson spot interferometer (PSI) is sketched in Figure 3.1. It has a cylindrical symmetry with respect to the interferometer axis z . The source, the obstacle and the detection plane are located at $z = 0$, $z = L_1$ and $z = L_1 + L_2$, respectively. In all practical implementations, the source is given by a circular pinhole of radius R_0 . It represents the circular analogue of the primary collimation slit in a conventional Young double-slit geometry, and it emits a rather uncollimated beam of particles (or light), which is to be diffracted at an opaque circular obstacle of radius R at the distance L_1 . In most cases, this obstacle is a thin disc (as depicted), but it could also be implemented by a sphere, as I will discuss later. The single-particle diffraction pattern is then detected

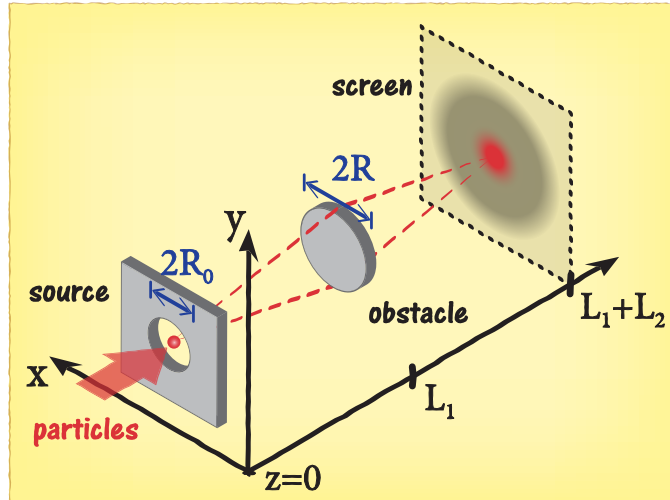


Figure 3.1. Sketch of the Poisson spot interferometer (PSI) layout for matter waves. An uncollimated beam of particles enters the interferometer through a source pinhole of radius R_0 , it crosses the distance L_1 along the z -axis to the circular obstacle of radius R , and it is detected on a screen after another distance L_2 . Multi-path interference around the obstacle leads to the appearance of a bright spot in the center of the shadow region behind the obstacle. It is named after S. D. Poisson, who predicted the effect for light in 1818 [99].

on a screen at the distance L_2 behind the obstacle. Its most prominent feature, Poisson's spot, is a bright diffraction maximum in the center, surrounded by higher-order maxima. They are the result of constructive interference between the wavelets diffracted all around the obstacle. Outside of the classical shadow projection of the obstacle the intensity on the screen approaches the classically expected flat density.

The required transverse coherence of the matter-wave (or light) beam is achieved when the source pinhole is placed sufficiently far away from the obstacle, $L_1 \gg R, R_0$. In this case, only a well-collimated sub-ensemble of particles (or light rays) will actually reach the vicinity of the obstacle and take part in the diffraction process. (In the far-field limit, $L_1 \rightarrow \infty$, the obstacle would be illuminated by a plane wave.) The brightest spot is produced by a perfect point source, $R_0 \rightarrow 0$; it ejects an ideal Huygens wavelet whose diffraction components coincide in phase at the center of the screen.

Basic properties of the elementary Poisson-spot effect Before moving on to a full assessment of Poisson's spot with matter waves, let me first summarize the basic effect in the idealized situation where monochromatic matter (or light) waves of wavelength λ illuminate a perfectly thin disc [111, 112]. Most of its characteristic features and parameters can be already understood under these restrictions, before presenting all the technical details of the full theory afterwards.

In the ideal case, the central bright spot is a direct indication of the wave nature of the particles emitted by the source. No signal would be detected in the shadow region behind the disc according to a classical ballistic description, where the particles are assumed to follow rectilinear trajectories from the source to the screen¹. The parameter $\ell = (L_1 + L_2) / L_1$ determines the radius of the shadow

¹ The ballistic description corresponds to the limit of geometric ray optics in the case of light.

projection of the obstacle on the detection screen, $R_{cl} = \ell R$, as follows from elementary geometry (intercept theorem).

Poisson's spot can be observed with waves both in the near field and in the far field behind the obstacle. The regimes are distinguished by the parameter $k = R^2/L_2\lambda$, which compares the characteristic length scale R^2/λ of diffraction patterns to the screen distance L_2 . The far-field regime is given by $k \ll 1$. The quasi-classical short-wave limit $\lambda \rightarrow 0$, on the other hand, implies $k \rightarrow \infty$.

Some characteristics of the ideal Poisson spot can be understood in terms of the *Fresnel zone construction* [99]: The radius $r_n = \sqrt{n\lambda L_1 L_2 / (L_1 + L_2)} = R\sqrt{n/k\ell}$ defines the n th Fresnel zone on the obstacle plane ($n > k\ell$). It implies a path length of about $L_1 + L_2 + n\lambda/2$ from the center of the source to the center of the screen. That is, the spherical Huygens wavelets emanating from neighbouring zones interfere *destructively* at the screen center. Since the diffraction angle required to reach the screen center from the n th zone (the so-called inclination angle according to [99]) grows with n , higher-order zones contribute less to the central maximum on the screen. We thus expect a most pronounced Poisson spot at small values of $k\ell \sim 1$, which permits contributions of low orders n .

The exact shape of the *ideal* diffraction pattern on the screen can be deduced with help of *Babinet's principle* [99]: The superposition principle implies that the wave amplitudes $\psi_P(r)$ behind a circular pinhole of radius R and $\psi_D(r)$ behind the corresponding disc of the same radius must sum up to the flat undisturbed solution in the absence of any diffractive element, $\psi_P(r) + \psi_D(r) = 1$. The same principle holds trivially for the geometric shadow projections $I_D(r) = \Theta(r - \ell R)$ and $I_P(r) = 1 - I_D(r)$ obtained from a simple ray model. Hence, the diffraction amplitudes *on top of* the geometric shadow projection differs in both cases merely by a negative sign, $\psi_P(r) - I_P(r) = I_D(r) - \psi_D(r)$.

Moreover, if the disc is illuminated by a perfect point source, we can roughly estimate the width of the central diffraction maximum: The distances between points $\mathbf{r}_1 = (R \cos \phi, R \sin \phi)$ on the disc edge to a point $\mathbf{r}_s = (R_s, 0)$ on the screen range approximately between $L_2 + (R \pm R_s)^2 / 2L_2$. The average path difference of two arbitrary points $\mathbf{r}_{1,2}$ on the disc and the screen coordinate \mathbf{r}_s reads as RR_s/L_2 . If we assume that the first dark ring around the center spot corresponds to a mean path difference of $\lambda/2$, we arrive at the estimate $R_s \approx L_2\lambda/2R = R/2k$ for the radius of the Poisson spot.

In all realistic cases the Poisson spot is washed out due to the finite source coherence related to a nonzero radius R_0 of the source pinhole. For each off-center point in the source the Poisson spot moves away from the screen center by at most $L_2 R_0 / L_1$. A pronounced spot is observed as long as this shift is small compared to the spot size R_s , which results in the condition $R_0 < L_1\lambda/2R = L_1 R / 2L_2 k$. At the same time, the source radius must be bounded by $R_0 < \ell R$, or else there would be no shadow region of the disc on the screen plane.

The informed reader may notice that the condition on the required source coherence is similar to the case of far-field diffraction at a grating [9]. Given the grating period d , an incoming beam must have a divergence angle smaller than λ/d . This leads to the condition $D < 2L_1\lambda/d$ for a collimation slit of width D placed at the distance L_1 . The advantage of the PSI setup lies in the condition $k\ell \sim 1$ for observing a pronounced spot: It admits disc radii R larger than typical grating periods d for a given wavelength λ , which should make the PSI suitable for heavy (and fast) particles with small de Broglie wavelengths.

On the other hand, important features of the diffraction pattern are modified in the presence of a dispersive interaction between the matter waves and the obstacle. We will find out in the following that this modifies the width and the height of the central Poisson spot, invalidating the Fresnel zone construction and Babinet's principle. More importantly, I will show that a central bright spot could also appear in the case of classical particles passing the obstacle on deflected trajectories due to the attractive force towards the obstacle. This obscures the distinction between the quantum and the classical description for large interaction strengths, such that the appearance of the spot *per se* does not indicate the wave nature of the particles.

3.1.1. Phase-space description of the ideal effect

The present theoretical model of the PSI for matter waves will be based on the phase-space representation of quantum states in terms of Wigner functions, which I have used already in Chapter 2. The basic features of this representation are given in Appendix A.3. Most notably, it serves as a common and descriptive framework for both quantum and classical descriptions of the setup.

Moreover, I will consider only the paraxial regime, where the diffraction effect is confined to those transverse coordinates $\mathbf{r} = (x, y)$ on the source, the obstacle, and the detection plane, which are small compared to the longitudinal extension of the interferometer, $R, R_0 \ll L_{1,2}$. This represents the standard regime for many matter-wave diffraction experiments with collimated beams of particles. In this case the dimensionality of the problem reduces effectively to the two transverse coordinates (x, y) . The only role of the longitudinal velocity v_z is to determine the arrival times $T_{1,2} = L_{1,2}/v_z$ at the obstacle and the detection screen, and we may simply average the resulting density pattern on the screen over the velocity distribution of the particle ensemble.

In the following I derive the diffraction and shadow effect at an ideal circular aperture, that is, at an arbitrarily thin and non-interacting disc of radius R . This will be the quantitative assessment of the previously discussed properties. The dispersive interaction between the particles and the obstacle will be implemented afterwards.

3.1.1.1. Ideal diffraction pattern

The two-dimensional Wigner function for a given quantum state of motion ρ reads as

$$w(\mathbf{r}, \mathbf{p}) = \frac{1}{(2\pi\hbar)^2} \int d^2s e^{i\mathbf{p}\cdot\mathbf{s}/\hbar} \langle \mathbf{r} - \frac{\mathbf{s}}{2} | \rho | \mathbf{r} + \frac{\mathbf{s}}{2} \rangle. \quad (3.1)$$

It resembles a classical phase-space probability distribution $f(\mathbf{r}, \mathbf{p})$ in the case of incoherent mixtures. I therefore describe the initially uncollimated ensemble state behind the source pinhole as

$$w_0(\mathbf{r}, \mathbf{p}) = \frac{1}{\pi R_0^2} \Theta(R_0 - r) D(\mathbf{p}) \equiv S(r) D(\mathbf{p}), \quad (3.2)$$

with Θ the Heaviside function and $D(p)$ an isotropic and normalized distribution of transverse momenta ejected from the source². An ideal point source would correspond to the pure state³ $w_0(\mathbf{r}, \mathbf{p}) = S(\mathbf{r}) = \delta(\mathbf{r})$.

The propagation of the beam from source to aperture is given by the shearing transformation

$$w_0(\mathbf{r}, \mathbf{p}) \mapsto w_0\left(\mathbf{r} - \frac{\mathbf{p}}{m} T_1, \mathbf{p}\right), \quad (3.3)$$

with m the particle mass. We arrive at the plane of the obstacle, which acts here as an ideal circular transmission mask for the matter waves. It modulates the matter-wave state by the isotropic transmission function $t(\mathbf{r}) = \Theta(\mathbf{r} - R)$ of the ideal disc, $\langle \mathbf{r} | \rho | \mathbf{r}' \rangle \mapsto t(\mathbf{r}) t^*(\mathbf{r}') \langle \mathbf{r} | \rho | \mathbf{r}' \rangle$ in the position representation. This corresponds to the Wigner function transformation [40, 59]

$$w(\mathbf{r}, \mathbf{p}) \mapsto \int d^2 q T(\mathbf{r}, \mathbf{p} - \mathbf{q}) w(\mathbf{r}, \mathbf{q}) \quad (3.4)$$

with the transmission kernel

$$T(\mathbf{r}, \mathbf{p}) = \frac{1}{(2\pi\hbar)^2} \int d^2 s e^{i\mathbf{p}\cdot\mathbf{s}/\hbar} t\left(\mathbf{r} - \frac{\mathbf{s}}{2}\right) t^*\left(\mathbf{r} + \frac{\mathbf{s}}{2}\right). \quad (3.5)$$

After a subsequent free propagation to the screen plane we arrive at the Wigner function

$$w(\mathbf{r}, \mathbf{p}) = \int d^2 q T\left(\mathbf{r} - \frac{\mathbf{p} T_2}{m}, \mathbf{p} - \mathbf{q}\right) w_0\left(\mathbf{r} - \frac{\mathbf{p} T_2}{m} - \frac{\mathbf{q} T_1}{m}, \mathbf{q}\right). \quad (3.6)$$

The density pattern $w(\mathbf{r})$ on the screen is obtained by integrating over the momentum coordinate. A substitution of the momentum coordinate leaves us with

$$w(\mathbf{r}) = \frac{m^2}{T_2^2} \int d^2 r_0 d^2 p_0 S(r_0) D(p_0) T\left(\mathbf{r}_0 + \frac{\mathbf{p}_0 T_1}{m}, m \frac{\mathbf{r} - \mathbf{r}_0}{T_2} - \frac{T_1 + T_2}{T_2} \mathbf{p}_0\right). \quad (3.7)$$

At this point I make use of the Fourier transform of the momentum distribution (i.e. its characteristic function),

$$\begin{aligned} \tilde{D}(\mathbf{s}) &= \tilde{D}(\mathbf{s}) = \int d^2 p e^{-i\mathbf{p}\cdot\mathbf{s}/\hbar} D(\mathbf{p}), \\ D(\mathbf{p}) &= \int \frac{d^2 s}{(2\pi\hbar)^2} e^{i\mathbf{p}\cdot\mathbf{s}/\hbar} \tilde{D}(\mathbf{s}) \end{aligned} \quad (3.8)$$

with $\tilde{D}(0) = 1$. After plugging the explicit form of the kernel (3.5) into the density pattern (3.7), several steps of calculation lead to the expression

$$w(\mathbf{r}) = \left[\frac{m}{2\pi\hbar(T_1 + T_2)} \right]^2 \int d^2 r_0 d^2 s S(r_0) \tilde{D}(\mathbf{s}) \psi\left[\mathbf{r} + \frac{T_2}{T_1} \left(\mathbf{r}_0 - \frac{\mathbf{s}}{2}\right)\right] \psi^*\left[\mathbf{r} + \frac{T_2}{T_1} \left(\mathbf{r}_0 + \frac{\mathbf{s}}{2}\right)\right], \quad (3.9)$$

² This is admissible as long as the transverse coherence of the ensemble is of no concern, that is, if the occupied phase-space region is much larger than Planck's quantum of action, $R_0 P_0 \gg \hbar$, with P_0 the width of the momentum distribution $D(p)$.

³ This state is an improper position eigenstate that cannot be normalized. The corresponding Wigner function does not contain a finite momentum distribution due to quantum uncertainty, whereas this would be very well possible in a classical model.

with the dimensionless amplitude term

$$\begin{aligned}\psi(\mathbf{r}) &= \frac{m\ell}{2\pi\hbar T_2} \int d^2r_1 \exp\left[\frac{im}{\hbar T_2} \left(\frac{\ell}{2}r_1^2 - \mathbf{r}_1 \cdot \mathbf{r}\right)\right] t(\mathbf{r}_1) \\ &= k\ell \int d^2u \exp\left[i\pi k\ell u^2 - 2\pi i k \frac{\mathbf{u} \cdot \mathbf{r}}{R}\right] t(R\mathbf{u}).\end{aligned}\quad (3.10)$$

Here I have introduced the dimensionless variable $\mathbf{u} = \mathbf{r}_1/R$, which represents a two-dimensional position vector on the obstacle plane in units of the obstacle radius. This admits a convenient notation in terms of the geometry parameters $k = mR^2/\hbar T_2$ and $\ell = (T_1 + T_2)/T_1$. See Appendix B.1 for details on how to compute the diffraction amplitude of an ideal disc in practice.

Weak-collimation approximation The amplitude term (3.10) can be read as the Fourier transform of a function of \mathbf{u} with the characteristic length scale of variation $\delta u \sim 1$, as mainly determined by the transmission function. It is then possible to write $\psi(\mathbf{r} + \delta\mathbf{r}) \approx \psi(\mathbf{r})$ for $|\delta\mathbf{r}| \ll R$. Specifically, we can apply this approximation to drop the \mathbf{s} -dependence in (3.9) if the ensemble exiting the source is poorly collimated, that is, if the spread P_0 of the momentum distribution $D(\mathbf{p})$ is large, $P_0 R \gg \hbar$. The reason is that the Fourier transform $\tilde{D}(\mathbf{s})$ is then confined to small arguments $|\mathbf{s}| \ll R$. This leaves us with the conventional form of the diffraction pattern,

$$w(R\mathbf{u}) = \frac{m^2 D(0)}{\pi(T_1 + T_2)^2} \int_{u_0 \leq 1} d^2u_0 \left| \psi\left(R\mathbf{u} + \frac{L_2}{L_1} R_0 \mathbf{u}_0\right) \right|^2, \quad (3.11)$$

which is completely sufficient for all practical purposes⁴. Note that I have plugged in the source aperture from (3.2) and introduced the dimensionless source coordinate $\mathbf{u}_0 = \mathbf{r}_0/R_0$. The prefactor

$$\mathcal{I}_0 = \frac{m^2 D(0)}{(T_1 + T_2)^2} \quad (3.12)$$

is given by the constant particle density on the screen that would be obtained if the diffracting disc were removed and the matter waves could transit unobstructedly. This is shown explicitly in Appendix B.1.

3.1.1.2. Poisson's spot

The characteristic features of the diffraction pattern behind an ideal disc are most pronounced if we assume the disc to be illuminated by a perfect point source in the center of the source plane. The density distribution on the screen then reduces to the simple expression $w(\mathbf{r}) = \mathcal{I}_0 |\psi(\mathbf{r})|^2$. We note that the diffraction image (3.11) of a finite-size source may be viewed as an average of displaced point-source images over the source aperture.

⁴ The approximation ceases to be valid only in the limit $k\ell \gg 1$, or if the obstacle were illuminated by a strongly collimated beam. The latter case would already imply diffraction at the source pinhole. The former case would result in a very narrow Poisson spot that could hardly be observed in an experiment.

In Appendix B.1, I simplify the expression (3.10) for the diffraction amplitude at an ideal disc,

$$\begin{aligned}\psi(\mathbf{r}) &= 2\pi k\ell \int_1^\infty du u \exp(i\pi k\ell u^2) J_0\left(2\pi k u \frac{r}{R}\right) \\ &= i \exp\left(-i\pi \frac{kr^2}{\ell R^2}\right) - \underbrace{2\pi k\ell \int_0^1 du u \exp(i\pi k\ell u^2) J_0\left(2\pi k u \frac{r}{R}\right)}_{\equiv \psi_1(\mathbf{r})}.\end{aligned}\quad (3.13)$$

The second line represents a numerically stable form of the solution which shall be used in the computational analysis of the effect. The first term in the second line is a pure phase factor of modulus one and the second term represents the diffraction amplitude $\psi_1(\mathbf{r})$ of a circular aperture of radius R , in accordance with Babinet's principle.

Let me first discuss the asymptotic behaviour of the diffraction amplitude far away from the screen center, $r \gg R/k$. For this we can approximate the Bessel function in the integral by its asymptotic form for large arguments [113], $J_0(x) \approx \sqrt{2/\pi x} \cos(x - \pi/4)$. I show in Appendix B.1 that the magnitude of $\psi_1(\mathbf{r})$ is bounded from above by

$$|\psi_1(\mathbf{r})| \leq \frac{4k\ell}{3} \sqrt{\frac{R}{kr}} \xrightarrow{kr/R \rightarrow \infty} 0. \quad (3.14)$$

This confirms the intuitive picture that far outside the shadow projection (but still inside the screen area illuminated by the weakly collimated matter-wave beam) the intensity on the screen is not affected by the diffraction at the obstacle, $w(\mathbf{r} \rightarrow \infty) \rightarrow \mathcal{I}_0$.

At the same time, the density distribution exhibits a central diffraction maximum in the shadow region behind the disc, Poisson's spot, as easily shown by evaluating the amplitude function (3.13) at $\mathbf{r} = 0$. We find that $\psi(0) = i \exp(i\pi k\ell)$, and that the central intensity, $w(0) = \mathcal{I}_0$, is as large as it would be without the obstacle. In other words, the ideal diffraction image of a point source always exhibits a peak in the center of the disc shadow, whose height and position are independent of the PSI geometry and the particle velocities.

Off center, however, the diffraction image does depend on these parameters, as demonstrated in Figure 3.2. There, I plot radial cuts of the Poisson-spot diffraction images of a perfect monochromatic point source for different geometry parameters. The density distributions are normalized to the unobstructed value \mathcal{I}_0 . The left and the right panels correspond respectively to $k = 0.2$ and $k = 2$. The distances $L_{1,2}$ are assumed to be equal, $\ell = 2$, in the top panels, whereas we chose an asymmetric configuration, $\ell = 1.2$, for the bottom panels. We observe that the width of the central spot depends mainly on the parameter k ; it gets narrower with larger values of k . We can estimate the width R_s of the central peak by the first zero of the Bessel function⁵ in (3.13), $J_0(2\pi k R_s/R) = 0$ at $R_s \approx 0.4R/k$. An upper limit for the source radius R_0 , at which a pronounced Poisson spot is still visible, is obtained in the same way,

$$R_0 \lesssim 0.4 \frac{L_1 R}{L_2 k} = 0.4 \frac{h T_1}{m R}. \quad (3.15)$$

⁵ For larger values $r > R_s$ the integral in the second line of (3.13) extends over positive and negative intervals of the Bessel function. They cancel in parts and should therefore decrease the diffraction amplitude $\psi_1(\mathbf{r})$ significantly. Of course, the quality of this estimate varies with different values of $k\ell$, which enters the same integral through the complex Gaussian function.

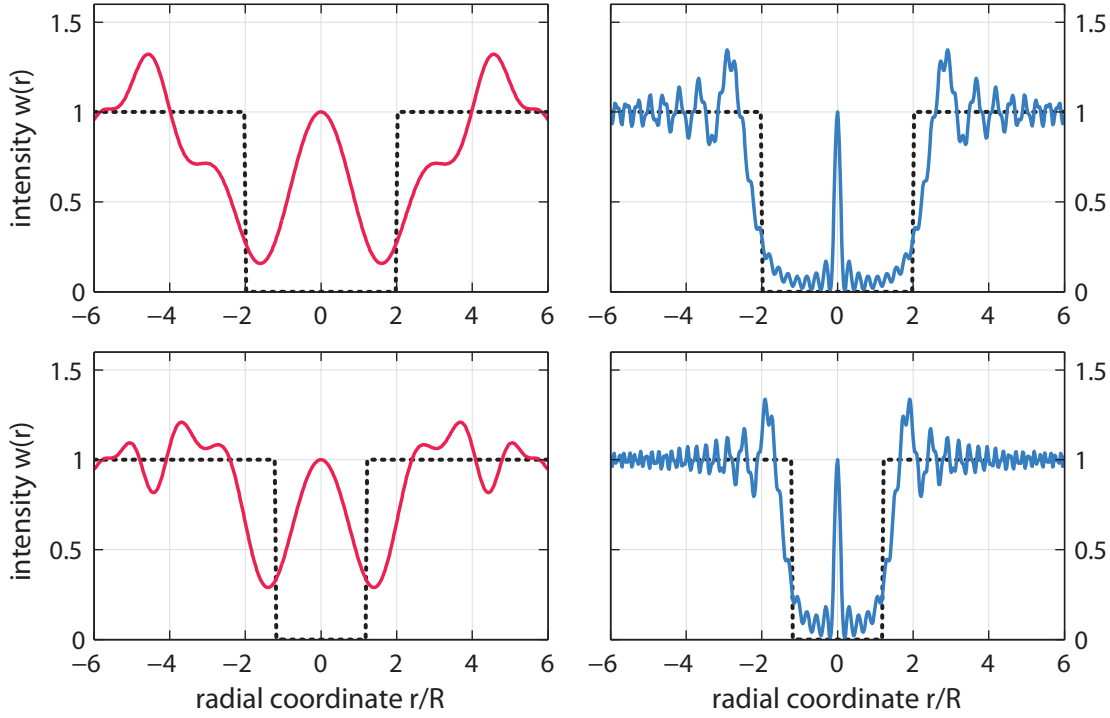


Figure 3.2. Radial cuts of the ideal Poisson spot pattern from a monochromatic point source for different geometry parameters k, ℓ (see text). The k -value is given by 0.2 in both panels on the left, and by 2 on the right. I plot the results for a symmetric configuration, $\ell = 2$, in the top row, and for the asymmetric case $\ell = 1.2$ in the bottom row. The black dotted line represents the geometric shadow projection of the obstacle on the screen. The vertical axis is normalized to the constant intensity \mathcal{I}_0 in the absence of the obstacle. All four cases exhibit a central diffraction maximum of the same height, Poisson's spot.

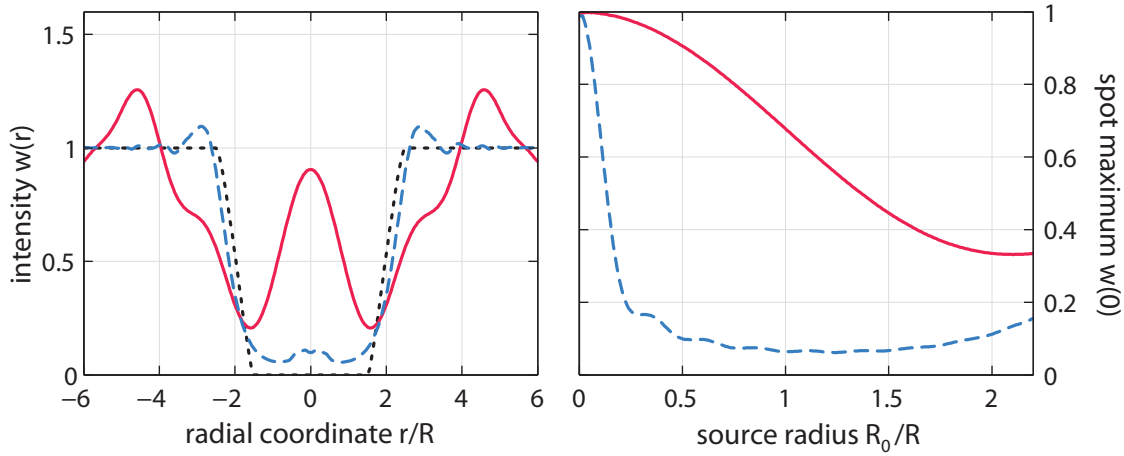


Figure 3.3. Influence of a finite source radius on the ideal Poisson spot in a symmetric interferometer configuration, $\ell = 2$. On the left the radial cut of two exemplary diffraction patterns (top panels in Figure 3.2) is shown for a source radius of $R_0 = R/2$. The solid line corresponds to $k = 0.2$, the dashed line to $k = 2$, and the dotted line represents the classical shadow projection. The right panel depicts the intensity of the central spot on the screen as a function of the source radius for both quantum cases.

At larger source radii, the Poisson spot would be smeared out by more than its own width.

Concludingly, we can distinguish two ramifications for a realistic implementation of the PSI with matter waves:

- ★ The diffraction pattern must be averaged over the finite longitudinal velocity distribution of the matter-wave beam. In the absence of any particle-obstacle interaction, this affects merely the geometry parameter $k = k(v_z)$, that is, the width of the Poisson spot and the off-center features of the diffraction pattern. It does not diminish the central spot—one of the crucial advantages of the PSI setup.
- ★ The diffraction pattern must be averaged over realistic source apertures $R_0 > 0$, which must be made large enough to transmit a detectable number of particles. This may diminish the visibility of the Poisson spot significantly in practical implementations with fast particles and large k -values, as shown in Figure 3.3. In the left panel I plot the ideal monochromatic diffraction images for $k = 0.2$ (solid line) and $k = 2$ (dashed line) assuming a source radius of $R_0 = R/2$ and $\ell = 2$. The central maximum almost vanishes in the latter case. This is to be compared to the corresponding point-source images in Figure 3.2. The quantitative depreciation of the Poisson spot maximum is shown in the right panel, where the height of the central spot is plotted as a function of the source radius for both cases.

A third main ramification, yet to be analyzed, is the influence of dispersive interactions between the particles and the obstacle. We will see below how this can modify the diffraction pattern dramatically in the case of large particles.

3.1.1.3. Classical ideal shadow projection

I mentioned the ideal geometric shadow projection of the obstacle in the preceding section to emphasize the quantum nature of the Poisson spot phenomenon. The shadow image on the screen of a disc of radius R illuminated by a perfect point source has a radius of ℓR . This follows from geometric considerations if we assume that the particles that are ejected from the source in all directions and travel to the screen on classical rectilinear trajectories.

We can describe this mathematically by replacing the two-dimensional Wigner function $w(\mathbf{r}, \mathbf{p})$ with the classical phase-space distribution function $f(\mathbf{r}, \mathbf{p})$ in the above phase-space framework. In fact, the initial mixed ensemble state $f_0(\mathbf{r}, \mathbf{p})$ at the source is identical to the initial Wigner function (3.2) of the quantum model. The essential difference between the classical and the quantum phase-space model lies in the state transformation at the obstacle. Classically, the ideal disc of radius R simply masks the incoming particle ensemble by blocking the ones that hit the disc, $f(\mathbf{r}, \mathbf{p}) \mapsto |t(\mathbf{r})|^2 f(\mathbf{r}, \mathbf{p})$. It results in the classical transmission kernel

$$T_{\text{cl}}(\mathbf{r}, \mathbf{p}) = |t(\mathbf{r})|^2 \delta(\mathbf{p}) = \Theta(r - R) \delta(\mathbf{p}), \quad (3.16)$$

which must be compared to the quantum kernel (3.5). The latter results in a partially negative Wigner function characterizing a quantum superposition state, whereas the former upholds the compulsory positivity of the classical distribution function.

By replacing the transmission kernel in the quantum formula (3.7) we arrive at the classical density distribution on the screen,

$$f(\mathbf{r}) = \frac{m^2}{(T_1 + T_2)^2} \int d^2 r_0 S(r_0) D\left(m \frac{\mathbf{r} - \mathbf{r}_0}{T_1 + T_2}\right) \left| t\left(\frac{T_1 \mathbf{r} + T_2 \mathbf{r}_0}{T_1 + T_2}\right) \right|^2. \quad (3.17)$$

Once again, if we restrict to screen coordinates $\mathbf{r} = R\mathbf{u}$ that are well within reach of the unobstructed particle beam we are left with the screen image of an uncollimated particle beam partially blocked by the disc,

$$f(R\mathbf{u}) = \frac{T_0}{\pi} \int_{u_0 \leq 1} d^2 u_0 \Theta\left(\left| \frac{L_1 R\mathbf{u} + L_2 R_0 \mathbf{u}_0}{L_1 + L_2} \right| - R\right). \quad (3.18)$$

This is the classical counterpart of (3.11). It vanishes for all $u < \ell - L_2 R_0 / L_1 R$. In other words, there exists a classical shadow region behind the disc as long as the source radius satisfies $R_0 < R(L_1 + L_2) / L_2$. Any observation of particles in this shadow region would indicate their quantum nature.

3.1.2. Modified effect in the presence of interaction

In practice, the quantum-classical distinction in a matter-wave PSI is obscured by the dispersive interaction between the circular obstacle and a passing particle. Given the polarizability of the particle and the dielectric properties of the obstacle material, mutually induced virtual dipoles give rise to a van der Waals-type potential attracting the particle towards the obstacle if it is sufficiently close to its walls. In the following I will restrict to (dielectric or metallic) spheres and thin discs, the most relevant obstacle candidates for practical implementations.

So far I have modelled the obstacle as an arbitrarily thin opaque disc on the obstacle plane at distance $z = L_1$ from the source, as sketched in Figure 3.1. In the following I will consider obstacles, which are sufficiently thin so that we can still specify an obstacle plane and a two-dimensional binary function $|t(\mathbf{r})|$ describing the transmission of matter waves through the plane⁶.

3.1.2.1. Modified diffraction pattern

The weak short-time interaction between a collimated matter-wave beam and a thin diffractive element can be assessed by means of the standard eikonal phase [40, 59, 60]

$$\phi(x, y) = -\frac{1}{\hbar v_z} \int dz V(x, y, z). \quad (3.19)$$

It approximates the classical action and the wave front curvature accumulated by the matter waves when they scatter at the interaction potential $V(x, y, z)$ with a large longitudinal velocity v_z . The expression is valid in the longitudinal high-energy limit, where the kinetic energy of the particles exceeds by far the average interaction strength, and where the transverse motion of the matter-wave state is restricted to small momenta, $|p_{x,y}| \ll mv_z$, playing no role during interaction. I refer the reader to my previous work [59, 60] for a detailed analysis of the eikonal approximation and its validity.

⁶ The use of thick obstacles would be counterproductive in practice, because it would also aggravate the interaction effect and its destructive influence on the quantum visibility.

Here we consider a cylindrically symmetric potential $V(x, y, z) = V(\sqrt{x^2 + y^2}, z)$ and append the corresponding eikonal phase factor $\exp[i\phi(r)]$ to the transmission function of the obstacle. In the case of an attractive potential we must not forget an important additional effect: Particles in close vicinity of the obstacle may be captured and absorbed by its walls, increasing the effective obstacle radius by ηR . The parameter η depends on the specific potential and on the particle velocity as well, which adds to the dispersive nature of the interaction effect. The modified transmission function reads as $t(\mathbf{r}) = \Theta(r - R - \eta R) \exp[i\phi(r)]$, and the modified diffraction pattern is obtained by replacing the amplitude function in (3.11) with

$$\psi(\mathbf{r}) = 2\pi k \ell \int_{1+\eta}^{\infty} du u \exp[i\pi k \ell u^2 + i\phi(Ru)] J_0\left(2\pi k u \frac{r}{R}\right). \quad (3.20)$$

The concrete evaluations of the modified amplitude will be implemented below using the numerically stable expression

$$\begin{aligned} \psi(\mathbf{r}) = & i \exp\left(-i\pi \frac{k r^2}{\ell R^2}\right) - 2\pi k \ell \int_0^{1+\eta} du u \exp(i\pi k \ell u^2) J_0\left(2\pi k u \frac{r}{R}\right) \\ & + 2\pi k \ell \int_{1+\eta}^{\infty} du u \exp(i\pi k \ell u^2) J_0\left(2\pi k u \frac{r}{R}\right) \left[e^{i\phi(Ru)} - 1\right]. \end{aligned} \quad (3.21)$$

The first line is given by the stable form of the ideal diffraction amplitude with an increased obstacle radius, the second line is an infinite integral over the difference between the ideal and the modified case. I note that the latter converges much better than (3.20) in numerical implementations because the integrand drops to zero outside the limited range of the interaction potential.

3.1.2.2. Modified shadow pattern

The particle-obstacle interaction potential $V(r, z)$ also modifies the classical shadow projection on the screen, as the attractive force $F_r = -\partial_r V(r, z)$ deflects those particles towards the screen center whose trajectories come close to the obstacle walls. The deflection of each particle can be approximated by the net momentum kick

$$\mathbf{q}(\mathbf{r}) = - \int \frac{dz}{v_z} \partial_r V(r, z) \frac{\mathbf{r}}{r} = \hbar \partial_r \phi(r) \frac{\mathbf{r}}{r} \quad (3.22)$$

given the same parameter constraints as for the eikonal phase (3.19). The classical transmission kernel (3.16) is turned into

$$T_d(\mathbf{r}, \mathbf{p}) = \Theta(r - R - \eta R) \delta[\mathbf{p} - \mathbf{q}(\mathbf{r})], \quad (3.23)$$

which represents the classical counterpart of the eikonal approximation [59, 60]. It will be convenient to express the momentum kick in terms of the dimensionless function

$$Q(r) = -\frac{R}{\hbar k} \mathbf{q}(\mathbf{r}) \cdot \frac{\mathbf{r}}{r} = \frac{R}{\hbar k v_z} \int dz \partial_r V(r, z) = -\frac{R \partial_r \phi(r)}{2\pi k}, \quad (3.24)$$

which is always non-negative in the case of an attractive interaction. Moreover, the momentum kick will induce arbitrarily large deflections of those trajectories that come close to the obstacle surface, $Q(u \rightarrow 1 + \eta) \gg 1$, if we assume a divergent van der Waals potential.

Putting everything together, the ideal classical density distribution (3.18) changes to

$$f(\mathbf{r}) = \frac{\mathcal{I}_0}{\pi R_0^2} \int d^2 r_0 \Theta \left[R_0 - \left| \mathbf{r}_0 - \frac{T_1}{T_2} \mathbf{r} + \mathbf{q} \left(\frac{T_2 \mathbf{r}_0}{\ell T_1} \right) \frac{T_1}{m} \right| \right] \Theta \left[r_0 - \frac{\ell T_1}{T_2} (1 + \eta) R \right]. \quad (3.25)$$

In particular, the intensity at the center of the screen becomes

$$f(0) = 2\mathcal{I}_0 \int_0^\infty du_0 u_0 \Theta \left[1 - \left| u_0 - \frac{RT_1}{R_0 T_2} Q \left(\frac{T_2 R_0 u_0}{\ell T_1} \right) \right| \right] \Theta \left[u_0 - \frac{RT_1}{R_0 T_2} \ell (1 + \eta) \right]. \quad (3.26)$$

We notice that the two Heaviside functions do overlap for those values of u_0 which correspond to sufficiently large momentum kicks close to the obstacle. This shows that the classical model also predicts a non-vanishing intensity at the center behind the obstacle, $f(0) > 0$. Therefore the observation of a signal at $\mathbf{r} = 0$ cannot be taken as a proof of the quantum nature of the matter waves in the presence of interactions any longer. This highlights that the analysis of matter-wave experiments must include a quantitative comparison of the data with both the quantum and the classical model.

The appearance of a ‘classical Poisson spot’ can be made more explicit in the limit of a perfect point source. In this case the classical shadow pattern on the screen plane becomes

$$f(\mathbf{r}) = \frac{\mathcal{I}_0 \ell^2}{r} \left\{ \frac{r_+}{|\ell - RQ'(r_+)|} + \frac{r_-}{|\ell - RQ'(r_-)|} \right\} \quad \text{for } r_\pm \geq (1 + \eta) R, \quad (3.27)$$

as shown in Appendix B.2. The density distribution at each point on the screen is thus made up by at most two contributions r_+ and r_- , which can be understood from basic reasoning. To see this, let us consider an arbitrary point \mathbf{r} on the screen plane. We may set $\mathbf{r} = (r, 0)$ without loss of generality due to the radial symmetry of the problem. Given that \mathbf{r} is the endpoint of rectilinear particle trajectories from the obstacle plane, only two such trajectories are allowed by the symmetry: One must originate from a point $(r_+, 0)$ on the positive x -axis, and one from another point $(-r_-, 0)$ on the negative x -axis. Given that these two points would be mapped to $(\pm \ell r_\pm, 0)$ on the screen plane in the absence of the interaction, the momentum kick must provide the appropriate deflection,

$$|\mathbf{q}(\mathbf{r}_\pm)| \frac{T_2}{m} = RQ(r_\pm) = \ell r_\pm \mp r. \quad (3.28)$$

The solutions of these two implicit equations, if there are any, represent the two coordinates r_\pm on the obstacle plane contributing to the density (3.27). Of course, they must also be larger than the effective obstacle radius, $r_\pm \geq R + \eta R$, to constitute valid solutions. The derivative of the condition (3.28) with respect to those coordinates determines the weight of both contributions, as it relates the particle flux through a surface element on the obstacle plane with the intensity arriving at a surface element on the screen.

If we assume an attractive force of the obstacle that diverges at its walls, then Equation (3.28) will yield non-vanishing contributions reaching the screen center, $r = 0$. We note that the corresponding density distribution (3.27) diverges like $1/r$ at the center. However, this constitutes a non-essential singularity, which disappears as soon as we integrate the particle density over a finite surface, or average it over a finite size of the source. The relevant quantities remain finite for all practical settings.

3.1.2.3. Interaction potential at dielectric discs and spheres

I proceed by specifying the obstacle-particle interaction for spheres and discs in order to assess the interaction effect in practical implementations of the PSI setup. Here, I will resort to a simplified and approximate treatment of the interaction. An exact description is beyond the scope of this work as it would require an in-depth analysis of the Casimir force between the polarizable particles and the obstacle material, as well as a detailed knowledge about their dielectric properties.

The simplified present model will be based on the asymptotic Casimir-Polder formula $V(d) = -C_4/d^4$ for the retarded van der Waals interaction between a polarizable point particle and an infinite conducting surface at the distance d [114]. This rough estimate certainly overestimates the interaction strength at large distances $d \gtrsim R$ from the obstacle surface, but a proper assessment would involve sophisticated numerical methods [115,116]. The present model depends solely on the static dipole polarizability $\chi = \chi(\omega = 0)$ of the particle, which determines the interaction strength through the asymptotic Casimir-Polder parameter $C_4 = (3\hbar c/8\pi) \chi/4\pi\epsilon_0$. I estimate the effective increase ηR of the obstacle radius by the critical distance to the surface below which a classical particle would hit the surface during passage. We distinguish two obstacle geometries:

Diffraction at a metallic sphere In the case of a spherical conductor obstacle centered in the obstacle plane at $z = L_1$, I estimate the potential by the asymptotic Casimir-Polder expression using $V(x, y, z) = -C_4/\left[\sqrt{x^2 + y^2 + (z - L_1)^2} - R\right]^4$. The corresponding eikonal phase integral (3.19) can be carried out explicitly [63],

$$\phi(Ru) = \frac{C_4}{\hbar v_z R^3} \left\{ \frac{2 + 13u^2}{3(u^2 - 1)^3} + \frac{u^4 + 4u^2}{(u^2 - 1)^{7/2}} \left[\frac{\pi}{2} + \arctan\left(\sqrt{\frac{1}{u^2 - 1}}\right) \right] \right\}. \quad (3.29)$$

The radial coordinate is once again written in units of the obstacle radius, $r = Ru$. The phase is measured in units of the prefactor

$$\phi_{\text{sph}} = \frac{C_4}{\hbar v_z R^3} = \frac{3c}{8\pi v_z} \frac{\chi}{4\pi\epsilon_0 R^3}, \quad (3.30)$$

while the coordinate dependence is entirely determined by the term in the curly brackets. The classical momentum kick (3.24) reads as

$$Q(Ru) = \frac{\phi_{\text{sph}}}{2\pi k} \left\{ \frac{5u(10 + 11u^2)}{3(u^2 - 1)^4} + \frac{u(3u^4 + 24u^2 + 8)}{(u^2 - 1)^{9/2}} \left[\frac{\pi}{2} + \arctan\left(\sqrt{\frac{1}{u^2 - 1}}\right) \right] \right\}. \quad (3.31)$$

The relative increase $\eta > 0$ of the obstacle size is derived in Appendix B.3 by means of a classical scattering approach. It is (implicitly) defined by the classical turning point of the particle trajectory deflected by the sphere,

$$\eta = \sqrt{\frac{2(v+1)^3}{v+2}} - 1, \quad \text{with } \frac{v^5}{v+2} = \frac{C_4}{ER^4}. \quad (3.32)$$

The term $E > 0$ denotes the kinetic energy of the incoming particle. In the paraxial limit considered here, the latter is almost entirely covered by the longitudinal motion, and we can safely approximate $E \approx mv_z^2/2$.

Diffraction at a metallic disc I model the van der Waals attraction of a disc obstacle of radius R and thickness b by the two-dimensional potential $V(x, y) = -C_4/(\sqrt{x^2 + y^2} - R)^4$, which only acts on the particle while it passes by the side wall of the disc. This happens during the time interval $t = b/v_z$, which results in the eikonal phase and momentum kick

$$\phi(Ru) = \frac{C_4 b}{\hbar v_z R^4} \frac{1}{(u-1)^4} \equiv \frac{\phi_{\text{disc}}}{(u-1)^4}, \quad (3.33)$$

$$Q(Ru) = \frac{2\phi_{\text{disc}}}{\pi k} \frac{1}{(u-1)^5}. \quad (3.34)$$

We obtain the effective increase η of the disc radius from the time t_c it takes a particle to hit the surface surrounding the disc if it is initially at rest above this surface. The particles that pass the disc in close proximity will be absorbed by its walls before they can leave, $t_c < b/v_z$. This results in the condition

$$t_c = \int_R^{R_c} dr \sqrt{-\frac{m}{2V(r)}} = \sqrt{\frac{m}{2C_4}} \frac{(R_c - R)^3}{3} \stackrel{!}{<} \frac{b}{v_z} \quad (3.35)$$

for all $R_c < (1 + \eta) R$. We find $\eta = \left(3b\sqrt{2C_4/m}/R^3 v_z\right)^{1/3}$.

A direct comparison between the disc and the sphere reveals that the characteristic interaction strengths differ in proportion to the disc thickness, $\phi_{\text{disc}}/\phi_{\text{sph}} = b/R$.

3.1.2.4. Numerical analysis of realistic scenarios

We are now in a position to analyze the modified Poisson spot pattern of realistic cluster particles in an exemplary PSI setup. The distances between the source, the obstacle and the screen shall be equal, $\ell = 2$, and the geometry parameter shall be fixed to $k = 0.2$. The obstacle shall be given by a suspended gold nanosphere of radius $R = 500$ nm or, alternatively, by a $b = 10$ nm-thick disc of the same radius. As test particles I shall consider

- (I) the C_{60} fullerene with the mass $m = 720$ amu, the longitudinal velocity $v_z = 200$ m/s, and the static polarizability $\chi/4\pi\epsilon_0 = 90 \text{ \AA}^3$ [117]. In this case the setup extends over the distances $L_1 = L_2 = 45$ cm. Bright beams of fullerenes are routinely created in the lab, and they have been used in diffraction experiments for more than a decade [12].
- (II) as a more ambitious particle, the nanocluster Au_{100} consisting of 100 gold atoms with the total mass $m = 19700$ amu, the velocity $v_z = 2$ m/s, and the polarizability⁷ $\chi/4\pi\epsilon_0 = 400 \text{ \AA}^3$. This requires distances of $L_1 = L_2 = 12$ cm. Gold clusters can be formed with the magnetron sputter technique [118], and they are considered good candidates for future interference experiments [10].

In order to detect the Poisson spot patterns, the particles could be deposited on a flat atomic surface and imaged by means of scanning tunneling microscopy. This lithographic detection method has already proven successful in other diffraction experiments with fullerenes [119].

⁷ I use the standard formula $\chi = 4\pi\epsilon_0 R^3$ for the static polarizability of an ideal metal sphere of radius R [52]. The latter is estimated by means of the bulk mass density $\rho = 19300 \text{ kg/m}^3$ of gold, $R = (3m/4\pi\rho)^{1/3} \approx 7.4 \text{ \AA}$.

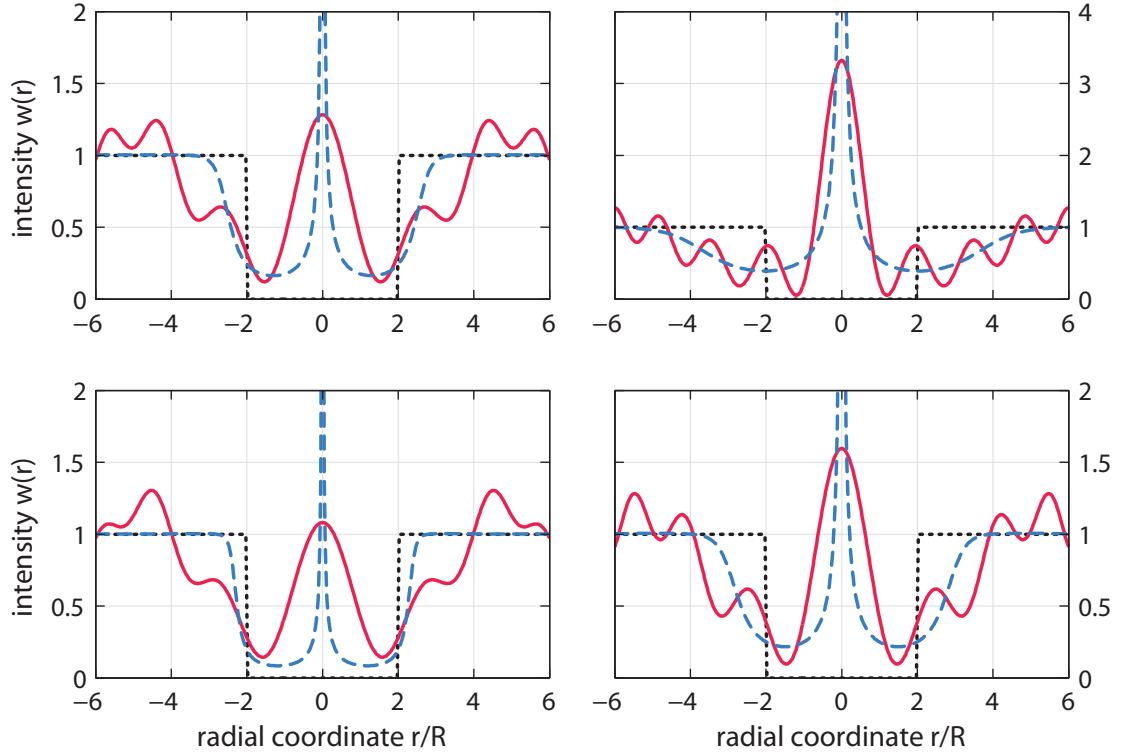


Figure 3.4. Radial cuts of the interaction-modified quantum (solid) and classical (dashed) Poisson spot pattern from a monochromatic point source for different particle-obstacle configurations. The geometry parameters are fixed at $(k, \ell) = (0.2, 2)$. The upper row corresponds to a spherical obstacle of radius $R = 500$ nm, the lower row to a disc of 10 nm thickness. The left and the right column represent particle species (I) and (II), respectively (see text). The ideal shadow projection of the obstacle (dotted line) is also plotted for reference. I have normalized the intensity to the unobstructed value \mathcal{I}_0 , as in Figure 3.2.

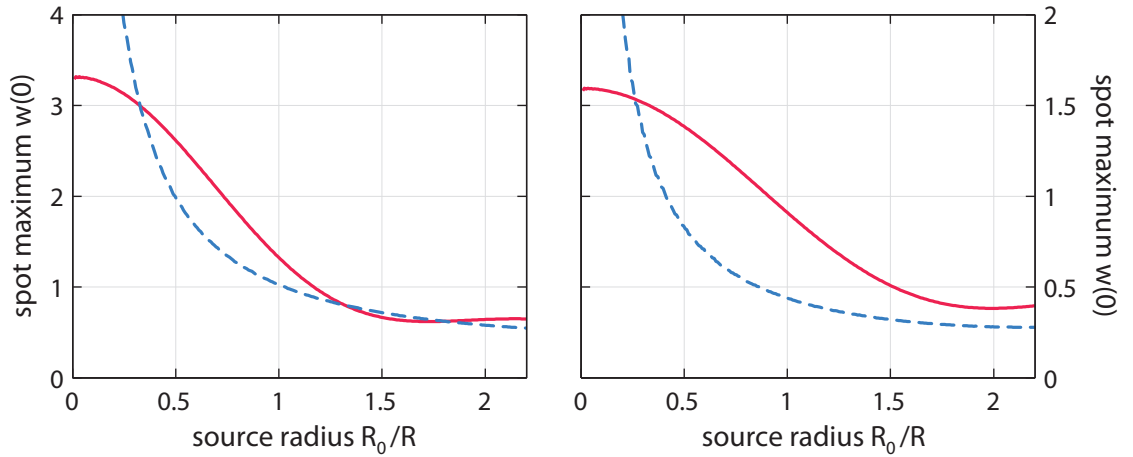


Figure 3.5. Quantum (solid) and classical (dashed) Poisson spot maximum as a function of the source radius R_0 . Once again, I have fixed the configuration at $(k, \ell) = (0.2, 2)$, and I assume that the gold clusters (II) are diffracted at a spherical obstacle (left) and at a disc (right) of 500 nm radius. The corresponding point-source patterns are shown in the left column of Figure 3.4.

In the upper panels of Figure 3.4 I plot the quantum diffraction and the classical shadow image of a spherical obstacle, which is illuminated by both particle species from a perfect point source. The left and the right panel correspond to species (I) and (II), respectively. The quantum (solid) and the classical (dashed) results were obtained by employing the above van der Waals interaction model and evaluating the expressions (3.21) and (3.27) numerically. The dotted black line represents the ideal geometric shadow projection of the obstacle for reference.

The plotted results are to be compared to the ideal diffraction pattern in the top-left panel of Figure 3.2. We notice an enhanced central diffraction maximum due to the focusing effect of the interaction, as well as the divergence of the classical intensity that we encountered in Section 3.1.2.2. Whereas the fullerene pattern is only slightly perturbed by the interaction effect, the gold results exhibit a drastic change with respect to the ideal pattern. The modification is less severe at the disc obstacle, as shown in the bottom panels of Figure 3.4.

In toto, the quantum and the classical point-source patterns are well distinguishable by their shape. This is no longer true when the density distribution on the screen is smeared out over realistic source radii. The central diffraction peak broadens and attenuates until it cannot be distinguished from the classical maximum. This is illustrated in Figure 3.5, where the height of the central maximum of the quantum (solid) and the classical (dashed) pattern is plotted as a function of the source radius. Here, we restrict ourselves to the gold clusters (II). The case of a sphere is depicted on the left, and the one of a disc on the right. Assuming a realistic source radius of $R_0 \approx R = 500$ nm, a clear distinction between the quantum and the classical Poisson spot can at most be made using the thin disc.

Finally, I should also mention the issue of surface corrugations, which cannot be avoided when using nanofabricated spheres or discs as obstacles. Such irregularities disturb the radial symmetry of the problem by adding a random angular fluctuation of the obstacle radius, which deteriorates the visibility of the central diffraction maximum. These fluctuations are expected to play no role as long as they are smaller than the interaction-induced increase ηR of the effective obstacle size. In fact, the fluctuations can be kept on the nanometer level with present-day technology, and they are thus not considered here.

The present analysis demonstrates that the PSI scheme, although useful to interfere relatively large molecules such as fullerenes [22], is not so well suited to test the quantum wave nature of heavy nanoparticles beyond the level of 10^4 amu, which can be achieved nowadays using optical diffraction gratings in the Talbot-Lau scheme [96]. The PSI shares this drawback with other schemes of matter-wave diffraction at material apertures. At one point or another, they all suffer from the destructive influence of dispersive particle-wall interactions, which makes it difficult to observe a distinguished quantum interference signal.

3.2. Talbot-Lau interferometer (TLI) scheme

After a detailed assessment of the PSI scheme, including its main drawbacks when it comes to heavy particles, I now turn to a different single-particle interference scheme in the near field, the Talbot-Lau interferometer (TLI). It is based on the Talbot effect of optical self-imaging at a periodic grating [120–123]: One observes a recurring image of the grating mask at multiples of the characteristic distance $L_T = d^2/\lambda$ behind the grating (of period d) if it is illuminated by a monochromatic plane wave of wavelength λ . Fractional images appear in the intensity distribution at other distances L in

between, which leads to the emergence of the so-called Talbot carpet [123]. In practice, the finite number of illuminated slits N confines this self-imaging effect to the near field behind the grating⁸, $L \leq NL_T$.

The multi-grating Talbot-Lau scheme produces a similar near-field interference effect and operates with less stringent coherence requirements [122–124], which facilitates matter-wave interference with thermal ensembles of particles [61]. The quantum interference effect appears in the form of a periodic fringe pattern whose amplitude varies strongly with the distance L between the gratings of the interferometer. Also here, recurrences appear in steps of the Talbot length L_T .

Until the present day, matter-wave TLI experiments have been conducted with atoms, molecules and molecular clusters [12, 18, 97]. I focus here on the molecular TLI experiments that have been performed in Vienna for more than a decade using three different implementations of the scheme. They are sketched in Figure 3.6.

The conventional TLI scheme [61] with three identical material gratings is depicted in Panel (a). An incoherent beam of particles⁹ enters the interferometer through the first grating mask G_1 , which acts as an array of collimation slits. This imprints a certain amount of spatial coherence over multiple grating periods d onto the matter-wave beam state, after it has traversed the distance L along the z -axis of the interferometer to the second grating G_2 . Here, the actual diffraction takes place, as G_2 modulates the amplitude and/or the phase of the impinging matter waves. The outgoing wavelets interfere and a periodic fringe pattern appears in the density distribution of the beam after *exactly* another distance L behind G_2 . In a sense, each slit of G_1 represents a partially coherent matter-wave source producing a Talbot interference image behind G_2 , but there is no phase coherence between neighbouring source slits. A visible fringe pattern can therefore only be established at fixed distances behind G_2 , where the individual Talbot images overlap ‘in phase’. Slight deviations from this ‘resonance configuration’ (of equal distances and equal grating periods)¹⁰ lead to the disappearance of the interference fringes.

The third grating G_3 merely serves the purpose of detecting the fringe pattern when a spatially resolving screen is unavailable or impractical¹¹. One simply shifts G_3 with respect to the other two in the direction of the grating, defined as the x -axis in the following. The fringe pattern is reconstructed by recording the total outgoing particle flux modulated by G_3 as a function of the shift.

⁸ The so-called Talbot length L_T gives the distance behind the grating where the two first order interference maxima between neighbouring grating slits are separated by a single grating period (in the paraxial approximation). At the distance $L = NL_T$ behind the grating, the maxima would be split over all N illuminated grating slits.

⁹ An incoherent beam is understood here as an essentially uncollimated beam with a broad distribution of velocity components along the grating axis x . This is equivalent to stating that the corresponding density operator ρ of the transverse motion does not exhibit any off-diagonal elements, i.e. spatial coherences, between neighbouring grating slits.

¹⁰ In general there is more than one such ‘resonance configuration’ of grating periods and distances permitting a visible Talbot-Lau fringe pattern [60, 61]. I will restrict most of the analysis to the symmetric arrangement implemented in Vienna, where all three gratings have the same period d and inter-grating distance L , as depicted in Figure 3.6. A generalization of the theory presented in Section 3.2.1 to arbitrary configurations will be sketched in Appendices B.4 and B.5.

¹¹ This is often the case considering that the grating period is of the order of a few hundred nanometers and that the source brightness and detection efficiency of many large molecules is low. Nevertheless, Talbot-Lau interference with fullerene molecules was demonstrated also by depositing the molecules on an silicon surface instead of using a third grating [119].

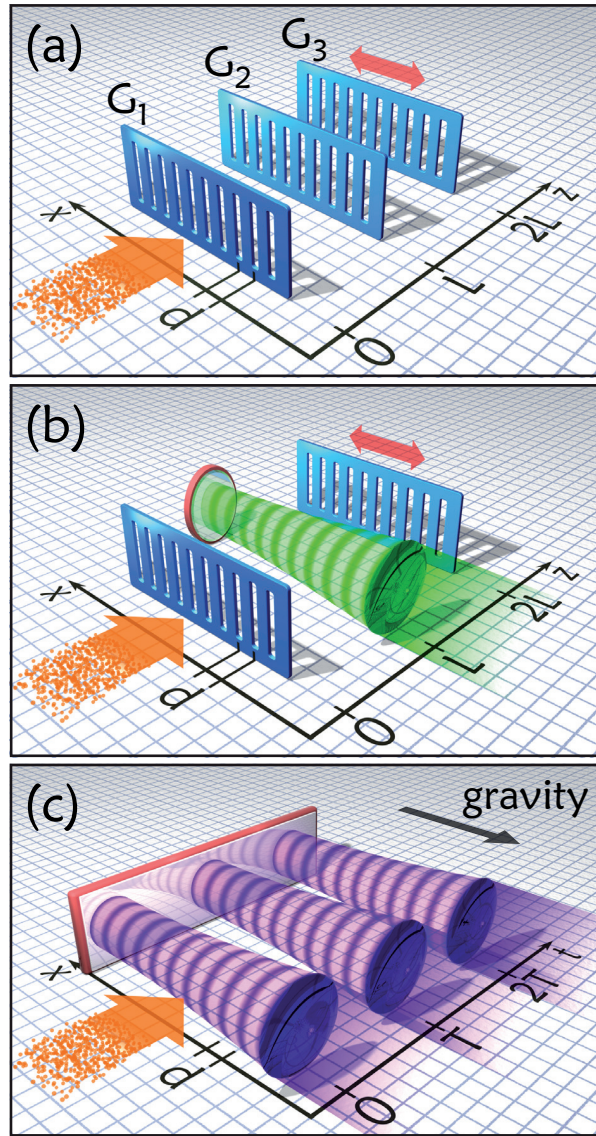


Figure 3.6. The three-grating configurations currently used in Talbot-Lau interferometry with molecules and clusters, as described in the text. An incoherent matter-wave ensemble enters from the left. Coherence is prepared at the first grating G_1 , diffraction takes place at G_2 , and the interference fringes are detected with help of a third grating G_3 . (a) The conventional TLI scheme with three identical grating apertures of equal period d and distance L . (b) The KDTLI scheme, where G_2 is implemented by a standing laser wave and the interference effect results from a pure phase modulation of the matter waves. (c) The OTITLI scheme with three optical standing-wave gratings, which are realized by ionizing laser pulses reflected off a mirror. The OTITLI is a time-domain configuration where the grating pulses illuminate a moving cloud of particles at three fixed instants in time, $t = 0, T, 2T$, whereas the (a) and (b) are stationary configurations where a continuous beam of particles passes a fixed spatial arrangement of gratings at $z = 0, L, 2L$.

The TLI is a single-particle near-field scheme where the different diffraction orders behind G_2 overlap in space and interfere to form the fringe pattern, as opposed to, say, a three-grating Mach-Zehnder configuration in the far field [125] where only a few diffraction orders are involved. Two points speak in favour of the near-field scheme. First, the setup requirements are less demanding for higher masses than in the far field. The fringe pattern can be observed when the distance between the gratings is at least of the order of the Talbot length, $L \gtrsim L_T = md^2 v_z / h$, with m and v_z the mass and the longitudinal velocity of the particles [12]. At fixed interferometer length L and growing mass m , the grating period d decreases merely like $1/\sqrt{mv_z}$, as opposed to a far-field scheme with linear scaling. Second, unlike in far-field diffraction, there is no need to collimate the initial matter-wave beam to a transverse momentum spread of less than the grating momentum h/d at the expense of most of the signal in order to observe the interference effect.

It turns out, however, that the dispersive van der Waals interaction between the particles and the walls of the second grating introduces a strong and uncontrollable velocity dependence of the interference fringes [5, 102]. This is because near-field interference involves many diffraction orders and is thus more sensitive to distortions of the exact shape and curvature of the diffracted matter-wave fronts, which are induced by the van der Waals interaction close the grating walls. Slower particles are more strongly affected since they spend more time in the vicinity of the grating. Hence the dispersive nature (i.e. velocity dependence) of the interaction effect.

For heavy particles a high fringe visibility can be achieved only by means of a narrow velocity selection at the cost of overall signal [102]. It was found that one could alleviate this problem by replacing the central grating with a standing laser wave [103], as depicted in Figure 3.6 (b). The interference effect in this Kapitza-Dirac Talbot-Lau Interferometer (KDTLI) scheme is induced by the pure phase modulation of matter waves at the light grating, rather than by diffraction at an aperture. The phase modulation is related to the dispersive dipole interaction of the particles with the optical field, which has a weaker velocity dependence and can be controlled by varying the laser power. We will have a closer look on the KDTLI in Section 3.2.2. It is currently the working-horse setup in Vienna and it has led to the latest mass records of the order of 10^4 amu [96].

Still, the dispersive nature of such a stationary grating configuration represents a major obstacle to reaching substantially greater masses, even more so since van der Waals interactions remain present in the first and the third grating. Although the interaction-induced phase modulation of the matter waves is of no concern at G_1 and G_3 (since their purpose is to act merely as a transmission mask), the attraction to the walls may become so strong that large particles will ultimately stick to them and clog the grating slits [10]. One could consider making the walls of the grating masks thinner, but then they are more prone to break upon the heavy-particle bombardment.

Such problems are alleviated by changing to a pulsed configuration with optical depletion gratings, that is, with standing-wave gratings that remove particles in the matter-wave state at the field antinodes. Figure 3.6 (c) depicts the current implementation of this scheme, the Optical Time-Domain Ionizing Talbot-Lau Interferometer (OTITLI), which has been applied so far to small molecular cluster particles [13]. Here, the gratings are generated by three equally timed vacuum-ultraviolet (VUV) laser pulses reflected off a single mirror [10, 104]. Photo-ionizable particles are injected in the form of dilute clouds flying alongside the mirror surface to the detector; they are exposed to the three grating pulses at fixed moments in time, $t = 0, T, 2T$, irrespectively of their precise position and velocity (as opposed to a stationary configuration where the timing depends on the particle velocity v_z). The gratings modulate both the phase and the amplitude of the illuminated

matter waves, as they ionize and remove particles from the ensemble via single-photon absorption in the field antinodes. In this way, the standing-wave pulses form absorptive masks, as required for the first and the third grating. I have presented the working principle of optical depletion or ionization gratings already in Chapter 2 on page 18ff. Here, I will develop a theoretical model of the OTITLI scheme in Section 3.2.3.

An important property of the TLI scheme in general is that it admits a classical moiré shadow effect. That is to say, a fringe pattern may as well appear in a classical hypothetical description of the scheme in terms of ballistic particle trajectories. As they are partially blocked and/or deflected by the grating apertures, a periodic density modulation can occur behind the second grating as well, albeit with a different dependence on the inter-grating distance (or particle velocity). Therefore, a non-vanishing fringe contrast by itself does not prove that the particles have interfered. As in Poisson's spot experiment, we must provide both the quantum and the classical model for the TLI and we must compare the results of both models quantitatively with the measured data.

3.2.1. Generic description of the Talbot-Lau scheme

Before discussing the details of the various manifestations of the TLI scheme, let me first present the underlying theoretical model applicable to all of them. It is based on the one-dimensional phase-space description of generic Talbot-Lau interferometry developed in [40, 59, 60]. The present formulation will be done entirely in the time domain, that is, I will describe the effect of the three gratings by quasi-instantaneous state transformations separated by two long stretches of free evolution in between [10]. The corresponding time intervals, T_1 and T_2 , will be of the order of the Talbot time,

$$T_T = \frac{md^2}{h}. \quad (3.36)$$

It depends on the particle mass m and on the grating period d . In a stationary TLI setup, where the gratings are arranged at fixed distances $L_{1,2}$ on the z -axis, the time intervals depend also on the longitudinal velocity v_z of the particles, $T_{1,2} = L_{1,2}/v_z$. This can easily be taken into account in the description by averaging the results over the initial velocity distribution of the matter-wave ensemble¹². In the following assessment of the dispersive TLI scheme we will always assume (and the results will be dependent on) a fixed velocity parameter v_z .

The transverse y -coordinate can be omitted, provided that the gratings are sufficiently extended along the y -axis and that the matter-wave ensemble is at all times located well within this extension. Generally speaking, I assume here that all particles see the same one-dimensional grating profiles, irrespectively of their y - z -position¹³. Hence, we may work with the one-dimensional Wigner function,

$$w(x, p) = \frac{1}{2\pi\hbar} \int ds e^{ips/\hbar} \left\langle x - \frac{s}{2} \left| \rho \left| x + \frac{s}{2} \right. \right. \right\rangle, \quad (3.37)$$

¹² This parametric treatment is only allowed in the paraxial limit, where the transverse state of the matter-wave beam remains separable from its longitudinal motion taking place at much larger velocities, and where the gratings act solely on the transverse part. The same formal limitation applies to the description of Poisson's spot, as noted in Section 3.1.1. It is automatically fulfilled in all relevant experiments, where the grating structures are much smaller in size than the required distances between them.

¹³ In the case of the pulsed OTITLI scheme, this implies that the lasers have a sufficiently wide beam profile and that the particle ensemble is well centered in the laser beam during each grating pulse.

as given in Appendix A.3. The classical description of the TLI will be given in the same framework, using the classical phase-space distribution $f(x, p)$ instead of the Wigner function.

3.2.1.1. Coherent grating transformation in phase space

The coherent state transformation at each of the short (resp. thin) gratings $k = 1, 2, 3$, is conventionally described in terms of a complex transmission function, $t^{(k)}(x) = |t^{(k)}(x)| \exp[i\phi^{(k)}(x)]$, modulating both the amplitude and the phase of the matter waves. I have introduced it in Section 2.1.4 on page 18ff. An incoming wavefunction transforms as $\langle x|\psi\rangle \mapsto t^{(k)}(x) \langle x|\psi\rangle$. The periodicity of the grating admits a Fourier expansion of the transmission function,

$$t^{(k)}(x) = \sum_{n=-\infty}^{\infty} b_n^{(k)} \exp\left(\frac{2\pi i n x}{d}\right), \quad (3.38)$$

which unfolds the grating transformation in momentum space: A momentum eigenstate $|p\rangle$ is transformed into a superposition of discrete plane-wave components $|p + nh/d\rangle$ separated by multiples of the elementary grating momentum h/d ,

$$\langle x|p\rangle \mapsto t^{(k)}(x) \langle x|p\rangle = \sum_{n=-\infty}^{\infty} b_n^{(k)} \exp\left(\frac{2\pi i n x}{d}\right) \langle x|p\rangle = \sum_{n=-\infty}^{\infty} b_n^{(k)} \langle x|p + n \frac{h}{d}\rangle. \quad (3.39)$$

Each Fourier component $b_n^{(k)}$ corresponds to a different order of diffraction.

The modulus of the transmission function is responsible for the amplitude modulation effect; its square determines the probability of transmission at each position x . The latter is given by the aperture function, $|t^{(k)}(x)|^2 = \sum_n \Theta(fd/2 - |x - nd|)$, for material gratings with a slit opening fraction $f \in (0, 1)$. The phase modulation term $\phi^{(k)}(x)$ is determined in the eikonal approximation by an action integral over the particle-grating interaction potential, Eq. (3.19). This approximation is valid only for short (resp. thin) gratings, where the free transverse evolution of the matter waves can be neglected during the interaction. We can describe the van der Waals-type interactions with the walls of a material grating in the same way as done in the PSI case in Section 3.1.2. A detailed model for the transmission function of optical standing-wave gratings is presented in the preceding chapter, Section 2.1.4 on page 18ff. Incoherent modifications of the grating transformation will be included below.

In the phase-space representation, the coherent grating transformation is given by a convolution, $w(x, p) \mapsto \int dp_0 T^{(k)}(x, p - p_0) w(x, p_0)$, with $T^{(k)}$ a one-dimensional transmission kernel of the same form as the two-dimensional kernel (3.5) in the Poisson-spot case. Let me introduce the *Talbot coefficients* in Fourier space to obtain a convenient Fourier notation of the kernel,

$$B_n^{(k)}(\xi) = \sum_{j=-\infty}^{\infty} b_j^{(k)} (b_{j-n}^{(k)})^* \exp[i\pi(n - 2j)\xi], \quad (3.40)$$

$$\begin{aligned} T^{(k)}(x, p) &= \sum_{j,n} \exp\left(\frac{2\pi i n x}{d}\right) b_j^{(k)} (b_{j-n}^{(k)})^* \delta\left[p - \left(j - \frac{n}{2}\right) \frac{h}{d}\right] \\ &= \frac{1}{2\pi\hbar} \sum_n \exp\left(\frac{2\pi i n x}{d}\right) \int ds e^{ips/\hbar} B_n^{(k)}\left(\frac{s}{d}\right). \end{aligned} \quad (3.41)$$

The effect of the grating transformation on momentum states in (3.39) is reflected in the explicit form of the transmission kernel (3.41), which sums over momentum displacements by multiples of h/d . Note that the Talbot coefficients are 2π -periodic in ξ , and that the Fourier components of the grating transmission probability $|t^{(k)}(x)|^2$ are given by $B_n^{(k)}(0) = B_n^{(k)}(2\pi N)$.

The classical phase-space transformation has two components, following the same line of argument as in the description of Poisson's spot in Sections 3.1.1.3 and 3.1.2.2. The first component is the ideal grating transformation, which masks an initial phase-space distribution by the aperture function, $f(x, p) \mapsto |t^{(k)}(x)|^2 f(x, p)$. This must be complemented a second component, the eikonal momentum kick, $q^{(k)}(x) = \hbar \partial_x \phi^{(k)}(x)$. It represents the integrated particle-grating force transferred to the classical ensemble, $f(x, p) \mapsto f(x, p - q^{(k)}(x))$. Both components can be expanded in a Fourier series. The combined classical transmission kernel reads as

$$\begin{aligned} T_{cl}^{(k)}(x, p) &= |t^{(k)}(x)|^2 \delta[p - q^{(k)}(x)] = \frac{1}{2\pi\hbar} \sum_n \exp\left(\frac{2\pi i n x}{d}\right) \int ds e^{ips/\hbar} C_n^{(k)}\left(\frac{s}{d}\right), \\ C_n^{(k)}(\xi) &= \sum_j B_{n-j}^{(k)}(0) c_j^{(k)}(\xi), \quad c_n^{(k)}(\xi) = \frac{1}{d} \int_{-d/2}^{d/2} dx \exp\left[-\frac{2\pi i n x}{d} - i\xi \frac{q^{(k)}(x)d}{\hbar}\right]. \end{aligned} \quad (3.42)$$

The classical Talbot coefficients $C_n^{(k)}(\xi)$ are a convolution of the transmission mask coefficients $B_n^{(k)}(0)$ with the eikonal kick coefficients $c_n^{(k)}(\xi)$. In contrast to the quantum coefficients, the classical ones are not periodic in the argument ξ . What can be said is that the quantum and the classical Talbot coefficients are identical at $\xi = 0$, where the particle-grating interaction has no influence, $C_n^{(k)}(0) = B_n^{(k)}(0)$.

3.2.1.2. Step-by-step derivation of the Talbot-Lau fringe pattern

With the transmission kernels (3.41) and (3.42) at hand I now derive the Talbot-Lau fringe pattern in a unified phase-space framework; the quantum and classical results can be directly related by interchanging $B_n^{(k)}(\xi) \leftrightarrow C_n^{(k)}(\xi)$ at each grating.

The initial particle ensemble in front of the first grating is assumed to be an incoherent mixture uniformly distributed over many grating slits¹⁴. In other words, the initial state occupies a large phase-space area with a spatial extension $X_0 \gg d$ and a momentum spread $P_0 \gg h/d$ making it indistinguishable from a classical mixture of the same size. Introducing the normalized and positive transverse momentum distribution $D(p)$, the initial Wigner function reads as $w_0(x, p) = D(p)/X_0$, and the passage through G_1 transforms it to $w_1(x, p) = \int dp_0 T^{(1)}(x, p - p_0) D(p_0)/X_0$.

Note that the initial momentum distribution may depend on the longitudinal momentum $p_z = mv_z$ of the particle ensemble in a stationary TLI configuration, where the particle beam is characterized by a fixed divergence angle $\alpha = P_0/p_z$ [60]. In the pulsed OTITLI scheme, the function $D(p)$ is given by the marginal of the full three-dimensional momentum distribution $\mu(\mathbf{p})$ of the particle cloud, $D(p) = \int dp_y dp_z \mu(p, p_y, p_z)$ [10].

¹⁴ I disregard any fringe effects related to the finite number of illuminated grating slits. A way to incorporate these effects is discussed in [59, 60] for material grating masks. Here, I will assume an unlimited periodicity of the gratings throughout the calculation.

The free evolution to G_2 is given by a shearing transformation in phase space, see (3.3) for the two-dimensional case. Let me add a constant acceleration a acting on the particles along the x -axis. It allows us to include, say, gravity or an external deflection field into the model, and it will lead to an effective shift of the resulting fringe pattern. Free propagation over a time t under the influence of a then shears and displaces both the quantum and the classical state according to the map $w(x, p) \mapsto w(x - pt/m + at^2/2, p - mat)$. We arrive at the particle state $w_3(x, p)$ at G_3 by subsequently applying on $w_1(x, p)$ the shearing-displacement rule for the time $t = T_1$, then applying the second grating kernel $T^{(2)}(x, p)$, and then another shearing-displacement for $t = T_2$.

$$w_3(x, p) = \frac{1}{X_0} \int dp_1 T^{(2)}\left(x - \frac{pT_2}{m} + \frac{a}{2}T_2^2, p - p_1 - maT_2\right) \times \int dp_0 T^{(1)}\left(x - \frac{pT_2}{m} - \frac{p_1T_1}{m} + \frac{a}{2}(T_1^2 + T_2^2), p_1 - p_0 - maT_1\right) D(p_0) \quad (3.43)$$

The Talbot-Lau fringe pattern is to appear in the spatial density distribution at G_3 , which we obtain by integrating the $w_3(x, p)$ over the momentum coordinate. After plugging in the Fourier expansions (3.41) of the transmission kernels and a few steps of calculation, we are left with

$$w_3(x) = \frac{1}{X_0} \sum_{\ell, k} \tilde{D}\left(\frac{kT_1 + \ell T_2}{T_T}d\right) B_k^{(1)}\left(\frac{kT_1 + \ell T_2}{T_T}\right) B_{\ell-k}^{(2)}\left(\frac{\ell T_2}{T_T}\right) \times \exp\left\{\frac{2\pi i}{d}\left[\ell x - \ell \frac{a}{2}(T_1 + T_2)^2 + (\ell - k)\frac{a}{2}T_1^2\right]\right\}. \quad (3.44)$$

Here, I have introduced the Fourier transform of the momentum distribution (i.e. its characteristic function),

$$\tilde{D}(x) = \int dp e^{-ipx/\hbar} D(p), \quad (3.45)$$

which is normalized to $\tilde{D}(0) = 1$ and whose characteristic width is given by $\hbar/P_0 \ll d$.

Resonance approximation The sharply peaked function \tilde{D} narrows down the number of index pairs (ℓ, k) that contribute appreciably to the Fourier sum in (3.44). Non-vanishing contributions can only come from indices that fulfill $|kT_1 + \ell T_2| \ll T_T$. This is always so for the zeroth component, $k = \ell = 0$, which represents the constant average particle density transmitted through G_1 and G_2 . Non-zero Fourier indices $k, \ell \neq 0$, which constitute the Talbot-Lau fringe oscillation, are uniquely paired through the above relation. For each integer ℓ there is at most one integer k fulfilling the above condition, if we restrict our attention to the relevant cases where the grating separation is at least of the order of the Talbot time, $T_{1,2} \gtrsim T_T$. Large integers $|k|, |\ell| \gg 1$ will hardly contribute to the signal as the corresponding high-order Talbot coefficients are expected to be vanishingly small. A pronounced fringe oscillation, if there is any, can only be due to small values of $|k|$ and $|\ell - k|$. It depends very much on the ratio of grating distances T_2/T_1 whether such index pairs exist at all, according to the above pairing condition.

Let us resort here to the most relevant case in practice, where the distance ratio is close to an integer, $T_1 = T$ and $T_2 = NT + \tau$, with $|\tau| \ll T_T$. The more general case, including also the possibility of different grating periods, is presented in Appendix B.4. We can now simplify the expression (3.44) for the fringe pattern by means of the *resonance approximation*,

$$\tilde{D}\left(\frac{kT_1 + \ell T_2}{T_T}d\right) \approx \delta_{k, -N\ell} \tilde{D}\left(\frac{\ell \tau}{T_T}d\right), \quad (3.46)$$

which explicitly yields the pairing relation $k = -N\ell$. We are left with the fringe pattern

$$w_3(x) = \frac{1}{X_0} \sum_{\ell} \tilde{D}\left(\frac{\ell\tau}{T_T}d\right) B_{-N\ell}^{(1)}\left(\frac{\ell\tau}{T_T}\right) B_{(N+1)\ell}^{(2)}\left(\ell\frac{NT+\tau}{T_T}\right) \exp\left[\frac{2\pi i\ell}{d}(x + \delta x_a)\right]. \quad (3.47)$$

It is effectively shifted by the amount

$$\delta x_a = -\frac{aT^2}{2}N(N+1) - aT\tau(N+1) - \frac{a\tau^2}{2} \quad (3.48)$$

due to the acceleration a acting on the particles. Equation (3.47) is a Fourier sum, where each non-vanishing component of order $\ell \neq 0$ contributes to the oscillation amplitude of the fringe pattern.

Detection signal and visibility The fringe pattern is detected in practice by measuring the total transmitted particle density $S(x_S)$ behind the third grating and varying its shift x_S with respect to the other two. Here, in order to obtain $S(x_S)$, we must apply the shifted transmission kernel of G_3 on the Wigner function (3.43) and integrate the transformed function over the whole phase space, $S(x_S) = \int dx dp dp_0 T^{(3)}(x - x_S, p - p_0) w_3(x, p_0)$. One can easily check that this boils down to a convolution of the fringe pattern $w_3(x)$ with the transmission probability at the shifted grating,

$$S(x_S) = \int dx w_3(x) \left| t^{(3)}(x - x_S) \right|^2 = \sum_{\ell} S_{\ell} \exp\left[\frac{2\pi i\ell}{d}(x_S + \delta x_a)\right],$$

$$S_{\ell} = \tilde{D}\left(\ell\frac{\tau}{T_T}d\right) B_{-N\ell}^{(1)}\left(\ell\frac{\tau}{T_T}\right) B_{(N+1)\ell}^{(2)}\left(\ell\frac{NT+\tau}{T_T}\right) B_{-\ell}^{(3)}(0). \quad (3.49)$$

The signal gives the per-particle probability for transmission through the three gratings of the TLI. As follows from its Fourier components, it contains all the fringe amplitudes of $w_3(x)$, multiplied by the Fourier coefficients $B_{-\ell}^{(3)}(0)$ of the third grating aperture. Hence, the third grating does nothing more than masking the outgoing particle state; the interaction of the particles with G_3 does not influence the signal¹⁵. We note that the fringe pattern can also be recorded without moving the third grating if one is able to vary the deflection shift δx_a in the external acceleration field a . The classical moiré signal is obtained by replacing the Talbot coefficients in (3.47) and (3.49) with their classical counterparts (3.42).

The amplitude of the fringe oscillation exhibited by the positive-valued and periodic signal is commonly measured in terms of the relative fringe contrast, or *visibility*,

$$\mathcal{V} = \frac{S_{\max} - S_{\min}}{S_{\max} + S_{\min}}. \quad (3.50)$$

The terms S_{\min} and S_{\max} represent the minimum and the maximum values of the fringe signal, respectively. The visibility ranges from zero (no fringes) to a maximum of 100% if the local minima of the signal are zero, $S_{\min} = 0$. Often the fringe oscillation is dominated by the first Fourier amplitude, which results in a near-sinusoidal pattern. The fringe contrast is then well described by the

¹⁵ This applies only to the interaction-induced phase modulation of the matter waves. The van der Waals attraction still reduces the effective slit opening of material gratings. Particles in close vicinity to the walls may hit them and will not be transmitted.

sinusoidal visibility,

$$\mathcal{V}_{\sin} = \left| \frac{2S_1}{S_0} \right| = 2 \left| \tilde{D} \left(\frac{\tau d}{T_T} \right) \frac{B_{-N}^{(1)}(\tau/T_T) B_{N+1}^{(2)}[(NT + \tau)/T_T] B_{-1}^{(3)}(0)}{B_0^{(1)}(0) B_0^{(2)}(0) B_0^{(3)}(0)} \right|. \quad (3.51)$$

One obtains this value experimentally by fitting a sine curve to the recorded signal data. This is the standard method of analysis in most TLI experiments. Note that \mathcal{V}_{\sin} may assume values larger than 100% if the underlying fringe signal differs from a sinusoidal pattern.

We find that the grating separation time T enters the detected fringe amplitudes (3.49) and the visibility (3.51) exclusively through the argument of the Talbot coefficients (3.41), which are periodic. This explains the periodic revival of interference fringes in unit steps of the Talbot time (3.36), which also constitutes the characteristic mass dependence of the Talbot-Lau interference effect and distinguishes it from a classical moiré effect.

Resonant and symmetric configuration In order to observe a significant fringe contrast in most realistic settings, the grating asymmetry number $N \in \mathbb{N}$ in (3.49) and the resonance deviation $|\tau| \ll T_T$ must be sufficiently small. From the visibility expression (3.51) we read that a large asymmetry N implies that the fringe oscillation is generated by high-order Talbot coefficients. These Fourier coefficients generally fall off rapidly with increasing order, which decreases the maximum achievable contrast to low values. Therefore, the symmetric configuration $N = 1$ is most suitable for all practical purposes where distinct fringes are intended.

For the same reason, the time deviation τ is also limited, $|\tau| \lesssim hT_T/P_0 d = md/P_0$, due to the momentum spread P_0 of the particle ensemble. The latter typically covers several thousand grating momenta in the molecular TLI experiments considered here, in which case we can safely neglect the influence of τ on the Talbot coefficients and on the fringe shift in (3.49),

$$S_\ell \approx \tilde{D} \left(\frac{\ell \tau}{T_T} d \right) B_{-N\ell}^{(1)}(0) B_{(N+1)\ell}^{(2)} \left(\frac{\ell NT}{T_T} \right) B_{-\ell}^{(3)}(0), \quad \delta x_a \approx -\frac{aT^2}{2} N(N+1). \quad (3.52)$$

This implies that a resonance mismatch $\tau \neq 0$ mainly diminishes the fringe visibility as it reduces the non-zero Fourier components of the fringe pattern (3.47) and (3.49) by the factor $|\tilde{D}(\ell \tau d/T_T)| < 1$ for $\ell \neq 0$. Moreover, the result shows that no fringes would appear if G_1 were a pure phase grating, since this would imply $|t^{(1)}(x)|^2 = 1$ and $B_n^{(1)}(0) = \delta_{n,0}$. Both G_1 and G_3 must be amplitude gratings; their phase modulation properties do not enter the result.

Let me remark that the situation is different if one works with a well-collimated ensemble of particles, where P_0 is of the order of the grating momentum h/d . In this case, larger time deviations τ are permitted, and an off-resonant fringe pattern at $\tau \neq 0$ may appear even if G_1 is a pure phase grating. Such a transient effect was demonstrated with thermal atom ensembles in standing-wave gratings [62, 126]. Here, we restrict our view to the resonant and symmetric configuration, $N = 1$ and $\tau = 0$, which is best suited to achieve high contrast with incoherent particle ensembles. This has been the standard configuration of all molecular TLI experiments so far. The quantum and classical fringe signal differ solely by the Talbot coefficients of G_2 ,

$$\begin{Bmatrix} S(x_S) \\ S_{\text{cl}}(x_S) \end{Bmatrix} = \sum_{\ell} B_{-\ell}^{(1)}(0) \begin{Bmatrix} B_{2\ell}^{(2)}(\ell T/T_T) \\ C_{2\ell}^{(2)}(\ell T/T_T) \end{Bmatrix} B_{-\ell}^{(3)}(0) \exp \left[\frac{2\pi i \ell}{d} (x_S - aT^2) \right]. \quad (3.53)$$

3.2.1.3. Incoherent effects and decoherence events

I have now presented a phase-space model for the coherent propagation of matter waves through a generic TLI scheme. Yet, this will not necessarily suffice to describe the Talbot-Lau effect in a realistic setting. Environmental decoherence and other stochastic processes may affect the coherence properties of the state and modify the interference effect depending on the experimental conditions. In the following, I distinguish incoherent grating effects and free-space decoherence events. The latter can occur randomly at any time and any place while the particles evolve freely from one grating to another. The former modify the grating transformation and take on the same periodic spatial dependence.

For our purposes it will suffice to consider only norm-preserving and stochastic momentum transfer processes, which are described by state transformations of the form $\langle x|\rho|x'\rangle \mapsto \mathcal{R}(x, x') \langle x|\rho|x'\rangle$. Such processes randomly redistribute momentum and thus affect the spatial coherence properties of the state, but they leave the spatial density distribution invariant, $\mathcal{R}(x, x) = 1$ for all x . The latter follows from norm conservation,

$$\int dx \mathcal{R}(x, x) \langle x|\rho|x\rangle = \int dx \langle x|\rho|x\rangle = 1, \quad (3.54)$$

which must hold for arbitrary density operators ρ . Explicit forms of the decoherence function $\mathcal{R}(x, x')$ will be specified later. The corresponding phase-space transformation is given by a momentum convolution,

$$\begin{aligned} w(x, p) &\mapsto \int dq \tilde{\mathcal{R}}(x, q) w(x, p - q), \\ \tilde{\mathcal{R}}(x, q) &= \frac{1}{2\pi\hbar} \int ds e^{iqs/\hbar} \mathcal{R}\left(x - \frac{s}{2}, x + \frac{s}{2}\right). \end{aligned} \quad (3.55)$$

A phase-space transformation of this type can also be conceived in a purely classical picture: A stochastic process that kicks a particle at position x with a random kick distribution $\tilde{\mathcal{R}}(x, q)$ can be described by the transformation $f(x, p) \mapsto \int dq \tilde{\mathcal{R}}(x, q) f(x, p - q)$. It washes out the momentum distribution of the ensemble state.

Incoherent grating effects Apart from the coherent modulation of the matter-wave state, each grating G_k may also contribute an incoherent process $\mathcal{R}^{(k)}(x, x')$ if it couples to internal degrees of freedom of the particles in an uncontrollable manner. The absorption and the elastic scattering of single photons from an optical standing-wave grating are the most important processes, which will be of relevance. I have elaborated on the corresponding decoherence functions, $\mathcal{R}_{\text{abs, sca}}(x, x')$, in the context of the light-matter interaction in Section 2.1.4.3, see Eqs. (2.48) and (2.50) on page 24f. The periodicity of the grating implies that the decoherence function is periodic in both x and x' , too. Hence, we can perform a Fourier expansion with respect to $(x + x')/2$,

$$\begin{aligned} \mathcal{R}^{(k)}(x, x') &= \sum_{n=-\infty}^{\infty} R_n^{(k)} \left(\frac{x' - x}{d} \right) \exp \left[\frac{2\pi i n}{d} \left(\frac{x + x'}{2} \right) \right], \\ R_n^{(k)}(\xi) &= \frac{1}{d} \int_{-d/2}^{d/2} dx \mathcal{R}^{(k)} \left(x - \xi \frac{d}{2}, x + \xi \frac{d}{2} \right) \exp \left(-\frac{2\pi i n x}{d} \right), \end{aligned} \quad (3.56)$$

where $R_n^{(k)}(0) = \delta_{n,0}$. Putting the coherent and the incoherent part together yields a double convolution of the Wigner function with the coherent transmission kernel $T^{(k)}(x, p)$ and the incoherent kernel $\tilde{\mathcal{R}}^{(k)}(x, p)$, which can be subsumed under the modified grating kernel,

$$\begin{aligned}\tilde{T}^{(k)}(x, p) &= \int dq \tilde{\mathcal{R}}^{(k)}(x, p - q) T^{(k)}(x, q) \\ &= \frac{1}{2\pi\hbar} \sum_n \exp\left(\frac{2\pi i n x}{d}\right) \int ds e^{ips/\hbar} \sum_j B_{n-j}^{(k)}\left(\frac{s}{d}\right) R_j^{(k)}\left(\frac{s}{d}\right).\end{aligned}\quad (3.57)$$

We obtain the modified fringe pattern if we replace the quantum and classical Talbot coefficients by the modified versions,

$$\tilde{B}_n^{(k)}(\xi) = \sum_j B_{n-j}^{(k)}(\xi) R_j^{(k)}(\xi), \quad \tilde{C}_n^{(k)}(\xi) = \sum_j C_{n-j}^{(k)}(\xi) R_j^{(k)}(\xi). \quad (3.58)$$

Here, I implicitly assume that $\tilde{\mathcal{R}}^{(k)}$ can be interpreted as a momentum averaging process that would act on a classical particle ensemble in the same way as it acts on a quantum state in phase space.

We notice that the value of the Talbot coefficients at $\xi = 0$ remains unchanged, $\tilde{B}_n^{(k)}(0) = B_n^{(k)}(0)$. The incoherent modification is therefore only relevant at the second grating, $k = 2$, where the spatial coherence properties (the momentum structure) of the particle state affect the final fringe signal (3.53).

Free-space decoherence events The other important class of incoherent modifications of the Talbot-Lau effect are free-space events that may occur uniformly during the propagation time. They include, for instance, environmental decoherence by gas collisions, or by the absorption, emission, and scattering of thermal photons. Moreover, they can be employed in metrological applications, where such events are evoked on purpose to manipulate the fringe contrast in a controlled way. I will discuss the example of absorption spectroscopy in Section 3.3.

Let us consider a single decoherence event \mathcal{R} occurring at a time $t \in [-T_1, T_2]$ before or after the second grating. If we assume that the underlying process is uniform in space, then the state transformation will not depend on the position of each ensemble particle, $\mathcal{R}(x, x') = \mathcal{R}(x' - x)$ and $\tilde{\mathcal{R}}(x, p) = \tilde{\mathcal{R}}(p)$ in (3.55). This momentum averaging transformation must be inserted at the right moment into the phase-space scheme that has led us to the Wigner function (3.43) and to the fringe pattern $w_3(x)$ at G_3 . I do this explicitly for the general case in Appendix B.5. Here, the discussion is restricted to the resonant symmetric configuration where the fringe pattern is effectively smeared out by the kick distribution, $\tilde{w}_3(x) = \int dq \tilde{\mathcal{R}}(q) w_3[x - q(T - |t|)/m]$, as follows from (B.25). The form of the equation implies that the averaging effect is most severe if the event occurs directly at the second grating, $t = 0$, and it does not depend on whether the event takes place before or after G_2 . The modulated Fourier components of the detection signal (and of the fringe pattern) read as

$$\tilde{S}_\ell = \mathcal{R}\left(\ell d \frac{T - |t|}{T_T}\right) S_\ell. \quad (3.59)$$

Environmental decoherence can be understood as a random series of such events that may occur uniformly at all times t . One can establish a time-dependent rate equation based on the individual event transformation (3.59) and solve it to obtain the mean overall contrast reduction by decoherence [40].

3.2.2. The Kapitza-Dirac Talbot-Lau interferometer (KDTLI)

Let me illustrate the just developed phase-space model by discussing the basic features of the KDTLI setup, Figure 3.6 (b), as currently operated in Vienna in measurements on large organic molecules. It replaces the former TLI setup with three material gratings, which had become obsolete due to the growing highly dispersive van der Waals interaction between the molecules and the grating walls. On the theoretical side, the beauty of the KDTLI scheme lies in the fact that it can be assessed in analytic terms.

The Vienna KDTLI is a horizontal grating arrangement, where G_2 is a standing wave of period $d = \lambda/2 = 266$ nm, as generated in the focus of a green laser of wavelength λ illuminating a mirror. The other gratings are material masks of the same period with an opening fraction $f \lesssim 0.5$. The grating distance is set to $L = 10.5$ cm, and the corresponding time T varies with the velocity of the interfered particle species.

Normally, there is no external acceleration acting on the particles, $a = 0$, that would shift the final fringe pattern¹⁶. For metrological applications, however, a static electric field E can be applied between two electrodes, which deflects the particles on their way from G_1 to G_2 and shifts the interference fringe pattern by the same amount. The deflection is proportional to the dipole force, $F_x = \chi(0) \partial_x |E|^2 / 2$, that acts on the particle while it passes the electrodes. The interference fringe pattern allows one to resolve the deflection on the sub-micrometer level and, therefore, to measure the static electric polarizability $\chi(0)$ of the particles at high precision [105, 106, 117, 127, 128].

3.2.2.1. Coherent description

I will now give an overview of the theoretical description of the KDTL interference effect in the absence of free-space Rayleigh scattering and absorption at the grating. An exhaustive treatment can also be found in [7]. The results will be required in the subsequent modification of the effect due to single-photon absorption, drawing from the results of Chapter 2, page 18ff. There, I have developed a detailed description of the optical grating interaction.

According to Section 2.1.4.1, the transmission function of a pure standing-wave phase grating can be written as $t^{(2)}(x) = \exp(i\phi_0 \cos^2 kx)$, with $k = 2\pi/\lambda = \pi/d$ the wave number of the laser and ϕ_0 the eikonal phase factor (2.39) defined on page 21. The latter is related to the dipole interaction with the laser field; it is proportional to the polarizability of the particle, the laser power, and the inverse of the longitudinal velocity v_z . The d -periodic transmission function can be expanded as a Fourier sum of Bessel functions [113], Equation (3.38) with $b_n^{(2)} = i^n \exp(i\phi_0/2) J_n(\phi_0/2)$. The associated Talbot coefficients (3.40) are obtained with help of Graf's addition theorem for Bessel functions [113]. It states that

$$\left[\frac{u - v \exp(-i\varphi)}{u - v \exp(i\varphi)} \right]^{\pm n/2} J_n(w) = \sum_{j=-\infty}^{\infty} J_{j+n}(u) J_j(v) e^{\pm i j \varphi}, \quad (3.60)$$

where $\varphi \in [0, \pi]$ without loss of generality. (The sign change allows for larger phase angles φ .) The term $w = \sqrt{u^2 + v^2 - 2uv \cos \varphi} = u \sqrt{1 + (v/u)^2 - 2v \cos \varphi / u}$ is the analytic continuation of the positive root, $w \rightarrow +u$, in the limit $v \rightarrow 0$.

¹⁶ Inertial forces such as the Coriolis force can be safely neglected in the velocity and mass regime considered so far.

In the present case, we have $u = v = \phi_0/2$ and $\varphi = 2\pi\xi$, which leads to the Talbot coefficients

$$B_n^{(2)}(\xi) = i^n e^{i\pi n \xi} \sum_j J_j\left(\frac{\phi_0}{2}\right) J_{j-n}^*\left(\frac{\phi_0}{2}\right) e^{-2\pi i j \xi} = J_n(\phi_0 \sin \pi \xi). \quad (3.61)$$

We immediately find that $B_n^{(2)}(N) = \delta_{n,0}$ for $N \in \mathbb{N}_0$, as expected from a pure phase grating. The classical Talbot coefficients are obtained from (3.42), using the eikonal momentum kick expression $q^{(2)}(x) = -(\pi\hbar/d) \sin 2\pi x/d$ [7]. This yields

$$C_n^{(2)}(\xi) = c_n^{(2)}(\xi) = J_n(\phi_0 \pi \xi). \quad (3.62)$$

The first and the third gratings are given by a periodic mask of material slit apertures, $|t^{(1,3)}(x)|^2 = \sum_n \Theta(f_{1,3}d/2 - |x - nd|)$, with the slit opening fractions $f_{1,3}$. Their Fourier coefficients read as $B_n^{(1,3)}(0) = f_{1,3} \text{sinc}(\pi n f_{1,3})$. This leaves us with the quantum and classical Fourier components of the detection signal,

$$\begin{Bmatrix} S(x_S) \\ S_{cl}(x_S) \end{Bmatrix} = \sum_\ell f_1 f_3 \text{sinc}(\pi \ell f_1) \text{sinc}(\pi \ell f_3) \begin{Bmatrix} J_{2\ell}(\phi_0 \sin \pi \ell T/T_T) \\ J_{2\ell}(\phi_0 \pi \ell T/T_T) \end{Bmatrix} \exp\left(\frac{2\pi i \ell x_S}{d}\right). \quad (3.63)$$

It depends on the longitudinal particle velocities through ϕ_0 and $T = L/v_z$, and it must be averaged over a realistic v_z -distribution when comparing it to experimental data. We notice that the quantum and the classical expression converge in the quasi-classical limit, $v_z \rightarrow \infty$, or $T/T_T \ll 1$.

The sinusoidal visibilities (3.51) read as

$$\begin{Bmatrix} \mathcal{V}_{\sin} \\ \mathcal{V}_{\sin}^{cl} \end{Bmatrix} = 2 \left| \text{sinc}(\pi f_1) \text{sinc}(\pi f_3) \begin{Bmatrix} J_2(\phi_0 \sin \pi T/T_T) \\ J_2(\phi_0 \pi T/T_T) \end{Bmatrix} \right|. \quad (3.64)$$

The fringe contrast vanishes at $T = 0$ in both cases. However, only the quantum interference signal exhibits a periodic revival of this zero in visibility at integer multiples of the Talbot time. This is where the phase modulation at G_2 cancels, and where a Talbot-Lau fringe pattern mimics the ideal shadow projection of the aperture, as in the case of the ideal Talbot effect. A pure phase grating cannot produce any interference fringes there, whereas the classical model may lead to visible fringes due to the deflection of the particle trajectories in the standing-wave field. At the same time, the achievable shadow fringe contrast decreases with growing grating separation T as the oscillation amplitude of the Bessel function converges to zero. The sinusoidal visibility is largest when the Bessel function $J_2(x)$ assumes its maximum, $\max J_2(x) \approx 0.49$, at $x \approx \pm 3.05$. Fixing the grating phase shift at $\phi_0 \gtrsim \pi$, this can only be reached at a single time $T < T_T$ in the classical case, whereas it appears repeatedly for periodic T -values between two subsequent Talbot orders in the quantum case. The quantum nature of the fringe pattern can thus be easily verified in the experiment by varying the grating distance L or the particle velocity v_z .

3.2.2.2. Modification due to the absorption of grating photons

The coherent description of the KDTLI is only valid for subwavelength particles with negligible absorption and Rayleigh scattering cross sections, that is, if the mean number of absorbed and

scattered grating photons $n_{0,\text{sca}} \ll 1$. See Eqs. (2.42) on page 23 and (2.50) on page 25 for a definition of these terms. This limit can be appropriate for the assessment of experiments with a subset of non-absorbing molecules, such as the C_{60} -fullerene. But there are other examples, such as C_{70} , where the absorption of single photons does influence the interference contrast noticeably [7]. On the other hand, Rayleigh scattering has not yet been an issue since all particles used so far were orders of magnitude smaller than the grating wavelength.

I have layed out everything necessary to incorporate the influence of absorption and scattering on the overall grating transformation in a few steps of calculation. The combined decoherence function, $\mathcal{R}^{(2)}(x, x') = \mathcal{R}_{\text{abs}}(x, x') \mathcal{R}_{\text{sca}}(x, x')$, consists of the absorption term (2.48) and the scattering term (2.50), which were obtained by solving the associated master equations in Section 2.1.4.3. The coefficients of the Fourier expansion (3.56) can be given explicitly in terms of modified Bessel functions [113] after applying a few trigonometric identities,

$$R_n^{(2)}(\xi) = \exp \left\{ -n_0 \frac{1 - \cos \pi \xi}{2} - \frac{n_{\text{sca}}}{2} \left[1 - 3 \cos \pi \xi \frac{\sin \pi \xi - j_1(\pi \xi)}{2\pi \xi} \right] \right\} \\ \times I_n \left\{ n_0 \frac{1 - \cos \pi \xi}{2} + \frac{n_{\text{sca}}}{2} \left[3 \frac{\sin \pi \xi - j_1(\pi \xi)}{2\pi \xi} - \cos \pi \xi \right] \right\}. \quad (3.65)$$

With this we arrive at the modified quantum and classical Talbot coefficients (3.58) that include both effects.

Let us now restrict to the point-particle limit where no free-space scattering takes place in the grating, $n_{\text{sca}} \approx 0$. We can apply Graf's addition theorem (3.60) another time¹⁷ to obtain an explicit form of the modified Talbot coefficients,

$$\widetilde{B}_n^{(2)}(\xi) = e^{-\zeta_{\text{abs}}(\xi)} \left[\frac{\zeta_{\text{coh}}(\xi) + \zeta_{\text{abs}}(\xi)}{\zeta_{\text{coh}}(\xi) - \zeta_{\text{abs}}(\xi)} \right]^{n/2} J_n \left[\text{sgn} \{ \zeta_{\text{coh}}(\xi) - \zeta_{\text{abs}}(\xi) \} \sqrt{\zeta_{\text{coh}}^2(\xi) - \zeta_{\text{abs}}^2(\xi)} \right], \quad (3.66)$$

with $\zeta_{\text{coh}}(\xi) = \phi_0 \sin \pi \xi$ and $\zeta_{\text{abs}}(\xi) = n_0 \sin^2(\pi \xi/2) = \beta \phi_0 (1 - \cos \pi \xi)$. The modified sinusoidal visibility reads as

$$\mathcal{V}_{\text{sin}} = 2 |\text{sinc}(\pi f_1) \text{sinc}(\pi f_3)| \exp \left\{ \beta \phi_0 \left[\cos \left(\frac{\pi T}{T_T} \right) - 1 \right] \right\} \\ \times \left| \frac{\beta + \sin(\pi T/T_T) - \beta \cos(\pi T/T_T)}{\beta - \sin(\pi T/T_T) - \beta \cos(\pi T/T_T)} J_2 \left[\phi_0 \sqrt{\sin^2 \left(\frac{\pi T}{T_T} \right) - 4\beta^2 \sin^4 \left(\frac{\pi T}{2T_T} \right)} \right] \right|. \quad (3.67)$$

Both ϕ_0 and n_0 are controlled by the laser power. In order to mimic this dependence, it will be convenient to introduce the parameter

$$\beta = \frac{n_0}{2\phi_0} = \frac{\sigma_{\text{abs}} \lambda \varepsilon_0}{2\pi \Re \{ \chi \}} = \frac{\sigma_{\text{abs}} d}{4\pi^2 \alpha}, \quad (3.68)$$

¹⁷ Here, we make use of the specific formulation [7]

$$\left[\frac{u - v}{u + v} \right]^{n/2} J_{-n} \left[\text{sgn}(u + v) \sqrt{u^2 - v^2} \right] = \sum_{j=-\infty}^{\infty} J_j(u) I_{j+n}(v)$$

for $u, v \in \mathbb{R}$, $u \neq v$. It can be derived from the general form (3.60) using the relation $I_n(v) = (-i)^n J_n(iv)$.

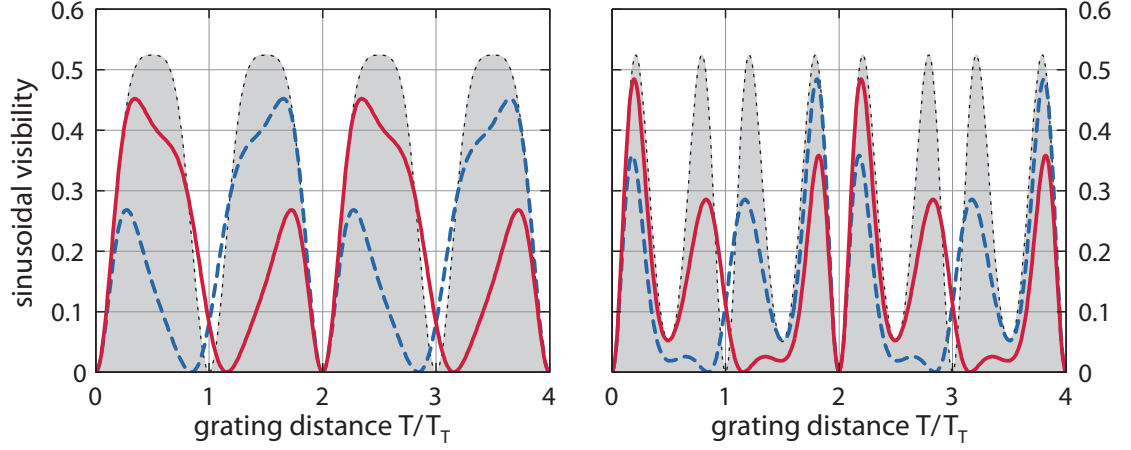


Figure 3.7. Absorption-modified sinusoidal visibility in an exemplary KDTLI setup versus the grating distance T in units of the Talbot time. The left and the right panel correspond to different laser powers, respectively $\phi_0 = 3$ and $\phi_0 = 5$. The modified visibility (3.67) is plotted as a solid line, whereas the dashed line represents the analogous result as predicted in [7]. I take $\beta = 0.25$, and I use the same slit opening fraction as in [7], $f_1 = f_3 = 0.42$, for the two material grating masks $G_{1,3}$. The shaded area depicts the interference contrast (3.64) in the absence of absorption.

a constant which depends solely on the grating period and on the absorption cross section σ_{abs} and dipole polarizability $\alpha = \Re\{\chi\}/4\pi\epsilon_0$ (in cgs units) of the particle. A variation of the laser power changes both ϕ_0 and n_0 proportionally while leaving the ratio β unchanged. Given the grating power P_L , its y -waist w_y , and the particle velocity v_z , we can write $\phi_0 = 8\sqrt{2\pi}\alpha P_L/\hbar c v_z w_y$ and $n_0 = 2\beta\phi_0$.

Expression (3.66) must be compared to the result in the previous treatment of the KDTLI scheme in [7]. There, the absorption of single photons from the standing-wave grating was described by a classical random walk model which did not properly incorporate the coherence of the standing-wave field in the absorption process. The two counter-propagating running-wave components of the standing-wave mode were implicitly taken to be *distinguishable*. For instance, this implied that the absorption of one photon would transform the pure matter-wave eigenstate $|p\rangle$ into a *mixture* of two contradirectionally kicked eigenstates $|p \pm \hbar k\rangle$. In fact, the running-wave components are *indistinguishable* and the momentum state must be transformed into a *superposition* of kicked eigenstates, accordingly. I have given the underlying master equation model (2.47) in Section 2.1.4.3, page 24. Here, it is only the conditional state transformations corresponding to different numbers of absorbed photons which are mixed incoherently. The difference between the present and the former result amounts to a mere sign flip¹⁸, $\zeta_{\text{coh}}(\xi) \rightarrow -\zeta_{\text{coh}}(\xi)$.

I illustrate the difference in Figure 3.7 where the sinusoidal interference visibility is plotted versus the grating distance T in units of the Talbot time. The laser power is assumed to be fixed at a value that corresponds to the eikonal phase $\phi_0 = 3$ (right panel) and $\phi_0 = 5$ (left panel). Here, I assume a fictitious particle with a rather large absorption cross section, $\beta = 0.25$, to see a pronounced modification. That is, each value of ϕ_0 corresponds to $n_0 = 0.5\phi_0$. The solid line represents the

¹⁸ Note that the former treatment is based on a sine-type standing wave mode, whereas I use a cosine mode. However, this difference merely determines the parity of the resulting fringe pattern, but it is not responsible for a change in the fringe visibility.

present model, Equation (3.67), whereas the dashed line represents the result taken from [7]. The unmodified visibility ($\beta = 0$) is depicted as a shaded area in the background. We observe that the absorption effect generally diminishes the interference contrast, but it suppresses only every second Talbot order to a large extent. The present result affects exactly those Talbot orders more, which are less affected by the former result, and vice versa.

3.2.3. The optical time-domain ionizing Talbot-Lau interferometer (OTITLI)

Let me now turn to the most recent version of the TLI scheme using a pulsed arrangement of ionizing laser gratings in the time domain, as depicted in Figure 3.6 (c) on page 85. We proposed the OTITLI scheme as a viable method to interfere large polarizable nanoparticles in [10], where we also gave a full feasibility study for the realization of this scheme with metal clusters of less than 10^6 amu. Meanwhile, the experiment has been set up in Vienna, and it has led to the first proof-of-principle results with small clusters of anthracene molecules [13].

In this section I formulate the theoretical description and assess its main predictions. Details on the experiment, as well as general mass limits of the OTITLI will be studied in Section 3.4.

3.2.3.1. Coherent description and results

The coherent description of the OTITLI scheme follows straightforwardly from the theory of optical depletion gratings presented in Section 2.1.4.2, page 22f. Here, I assume that the absorption of a single photon from the grating always ionizes the particle and removes it from the interrogated ensemble. The associated transmission function reads as $t^{(k)}(x) = \exp\left[\left(i\phi_0^{(k)} - n_0^{(k)}/2\right)\cos^2\pi x/d\right]$, with $\phi_0^{(k)}$ and $n_0^{(k)}$ the eikonal phase and the mean number of absorbed photons in the antinodes of G_k . The associated Fourier components are given by modified Bessel functions,

$$b_n^{(k)} = \exp\left(i\frac{\phi_0^{(k)}}{2} - \frac{n_0^{(k)}}{4}\right) I_n\left(i\frac{\phi_0^{(k)}}{2} - \frac{n_0^{(k)}}{4}\right). \quad (3.69)$$

We arrive at the Talbot coefficients by applying Graf's addition theorem (3.60) once again,

$$B_n^{(k)}(\xi) = e^{-n_0^{(k)}/2} \left[\frac{\zeta_{\text{coh}}(\xi) - \zeta_{\text{ion}}(\xi)}{\zeta_{\text{coh}}(\xi) + \zeta_{\text{ion}}(\xi)} \right]^{n/2} J_n \left[\text{sgn}\{\zeta_{\text{coh}}(\xi) + \zeta_{\text{ion}}(\xi)\} \sqrt{\zeta_{\text{coh}}^2(\xi) - \zeta_{\text{ion}}^2(\xi)} \right], \quad (3.70)$$

with $\zeta_{\text{coh}} = \phi_0^{(k)} \sin \pi \xi$ and $\zeta_{\text{ion}} = (n_0^{(k)}/2) \cos \pi \xi$. Notice the subtle but essential differences between this expression and the absorption-modified KDTLI coefficients (3.66). In particular, the coefficients here do not vanish at $\xi = 0$,

$$B_n^{(k)}(0) = (-)^n \exp\left(-\frac{n_0^{(k)}}{2}\right) I_n\left(\frac{n_0^{(k)}}{2}\right). \quad (3.71)$$

As mentioned above, these terms represent the Fourier coefficients of the transmission probability at each standing-wave grating pulse G_k , and they are all that is needed to describe the first and the third grating mask of the OTITLI scheme. A convolution of these terms with the eikonal kick coefficients yields the classical version (3.42) of the Talbot coefficients. We note that the kick coefficients

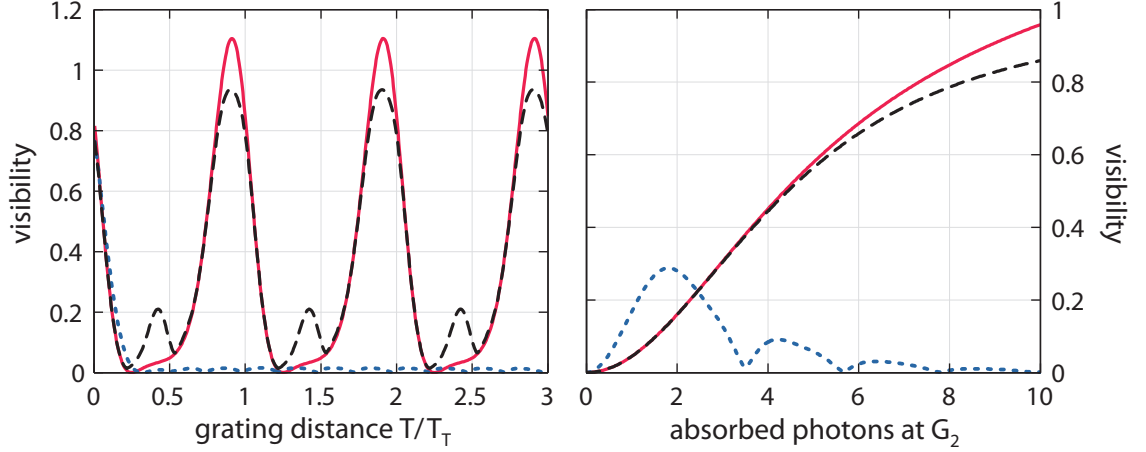


Figure 3.8. Predicted OTITLI fringe visibility as a function of the grating distance T in units of the Talbot time (left) and of the mean number $n_0^{(2)}$ of absorptions at the second grating (right). The other two gratings are kept fixed at $n_0^{(1,3)} = 8$, and the particles shall be characterized by $\beta = 1$. The data on the left and on the right are evaluated at $n_0^{(2)} = 8$ and $T = T_T$, respectively. I plot the sinusoidal quantum visibility (solid line), the conventional quantum contrast (dashed line), and the classical ‘shadow’ contrast (dotted line).

are the same as in the KDTLI scheme, $c_n^{(k)}(\xi) = J_n(\phi_0^{(k)}\pi\xi)$. We thus find that the classical Talbot coefficients $C_n^{(k)}(\xi)$ can be brought into the same form as the quantum coefficients (3.70), but with different parameters, $\zeta_{\text{coh}}^{\text{cl}} = \phi_0^{(k)}\pi\xi$ and $\zeta_{\text{ion}}^{\text{cl}} = n_0^{(k)}/2$. This implies that the quantum and the classical description converge in the limit $\xi \rightarrow 0$. In practice, this corresponds to the limit of large masses and relatively small pulse separation times, $T \ll T_T$. The sinusoidal interference visibility reads as

$$\mathcal{V}_{\text{sin}} = 2 \frac{I_1\left(\frac{n_0^{(1)}}{2}\right) I_1\left(\frac{n_0^{(3)}}{2}\right)}{I_0\left(\frac{n_0^{(1)}}{2}\right) I_0\left(\frac{n_0^{(3)}}{2}\right)} \left| \frac{\beta \cos\left(\frac{\pi T}{T_T}\right) - \sin\left(\frac{\pi T}{T_T}\right)}{\beta \cos\left(\frac{\pi T}{T_T}\right) + \sin\left(\frac{\pi T}{T_T}\right)} J_2\left[\frac{n_0^{(2)}}{2\beta} \sqrt{\sin^2\left(\frac{\pi T}{T_T}\right) - \beta^2 \cos^2\left(\frac{\pi T}{T_T}\right)}\right] \right|, \quad (3.72)$$

and the classical counterpart is obtained by substituting $\cos(\pi T/T_T)$ by 1 and $\sin(\pi T/T_T)$ by $\pi T/T_T$.

In Figure 3.8 I plot the sinusoidal interference visibility as a function of the grating separation T/T_T (left panel, fixing $n_0^{(2)} = 8$) and of the mean absorption number $n_0^{(2)}$ at G_2 (right panel, fixing $T = T_T$). It is given by the solid line in the plot. The dashed line represents the conventional interference contrast \mathcal{V} , as defined by the relative difference between the maximum and the minimum of the fringe signal in (3.50). By construction, it cannot be greater than unity, whereas the sinusoidal visibility may exceed this value. The reason is that the fringe signal deviates from a sinusoidal pattern in the high-contrast regions close to integer values of T/T_T , where higher-order Fourier components must be taken into account. The same is true in between the integer Talbot orders, where the first-order Fourier components of the signal, and with them the sinusoidal visibility, vanish. The theory then predicts the appearance of a higher-order harmonic fringe oscillation, which is reflected in

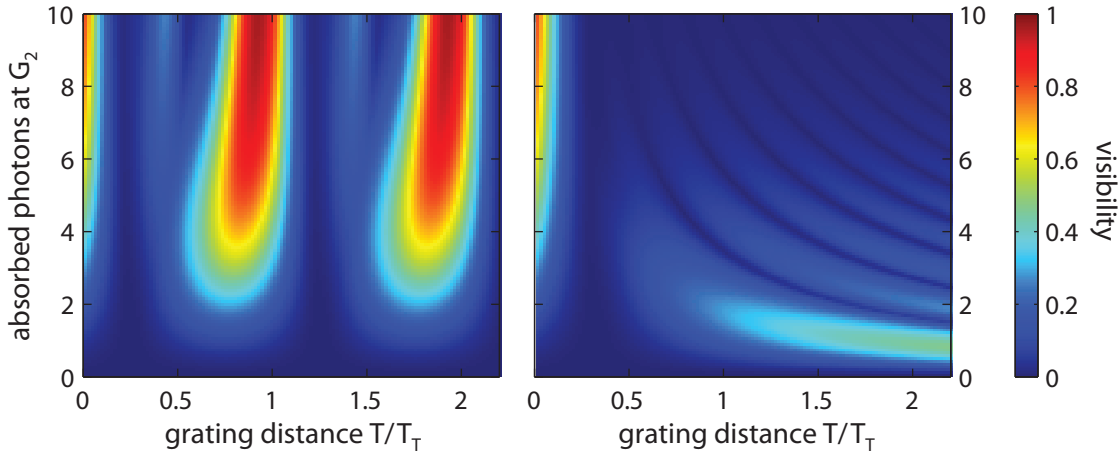


Figure 3.9. Density diagrams of the quantum (left) and the classical (right) fringe contrast as a function of the grating separation time and the absorption number at the second grating. I plot the conventional visibility \mathcal{V} using the same OTITLI configuration as in Figure 3.8, $n_0^{(1,3)} = 8$ and $\beta = 1$.

the conventional visibility \mathcal{V} (dashed line in the left panel). The classical moiré visibility is represented by the dotted line in the two panels. Its dependence on the laser power (through $n_0^{(2)}$) and on the separation time is very different from the quantum version. In particular, it does not exhibit the recurring visibility maxima at integer Talbot orders, which are characteristic for the Talbot-Lau interference effect.

This striking difference between the quantum and the classical model is also clearly demonstrated in Figure 3.9. It depicts the interference (left) and the ‘shadow’ (right) fringe contrast \mathcal{V} as a density plot versus the grating separation and the absorption number. For the results plotted here and in Figure 3.8 I have assumed a fixed material parameter $\beta = 1$, as well as a fixed laser power at G_1 and G_3 , $n_0^{(1)} = n_0^{(3)} = 8$.

At first sight, a material constant β of the order of unity seems not like a generic choice, but it actually covers the specific implementations of the OTITLI with metal clusters conceived in our original proposal [10]. If we describe the cluster by a homogeneous dielectric sphere of radius R and relative permittivity ϵ , then we obtain both its dipole polarizability, $\alpha = \Re\{\chi\}/4\pi\epsilon_0$, and its absorption cross section, $\sigma_{\text{abs}} = k\Im\{\chi\}/\epsilon_0$, from the complex polarizability $\chi = 4\pi\epsilon_0 R^3 (\epsilon - 1)/(\epsilon + 2)$. See Section 2.3 on page 48ff. for details on this model. It is valid as long as the sphere is much smaller than the grating wavelength, $kR \ll 1$. The associated β -parameter,

$$\beta = \frac{3\Im\{\epsilon\}}{|\epsilon|^2 + \Re\{\epsilon\} - 2}, \quad (3.73)$$

depends solely on the dielectric function, which we can estimate by the bulk value of the material [52]. The latter can be found in the literature for various materials and light wavelengths [50]. In the case of VUV light of 157 nm wavelength, for instance, we find $\beta = 1.0$ for gold, $\beta = 9.2$ for silver, and $\beta = -1.3$ for cesium. The last value is negative because cesium behaves like a low-field seeker at this wavelength.

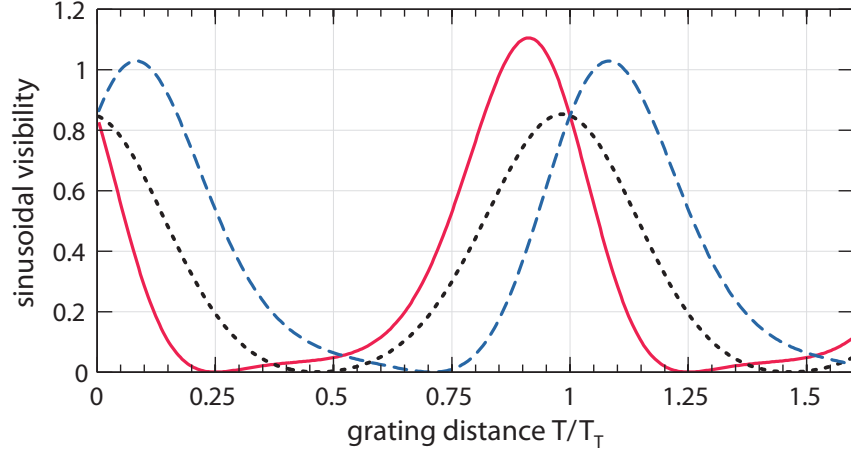


Figure 3.10. Sinusoidal interference visibility for different particles versus the grating distance in units of the Talbot time. The solid, the dashed and the dotted line are associated to particle species with β -values of 1.0, -1.3 and 9.2 , respectively (see text). The three laser gratings are always set to the same absorption number, $n_0^{(1,2,3)} = 8$.

The three exemplary cases are compared in a visibility-versus-time plot in Figure 3.10. The solid line ($\beta = 1.0$) is a part of the respective curve in the left panel of Figure 3.8, whereas the dashed and the dotted lines correspond to the cesium ($\beta = -1.3$) and the silver ($\beta = 9.2$) case. All other parameters are fixed at the same values as before, $n_0^{(1,2,3)} = 8$. We observe that small values of $|\beta|$ shift the visibility maximum further away from integer multiples of the Talbot time than large values. The reason lies in the growing influence of the coherent phase modulation at the grating the smaller the magnitude of β .

Last but not least, the fringe contrast is also varied by tuning the laser power of the first and the third grating. The solid line in the left panel of Figure 3.11 shows how the sinusoidal visibility grows as the increasing absorption number $n_0^{(3)}$ shrinks the effective aperture of transmission through the nodes of the third grating mask. The right panel plots the associated overall transmission probability through the interferometer on a logarithmic scale. It is given by the zeroth Fourier coefficient of the fringe signal, $S_0 = B_0^{(1)}(0) B_0^{(2)}(0) B_0^{(3)}(0)$, and the plot looks the same no matter whether the power of the first, the second or the third grating is varied. Here, we vary only $n_0^{(3)}$, keeping the other gratings fixed at $n_0^{(1,2)} = 8$, and setting $T = T_T$ and $\beta = 1$.

The dashed line shows the predicted visibility and transmission in an inverted detection scheme, where the recorded OTITLI fringe signal is not comprised of the neutral particles transmitted, but of the particles ionized at the third grating. This may be useful to facilitate the detection of particles behind G_3 as it allows one to dispense with the ionization stage in conventional mass spectrometers. The inverted grating is straightforwardly incorporated into the theoretical model by inverting the transmission probability, $|t^{(3)}(x)|^2 \mapsto 1 - |t^{(3)}(x)|^2$. This results in a change of the associated Fourier coefficients, $B_n^{(3)}(0) \mapsto \delta_{n,0} - B_n^{(3)}(0)$. In this case we find that the transmissivity increases with growing laser power since a larger fraction of the particle cloud is ionized at G_3 . However, this comes at the price of an overall reduction of visibility, because the antinodes of an inverted grating

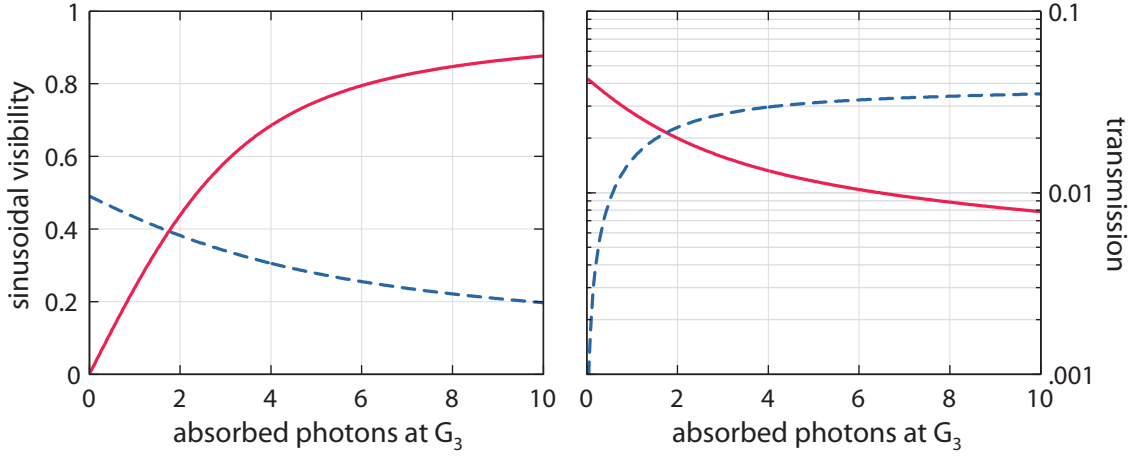


Figure 3.11. Influence of a varying power of the third grating laser on the sinusoidal interference visibility (left) and on the transmission probability through the interferometer (right). The laser power is given in terms of the absorbed photon number $n_0^{(3)}$. The other parameters are fixed at the reference values of the preceding diagrams, $n_0^{(1,2)} = 8$, $T = T_T$ and $\beta = 1$. The dashed line corresponds to the inverted configuration, where the ionized particles are detected behind G_3 instead of the neutrally transmitted ones.

mimic an aperture with a broader effective slit width than the nodes of a conventional ionization grating.

3.2.3.2. Incoherent modification due to Rayleigh scattering

Judging from the concrete predictions of the coherent model I have just assessed in detail, the OTI-TLI scheme appears to be the most promising implementation of the Talbot-Lau effect with heavy particles. It offers full and flexible control over all relevant setup parameters, while avoiding most of the limitations associated to a stationary TLI configuration (with material grating masks). On the other hand, one incurs additional decoherence effects by employing optical gratings, which may restrict the scope of the interferometer to a limited range of particle species. We have observed in Section 3.2.2.2 how the interference visibility in the KDTLI scheme is diminished for particles with large absorption cross sections.

Here, photon absorption, if it is always accompanied by ionization, is an explicit prerequisite for the ionization gratings to work, and radiative decoherence may only arise due to the elastic scattering of grating photons into free space. The Fourier coefficients $R_n^{(2)}(\xi)$ of the scattering decoherence function can be taken from Equation (3.65), which describes the combined decoherence effect of scattering and absorption in a pure phase grating. Setting the absorption number $n_0 = 0$ in that expression leaves us with the mere scattering effect,

$$R_n^{(2)}(\xi) = \exp \left\{ \frac{n_{\text{sca}}^{(2)}}{2} \left[3 \cos \pi \xi \frac{\sin \pi \xi - j_1(\pi \xi)}{2\pi \xi} - 1 \right] \right\} I_n \left\{ \frac{n_{\text{sca}}^{(2)}}{2} \left[3 \frac{\sin \pi \xi - j_1(\pi \xi)}{2\pi \xi} - \cos \pi \xi \right] \right\}. \quad (3.74)$$

The modified Talbot coefficients of the second grating are then given by the convolution (3.58) of these coefficients with the coherent Talbot coefficients (3.70). The modification influences neither the first nor the third grating mask since $R_n^{(1,3)}(0) = \delta_{n,0}$, as already noted above.

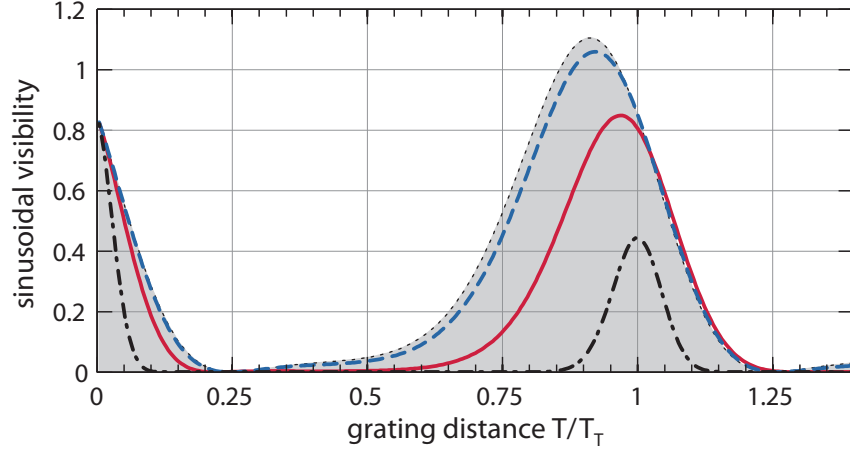


Figure 3.12. Interference visibility as a function of the grating separation time in the presence of light scattering. I evaluate the visibility for different scattering cross sections, while keeping the other parameters fixed at $\beta = 1$ and $n_0^{(1,2,3)} = 8$. The dashed, the solid and the dash-dotted line correspond respectively to a scattering cross section of 0.1, 1 and 10 times the size of the absorption cross section. The shaded area in the background represents the visibility in the absence of scattering.

The impact of the scattering-induced decoherence on the fringe visibility depends once again on the particle properties via the ratio of the scattering and absorption cross section, $n_{\text{sca}}^{(2)}/n_0^{(2)} = \sigma_{\text{sca}}/\sigma_{\text{abs}}$. This ratio should be minimized for an optimal interference effect, as demonstrated in Figure 3.12. There, I plot the sinusoidal fringe visibility versus the grating separation time using three different ratios: $\sigma_{\text{sca}}/\sigma_{\text{abs}} = 0.1, 1$ and 10 , respectively for the dashed, the solid and the dash-dotted line. All other parameters are set to the same values as before, $n_0^{(1,2,3)} = 8$ and $\beta = 1$. The fringe visibility for the coherent case $\sigma_{\text{sca}} = 0$ is depicted by the shaded area. We observe a strong deterioration of contrast when the scattered power gets comparable to the absorbed power.

In practice, however, the scattering modification is rarely of concern since the OTITLI scheme will be mostly applied to polarizable subwavelength particles with a large absorption cross section¹⁹. The associated scattering cross section, which is of second order in the particle's linear response to the field, is then expected to be smaller, as discussed in detail on page 8ff. in Chapter 2. For spherical cluster particles in the dipole approximation²⁰, we find

$$\frac{\sigma_{\text{sca}}}{\sigma_{\text{abs}}} = \frac{2}{9} (kR)^3 \frac{|\varepsilon - 1|^2}{\Im\{\varepsilon\}} = \frac{4\pi^2 m}{3\rho\lambda^3} \frac{|\varepsilon - 1|^2}{\Im\{\varepsilon\}}. \quad (3.75)$$

Here, m and R denote the mass and the radius of the sphere, while ρ and ε are the mass density and the relative permittivity of the cluster material. To give an example, the ratio is of the order of 10^{-9} per atomic mass unit for the case of gold clusters in VUV laser gratings at $\lambda = 157$ nm. This case corresponds also to $\beta = 1.0$, and we may thus associate a mass to each of the curves in Figure

¹⁹ I assume that the absorption of a single photon ionizes the particle at 100% efficiency. This generally implies a pronounced imaginary part of the complex dipole polarizability, that is, $\beta \sim 1$.

²⁰ The scattering and absorption cross sections of a polarizable point particle read as $\sigma_{\text{sca}} = k^4 |\chi|^2 / 6\pi\varepsilon_0^2$ and $\sigma_{\text{abs}} = k\Im\{\chi\} / \varepsilon_0$. The complex polarizability of small dielectric spheres of radius $R \ll \lambda$ is given by $\chi = 4\pi\varepsilon_0 R^3 (\varepsilon - 1) / (\varepsilon + 2)$ [52].

3.12. The dashed line corresponds to gold spheres of 10^8 amu in mass and 26 nm in diameter, which is where light scattering at G_2 starts to affect the interference effect. The solid and the dash-dotted lines would then be related to a mass of 10^9 amu (56 nm diameter) and 10^{10} amu (121 nm diameter), respectively.

At about 10^9 amu, however, we are leaving the subwavelength regime and the present theoretical model ceases to be valid. It turns out that this point constitutes a major mass limitation for conceivable implementations of the OTITLI scheme, as I will discuss in Section 3.4.

3.3. Absolute absorption spectroscopy in the TLI scheme

After having studied the theoretical description of Talbot-Lau interferometry in the preceding section, and before assessing its limits in the next section, I now turn to its application for the metrology of large polarizable particles. In the beginning of Section 3.2.2 I mentioned already that the present KDTLI experiment in Vienna is regularly used for deflectometric measurements of the dipole polarizability of the interfering molecules [105, 106, 117, 127, 128]. Let me focus here on a different example proposed in [6], which is yet to be implemented in the lab.

We can exploit the sensitivity of the Talbot-Lau interferogram to single-photon momenta imparted on the interfering particles to devise an absolute and precise measurement of their absorption cross-section. This is of potential value in the field of molecule and cluster spectroscopy [52, 129, 130], where the absolute absorption cross-sections of many large molecules and clusters are poorly known. Conventional optical methods can be used to measure the overall absorption power of a given particle gas or beam, but this does not convey much information about the single-particle cross section without prior knowledge about the particle density. In fact, optical absorption spectra are routinely measured nowadays, even with large nanoparticles, but the data is often insignificant or imprecise when it comes to absolute values for the single-particle cross-sections (due to the difficulty of measuring particle densities precisely). Obviously, it would suffice to measure the absolute cross-section $\sigma_{\text{abs}}(\omega)$ at a single optical frequency to normalize the whole spectrum.

In the following I will present an interferometric technique to measure the value of σ_{abs} in a non-destructive manner: By shining a laser in between the gratings of the TLI one can induce a controlled modulation of the interference fringe pattern as a function of the laser power and position. I will show that this allows one to extract information about the optical absorption and fluorescence properties of individual molecules.

3.3.1. Experimental setup and theoretical description

Talbot-Lau interferograms are periodic fringe structures sensitive to any kind of deflection of the matter waves between the gratings and on the scale of the fringe period. The basic idea behind the following measurement scheme is to trigger such deflections by the absorption of one or more photons from a running-wave laser (pulse) that is added to the interferometer and that illuminates the interfering particles either before or after the second grating G_2 . This results in a modified fringe pattern which is a mixture of discretely shifted interferograms, and, therefore, exhibits a reduced overall contrast depending on the laser parameters and on σ_{abs} .

The complemented three-grating Talbot-Lau arrangement is sketched in Figure 3.13 for the exemplary case of a KDTLI scheme, where G_2 is an optical phase grating. The reasoning applies also

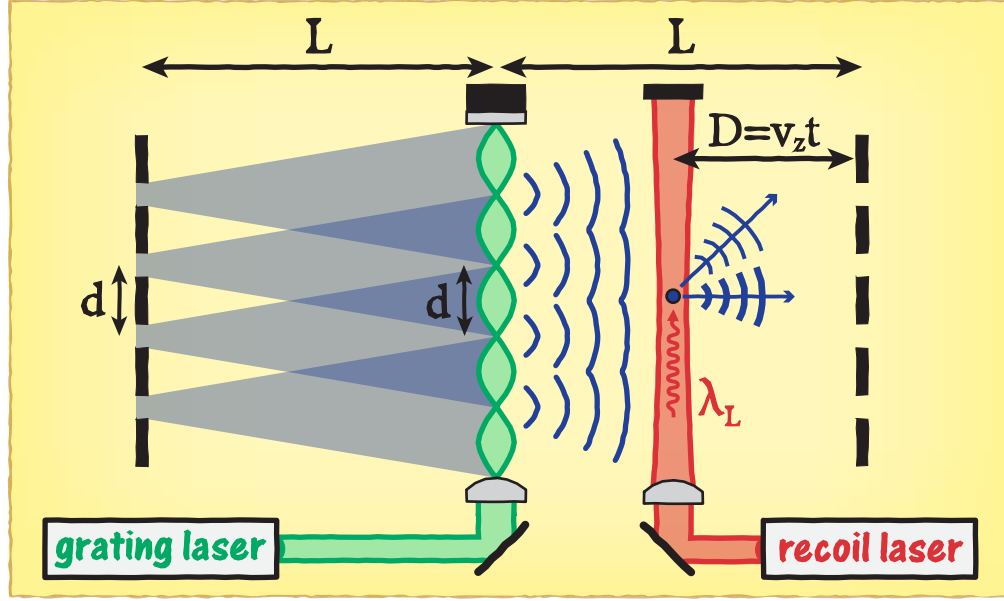


Figure 3.13. Sketch of the proposed arrangement for measuring the absorption cross section of particles interfering in a symmetric Kapitza-Dirac Talbot-Lau setup (with grating distance L and period d , see Figure Section 3.2.2). A recoil laser is added between the gratings G_2 and G_3 , which generates a thin running-wave beam of wavelength λ_L parallel to the grating fringes at the distance D to G_3 . Interfering particles may experience a momentum recoil by absorbing one or more photons when they cross the beam. The shifted interferograms sum up to a modified interference signal, which depends on the absorption probability per particle.

to any other implementation of the TLI, but I will focus here on the present KDTLI and OTITLI setups.

The standard KDTLI scheme in the sketch consists of two material grating apertures $G_{1,3}$ and a standing-wave phase grating G_2 of the same period d placed at equal distances $L = v_z T$, with T the grating separation time for a fixed longitudinal velocity class. The additional recoil laser is now introduced at a distance $D = v_z t$ in front of G_3 . It shall produce a running-wave beam of the wavelength λ_L that runs parallel to the gratings along the positive x -axis. Just like for the grating laser, we require the beam profile to be narrow in the z -dimension and widely extended in the y -direction such that it illuminates all the interfering particles uniformly. The analogous arrangement in the OTITLI scheme would be three identical standing-wave pulses separated by the time T and another short running-wave pulse at the time t before G_3 , which also covers the whole interfering particle cloud.

3.3.1.1. Theoretical description

Given a power P_L and a Gaussian beam profile of the recoil laser, each particle absorbs on average $n_0^{(\text{rec})} = \sqrt{2/\pi} \sigma_{\text{abs}} P_L \lambda_L / \hbar c w_y v_z$ photons from the beam²¹, with w_y the waist parameter in y -direction. A recoil laser pulse of energy E_L and spot area a_L in the time-domain configuration

²¹ Once again, I assume that the beam is sufficiently thin in the z -direction, such that we can neglect the transverse motion of the particles while they cross it.

corresponds to the mean number $n_0^{(\text{rec})} = \sigma_{\text{abs}} E_L \lambda_L / h c a_L$, accordingly. I refer the reader to the preceding chapter for a detailed derivation of the absorption effect. In particular, we have found on page 26 that the probabilistic absorption of running-wave photons leads to the random unitary state transformation (2.53). The short particle-laser interaction transforms the one-dimensional quantum state of motion as

$$\rho \mapsto \sum_{n=0}^{\infty} P_n(n_0^{(\text{rec})}) \exp\left(\frac{2\pi i n x}{\lambda_L}\right) \rho \exp\left(-\frac{2\pi i n x}{\lambda_L}\right), \quad \text{with } P_n(n_0^{(\text{rec})}) = \frac{(n_0^{(\text{rec})})^n \exp(-n_0^{(\text{rec})})}{n!}. \quad (3.76)$$

The term $P_n(n_0^{(\text{rec})})$ represents the Poisson probability of absorbing n photons. No quantum coherence is generated in this transformation, and we can understand it in classical terms. The corresponding Wigner function transformation,

$$w(x, p) \mapsto \sum_{n=0}^{\infty} P_n(n_0^{(\text{rec})}) w\left(x, p - n \frac{h}{\lambda_L}\right), \quad (3.77)$$

resembles a random distribution of discrete momentum kicks. Its impact on the final Talbot-Lau fringe signal is readily obtained using the generic decoherence formalism outlined in Section 3.2.1.3. Introducing the kick distribution $\tilde{\mathcal{R}}(q) = \sum_n P_n(n_0^{(\text{rec})}) \delta(q - nh/\lambda_L)$ we arrive at the expected result for the modified fringe pattern $\tilde{w}_3(x)$, which is a weighted sum of the shifted Talbot-Lau fringe patterns,

$$\tilde{w}_3(x) = \sum_{n=0}^{\infty} P_n(n_0^{(\text{rec})}) w_3\left(x - \frac{nh t}{m \lambda_L}\right). \quad (3.78)$$

Due to the symmetric grating configuration, the same result is obtained if we insert the recoil laser between G_1 and G_2 , at the time t (distance D) after the first grating. Note that the per-photon shift $ht/m\lambda_L$ contributes an additional velocity dependence in the KDTLI case, where $t = D/v_z$.

The associated modulation of the fringe signal follows from Equation (3.59),

$$\tilde{S}_\ell = S_\ell \exp\left[n_0^{(\text{rec})} \exp\left(-\frac{2\pi i \ell t d}{T_L \lambda_L}\right) - n_0^{(\text{rec})}\right] \equiv R_\ell^{(\text{rec})} S_\ell. \quad (3.79)$$

In particular, the sinusoidal fringe visibility \mathcal{V}_{sin} reduces by the factor $|R_1^{(\text{rec})}|$. The strongest reduction, $R_1^{(\text{rec})} = \exp(-2n_0^{(\text{rec})})$, occurs when the recoil laser is positioned such that each absorbed photon shifts the interferogram by half a period, $ht/m\lambda_L = (2k+1)d/2$ with integer k . In this case, the modified fringe pattern (3.78) simplifies to

$$\tilde{w}_3(x) = \exp(-n_0^{(\text{rec})}) \left[\cosh(n_0^{(\text{rec})}) w_3(x) + \sinh(n_0^{(\text{rec})}) w_3\left(x - \frac{d}{2}\right) \right]. \quad (3.80)$$

On the other hand, the fringe pattern remains unaltered when the interferogram is shifted by multiple periods per photon, that is, when the timing condition $ht/m\lambda_L = kd$ is precisely met²².

The probabilistic recoil shift does not only manifest in the reduction of contrast, but it may also lead to the appearance of characteristic new features in the fringe signal. This happens when the

²² This is impossible in the KDTLI experiment because of the finite velocity spread of the particle beam.

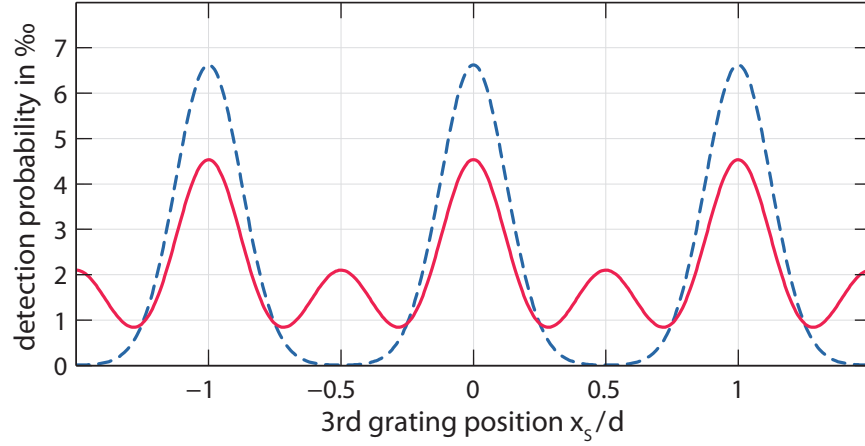


Figure 3.14. Modified interference signal of a OTITLI setup in the presence of a recoil laser that induces half-period recoil shifts per absorbed photon. It is given in terms of the per-particle detection probability (vertical axis). The dashed curve corresponds to the unmodified fringe signal, as predicted by the model in Section 3.2.3 for the parameters $T = T_T$ and $n_0^{(1,2,3)} = 20$. I assume that the third grating can be effectively scanned over three periods d (horizontal axis). The recoil laser intensity shall yield an average of $n_0^{(\text{rec})} = 0.5$ photon absorptions per particle.

latter is a sharply peaked pattern so that the emergence of shifted fringes with growing laser power becomes clearly visible against a flat background. Let me exemplify this for the OTITLI case in Figure 3.14, where I compare the fringe signal with and without recoil²³. The OTITLI interferogram typically exhibits pronounced fringes at integer Talbot orders, $T = NT_T$, when the optical grating pulses are cranked up in energy and hardly transmit particles through the antinodes. The dashed curve represents the interferogram predicted by the coherent model in Section 3.2.3, using a mean absorption number of $n_0^{(1,2,3)} = 20$. Suppose now that we insert the recoil laser pulse between the second and the third grating in such a way that it induces a half-period shift per photon. According to Equation (3.80), additional peaks should then appear in the middle between the original fringes, whereas the latter are partly depleted with growing recoil laser power. This is depicted as the solid curve, assuming a mean absorption of $n_0^{(\text{rec})} = 0.5$ photons. The side peaks grow until the shifted and the unshifted fringe pattern are equally occupied in the limit of large absorptions, $n_0^{(\text{rec})} > 1$, where the sinh-term and the cosh-term in (3.80) are approximately equal.

In most practical situations, however, we are faced with almost sinusoidal fringe patterns, and the sole noticeable effect of the recoil laser is a reduction of fringe visibility. It can be used for a quantitative analysis of the absorption properties of the particle, as I will show in the following. First I should remark, however, that the present treatment implies a few additional assumptions, which may not be automatically fulfilled and must be checked in practice:

- ★ Modelling the probabilistic absorption of recoil photons as a homogeneous Poisson process implies treating subsequent absorptions as statistically independent. That is, I assume that the absorption cross-section of the particle does not significantly change upon photoexcitation.

²³ A similar diagram was presented in our article [6]. There, we studied the effect using the specific example of an H_2TPP molecule in a conventional TLI setup with three material gratings of 991 nm period. Since such a TLI setup is no longer used, I give a more relevant OTITLI example here.

This is not guaranteed in practice, some molecules are indeed known to be ‘optically limited’ absorbers [131]. We can minimize the influence of such uncertainties if we restrict our analysis to low absorption powers, $n_0^{(\text{rec})} < 1$.

- ★ Expression (3.79) for the recoil-induced fringe reduction implies that the detection efficiency of the particles behind the third grating does not depend on their internal state, that is, on the number of absorbed photons. In principle, this assumption could be tested separately by looking at the average transmission through the interferometer as a function of the absorption power
- ★ An additional contrast reduction may occur if the excited particles that have absorbed one or more recoil photons decohere either by fluorescence or by emitting thermal radiation. The latter effect is expected to be negligible for large molecules with a heat capacity $C \gg k_B$. Their internal temperature can only rise by at most $\Delta T = hc/\lambda_L C$ per photon. The fluorescence effect, on the other hand, must be taken into account if present. We can assess it separately in settings where the recoil laser induces full-period shifts per photon, as I will discuss below in Section 3.3.2.
- ★ Last but not least, I assume that it is possible to induce half- and full-period shifts by positioning or timing the recoil laser adequately. However, the largest possible shift is limited by the restriction that the recoil laser cannot be farther away from the first or third grating than the second one, $t < T$. Hence, a full-period shift can only be achieved if $hT/m\lambda_L \geq d$. That is, one must go beyond the first Talbot order if one uses a spectroscopy laser with a wavelength larger than the grating period, $T/T_T \geq \lambda_L/d$.

3.3.1.2. Quantitative analysis

Based on the explicit description of the recoil effect on the fringe signal, Equation (3.79), let me now devise a measurement routine for the absorption cross-section of the interfering particle species: One first measures the unmodified fringe visibility \mathcal{V}_{sin} in a given Talbot-Lau experiment with the recoil laser switched off. Then one measures the reduced visibility, $\tilde{\mathcal{V}}_{\text{sin}}(P_L) = |R_1^{(\text{rec})}| \mathcal{V}_{\text{sin}}$, for different powers P_L of the recoil laser and plots the data on a logarithmic scale versus P_L . The above model predicts a linear dependence,

$$\ln \tilde{\mathcal{V}}_{\text{sin}} = \ln \mathcal{V}_{\text{sin}} - n_0^{(\text{rec})} \left[1 - \cos \left(\frac{2\pi t d}{T_T \lambda_L} \right) \right], \quad (3.81)$$

since the mean number of absorbed photons is proportional to the product of the absorption cross-section and the power, $n_0^{(\text{rec})} \propto \sigma_{\text{abs}} P_L$. The slope parameter of a straight line fit through the data reveals the absorption cross-section, given the power and the time of the laser. Note that the particle density does not enter the measurement result here (as opposed to other spectroscopy schemes) since it is based on single-particle interference effect. In a time-domain setting the power variable is replaced by the pulse energy E_L .

The relevant fitting parameter is independent of the unmodified visibility; only the recoil-induced reduction relative to the original value enters the routine. In principle, this renders our method independent of the precise theoretical prediction of the fringe contrast and robust against many

phase-averaging and decoherence effects in the experiment (that is, if they do not fluctuate between different steps of the measurement procedure). In practice, however, this is only strictly true in the OTITLI setting where the velocity of the particles does not enter the description. In a conventional KDTLI scheme both the timing t and the absorption strength $n_0^{(\text{rec})}$ are inversely proportional to the longitudinal particle velocity v_z , and we must average the results over a given velocity distribution. We are left with a more complicated expression of the ratio between the reduced and the unreduced fringe visibility,

$$\bar{R} = \left| \left\langle B_2^{(2)} \left(\frac{\pi L}{v_z T_T} \right) \right\rangle_{v_z}^{-1} \left\langle B_2^{(2)} \left(\frac{\pi L}{v_z T_T} \right) \exp \left\{ \sqrt{\frac{2}{\pi}} \frac{\sigma_{\text{abs}} P_L \lambda_L}{\hbar c w_y v_z} \left[\exp \left(-\frac{2\pi i D d}{T_T \lambda_L v_z} \right) - 1 \right] \right\} \right\rangle_{v_z} \right|, \quad (3.82)$$

where L denotes the grating distance and $B_2^{(2)}$ is the Talbot coefficient (3.66) determining the KDTLI fringe visibility (3.67). The measured reduction must be compared to the averaged expression \bar{R} , and a simple fit based on the linear form (3.81) for a fixed velocity will introduce errors in the measurement result for σ_{abs} . It can be kept at a minimum by optimizing the velocity dependence of the original fringe visibility and of the recoil shift per photon, $\hbar D / m v_z \lambda_L$. The former is achieved by adjusting the KDTLI setup to a visibility maximum, where $\partial \mathcal{V}_{\text{sin}} / \partial v_z$ is small at a given mean velocity \bar{v}_z of the particles. The latter is achieved by keeping the mean recoil shift small but effective; the ideal value is one half period, $\hbar D / m \bar{v}_z \lambda_L = d/2$. Larger shifts would only lead to a larger variation of the reduction effect over the velocity.

To be specific, let us consider a symmetric distribution of velocities over the interval of length $2\Delta v_z$ around its mean value \bar{v}_z , which fulfills those minimality criteria. In particular, the contrast reduction shall converge to $\exp(-2n_0^{(\text{rec})})$ for $\Delta v_z \rightarrow 0$. By performing a second-order Taylor expansion of the bracketed terms in (3.82) with respect to the velocity deviation from the mean, $v_z - \bar{v}_z$, we find that the velocity-averaged reduction varies around this value like

$$\bar{R} \approx \exp(-2n_0^{(\text{rec})}) \left\{ 1 + 2n_0^{(\text{rec})} \left(\frac{\Delta v_z}{\bar{v}_z} \right)^2 \left[\left(n_0^{(\text{rec})} - 1 \right) \left(1 - \frac{\pi^2}{4} \right) + \bar{v}_z \frac{\partial \ln \mathcal{V}_{\text{sin}}}{\partial \bar{v}_z} \right] \right\}. \quad (3.83)$$

Here, $n_0^{(\text{rec})}$ and \mathcal{V}_{sin} are evaluated at the mean velocity \bar{v}_z . The relative uncertainty in the fringe reduction is of merely quadratic order in the velocity width Δv_z . Hence, the systematic error $\Delta \sigma_{\text{abs}}$ on the measured cross section, which we would disregard by modelling the data according to the simple linear relation (3.81) at $v_z = \bar{v}_z$, is of the same order in the velocity variance.

Figure 3.15 demonstrates that a reasonable velocity selection of $\Delta v_z / \bar{v}_z \lesssim 10\%$ suffices to measure the absorption cross-section with a precision on the percent level in practice. For this I have simulated a realistic KDTLI experiment with a blue recoil laser of $\lambda_L = 420$ nm wavelength in the existing Vienna setup ($L = 10.5$ cm, $d = 266$ nm, $w_y = 900$ μm , $f_1 = f_3 = 0.42$)²⁴. I take H₂TPP molecules at $\bar{v}_z = 175$ m/s as test particles using an absorption cross-section of $\sigma_{\text{abs}} = 15$ \AA^2 for the blue recoil photons, and 0.17 \AA^2 for the green grating photons at 532 nm wavelength [38,39]. The polarizability is approximated by the measured static value [132], $\alpha = 105$ \AA^3 , which yields a β -parameter of 0.11, according to Equation (3.68). The grating laser shall have 8 W input power, which corresponds to the phase modulation factor $\phi_0 = 3.4$ and to $\mathcal{V}_{\text{sin}} = 29\%$. A recoil shift of $d/2$ is attained by placing the recoil laser at $D = 1.5$ cm distance from the third grating. Both lasers in the experiment shall have the same waist.

²⁴ See Section 3.2.2 for all necessary details to compute the KDTLI fringe signal.

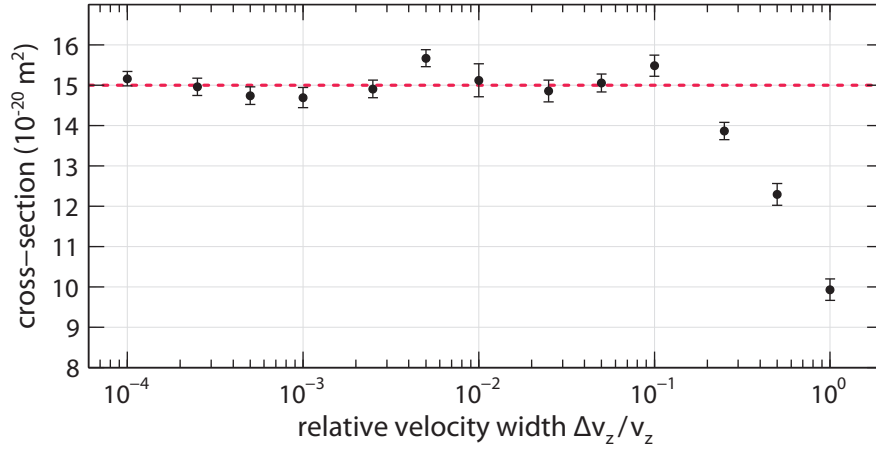


Figure 3.15. Simulated measurement of the absorption cross-section of H_2TPP molecules at 420 nm wavelength with help of a recoil laser in the KDTLI setup. The dotted line marks the actual value, $\sigma_{\text{abs}} = 15 \text{ \AA}^2$, and the data points are the simulated results for molecule beams of different velocity spreads (horizontal axis). Details on the experimental settings are given in the text. The error bars show the statistical uncertainty at 95% confidence (see text).

I performed a Monte Carlo simulation of the cross-section measurement in 14 runs, each corresponding to a different width parameter Δv_z of a Gaussian velocity distribution around the mean value \bar{v}_z . The results plotted in Figure 3.15 are based on the following algorithm:

- (A)** A sample of 10^4 molecules is generated by drawing random velocities v_z from a Gaussian distribution with the mean value $\bar{v}_z = 175 \text{ m/s}$ and a given standard deviation Δv_z . Given also the recoil laser power P_L and the position x_S of the third grating, the detection probability for each molecule in the sample is computed by means of the above theoretical model. It is then used to generate a random number $N(x_S, P_L; \Delta v_z)$ of detected molecules.
- (B)** Routine (A) is iterated over 100 positions x_S of the third grating, which is scanned over five grating periods in steps of $d/20$. A sine curve is fitted through these 100 data points, and the ratio between amplitude and offset then gives a ‘measured’ value for the sinusoidal fringe visibility, $\mathcal{V}_{\text{sin}}(P_L; \Delta v_z)$, for a fixed recoil laser power and velocity width. The statistical error of the fit is recorded as well.
- (C)** The recoil laser power P_L is ramped up from zero to 0.5 W in 20 steps, and (B) is repeated in each step. The resulting visibility values are weighted by their fitting error and plotted on a logarithmic scale against P_L . The mean velocity \bar{v}_z is then inserted into Equation (3.81) and used as the basis of a linear fit through the data. This serves as an estimate of the absorption cross-section, $\sigma_{\text{abs}}(\Delta v_z)$, including statistical uncertainties.
- (D)** Routine (C) is repeated for various standard deviations of the Gaussian velocity distribution, and the results are plotted in Figure 3.15.

We observe that the actual value of σ_{abs} is well reproduced by the simulated measurement when the molecular beam is velocity-selected to less than 10% deviation from the mean. At this point the velocity spread hardly adulterates the measurement. The statistical error in the data is mostly determined by the shot noise, which could be reduced using larger molecule samples.

Note that the suggested method is minimally invasive on the molecules because it does not rely on a strong optical depletion process to measure the net absorption of the molecular ensemble. The recoil laser in the given example yields an average of less than one photon absorption per molecule. Nevertheless, we can attain a shot-noise limited measurement accuracy on the percent level in realistic settings²⁵, irrespectively of the precise particle flux. Moreover, the latter could be much smaller than what would be required for a conventional extinction measurement of the net absorption. In fact, Talbot-Lau interference is still observable with dilute and optically thin molecular beams.

3.3.2. Dealing with fluorescence

The simulation results suggest that an interferometric measurement of σ_{abs} is viable by means of the recoil-induced contrast reduction in the existing KDTLI setup. However, I have ignored here another contrast-reducing factor related to the absorption: fluorescence. As long as no photo-depletion effect occurs, an excited molecule can either distribute the extra photon energy internally among its rovibrational degrees of freedom or it can reemit the energy in the form of a fluorescence photon. The former would lead to internal heating, which is often negligible in the case of large molecules. The latter corresponds to an immediate decoherence event, which is likely to occur within nanoseconds after the excitation. The likelihood of this event is referred to as the *quantum yield*, $P_{\text{flu}} \leq 1$, of a given molecule. It is about 11% in the above example of H₂TPP.

The fluorescence effect is readily incorporated into the model by employing once again the generic description of decoherence events outlined in Section 3.2.1.3. We merely require the knowledge of the relative fluorescence spectrum, $F(\omega)$, as an additional input. No absolute emission rates are required, and the spectrum shall be normalized to $\int d\omega F(\omega) = 1$. Moreover, it is reasonable to assume that each photon is emitted isotropically. Putting everything together, a single fluorescence event effectively transforms the one-dimensional center-of-mass state of the molecule as $\rho \mapsto \int d^3k c F(c k) \exp(-ik_x x) \rho \exp(ik_x x)$. The associated decoherence function reads as $\mathcal{R}_{\text{flu}}(x) = \int_0^\infty d\omega F(\omega) \text{sinc}(\omega x/c)$, and the Fourier components of the interference fringe signal are modulated by $\mathcal{R}_{\text{flu}}(\ell dt/T_T)$, according to Equation (3.59). Because of the short fluorescence time scales, we may assume that the absorption and the emission events occur approximately at the same point t in the interferometer.

With these ingredients the fluorescence effect can be incorporated into the probabilistic recoil model in Equation (3.79). Given that n photons have been absorbed from the recoil laser, we model the conditional probability of reemitting $k < n$ photons by a binomial distribution, $p(k|n) = \binom{n}{k} P_{\text{flu}}^k (1 - P_{\text{flu}})^{n-k}$. Once again, this implies that P_{flu} does not change with the number of excitations, like the absorption cross-section before. It is an uncritical assumption if we restrict to low absorption numbers, $n_0^{(\text{rec})} < 1$. The emission of k photons modulates the fringe signal by $[\mathcal{R}_{\text{flu}}(\ell dt/T_T)]^k$ in Fourier space; an average over all possible k leads to the fluorescence-modified

²⁵ Systematic errors due to the imprecise knowledge of the setup parameters, say, the laser powers, must be included in practical implementations.

fringe amplitudes,

$$S_\ell^{(n)} = \sum_{k=0}^n P(k|n) \left[\mathcal{R}_{\text{fluo}} \left(\frac{\ell dt}{T_T} \right) \right]^k S_\ell = \sum_{k=0}^n \binom{n}{k} (1 - P_{\text{fluo}})^{n-k} \left[P_{\text{fluo}} \mathcal{R}_{\text{fluo}} \left(\frac{\ell dt}{T_T} \right) \right]^k S_\ell$$

$$= \left[1 - P_{\text{fluo}} + P_{\text{fluo}} \mathcal{R}_{\text{fluo}} \left(\frac{\ell dt}{T_T} \right) \right]^n S_\ell. \quad (3.84)$$

given the absorption of n recoil photons. Finally, we multiply this conditional result by the phase factor $\exp(2\pi i \ell n t d / T_T \lambda_L)$ associated to n recoil shifts and average it over n to arrive at the reduced fringe amplitudes,

$$\tilde{S}_\ell = \sum_{n=0}^{\infty} P_n(n_0^{(\text{rec})}) \exp\left(\frac{2\pi i \ell n t d}{T_T \lambda_L}\right) S_\ell^{(n)}$$

$$= \exp\left\{ n_0^{(\text{rec})} \left[1 - P_{\text{fluo}} + P_{\text{fluo}} \mathcal{R}_{\text{fluo}} \left(\frac{\ell dt}{T_T} \right) \right] \exp\left(\frac{2\pi i \ell t d}{T_T \lambda_L}\right) - n_0^{(\text{rec})} \right\} S_\ell. \quad (3.85)$$

This is the generalization of the above result (3.79) to nonzero quantum yields, $P_{\text{fluo}} > 0$.

Let me close this section by discussing the primary cases of interest, half- and full-period shifts. Here, the sinusoidal fringe visibility reduces in the following way:

$$\ln \tilde{\mathcal{V}}_{\text{sin}} = \ln \mathcal{V}_{\text{sin}} - 2n_0^{(\text{rec})} + P_{\text{fluo}} n_0^{(\text{rec})} \left[1 - \mathcal{R}_{\text{fluo}} \left(\frac{\lambda_L}{2} \right) \right] \quad \text{if } \frac{td}{T_T \lambda_L} = \frac{1}{2} \quad (3.86)$$

$$\ln \tilde{\mathcal{V}}_{\text{sin}} = \ln \mathcal{V}_{\text{sin}} - P_{\text{fluo}} n_0^{(\text{rec})} [1 - \mathcal{R}_{\text{fluo}}(\lambda_L)] \quad \text{if } \frac{td}{T_T \lambda_L} = 1 \quad (3.87)$$

Such linear models are valid descriptions for time-domain interference, and they can also be good approximations for velocity-selected molecule beams in the KDTLI configuration, as I have verified explicitly in the zero-fluorescence case. Here, we find the combined effect of reduction by recoil and by fluorescence. Although the effect is still strongest for half-period shifts, the absorption cross section σ_{abs} is no more accessible by the devised measurement if the quantum yield P_{fluo} is not known either. The latter should then be measured separately in a configuration where the recoil laser induces a full-period shift. The contrast is then solely affected by the reemission of photons, and a fit of Equation (3.87) to the data would reveal the value of the term $P_{\text{fluo}} \sigma_{\text{abs}}$, provided the relative fluorescence spectrum is known. Combining this with the results of the other half-period measurement would then result in a value for both σ_{abs} and P_{fluo} . One could take this principle even further and map the whole parameter space of absorption and fluorescence with a movable and tunable recoil laser.

Note, however, that this interferometric method can only measure thermally averaged values of the cross-section and the quantum yield, which are predetermined by the available molecule sources. Additional measurement uncertainties not covered here could be caused by optical limiting or enhanced thermal radiation, as listed at the end of Section 3.3.1.1. A nonlinear power dependence of the logarithmic contrast reduction would be a first indication of whether such effects might be relevant for a specific molecule. One should then restrict the analysis to the linear regime at sufficiently small powers. The thermal effects could be studied separately by systematic heating experiments.

3.4. Mass limits of the OTITLI scheme

I close this chapter with an outlook into the future of matter-wave interferometry with ultra-heavy objects, specifically for Talbot-Lau interferometry with nanoclusters. What is the highest mass that could be brought to interference in a feasible experiment using available matter-wave techniques? In the following I will answer this question on the basis of the Talbot-Lau interferometer scheme with optical ionization gratings operating in the time domain. This OTITLI scheme was worked out in [10] and described in detail in Section 3.2.3.

So far, Talbot-Lau interferometry has proven to be the method of choice for demonstrating the quantum wave nature of ever larger objects. It holds the current mass record, and it offers a greater flexibility and more favorable mass scaling than other more conventional interference techniques, as I have illustrated throughout this chapter. In particular, the OTITLI scheme has been designed and optimized precisely for the purpose of reaching the highest possible masses. Its limitations, which I discuss in the following, will apply in a similar manner, if not more severely, to other conceivable matter-wave experiments.

Finally, we will see in Section 3.4.3 that a class of alternative theories beyond the level of standard quantum mechanics will become testable in the reachable high-mass regime. These theories predict a breakdown of the superposition principle and induce classical behaviour on the macro-scale.

3.4.1. Experimental methods and challenges

A concrete study of the required technology and the effort necessary to implement the OTITLI scheme of Section 3.2.3 with heavy metal clusters was provided when we first proposed it [10]. In addition, the first experimental demonstration with small molecular clusters in [13] has proven that the proposed design is indeed feasible with present-day technology.

Let me give a short overview of the experimental methods and challenges related to this implementation, including the interferometer design as well as the creation and detection of appropriate particle ensembles.

3.4.1.1. Particle candidates and sources

The amplitude modulation effect of the optical gratings in the proposed OTITLI scheme is based on single-photon ionization. We must therefore choose the particles according to whether they ionize at a given wavelength of the grating lasers. Moreover, the ionization process should take place on a short time scale and at an efficiency close to 100%, since absorption events without subsequent ionization would lead to additional decoherence. The proposed VUV laser gratings at 157 nm wavelength provide a single-photon energy of 7.9 eV, which exceeds the ionization threshold of many large molecules²⁶ or the work function of most cluster materials. The latter has a typical value of around 5 eV such that ultraviolet or optical laser gratings with wavelengths larger than about 250 nm would narrow down the range of usable materials significantly. Nevertheless, optical depletion processes, such as multi-photon ionization, photo-isomerization or fragmentation, may still facilitate Talbot-Lau interferometry with optical absorptive gratings.

²⁶ Complex biomolecules often do not photoionize, or at best at low efficiency, even if the absorbed photon provides enough energy. The latter is then deposited and distributed among many other internal degrees of freedom of the molecule.

The availability of large ionizable particles for OTITLI experiments is mostly related to the availability of stable sources volatilizing a sufficient amount of these particles that can be passed on to the grating pulses. Viable sources for large and complex molecules exist for tailor-made species on the 10^3 - 10^4 amu scale [19]. However, it seems more sensible with current technology to focus on atomic or molecular cluster aggregation sources, which offer a broad range of masses and hold out the prospect of generating pulsed beams of nanoparticles up to 10^6 amu and beyond. Here, individual atoms and molecules are typically desorbed or sputtered from a substrate and then swept away in a cold gas jet where they condense and aggregate to clusters of a broad size distribution [118]. If necessary, the ejected cluster ensemble can be slowed down in a buffer gas cooling stage [133] to achieve sufficiently long residence times in the active interferometer region. The anthracene clusters in the first demonstration of the OTITLI scheme were formed in a cold jet of noble gas after the pulsed injection of anthracene vapour from an Even-Lavie valve [13, 134]. Although their interference was clearly observed, a systematic *ab initio* assessment of the measured results was obstructed by the fact that the optical properties of these clusters were practically unknown.

Laser acoustic desorption from atomic surfaces [135] represents an alternative way of producing large nano- or even microclusters that could be used in matter-wave interferometry. Recently, there has been growing interest and progress in optical manipulation, cooling, and interference techniques with single levitated nanospheres on the quantum level of motion [23–25, 136, 137].

3.4.1.2. Interferometer design

Having a working pulsed particle source at hand, the design of the interferometer is a relatively simple matter. The basic OTITLI setup consists of a single flat high-reflectivity mirror and a set of one to three identical pulsed laser systems with tunable pulse energy and timing. I restrict here to the working setup [13] with three F_2 excimer lasers producing 7 ns long pulses of a few mJ energy at the vacuum ultraviolet (VUV) wavelength $\lambda = 157.63$ nm. They illuminate a polished highly reflective CaF_2 surface of two inches in diameter vertically from below. Each pulse is retroreflected from the mirror and forms a short standing-wave grating of 80 nm period that extends coherently over a longitudinal coherence length of roughly 1 cm. A weak electric field is applied in the vacuum chamber containing the mirror to remove the particles ionized in each grating.

For the interference effect to occur it is vital to have precise control over the pulse timing. We read from the resonance approximation in Section 3.2.1.2 that the delay times between the three grating pulses must be equal up to a small deviation $|\tau| \ll T_T$. The time window left for unavoidable pulse jitters and timing imprecisions can be adjusted by the initial collimation of the matter-wave ensemble along the standing-wave axis. It was measured to be 48 ns in the anthracene experiment [13], a value larger than the pulse duration and the jitter of the lasers.

Besides the initial collimation of the particles, it might be necessary to guarantee that they are sufficiently slow and do not average over the standing-wave profile for the duration of each grating pulse. The dimensions and positions of the laser spots must be optimized accordingly, because different parts of the particle cloud may experience different laser intensities, and the observed visibility is averaged over the ensemble spread in velocity and position.

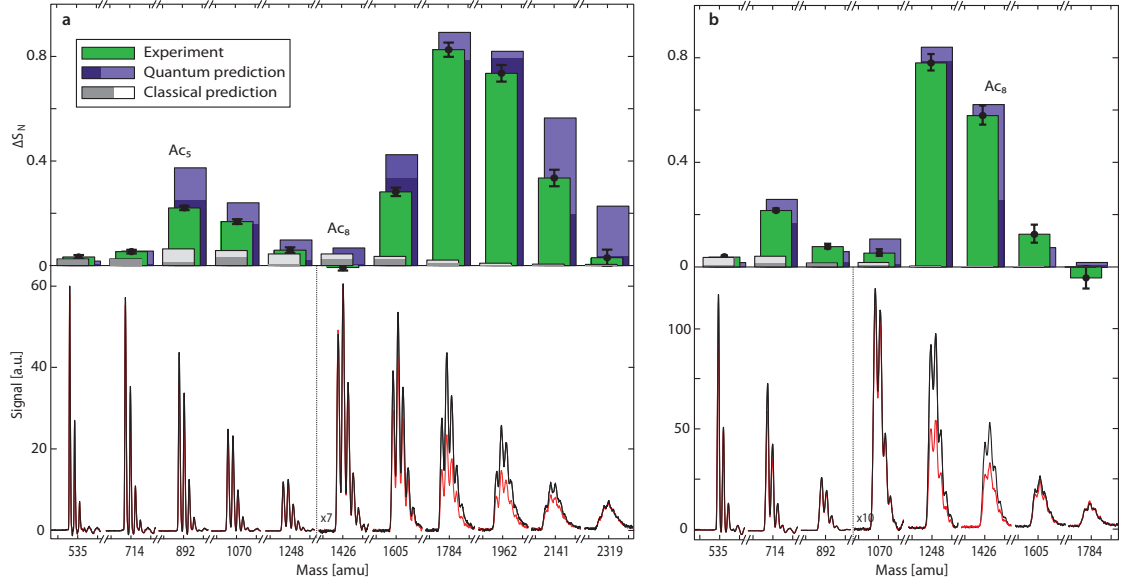


Figure 3.16. Signature of anthracene cluster interference in the mass spectrum [138], as observed in the first OTITLI experiment [13] for two different pulse delays, $T = 26 \mu\text{s}$ (left) and $19 \mu\text{s}$ (right). The bottom panels contain the resonant (black) and the off-resonant (red) mass spectra; their relative difference is given by the green bars in the histograms above. Fringes can appear only in the resonant case, and so the normalized signal difference is a direct measure for the fringe contrast. A comparison to the theoretical predictions plotted in the same histogram verifies the quantum nature of the fringes. The figure is courtesy of the authors of [13] and reprinted with their permission.

3.4.1.3. Signal detection

The number of particles passing the three grating pulses is measured in a time-of-flight mass spectrometer with help of an additional ionization laser. This admits the simultaneous detection of a broad distribution of cluster sizes in each shot of the experiment. However, there is no straightforward way to scan the interference fringe pattern by shifting the third grating with respect to the other two, because all three standing waves are defined by the same mirror surface. Hence, one is forced to seek different means to effectively observe the fringe pattern:

- ★ One obtains a first fringe signature by varying the pulse delay time and by comparing the on-resonant signal at $\tau = 0$ with the off-resonant case at $\tau \neq 0$. The fringe amplitude vanishes if τ is increased beyond the above mentioned resonance time window, implying that one should observe a change in the detection signal (i.e. number of particles detected in the mass spectrometer). The signal difference is proportional to the fringe contrast. Hence, by subtracting the on- and off-resonant mass spectra in the detector, one expects to see the same characteristic mass dependence as predicted by the theory and depicted in the diagrams of Section 3.2.3 Figure 3.16 is an excerpt from the publication [13] of the anthracene experiment, where the difference in the recorded mass spectra is plotted for two different runs of the experiment. The on- and off-resonant mass spectra are depicted as black and red curves in the lower panel, whereas the normalized signal difference is plotted in the top panel. The uncertainty between the data and the theoretical prediction is due to the lack of knowledge about the cluster properties.

- ★ An effective grating scan was also achieved in the anthracene experiment with help of a simple trick: By varying slightly the incidence angle of one of the lasers onto the mirror, the authors effected a change in the grating period along the standing-wave axis. This change was small enough to not affect the Talbot-Lau resonance and the grating coherence length too much, but it accumulated a sufficiently large grating shift of up to one period a few millimeters away from the mirror surface.
- ★ A cleaner way to scan and resolve the interference fringe pattern is to make use of an external acceleration, which deflects the particle trajectories in a controlled manner between the gratings. A constant acceleration a along the standing-wave axis yields the effective shift $\delta x_a = -aT^2$ of the fringe pattern, as discussed in Section 3.2.1.2. The fringes can be scanned by varying either a or the grating separation time T . The latter also influences the fringe visibility. A tunable acceleration, for instance, could be generated by a static electric field that produces a constant dipole force on polarizable particles along the grating axis. This technique is commonly used for deflectometric measurements in the KDTLI setup, as mentioned in Section 3.2.2. Alternatively, one can simply employ gravity, $a = g$, in the vertical grating alignment if the particles are sufficiently massive. A particle of, say, 10^5 amu corresponds to the Talbot time $T_T \approx 1.6$ ms, and it would fall more than 300 grating periods in the current OTITLI setup if we assume a pulse separation of $T = T_T$. That is, one could easily scan the fringe pattern by varying T over less than one per cent.

3.4.2. Standard mass limitations

Having discussed the experimental techniques, I proceed with the relevant mass-limiting factors in the OTITLI scheme, as published in [11]. I resort to the currently available implementation using VUV lasers with a grating period of $d = 80$ nm and variable separation time T . Spherical gold clusters of variable radius R in the nanometer regime will be used as reference particles of mass $m = 4\pi\rho R^3/3$, adopting the bulk values for the mass density and the relative dielectric permittivity, $\rho = 19320$ kg/m³ and $\varepsilon = 0.9 + 3.2i$ [50].

3.4.2.1. Temporal stability and inertial forces

The most obvious limitation is related to the feasibility and stability of long-time interferometers. Given a mass-proportional Talbot time of 16 ns per atomic mass unit, a reliable and distinguished observation of quantum interference fringes requires the particles not to leave the interferometer for at least $2T \sim 32$ ns per amu. This implies the following practical mass limitations:

- ★ **Velocity limit** A sufficiently rigid and flat reference mirror for all three laser gratings cannot be made arbitrarily large, and the use of separate mirrors for each grating would come at the price of harsh stability and adjustment requirements. Particles must therefore be slow enough to stay within the range of the mirror for at least the time $2T$. Let us assume a realistic mirror length of about 5 cm, as currently used in the lab. A particle of, say, 10^6 amu must then be injected with a velocity of less than 1.6 m/s to not traverse the mirror in less than the required 32 ms²⁷. Most known sources produce much faster particle ensembles. That

²⁷ A similar velocity limit applies along the other spatial directions in order to prevent the particles from leaving the coherent high-intensity parts of the standing-wave beam profile.

is, one must first develop and implement efficient methods to slow, guide, or even trap the motion of polarizable particles before being able to do interference experiments with masses of more than 10^5 amu. In this respect, optical and electromagnetic manipulation techniques have attracted growing interest and undergone progress over the years, see e.g. [8, 23, 48, 136, 139–142].

★ **Gravitational limit** I have mentioned above that the presence of gravity may be of help in resolving the interference fringe pattern of large particles. At even higher masses, however, the free fall of particles must be balanced or suppressed in order to keep them in place for a sufficiently long time. The free-fall distance during interference increases quadratically with the Talbot time from already 5 mm at 10^6 amu to the out-of-reach value of 5 km at 10^9 amu. This would have to be counteracted on the nanometer or millimeter level in a vertical or horizontal grating arrangement. Experiments with trapped particles or in a microgravitational environment [143] might be the only possibilities to beat the level of a million mass units.

3.4.2.2. Decoherence

Environmental decoherence is another limiting factor in high-mass interferometry. It is a well-understood phenomenon that was assessed both theoretically and experimentally in the context of Talbot-Lau interferometry with molecules [40, 144, 145]. The two relevant free-space decoherence processes for matter waves propagating through the interferometer are due to collisions with residual gas particles and due to the interaction with thermal radiation. The third relevant process, grating decoherence due to the elastic scattering of laser photons in each pulse, will be omitted here. It has been covered in Section 3.2.3.2, and I have shown that it is hardly of significance for subwavelength particles with masses $< 10^9$ amu.

The overall free-space decoherence rate depends on the internal temperature of the particles and on the background pressure and temperature of the environment. The shielding of ever larger particles from decoherence requires us to decrease both temperature and vacuum pressure to the same extent as the cross-section for gas collisions, and for the emission, absorption, and Rayleigh scattering of thermal radiation increases.

The influence of free-space decoherence on the interference visibility can be obtained using the formalism layed out in [40] and the terminology developed in Section 3.2.1.3. Each type of decoherence is modelled as an independent random process of scattering events with a mean event rate $\Gamma(t)$. A single scattering event transfers a randomly distributed momentum recoil $\hbar \mathbf{k}$ to the particle, as described by the random unitary transformation, $\rho \mapsto \int d^3k P(\mathbf{k}) \exp(i\mathbf{k}_x \mathbf{x}) \rho \exp(-i\mathbf{k}_x \mathbf{x})$, of the reduced one-dimensional state of motion. The probability distribution $P(\mathbf{k})$ is normalized to unity. Following the argumentation in Section 3.2.1.3, we arrive at the associated decoherence function in the position representation, $\mathcal{R}(\Delta x) = \int d^3k P(\mathbf{k}) \exp(-i\mathbf{k}_x \Delta x)$. If we suppose that the event occurs at the time t before or after the second grating, we can use (3.59) to establish the rate equation,

$$\frac{d}{dt} \tilde{S}_\ell = \Gamma(t) \left[\mathcal{R} \left(\ell d \frac{T - |t|}{T_T} \right) - 1 \right] \tilde{S}_\ell, \quad (3.88)$$

for the decay of the ℓ th Fourier component of the interference fringe signal. Solving this differential equation yields a relation between the decohered and the unmodified signal components,

$$R_\ell = \frac{\tilde{S}_\ell}{S_\ell} = \exp \left\{ \int_{-T}^T dt \Gamma(t) \left[\mathcal{R} \left(\ell d \frac{T - |t|}{T_T} \right) - 1 \right] \right\}, \quad (3.89)$$

with $R_0 = 1$. Each independent decoherence process contributes a separate reduction factor R_ℓ . I assume, for simplicity, that each scattering event is isotropic²⁸, $P(\mathbf{k}) = P(k)$, and that the event rate Γ does not change over time in all the following processes. So we are left with reduction factors of the form

$$R_\ell = \exp \left\{ -2\Gamma \left[T - \int_0^T dt \int_0^\infty dk 4\pi k^2 P(k) \operatorname{sinc} \left(\ell k d \frac{t}{T_T} \right) \right] \right\}. \quad (3.90)$$

Absorption and emission of thermal radiation The interfering nanoclusters can be regarded as hot composite systems constantly absorbing and emitting thermal photons from and into the radiation field of the environment. For the present estimates I assume the clusters to be in thermal equilibrium with the environment, as also described in Section 2.1.2.2. Corrections of the radiation law due to the finite heat capacitance of the clusters, as given in [40], will be neglected. The spectral absorption and emission rates are identical and given by the Planck formula, Equation (2.23) on page 12, at the temperature T_{env} ,

$$4\pi\Gamma k^2 P(k) dk = \gamma_{\text{emi}}(\omega) d\omega = \frac{\sigma_{\text{abs}}(\omega) \omega^2 d\omega}{\pi^2 c^2 [\exp(\hbar\omega/k_B T_{\text{env}}) - 1]}. \quad (3.91)$$

By plugging this into (3.90) we obtain the reduction factors of emission and absorption, $R_\ell^{(\text{abs})} = R_\ell^{(\text{emi})}$. In the alternative case of a hot particle, $T_{\text{int}} \gg T_{\text{env}}$, the decoherence is dominantly due to emission, and the temperature dependence of the spectral rate is given by a Boltzmann factor, Equation (2.22),

$$4\pi\Gamma k^2 P(k) dk = \frac{\sigma_{\text{abs}}(\omega) \omega^2 d\omega}{\pi^2 c^2} \exp \left(-\frac{\hbar\omega}{k_B T_{\text{int}}} \right). \quad (3.92)$$

Elastic scattering of thermal radiation An elastic photon scattering event can be understood as a combined absorption and emission process, averaged over the in- and outgoing wave vector with the scattering probability $P(\mathbf{k} \rightarrow \mathbf{k}')$ proportional to $\gamma_{\text{sca}}(ck) \delta(k - k')$ and the unitary double-recoil operator given by $\exp[i(k_x - k'_x)x]$. The associated decoherence function reads as $\mathcal{R}(\Delta x) = \int d^3k d^3k' P(\mathbf{k} \rightarrow \mathbf{k}') \exp[-i(k_x - k'_x)\Delta x]$, and the reduction factor becomes

$$R_\ell^{(\text{sca})} = \exp \left\{ -2 \int_0^\infty d\omega \gamma_{\text{sca}}(\omega) \left[T - \int_0^T dt \operatorname{sinc}^2 \left(\ell \frac{d\omega t}{c T_T} \right) \right] \right\}. \quad (3.93)$$

In full equivalence to the spectral emission rate (3.91), the scattering rate per frequency ω is taken to be proportional to the Rayleigh scattering cross-section times the Planck energy density of the surrounding radiation field, $\gamma_{\text{sca}}(\omega) = (\omega/\pi)^2 \sigma_{\text{sca}}(\omega) [\exp(\hbar\omega/k_B T_{\text{env}}) - 1]^{-1}$. We expect that the impact of scattering on nanoparticle interference is small, given the large average wavelengths of thermal photons at temperatures below 1000 K.

²⁸ The overall effect is practically the same whether the scattering pattern is isotropic or, say, a dipolar pattern with respect to a fixed polarization axis.

Collisions with gas particles The decoherence by elastic scattering of background gas particles can be modeled in full analogy to the elastic light scattering. In addition, we can make use of a further simplification [146]: In contrast to thermal blackbody photons, most gas particles deliver (and experience) a comparatively large momentum recoil upon collision, which exceeds by far the elementary grating momentum \hbar/d describing the reciprocal interference path separation. In other words, we may assume that each collision event by itself leads to a complete loss of coherence on the length scale d , and that the resulting interference fringes decay uniformly with the mean number of collisions in the interferometer, $R_\ell^{(\text{col})} \approx \exp(-2\Gamma_{\text{col}} T)$ for all $\ell \neq 0$. The collision rate follows from a van der Waals scattering model [40, 146],

$$\Gamma_{\text{col}} \approx \frac{4\pi\Gamma(0.9)}{5 \sin(\pi/5)} \left(\frac{3\pi C_6}{2\hbar} \right)^{2/5} \frac{p_g v_g^{3/5}}{k_B T_{\text{env}}}, \quad (3.94)$$

given the pressure p_g and the temperature T_{env} of the residual gas. The approximation holds for nanoclusters that are slow with respect to the mean thermal velocity $v_g = \sqrt{2k_B T_{\text{env}}/m_g}$ of the gas particles of mass m_g . We estimate the van der Waals coupling constant by means of the London formula [147], $C_6 \approx 3\alpha_g I_g \alpha I / 2(I + I_g)$, based on the static polarizability α in cgs units and the ionization energies I_g and I of the gas and the cluster particles.

Putting everything together, environmental decoherence reduces the sinusoidal fringe visibility \mathcal{V}_{sin} by the combined factor R_1 ,

$$\begin{aligned} \ln R_1 = & -2\Gamma_{\text{col}} T - 4 \int_0^\infty d\omega \gamma_{\text{abs}}(\omega) \left[T - \frac{cT_T}{d\omega} \text{Si}\left(\frac{d\omega T}{cT_T}\right) \right] \\ & - 2 \int_0^\infty d\omega \gamma_{\text{sca}}(\omega) \left\{ T \left[1 + \text{sinc}^2\left(\frac{d\omega T}{cT_T}\right) \right] - \frac{cT_T}{d\omega} \text{Si}\left(\frac{2d\omega T}{cT_T}\right) \right\}, \end{aligned} \quad (3.95)$$

where $\text{Si}(x)$ denotes the sine integral function²⁹ [113].

Figure 3.17 shows under which temperature and vacuum conditions one may still observe interference with gold clusters ranging from 10^5 to 10^9 amu in the OTITLI. The contour lines correspond to those background pressures p_g and temperatures T_{env} where the sinusoidal fringe visibility is reduced by a factor of two at $m = 10^{6..9}$ amu. That is, the interference effect should be largely visible within the enclosed parameter region, whereas it is prevented by decoherence everywhere in the shaded outside area. I have taken N_2 as the background gas, with $I_g = 15.6$ eV and $\alpha_g = 1.74 \text{ \AA}^3$ [148]. The grating separation time is set to $T = 2T_T$ for each mass. Everything is assumed to be in thermal equilibrium. The dielectric properties of the gold clusters for all relevant thermal wavelengths are estimated by means of the Drude model,

$$\varepsilon(\omega) = 1 - \frac{\omega_p^2}{\omega^2} + i\gamma_p \frac{\omega_p^2}{\omega^3}, \quad (3.96)$$

using the bulk values for the plasma frequency and width, $\omega_p = 1.3 \times 10^{16}$ Hz and $\gamma_p = 1.1 \times 10^{14}$ Hz [149]. Given the cluster radius R and the complex polarizability $\chi = 4\pi\epsilon_0 R^3 (\varepsilon - 1) / (\varepsilon + 2)$, this

²⁹ It is defined by the integral $\text{Si}(x) = \int_0^x dy \text{sinc}(y)$. In addition, I have used the integral identity

$$\int_0^x dy \text{sinc}^2(ay) = \frac{1}{a} \text{Si}(2ax) - x \text{sinc}^2(ax).$$

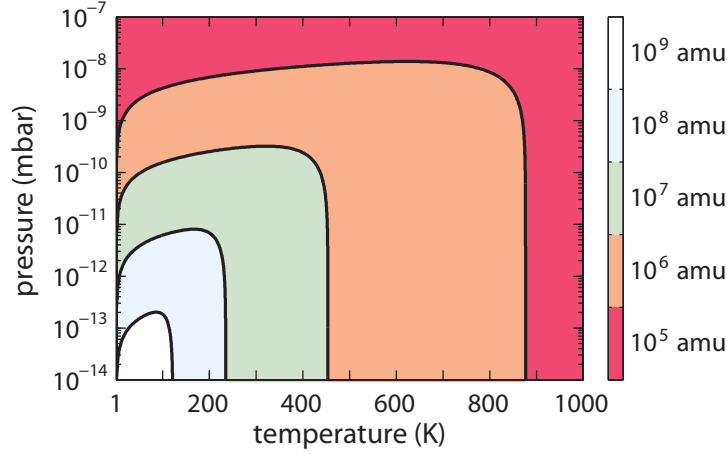


Figure 3.17. Area plot of the ambient temperatures and pressures required for interfering gold clusters of various masses. The contour line associated to each of the depicted masses gives the critical temperatures and residual gas pressures where decoherence reduces the visibility by a factor of two. Interference is largely suppressed in the shaded exterior areas. I assume that interference is observed in the second Talbot order, $T = 2T_T$, and that the particles and the apparatus are in thermal equilibrium.

sets the values for the absorption and scattering cross sections at all relevant frequencies. Moreover, the static polarizability is approximated by the ideal metal value, $\alpha = R^3$, and the work function of the bulk material is taken as an estimate for the ionization energy, $I = 5.4$ eV.

Although decoherence does not pose an absolute mass limit in interferometry, we find that it would be quite demanding to shield large nanoclusters sufficiently well from the environment. A pressure of about 10^{-9} mbar at room temperature, which is easily achieved in practice, may be just enough for 10^6 amu clusters. But it is already too high for greater masses. The setup would have to be cooled and evacuated to below 200 K and 10^{-12} mbar in order to see 10^8 amu clusters interfere.

3.4.2.3. Particle size effect

Probably the most fundamental and inevitable mass limit in Talbot-Lau interferometry with optical depletion gratings is related to the growing size of the particles. The point-particle approximation used so far breaks down as soon as they approach the dimension of the grating fringes, and this alters the amplitude and phase modulation properties of the optical gratings severely. Although this does not necessarily imply that the grating modulation, and with it the interference effect, will vanish, it does mean that the effect will ultimately become unobservable in practice.

We can study the implications of finite-sized particles for the case of spherical gold clusters by applying the Mie theory description of the interaction between dielectric spheres and standing waves given in Chapter 2, page 48ff. According to the results of Section 2.3.2, we can allow for a finite sphere radius R in our description of the OTITLI (in Section 3.2.3) if we replace each grating transmission function $t^{(k)}(x)$ by the modified version (2.136),

$$t^{(k)}(x) = \exp \left[-n_+^{(k)} + \left(\frac{i}{2} \tilde{\phi}_0^{(k)} - n_-^{(k)} \right) \cos \left(\frac{2\pi x}{d} \right) \right]. \quad (3.97)$$

The transverse coordinate x represents the center-of-mass position of the sphere. The mean absorption $n_+^{(k)}$ and the amplitude and phase modulation factors, $n_-^{(k)}$ and $\tilde{\phi}_0^{(k)}$, are defined by the Mie expressions (2.135) on page 58. They reduce to the point-particle parameters, $n_\pm^{(k)} \approx n_0^{(k)}/2$ and $\tilde{\phi}_0^{(k)} \approx \phi_0^{(k)}$, in the subwavelength limit, $R/d \ll 1$.

The phase-space model of the interferometer is retained, and we accomodate the generalized grating parameters by changing the Talbot coefficients (3.70) into

$$B_n^{(k)}(\xi) = e^{-n_+^{(k)}} \left[\frac{\zeta_{\text{coh}}(\xi) - \zeta_{\text{ion}}(\xi)}{\zeta_{\text{coh}}(\xi) + \zeta_{\text{ion}}(\xi)} \right]^{n/2} J_n \left[\text{sgn} \{ \zeta_{\text{coh}}(\xi) + \zeta_{\text{ion}}(\xi) \} \sqrt{\zeta_{\text{coh}}^2(\xi) - \zeta_{\text{ion}}^2(\xi)} \right],$$

with $\zeta_{\text{coh}}(\xi) = \tilde{\phi}_0^{(k)} \sin \pi \xi$, $\zeta_{\text{ion}}(\xi) = n_-^{(k)} \cos \pi \xi$. (3.98)

The classical Talbot coefficients are modified accordingly, using $\zeta_{\text{coh}}^{\text{cl}}(\xi) = \tilde{\phi}_0^{(k)} \pi \xi$ and $\zeta_{\text{ion}}^{\text{cl}} = n_-^{(k)}$.

A comparison with Equation (3.70) shows that the change is subtle, but its implications are far-reaching. On the one hand, we find that the visibility of the interference effect does not depend on the mean absorption $n_+^{(k)}$, which appears only in the form of a constant exponential damping factor in the Talbot coefficients. The mean value grows monotonously with the sphere size, whereas the modulation terms, $\tilde{\phi}_0^{(k)}$ and $n_-^{(k)}$, are bound to much lower values and regularly flip signs at large radii, see Figures 2.9 and 2.10. The dotted curves on the left and the right of Figure 2.9 on page 52 depict the mean absorption (in different dimensionless units) and the ratio $n_-^{(k)}/n_+^{(k)}$ as a function of the cluster size, respectively. The solid line in the left panel of Figure 2.10 represents $\tilde{\phi}_0^{(k)}$ (in different units). All this implies that even the largest gold spheres (except for the critical sizes at which the modulation terms vanish) could in principle be interfered at high contrast with the right experimental parameters.

On the other hand, the total transmissivity of the interferometer, as given by the zeroth Fourier component of the fringe signal, does depend on the mean absorption. For the specific case where all three grating pulses are equal, $n_\pm^{(1,2,3)} = n_\pm$, we find

$$S_0 = B_0^{(1)}(0) B_0^{(2)}(0) B_0^{(3)}(0) = \exp(-3n_+) I_0^3(n_-). \quad (3.99)$$

High contrast can be attained at the same time if we match the pulse timing to one of the Talbot orders, $T = NT_T$, where the sinusoidal fringe visibility (3.72) simplifies to

$$\mathcal{V}_{\text{sin}} = 2 \frac{I_1^2(n_-) I_2(n_-)}{I_0^3(n_-)}. \quad (3.100)$$

Suppose that we adjust the laser power in each grating pulse to, say, $n_- = 4$, which yields a pronounced fringe visibility of $\mathcal{V}_{\text{sin}} = 85\%$. This amounts to an average of $n_0 = 8$ absorbed photons at the grating antinodes and to a transmissivity of $S_0 = 1\%$ in the point-particle limit, where $n_+ = n_- = n_0/2$. However, a realization of the same fringe visibility with wavelength-sized gold spheres is accompanied by a drastic loss in transmissivity. This is shown in Figure 3.18 where I plot the transmissivity S_0 as a function of the sphere mass at a fixed 85% visibility (solid line, left scale). The energy flux E_L/a_L in each grating pulse (dashed line, right scale) must be decreased accordingly to keep $n_- = 4$ and the visibility constant. (E_L denotes the energy and a_L the spot area of the grating pulse, as defined on page 21 in Section 2.1.4.1.)

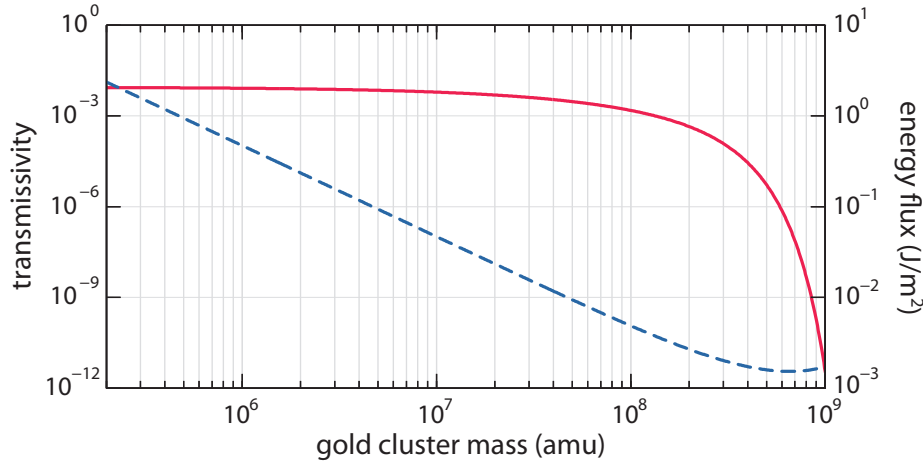


Figure 3.18. Transmissivity of the OTITLI setup for gold nanospheres as a function of their mass. The transmissivity (solid line) is given by the probability that a neutral cluster is transmitted by the three laser gratings and arrives at the detector. The dashed line represents the energy flux of each grating (right scale) required to fix the sinusoidal fringe visibility at 85% for all masses. This plot was published in [11].

A 10^6 amu gold sphere with a radius of less than 3 nm can still be regarded as a point particle, and it is transmitted with 1% probability, according to the data in the diagram. The transmissivity drops by almost one order of magnitude to about 0.1% at $m = 10^8$ amu and $R = 13$ nm. From this point onwards, however, the overall signal loss grows exponentially to an unfeasibly large degree. We find an unacceptably low transmission probability of 4×10^{-12} at the other end of the plotted scale, where the clusters are 10^9 amu heavy and 27 nm in radius.

In practice, the OTITLI experiment is thus limited to masses of the order of 10^8 amu and below. Moreover, we should keep in mind that the size effect may lead to more restrictive mass limits if other, less dense cluster materials than gold are used. One can only gain in mass by increasing the grating wavelength, but this is only possible to a limited extent: the photon energy must suffice for the photo-ionization of the clusters, or for another absorption-induced depletion effect. Conceptually different interferometer schemes in the high-mass regime, such as the cavity-based double slit for silica nanospheres [25], are less sensitive to the discussed size effect. Then again, they are typically bound by prohibitively strict initial conditions and coherence requirements. For example, the scheme proposed in [25] requires the nanospheres to be initially trapped close to the quantum ground state of an optical potential.

3.4.3. Test of spontaneous localization models

We have concluded that Talbot-Lau interferometry with heavy nanoparticles is limited to masses below 10^9 amu. While this will probably not be the ultimate limit for matter-wave interferometry in general, it sets an evident feasibility bound for the discussed setup (and other endeavours of this kind) at the moment. Nevertheless, this bound still lies orders of magnitude above what has been achieved today. Hence, it is worthwhile to look whether hints of new physics besides standard decoherence may appear at yet unprecedented mass scales and bridge the gap between the quantum and the classical world.

The majority of postulates and theories on this matter build upon the concept of macrorealism, as coined by Leggett [3]. One modifies standard quantum theory in such a way that a realist ‘classical’ description of physics emerges on a macroscopic scale, whereas quantum superpositions of distinct states are confined to the microscopic world. The growing influence of gravity in large and massive systems is often held responsible for such a modification by researchers in this field [150–152]. Other suggestions stipulate a fundamental stochasticity of space or space-time that has the desired effect and amplifies with the system size [153–156]. They all have in common that they introduce a nonlinear stochastic addition to the Schrödinger equation, whose main observable consequence is the effective destruction of quantum coherence in large systems similar to the effect of environmental decoherence. I will study a broad class of such models from a more general perspective in Chapter 4.

Here, we will focus on one of the best studied models of this kind, the full-fledged theory of continuous spontaneous localization (CSL) [154, 155, 157]. I will assess its concrete predictions for high-mass interferometry and show that it will become testable in the proposed OTITLI setup with the heaviest gold clusters.

3.4.3.1. The CSL master equation

The CSL model adds a stochastic momentum diffusion term to the Schrödinger equation of mechanical systems, which continuously localizes the wave function in space. This diffusion occurs spontaneously and is not related to any kind of environmental interaction, as in the case of Brownian diffusion, for instance. On the microscopic level, the predicted effect is too weak to be observed in quantum experiments to date. On the macroscopic level, however, the effect is amplified by the system mass to such an extent that any delocalized wave function would localize within unobservably short times.

The elementary quantum description of composite mechanical objects is given in terms of many constituent species of bosons and fermions. According to the CSL hypothesis, each such constituent particle experiences the localization effect in proportion to its mass m_k , and the many-body wave function is then subject to an amplified diffusion process that is the sum of the individual effects. In a second-quantization formulation, it is represented by the position-averaged mass density operator

$$\mathbf{m}(\mathbf{r}) = \int d^3 r' g(\mathbf{r} - \mathbf{r}') \sum_k m_k \mathbf{n}_k(\mathbf{r}'), \quad (3.101)$$

with $\mathbf{n}_k(\mathbf{r}) = \hat{\psi}_k^\dagger(\mathbf{r}) \hat{\psi}_k(\mathbf{r})$ the number density operator of the k th species. The function $g(\mathbf{r}) = (2\pi)^{-3/2} r_c^{-3} \exp(-r^2/2r_c^2)$ is a normalized and isotropic Gaussian distribution, whose width r_c is a free parameter of the model. It is commonly fixed at $r_c = 100$ nm in the literature [155, 157, 158], although the precise value may differ within one order of magnitude [159, 160]. An arbitrary many-body density operator $\hat{\rho}$ (in second quantization) is now subject to the modified time evolution $\partial_t \hat{\rho} = -i[\mathbf{H}, \hat{\rho}]/\hbar + \mathcal{L}_{\text{CSL}} \hat{\rho}$, where the von Neumann equation is complemented by the Lindblad term³⁰

$$\mathcal{L}_{\text{CSL}} \hat{\rho} = \frac{8\pi^{3/2} r_c^3 \lambda_0}{m_0^2} \int d^3 r \left[\mathbf{m}(\mathbf{r}) \hat{\rho} \mathbf{m}(\mathbf{r}) - \frac{1}{2} \{ \hat{\rho}, \mathbf{m}^2(\mathbf{r}) \} \right]. \quad (3.102)$$

³⁰ Note that I will study generalized modifications of this kind in Chapter 4. There, I will construct them from basic principles, and their Lindblad operators will exhibit a similar mass dependence. Note also that the second-quantization form already implies that the exchange symmetry of indistinguishable particles is conserved by the model.

The constant λ_0 , the second free parameter of the model, denotes the localization rate at a fixed but arbitrary reference mass m_0 . The reference rate is conventionally given at the nucleon mass, $m_0 = 1$ amu. Superposition states of nuclei delocalized over more than $r_c = 100$ nm are decayed into mixtures at this rate. It was originally assumed to be $\lambda_0 = 10^{-16}$ Hz [153], a conservative estimate, which made the originally proposed model [153] consistent with all quantum experiments on microscopic scales at the time. Later reasonings based on the image formation on photographic plates or in the human eye, for instance, have led to the substantially larger estimate $\lambda_0 = 10^{10 \pm 2}$ Hz [159, 161, 162].

The divergence in the estimates is related to the quadratic mass dependence of the effective localization rate in heavier compound systems, such as molecules or nanoparticles. As long as they are smaller in size than the localization length r_c , their center-of-mass degree of freedom evolves under the modified master equation $\partial_t \rho = -i [\mathbf{H}, \rho] / \hbar + \mathcal{L} \rho$,

$$\mathcal{L} \rho = \left(\frac{m}{m_0} \right)^2 \lambda_0 \left[8\pi^{3/2} r_c^3 \int d^3 r g(\mathbf{R} - \mathbf{r}) \rho g(\mathbf{R} - \mathbf{r}) - \rho \right]. \quad (3.103)$$

Here, m and \mathbf{R} denote the mass and the center-of-mass position operator of the object. The origin of this Lindblad form can also be understood in terms of a stochastic process of single random events (instead of a continuous diffusion process), where the events occur at the rate $\lambda = \lambda_0 (m/m_0)^2$ and project the wave function of the compound to localized Gaussian states of the form $g(\mathbf{R} - \mathbf{r})$.

This indicates a formal resemblance to decoherence master equations [163]. In fact, a Fourier transform of the Gaussian functions converts the CSL term (3.103) into the form

$$\mathcal{L} \rho = \left(\frac{m}{m_0} \right)^2 \lambda_0 \left[\left(\frac{r_c}{\sqrt{\pi}} \right)^3 \int d^3 k e^{-k^2 r_c^2} \exp(i\mathbf{k} \cdot \mathbf{R}) \rho \exp(-i\mathbf{k} \cdot \mathbf{R}) - \rho \right]. \quad (3.104)$$

It resembles the standard collisional decoherence master equation with a Gaussian distribution of momentum kicks exerted on the particle.

3.4.3.2. Contrast reduction predicted by the model

The converted form (3.104) of the CSL modification allows us to treat it in full analogy to the decoherence effects of Section 3.4.2.2. The decoherence function becomes $\mathcal{R}(x) = \exp(-x^2/4r_c^2)$, and we find that the corresponding reduction factors (3.89) take on the form

$$\ln R_\ell = -2\lambda_0 T \left(\frac{m}{m_0} \right)^2 \left[1 - \frac{\sqrt{\pi} r_c T_T}{\ell d T} \operatorname{erf} \left(\frac{\ell d T}{2 r_c T_T} \right) \right]. \quad (3.105)$$

They describe the reduction of the interference fringe amplitudes in the OTITLI setup as predicted by the CSL model. In particular, the sinusoidal fringe visibility reduces by

$$\mathcal{V}_{\sin} \rightarrow \mathcal{V}_{\sin} \exp \left\{ -2\xi \lambda_0 T_0 \left(\frac{m}{m_0} \right)^3 \left[1 - \frac{\sqrt{\pi} r_c}{\xi d} \operatorname{erf} \left(\frac{\xi d}{2 r_c} \right) \right] \right\}. \quad (3.106)$$

Let me express the pulse separation in units of the Talbot time, $T = \xi T_T$, and introduce the reference Talbot time $T_0 = m_0 d^2 / \hbar \approx 16$ ns in order to highlight the cubic mass dependence of the predicted

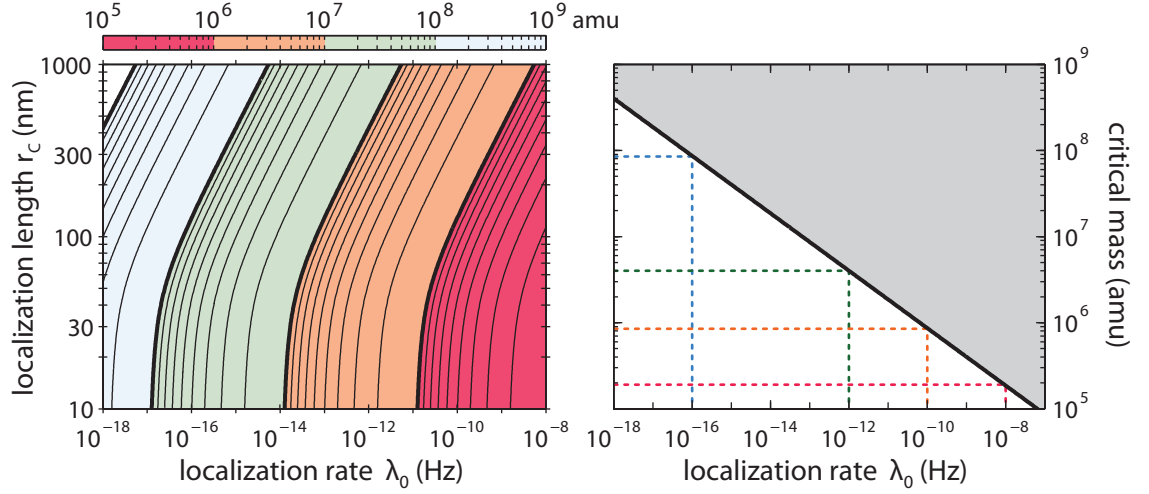


Figure 3.19. Required mass for testing the CSL model with gold cluster interferometry as a function of the localization rate λ_0 and the localization length r_c (right panel), and as a function of only the rate parameter λ_0 (left panel). The solid curves give the critical mass at which the interference visibility is predicted to decrease by a factor of two when the grating separation is fixed at the second Talbot order, $T = 2T_T$. The dashed lines on the right mark the critical masses associated to the existing estimates for the localization rate λ_0 .

decay³¹. The square-bracketed term is always positive and smaller than unity. It converges to unity in the limit where the effective separation of neighbouring interference paths is large compared to the CSL length, $\xi d \gg r_c$.

In Figure 3.19 I plot the critical mass of gold clusters (solid lines) at which the OTITLI fringe visibility would be reduced by a factor of two due to CSL, at a fixed $\xi = 2$. The right diagram shows it as a function of the localization rate parameter λ_0 , assuming the standard value for the localization length, $r_c = 100$ nm. All masses below the solid line experience a visibility reduction of less than 1/2, whereas the shaded area above the line marks the mass regime where interference is essentially prohibited by CSL. The dashed lines indicate the masses that must be reached in order to test the existing (old and new) estimates for the rate parameter, $\lambda_0 = 10^{-16}$ Hz and $10^{-10 \pm 2}$ Hz. The left panel is a contour plot of the critical mass, where I allow the localization length r_c to deviate from the standard value by at most one order of magnitude. (The diagrams were published in [12] and [11].)

Concludingly, we find that the old and the new estimate for the CSL rate will become testable with gold clusters of 9×10^7 and $10^{5.9 \pm 0.7}$ amu, respectively. We have seen in the preceding sections that this mass regime can still be reached, in principle, with the proposed OTITLI scheme if we are able to keep the particles on a stable trajectory and sufficiently well shielded from the environment. The limiting size effect of Section 3.4.2.3 kicks in significantly only at larger masses. If present, the CSL effect could also be distinguished from standard decoherence effects by measuring the contrast reduction as a function of varying pressure and temperature of the apparatus.

In the next chapter, I will exploit the idea of testing modifications of standard quantum theory by means of experiments further and from a more general perspective. By constructing a broad generic class of such modifications and matching its predictions with observational data we will be able to quantify and compare the amount of 'macroscopicity' in different quantum experiments.

³¹ It stems from the fact that we require $\xi \sim 1$ (i.e. $T = T_T$) for a successful proof of quantum interference.

Chapter 4.

Classicalization and the macroscopicity of quantum superposition states

“Under the ideal measure of values there lurks the hard cash.”
— Karl Marx

The attentive reader should have recognized as a leitmotif throughout this thesis the exploration of the fundamental limits to controlling and interfering massive particles at the borderline to the classical world. A concrete assessment of these limits was done in Section 3.4 of the preceding chapter, which showed the potential of the OTITLI scheme for time-domain Talbot-Lau interferometry with nanoclusters. We have seen there that, apart from classical confounding factors due to inertial forces, finite particle size or setup imprecisions, the interference of heavy particles would mainly be affected by environmental decoherence or by certain objective collapse models which have been proposed for the sake of macroscopic realism [3]. Both effects lead to a decay of superposition states in the position and in the momentum variable of the interfering particle over time, while at the same time maintaining the classical correspondence of the respective expectation values, as given by the Ehrenfest theorem [164]. One generally describes the observable consequences of such a modified time evolution by adding a term to the von Neumann equation of the state operator ρ that represents the motion of the particle. I will refer to the modification as *classicalization*, or *classicalizing modification*, in the following.

In this chapter I take a broader perspective and turn the question of the classical limitation to heavy-particle interference into the question of the *macroscopicity* of quantum superposition states in general. What makes, say, a particular many-body superposition state more macroscopic than another one? If we stick to an intuitive conception of macroscopicity as some kind of yardstick indicating how far beyond the microscopic (atomic) scale quantum behaviour might still be *observed* in nature, then the answer to the latter question must be grounded in *empirical* facts. So the macroscopicity should rather be assigned to a concrete physical observation than to the formal representation of the quantum state itself. Recall that I motivated this argument already in the Introduction Chapter by referring to Leggett’s hypothesis of macroscopic realism [3, 165]. It will be carried out rigorously in what is to follow.

The demonstration of the quantum superposition principle with ever larger systems has in fact become a key challenge in modern-day experiments. They range from atom interference with large path separations and long interrogation times [166, 167], observed superpositions with many supercondensed electrons [1, 2, 168] or Bose-Einstein condensates [169], to proposed measurements of

quantum coherence with micromirrors in their oscillatory ground state [170]. In the cited examples, as well as in many other realized and conceivable superposition experiments, the systems under investigation consist of material degrees of freedom with a direct correspondence in classical mechanics: One may associate with them a distribution of moving point masses. The time evolution of the corresponding quantum states of motion is expected to be affected in a similar way both by the same decoherence effects and by (speculative) classicalizing modifications. So, in a sense, all those experiments are testing the same basic hypothesis, the validity of quantum mechanics, in different settings and to a different degree—a common feature that may ultimately serve as a basis to compare all those experiments in an unbiased way.

The central result of this chapter will be the definition of an objective measure of macroscopicity in Section 4.3, which allows us to quantify how macroscopic various quantum superposition states are, which have been or may soon be observed in past and future experiments on mechanical systems. To achieve this I will first construct a generic class of classicalizing modifications in Section 4.1, which affect standard quantum theory only minimally and leave its basic symmetry and consistency principles intact. Having studied their observable consequences in Section 4.2, we can then assess the macroscopicity of quantum superposition states by quantifying the extent to which such minimal modifications are ruled out once they are observed in an experiment¹.

The present approach differs from the reasoning behind other measures of macroscopicity that can be found in the literature [3, 165, 171–176]. These measures are often restricted to a subclass of quantum systems and state representations, or they refer to a preferred choice of macroscopically distinct observables or operational resources required to analyze a given quantum state. Hence they reveal an inherent problem underlying the definition of macroscopicity within quantum theory: The Hilbert space of complex many-body systems can be decomposed into many different tensor products, in some of which specific quantum states may look elementarily simple or particularly complex. De Broglie interference of large molecules is, after all, described by one single center-of-mass degree of freedom. I will discuss in this chapter in which sense molecule interference should be regarded more macroscopic than, say, neutron interference. The results of this work were published in a condensed form in [14].

4.1. A minimal modification of quantum mechanics

As a first step let me specify the form and the properties of a hypothetical modification of quantum mechanics which shall be weakly invasive in the sense that it conserves basic symmetry principles as well as the operational framework underlying both quantum and classical mechanics. The principal focus here lies on the conservation of Galilean invariance in order to avoid a preferred reference frame of the modification, but we shall also account for the exchange symmetry of identical quantum particles. Moreover, the modification shall consistently scale and apply to arbitrary systems of mechanical degrees of freedom, from the free motion of individual particles to the complex dynamics of interacting many-body systems.

The conditions sketched above will be sufficient to specify the observable consequences of this minimal modification, that is, its explicit form on the level of the density operator ρ for the motional

¹ The concept of macroscopicity presented here only applies to quantum systems with a direct classical correspondence in nonrelativistic mechanics. This excludes, by definition, systems of genuinely quantum degrees of freedom such as spins.

state of an arbitrary mechanical system. It is important to note that there exist already explicit macro-realistic theories [150, 155, 157, 177], which enforce classical behaviour on the macroscale by adding a nonlinear and stochastic term to the Schrödinger equation of a system of material particles. They meet the above requirements and can thus be regarded as special cases of a classicalizing modification.

4.1.1. The operational framework and the dynamical semigroup assumption

The theory of both quantum and classical mechanics can be elegantly formulated in a common operational framework [178, 179] of preparations, transformations and measurements. This approach, minimizing the interpretational overhead on top of the pure mathematical formalism, underlines the empirical and statistical nature of both theories and allows us to assess their common features most clearly.

One of these features is the general concept of the state ρ associated to a given ensemble of preparations of a system, a mathematical object that contains all the necessary information to reproduce the statistics of any measurement on that system. In quantum theory the state is given by a linear, positive and normalized² operator $\rho \in \mathcal{B}(\mathcal{H})$ on the Hilbert space \mathcal{H} associated to the underlying quantum system. The most elementary quantum system with a counterpart in classical mechanics is that of an elementary moving point mass m in free space, $\mathcal{H} = L^2(\mathbb{R}^3)$. In this case, a given quantum state ρ may be represented in terms of the *real-valued and normalized* Wigner function $w(\mathbf{r}, \mathbf{p})$ in phase space (see Appendix A.3 for the one-dimensional case). A classical state of the same system is given by a *positive and normalized* distribution function $f(\mathbf{r}, \mathbf{p})$ of the phase space coordinates $(\mathbf{r}, \mathbf{p}) \in \mathbb{R}^6$. The respective distribution functions for general mechanical systems consisting of N particles with arbitrary masses are then defined on the $6N$ -dimensional phase space \mathbb{R}^{6N} .

An important aspect of the operational concept of states is state mixing: Repeating many times a routine P , where a given system is prepared in the state ρ_1 with probability p_1 or in a different state ρ_2 with probability $p_2 = 1 - p_1$, yields the state $\rho = p_1\rho_1 + p_2\rho_2$ for the overall ensemble. That is to say, the set of all possible states is convex. Moreover, if the experimenter decides to transform the state by $\Phi : \rho \mapsto \Phi(\rho)$ each time after preparing it, we can speak of a different mixing routine P' of the states $\rho'_1 = \Phi(\rho_1)$ and $\rho'_2 = \Phi(\rho_2)$. Consistency then requires the transformation to be a convex linear map,

$$\Phi(p_1\rho_1 + p_2\rho_2) = p_1\Phi(\rho_1) + p_2\Phi(\rho_2). \quad (4.1)$$

In addition, the map Φ must then also conserve the normalization and the positivity of states (even when the transformation is performed only on parts of a larger system). One speaks of a linear, completely positive and trace-preserving (LCPT) map. This must hold, in particular, for the free time evolution of states, as described by a family of transformations $\{\Phi_t \mid t \geq 0\}$. It should then be clear that any modification of the standard quantum time evolution must be LCPT in order to stay consistent with the underlying operational framework.

Standard time evolutions in both quantum and classical mechanics exhibit another important property – their dynamical semigroup character – which should not be easily abandoned when modifying it. The semigroup property of a given one-parameter family $\{\Phi_t \mid t \geq 0\}$ of LCPT time

² The normalization $\text{tr}(\rho) = 1$ implies that the state is a norm-bounded operator. The set of bounded operators $\mathcal{B}(\mathcal{H})$ on a separable Hilbert space \mathcal{H} is also a Hilbert space.

transformations means that the time evolution of a state can be decomposed into successive time steps by splitting the respective time evolution as $\Phi_t \circ \Phi_s = \Phi_{t+s}$, with $t, s \geq 0$ and $\Phi_0 = \text{id}$ [180]. This property is also known as the Markov condition, which is usually only violated when the evolving system is part of a larger system, and the (delayed) back-action of its other part on the degrees of freedom of the subsystem cannot be neglected.

Nevertheless, we may always consider, at least in principle, mechanical systems that are sufficiently well isolated from any environment and that evolve coherently in time, according to the von Neumann equation $\partial_t \rho = -i [\mathbf{H}, \rho] / \hbar$ or its classical counterpart. It is therefore natural to assume that a modification of the coherent time evolution (of isolated systems) conserves the semigroup property of this equation. Recall that the modification is introduced solely for the purpose of inducing the quantum-classical transition on the macro-scale, where in both limits the time evolution for arbitrary self-contained systems is Markovian. One might argue that a physical realization of such a modification could embody non-Markovian back-action effects on the small time scales of an underlying physical process. We do not exclude this possibility from our considerations, implying that the Markov condition might be strictly fulfilled only on the coarse-grained time scales of actual experiments.

The quantum dynamical semigroup of the modified time evolution Φ_t can be expressed in terms of the master equation³

$$\partial_t \rho(t) = \mathcal{L}_\Phi \rho(t) = -\frac{i}{\hbar} [\mathbf{H}, \rho(t)] + \mathcal{L} \rho(t), \quad (4.2)$$

with $\rho(t) = \Phi_t(\rho)$ the time-evolved initial state ρ and \mathcal{L}_Φ the *generator* of the semigroup [180]. After subtracting the (unmodified) coherent time evolution under the influence of the Hamilton operator \mathbf{H} , one arrives at the generator \mathcal{L} of the modification. It is of the Lindblad form [180–182]

$$\mathcal{L} \rho = \sum_j \gamma_j \left(\mathbf{L}_j \rho \mathbf{L}_j^\dagger - \frac{1}{2} \{ \mathbf{L}_j^\dagger \mathbf{L}_j, \rho \} \right). \quad (4.3)$$

The constituting Lindblad operators \mathbf{L}_j and coefficients $\gamma_j \geq 0$ will be specified further using basic symmetry and consistency arguments in the following.

4.1.2. Galilean covariance

We are looking for a modification whose form is invariant under arbitrary Galilean symmetry transformations, that is, the modified time evolution must be interchangeable with arbitrary coordinate transformations between different inertial reference frames. This property is called *Galilean covariance*. It should hold universally, even if the concrete Hamiltonian \mathbf{H} of the mechanical system under consideration is not invariant under Galilean transformations due to an external potential, for instance.

In general, the symmetry covariance of a dynamical semigroup is defined with respect to a group \mathcal{G} of symmetry transformations $g \in \mathcal{G}$. In a mechanical system they are given by transformations of the phase space coordinates $(\mathbf{r}_1, \dots, \mathbf{r}_N, \mathbf{p}_1, \dots, \mathbf{p}_N)$ of N arbitrary particles. The corresponding

³ An additional technical assumption is required apart from the semigroup property and the LCPT nature of the one-parameter family $\{\Phi_t \mid t \geq 0\}$: Expectation values must evolve continuously in time, that is, the function $\langle \mathbf{A}(t) \rangle = \text{tr}(\mathbf{A} \Phi_t(\rho))$ must be continuous in t for any state ρ and any bounded operator $\mathbf{A} \in \mathcal{B}(\mathcal{H})$.

transformations of a quantum state are represented by unitary operators U_g associated to each group element. The semigroup of maps Φ_t is covariant with respect to \mathcal{G} if $\Phi_t(U_g \rho U_g^\dagger) = U_g \Phi_t(\rho) U_g^\dagger$ holds for all ρ, g and t . Written in terms of the generator the covariance condition reads as

$$\mathcal{L}_\Phi(U_g \rho U_g^\dagger) = U_g \mathcal{L}_\Phi(\rho) U_g^\dagger \quad \forall g, \rho. \quad (4.4)$$

By inspecting Equations (4.2) and (4.3) one easily sees that covariance is fulfilled for \mathcal{G} -symmetric Hamiltonians $H = U_g H U_g^\dagger$ and for Lindblad operators that are symmetric up to a complex phase, $U_g L_j U_g^\dagger = e^{i\phi_j} L_j$.

Things are a bit more complicated in case of Galilean transformations, which can be explicitly time-dependent. A different equality holds then for the generator of the time evolution, corrected by the kinetic energy of a mechanical system. The Lindblad-generator \mathcal{L} of the modification, however, fulfills the above covariance condition (4.4), as will be shown in Section 4.1.2.3 below.

4.1.2.1. The Galilei symmetry group

The Galilei group \mathcal{G} of transformations between inertial reference frames consists of time translations, spatial translations, velocity boosts, rotations and combinations of those [183]. A space-time point transforms as

$$g : (\mathbf{r}, t) \mapsto (R_g \mathbf{r} + \mathbf{s}_g + \mathbf{w}_g t, t + t_g), \quad (4.5)$$

where R_g denotes a three-dimensional rotation matrix. Hence the group \mathcal{G} is a direct product of the one-parameter group of time translations, the rotation group and the six-parameter group \mathcal{G}_B of Galilean boosts in position and velocity. The most natural physical representation of the Galilei symmetry is a free particle of mass m [183].

I focus here on the boost subgroup \mathcal{G}_B , rotations will be discussed separately at a later stage. Time translations will have to be excluded from our considerations. The invariance of a system under time translations implies energy conservation, which is generally not compatible with a classicalizing modification of the time evolution that leads to an overall loss of quantum coherence in mechanical systems, as we will see later⁴.

We are now left with the abelian subgroup of general boost transformations

$$\begin{aligned} \mathcal{G}_B \ni g_{\mathbf{s}, \mathbf{w}} : (\mathbf{r}, t) &\mapsto (\mathbf{r} + \mathbf{s} + \mathbf{w} t, t), \\ g_{\mathbf{s}, \mathbf{w}} \circ g_{\mathbf{s}', \mathbf{w}'} &= g_{\mathbf{s} + \mathbf{s}', \mathbf{w} + \mathbf{w}'}. \end{aligned} \quad (4.6)$$

Each group element is determined by a position translation \mathbf{s} and a velocity translation \mathbf{w} . Obviously, the group is abelian and isomorphic to \mathbb{R}^6 . In order to find a representation of the group in terms of unitary transformations of quantum states in arbitrary mechanical systems, we need to introduce the concept of *characters*: They are the irreducible one-dimensional representations of abelian groups such as \mathcal{G}_B and serve as the building blocks of the unitary representations on infinite dimensional Hilbert spaces that we will be using [184]. A character χ is a continuous homomorphism from \mathcal{G}_B to the set $\mathcal{T} = \{z \in \mathbb{C} \mid |z| = 1\}$ of complex numbers of modulus one,

$$\chi : \mathcal{G}_B \rightarrow \mathcal{T} \text{ continuous,} \quad \chi(g \circ h) = \chi(g) \chi(h) \quad \forall g, h \in \mathcal{G}_B. \quad (4.7)$$

⁴ The unitary representation of time translations in a system with Hamiltonian H is given by the time evolution operators $U(t_g) = \exp[-iHt_g/\hbar]$. The time translation-covariant Lindblad generator of a modification of the coherent time evolution would require the Lindblad operators to commute with $U(t_g)$ up to a complex phase.

The set of all characters, together with the pointwise multiplication, forms the dual group $\widetilde{\mathcal{G}}_B$, which is again isomorphic to \mathbb{R}^6 . That is to say, every character is specified by two coordinates \mathbf{r}, \mathbf{v} and can conveniently be written as

$$\chi_{\mathbf{r}, \mathbf{v}} : g_{\mathbf{s}, \mathbf{w}} \mapsto \exp \left[\frac{i}{\hbar} m_0 (\mathbf{v} \cdot \mathbf{s} - \mathbf{w} \cdot \mathbf{r}) \right], \quad (4.8)$$

with m_0 an arbitrary reference mass to set the unit dimensions right.

4.1.2.2. The projective unitary representation of Galilean boosts

The standard representation of Galilean boosts on the Hilbert space $L^2(\mathbb{R}^3)$ of a free particle of mass m is expressed in terms of the unitary *Weyl operators* [183, 185],

$$\begin{aligned} W_1(\mathbf{s}, \mathbf{w}) &= \exp \left[\frac{i}{\hbar} (\mathbf{p} \cdot \mathbf{s} - m\mathbf{w} \cdot \mathbf{r}) \right] \\ &= \exp \left[\frac{im\mathbf{w} \cdot \mathbf{s}}{2\hbar} \right] \exp \left[\frac{i\mathbf{p} \cdot \mathbf{s}}{\hbar} \right] \exp \left[-\frac{im\mathbf{w} \cdot \mathbf{r}}{\hbar} \right] \\ &= \exp \left[-\frac{im\mathbf{w} \cdot \mathbf{s}}{2\hbar} \right] \exp \left[-\frac{im\mathbf{w} \cdot \mathbf{r}}{\hbar} \right] \exp \left[\frac{i\mathbf{p} \cdot \mathbf{s}}{\hbar} \right], \end{aligned} \quad (4.9)$$

with \mathbf{r} and \mathbf{p} the position and momentum operators⁵. The Weyl operators are the quantum pendant of a phase space translation, as can be seen from

$$W_1(\mathbf{s}, \mathbf{w})|\mathbf{r}\rangle = e^{-im\mathbf{w} \cdot (2\mathbf{r} - \mathbf{s})/2\hbar} |\mathbf{r} - \mathbf{s}\rangle, \quad (4.10)$$

$$W_1(\mathbf{s}, \mathbf{w})|\mathbf{p}\rangle = e^{i(2\mathbf{p} - m\mathbf{w}) \cdot \mathbf{s}/2\hbar} |\mathbf{p} - m\mathbf{w}\rangle, \quad (4.11)$$

$$W_1(\mathbf{s}, \mathbf{w}) \begin{pmatrix} \mathbf{r} \\ \mathbf{p} \end{pmatrix} W_1^\dagger(\mathbf{s}, \mathbf{w}) = \begin{pmatrix} \mathbf{r} + \mathbf{s} \\ \mathbf{p} + m\mathbf{w} \end{pmatrix}. \quad (4.12)$$

The operators form a *projective* unitary representation (or unitary *ray* representation) of Galilean boosts [183–185], that is, they conserve the group operation and commute with each other *up to a complex phase*,

$$\begin{aligned} W_1(\mathbf{s}_1, \mathbf{w}_1) W_1(\mathbf{s}_2, \mathbf{w}_2) &= e^{im(\mathbf{w}_1 \cdot \mathbf{s}_2 - \mathbf{w}_2 \cdot \mathbf{s}_1)/2\hbar} W_1(\mathbf{s}_1 + \mathbf{s}_2, \mathbf{w}_1 + \mathbf{w}_2) \\ &= e^{im(\mathbf{w}_1 \cdot \mathbf{s}_2 - \mathbf{w}_2 \cdot \mathbf{s}_1)/\hbar} W_1(\mathbf{s}_2, \mathbf{w}_2) W_1(\mathbf{s}_1, \mathbf{w}_1). \end{aligned} \quad (4.13)$$

This is also known as the *Weyl relation* [186]. The phase factor in the second line is given by the character (4.8), with $m_0 = m$.

⁵ An operator exponential can be split according to $e^{X+Y} = e^X e^Y e^{-[X,Y]/2}$ when the commutator is a \mathbb{C} -number. From this follows also the identity $e^X Y e^{-X} = Y + [X, Y]$.

In the general case of N particles (with masses m_1, \dots, m_N) the boosts are represented by a tensor product of the single-particle representations,

$$\begin{aligned} W_N(\mathbf{s}, \mathbf{w}) &= \bigotimes_{n=1}^N \exp \left[\frac{i}{\hbar} (\mathbf{p}_n \cdot \mathbf{s} - m_n \mathbf{w} \cdot \mathbf{r}_n) \right] = \exp \left[\frac{i}{\hbar} (\mathbf{P} \cdot \mathbf{s} - M \mathbf{w} \cdot \mathbf{R}) \right] \\ &= \exp \left[\frac{iM \mathbf{w} \cdot \mathbf{s}}{2\hbar} \right] \bigotimes_{n=1}^N \exp \left[\frac{i\mathbf{p}_n \cdot \mathbf{s}}{\hbar} \right] \exp \left[-\frac{im_n \mathbf{w} \cdot \mathbf{r}_n}{\hbar} \right] \\ &= \exp \left[-\frac{iM \mathbf{w} \cdot \mathbf{s}}{2\hbar} \right] \bigotimes_{n=1}^N \exp \left[-\frac{im_n \mathbf{w} \cdot \mathbf{r}_n}{\hbar} \right] \exp \left[\frac{i\mathbf{p}_n \cdot \mathbf{s}}{\hbar} \right]. \end{aligned} \quad (4.14)$$

Comparing the right hand side of the first line with (4.9) we see that this effectively boosts only the center-of-mass coordinates $\mathbf{R} = \sum_n m_n \mathbf{r}_n / M$ and $\mathbf{P} = \sum_n \mathbf{p}_n$, with $M = \sum_n m_n$ the total mass. The respective Weyl relation reads as

$$W_N(\mathbf{s}_1, \mathbf{w}_1) W_N(\mathbf{s}_2, \mathbf{w}_2) = e^{iM(\mathbf{w}_1 \cdot \mathbf{s}_2 - \mathbf{w}_2 \cdot \mathbf{s}_1)/2\hbar} W_N(\mathbf{s}_1 + \mathbf{s}_2, \mathbf{w}_1 + \mathbf{w}_2). \quad (4.15)$$

The many-particle Weyl operators can also be formulated in second quantization by expressing the position and momentum operators of identical particles in terms of Fock operators,

$$W(\mathbf{s}, \mathbf{w}) = \exp \left[\frac{i}{\hbar} \sum_k \left(\int d^3p \, \mathbf{p} \cdot \mathbf{s} a_k^\dagger(\mathbf{p}) a_k(\mathbf{p}) - m_k \int d^3r \, \mathbf{w} \cdot \mathbf{r} \hat{\psi}_k^\dagger(\mathbf{r}) \hat{\psi}_k(\mathbf{r}) \right) \right]. \quad (4.16)$$

Here, the sum extends over different bosonic or fermionic particle species labeled by k . In particular, it extends over the different spin states of each particle. The terms $a_k(\mathbf{p})$ and $\hat{\psi}_k(\mathbf{r})$ denote the Fock annihilation operators for momentum \mathbf{p} and position \mathbf{r} , respectively. The Weyl relation becomes

$$W(\mathbf{s}_1, \mathbf{w}_1) W(\mathbf{s}_2, \mathbf{w}_2) = e^{iM(\mathbf{w}_1 \cdot \mathbf{s}_2 - \mathbf{w}_2 \cdot \mathbf{s}_1)/2\hbar} W(\mathbf{s}_1 + \mathbf{s}_2, \mathbf{w}_1 + \mathbf{w}_2), \quad (4.17)$$

with the operator $M = \sum_k m_k N_k$ counting the total mass via the number operators N_k of each species. Projective unitarity holds within each subspace of fixed particle number, where the exponential term reduces to a phase factor, as in (4.15). I will mostly use the first quantization form in the following, when discussing the general implications of Galilean covariance on the modified time evolution of mechanical systems.

4.1.2.3. Galilean covariance of the modified time evolution

The modified time evolution Φ_t of a mechanical system is covariant with respect to the Galilean boost transformations (4.6) if it stays the same whether one applies it in, say, the system's rest frame or in another inertial frame. In mathematical terms, this condition reads as [187, 188]

$$\Phi_t [W_N(\mathbf{s}, \mathbf{w}) \rho W_N^\dagger(\mathbf{s}, \mathbf{w})] = W_N(\mathbf{s} - \mathbf{w}t, \mathbf{w}) \Phi_t(\rho) W_N^\dagger(\mathbf{s} - \mathbf{w}t, \mathbf{w}) \quad \forall \rho, \mathbf{s}, \mathbf{w}, t. \quad (4.18)$$

It differs from the covariance condition (4.4) due to the explicit time-dependence of the boost transformation: The system coordinates with respect to the moving reference frame are constantly relocated by $\mathbf{w}t$ over time. The covariance condition for the generator \mathcal{L}_Φ is obtained by differentiating with respect to time at $t = 0$,

$$\mathcal{L}_\Phi [W_N(\mathbf{s}, \mathbf{w}) \rho W_N^\dagger(\mathbf{s}, \mathbf{w})] = W_N(\mathbf{s}, \mathbf{w}) \left\{ \mathcal{L}_\Phi(\rho) - \frac{i}{\hbar} \mathbf{w} \cdot \left[\sum_n \mathbf{p}_n, \rho \right] \right\} W_N^\dagger(\mathbf{s}, \mathbf{w}). \quad (4.19)$$

As already mentioned, this only holds in systems where the coherent time evolution is governed by a Galilei-invariant Hamiltonian without external potential. In fact, the second term in the curly brackets corrects for the phase-space translation of the kinetic energy term $\mathcal{L}_0(\rho) = -i \sum_n [\mathbf{p}_n^2/2m_n, \rho]/\hbar$, which is always part of the Hamiltonian. One checks this easily using the identity (4.12). By subtracting the coherent part from the generator of the time evolution one finds that the Galilei-covariant modification (4.3) then must fulfill the condition (4.4) in terms of the Weyl operators,

$$\mathcal{L} [W_N(\mathbf{s}, \mathbf{w}) \rho W_N^\dagger(\mathbf{s}, \mathbf{w})] = W_N(\mathbf{s}, \mathbf{w}) \mathcal{L}(\rho) W_N^\dagger(\mathbf{s}, \mathbf{w}). \quad (4.20)$$

The identity shall hold universally, including the cases where the Hamiltonian H breaks the Galilean covariance of the coherent time evolution.

4.1.2.4. Implications for the form of the modification

A theorem by Holevo [189, 190] restricts the form of the modification generator \mathcal{L} based on the above condition (4.20). He studied the generic form of quantum dynamical semigroups which are covariant with respect to a certain class of abelian symmetry groups, including the Galilean boost group \mathcal{G}_B studied here. I follow the proof presented in [189], which does not only apply to single-particle Hilbert spaces but to arbitrary many-body systems. Holevo states his result for unitary representations of the symmetry group, but the relevant steps in the proof remain valid also for projective unitary representations, as in the present case. The result is valid for norm-bounded quantum dynamical semigroups $\{\Phi_t\}$, that is, $\|\Phi_t(A)\| \leq C \|A\| \quad \forall A \in \mathcal{B}(\mathcal{H})$, with $C \geq 0$ and $\|A\|$ the operator norm [191].

According to Holevo's theorem, the \mathcal{G}_B -covariant generator (4.20) can be decomposed in terms of an integral over the dual group $\tilde{\mathcal{G}}_B \cong \mathbb{R}^6$ of characters (4.8),

$$\mathcal{L}(\rho) = \sum_j \int d^3s d^3w \left[L_j(\mathbf{s}, \mathbf{w}) \rho L_j^\dagger(\mathbf{s}, \mathbf{w}) - \frac{1}{2} \{L_j^\dagger(\mathbf{s}, \mathbf{w}) L_j(\mathbf{s}, \mathbf{w}), \rho\} \right]. \quad (4.21)$$

The Lindblad operators fulfill the relation

$$\begin{aligned} L_j(\mathbf{s}, \mathbf{w}) W_N(\mathbf{s}', \mathbf{w}') &= \chi_{\mathbf{s}, \mathbf{w}}(g_{\mathbf{s}', \mathbf{w}'}) W_N(\mathbf{s}', \mathbf{w}') L_j(\mathbf{s}, \mathbf{w}) \\ &= \exp \left[\frac{i}{\hbar} m_0 (\mathbf{w} \cdot \mathbf{s}' - \mathbf{w}' \cdot \mathbf{s}) \right] W_N(\mathbf{s}', \mathbf{w}') L_j(\mathbf{s}, \mathbf{w}), \end{aligned} \quad (4.22)$$

and the operator-valued integral $\int d^3s d^3w \sum_j L_j^\dagger(\mathbf{s}, \mathbf{w}) L_j(\mathbf{s}, \mathbf{w})$ is pointwise convergent (i.e. it converges to a finite value with respect to the weak-* topology in $\mathcal{B}(\mathcal{H})$ [191]). The latter, however, means that unbounded diffusion terms such as double commutators $[\mathbf{r}, [\mathbf{r}, \rho]]$ are excluded [188, 192]. Such terms occur in the Caldeira-Leggett model of quantum Brownian motion [35, 193], for instance. They are typically the result of approximating scattering processes in the limit of weak momentum exchange [194], and they give rise to a significantly more drastic classicalizing modification of the coherent time evolution when they are universally applied beyond that limit. I have therefore omitted unbounded terms in the construction of a minimally invasive modification.

We still have to account for the rotation transformations to obtain full Galilean covariance of the modification. However, it will be more convenient to incorporate them after studying the concrete implications of the covariance condition (4.22) on the Lindblad operators $L_j(\mathbf{s}, \mathbf{w})$.

4.1.3. The modified time evolution of a single particle

In the case of a single particle of mass m one can explicitly construct the Lindblad operators of the modification (4.21) from the covariance condition (4.22), which reduces to

$$\exp\left[-\frac{i}{\hbar}(\mathbf{p} \cdot \mathbf{s}' - m\mathbf{w}' \cdot \mathbf{r})\right] L_j(\mathbf{s}, \mathbf{w}) \exp\left[\frac{i}{\hbar}(\mathbf{p} \cdot \mathbf{s}' - m\mathbf{w}' \cdot \mathbf{r})\right] = e^{im_0(\mathbf{w} \cdot \mathbf{s}' - \mathbf{w}' \cdot \mathbf{s})/\hbar} L_j(\mathbf{s}, \mathbf{w}). \quad (4.23)$$

Since this must hold for arbitrary $(\mathbf{s}', \mathbf{w}') \in \mathbb{R}^6$, we obtain two independent conditions by setting either the position or the velocity variable to zero. For $\mathbf{w}' = 0$ the matrix elements of the operator in momentum representation fulfill the identity

$$e^{i(\mathbf{p}' - \mathbf{p}) \cdot \mathbf{s}'/\hbar} \langle \mathbf{p}' | L_j(\mathbf{s}, \mathbf{w}) | \mathbf{p}' \rangle = e^{im_0 \mathbf{w} \cdot \mathbf{s}'/\hbar} \langle \mathbf{p}' | L_j(\mathbf{s}, \mathbf{w}) | \mathbf{p}' \rangle \quad \forall \mathbf{s}'. \quad (4.24)$$

A non-zero value of the matrix element is only possible for $\mathbf{p}' = \mathbf{p} + m_0 \mathbf{w}$. Using the transformation rule (4.11) we may thus expand the operator as

$$L_j(\mathbf{s}, \mathbf{w}) = L_j(\mathbf{s}, \mathbf{w}; \mathbf{p}) \exp\left[\frac{i}{\hbar} m_0 \mathbf{w} \cdot \mathbf{r}\right], \quad (4.25)$$

where the function L_j can only depend on the momentum operator \mathbf{p} of the particle. Plugging this into (4.23) for $\mathbf{s}' = 0$ leads to the condition

$$e^{im\mathbf{w}' \cdot (\mathbf{r} - \mathbf{r}')/\hbar} \langle \mathbf{r}' | L_j(\mathbf{s}, \mathbf{w}; \mathbf{p}) | \mathbf{r}' \rangle = e^{-im_0 \mathbf{w}' \cdot \mathbf{s}/\hbar} \langle \mathbf{r}' | L_j(\mathbf{s}, \mathbf{w}; \mathbf{p}) | \mathbf{r}' \rangle \quad \forall \mathbf{w}', \quad (4.26)$$

in position representation. Here, a non-zero matrix element is only possible for $\mathbf{r}' = \mathbf{r} + m_0 \mathbf{s}/m$. The form of L_j is thus obtained from the rule (4.10) and we are finally left with

$$L_j(\mathbf{s}, \mathbf{w}) = \ell_j(\mathbf{s}, \mathbf{w}) \exp\left[\frac{i}{\hbar} m_0 \left(\mathbf{w} \cdot \mathbf{r} - \frac{\mathbf{p} \cdot \mathbf{s}}{m}\right)\right] = \ell_j(\mathbf{s}, \mathbf{w}) W_1^\dagger\left(\frac{m_0}{m} \mathbf{s}, \frac{m_0}{m} \mathbf{w}\right), \quad (4.27)$$

where ℓ_j denotes an arbitrary complex-valued function. It must be square-integrable since the modification (4.21) is norm-bounded. This allows us to introduce a time parameter $\tau > 0$ and a positive phase-space distribution function $g(\mathbf{s}, \mathbf{q})$ by

$$\frac{1}{\tau} = \int d^3s d^3w \sum_j |\ell_j(\mathbf{s}, \mathbf{w})|^2, \quad (4.28)$$

$$g(\mathbf{s}, \mathbf{q}) = \frac{m^3 \tau}{m_0^6} \sum_j \left| \ell_j\left(\frac{m}{m_0} \mathbf{s}, \frac{\mathbf{q}}{m_0}\right) \right|^2, \quad (4.29)$$

where the latter is normalized to $\int d^3s d^3q g(\mathbf{s}, \mathbf{q}) = 1$. The time parameter and the position-momentum distribution function specify completely the modification for a single particle,

$$\mathcal{L}_1(\rho) = \frac{1}{\tau} \left[\int d^3s d^3q g(\mathbf{s}, \mathbf{q}) W_1^\dagger\left(\mathbf{s}, \frac{\mathbf{q}}{m}\right) \rho W_1\left(\mathbf{s}, \frac{\mathbf{q}}{m}\right) - \rho \right]. \quad (4.30)$$

4.1.3.1. Covariance with respect to rotations

In order to achieve full Galilean covariance of (4.30) rotational transformations must be considered as well. They are described in terms of orthogonal rotation matrices $R \in SO(3)$, $RR^T = R^T R = \mathbb{I}$, with unit determinant. Their unitary representation in mechanical systems transforms the position and momentum operator of a particle as

$$U_R \begin{pmatrix} \mathbf{r} \\ \mathbf{p} \end{pmatrix} U_R^\dagger = \begin{pmatrix} R\mathbf{r} \\ R\mathbf{p} \end{pmatrix}. \quad (4.31)$$

The identity $\mathbf{a} \cdot R\mathbf{b} = (R^T \mathbf{a}) \cdot \mathbf{b}$ holds for scalar products of three-dimensional vectors. Given an arbitrary rotation R , we find that the generator (4.30) transforms as

$$\begin{aligned} U_R \mathcal{L}_1(\rho) U_R^\dagger &= \frac{1}{\tau} \left[\int d^3 s d^3 q g(\mathbf{s}, \mathbf{q}) W_1^\dagger \left(R^T \mathbf{s}, \frac{R^T \mathbf{q}}{m} \right) U_R \rho U_R^\dagger W_1 \left(R^T \mathbf{s}, \frac{R^T \mathbf{q}}{m} \right) - U_R \rho U_R^\dagger \right] \\ &= \frac{1}{\tau} \left[\int d^3 s d^3 q g(R\mathbf{s}, R\mathbf{q}) W_1^\dagger \left(\mathbf{s}, \frac{\mathbf{q}}{m} \right) U_R \rho U_R^\dagger W_1 \left(\mathbf{s}, \frac{\mathbf{q}}{m} \right) - U_R \rho U_R^\dagger \right] \end{aligned} \quad (4.32)$$

Rotational covariance is then obtained for isotropic (and inversion-symmetric) distribution functions, $g(\mathbf{s}, \mathbf{q}) = g(s, q)$, where $s = |\mathbf{s}|$ and $q = |\mathbf{q}|$. The final form of the Galilei-covariant modification of the time evolution of a single particle then reads as

$$\mathcal{L}_1(\rho) = \frac{1}{\tau} \left[\int d^3 s d^3 q g(s, q) W_1 \left(\mathbf{s}, \frac{\mathbf{q}}{m} \right) \rho W_1^\dagger \left(\mathbf{s}, \frac{\mathbf{q}}{m} \right) - \rho \right]. \quad (4.33)$$

4.1.3.2. Decay of coherence

The main feature of the Galilei-covariant modification is its inherent classicalizing effect on the quantum state of a single particle. It induces a combined decay of off-diagonal matrix elements of the state operator ρ in both position and momentum representation. This becomes evident already in the specific case where translations occur only in the momentum direction, $g(\mathbf{s}, \mathbf{q}) = \delta(\mathbf{s}) h(q)$. The modification (4.33) then resembles the generic form of collisional decoherence master equations [195]. Such master equations can be interpreted as a random position measurement with a limited spatial resolution given by the spread of the Fourier transform of $h(q)$. Quantum states remain practically unaffected if they are localized below this limit, whereas coherent superpositions stretching over a larger distance decay into a classical mixture within the time scale τ .

Moreover, the observable consequences of certain objective collapse models [150, 153, 155, 157, 177], which explicitly modify the quantum dynamics of mechanical systems on the level of the Schrödinger equation, are described by the same generic form [163]. In the model of continuous spontaneous localization [155, 157], for instance, the function $h(q)$ is given by a Gaussian distribution (and the same holds true in the previous version [153] of that model). Diósi's gravitational collapse model [150, 177] leads to the modification term

$$\mathcal{L}_D(\rho) = -\frac{\kappa G}{4\hbar} \int d^3 s_1 d^3 s_2 \frac{1}{|\mathbf{s}_1 - \mathbf{s}_2|} [f(\mathbf{s}_1 - \mathbf{r}), [f(\mathbf{s}_2 - \mathbf{r}), \rho]] \quad (4.34)$$

for a single particle, with G the gravitational constant, κ a free scaling factor of the collapse rate and $f(\mathbf{r})$ the local mass density of the particle⁶. The expression can be brought into the covariant standard form (4.33) by introducing the Fourier transform $\tilde{f}(\mathbf{q})$ of the mass density $f(\mathbf{s}) = \int d^3q e^{i\mathbf{q}\cdot\mathbf{s}/\hbar} \tilde{f}(\mathbf{q}) / (2\pi\hbar)^3$, and by noting that the gravitational potential transforms as

$$\int d^3s \frac{\exp(i\mathbf{k}\cdot\mathbf{s})}{s} = \lim_{\alpha \rightarrow 0} \int d^3s \frac{\exp(-\alpha s + i\mathbf{k}\cdot\mathbf{s})}{s} = \frac{4\pi}{k^2} \quad (4.35)$$

into Fourier space. We arrive at

$$\mathcal{L}_D(\rho) = \frac{\kappa G}{(2\pi\hbar)^2} \int d^3q \frac{|\tilde{f}(\mathbf{q})|^2}{q^2} \left[W_1\left(0, \frac{\mathbf{q}}{m}\right) \rho W_1^\dagger\left(0, \frac{\mathbf{q}}{m}\right) - \rho \right], \quad (4.36)$$

which is Galilei-covariant if $f(\mathbf{s}) = f(s)$.

In the more general case (4.33) the classicalizing effect can be made explicit by representing the state in terms of its *characteristic function*. The latter is given by the expansion coefficients of the state operator ρ in terms of the Weyl operators, which form a complete basis set of bounded operators,

$$\chi(\mathbf{r}, \mathbf{p}) := \text{tr} \left(\rho W_1^\dagger \left(\mathbf{r}, \frac{\mathbf{p}}{m} \right) \right) = \int d^3r' d^3p' w(\mathbf{r}', \mathbf{p}') e^{i(\mathbf{p}\cdot\mathbf{r}' - \mathbf{p}'\cdot\mathbf{r})/\hbar}. \quad (4.37)$$

It is normalized to $\chi(0, 0) = 1$, and it relates to the Wigner function $w(\mathbf{r}, \mathbf{p})$ by a Fourier transform. Spatial coherences, that is, off-diagonal matrix elements of ρ in position representation, can be extracted from the characteristic function via

$$\left\langle \mathbf{r}_0 - \frac{\mathbf{r}}{2} \right| \rho \left| \mathbf{r}_0 + \frac{\mathbf{r}}{2} \right\rangle = \int \frac{d^3p}{(2\pi\hbar)^3} e^{-i\mathbf{p}\cdot\mathbf{r}_0/\hbar} \chi(\mathbf{r}, \mathbf{p}), \quad (4.38)$$

and similarly for momentum coherences. The above single-particle modification (4.33) maps the characteristic function to

$$\begin{aligned} \mathcal{L}_1 : \chi(\mathbf{r}, \mathbf{p}) &\mapsto \frac{1}{\tau} \left[\int d^3s d^3q g(s, q) e^{i(\mathbf{q}\cdot\mathbf{r} - \mathbf{p}\cdot\mathbf{s})/\hbar} - 1 \right] \chi(\mathbf{r}, \mathbf{p}) \\ &= -\frac{1}{\tau} [1 - \tilde{g}(r, p)] \chi(\mathbf{r}, \mathbf{p}), \end{aligned} \quad (4.39)$$

where I have introduced the Fourier transform of the phase space distribution function

$$\begin{aligned} \tilde{g}(r, p) &= \int d^3s d^3q g(s, q) \exp \left[-\frac{i}{\hbar} (\mathbf{p}\cdot\mathbf{s} + \mathbf{r}\cdot\mathbf{q}) \right] \\ &= \int_0^\infty ds d^3q (4\pi qs)^2 g(s, q) \text{sinc} \left(\frac{ps}{\hbar} \right) \text{sinc} \left(\frac{qr}{\hbar} \right). \end{aligned} \quad (4.40)$$

It is real and bounded by $|\tilde{g}(r, p)| \leq 1$ due to the normalization of the distribution g . The modification thus effects a decay of the characteristic function in (4.39) and, as a consequence, of off-diagonal matrix elements in position and momentum representation. This happens at a decay time scale given by the parameter τ . The range of affected superposition states is limited, as the decay is

⁶ Point particles with $f(\mathbf{r}) = m\delta(\mathbf{r})$ are not allowed in this model because they would lead to a diverging modification term. One must assume a finite mass density, or finite size, for every particle, even including electrons, for instance.

suppressed for small-scale coherences extending only over distances r in position or p in momentum for which $\tilde{g}(r, p) \approx 1$.

It is interesting to note that the modification (4.33) for a free particle is covariant with respect to time translations in the specific case of zero momentum translations, $g(s, q) = h(s) \delta(q)$. This is because the Lindblad operators commute with the free unitary time evolution operator $U_0(t) = \exp[-i\mathbf{p}^2 t / 2m\hbar]$, and the modification does not affect the conservation of energy. However, this also means that plane wave states⁷ $\rho = |\mathbf{p}\rangle\langle\mathbf{p}|$, which are delocalized and clearly non-classical, are not affected by the modification. Momentum translations are therefore necessary to classicalize the motion of free particles.

4.1.4. The modified time evolution of a many-particle system

While the form of the modification for a single particle can be specified up to a time constant and a phase space distribution function, this is not so in the case of $N > 1$ particles. Using (4.14) the covariance condition (4.22) for the Lindblad operators can be stated as

$$\begin{aligned} \exp\left[-\frac{i}{\hbar}(\mathbf{P} \cdot \mathbf{s}' - M\mathbf{w}' \cdot \mathbf{R})\right] L_j(\mathbf{s}, \mathbf{w}) \exp\left[\frac{i}{\hbar}(\mathbf{P} \cdot \mathbf{s}' - M\mathbf{w}' \cdot \mathbf{R})\right] \\ = e^{im_0(\mathbf{w} \cdot \mathbf{s}' - \mathbf{w}' \cdot \mathbf{s})/\hbar} L_j(\mathbf{s}, \mathbf{w}) \quad \forall \mathbf{s}', \mathbf{w}', \end{aligned} \quad (4.41)$$

with $M = \sum_{n=1}^N m_n$ the total mass. This relation means that the Lindblad operators must translate the center-of-mass momentum $\mathbf{P} = \sum_n \mathbf{p}_n$ by the amount $-m_0\mathbf{w}$, and the center-of-mass position $\mathbf{R} = \sum_n m_n \mathbf{r}_n / M$ by $-m_0\mathbf{s}/M$. Let us therefore switch to center-of-mass and relative coordinates and factorize the operator as

$$L_j(\mathbf{s}, \mathbf{w}) = L_j^{\text{rel}}(\mathbf{s}, \mathbf{w}) \otimes \exp\left[\frac{i}{\hbar} m_0 \left(\mathbf{w} \cdot \mathbf{R} - \frac{\mathbf{P} \cdot \mathbf{s}}{M}\right)\right] = L_j^{\text{rel}}(\mathbf{s}, \mathbf{w}) \otimes W_N^\dagger\left(\frac{m_0}{M}\mathbf{s}, \frac{m_0}{M}\mathbf{w}\right) \quad (4.42)$$

where the factor $L_j^{\text{rel}}(\mathbf{s}, \mathbf{w})$ represents an operator acting solely on the Hilbert space of the relative coordinates of the N -particle system. With this the covariance condition is fulfilled by construction.

The possible choices of the remaining factor correspond to different ways of distributing the phase-space translation of the center of mass over the individual constituents. The simplest way is to divide the translation equally among all constituents, which yields a unitary representation in terms of the N -particle Weyl operator,

$$L^{(U)}(\mathbf{s}, \mathbf{w}) = \sqrt{\frac{M^3}{\tau^{(N)}}} g^{(N)}(\mathbf{s}, M\mathbf{w}) W_N^\dagger(\mathbf{s}, \mathbf{w}). \quad (4.43)$$

It represents a straightforward generalization of the single-particle form (4.30), where I have re-scaled the argument of the Weyl operator accordingly and omitted the j -index. The parameter $\tau^{(N)}$ determines the time scale at which coherence decays in the system, while $g^{(N)}$ denotes a positive and normalized phase-space distribution function. The latter must be isotropic to fix the rotational covariance, as in the single-particle case. However, it will be explained below that this N -particle

⁷ Although plane waves are improper states, i.e. not normalizable, they serve as a helpful idealization in many concrete situations.

form is not suitable to consistently describe a universal classicalizing modification for arbitrary many-particle systems.

Another natural way to effect the above center-of-mass translation is to superimpose individual single-particle translations of all constituents,

$$\mathcal{L}^{(S)}(\mathbf{s}, \mathbf{w}) = \sum_{n=1}^N \ell_n(s, w) \exp \left[\frac{i}{\hbar} \left(m_0 \mathbf{w} \cdot \mathbf{r}_n - \frac{m_0}{m_n} \mathbf{p}_n \cdot \mathbf{s} \right) \right], \quad (4.44)$$

where the weights ℓ_n of the summands must be equal for indistinguishable particles in order to conserve the exchange symmetry of bosons and fermions. Each summand describes the translation of the position and momentum of the n th particle by $-m_0 \mathbf{s}/m_n$ and $-m_0 \mathbf{w}$, which effects a net shift of the center-of-mass coordinates by $-m_0 \mathbf{s}/M$ and $-m_0 \mathbf{w}$. Rotational covariance is again achieved by isotropic coefficient functions⁸ $\ell_n(s, w)$, in analogy to the single-particle case discussed in Section 4.1.3.1. The representation (4.44) treats individual particles independently, and a consistent scaling of the classicalization effect to arbitrary mechanical systems can be achieved, as will be demonstrated below.

In principle, the N -particle Lindblad operators could also be constructed out of phase-space translations of arbitrary subsets of $2, \dots, N-1$ particles, or a linear combination of all these possibilities. Picking one of these possibilities, however, would be an unduly complication of matters without any clear advantages to the natural N -particle form (4.44). In particular, it seems unlikely that a scale invariance property similar to the one explained in Section 4.1.4.4 below would hold in such a case.

Finally there is also the possibility to ascribe independent generators $\mathcal{L}_1^{(n)}(\rho)$ to the individual particles and add them up⁹ to $\mathcal{L}_N(\rho) = \sum_{n=1}^N \mathcal{L}_1^{(n)}(\rho)$ in the N -particle case. Each generator must then be of the single-particle form (4.33). Such an approach was in fact pursued by the authors of the so-called GRW model [153], an earlier version of the continuous spontaneous localization model [155] which falls under the class of classicalizing modifications studied here. This form, however, breaks the fundamental exchange symmetry in systems of indistinguishable quantum particles (as was pointed out in [196] for the GRW case). Separate generators $\mathcal{L}^{(k)}$ could be admissible only for different particle species k , which are inherently distinguishable, but this would lead to a complicated nonuniform scaling behaviour of the classicalizing effect in large systems consisting of various kinds of particles. I have avoided this complication by restricting to a single Lindblad generator to describe the modification in any mechanical system of N particles, that is, I dropped the j -summation in the general form of the generator (4.21).

4.1.4.1. Basic consistency and scaling requirements

The selection of a specific N -particle form of the modification must be based on two other formal requirements besides the Galilean covariance, which guarantee that the modification is universally applicable to any system of mechanical degrees of freedom.

⁸ The coefficient functions could actually share a common phase factor $\exp[i\theta(\mathbf{s}, \mathbf{w})]$ which needs not be isotropic. Such a global phase factor in the Lindblad operator $\mathcal{L}^{(S)}(\mathbf{s}, \mathbf{w})$ may, however, always be omitted without loss of generality.

⁹ This corresponds to the j -summation in the general Galilei-covariant form of the modification (4.21), which is otherwise omitted.

Bystander criterion Firstly, we demand a consistent treatment of single particles, whether they are isolated or constituents in a larger (possibly interacting) system of particles. No additional correlations between individual particles should originate from the N -particle modification. That is to say, the single-particle form (4.33) must always be reobtained from the general N -particle modification (4.21) after tracing over $N - 1$ ‘bystanding’ particles. In particular, the local description of the state of a particle should not be altered by appending the state of an uncorrelated system of particles, which may be completely detached and far away from the particle of interest. This avoids any superluminal action at a distance induced by the modification.

Composition criterion In both quantum and classical mechanics we can describe the time evolution of a compound many-body system by a single center-of-mass degree of freedom if its internal structure does not influence the overall motion. The notion of a ‘single particle’ thus not only applies to elementary building blocks of matter, but may also be used to describe the motion of composite objects. In the same vein, we demand that the single-particle form (4.33) must effectively apply to the center-of-mass description of a compound N -particle object, if the modification does not affect notably the (coherent) internal dynamics of the constituents. This may be applicable (i) if the compound can be regarded as a *point-like particle*, that is, if the constituent particles extend over a small region where the modification shows no ponderable impact¹⁰, or (ii) if the constituent particles of a larger compound are rigidly localized around their equilibrium positions in the body-fixed frame. In both cases we demand that the Lindblad operators (4.42) should (in some approximate sense) reduce to

$$\mathcal{L}(s, w) \approx e^{i\theta(s, w)} \sqrt{\frac{m_0^6}{M^3 \tau_{\text{cm}}}} g_{\text{cm}}\left(\frac{m_0}{M}s, m_0 w\right) W_N^\dagger\left(\frac{m_0}{M}s, \frac{m_0}{M}w\right), \quad (4.45)$$

to obtain the form (4.33) for the center-of-mass degree of freedom, with a time parameter τ_{cm} and distribution function $g_{\text{cm}}(s, q)$ determining the effective strength of the classicalizing effect on the motion of the compound. A complex phase θ_j may appear in the approximation, which drops out again in the corresponding generator.

To achieve the required classicalization on macroscopic scales, the modification should act more strongly on the whole compound than on each constituent individually; there must be an *amplification* of the effect with growing size of the compound object. I will show how this influences the general form of the modification in many-particle systems. Let me denote, in the following, by τ_n and g_n the time parameter and the distribution function of the n th particle in the system.

4.1.4.2. Center-of-mass translations

As already mentioned, the simplest generalization of the modification to arbitrary states ρ of N particles is given by the Weyl operator (4.43),

$$\mathcal{L}_N^{(\text{U})}(\rho) = \frac{1}{\tau^{(N)}} \left[\int d^3s d^3q g^{(N)}(s, q) W_N\left(s, \frac{q}{M}\right) \rho W_N^\dagger\left(s, \frac{q}{M}\right) - \rho \right], \quad (4.46)$$

¹⁰ It was noted in Section 4.1.3.2 that the single-particle modification is characterized by a minimal length scale where it affects superpositions. Smaller-scale coherences are hardly influenced, and the internal dynamics of a sufficiently small compound object should therefore remain unaffected under the same conditions.

with $M = \sum_n m_n$ the total mass. Tracing over all but the n th particle in the system yields the expression

$$\begin{aligned} \text{tr}_{N-1} [\mathcal{L}_N^{(U)}(\rho)] &= \frac{1}{\tau^{(N)}} \left[\int d^3s d^3q g^{(N)}(s, q) W_1\left(s, \frac{q}{M}\right) \rho_n W_1^\dagger\left(s, \frac{q}{M}\right) - \rho_n \right] \\ &= \frac{1}{\tau^{(N)}} \left[\frac{M^3}{m_n^3} \int d^3s d^3q g^{(N)}\left(s, \frac{M}{m_n} q\right) W_1\left(s, \frac{q}{m_n}\right) \rho_n W_1^\dagger\left(s, \frac{q}{m_n}\right) - \rho_n \right] \end{aligned} \quad (4.47)$$

for its reduced state $\rho_n = \text{tr}_{N-1}[\rho]$. We find that for $\tau^{(N)} = \tau_n$ and $g^{(N)}(s, q) = (m_n/M)^3 g_n(s, m_n q/M)$ the bystander criterion is met, that is, the expression equals the single-particle form (4.33) for ρ_n . On the other hand, the composition criterion is met by construction, with $\tau_{\text{cm}} = \tau^{(N)}$ and $g_{\text{cm}} = g^{(N)}$, as (4.46) acts only on the center-of-mass coordinate.

With both criteria taken into account the present form of the modification is not capable of inducing classical behaviour on the macro-scale, while imposing only a negligible disturbance of the dynamics of microscopic quantum systems. This is because the rate of coherence decay induced by the modification does not amplify with the size of a compound system. The time parameter $\tau^{(N)} = \tau_n = \tau$ is the same for all kinds of particles, irrespective of their mass and composition. The only feature that grows with the mass M of the compound is the momentum spread of the phase-space distribution function $g^{(N)}$, which merely increases the range of affected superposition states, as discussed in Section 4.1.3.2. In addition, the time evolution of the relative coordinates within a (possibly large) compound system is not subject to any effect, because the modification only acts on center-of-mass coordinates. No matter how macroscopic the system may be, its internal degrees of freedom could stay in a superposition and would never be classicalized.

4.1.4.3. Single-particle translations

Having discarded the representation in terms of N -particle Weyl operators, let us proceed to describe the N -particle Lindblad operators as the sum of single-particle translations (4.44),

$$\begin{aligned} \mathcal{L}_N^{(S)}(\rho) &= \sum_{k,n=1}^N \int d^3s d^3w \ell_n(s, w) \ell_k^*(s, w) \left[W_1^\dagger\left(\frac{m_0}{m_n} s, \frac{m_0}{m_n} w\right) \rho W_1\left(\frac{m_0}{m_k} s, \frac{m_0}{m_k} w\right) \right. \\ &\quad \left. - \frac{1}{2} \left\{ W_1\left(\frac{m_0}{m_k} s, \frac{m_0}{m_k} w\right) W_1^\dagger\left(\frac{m_0}{m_n} s, \frac{m_0}{m_n} w\right), \rho \right\} \right]. \end{aligned} \quad (4.48)$$

Here and in the following, the single-particle Weyl operators act on the Hilbert space of the particle n that is indicated by the mass variable m_n in their argument. In order to check the bystander criterion we must trace again over all but the n th particle, as denoted by tr_{N-1} , and obtain

$$\text{tr}_{N-1} [\mathcal{L}_N^{(S)}(\rho)] = \int d^3s d^3w |\ell_n(s, w)|^2 \left[W_1^\dagger\left(\frac{m_0}{m_n} s, \frac{m_0}{m_n} w\right) \rho_n W_1\left(\frac{m_0}{m_n} s, \frac{m_0}{m_n} w\right) - \rho_n \right] + \Delta\rho, \quad (4.49)$$

with $\Delta\rho$ given by (4.51). Comparing the first Lindblad term to the single-particle form gives

$$\ell_n(s, w) = e^{i\theta_n(s, m_0 w)} \sqrt{\frac{m_0^6}{m_n^3 \tau_n} g_n\left(\frac{m_0}{m_n} s, m_0 w\right)}, \quad (4.50)$$

with $\theta_n(s, w)$ an arbitrary phase that may be different for each (distinguishable) particle in the system. The bystander criterion is now met if the remaining term,

$$\Delta\rho = i \sum_{k \neq n} \int d^3s d^3w \Im \{ \ell_n(s, w) \ell_k^*(s, w) \} \times \left[W_1^\dagger \left(\frac{m_0}{m_n} s, \frac{m_0}{m_n} w \right), \text{tr}_{N-1} \left(W_1 \left(\frac{m_0}{m_k} s, \frac{m_0}{m_k} w \right) \rho \right) \right], \quad (4.51)$$

vanishes. This is achieved if the phases θ_n are multiples of π , notwithstanding any global phase for all single-particle contributions. Moreover, the phases must be zero for identical particles to conserve their bosonic or fermionic exchange symmetry¹¹.

The composition criterion is also met, as can be seen explicitly by neglecting the relative motion of the constituents in a point-like compound and approximating the coordinates of each particle by $\mathbf{r}_n \approx \mathbf{R}$ and $\mathbf{p}_n \approx m_n \mathbf{P}/M$. This leads to approximate Lindblad operators of the form (4.45), where the modification parameters for the center-of-mass motion are given by

$$\frac{1}{\tau_{\text{cm}}} g_{\text{cm}}(s, q) = \left| \sum_{n=1}^N e^{i\theta_n(Ms/m_0, q)} \sqrt{\frac{M^3}{m_n^3 \tau_n}} g_n \left(\frac{M}{m_n} s, q \right) \right|^2. \quad (4.52)$$

Integrating this expression yields the decay rate $1/\tau_{\text{cm}}$ of center-of-mass coherence,

$$\frac{1}{\tau_{\text{cm}}} = \sum_n \frac{1}{\tau_n} + 2 \sum_{k < n} \int \frac{d^3s d^3q}{\sqrt{\tau_n \tau_k}} \sqrt{\frac{m_0^6}{m_n^3 m_k^3}} g_n \left(\frac{m_0}{m_n} s, q \right) g_k \left(\frac{m_0}{m_k} s, q \right) \underbrace{\cos[\theta_n(s, q) - \theta_k(s, q)]}_{=\pm 1}. \quad (4.53)$$

A clearer view is obtained by introducing the normalized functions

$$f_n(s, q) = \sqrt{\frac{m_0^3}{m_n^3} g_n \left(\frac{m_0}{m_n} s, q \right)} \underbrace{e^{i\theta_n(s, q)}}_{=\pm 1} \quad (4.54)$$

for the square root of the phase-space distributions g_n appearing in (4.50). The particle mass m_n must be replaced by the total mass M in the case of the center-of-mass compound, as represented by f_{cm} . Each function is real and square-integrable, $f_n \in L^2(\mathbb{R}^6)$, with norm $\|f_n\| = \sqrt{(f_n, f_n)} = 1$ by construction. The L^2 -scalar product is defined in the usual way as $(f, g) = \int d^3s d^3q f^*(s, q) g(s, q)$, and the Cauchy-Schwarz inequality implies $-1 \leq (f_k, f_n) \leq 1 \forall k, n$.

Using this notation the composition criterion (4.52) can be expressed as

$$\frac{1}{\sqrt{\tau_{\text{cm}}}} f_{\text{cm}}(s, q) = \sum_{n=1}^N \frac{1}{\sqrt{\tau_n}} f_n(s, q), \quad (4.55)$$

and, in particular,

$$\frac{1}{\tau_{\text{cm}}} = \left\| \sum_{n=1}^N \frac{1}{\sqrt{\tau_n}} f_n \right\|^2 \leq \left| \sum_{n=1}^N \frac{1}{\sqrt{\tau_n}} \right|^2. \quad (4.56)$$

¹¹ Invariance with respect to particle exchange is fulfilled if the Lindblad operators $L^{(s)}(s, w)$ of the modification commute with the exchange of any two out of N identical particles n, m up to a complex phase factor $\exp[i\phi_{nm}(s, w)]$. Since this must generally hold for any $N \geq 2$, all relative phases θ_n between indistinguishable particles in (4.50) must be set to zero. This makes the Lindblad operators exchange-symmetric sums of single-particle operators.

Here it becomes evident how the use of single-particle translations produces the intended amplification of the classicalizing effect with the system size (as opposed to the description in Section 4.1.4.2): The center-of-mass coherence decay rate grows quadratically with the number N of constituents (for a finite number of particle species). Concretely, one obtains $\tau_{\text{cm}} = \tau/N^2$ in the case of N identical particles, with $\tau_n = \tau$.

4.1.4.4. Universality and scale invariance of the modification

Using the single-particle description we are left with the freedom of choosing the time parameters τ_n and the real functions $f_n(s, q)$ of each individual particle species in order to fully specify the general form of the classicalizing modification. Different functions (by e.g. varying their shapes, widths and signs) for different constituents would lead to even another distribution for the compound particle, according to the composition rule (4.55). This compound could then be combined with another species to a different compound, and so on, and each with its own distribution function. Ultimately, one would have to deliberately choose a fixed reference set of elementary point particles, which serve as the building blocks for all matter subject to the classicalization, and assign individual phase-space distribution functions and rate parameters to each of them. Should one decompose the superposition of, say, a C₆₀-fullerene in terms of 60 carbon atoms or in terms of an overall 1080 protons, neutrons and electrons?

We can avoid such questions of preferred choice by once again taking advantage of the composition rule (4.55). It implies that the weighted function $f_n/\sqrt{\tau_n}$ is an extensive property of (point-like) composite systems which increases with each constituent. We thus obtain a universal description, which does not favour a particular decomposition of compound objects into smaller units, by relating the composition rule (4.55) to the mass—the basic extensive property of mechanical objects, which comes naturally with the Galilean covariance condition. That is to say, we can define the weighted root function of *any* point-like particle with mass m_n relative to a fixed reference mass m_0 ,

$$\frac{1}{\sqrt{\tau_n}} f_n(s, q) := \frac{m_n}{m_0} \frac{1}{\sqrt{\tau_0}} f_0(s, q), \quad (4.57)$$

by introducing only a single reference time parameter τ_0 and a single reference function f_0 . The latter boils down (without loss of generality) to a positive, normalized and isotropic reference distribution function $g_0(s, q) = |f_0(s, q)|^2$, according to (4.54). The time parameter and the distribution for each particle species n is then given by

$$\tau_n = \left(\frac{m_0}{m_n}\right)^2 \tau_0, \quad g_n(s, q) = \left(\frac{m_n}{m_0}\right)^3 g_0\left(\frac{m_n}{m_0}s, q\right), \quad (4.58)$$

which holds consistently for point-like compound particles,

$$\tau_{\text{cm}} = \left(\frac{m_0}{M}\right)^2 \tau_0, \quad g_{\text{cm}}(s, q) = \left(\frac{M}{m_0}\right)^3 g_0\left(\frac{M}{m_0}s, q\right), \quad (4.59)$$

as follows from the identities (4.55) and (4.56). The classicalization of point-like particles is thus universally described by the (mass-rescaled) expressions (4.58), which are independent of decom-

posing those particles into smaller mass units¹². The classicalizing effect is obviously amplified for large particles, as the coherence decay time parameter τ_{cm} decreases quadratically with growing mass, according to (4.59). At the same time the distribution function is compressed in the position coordinate, weakening the classicalization-induced position diffusion for heavy objects.

4.1.4.5. General form of the modification

Putting everything together we arrive at a universal and consistent form of the classicalizing modification for arbitrary mechanical systems comprised of N point-like particles,

$$\mathcal{L}_N(\rho) = \frac{1}{\tau_0} \int d^3s d^3q g_0(s, q) \left[A_N(s, q) \rho A_N^\dagger(s, q) - \frac{1}{2} \{A_N^\dagger(s, q) A_N(s, q), \rho\} \right], \quad (4.60)$$

$$A_N(s, q) = \sum_{n=1}^N \frac{m_n}{m_0} \exp \left[\frac{i}{\hbar} \left(\mathbf{p}_n \cdot \frac{m_0}{m_n} \mathbf{s} - \mathbf{q} \cdot \mathbf{r}_n \right) \right] = \sum_{n=1}^N \frac{m_n}{m_0} W_1 \left(\frac{m_0}{m_n} \mathbf{s}, \frac{\mathbf{q}}{m_n} \right). \quad (4.61)$$

It is completely determined by specifying the time parameter τ_0 and the distribution function $g_0(s, q)$ at the reference mass m_0 .

4.1.4.6. Second quantization formulation

The general Lindblad operators (4.61) are sums of single-particle operators. Due to the constant weight for particles of identical mass, they conserve the exchange symmetry of indistinguishable bosons and fermions, that is, quantum particles of the same species j and in the same spin state σ . It follows that we may consistently formulate the modification generator (4.60) in second quantization,

$$\mathcal{L}(\rho) = \frac{1}{\tau_0} \int d^3s d^3q g_0(s, q) \left[A(s, q) \rho A^\dagger(s, q) - \frac{1}{2} \{A^\dagger(s, q) A(s, q), \rho\} \right], \quad (4.62)$$

Here, the Lindblad operators can be expanded in terms of the single-particle creation and annihilation operators in the momentum or position basis,

$$\begin{aligned} A(s, q) &= \sum_{j, \sigma} \int d^3p d^3p' A_{j, \sigma}(s, q; \mathbf{p}, \mathbf{p}') a_{j, \sigma}^\dagger(\mathbf{p}) a_{j, \sigma}(\mathbf{p}') \\ &= \sum_{j, \sigma} \int d^3r d^3r' A_{j, \sigma}(s, q; \mathbf{r}, \mathbf{r}') \psi_{j, \sigma}^\dagger(\mathbf{r}) \psi_{j, \sigma}(\mathbf{r}'), \end{aligned} \quad (4.63)$$

or in any other basis of single-particle wavefunctions over configuration space¹³ [197, 198]. The momentum and the position basis represent the most natural choices; they fulfill the *canonical*

¹² Evidently, I assume that there exist (besides elementary point particles) point-like compound particles whose internal structure remains practically unaffected by the classicalizing effect. This is certainly a weaker prerequisite than establishing a fixed reference set of elementary particles with individual classicalization rates and distribution functions, and it can be justified a posteriori by limiting the strength of the classicalization effect in compliance with experimental observations on the microscopic scale. In practice one should describe electrons, protons, neutrons and nuclei as point particles, or otherwise even femtometer-sized superpositions of elementary particles would be affected. In this case one could keep microscopic systems unaffected only by limiting the classicalization rate of macroscopic systems to unsatisfactorily low values, as was discussed in the case of spontaneous localization models in [160].

¹³ Spins are finite-dimensional degrees of freedom and their basis states are thus labelled by a single running index σ . The classicalizing modification only acts on mechanical degrees of freedom, and the internal dynamics of spin states remains unaffected.

commutation relations (CCR)

$$\begin{aligned} [\mathbf{a}_\sigma(\mathbf{p}), \mathbf{a}_{\sigma'}(\mathbf{p}')]_{\pm} &= [\mathbf{a}_\sigma^\dagger(\mathbf{p}), \mathbf{a}_{\sigma'}^\dagger(\mathbf{p}')]_{\pm} = 0, \quad [\mathbf{a}_\sigma(\mathbf{p}), \mathbf{a}_{\sigma'}^\dagger(\mathbf{p}')]_{\pm} = \delta_{\sigma\sigma'} \delta(\mathbf{p} - \mathbf{p}'), \\ [\hat{\psi}_\sigma(\mathbf{r}), \hat{\psi}_{\sigma'}(\mathbf{r}')]_{\pm} &= [\hat{\psi}_\sigma^\dagger(\mathbf{r}), \hat{\psi}_{\sigma'}^\dagger(\mathbf{r}')]_{\pm} = 0, \quad [\hat{\psi}_\sigma(\mathbf{r}), \hat{\psi}_{\sigma'}^\dagger(\mathbf{r}')]_{\pm} = \delta_{\sigma\sigma'} \delta(\mathbf{r} - \mathbf{r}'), \end{aligned} \quad (4.64)$$

where the anticommutator (+) is used for fermions and the commutator (−) for bosons. Any (spin-independent) single-particle operator is readily translated into second quantization by first expanding it, say, in the momentum representation and then mapping $|\mathbf{p}'\rangle\langle\mathbf{p}| \mapsto \sum_\sigma \mathbf{a}_\sigma^\dagger(\mathbf{p}') \mathbf{a}_\sigma(\mathbf{p})$. The Lindblad operators (4.61) of the modification then become

$$\begin{aligned} \mathbf{A}(\mathbf{s}, \mathbf{q}) &= \sum_j \frac{m_j}{m_0} \int d^3 p \, e^{i\mathbf{p} \cdot \mathbf{m}_0 \mathbf{s} / m_j \hbar} \sum_\sigma \mathbf{a}_{j,\sigma}^\dagger(\mathbf{p} - \mathbf{q}) \mathbf{a}_{j,\sigma}(\mathbf{p}) \\ &= \sum_j \frac{m_j}{m_0} \int d^3 r \, e^{-i\mathbf{q} \cdot \mathbf{r} / \hbar} \sum_\sigma \hat{\psi}_{j,\sigma}^\dagger\left(\mathbf{r} - \frac{m_0}{m_j} \mathbf{s}\right) \hat{\psi}_{j,\sigma}(\mathbf{r}), \end{aligned} \quad (4.65)$$

up to an irrelevant complex phase factor. The second line follows from the first with help of the basis transformation rule

$$\hat{\psi}(\mathbf{r}) = \int \frac{d^3 p}{(2\pi\hbar)^{3/2}} \mathbf{a}(\mathbf{p}) e^{i\mathbf{p} \cdot \mathbf{r} / \hbar} \quad \leftrightarrow \quad \mathbf{a}(\mathbf{p}) = \int \frac{d^3 r}{(2\pi\hbar)^{3/2}} \hat{\psi}(\mathbf{r}) e^{-i\mathbf{p} \cdot \mathbf{r} / \hbar}. \quad (4.66)$$

In the case of one particle species of mass m the modification reads as

$$\begin{aligned} \mathcal{L}(\rho) &= \frac{1}{\tau} \int d^3 s d^3 q \, g(\mathbf{s}, \mathbf{q}) \left[\mathbf{A}(\mathbf{s}, \mathbf{q}) \rho \mathbf{A}^\dagger(\mathbf{s}, \mathbf{q}) - \frac{1}{2} \{ \mathbf{A}^\dagger(\mathbf{s}, \mathbf{q}) \mathbf{A}(\mathbf{s}, \mathbf{q}), \rho \} \right], \\ \mathbf{A}(\mathbf{s}, \mathbf{q}) &= \int d^3 p \, e^{i\mathbf{p} \cdot \mathbf{s} / \hbar} \sum_\sigma \mathbf{a}_\sigma^\dagger(\mathbf{p} - \mathbf{q}) \mathbf{a}_\sigma(\mathbf{p}), \\ g(\mathbf{s}, \mathbf{q}) &= \left(\frac{m}{m_0} \right)^3 g_0\left(\frac{m}{m_0} \mathbf{s}, \mathbf{q} \right), \quad \tau = \left(\frac{m_0}{m} \right)^2 \tau_0. \end{aligned} \quad (4.67)$$

The effect of the modification (4.62) on single-particle expectation values of the form $\langle \hat{\psi}_\sigma^\dagger(\mathbf{r}') \hat{\psi}_\sigma(\mathbf{r}) \rangle$, or arbitrary linear combinations of this, is the same as for the corresponding matrix elements of the single-particle density operator, as discussed in Section 4.1.3.2.

Formulation with discretized momenta So far this chapter has covered the motion of particles in free space, with a continuum of positions and momenta. When the motion is confined to a finite volume V , as is the case for electrons in a crystal lattice, we must work instead with discrete momenta and a discretized formulation of the modification.

A box geometry of the dimension $V = L_x L_y L_z$ yields discrete momenta in steps of $\Delta p_j = 2\pi\hbar/L_j$, $j \in \{x, y, z\}$, each of which occupies a momentum cell of volume $V_c = (2\pi\hbar)^3/V$. Following the convention to express momenta in terms of wave vectors $\mathbf{k} = \mathbf{p}/\hbar$, let us introduce the discrete momentum annihilation operators

$$\mathbf{c}_\sigma(\mathbf{k}) = \int_V \frac{d^3 r}{\sqrt{V}} \hat{\psi}_\sigma(\mathbf{r}) e^{-i\mathbf{k} \cdot \mathbf{r}} \quad \leftrightarrow \quad \hat{\psi}_\sigma(\mathbf{r}) = \frac{1}{\sqrt{V}} \sum_{\mathbf{k}} \mathbf{c}_\sigma(\mathbf{k}) e^{i\mathbf{k} \cdot \mathbf{r}}, \quad (4.68)$$

which fulfill the CCR $[\mathbf{c}_\sigma(\mathbf{k}), \mathbf{c}_{\sigma'}^\dagger(\mathbf{k}')]_{\pm} = \delta_{\sigma\sigma'}\delta_{\mathbf{k}\mathbf{k}'}$. The summation extends over wave vectors of the form $k_j = 2\pi n/L_j$, $n \in \mathbb{Z}$. By integrating the phase-space distribution $g(s, q)$ for identical particles in (4.67) over the occupied momentum cell around each \mathbf{k} we obtain the discretized distribution function

$$G(s, \mathbf{k}) = \int_{-\pi\hbar/L_x}^{\pi\hbar/L_x} dq_x \int_{-\pi\hbar/L_y}^{\pi\hbar/L_y} dq_y \int_{-\pi\hbar/L_z}^{\pi\hbar/L_z} dq_z g(s, |\hbar\mathbf{k} - \mathbf{q}|) = \int_{V_c} d^3q g(s, |\hbar\mathbf{k} - \mathbf{q}|). \quad (4.69)$$

It simplifies in two limiting cases: (i) if the elementary cell volume V_c is so large that it covers the support of g in the momentum coordinate we have $G(s, \mathbf{k}) \approx \delta_{\mathbf{k},0} \int d^3q g(s, q)$, and (ii) if the volume V_c is so small that g is approximately constant there then $G(s, \mathbf{k}) \approx V_c g(s, \hbar\mathbf{k})$.

In the generic case that the volume V is much larger than the support of the discretized distribution in the s -coordinate, the latter is normalized to

$$\int_V d^3s \sum_{\mathbf{k}} G(s, \mathbf{k}) \approx \int d^3s \sum_{\mathbf{k}} G(s, \mathbf{k}) = 1. \quad (4.70)$$

The discretized modification then reads as

$$\begin{aligned} \mathcal{L}(\rho) &= \frac{1}{\tau} \int_V d^3s \sum_{\mathbf{k}} G(s, \mathbf{k}) \left[\mathbf{A}(s, \mathbf{k}) \rho \mathbf{A}^\dagger(s, \mathbf{k}) - \frac{1}{2} \{ \mathbf{A}^\dagger(s, \mathbf{k}) \mathbf{A}(s, \mathbf{k}), \rho \} \right], \\ \mathbf{A}(s, \mathbf{k}) &= \sum_{\sigma, \ell} e^{i\ell \cdot s} \mathbf{c}_\sigma^\dagger(\ell - \mathbf{k}) \mathbf{c}_\sigma(\ell). \end{aligned} \quad (4.71)$$

In the limit of truly macroscopic volumes V , a *continuum approximation* may be applied after carrying out calculations in the discretized picture in order to evaluate the resulting expressions numerically. It consists of replacing sums over momentum-dependent terms by integrals,

$$\sum_{\mathbf{k}} f(\mathbf{k}) \longrightarrow \frac{V}{(2\pi)^3} \int d^3k f(\mathbf{k}) = \frac{1}{V_c} \int d^3p f\left(\frac{\mathbf{p}}{\hbar}\right). \quad (4.72)$$

This is a valid approximation, for instance, in large crystals where the dimensions are orders of magnitude larger than the lattice constants. It turns the discretized modification (4.71) into the original one.

4.1.5. Center-of-mass motion of rigid compounds

With the general N -particle modification (4.60) at hand, one can compute the classicalizing effect on large compound systems, and see how it amplifies with growing system size. While this can be a hard task when studying the full N -body problem, the effective description of the classicalizing effect on the collective motion of the compound turns out to be manageable. Many tests of the quantum superposition principle with mechanical systems are in fact done by interfering compound objects (atoms, nanoparticles, micromirrors) in their center-of-mass coordinates, as will be discussed below.

It was shown in the previous section 4.1.4.4 how the composition property leads to an effective single-particle treatment of the center-of-mass motion of point-like compound objects, where the joint contribution of all constituents collectively enhances the classicalization of the center of mass.

This is related to the fact that a superposition state in the center-of-mass coordinate of the compound should in fact be viewed as an entangled state, where the N constituent particles are either *all* here or *all* there; even if only a single one of them gets localized due to classicalization the whole superposition state reduces to a classical mixture. In the following, this argument will be generalized to spatially extended compounds of rigidly bound particles, provided that the constituents are confined around their fixed equilibrium positions and that the center-of-mass motion decouples from their relative motion.

On the other hand, we expect a different behaviour of the classicalizing effect in a system of N noninteracting particles, which need not be correlated and may even be located far away from each other. They are subject to individual classicalizing modifications, in accordance with the bystander property of Section 4.1.4.1. Therefore it is in general not possible to describe the center-of-mass coordinate as a single rigid particle.

4.1.5.1. Case study: The two-particle modification

The different behaviour of compound and non-interacting systems of particles can be illustrated instructively for the case of two particles of equal mass m , which for simplicity shall be given by the reference mass, $m = m_0$. Rewriting the two position and momentum operators $\mathbf{r}_{1,2}$ and $\mathbf{p}_{1,2}$ in terms of the center-of-mass and relative coordinates, $\mathbf{r}_{1,2} = \mathbf{R} \pm \mathbf{r}/2$ and $\mathbf{p}_{1,2} = \mathbf{P}/2 \pm \mathbf{p}$, we find that the Lindblad operators (4.61) of the modification factorize as

$$\begin{aligned} A_2(s, q) &= \exp\left[\frac{i}{\hbar}\left(\frac{\mathbf{P} \cdot \mathbf{s}}{2} - \mathbf{q} \cdot \mathbf{R}\right)\right] \otimes \left(\exp\left[\frac{i}{\hbar}\left(\mathbf{p} \cdot \mathbf{s} - \frac{\mathbf{q} \cdot \mathbf{r}}{2}\right)\right] + h.c.\right) \\ &= 2 \exp\left[\frac{i}{\hbar}\left(\frac{\mathbf{P} \cdot \mathbf{s}}{2} - \mathbf{q} \cdot \mathbf{R}\right)\right] \otimes \cos\left(\frac{\mathbf{p} \cdot \mathbf{s}}{\hbar} - \frac{\mathbf{q} \cdot \mathbf{r}}{2\hbar}\right). \end{aligned} \quad (4.73)$$

We trace over the relative coordinates in the two-particle modification (4.60) to obtain the reduced center-of-mass form

$$\begin{aligned} \text{tr}_{\text{rel}}[\mathcal{L}_2(\rho)] &= \frac{4}{\tau_0} \int d^3s d^3q g_0(s, q) \left(\exp\left[\frac{i}{\hbar}\left(\frac{\mathbf{P} \cdot \mathbf{s}}{2} - \mathbf{q} \cdot \mathbf{R}\right)\right] \text{tr}_{\text{rel}}\left[\cos^2\left(\frac{\mathbf{p} \cdot \mathbf{s}}{\hbar} - \frac{\mathbf{q} \cdot \mathbf{r}}{2\hbar}\right)\rho\right] \right. \\ &\quad \left. \times \exp\left[-\frac{i}{\hbar}\left(\frac{\mathbf{P} \cdot \mathbf{s}}{2} - \mathbf{q} \cdot \mathbf{R}\right)\right] - \text{tr}_{\text{rel}}\left[\cos^2\left(\frac{\mathbf{p} \cdot \mathbf{s}}{\hbar} - \frac{\mathbf{q} \cdot \mathbf{r}}{2\hbar}\right)\rho\right] \right). \end{aligned} \quad (4.74)$$

This form resembles the generator \mathcal{L}_1 of the single-particle modification for a particle of total mass $2m_0$, but it does not act directly on the reduced center-of-mass state $\rho_{\text{cm}} = \text{tr}_{\text{rel}}(\rho)$. Instead, the state of relative motion influences the center-of-mass classicalization by modulating the effective distribution of phase-space translations imposed on the center of mass. This can be made explicit in the case of a product state $\rho = \rho_{\text{cm}} \otimes \rho_{\text{rel}}$, where the reduced center-of-mass generator,

$$\begin{aligned} \text{tr}_{\text{rel}}[\mathcal{L}_2(\rho)] &= \frac{4}{\tau_0} \int d^3s d^3q g_0(s, q) \left\langle \cos^2\left(\frac{\mathbf{p} \cdot \mathbf{s}}{\hbar} - \frac{\mathbf{q} \cdot \mathbf{r}}{2\hbar}\right) \right\rangle_{\text{rel}} \\ &\quad \times \left(\exp\left[\frac{i}{\hbar}\left(\frac{\mathbf{P} \cdot \mathbf{s}}{2} - \mathbf{q} \cdot \mathbf{R}\right)\right] \rho_{\text{cm}} \exp\left[-\frac{i}{\hbar}\left(\frac{\mathbf{P} \cdot \mathbf{s}}{2} - \mathbf{q} \cdot \mathbf{R}\right)\right] - \rho_{\text{cm}} \right), \end{aligned} \quad (4.75)$$

is actually equivalent to the single-particle form (4.33), but with an effective time parameter and distribution function¹⁴

$$\frac{1}{\tau_{\text{cm}}} = \frac{4}{\tau_0} \int d^3s d^3q g_0(s, q) \left\langle \cos^2 \left(\frac{\mathbf{p} \cdot \mathbf{s}}{\hbar} - \frac{\mathbf{q} \cdot \mathbf{r}}{2\hbar} \right) \right\rangle_{\text{rel}}, \quad (4.76)$$

$$g_{\text{cm}}(\mathbf{s}, \mathbf{q}) = \frac{4\tau_{\text{cm}}}{\tau_0} 8g_0(2s, q) \left\langle \cos^2 \left(\frac{2\mathbf{p} \cdot \mathbf{s}}{\hbar} - \frac{\mathbf{q} \cdot \mathbf{r}}{2\hbar} \right) \right\rangle_{\text{rel}}, \quad (4.77)$$

which both depend on the state of relative motion ρ_{rel} . We distinguish three limiting cases:

★ **Point-like compound** The two particles are closely bound in a point-like configuration, such that

$$\left\langle \cos^2 \left(\frac{\mathbf{p} \cdot \mathbf{s}}{\hbar} - \frac{\mathbf{q} \cdot \mathbf{r}}{2\hbar} \right) \right\rangle_{\text{rel}} \approx 1 \quad (4.78)$$

for all \mathbf{s}, \mathbf{q} where the distribution function $g_0(s, q)$ differs (noticeably) from zero. If we characterize this region in phase space by the standard deviations σ_s and σ_q of g_0 , then the point-like configuration is attained once the variance in relative position and momentum is confined by $\Delta r = \sqrt{\langle \mathbf{r}^2 \rangle - \langle \mathbf{r} \rangle^2} \ll \hbar/\sigma_q$ and $\Delta p \ll \hbar/\sigma_s$, respectively. In practice, this would be realized by, say, a diatomic molecule much smaller in size than \hbar/σ_q . In this case the center of mass can be treated like a point particle of total mass $M = 2m_0$, as already discussed in Section 4.1.4.4. The classicalization rate $1/\tau_{\text{cm}} \approx 4/\tau_0$ is quadratically enhanced by the mass since the contributions of both particles are added ‘in phase’.

★ **Rigid dumbbell** The above case can be generalized to a dumbbell-shaped configuration, where the two particles are rigidly bound at a relative position $\bar{\mathbf{r}} = \langle \mathbf{r} \rangle$ like two weights fixed to the ends of a rod,

$$\left\langle \cos^2 \left(\frac{\mathbf{p} \cdot \mathbf{s}}{\hbar} - \frac{\mathbf{q} \cdot \mathbf{r}}{2\hbar} \right) \right\rangle_{\text{rel}} \approx \cos^2 \left(\frac{\mathbf{q} \cdot \bar{\mathbf{r}}}{2\hbar} \right) = \frac{1}{2} + \frac{1}{2} \cos \left(\frac{\mathbf{q} \cdot \bar{\mathbf{r}}}{\hbar} \right). \quad (4.79)$$

The fluctuations of the relative coordinate around $\bar{\mathbf{r}}$ are neglected for all relevant \mathbf{s}, \mathbf{q} in this case. Once again, this implies $\Delta r \ll \hbar/\sigma_q$ and $\Delta p \ll \hbar/\sigma_s$, whereas the fixed equilibrium distance \bar{r} can be arbitrarily large, in principle. One could think of two atoms bound in a stiff crystal lattice at a distance $\sim \hbar/\sigma_q$, for instance. The center of mass classicalizes like a single $2m_0$ -particle at a reduced rate, $1/\tau_{\text{cm}} \approx 2(1 + \tilde{g}_0(\bar{r}, 0))/\tau_0$, with \tilde{g}_0 the Fourier transform of the distribution g_0 (which is real-valued and ≤ 1). It vanishes for large distances \bar{r} in the case of reasonably smooth distribution functions g_0 .

★ **Unbound system** If the particles are moving independently and far apart from each other such that their motional state covers a broad distribution with large values of the relative coordinates, we may approximate

$$\left\langle \cos^2 \left(\frac{\mathbf{p} \cdot \mathbf{s}}{\hbar} - \frac{\mathbf{q} \cdot \mathbf{r}}{2\hbar} \right) \right\rangle_{\text{rel}} \approx \frac{1}{2} \quad (4.80)$$

¹⁴ Note that the modulated distribution function in (4.75) is not normalized; a renormalization to unity leads to an effective center-of-mass time parameter $1/\tau_{\text{cm}} < 4/\tau_0$. Note also that we have to substitute the integration variable \mathbf{s} by $\mathbf{s}/2$ to arrive at the single-particle form (4.33).

almost everywhere¹⁵. The center of mass then classicalizes at double the rate of each particle, $1/\tau_{\text{cm}} \approx 2/\tau_0$; a value one arrives at by treating the two particles independently and adding up their separate single-particle modifications \mathcal{L}_1 . This conforms to the general rule of treating uncorrelated states of separated systems individually.

4.1.5.2. Rigid compounds of many particles

The rigid dumbbell configuration of two particles can be readily generalized to a rigid configuration of N constituents in extended molecules, clusters or solids, for example. To this end, one expands the single-particle position and momentum operators in terms of the center-of-mass operators $\mathbf{R} = \sum_n m_n \mathbf{r}_n / M$ and $\mathbf{P} = \sum_n \mathbf{p}_n$, and the set of $N - 1$ relative coordinates,

$$\mathbf{r}_n = \mathbf{R} + \sum_{j=1}^{N-1} c_{nj} \tilde{\mathbf{r}}_j, \quad \mathbf{p}_n = \frac{m_n}{M} \mathbf{P} + \sum_{j=1}^{N-1} d_{nj} \tilde{\mathbf{p}}_j. \quad (4.81)$$

The position expectation values of the N constituent particles in the body-fixed frame are denoted by $\bar{\mathbf{r}}_n = \left\langle \sum_{j=1}^{N-1} c_{nj} \tilde{\mathbf{r}}_j \right\rangle$, defined over the Hilbert space of the $N - 1$ relative coordinates¹⁶.

A rigid configuration is given if the deviations of the relative coordinates from the mean equilibrium configuration of the N -particle compound are negligible within the range of the classicalizing modification (4.60), as set by the standard deviations $\sigma_{s,q}$ of the reference distribution g_0 . (Such deviations include vibrations of the constituents around their (stable) equilibria as well as rotations of the whole object.) In concrete terms, the variances of the N body-fixed positions and momenta must be small compared to \hbar/σ_q and \hbar/σ_s , respectively, in order to justify the approximation $\mathbf{r}_n \approx \mathbf{R} + \bar{\mathbf{r}}_n$ and $\mathbf{p}_n \approx m_n \mathbf{P} / M$. The Lindblad operators (4.61) of the modification then reduce to

$$A_N(\mathbf{s}, \mathbf{q}) \approx \sum_n \frac{m_n}{m_0} \exp \left[\frac{i}{\hbar} \left(\mathbf{P} \cdot \frac{m_0}{M} \mathbf{s} - \mathbf{q} \cdot (\mathbf{R} + \bar{\mathbf{r}}_n) \right) \right] = \frac{\tilde{\varrho}(\mathbf{q})}{m_0} \exp \left[\frac{i}{\hbar} \left(\mathbf{P} \cdot \frac{m_0}{M} \mathbf{s} - \mathbf{q} \cdot \mathbf{R} \right) \right]. \quad (4.82)$$

The term

$$\tilde{\varrho}(\mathbf{q}) = \sum_n m_n e^{-i\mathbf{q} \cdot \bar{\mathbf{r}}_n / \hbar} = \int d^3 r \varrho(\mathbf{r}) e^{-i\mathbf{q} \cdot \mathbf{r} / \hbar} \quad (4.83)$$

represents the Fourier transform of the *local mass density* of the compound in the body-fixed frame¹⁷,

$$\varrho(\mathbf{r}) = \sum_n m_n \delta(\mathbf{r} - \bar{\mathbf{r}}_n), \quad \int d^3 r \varrho(\mathbf{r}) = \tilde{\varrho}(0) = M. \quad (4.84)$$

The density can be replaced by a constant average value in the case of homogeneous solids, provided that the microscopic structure of the crystal lattice is not affected by the classicalization. The contribution of free electrons in the solid can safely be neglected due to their much smaller mass.

With the approximate Lindblad operators (4.82) we find that the center of mass classicalizes like a single particle, as given by equation (4.33), with an effective mass

$$m_{\text{eff}} = \sqrt{\int d^3 s d^3 q |\tilde{\varrho}(\mathbf{q})|^2 g_0(\mathbf{s}, \mathbf{q})} \leq M. \quad (4.85)$$

¹⁵ The approximation ceases to be valid sufficiently close to the origin $\mathbf{s} = \mathbf{q} = 0$, but we neglect this contribution to the integral over the phase space distribution $g_0(\mathbf{s}, \mathbf{q})$.

¹⁶ The N vectors $\bar{\mathbf{r}}_n$ are linearly dependent. They sum up to $\sum_n m_n \bar{\mathbf{r}}_n = 0$.

¹⁷ This resembles the continuum approximation in [155, 157] for the specific case of spontaneous collapse models.

It determines the scaling of the effective single-particle time parameter and distribution function for the center-of-mass motion,

$$\tau_{\text{eff}} = \left(\frac{m_0}{m_{\text{eff}}} \right)^2 \tau_0, \quad g_{\text{eff}}(s, \mathbf{q}) = \left(\frac{M}{m_0} \right)^3 g_0 \left(\frac{M}{m_0} s, \mathbf{q} \right) \frac{|\tilde{\varrho}(\mathbf{q})|^2}{m_{\text{eff}}^2}. \quad (4.86)$$

Note that the effective distribution function is not isotropic in \mathbf{q} anymore if the shape of the compound is anisotropic, but the inversion symmetry $\mathbf{q} \mapsto -\mathbf{q}$ still holds. The effective mass is smaller than the total mass M , and for fixed M it decreases with growing size of the compound. It reaches its maximum, $m_{\text{eff}} \approx M$, in the limit of a point-like compound, as discussed above. We can generally distinguish two limiting cases by looking at the expressions (4.85) and (4.86):

- ★ **Point-like compound** If the mass density $\varrho(\mathbf{r})$ is sufficiently localized around the origin $\mathbf{r} = 0$, such that $\tilde{\varrho}(\mathbf{q}) \approx \tilde{\varrho}(0) = M$ holds for all momenta \mathbf{q} covered by the distribution function g_0 , the effective mass (4.85) becomes $m_{\text{eff}} \approx M$. The compound can then be treated as a point particle of total mass M , since its internal structure is practically not affected by the classicalization. This is exactly true for $\varrho(\mathbf{r}) = M\delta(\mathbf{r})$.
- ★ **Large rigid body** In the limit of large and dense compounds (e.g. macroscopic pieces of solid matter) the Fourier transform of the density $\tilde{\varrho}(\mathbf{q})$ is narrowly peaked around $\mathbf{q} = 0$. Once the peak width is smaller than the standard deviation σ_q , one may set

$$m_{\text{eff}} \approx \sqrt{\int d^3q |\tilde{\varrho}(\mathbf{q})|^2 \int d^3s g_0(s, 0)}, \quad (4.87)$$

$$g_{\text{eff}}(s, \mathbf{q}) \approx \frac{m_{\text{eff}}}{m_0^3} g_0 \left(\frac{m_{\text{eff}}}{m_0} s, 0 \right) |\tilde{\varrho}(\mathbf{q})|^2. \quad (4.88)$$

The momentum dependence of the effective phase-space distribution function is then mainly determined by the mass density and geometrical shape of the compound.

4.2. Observable consequences of the modification

Having derived the specific form of the classicalizing modification let me now analyze its effect in concrete physical situations where superposition states of mechanical systems are observed. I study in the following the destructive influence of the modification on single-particle interference, including the accompanying diffusion effect, as well as on superposition states of condensed quantum gases.

4.2.1. Effects of the single-particle classicalization

Many interference experiments can be described by the state ρ of a single mechanical degree of freedom of mass m , which evolves under the influence of a Hamiltonian H . The modified time evolution is of the form

$$\partial_t \rho = -\frac{i}{\hbar} [H, \rho] + \frac{1}{\tau} \left[\int d^3s d^3q g(s, \mathbf{q}) e^{i(\mathbf{p} \cdot \mathbf{s} - \mathbf{q} \cdot \mathbf{r})/\hbar} \rho e^{-i(\mathbf{p} \cdot \mathbf{s} - \mathbf{q} \cdot \mathbf{r})/\hbar} - \rho \right]. \quad (4.89)$$

The terms τ and g are given by the expressions (4.58) in the case of a point particle, or by (4.86) in the case of a rigid compound. It was already discussed in Section 4.1.3.2 that the modification induces a decay of coherences in both the position and the momentum representation of the state.

This alone, however, does not yet guarantee the emergence of classical behaviour. It should be granted additionally that the particle moves according to the classical equations of motion of the system governed by the classical Hamilton function $H(\mathbf{r}, \mathbf{p}) = \mathbf{p}^2/2m + V(\mathbf{r})$ corresponding to H . To this end, we must confirm the validity of Ehrenfest's theorem [199] under the influence of the modification, because it predicts that the centers of well-localized wave packets basically move on classical trajectories in phase space. This is due to the quasi-classical time evolution equations for the expectation values of the position and momentum operators. They are indeed unaffected by the modification,

$$\partial_t \langle \mathbf{r} \rangle = \frac{\langle \mathbf{p} \rangle}{m} + \frac{1}{\tau} \mathcal{E}[\mathbf{s}] = \frac{\langle \mathbf{p} \rangle}{m}, \quad (4.90)$$

$$\partial_t \langle \mathbf{p} \rangle = -\langle \nabla V(\mathbf{r}) \rangle + \frac{1}{\tau} \mathcal{E}[\mathbf{q}] = -\nabla \langle V(\mathbf{r}) \rangle, \quad (4.91)$$

since the first moments $\mathcal{E}[\mathbf{s}]$ and $\mathcal{E}[\mathbf{q}]$ of the distribution function g vanish due to its inversion symmetry. Here, I denote expectation values with respect to g by

$$\mathcal{E}[f(\mathbf{s}, \mathbf{q})] = \int d^3s d^3q g(\mathbf{s}, \mathbf{q}) f(\mathbf{s}, \mathbf{q}). \quad (4.92)$$

4.2.1.1. Diffusion and energy increase

Whereas the time evolution equations for the expectation values of position and momentum are unaffected by the modification, this does not hold for higher-order expectation values. In particular, the position and momentum variances of the particle are influenced, as the second moments $\mathcal{E}[q^2]$ and $\mathcal{E}[s^2]$ are generally positive (whereas $\mathcal{E}[\mathbf{q} \cdot \mathbf{s}] = 0$). This leads to position and momentum diffusion, as described by

$$\partial_t \langle \mathbf{r}^2 \rangle = \frac{1}{m} \langle \mathbf{p} \cdot \mathbf{r} + \mathbf{r} \cdot \mathbf{p} \rangle + \frac{1}{\tau} \mathcal{E}[s^2], \quad (4.93)$$

$$\partial_t \langle \mathbf{p} \cdot \mathbf{r} \rangle = \frac{1}{m} \langle \mathbf{p}^2 \rangle - \langle \mathbf{r} \cdot \nabla V(\mathbf{r}) \rangle = \partial_t \langle \mathbf{r} \cdot \mathbf{p} \rangle, \quad (4.94)$$

$$\partial_t \langle \mathbf{p}^2 \rangle = -\langle \mathbf{p} \cdot \nabla V(\mathbf{r}) + \nabla V(\mathbf{r}) \cdot \mathbf{p} \rangle + \frac{1}{\tau} \mathcal{E}[q^2]. \quad (4.95)$$

These equations, together with (4.90) and (4.91), are an explicitly solvable closed set of equations in the case of free propagation ($V = 0$), constant acceleration ($V \propto \mathbf{r}$), or harmonic oscillation ($V \propto \mathbf{r}^2$).

As an important consequence, the modification induces an increase of the particle's energy over time at an average rate given (for time-independent Hamiltonians) by

$$\partial_t \langle H \rangle = \frac{1}{2m\tau} \mathcal{E}[q^2] + \frac{1}{\tau} \langle \mathcal{E}[V(\mathbf{r} + \mathbf{s}) - V(\mathbf{r})] \rangle \approx \frac{1}{2m\tau} \mathcal{E}[q^2] + \frac{1}{2\tau} \mathcal{E}[s^2] \langle \nabla \cdot \nabla V(\mathbf{r}) \rangle. \quad (4.96)$$

On the right the potential is Taylor-expanded up to second order, using the fact that the isotropy of the distribution g in \mathbf{s} yields the relation $\mathcal{E}[s_j s_k] = \mathcal{E}[s^2] \delta_{jk}/3$. In the case of free motion or constant acceleration the particle heats solely by the rate $\mathcal{E}[q^2]/2m\tau$. A particle that is harmonically

bound with trapping frequencies $\omega_{x,y,z}$ experiences a mean heating rate of

$$\partial_t \langle H \rangle = \frac{1}{2m\tau} \mathcal{E}[q^2] + \frac{m(\omega_x^2 + \omega_y^2 + \omega_z^2)}{2\tau} \mathcal{E}[s^2], \quad (4.97)$$

which constitutes a measureable side effect of the classicalization. Considering that no significant heating effects of this kind have been observed in experiments on quantum systems so far, this introduces empirical upper bounds for the rate $1/\tau$ and for the second moments of the distribution function¹⁸. The classicalization-induced heating, however, does not depend on how nonclassical a given system state is. Classically mixed states are affected in the same way as genuine quantum superposition states.

In the case of a point-like particle we can express the heating rate in terms of the reference time parameter, $\tau = (m_0/m)^2 \tau_0$, and in terms of the standard deviations σ_s and σ_q of the reference distribution function $g_0(s, q)$, by noting that $\mathcal{E}[s^2] = (m_0/m)^2 \sigma_s^2$ and $\mathcal{E}[q^2] = \sigma_q^2$, as follows from equation (4.58). We arrive at a heating rate expression proportional to the mass, $\partial_t \langle H \rangle = (m/m_0) [\sigma_q^2/2m_0\tau_0 + m_0\sigma_s^2(\omega_x^2 + \omega_y^2 + \omega_z^2)/2\tau_0]$. Similarly, the average increase of internal energy U for an ideal gas of particles without internal degrees of freedom increases with growing particle number M/m , $\partial_t U = M\sigma_q^2/2m_0^2\tau_0$, where M denotes the total mass of the gas.

4.2.1.2. Discussion of the coherence decay effect

I have already discussed in Section 4.1.3.2 how the classicalizing modification leads to a decay of coherences in both position and momentum representation. The effect is most easily evaluated in the characteristic function representation (4.37) of the single-particle state, where the modification reads as $\mathcal{L}_1[\chi(\mathbf{r}, \mathbf{p})] = [\tilde{g}(\mathbf{r}, \mathbf{p}) - 1] \chi(\mathbf{r}, \mathbf{p})/\tau$, as given by (4.39). The Fourier transform \tilde{g} of the distribution function g is defined in Equation (4.40). Since g is a positive and normalized distribution function with finite moments, its Fourier transform \tilde{g} can also be regarded a well-behaved function that is bounded by $|\tilde{g}(\mathbf{r}, \mathbf{p})| \leq \tilde{g}(0, 0) = 1$ and that decays sufficiently fast for large arguments (\mathbf{r}, \mathbf{p}) . The values of the characteristic function at different positions \mathbf{r} or momenta \mathbf{p} reflect the off-diagonal elements of the density operator in position or momentum representation, as seen from the expressions

$$\chi(\mathbf{r}, 0) = \int d^3 r_0 \langle \mathbf{r}_0 - \frac{\mathbf{r}}{2} | \rho | \mathbf{r}_0 + \frac{\mathbf{r}}{2} \rangle, \quad (4.98)$$

$$\chi(0, \mathbf{p}) = \int d^3 p_0 \langle \mathbf{p}_0 - \frac{\mathbf{p}}{2} | \rho | \mathbf{p}_0 + \frac{\mathbf{p}}{2} \rangle, \quad (4.99)$$

for the accumulated off-diagonals.

Disregarding the coherent evolution of the quantum state, the modification \mathcal{L}_1 describes a continuous decay of the characteristic function almost everywhere, with the exception of small arguments (\mathbf{r}, \mathbf{p}) close to the origin where $\tilde{g}(\mathbf{r}, \mathbf{p}) \approx 1$. That is to say, after waiting a sufficiently long time the

¹⁸ Note that, in particular, the classicalizing modification can only make physical sense if the distribution $g(s, q)$ is a well-behaved function with finite moments.

characteristic function is basically reduced to a narrow peak around its fixed value $\chi(0, 0) = 1$ at the origin—a state resembling a hot classical mixture¹⁹.

Moreover, the rate at which coherences decay is limited by the time scale τ , the latter being determined by the reference time parameter τ_0 . Even superposition states of arbitrarily distant positions and momenta will maintain coherence for a time scale of τ , if they are only subject to the classicalization. Generally speaking, *the coherence time of a mechanical object of mass m evolving under the influence of the classicalizing modification must be at least $(m_0/m)^2 \tau_0$* , given a fixed time parameter τ_0 at the reference mass m_0 . This statement is not restricted to point particles; it holds for arbitrary compound systems of total mass m where the center-of-mass classicalization depends more weakly on m , as was shown in Section 4.1.5.

Putting everything together, we conclude that the main observable consequence of the modification is the *classicalization* of the motion of particles in the sense originally introduced in the beginning of this Chapter: On the one hand, it predicts the described gradual decay of quantum coherence over time. On the other hand, it leaves the Ehrenfest equations for position and momentum unaffected, (4.90) and (4.91). Both aspects indicate the emergence of classical behaviour in mechanical systems over time. This is supported by the fact that the single-particle modification can be viewed as a generalization of the well-studied class of collisional decoherence master equations with velocity-independent scattering amplitudes [194, 195], for which $\sigma_s = 0$. This class is known to have solitonic pointer states as stable solutions in the long-time limit, which move on classical trajectories [200].

The classicalization effect may happen almost instantaneously at the macro-scale and, at the same time, be practically negligible if only a few elementary masses are involved, depending on the choice of time parameter τ_0 and reference distribution g_0 .

Finally, I would like to add that the existence of a minimal coherence time is related to the norm-boundedness of the modification, and it will be essential for defining a measure of macroscopicity based on the modification. This would be different if unbounded diffusion terms were present. In fact, a standard diffusion master equation,

$$\mathcal{L}_{\text{diff}}(\rho) = -\frac{\gamma_{pp}}{2} [\mathbf{p}, [\mathbf{p}, \rho]] - \frac{\gamma_{rr}}{2} [\mathbf{r}, [\mathbf{r}, \rho]] - \gamma_{pr} [\mathbf{p}, [\mathbf{r}, \rho]], \quad (4.100)$$

also classicalizes the motion of a single particle, leaves the Ehrenfest equations untouched, yields a constant energy increase per time, and is even Galilei-covariant, as can be easily checked. (The diffusion matrix γ_{ij} must be positive semi-definite in this case.) What distinguishes it from the bounded single-particle modification \mathcal{L}_1 is the rate at which it destroys coherences. We see this again most clearly in the characteristic function representation, where

$$\mathcal{L}_{\text{diff}}[\chi(\mathbf{r}, \mathbf{p})] = -\left(\frac{\gamma_{pp}}{2} p^2 + \frac{\gamma_{rr}}{2} r^2 + \gamma_{pr} \mathbf{p} \cdot \mathbf{r}\right) \chi(\mathbf{r}, \mathbf{p}). \quad (4.101)$$

¹⁹ The thermal state $\rho = \exp(-\mathbf{p}^2/2mk_B T) / (2\pi mk_B T)^{3/2}$ of a free particle corresponds to the characteristic function $\chi(\mathbf{r}, \mathbf{p}) = \delta(\mathbf{p}) \exp(-mk_B T \mathbf{r}^2/2\hbar^2)$. It is improperly normalized because the spatial coordinate extends over the whole coordinate space \mathbb{R}^3 . Regardless of this issue, which could be fixed by restricting to a finite volume, with growing temperature T the peak of the characteristic function around the origin gets more narrow. The same happens to the state under the influence of the classicalizing modification with growing time, which relates to the classicalization-induced diffusion heating discussed before.

The decay rate grows quadratically with \mathbf{r} and \mathbf{p} , which approximates the bounded case in the limit of small arguments²⁰. However, the unbounded case is valid for arbitrary arguments, that is, superpositions of far apart positions or momenta decay almost instantaneously. There is no lower limit to the coherence time, not even for elementary particles. I have therefore discarded this much more invasive possibility in the first place by restricting to a norm-bounded modification.

4.2.2. Explicit solution for harmonic potentials

The modified time evolution for a single particle, $\partial_t \rho = -i [\mathbf{H}, \rho] / \hbar + \mathcal{L}_1(\rho)$, can be integrated explicitly in the presence of at most harmonic potentials, that is, potentials with a linear or quadratic dependence on the position. The solution obtained can be used to describe many standard matter-wave interference experiments. Let me proceed by deriving the general solution in a rather lengthy but straightforward calculation, before I state the results for the most common cases.

4.2.2.1. Derivation of the explicit solution

It is well known that there exists an analytic solution to the Schrödinger evolution of a single-particle state ρ in the presence of a harmonic potential,

$$V(\mathbf{r}) = V_0 - m\mathbf{a} \cdot \mathbf{r} + \frac{1}{2} \mathbf{r}^T \cdot K \cdot \mathbf{r}, \quad K = K^T. \quad (4.102)$$

The time evolution resembles its classical counterpart in the phase space representation, that is, the Wigner function propagates in phase space along the classical trajectories corresponding to the potential, exactly like the classical phase space distribution does [77]. This is related to the fact that the classical equations of motion are linear and hence there exist closed expressions for the corresponding time-evolved quantum observables in the Heisenberg picture. The classical equations for the position \mathbf{r}_t and the momentum \mathbf{p}_t as a function of the initial values \mathbf{r}_0 and \mathbf{p}_0 read as

$$\frac{d}{dt} \begin{pmatrix} \mathbf{r}_t(\mathbf{r}_0, \mathbf{p}_0) \\ \mathbf{p}_t(\mathbf{r}_0, \mathbf{p}_0) \end{pmatrix} = \underbrace{\begin{bmatrix} 0 & \mathbb{I}/m \\ -K & C \end{bmatrix}}_{=:A} \begin{pmatrix} \mathbf{r}_t(\mathbf{r}_0, \mathbf{p}_0) \\ \mathbf{p}_t(\mathbf{r}_0, \mathbf{p}_0) \end{pmatrix} + \begin{pmatrix} 0 \\ m\mathbf{a} \end{pmatrix}. \quad (4.103)$$

Here I have introduced the additional traceless matrix C , $\text{tr}(C) = 0$, to account later for possible conservative velocity-dependent forces such as the Coriolis force. Together with the spring matrix K of the potential, it forms the full evolution matrix $A \in \mathbb{R}^{6 \times 6}$ which yields the solution (and its inverse)

$$\begin{pmatrix} \mathbf{r}_t \\ \mathbf{p}_t \end{pmatrix} = e^{At} \begin{pmatrix} \mathbf{r}_0 \\ \mathbf{p}_0 \end{pmatrix} + \int_0^t d\tau e^{A(t-\tau)} \begin{pmatrix} 0 \\ m\mathbf{a} \end{pmatrix},$$

²⁰ To see the small-argument limit explicitly, expand the Fourier transform $\tilde{g}(\mathbf{r}, \mathbf{p})$ of the distribution function to the lowest non-vanishing order around the origin, $\tilde{g}(\mathbf{r}, \mathbf{p}) \approx 1 - \mathcal{E}[s^2] p^2 / 2\hbar^2 - \mathcal{E}[q^2] r^2 / 2\hbar^2$. This leads to

$$\mathcal{L}_1[\chi(\mathbf{r}, \mathbf{p})] \approx - \left(\frac{\mathcal{E}[s^2]}{2\hbar^2 \tau} p^2 + \frac{\mathcal{E}[q^2]}{2\hbar^2 \tau} r^2 \right) \chi(\mathbf{r}, \mathbf{p}),$$

which is equivalent to the diffusion expression (4.101).

$$\begin{pmatrix} \mathbf{r}_0 \\ \mathbf{p}_0 \end{pmatrix} = e^{-At} \begin{pmatrix} \mathbf{r}_t \\ \mathbf{p}_t \end{pmatrix} - \int_0^t d\tau e^{-A\tau} \begin{pmatrix} 0 \\ m\mathbf{a} \end{pmatrix}. \quad (4.104)$$

The inversion is guaranteed by construction because the matrix exponential is norm-conserving, $\det[\exp(At)] = \exp[\text{tr}(A)t] = \exp[\text{tr}(C)t] = 1$. The coherent time evolution of the quantum state in the Wigner function representation is then given by

$$w_t(\mathbf{r}, \mathbf{p}) \equiv w_t \left[\begin{pmatrix} \mathbf{r} \\ \mathbf{p} \end{pmatrix} \right] = w_0 \left[e^{-At} \begin{pmatrix} \mathbf{r} \\ \mathbf{p} \end{pmatrix} - \int_0^t d\tau e^{-A\tau} \begin{pmatrix} 0 \\ m\mathbf{a} \end{pmatrix} \right]. \quad (4.105)$$

Note that I use here a more convenient phase-space vector notation for the arguments which is better suited to implement the expression (4.104) for the classical trajectory. Let me rephrase the characteristic function (4.37) in a similar manner as

$$\chi_t(\mathbf{r}, \mathbf{p}) \equiv \chi_t \left[\begin{pmatrix} \mathbf{p} \\ -\mathbf{r} \end{pmatrix} \right] = \int d^3r' d^3p' w_t \left[\begin{pmatrix} \mathbf{r}' \\ \mathbf{p}' \end{pmatrix} \right] \exp \left[\frac{i}{\hbar} \begin{pmatrix} \mathbf{p} \\ -\mathbf{r} \end{pmatrix}^T \begin{pmatrix} \mathbf{r}' \\ \mathbf{p}' \end{pmatrix} \right]. \quad (4.106)$$

A negative sign is added to the argument in order to keep track of the variable substitutions in the following steps. The time evolution is solved by plugging in the form of the time-evolved Wigner function (4.105) making a change of variables in the integral. We find

$$\chi_t \left[\begin{pmatrix} \mathbf{p} \\ -\mathbf{r} \end{pmatrix} \right] = \exp \left[\frac{i}{\hbar} \left[e^{A^T t} \begin{pmatrix} \mathbf{p} \\ -\mathbf{r} \end{pmatrix} \right]^T \int_0^t d\tau e^{-A\tau} \begin{pmatrix} 0 \\ m\mathbf{a} \end{pmatrix} \right] \chi_0 \left[e^{A^T t} \begin{pmatrix} \mathbf{p} \\ -\mathbf{r} \end{pmatrix} \right]. \quad (4.107)$$

The time dependence can be absorbed by inverting the above expression (4.107),

$$\tilde{\chi}_t \left[\begin{pmatrix} \mathbf{p} \\ -\mathbf{r} \end{pmatrix} \right] := \exp \left[-\frac{i}{\hbar} \begin{pmatrix} \mathbf{p} \\ -\mathbf{r} \end{pmatrix}^T \int_0^t d\tau e^{-A\tau} \begin{pmatrix} 0 \\ m\mathbf{a} \end{pmatrix} \right] \chi_t \left[e^{-A^T t} \begin{pmatrix} \mathbf{p} \\ -\mathbf{r} \end{pmatrix} \right]. \quad (4.108)$$

This adapted form is identical to the characteristic function at initial time, $\tilde{\chi}_0(\mathbf{s}, \mathbf{q}) = \chi_0(\mathbf{s}, \mathbf{q})$, and it remains constant over time, $\partial_t \tilde{\chi}_t = 0$.

We are now in a position to add the classicalizing modification \mathcal{L}_1 from Equation (4.39) to the coherent time evolution of the characteristic function,

$$\begin{aligned} \mathcal{L}_1 \left\{ \chi_t \left[\begin{pmatrix} \mathbf{p} \\ -\mathbf{r} \end{pmatrix} \right] \right\} &= \frac{1}{\tau} \left\{ \int d^3s d^3q g(\mathbf{s}, \mathbf{q}) \exp \left[-\frac{i}{\hbar} \begin{pmatrix} \mathbf{p} \\ -\mathbf{r} \end{pmatrix}^T \begin{pmatrix} \mathbf{s} \\ \mathbf{q} \end{pmatrix} \right] - 1 \right\} \chi_t \left[\begin{pmatrix} \mathbf{p} \\ -\mathbf{r} \end{pmatrix} \right] \\ &= \frac{1}{\tau} \left\{ \tilde{g} \left[\begin{pmatrix} \mathbf{p} \\ -\mathbf{r} \end{pmatrix} \right] - 1 \right\} \chi_t \left[\begin{pmatrix} \mathbf{p} \\ -\mathbf{r} \end{pmatrix} \right]. \end{aligned} \quad (4.109)$$

The only effect of this term is that it equips the adapted function (4.108) with a time dependence,

$$\partial_t \tilde{\chi}_t \left[\begin{pmatrix} \mathbf{p} \\ -\mathbf{r} \end{pmatrix} \right] = \frac{1}{\tau} \left\{ \tilde{g} \left[e^{-A^T t} \begin{pmatrix} \mathbf{p} \\ -\mathbf{r} \end{pmatrix} \right] - 1 \right\} \tilde{\chi}_t \left[\begin{pmatrix} \mathbf{p} \\ -\mathbf{r} \end{pmatrix} \right]. \quad (4.110)$$

This time-differential equation is easily integrated, and via the relation (4.108) we arrive at the final solution of the modified time evolution,

$$\begin{aligned} \chi_t \left[\begin{pmatrix} \mathbf{p} \\ -\mathbf{r} \end{pmatrix} \right] &= \chi_0 \left[e^{A^T t} \begin{pmatrix} \mathbf{p} \\ -\mathbf{r} \end{pmatrix} \right] \exp \left[\frac{i}{\hbar} \begin{pmatrix} \mathbf{p} \\ -\mathbf{r} \end{pmatrix}^T \int_0^t d\tau e^{A\tau} \begin{pmatrix} 0 \\ m\mathbf{a} \end{pmatrix} \right] \\ &\times \exp \left[\frac{1}{\tau} \int_0^t d\tau \left\{ \tilde{g} \left[e^{A^T \tau} \begin{pmatrix} \mathbf{p} \\ -\mathbf{r} \end{pmatrix} \right] - 1 \right\} \right]. \end{aligned} \quad (4.111)$$

The vector notation of the arguments will be dropped in the following discussion of common examples.

4.2.2.2. Free propagation in the presence of a constant acceleration

In many cases of single-particle interference, the particles propagate freely or under the influence of a constant acceleration, say earth's gravity. The free evolution matrix then reads as

$$A = \begin{bmatrix} 0 & \mathbb{I}/m \\ 0 & 0 \end{bmatrix}, \quad A^2 = 0 \quad \Rightarrow \quad e^{At} = \begin{bmatrix} \mathbb{I} & \mathbb{I}t/m \\ 0 & \mathbb{I} \end{bmatrix}, \quad (4.112)$$

and the modified time evolution of the state (4.111) yields

$$\chi_t(\mathbf{r}, \mathbf{p}) = \chi_0 \left(\mathbf{r} - \mathbf{p} \frac{t}{m}, \mathbf{p} \right) \exp \left\{ \frac{i}{\hbar} \left(\mathbf{p} \cdot \mathbf{a} \frac{t^2}{2} - m\mathbf{a}t \cdot \mathbf{r} \right) + \frac{1}{\tau} \left[\int_0^t d\tau \tilde{g} \left(\mathbf{r} - \mathbf{p} \frac{\tau}{m}, \mathbf{p} \right) - t \right] \right\}, \quad (4.113)$$

where it was used that \tilde{g} is of even parity in both arguments. The constant acceleration, if present, merely contributes a phase factor, but it does not affect the classicalization-induced decay term. This is because it does not affect the path difference in phase space between two interfering trajectories of a superposition state.

At this point it is appropriate to make a side remark on the role of the position and momentum distribution $g(\mathbf{s}, \mathbf{q})$ of the modification. If we assume that the distribution involves only momenta, $g(\mathbf{s}, \mathbf{q}) = h(\mathbf{q}) \delta(\mathbf{s})$, then quantum coherence will still be guaranteed to decay over time under any circumstances. The reason is that the Fourier transform $\tilde{g}(\mathbf{r}, \mathbf{p}) = \tilde{h}(\mathbf{r})$ predicts an exponential decay of the characteristic function in (4.113) for *all* arguments $(\mathbf{r}, \mathbf{p}) \neq (0, 0)$. The classicalizing effect does not vanish in the absence of position diffusion.

The situation is quite different in the absence of momentum translations, $g(\mathbf{s}, \mathbf{q}) = f(\mathbf{s}) \delta(\mathbf{q})$, where the freely evolving characteristic function would not be affected on the whole position axis $(\mathbf{r}, 0)$ ²¹. Consequently, a delocalized and therefore highly nonclassical plane wave state $\rho = |\mathbf{p}_0\rangle\langle\mathbf{p}_0|$, whose characteristic function is given by $\chi(\mathbf{r}, \mathbf{p}) = \delta(\mathbf{p}) \exp(-i\mathbf{p}_0 \cdot \mathbf{r}/\hbar)$, would not lose any of its coherence. We see that the absence of momentum diffusion undermines the classicalizing effect of the modification and should be excluded from our considerations. The reference distribution $g_0(\mathbf{s}, \mathbf{q})$ underlying the classicalizing modification must therefore extend over finite momenta, $\sigma_q \neq 0$. Naturally, this comes at the price of an increase in kinetic energy over time.

²¹ This case might be appealing as it also conserves the energy of a free particle, i.e. the invariance under time translations.

4.2.2.3. The description of lower dimensional motion

Many mechanical superposition experiments probe coherence only with respect to the motion in one or two dimensions. The modified time evolution for the lower-dimensional degrees of freedom is then obtained by tracing over the irrelevant dimension(s) in the single-particle modification \mathcal{L}_1 , which amounts to using the reduced phase-space distributions

$$g_{2D}(s_x, s_y, q_x, q_y) = \int ds_z dq_z g(s, q), \quad g_{1D}(s_x, q_x) = \int ds_y dq_y ds_z dq_z g(s, q). \quad (4.114)$$

In practice, the formal solution (4.111) is readily applied also to characteristic functions of one- or two-dimensional quantum states by replacing the term $\tilde{g}(\mathbf{r}, \mathbf{p})$ with its one- or two-dimensional counterpart $\tilde{g}_{1D}(x, p) = \tilde{g}(x, 0, 0, p, 0, 0)$ or $\tilde{g}_{2D}(x, y, p_x, p_y) = \tilde{g}(x, y, 0, p_x, p_y, 0)$, respectively.

4.2.2.4. Harmonic solution in 1D

As a final example, let us consider the case of a one-dimensional harmonic oscillator. Assuming a point mass m oscillating with a frequency ω , we obtain the time evolution matrix for position and momentum as

$$A = \begin{bmatrix} 0 & 1/m \\ -m\omega^2 & 0 \end{bmatrix}, \quad A^2 = -\omega^2 \mathbb{I} \quad \Rightarrow \quad e^{At} = \begin{bmatrix} \cos \omega t & \frac{\sin \omega t}{m\omega} \\ -m\omega \sin \omega t & \cos \omega t \end{bmatrix}. \quad (4.115)$$

Plugging this into the formal solution (4.111), reduced to one dimension, we find

$$\begin{aligned} \chi_t(x, p) = & \exp \left\{ \frac{1}{\tau} \left[\int_0^t dt' \tilde{g}_{1D} \left(x \cos \omega t' - \frac{p}{m\omega} \sin \omega t', p \cos \omega t' + m\omega x \sin \omega t' \right) - t \right] \right\} \\ & \times \chi_0 \left(x \cos \omega t - \frac{p}{m\omega} \sin \omega t, p \cos \omega t + m\omega x \sin \omega t \right). \end{aligned} \quad (4.116)$$

4.2.3. Classicalization of Bose-Einstein condensates

After the detailed study of the classicalizing effect on the dynamics of single particles and point-like compounds let us turn to quantum many-body systems. Bose-Einstein condensation is one of the most prominent and best-studied collective quantum effects, and such condensates have become a standard tool in the experimental observation of many-body phenomena [201].

The coherence properties are related to the bosonic single-particle nature of the condensate wave function, which gets macroscopically occupied when the BEC phase is formed below a certain critical temperature. The state of the condensate may then be represented by a single collective matter-wave field $\Psi(\mathbf{r}, t)$, the “condensate wave function”. It follows the nonlinear Gross-Pitaevski equation [202], which accounts for interactions between the condensed particles. This description, however, disguises the microscopic single-particle origin of the BEC state. It remains largely unaffected by the loss of single particles due to heating or diffusion mechanisms, as induced also by the classicalizing modification, for instance.

Interference experiments with spatially separated BECs (e.g. [169, 203]) have clearly demonstrated the coherence of the condensate state. So the natural question to ask is how this amount of coherence compares to superposition states of single atoms in the same configuration.

Note that the influence of interactions on BEC interference will not be discussed in this work. It was shown elsewhere [204] that they do considerably modify the coherent time evolution of the condensate wave function $\Psi(\mathbf{r}, t)$, and thus the observed interference pattern²². Here, we focus our attention on the expectation values of the observables that are actually used in the experiment to detect the interference effect, and on how they are classicalized over time.

In the first observation of interference between two separated sodium BECs [169], and in many following experiments, the fringe pattern typically appears in snapshots of the single-particle density $n(x) = \hat{\psi}^\dagger(x) \hat{\psi}(x)$ of the interfering condensates for each single run of the experiment. The motion of the condensed atoms is described by a one-dimensional degree of freedom in second quantization, where $\hat{\psi}(x)$ denotes the annihilation operator of a bosonic atom of mass m . The experiment [169] resembles the well-known double-slit configuration: Initially, a superposition of two condensates separated by the center-to-center distance d is created in a double-well trap potential. It is then released, and a snapshot of the density is recorded after a free time of flight t when both condensates have overlapped. In the ideal non-interacting case one should expect to see a fringe modulation of the density with period $\lambda = \hbar t / md$. The latter must be adapted in the presence of interactions [204].

The phase of the fringe pattern is random in each run since the relative phase between both condensates is not controlled when the double condensate is created. Consequently, the expectation value $\langle n(x) \rangle$ does not reproduce the fringe pattern since it corresponds to an average over many runs. The in-depth analysis provided in [204, 208] suggests two approaches to model the interference effect in single runs theoretically. In the first approach the single-run interference pattern can be recovered in the single-particle density $n(x)$ by replacing the bosonic operator $\hat{\psi}(x)$ with the collective wave function $\Psi(x, t)$ of the double condensate. The second, and more rigorous, solution is to seek signatures of the interference effect in second order correlation functions of the condensate, rather than directly in the expectation value of the single-particle density.

I will now discuss the influence of classicalization in both approaches, using the second quantization formulation of the modification (4.67) for a single spinless boson species of mass m in one dimension,

$$\begin{aligned} \mathcal{L}(\rho) &= \frac{1}{\tau} \int ds dq g_{1D}(s, q) \left[A(s, q) \rho A^\dagger(s, q) - \frac{1}{2} \{A^\dagger(s, q) A(s, q), \rho\} \right], \\ A(s, q) &= \int dp e^{ips/\hbar} a^\dagger(p - q) a(p) = \int dx e^{-iqx/\hbar} \hat{\psi}^\dagger(x) \hat{\psi}(x + s). \end{aligned} \quad (4.117)$$

4.2.3.1. Effective single-particle description of BEC interference

The free expansion of a BEC can be fully accounted for by using the second-quantization Heisenberg picture in the absence of interactions. The expectation values of single-particle observables B , that is, operators of the form $\hat{\psi}^\dagger(\mathbf{r}) \hat{\psi}(\mathbf{r}')$ and linear combinations thereof, evolve like their counterparts in first quantization (see Section 4.1.4.6 on page 144, where the second quantization form

²² Controllable nonlinear interactions are the crucial ingredient in interference experiments with squeezed multi-component BECs to achieve longer coherence times and better phase sensitivity [205–207].

of the modification is introduced). Their time evolution is effectively described by the Heisenberg equation of motion for the observable²³, $\partial_t B = i [H, B] / \hbar + \mathcal{L}(B)$.

As a consequence, the single-particle density $n(x)$ evolves effectively like the spatial probability distribution of a single particle. This can be made explicit by introducing the second quantization form of the characteristic function,

$$\hat{\chi}(x, p) = \int dx_0 e^{ipx_0/\hbar} \hat{\psi}^\dagger\left(x_0 + \frac{x}{2}\right) \hat{\psi}\left(x_0 - \frac{x}{2}\right) = \int dp_0 e^{-ip_0 x/\hbar} a^\dagger\left(p_0 + \frac{p}{2}\right) a\left(p_0 - \frac{p}{2}\right), \quad (4.118)$$

in close analogy to the line of arguments in [204]. It effectively evolves in time like its counterpart in first quantization. In particular, one can easily verify by means of the bosonic CCR (4.64) that it classicalizes like a single particle of mass m ,

$$\mathcal{L}[\hat{\chi}(x, p)] = \frac{1}{\tau} [\tilde{g}_{1D}(x, p) - 1] \hat{\chi}(x, p). \quad (4.119)$$

Solving the modified Heisenberg evolution of $\hat{\chi}(x, p)$ for freely expanding BECs then yields the same analytic result as given in Section 4.2.2.2 for a single particle.

At the same time, the characteristic function is directly related to the Fourier amplitude of a fringe modulation of the single-particle density with period λ ,

$$\hat{\chi}\left(0, -\frac{\hbar}{\lambda}\right) = \int dx e^{-2\pi i x/\lambda} n(x). \quad (4.120)$$

This expression serves to quantify the interference visibility observed in each run of a BEC interference experiment. If no coherence is lost, the visibility is obtained by substituting the number operator with the fully evolved condensate wave function [204], $n(x) \mapsto |\Psi(x, t)|^2$. The exact form of the wave function, as well as the amplitude and the period of the resulting fringe pattern, change in the presence of interactions.

The Heisenberg analysis of the modified time evolution of $\hat{\chi}(x, p)$, cf. Equation (4.119), indicates that the collective BEC interference effect is merely subject to single-particle classicalization. That is to say, the double-condensate wave function decays at the rate of a comparable single-atom superposition state. This is confirmed by the following analysis.

4.2.3.2. Interference in terms of second order correlation functions

A more rigorous way to unveil the single-run BEC interference pattern was discussed in [208]. Instead of looking at the expectation value of the single-particle density $\langle n(x) \rangle$, which ensemble-averages over the random relative phase of the double condensate, one should analyze the interference effect by means of the normally ordered second-order correlation function $C(x, \Delta) = \langle \hat{\psi}^\dagger(x) \hat{\psi}^\dagger(x + \Delta) \hat{\psi}(x + \Delta) \hat{\psi}(x) \rangle$. The latter is related to the joint probability of finding a boson at position x and, at the same time, a second boson at position $x + \Delta$. It is intuitively clear that this joint probability must reveal the interference fringe pattern irrespectively of its phase, given a fixed

²³ The effective Heisenberg equation of motion for an observable B is obtained by taking the time derivative of the expectation value, $\langle \partial_t B \rangle \equiv \partial_t \langle B \rangle = \partial_t \text{tr}(\rho B)$, and using the cyclic property of the trace to shift the master equation $\partial_t \rho = -i [H, \rho] / \hbar + \mathcal{L}(\rho)$ to B . This results in the conjugate equation $\partial_t B = i [H, B] / \hbar + \mathcal{L}^\dagger(B)$, where $\mathcal{L}^\dagger(B) = \mathcal{L}(B)$ holds due to the isotropy of the classicalizing modification (4.117).

fringe period. We can illustrate this by the idealized case of a BEC superposition state, $\rho = |\Psi\rangle\langle\Psi|$, where $2N$ atoms are condensed in two different plane wave states,

$$|\Psi\rangle = \sqrt{\frac{2\pi\hbar}{L}} \frac{1}{N!} [a^\dagger(-p_0)]^N [a^\dagger(p_0)]^N |0\rangle. \quad (4.121)$$

Here, the state vector is normalized with respect to a finite trap length L . One immediately checks that the single-particle density does not show any signature of interference, $\langle n(x) \rangle = 2N/L$, whereas the correlation function exhibits a fringe modulation with period $\lambda = h/2p_0$,

$$C(x, \Delta) L^2 = 4N^2 - 2N + 2N^2 \cos\left(\frac{2p_0\Delta}{\hbar}\right). \quad (4.122)$$

In order to account for the influence of classicalization on this second order interference effect, it is expedient to introduce the normally ordered second-quantization counterpart of the two-particle characteristic function,

$$\hat{\chi}_2(x_1, p_1, x_2, p_2) = \int dx_0 dy_0 e^{i(p_1 x_0 + p_2 y_0)/\hbar} \hat{\psi}^\dagger\left(x_0 + \frac{x_1}{2}\right) \hat{\psi}^\dagger\left(y_0 + \frac{x_2}{2}\right) \hat{\psi}\left(y_0 - \frac{x_2}{2}\right) \hat{\psi}\left(x_0 - \frac{x_1}{2}\right). \quad (4.123)$$

The correlation function can be obtained from this expression by

$$C(x, \Delta) = \int \frac{dp_1 dp_2}{(2\pi\hbar)^2} \langle \hat{\chi}_2(0, p_1, 0, p_2) \rangle e^{-ip_1 x/\hbar - ip_2(x+\Delta)/\hbar}. \quad (4.124)$$

The modified Heisenberg time evolution of $\hat{\chi}_2$ follows from a tedious but straightforward calculation that mainly relies on the use of the bosonic CCR. In the absence of external forces one arrives at the integro-differential equation

$$\begin{aligned} \partial_t \langle \hat{\chi}_2(x_1, p_1, x_2, p_2) \rangle &= \left[-\frac{p_1}{m} \partial_{x_1} - \frac{p_2}{m} \partial_{x_2} + \frac{\tilde{g}_{1D}(x_1, p_1) + \tilde{g}_{1D}(x_2, p_2) - 2}{\tau} \right] \langle \hat{\chi}_2(x_1, p_1, x_2, p_2) \rangle \\ &\quad - \frac{4}{\tau} \int ds dq g_{1D}(s, q) \sin\left(\frac{p_2 s - q x_2}{2\hbar}\right) \sin\left(\frac{p_1 s - q x_1}{2\hbar}\right) \langle \hat{\chi}_2(x_1 + s, p_1 + q, x_2 - s, p_2 - q) \rangle. \end{aligned} \quad (4.125)$$

Although a general solution of this equation is hard to find, an upper bound to the rate of the coherence decay can be given. Recall that $\langle \hat{\chi}_2 \rangle$ corresponds to the characteristic function of a two-particle state in first quantization. As such, its classicalization rate cannot be larger than four times the single-particle rate $1/\tau$, as seen in the exemplary discussion of the two-particle modification in Section 4.1.5.1. If the double-condensate superposition were to be observed by means of the second-order correlation function $C(x, \Delta)$, it would classicalize not more than a single particle of mass $2m$. This should come as no surprise: Genuine N -partite coherence, as would be the case if the particles were entangled in a so-called NOON superposition state of being either altogether in the left or in the right well, can neither be established nor identified on the level of two-particle observables alone.

In summary, collective interference with many Bose-condensed atoms is not subject to an enhanced classicalization effect beyond the level of a single or few atoms as far as only single- or few-particle observables are concerned. The situation changes when higher order correlations are taken

into consideration, e.g. in experiments with so-called NOON states. They may offer a high degree of N -atom entanglement similar to center-of-mass superposition states of atomic compounds such as molecules or clusters. Hence, they can be subject to an enhanced many-particle classicalization, but they are also increasingly hard to handle both experimentally and theoretically.

On the other hand, a detailed analysis of the coherence properties of strongly interacting condensates, where repulsive interactions countervail the bosonic nature of the constituent particles, would require a better understanding of the many-body structure underlying the collective wave function Ψ . Interference experiments with such condensates might be more strongly affected by classicalization than on the level of single particles, depending on what observables would be measured. I leave this as a matter for future studies.

4.2.4. Classicalization of Cooper-paired electrons

Now that we have seen the influence of classicalization on collective quantum interference effects with Bose-condensed atoms, let me turn to macroscopic quantum superposition phenomena in fermionic many-body systems. The single-particle nature of the collectively occupied condensate state did not give rise to a pronounced many-particle amplification of the total classicalizing effect in the bosonic case. With fermions, however, the situation is somewhat different since no two fermions may occupy the same state. Collective quantum phenomena involve the condensation of fermions into Cooper-pairs as in the case of electrons in superconductors [202].

In close analogy to the BEC case one may associate a macroscopic wave function $\Psi(\mathbf{r}, t) = \sqrt{N_s/V} \exp(i\varphi(\mathbf{r}, t))$ to the condensate, which represents the collective state occupied by N_s Cooper pairs and which embodies their macroscopic phase coherence throughout the superconductor of volume V [3]. It can be used to explain the characteristic electrodynamical properties of a superconductor: its perfect conductance and its perfect diamagnetism. The latter prevents magnetic fields from entering the superconducting material by building up a phase gradient in the pair wave function that compensates the corresponding electromagnetic vector potential, $\hbar \nabla \varphi(\mathbf{r}, t) = 2e\mathbf{A}(\mathbf{r}, t)$. This results in the flux quantization effect [209, 210]: The magnetic flux Φ threading a closed superconducting loop must be quantized in units of the Cooper pair flux quantum $\Phi_0 = h/2e$, because the wave function Ψ is only well defined if the total phase accumulated over the loop $\oint \nabla \varphi \cdot d\mathbf{r} = 2e \oint \mathbf{A} \cdot d\mathbf{r} / \hbar = 2e\Phi / \hbar$ is a multiple of 2π .

I focus here on the exemplary situation where the many-electron state of a superconducting ring is brought into a superposition of counter-rotating persistent current states; this was observed in various experiments [1, 2, 168] and is commonly regarded as a paradigm of macroscopic quantum phenomena [3, 211]. The basic effect is intuitively understood by means of the flux quantization condition. If an external flux of $\Phi_0/2$ is applied to the loop, the superconducting state may take on two equivalent possibilities. One where a negative flux is induced to counteract the external flux, $\Phi = 0$, or one where the external flux is augmented to one quantum, $\Phi = \Phi_0$. The two states have opposite phase gradients and can be understood as states of counter-rotating persistent currents, as will shortly be discussed. Breaking the loop with a so-called Josephson junction allows both states to tunnel and couple with each other giving rise to superposition states.

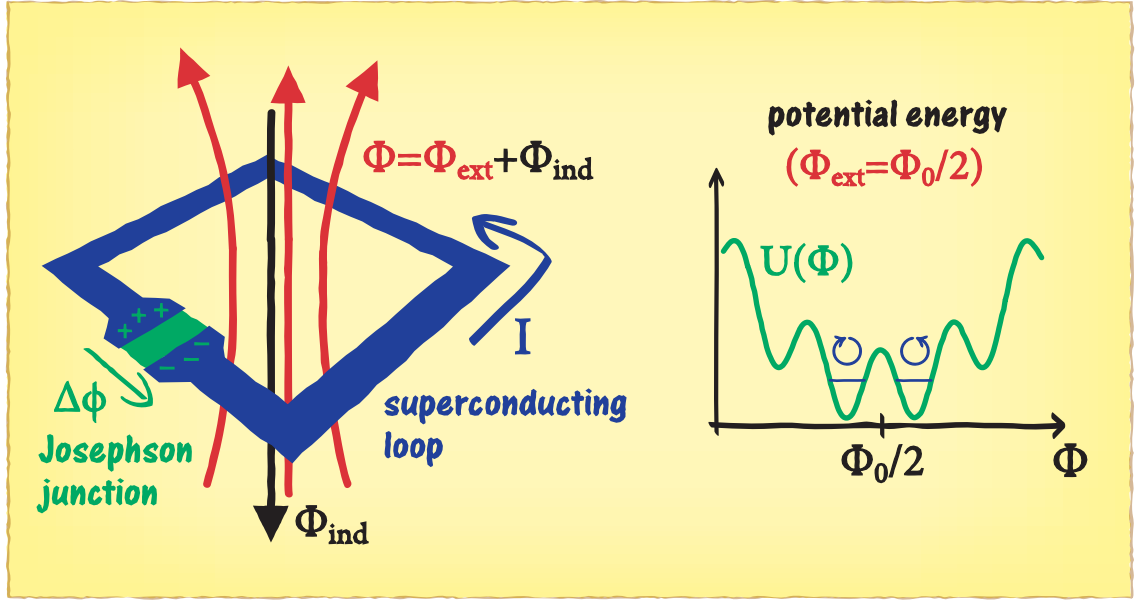


Figure 4.1. Schematic of a superconducting loop geometry with a single Josephson junction. Given the magnetic flux Φ threading the area surrounded by the superconducting lead, a phase difference $\Delta\phi$ falls off across the thin slab of insulating material (see text). It drives the tunneling current $I = I_c \sin \Delta\phi$ of Cooper pairs and builds up the charge imbalance $Q = C(d\Phi/dt)$ across the junction. The flux Φ consists of the externally applied Φ_{ext} and the flux induced by the ring current $\Phi_{\text{ind}} = LI$. On the right, the potential energy of the loop $U(\Phi)$ is sketched for one quantum of external flux, $\Phi_{\text{ext}} = \Phi_0/2$. The associated quantum ground state corresponds to a superposition of persistent loop currents.

4.2.4.1. Experimental situation

The experimental configuration can essentially be broken down to the geometry sketched in Figure 4.1 [212]: a closed loop of superconducting material, which is interrupted by one or more thin slabs of insulating material (Josephson junctions), in the presence of a tunable magnetic field [1, 213, 214]. The Josephson junction acts as a tunnel barrier for Cooper pairs, and a net tunnel current $I = I_c \sin \Delta\phi$ may flow if the phase of the pair wave function Ψ differs by $\Delta\phi$ across the junction. A sufficiently thin tunnel junction is fully characterized by the critical current parameter I_c , its coupling energy is given by $E_J = -I_c (\Phi_0/2\pi) \cos \Delta\phi$ [202]. The phase difference across the junction arises as one modifies the flux Φ through the loop by switching on the magnetic field. This is because the phase difference across the junction must again match the phase accumulated in the superconductor due to the flux, $\Delta\phi + 2\pi\Phi/\Phi_0 = 2\pi n$. At the same time, any flux $\Phi - \Phi_{\text{ext}}$ induced by the Cooper pairs as a reaction to the applied flux Φ_{ext} increases the energy of the system by the inductive term $E_L = (\Phi - \Phi_{\text{ext}})^2/2L$, with L the self-inductance of the loop [3]. The dynamical flux variable Φ thus fully determines the potential energy of the system,

$$U(\Phi) = E_L + E_J = \frac{(\Phi - \Phi_{\text{ext}})^2}{2L} - \frac{I_c \Phi_0}{2\pi} \cos\left(2\pi \frac{\Phi}{\Phi_0}\right). \quad (4.126)$$

On the other hand, the charge imbalance across the Josephson junction building up with growing phase difference must also be taken into account. It gives rise to a ‘kinetic’ energy term $E_C = C (\mathrm{d}\Phi/\mathrm{d}t)^2 / 2$, with C the capacitance of the junction²⁴.

The potential exhibits several local minima in Φ depending on the externally applied flux Φ_{ext} and on the system parameters L, I_c . A symmetric double-well potential appears in the case of $\Phi_{\text{ext}} = \Phi_0/2$, as depicted on the right of Figure 4.1. The minima are separated by a tunnel barrier at the point $\Phi = \Phi_0/2$ where no flux is induced by the Cooper pairs. The two wells correspond to clockwise (\odot) and anti-clockwise (\ominus) persistent loop currents, that is, to phase gradients of opposite sign in the collective Cooper pair wave function.

The quantum mechanical ground state of such a double-well configuration is then given by a symmetric combination of both single-well ground states with a reduced energy, $(|\odot\rangle + |\ominus\rangle)/\sqrt{2}$, while the antisymmetric combination corresponds to a higher energy. A similar configuration holds when the loops are interrupted by more than a single Josephson junction [215].

Microwave spectroscopy serves to measure the level splitting (also known as *anti-crossing*) in the experiments [1, 2, 168], thereby verifying that the system has occupied the superposition state for a sufficient lifetime inversely proportional to the energy difference.

4.2.4.2. Theoretical description of the superconducting state

The microscopic derivation and many-body description of the superconducting state of a metal is covered by the famous BCS theory [216]. It explains the pairing of conduction electrons in a solid material by means of an attractive electron-electron interaction which is mediated by the polarization of the crystal lattice reacting to the Coulomb charge of a moving electron. That is to say, two electrons may attract each other through the exchange of virtual phonons.

When no external forces are present this leads to the pairing of electrons with opposite spin and momentum²⁵ ($\mathbf{k} \uparrow, -\mathbf{k} \downarrow$) close to the Fermi surface where electron-phonon scattering is not forbidden by the Pauli principle. The wave functions associated to the electron pairs are superpositions of those momenta, $\Psi_{12}(\mathbf{r}_1, \mathbf{r}_2) = \sum_{\mathbf{k}} A_{\mathbf{k}} \exp[i\mathbf{k}(\mathbf{r}_1 - \mathbf{r}_2)]$, which exhibit a large spatial extension²⁶ [210]. From the coherent overlap of these states emerges the superconducting zero-current phase. The associated collective wave function $\Psi(\mathbf{R})$ is determined by the center-of-mass dependence exhibited by the states $\Psi_{12}(\mathbf{R} + \mathbf{r}/2, \mathbf{R} - \mathbf{r}/2)$ of the participating Cooper pairs [202]. One finds that $\Psi(\mathbf{R}) = \sqrt{N_s/V} \exp(i\varphi)$ is constant, and no phase gradient $\nabla\varphi$ is present, since the momenta of each pair cancel. We will see later that this changes for finite-current states where each Cooper pair carries a non-zero momentum.

The microscopic many-body nature of the superconducting state is made evident in the second quantization formulation of Bardeen, Cooper and Schrieffer [216]. At zero temperature the Fermi

²⁴ The law of induction tells us that any change of magnetic flux through an open loop induces an electric potential difference $u = -\mathrm{d}\Phi/\mathrm{d}t$. Here, the voltage u must build up across the tunneling junction, which can be regarded as a capacitor C . This is in accordance with the *Josephson equation* $\mathrm{d}\Delta\phi/\mathrm{d}t = 2eu/\hbar = 2\pi u/\Phi_0$ that generally relates the phase difference with the voltage across a Josephson junction [202]. The voltage gives rise to a charge imbalance $Q = Cu$ and to a capacitive energy $E_C = Cu^2/2$.

²⁵ We restrict our view to *s*-type superconductors with electrons pairing in a spin singlet state.

²⁶ The momentum spread of the superposition is much smaller than the Fermi wave number k_F as only the momentum states close to the Fermi surface are accessible by electron-phonon scattering. The spatial extension of the superposition is therefore much larger than the de Broglie wavelength $2\pi/k_F$ of the Fermi electrons.

sea of conductance electrons in a superconducting metal occupies the BCS ground state²⁷

$$|0\rangle = \prod_{\mathbf{k}} \left[u_{\mathbf{k}} + v_{\mathbf{k}} c_{\uparrow}^{\dagger}(\mathbf{k}) c_{\downarrow}^{\dagger}(-\mathbf{k}) \right] |\text{vac}\rangle, \quad (4.127)$$

where $|\text{vac}\rangle$ represents the electronic vacuum state. The product ranges over all discrete electron wave numbers \mathbf{k} in the solid crystal, and $v_{\mathbf{k}}^2$ ($u_{\mathbf{k}}^2 = 1 - v_{\mathbf{k}}^2$) represents the probability that the respective pair of electrons ($\mathbf{k} \uparrow, -\mathbf{k} \downarrow$) is occupied (unoccupied),

$$v_{\mathbf{k}}^2 = \frac{1}{2} \left(1 - \frac{k^2 - k_F^2}{\sqrt{(k^2 - k_F^2)^2 + (2m_e \Delta_{\mathbf{k}}/\hbar^2)^2}} \right). \quad (4.128)$$

Electrons close to the Fermi surface, $k \approx k_F$, form Cooper pairs due to the phonon-mediated attractive interaction. This reduces their total energy by the pairing energy $\Delta_{\mathbf{k}} > 0$, whereas $\Delta_{\mathbf{k}} = 0$ for momentum states further away from the Fermi surface, which are inaccessible by phonon scattering. Given the characteristic Debye cutoff frequency ω_D of the lattice vibrations, Cooper pairs are only formed in a small energy shell at the Fermi surface, $|k^2 - k_F^2| \leq 2m_e \omega_D/\hbar$. The occupation of momentum states outside of the shell is the same as in a normal metal at zero temperature, $v_{\mathbf{k}} = \Theta(k_F - k)$.

The pairing term $\Delta_{\mathbf{k}}$ plays the role of an energy gap; it stabilizes the superconducting phase against disturbances, since any excitation of the BCS ground state requires an energy input of at least $2\Delta_{\mathbf{k}}$ to break a Cooper pair. If we approximate $\Delta_{\mathbf{k}}$ by a constant value Δ within the Debye shell (and zero elsewhere), we can identify Δ with the phenomenological value for the zero-temperature energy gap $\Delta = 1.76k_B T_c$, with T_c the critical temperature of the superconductor.

After discussing the state of a superconductor ‘at rest’ let me turn to the description of stationary dissipationless supercurrents. Assume that a given current density $\mathbf{j}_s = 2en_s \mathbf{v}_s$ is carried by the entire pair condensate of density $n_s = N_s/V$, which must be moving at the constant velocity \mathbf{v}_s . The continuity equation for probability then relates the velocity to the phase gradient of the condensate wave function, as the current density associated to $\Psi(\mathbf{R})$ is given by $\mathbf{j}_s(\mathbf{R}) = 2e\hbar n_s \nabla \varphi(\mathbf{R})/2m_e$. This requires that the electrons are paired in the configuration $(\mathbf{k} + m_e \mathbf{v}_s/\hbar \uparrow, -\mathbf{k} + m_e \mathbf{v}_s/\hbar \downarrow)$ with total momentum $2m_e \mathbf{v}_s$, giving $\Psi(\mathbf{R}) \propto \exp(2m_e \mathbf{v}_s \cdot \mathbf{R}/\hbar)$.

Hence, the quantum state underlying the persistent supercurrent derives from a momentum translation of the zero-current BCS state. One achieves this formally applying the second quantization Weyl operator (4.16),

$$W(0, \mathbf{v}_s) = \exp \left\{ -\frac{i}{\hbar} \int d^3r m_e \mathbf{v}_s \cdot \mathbf{r} \left[\hat{\psi}_{\uparrow}^{\dagger}(\mathbf{r}) \hat{\psi}_{\uparrow}(\mathbf{r}) + \hat{\psi}_{\downarrow}^{\dagger}(\mathbf{r}) \hat{\psi}_{\downarrow}(\mathbf{r}) \right] \right\}, \quad (4.129)$$

²⁷ Strictly speaking, the BCS ground state does not describe a fixed number of electrons, but rather a distribution of numbers around the expectation value $N = \langle \text{BCS} | N | \text{BCS} \rangle$. The effect of this uncertain number of electrons can be neglected as N is very large in most practical cases.

to the crystal electrons²⁸. It describes a displacement of the electronic Fermi sphere in momentum space, and the BCS state associated to the persistent supercurrent $\mathbf{j}_s = 2en_s\mathbf{v}_s$ reads as

$$|\mathbf{j}_s\rangle = W^\dagger(0, \mathbf{v}_s)|0\rangle = \prod_{\mathbf{k}} \left[u_{\mathbf{k}} + v_{\mathbf{k}} c_{\uparrow}^\dagger \left(\mathbf{k} + \frac{m_e \mathbf{v}_s}{\hbar} \right) c_{\downarrow}^\dagger \left(-\mathbf{k} + \frac{m_e \mathbf{v}_s}{\hbar} \right) \right] |\text{vac}\rangle. \quad (4.130)$$

Note that, in realistic situations, the Cooper pair current density \mathbf{j}_s is accompanied by the presence of external fields represented by a vector potential $\mathbf{A}(\mathbf{r})$. In this case the measured net electrical current density $\mathbf{j} = \mathbf{j}_s + \mathbf{j}_e$ contains also the canonical term $\mathbf{j}_e(\mathbf{r}) = -2e^2 n_s \mathbf{A}(\mathbf{r}) / m_e$. The flux quantization effect discussed above follows from the condition $\mathbf{j} = 0$ inside a superconducting lead which encircles an external magnetic field.

4.2.4.3. Classicalization of current superposition states

Let me now show how the classicalization effect acts on superposition states of different supercurrents, as they have been observed in experiments with Josephson loops. We shall assume in the following that the two branches of the superposition correspond to the pure BCS states $|\mathbf{j}_1\rangle$ and $|\mathbf{j}_2\rangle$, disregarding impurities due to finite temperature. These states can be understood as BCS-Fermi spheres which are displaced by the momentum $\hbar\Delta\mathbf{k} = m_e(\mathbf{j}_1 - \mathbf{j}_2)/2en_s$ with respect to each other. We shall further assume macroscopically distinct supercurrents, that is, a significant displacement $\Delta\mathbf{q}$ between the branches so that the two Fermi spheres differ by more than a few electrons (in the non-overlapping region). In particular, this implies orthogonality, $\langle \mathbf{j}_1 | \mathbf{j}_2 \rangle = 0$.

The classicalizing modification (4.71) of the electron motion in the crystal volume V reads as

$$\begin{aligned} \mathcal{L}(\rho) &= \frac{1}{\tau} \int_V d^3s \sum_{\mathbf{k}} G(s, \mathbf{k}) \left[A(s, \mathbf{k}) \rho A^\dagger(s, \mathbf{k}) - \frac{1}{2} \{A^\dagger(s, \mathbf{k}) A(s, \mathbf{k}), \rho\} \right], \\ A(s, \mathbf{k}) &= \sum_{\boldsymbol{\ell}} e^{i\boldsymbol{\ell} \cdot \mathbf{s}} \left[c_{\uparrow}^\dagger(\boldsymbol{\ell} - \mathbf{k}) c_{\uparrow}(\boldsymbol{\ell}) + c_{\downarrow}^\dagger(\boldsymbol{\ell} - \mathbf{k}) c_{\downarrow}(\boldsymbol{\ell}) \right]. \end{aligned} \quad (4.131)$$

Here, the Lindblad operator A describes the phase-space displacement of a single (spin- \uparrow or \downarrow) electron by the momentum $\hbar\mathbf{k}$ and the position \mathbf{s} .

The above assumptions imply that the modification cannot induce direct transitions between states of distinct supercurrents,

$$\langle \mathbf{j}_1 | A(s, \mathbf{k}) | \mathbf{j}_2 \rangle = 0, \quad \langle \mathbf{j}_1 | A^\dagger(s, \mathbf{k}) A(s, \mathbf{k}) | \mathbf{j}_2 \rangle = 0. \quad (4.132)$$

Nevertheless, it gradually undermines the coherence of the respective superposition by progressional dephasing and diffusion of the displaced Fermi spheres.

This can be estimated by means of the classicalization-induced decay rate of the nondiagonal matrix element $\langle \mathbf{j}_1 | \rho_t | \mathbf{j}_2 \rangle$ at initial time, $\Gamma = -\langle \mathbf{j}_1 | \mathcal{L}(\rho_0) | \mathbf{j}_2 \rangle / \langle \mathbf{j}_1 | \rho_0 | \mathbf{j}_2 \rangle$, given that the initial state is a coherent superposition of the form $\rho_0 = (a|\mathbf{j}_1\rangle + b|\mathbf{j}_2\rangle)(h.c.)$. Note that a similar approach was followed in [217] to study the impact of the continuous spontaneous localization model on

²⁸ Discretized momenta must be used, as introduced in Section 4.1.4.6 on page 145. The Weyl operator $W(\mathbf{r}, \mathbf{v})$ describes a translation of both the position and the momentum coordinate, which transforms the momentum creation operator to $W(\mathbf{r}, \mathbf{v}) c_{\sigma}^\dagger(\mathbf{k}) W^\dagger(\mathbf{r}, \mathbf{v}) = \exp(i\mathbf{k} \cdot \mathbf{r} - m_e \mathbf{v} \cdot \mathbf{r} / 2\hbar) c_{\sigma}^\dagger(\mathbf{k} - m_e \mathbf{v} / \hbar)$, as can be checked in a straightforward calculation using the CCR (4.64) on page 145.

superposition states of distinct currents. The present treatment contains the previous study as a special case²⁹.

At this point, it helps to recall the Galilean covariance of the modification. The Lindblad operators $A(\mathbf{s}, \mathbf{k})$ commute with the Weyl translations $W(\mathbf{r}, \mathbf{v})$ up to a phase,

$$W(\mathbf{r}, \mathbf{v}) A(\mathbf{s}, \mathbf{k}) = e^{im_e \mathbf{v} \cdot \mathbf{s} / \hbar - i \mathbf{k} \cdot \mathbf{r}} A(\mathbf{s}, \mathbf{k}) W(\mathbf{r}, \mathbf{v}), \quad (4.133)$$

as easily checked using the identity given in footnote 28. Combining this with the definition of the Weyl-translated BCS ground state (4.130), and with the above assumption (4.132), leads to the expression

$$\Gamma = \frac{1}{\tau} \int_V d^3 s \sum_{\mathbf{k}} G(\mathbf{s}, \mathbf{k}) \left[\langle 0 | A^\dagger(\mathbf{s}, \mathbf{k}) A(\mathbf{s}, \mathbf{k}) | 0 \rangle - e^{i \Delta \mathbf{k} \cdot \mathbf{s}} |\langle 0 | A(\mathbf{s}, \mathbf{k}) | 0 \rangle|^2 \right]. \quad (4.134)$$

Both the overlap of the BCS ground state with the vector $A(\mathbf{s}, \mathbf{k}) | 0 \rangle$ and the norm of the latter can be computed using the explicit form of the BCS ground state (4.127). The term $A(\mathbf{s}, \mathbf{k}) | 0 \rangle$ describes a state where all but two electrons are paired with opposite momenta in the BCS configuration, while one of the two remaining electrons obtains a phase shift and gets displaced in momentum by $-\hbar \mathbf{k}$ (provided the displaced momentum state is yet unoccupied).

It follows immediately that the transformed vector overlaps with the unmodified BCS state $| 0 \rangle$ only if no displacement takes place, $\mathbf{k} = 0$. In this case the Lindblad operator simplifies to the expression $A(\mathbf{s}, 0) = \sum_{\ell} [\mathbf{n}_{\uparrow}(\ell) + \mathbf{n}_{\downarrow}(\ell)] \exp(i \ell \cdot \mathbf{s})$, which gives a phase shift to each occupied momentum state. Applied to the BCS state it yields

$$\begin{aligned} A(\mathbf{s}, 0) | 0 \rangle &= \sum_{\ell} \prod_{\mathbf{k}' \neq \ell} [u_{\mathbf{k}'} + v_{\mathbf{k}'} c_{\uparrow}^\dagger(\mathbf{k}') c_{\downarrow}^\dagger(-\mathbf{k}')] e^{i \ell \cdot \mathbf{s}} v_{\ell} |\ell \uparrow, -\ell \downarrow \rangle \\ &\quad + \sum_{\ell} \prod_{\mathbf{k}' \neq -\ell} [u_{\mathbf{k}'} + v_{\mathbf{k}'} c_{\uparrow}^\dagger(\mathbf{k}') c_{\downarrow}^\dagger(-\mathbf{k}')] e^{i \ell \cdot \mathbf{s}} v_{-\ell} |-\ell \uparrow, \ell \downarrow \rangle \\ &= \sum_{\ell} 2v_{\ell} \cos(\ell \cdot \mathbf{s}) \prod_{\mathbf{k}' \neq \ell} [u_{\mathbf{k}'} + v_{\mathbf{k}'} c_{\uparrow}^\dagger(\mathbf{k}') c_{\downarrow}^\dagger(-\mathbf{k}')] |\ell \uparrow, -\ell \downarrow \rangle. \end{aligned} \quad (4.135)$$

Here, $|\mathbf{k}_1 \uparrow, \mathbf{k}_2 \downarrow \rangle = c_{\uparrow}^\dagger(\mathbf{k}_1) c_{\downarrow}^\dagger(\mathbf{k}_2) |\text{vac}\rangle$ denotes the vacuum state occupied by two electrons; one with spin- \uparrow in the \mathbf{k}_1 -state and one with spin- \downarrow in the \mathbf{k}_2 -state. We thus find the results

$$\langle 0 | A(\mathbf{s}, \mathbf{k}) | 0 \rangle = \delta_{\mathbf{k}, 0} \sum_{\ell} 2v_{\ell}^2 \cos(\ell \cdot \mathbf{s}), \quad (4.136)$$

$$\langle 0 | A^\dagger(\mathbf{s}, 0) A(\mathbf{s}, 0) | 0 \rangle = \left[\sum_{\ell} 2v_{\ell}^2 \cos(\ell \cdot \mathbf{s}) \right]^2 + \sum_{\ell} 4u_{\ell}^2 v_{\ell}^2 \cos^2(\ell \cdot \mathbf{s}). \quad (4.137)$$

Clearly, the first term of the right hand side in the second line is identical to the square of the first line (for $\mathbf{k} = 0$). They both cancel in the expression (4.134) for the decay rate at $\mathbf{k} = \mathbf{s} = 0$, that is, when neither dephasing nor diffusion are present. The physical nature of the second term in (4.137), however, must be doubted. This is because it would produce a nonzero decay rate even in

²⁹ Recall that the observable consequences of the CSL model [155,157] are described by a specific classicalizing modification of the present form with a Gaussian momentum distribution and no position diffusion, as discussed in Section 4.1.3.2 on page 136.

the limit of vanishing classicalization, that is, if we switch off the classicalizing effect by setting the distribution function to $G(\mathbf{s}, \mathbf{k}) = \delta(\mathbf{s}) \delta_{\mathbf{k},0}$,

$$\Gamma \xrightarrow{\text{no effect}} \frac{1}{\tau} \sum_{\ell} 4u_{\ell}^2 v_{\ell}^2 \neq 0. \quad (4.138)$$

The reason for the appearance of this term lies in the definition of the BCS ground state (4.127), which is *not* a Fock state of electrons, that is, an eigenstate of the number operator $N = \sum_{\ell,\sigma} n_{\sigma}(\ell)$. The second quantization form of the classicalizing modification, however, presupposes a fixed electron number. Considering that $A(0,0) = N$, the above term in fact represents the variance in the total electron number. A fully realistic description of the superconducting state must assume a fixed number of electrons, and the term must therefore be regarded as an artefact of the BCS model. It will be subtracted from the expression (4.137) in the following.

What remains open is the generalization of the expression (4.137) to the case of nonzero momentum displacement $\mathbf{k} \neq 0$. Here, the transformed vector

$$\begin{aligned} A(\mathbf{s}, \mathbf{k}) |0\rangle &= \sum_{\ell} \prod_{\mathbf{k}' \neq \ell, \ell-\mathbf{k}} \left[u_{\mathbf{k}'} + v_{\mathbf{k}'} c_{\uparrow}^{\dagger}(\mathbf{k}') c_{\downarrow}^{\dagger}(-\mathbf{k}') \right] e^{i\ell \cdot \mathbf{s}} u_{\ell-\mathbf{k}} v_{\ell} |\ell - \mathbf{k} \uparrow, -\ell \downarrow\rangle \\ &\quad + \sum_{\ell} \prod_{\mathbf{k}' \neq -\ell, \mathbf{k}-\ell} \left[u_{\mathbf{k}'} + v_{\mathbf{k}'} c_{\uparrow}^{\dagger}(\mathbf{k}') c_{\downarrow}^{\dagger}(-\mathbf{k}') \right] e^{i\ell \cdot \mathbf{s}} u_{\mathbf{k}-\ell} v_{-\ell} |-\ell \uparrow, \ell - \mathbf{k} \downarrow\rangle \\ &= \sum_{\ell} \prod_{\mathbf{k}' \neq \ell, \ell-\mathbf{k}} \left[u_{\mathbf{k}'} + v_{\mathbf{k}'} c_{\uparrow}^{\dagger}(\mathbf{k}') c_{\downarrow}^{\dagger}(-\mathbf{k}') \right] \left(u_{\ell-\mathbf{k}} v_{\ell} e^{i\ell \cdot \mathbf{s}} + u_{\ell} v_{\ell-\mathbf{k}} e^{i(\mathbf{k}-\ell) \cdot \mathbf{s}} \right) |\ell - \mathbf{k} \uparrow, -\ell \downarrow\rangle \end{aligned} \quad (4.139)$$

represents a sum over BCS states where all but two of the Cooper pair states $(\mathbf{k}' \uparrow, -\mathbf{k}' \downarrow)$ are occupied by either no or both electrons. The remaining ℓ -th and $\ell - \mathbf{k}$ -th Cooper pair configurations are only singly occupied. Therefore, in the scalar product of the vector (4.139) with itself, the only nonzero summands are those where the same pairs are broken on both sides,

$$\langle 0 | A^{\dagger}(\mathbf{s}, \mathbf{k}) A(\mathbf{s}, \mathbf{k}) | 0 \rangle = \sum_{\ell} \left\{ v_{\ell}^2 u_{\ell-\mathbf{k}}^2 + v_{\ell-\mathbf{k}}^2 u_{\ell}^2 + 2v_{\ell} u_{\ell-\mathbf{k}} v_{\ell-\mathbf{k}} u_{\ell} \cos[(2\ell - \mathbf{k}) \cdot \mathbf{s}] \right\}. \quad (4.140)$$

Altogether, the coherence decay rate (4.134) consists of two distinct contributions, $\Gamma = \Gamma_{\text{deph}} + \Gamma_{\text{diff}}$. The first is a pure dephasing term which does not rely on any momentum displacement induced by the classicalizing modification,

$$\Gamma_{\text{deph}} = \frac{1}{\tau} \int_V d^3s G(\mathbf{s}, 0) \left[\sum_{\ell} 2v_{\ell}^2 \cos(\ell \cdot \mathbf{s}) \right]^2 (1 - e^{i\Delta \mathbf{k} \cdot \mathbf{s}}). \quad (4.141)$$

It is sensitive to the momentum difference $\hbar \Delta \mathbf{k}$ between the two displaced Fermi spheres of the superposition. The further they are apart the more which-state information can be extracted by the classicalization-induced dephasing. The rate thus grows quadratically with the number of electrons in each Fermi sphere which do not overlap with the other Fermi sphere, $\Gamma_{\text{deph}} \sim (N \Delta k / k_F)^2$, as follows from a thorough assessment of the decay rates in Appendix C.1. In a sense, it is merely the electrons in those disjunct zones at the opposite ends of the two spheres that constitute the two separate ‘arms’ of the superposition in momentum space. The bulk of indistinguishable electrons occupies the same states in both branches, $|j_1\rangle$ and $|j_2\rangle$. Hence, the quadratic dependence of

the dephasing rate on the electron number (i.e. mass) in the two disjunct arms can be viewed as the analogue to the quadratic mass dependence of the coherence decay rate for the center-of-mass superpositions of compound particles studied in Section 4.1.5.

The second decay term Γ_{diff} is related to heating (and pair-breaking) by momentum diffusion,

$$\Gamma_{\text{diff}} = \frac{1}{\tau} \int_V d^3s \sum_{\mathbf{k} \neq 0} G(s, \mathbf{k}) \sum_{\ell} \{v_{\ell}^2 u_{\ell-\mathbf{k}}^2 + v_{\ell-\mathbf{k}}^2 u_{\ell}^2 + 2v_{\ell} u_{\ell-\mathbf{k}} v_{\ell-\mathbf{k}} u_{\ell} \cos[(2\ell - \mathbf{k}) \cdot \mathbf{s}]\}, \quad (4.142)$$

which leads to a gradual coalescence of both Fermi spheres. Note that this decay rate generally embodies the heating loss of the occupation of the BCS ground state (whether it carries a supercurrent or not), and therefore does not depend on the actual displacement of the two superimposed persistent current states. Similar to the diffusion heating of compound objects studied in Section 4.2.1.1, one would expect the diffusion rate Γ_{diff} to grow linearly in proportion to the total number of available electrons $N = 2N_s$. It is shown in Appendix C.1 that the rate is in fact limited by $\Gamma_{\text{diff}} \leq N/\tau$. This maximum, however, is only reached once the momentum standard deviation of the distribution function $G(s, \mathbf{k})$ is greater than the Fermi momentum, $\sigma_q > \hbar k_F$. For lower values of σ_q , the inner electrons of the Fermi sea are inaccessible and cannot be lifted into unoccupied momentum states due to the Pauli exclusion principle and the superconducting energy gap.

In summary, the classicalization-induced decay of a superposition state of distinct supercurrents is generally enhanced by the number N of electrons in the metal. The larger the underlying superconducting loop the stronger the classicalizing effect would act on such superpositions in the experiment. It turns out that, in practice, the diffusion effect outdoes the dephasing part for the most part, and so the coherence decay scales at most linearly with the loop size. A concrete example will follow in Section 4.3.2.4.

4.3. The measure of macroscopicity

After the detailed discussion of the implications of generic classicalizing modifications, we are finally in a position to formulate the central result of this chapter: a quantitative measure of macroscopicity. This measure μ , which will be introduced in the following, quantifies the class of classicalizing modifications which are ruled out by the concrete observation of a quantum phenomenon, that is, the extent to which the validity of quantum mechanics is tested against the hypothesis of classical macroscopic realism. The latter being grounded in the striking empirical evidence that the everyday world follows the laws and principles of classical (Newtonian) physics, it qualifies as the most natural footing for quantifying and comparing the degree of macroscopicity achieved in quantum experiments on arbitrary mechanical systems.

The benefits of such an approach are clear. It depends neither on the formal representation of quantum phenomena in terms of specific classes of states and observables nor on the complexity thereof. Quite contrarily, the measure μ is derived from the hypothetical predictions of classicalizing modifications and their falsification by observation. The natural scaling behaviour of the classicalization effect with the size and complexity of mechanical systems is based on only two basic invariance principles (see Section 4.1.4.1), and it thus provides a minimal and unbiased gauge for the quantum-to-classical transition. Even more so, the approach respects and builds upon the well-established symmetry principles behind both Schrödinger quantum mechanics and Newtonian mechanics, most prominently Galilean covariance. It does not refer to any particular macro-realistic

extension of the standard Schrödinger equation by nonlinear and stochastic terms which might embody new physics beyond the scope of standard nonrelativistic quantum theory, such as quantum effects of gravity [151,177]. Instead it refers merely to the observable consequences of a generic hypothetical classicalization effect that are described by the minimally invasive modification of the time evolution of the many-body state operator studied in this chapter. Quantum superposition states decay into classical mixtures over time while the Newtonian equations of motion are kept intact.

4.3.1. Definition of the macroscopicity measure

The strength of the classicalization effect is determined by the distribution function $g_0(s, q)$ and the time parameter τ_0 associated with a fixed but arbitrary reference mass m_0 . The realization of nonclassical states in a given experiment immediately rules out a certain parameter set of the hypothetical modification which would predict a higher loss of quantum coherence than observed. The rationale behind the present measure of macroscopicity is to call one quantum state more macroscopic than another if the experimental demonstration of the former rules out a larger parameter set than the latter. What remains to be found is a robust way of quantifying the size of the excluded parameter set.

As will be shown in the following, the time parameter τ_0 turns out to be the apparent and most natural candidate. The reason is that the classicalizing modification always predicts a minimal coherence time for every given mechanical system and irrespectively of the functional form of the distribution g_0 . It is, in a sense, the universal property of all modifications falling under the generic class studied here. Nevertheless, a concrete numerical assessment of the macroscopicity requires additional restrictions on the form of the distribution function (without affecting the generality of the results). They will be motivated in the following, before the formal definition of μ will eventually be given in Section 4.3.1.4. The remainder of this chapter will then be spent applying the measure to the various manifestations of quantum superpositions in large mechanical systems which have been and will be observed in past and future experiments.

4.3.1.1. The electron as a natural reference point particle

At this point it is time to decide for the reference mass m_0 fixing the reference time parameter and the reference phase-space distribution in all the quantitative considerations to follow. The domain of standard, nonrelativistic, quantum mechanics begins at the level of electrons and nuclei, and the theory was originally developed to understand and assess the nonclassical behaviour of atoms. The quantum description of more complex systems of matter is often broken down into these elementary building blocks whose physical behaviour is well understood. Indeed, when observing quantum behaviour in larger systems of matter, scientists are often inclined to count the number of electrons or atoms involved in order to get an idea about the ‘size’ of the quantum observation.

Hence the electron, being the canonical elementary point particle in (nonrelativistic) quantum mechanics, qualifies naturally as the reference mass unit for the present purposes. From now on, the reference mass is once and for all set to $m_0 = m_e$. The classicalization effect is then fully determined by specifying the coherence time parameter $\tau_0 = \tau_e$ and the distribution function $g_0(s, q) = g_e(s, q)$ for an electron.

4.3.1.2. Minimizing parameter space with a Gaussian distribution

Throughout the discussion we have found that, when it comes to parametrizing the strength of the classicalization effect, three parameters mainly determine its generic behaviour: The time parameter τ_e and the two standard deviations σ_s and σ_q of the positive, normalized and isotropic distribution function $g_e(s, q)$. The most natural implementation of these parameters is then obtained by means of the Gaussian form

$$g_e(s, q) = \frac{1}{(2\pi\sigma_s\sigma_q)^3} \exp\left(-\frac{s^2}{2\sigma_s^2} - \frac{q^2}{2\sigma_q^2}\right). \quad (4.143)$$

It represents the most natural choice of a zero-mean distribution function, which is solely determined by its second moments, and it does not exhibit any particular difficult-to-justify features that would involve additional parameters to describe them. I therefore operate with this Gaussian form in the following in order to minimize the numerical effort as well as the number of ad-hoc parameters introduced with the classicalization effect. The Fourier transform (4.40) of the reference distribution reads as

$$\tilde{g}_e(\mathbf{r}, \mathbf{p}) = \exp\left(-\frac{\sigma_q^2 r^2}{2\hbar^2} - \frac{\sigma_s^2 p^2}{2\hbar^2}\right). \quad (4.144)$$

4.3.1.3. Parameter limitations on the subatomic scale

At first sight, the three parameters $(\sigma_s, \sigma_q, \tau_e)$ of our model could in principle assume any value larger than zero, and they would only be constrained by the experimental observation of quantum phenomena in mechanical systems. There is, however, also a fundamental restriction due to the limited scope of the underlying framework. Although standard quantum theory is well suited to assess the electronic level structure of atoms, it fails in describing the internal binding and structure of nuclei. This is where nonrelativistic mechanics ceases to be valid, and, with it, the classicalizing modification that builds upon its basic principles. We must therefore exclude the (sub-)nuclear domain from our considerations by restricting the parameter space in the following way:

According to Section 4.1.5, the classicalization of a compound object will start depending on the internal motion of its constituents once their mean variance in the relative position and momentum coordinates becomes comparable to the parameters $\sigma_{s,q}$. For example, the classicalization of an atom will depend on its electronic level structure if $\hbar/\sigma_q \lesssim 1 \text{ \AA} \lesssim \sigma_s$. Similarly, the relative state of motion of protons and neutrons inside atomic nuclei becomes relevant for $\hbar/\sigma_q \lesssim 10 \text{ fm} \lesssim (m_e/1 \text{ amu}) \sigma_s$. In order to avoid this, the classicalization parameters should be limited to $\sigma_s \lesssim 20 \text{ pm}$ and $\hbar/\sigma_q \gtrsim 10 \text{ fm}$. The exact numbers will be of no relevance, and they could easily be varied by a few orders of magnitude without altering the upcoming results.

4.3.1.4. Formal definition of the macroscopicity

Let me finally state the formal definition of the measure of macroscopicity μ , assuming the Gaussian form (4.143) of the classicalization distribution and respecting the above nuclear constraint on $\sigma_{s,q}$. The macroscopicity of a quantum superposition state is defined with respect to a concrete experimental realization. Assuming the existence of the classicalizing modification, the measurement rules out those parameter values $(\sigma_s, \sigma_q, \tau_e)$ which would predict a lower ‘visibility’ of the

superposition state than observed. To be concrete, the experiment rules out all coherence time parameters smaller than a certain boundary value $\tau_e(\sigma_s, \sigma_q)$ for any fixed value of (σ_s, σ_q) . The function $\tau_e(\sigma_s, \sigma_q)$, which is defined on the constrained set of (σ_s, σ_q) in this way, separates the excluded parameter range from the rest.

I suggest to measure the macroscopicity by the maximum of this function, that is, by the *greatest excluded time parameter* τ_{\max}

$$\mu = \log_{10} \left(\frac{\tau_{\max}}{1 \text{ s}} \right). \quad (4.145)$$

The time is expressed in units of seconds to fix a scale, and the logarithm is taken to handle the vast spread of τ_{\max} -values when comparing the numerous real experiments with one another. Positive values of μ are obtained, for instance, by demonstrating the wave nature of electrons over more than one second.

In the following, I will illustrate with the help of concrete examples why the greatest excluded time parameter appears as the most natural and robust choice to quantify macroscopicity. I will then proceed with the evaluation of μ for a broad selection of quantum superposition experiments.

4.3.2. Assessing the macroscopicity of quantum experiments

In order to compute the macroscopicity μ for a concrete quantum experiment, the classicalizing modification must be incorporated into the underlying theoretical model, and the modified solution must be compared with the measurement data as a function of the classicalization parameters $(\sigma_s, \sigma_q, \tau_e) \in \mathbb{R}_+^3$. This calls for an individual procedure in each case which results in the specification of a functional dependence $\tau_e(\sigma_s, \sigma_q)$ describing the boundary between the compatible and the incompatible parameter region. Nevertheless, the general form of the boundary, as well as a generic estimate of the macroscopicity, can be obtained for most standard cases.

Figure 4.2 provides an overview of typical experiments that narrow down the allowed parameter range of the classicalization effect, as will be discussed one by one in the following. Here, the largest excluded time parameters are plotted as a function of the length scale \hbar/σ_q associated to the momentum width σ_q of the Gaussian reference distribution, and at the fixed position width $\sigma_s = 20 \text{ pm}$. The case of de Broglie interference with point particles is represented by the solid line, as obtained from the optical Mach-Zehnder type interference experiment with cesium atoms in [166]³⁰. A different behaviour is observed when the interfering particles are composed of more than a single nucleus. The dashed line in the diagram corresponds to the Talbot-Lau interference experiment with gold clusters of 10^7 amu proposed in [11] and discussed in Chapter 3, page 114ff. The other end of the spectrum, where the interfering object is much larger than the interference path separation, is represented by the dash-dotted line. It derives from the proposed superposition experiment [170] with oscillatory states of ground-state cooled micromirrors. Finally, the dotted curve stands for a genuine many-body quantum phenomenon: The superposition of counter-rotating persistent currents in a superconducting loop, as observed in [1].

Before proceeding in the discussion of the listed cases I note once again that the classicalization can also be tested by means of purely classical experiments. This is due to the inherent diffusion effect which leads to an average energy increase in both classical and quantum systems alike. As an

³⁰ The atom mass is mainly concentrated in the femtometer-sized nucleus, and the small contribution of the electrons is negligible. It can therefore be regarded as a point particle in the present context.

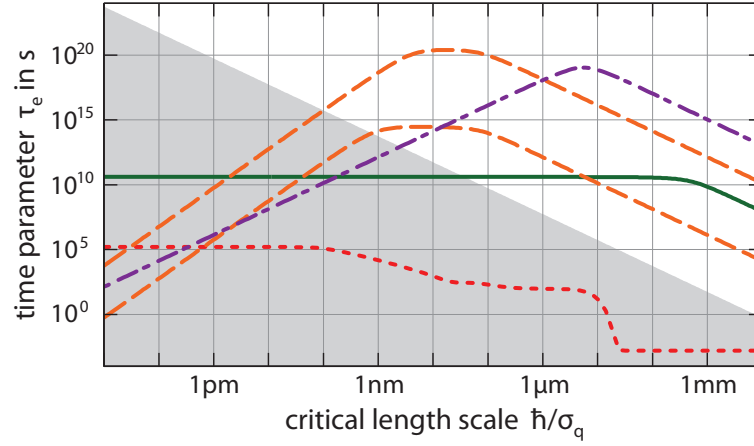


Figure 4.2. Upper bounds from various experiments on the excluded time parameter $\tau_e(\sigma_q)$ at the fixed position width $\sigma_s = 20$ pm. The curves are shown for the relevant range of momentum widths σ_q as a function of the associated length scale \hbar/σ_q . All parameter values below each curve are ruled out by the respective experiment. The solid line represents the single-atom interferometer realized in [166], while the dotted line results from the demonstration of superpositions of counter-rotating supercurrents in [1]. The dashed and the dash-dotted lines correspond to proposed interference experiments with heavy gold clusters [11] and oscillating micromirrors [170]. The shaded area represents the parameters ruled out by a classical temperature measurement (see text for details).

example, the shaded area in Figure 4.2 represents the parameter range excluded by a hypothetical precision measurement of temperature: Assume that one measures the temperature increase of a free gas of rubidium atoms to be less than, say, $1 \mu\text{K/s}$. Then the momentum diffusion rate would be limited by

$$\left(\frac{87 \text{ amu}}{m_e}\right)^2 \frac{\sigma_q^2}{2m_e \tau_e} < \frac{3}{2} k_B \times 1 \frac{\mu\text{K}}{\text{s}}. \quad (4.146)$$

It does not make sense, however, to ascribe a macroscopicity to such a classical experiment as it does not depend on the quantum behaviour of the system. Hence, it does not actually test quantum predictions against classical physics.

4.3.2.1. De Broglie interference of point-like particles

The simplest and most instructive class of mechanical superpositions is given by de Broglie interference experiments with point-like particles. They can be described by a single center-of-mass degree of freedom which dynamically evolves into a quantum superposition state (with the help of diffractive elements in the experimental setup).

From the perspective of the classicalization effect, a point particle is generally understood as a (rigid) body of total mass m , which is smaller than the length scale \hbar/σ_q associated to the momentum spread of the reference distribution. The internal structure of the object then remains unaffected, as discussed in Section 4.1.5. Disregarding the light electronic shell, atoms can always be regarded as point particles because the classicalization effect is restricted to the super-femtometer regime. The solid line in Figure 4.2 stands as a prime example for atomic point-particle interference. More generally, we may speak of point-particle interference if the particle size a is by orders of magnitude smaller than the interference path separation D of a given setup.

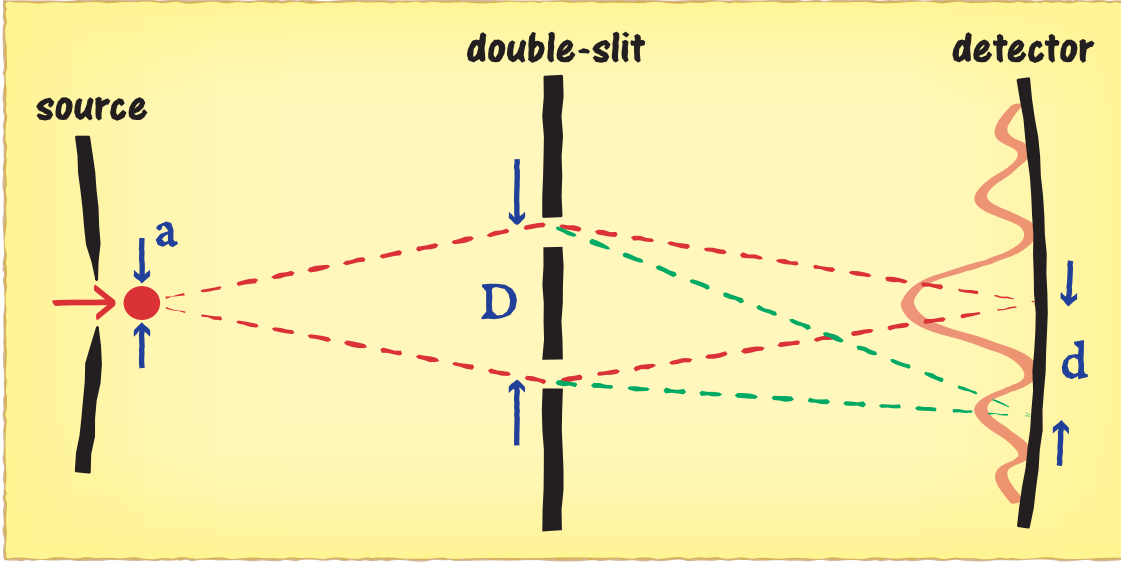


Figure 4.3. Schematic view of a double slit interferometer with point-like particles of diameter a . Given a sufficiently coherent initial state, the particles may traverse the interferometer along two distinct paths to the detection point on the screen. The characteristic path separation is determined by the slit distance D . Constructive interference is observed at points of distance d where the accumulated phase differs between the arms by multiples of 2π .

Let me illustrate this by the simple double-slit setup sketched in Figure 4.3. Many interferometer setups can be broken down to a similar scheme. An incoming point-like particle may follow two (or more) distinct paths from the source to the detection screen, which are separated by many times the particle size at almost every instant during passage. In the end an interference fringe pattern in the density distribution $\langle r|\rho|r \rangle$ is detected (e.g. on a screen). Its ‘visibility’ depends on the Fourier amplitude of the observed fringe oscillation, which can be expressed in terms of the characteristic function (4.37) of the state ρ . The expression

$$\chi\left(0, -\frac{h}{d}\mathbf{n}\right) = \int d^3r \langle r|\rho|r \rangle \exp\left(-\frac{2\pi i \mathbf{n} \cdot \mathbf{r}}{d}\right) \quad (4.147)$$

describes the Fourier component of an oscillatory contribution to the detection signal along the axis \mathbf{n} with period d . The latter determines the position of the first interference maximum, $d = ht/mD$, given the time of flight t to the detection plane.

The classicalization effect is easily implemented using the single-particle solution derived in Section 4.2.2. For every stretch of free propagation over the time t between the coherent source, the diffractive element(s) and the detector of a given setup the above visibility term (4.147) is damped by an exponential factor, as stated in Equation (4.113). Following the example of Figure 4.3, the time of flight between the double slit and the detection screen results in a reduction of the visibility by the factor

$$\begin{aligned} R_t\left(\frac{h}{d}\right) &= \exp\left\{\left(\frac{m}{m_e}\right)^2 \frac{1}{\tau_e} \left[\int_0^t dt' \tilde{g}_e\left(\frac{ht'}{md}\mathbf{n}, -\frac{m_e h}{md}\mathbf{n}\right) - t \right]\right\} \\ &= \exp\left\{\left(\frac{m}{m_e}\right)^2 \frac{t}{\tau_e} \left[\sqrt{\frac{\pi}{2}} \frac{\hbar}{\sigma_q D} \exp\left[-\frac{1}{2} \left(\frac{2\pi m_e \sigma_s}{md}\right)^2\right] \operatorname{erf}\left(\frac{\sigma_q D}{\sqrt{2}\hbar}\right) - 1 \right]\right\} \end{aligned} \quad (4.148)$$

The propagation from the coherent source to the double slit must be taken into account as well. It yields another factor of this form. The interference visibility is altogether reduced by $R_{t_0}R_t$, with $t_{\text{tot}} = t + t_0$ the time of flight from the source to the detector.

Note that the position spread σ_s of the classicalization is an irrelevant factor for all practical purposes, as it is bound by $\sigma_s \lesssim 20$ pm. The mass-rescaled width $m_e\sigma_s/m$ for the classicalization of atoms and other large particles is even smaller, and the fringe period d of any realistic interference pattern surpasses it by many orders of magnitude. The σ_s -dependence in (4.148) can safely be neglected.

We distinguish two limiting cases for the visibility reduction by classicalization.

- ★ **The saturated regime** The strongest effect is achieved in the limit of large momentum spreads σ_q of the classicalization distribution where the associated length scale is much smaller than the arm separation, $\hbar/\sigma_q \ll D$. The decay of coherence then saturates at the rate given by the mass-scaled coherence time scale, $1/\tau = (m/m_e)^2/\tau_e$, and we may approximate the reduction factor (4.148) by

$$R_t \approx \exp \left[- \left(\frac{m}{m_e} \right)^2 \frac{t}{\tau_e} \right]. \quad (4.149)$$

In total, the visibility is reduced by the factor $R_{t_0}R_t \approx \exp \left[-m^2 t_{\text{tot}}/m_e^2 \tau_e \right]$. This is the strongest reduction the classicalizing modification may cause. It explains the left part of the solid curve in Figure 4.2, which saturates at length scales below the 1 mm path separation of the interferometer [166]. It also explains the flat maximum of the dashed curve that roughly extends from $\hbar/\sigma_q \sim 10$ nm to 100 nm. The saturated classicalization of point-like particles is a valid approximation in the length scale regime $a \ll \hbar/\sigma_q \ll D$.

- ★ **The diffusive regime** If the momentum width σ_q is very small, $\hbar/\sigma_q \gg D$, the classicalization effect hardly distinguishes the different paths through the interferometer, and the visibility reduction is suppressed. We obtain the approximate reduction factor

$$R_t \approx \exp \left[- \frac{1}{6} \left(\frac{\sigma_q D}{\hbar} \right)^2 \left(\frac{m}{m_e} \right)^2 \frac{t}{\tau_e} \right] \quad (4.150)$$

after expanding the error function in (4.148) to the lowest order. The exponent is quadratically suppressed by $\sigma_q D/\hbar \ll 1$ with respect to the saturated case. As before, the time t must be replaced by the total time of flight t_{tot} to obtain the full visibility reduction. The quadratic dependence of the logarithmic reduction of visibility on the momentum width σ_q represents a general feature of the diffusive limit where spatial superposition states are too small to be resolved³¹. In particular, it explains that the solid, the dashed and the dash-dotted interference curves exhibit the same slope of 2 vertical orders of magnitude per horizontal order of magnitude on the right side of the double-logarithmic plot in Figure 4.2. This is easily checked by taking the logarithm of (4.150) and expressing the time parameter τ_e as a function of $\log(\hbar/\sigma_q)$.

³¹ One observes the same behaviour in the case of thermal decoherence at low temperatures [218], where the average photon wavelength is greater than the path separation.

The visibility reduction by classicalization can now be compared to the measured fraction $f < 1$ of the interference visibility predicted by standard quantum theory. In realistic interference experiments, the measurement is always affected by noise, uncertainties and limited accuracy, and it therefore never reaches the full 100% of the theoretically predicted visibility. Even if the recorded data fits to the theory within an error range of, say, 5%, then the fraction cannot be larger than $f = 95\%$.

By varying the momentum width parameter σ_q we obtain time parameters $\tau_e(\sigma_q)$ that are ruled out by the measurement, as plotted in Figure 4.2. Their maximum determines the macroscopicity value (4.145). For interference experiments with point-like particles the maximum is found in the saturated regime, where the visibility reduction factor reads as (4.149). Given the observed fraction f , the reduction factor is bound from below by $R_t \geq f$, and we may approximate the macroscopicity by

$$\mu \approx \log_{10} \left[\left| \frac{1}{\ln f} \right| \left(\frac{m}{m_e} \right)^2 \frac{t_{\text{tot}}}{1 \text{ s}} \right]. \quad (4.151)$$

The time t_{tot} should include all stretches of free propagation pieced together from the coherent source to the detection plane³². In the case of the cesium interferometer in [166] coherence was maintained for over $t_{\text{tot}} = 320$ ms, and a fringe visibility of $f = 62\%$ instead of the ideally expected 100% was recorded (see Figure 19 of [166]). Using a mass of $m = 137$ amu leads to the macroscopicity $\mu = 10.6$. That is to say, the greatest time parameter excluded by this experiment is $\tau_{\text{max}} = 4 \times 10^{10}$ s, the value to which the solid curve in Figure 4.2 saturates.

In principle, the expression (4.151) can be used to compute the macroscopicity of arbitrary de Broglie interference experiments with point-like particles (i.e. $a \ll D$). In practice, however, it is not always obvious how to obtain a value for the fraction f of confidently measured versus theoretically expected interference visibility. (If the latter is a loosely defined quantity, for instance.) I proceed by presenting methods to extract estimated values for f and μ from various matter-wave experiments.

Mach-Zehnder setup Mach-Zehnder-type interferometers [18] offer a direct relation between the observed fringe visibility and the reduction factor f . Many modern high-precision atom interferometers with large arm lengths and long interrogation times, e.g. [166, 167], are based on an optical Mach-Zehnder scheme comprised of a sequence of three laser pulses. Each pulse consists of two counterpropagating laser waves driving a Raman transition between the initial state $|0\rangle$ and the metastable state $|1\rangle$ of an atom. Each transition comes with a net momentum kick of $\pm \hbar k$ along the direction of the laser waves, denoted here as the x -axis. The center-of-mass motion of the atom may thus be treated in one dimension.

The first $\pi/2$ -pulse splits the incoming atoms coherently among two diverging paths corresponding to the internal states $|0\rangle$ and $|1\rangle$, where the latter differs in momentum by $\hbar k$. This is described by the unitary splitting transformation

$$U_{\pi/2} = \frac{1}{\sqrt{2}} (|0\rangle + e^{ikx}|1\rangle) \langle 0| + \frac{1}{\sqrt{2}} (|1\rangle - e^{-ikx}|0\rangle) \langle 1| \quad (4.152)$$

³² We must only include those parts of the setup where a loss of coherence in the particle state affects the interference visibility. This excludes, for instance, anything that happens before the first collimation slit in a double-slit experiment representing the point source. In a Talbot-Lau setup we must only consider the passage from the first to the second and from the second to the third grating.

acting on the initial product state of the atomic ensemble $\rho_0 \otimes |0\rangle\langle 0|$. The second π -pulse at time T flips the internal state and exerts opposite momentum kicks in each arm,

$$U_\pi = e^{ikx}|1\rangle\langle 0| + e^{i\Delta\phi}e^{-ikx}|0\rangle\langle 1|, \quad (4.153)$$

which makes both arms converge again. The term $\Delta\phi$ is added here to account for a tunable net phase difference between the two arms. They rejoin after another time T , where another $\pi/2$ -pulse is applied to close the path scheme. By detecting the atoms after the third pulse in one of its internal states, say $|0\rangle$, one records the sinusoidal interference pattern $I(\Delta\phi) = \langle 0|\text{tr}\left(U_{\pi/2}\rho_{2T}U_{\pi/2}^\dagger\right)|0\rangle$ as a function of the phase difference $\Delta\phi$. The state ρ_{2T} before applying the third laser pulse reads as

$$\rho_{2T} = \mathcal{T}\left\{U_\pi\left[\mathcal{T}\left(U_{\pi/2}\rho_0 \otimes |0\rangle\langle 0|U_{\pi/2}^\dagger\right)\right]U_\pi^\dagger\right\}, \quad (4.154)$$

where the superoperator \mathcal{T} denotes the modified free evolution³³ of the motional state by the time T . We find that the fringe contrast \mathcal{V} is directly given by the characteristic function of the quasi-state operator $\langle 0|\rho_{2T}|1\rangle$,

$$\mathcal{V} = 2\left|\langle 0|\text{tr}\left(e^{ikx}\rho_{2T}\right)|1\rangle\right| = 2\left|\chi_{\langle 0|\rho_{2T}|1\rangle}(0, \hbar k)\right|. \quad (4.155)$$

A visibility of $\mathcal{V} = 100\%$ is predicted in the absence of classicalization, and we may thus identify the fraction f with the measured interference contrast. The classicalizing modification contributes a reduction factor $R_T(\hbar k)$ of the form (4.148) for each free propagation \mathcal{T} , and the visibility reduces to

$$\mathcal{V} = R_T^2(\hbar k) = \exp\left\{\left(\frac{m}{m_e}\right)^2 \frac{2T}{\tau_e} \left[\sqrt{\frac{\pi}{2}} \frac{m}{\sigma_q k T} \text{erf}\left(\frac{\sigma_q k T}{\sqrt{2}m}\right) - 1\right]\right\}, \quad (4.156)$$

where the σ_s -term has been neglected. Identifying this reduction with the measured visibility $f < 1$ yields the critical time parameter,

$$\tau_e(\sigma_q) = \left|\frac{1}{\ln f}\right| \left(\frac{m}{m_e}\right)^2 \left[2T - \frac{\sqrt{2\pi}m}{\sigma_q k} \text{erf}\left(\frac{\sigma_q k T}{\sqrt{2}m}\right)\right]. \quad (4.157)$$

All values below $\tau_e(\sigma_q)$ are ruled out by the experiment. The solid curve in Figure 4.2 displays this function using the parameters $m = 133$ amu, $T = 160$ ms and $\hbar k/m = 7.0$ mm/s from [166].

The function (4.157) saturates at the maximum value $\tau_{\max} = 2Tm^2/m_e^2|\ln f|$ for large $\sigma_q \gg m/kT$, which confirms the macroscopicity formula (4.151). A more recent experiment of the same type [167] yielded a visibility of $f \approx 1/3$ (as extracted from Figure 3 in the reference) at a time of flight $2T = 800$ ms, which results in a macroscopicity of the same size, $\mu = 10.6$. Significantly higher values can be reached in atom interferometry only by increasing the interrogation time T beyond the currently feasible range. In [219] the authors proposed to realize a similar cesium interferometer with $T \approx 2000$ s between far apart satellites in space. It would correspond to $\mu = 14.5$ if a contrast of $f = 0.5$ were to be measured.

Apart from the three-pulse interferometer, Mach-Zehnder schemes are also realized by means of three material gratings [18]. The above reasoning applies here as well, except that the two arms are given by two subsequent diffraction orders at the grating.

³³ The presence of a constant acceleration would only contribute to the phase difference.

Specifically, let us consider the Na₂-interferometer setup with three identical 200 nm gratings and 30% opening fraction in [125]. The two arms originate from the 0th and the 1st order diffraction components of the first grating, followed by a 1st order and –1st order diffraction at the second grating. Standard diffraction theory states that their weight ratio P_1/P_2 is given by the squared ratio between the 1st and the 0th Fourier component of the periodic grating aperture function, $P_1/P_0 = (b_1/b_0)^2 = \text{sinc}^2(0.3\pi) = 0.74$. Interactions with the grating walls are negligible. The sinusoidal fringe pattern is detected through the movable third grating mask, which modulates the contrast by another factor $b_1/b_0 = 0.86$. In total, the unmodified interference visibility is limited to $\mathcal{V} = 2b_1\sqrt{P_1P_0}/b_0(P_1 + P_0) = 0.85$. The authors of [125] depict a fringe pattern with about 30% contrast in their Figure 4, that is, a fraction $f = 0.3/0.85 = 0.35$ of the theoretical value. The Na₂ molecules ($m = 46$ amu) traverse the total distance $L = 2.1$ m from the coherent source to the third grating at the mean velocity $v = 820$ m/s [125, 220], which results in the macroscopicity value $\mu = 7.2$.

Ramsey-Bordé setup Besides the optical Mach-Zehnder setup, the coherent path splitting by light coupled to an internal transition is also used in the Ramsey-Bordé interferometer scheme [221]. It consists of two separated pairs of co-propagating running-wave lasers, where each laser splits an incoming particle beam into two momentum-displaced arms corresponding to different internal states. The arms rejoin at the second laser pair pointing into the opposite direction, and the resulting interference pattern is measured by state-selective detection as a function of the phase shift between the arms. In general, however, more than two arms are mixed into the detection signal.

A Ramsey-Bordé experiment with I₂ molecules ($m = 254$ amu) was realized in [222], where a total of four different paths overlapped at the detector. Two of those paths are Doppler-shifted with respect to each other, that is, their phase difference depends on the transverse velocity of the particles. Their interference is thus averaged out over the velocity distribution of the particle beam, and the fringe pattern is only due to the other two paths. This limits the fringe contrast to 50%. We can read off a measured value of roughly $400/2400 = 1/6$ from the central fringe plotted in Figure 2 of [222], which results in the fraction $f = 1/3$. The I₂ molecules traverse the interferometer of about 35 mm length with a mean velocity of 350 m/s in $t = 100$ μ s. Formula (4.151) then yields an approximate macroscopicity of $\mu = 7.3$.

Diffraction at one-dimensional structures The biggest class of matter-wave interference experiments involves the diffraction at small one-dimensional structures in the near and far field. Slits, double-slits and thin gratings are the most commonly used diffractive elements; they are mathematically described by a transmission function $t(x)$, which is multiplied to the wave function upon traversal. Standard Fresnel diffraction theory in the paraxial approximation tells us that the resulting interference pattern for particles from a monochromatic point source at $x_0 = 0$ is given by $S_{v_z}(x) \propto |\int dx_1 \psi(x_1; x)|^2$, with

$$\psi(x_1; x) = t(x_1) \exp \left[\frac{im}{2\hbar} \left(\frac{x_1^2}{T_1} + \frac{x_1^2 - 2xx_1}{T_2} \right) \right]. \quad (4.158)$$

The x -variable represents the position on the detection plane, the terms T_1 and T_2 denote the times of flight from the source to the diffractive element and from there to the detection plane, respectively. In most cases the latter depend on the velocity v_z of the particles traversing the distances

L_1 and L_2 between the setup elements. We must therefore average the interference signal over the distribution $F(v_z)$ of velocities present in the beam. In addition, the signal must be averaged over the finite source aperture $A_S(x_S)$ to account for realistic orifices, and it must be convolved with the function $A_D(x_D)$ to account for the finite x -resolution of a realistic detector. The resulting signal formula,

$$S(x) = \int dv_z F(v_z) \int dx_S A_S(x_S) \int dx_D A_D(x_D) S_{v_z}\left(x + x_D - \frac{T_2}{T_1} x_S\right), \quad (4.159)$$

may then be used to predict realistic values for the fringe visibility observed in the experiment. On the other hand, the averaging is irrelevant in the assessment of the coherence-reducing effect due to the classicalizing modification. Once again we find that the latter modulates the ideal fringe pattern by reduction factors of the form (4.148),

$$\begin{aligned} S_{v_z}(x) &= \int dx_1 dx_2 R(x_2 - x_1) \psi(x_1; x) \psi^*(x_2; x), \\ R(x) &= R_{T_1}\left(\frac{mx}{T_1}\right) R_{T_2}\left(\frac{mx}{T_2}\right) \\ &\approx \exp\left\{\left(\frac{m}{m_e}\right)^2 \frac{T_1 + T_2}{\tau_e} \left[\sqrt{\frac{\pi}{2}} \frac{\hbar}{\sigma_q x} \operatorname{erf}\left(\frac{\sigma_q x}{\sqrt{2}\hbar}\right) - 1\right]\right\}. \end{aligned} \quad (4.160)$$

The influence of position translations is neglected in the last line; they are practically irrelevant as $\sigma_s \lesssim 20$ pm. Equation (4.160) is easily derived in the characteristic function representation, starting from the initial state of the coherent point source $\chi_0(x, p) \propto \delta(x)$ and ending at the signal formula $S_{v_z}(x) \propto \int dp \chi_{T_1+T_2}(0, p) \exp(-ipx/\hbar)/2\pi\hbar$. The diffraction transformation $\langle x|p|x'\rangle \mapsto t(x) \langle x|p|x'\rangle t^*(x')$ yields the convolution $\chi(x, p) \mapsto \int dq \tilde{T}(x, p - q) \chi(x, q)$, with the diffraction kernel³⁴

$$\tilde{T}(x, q) = \frac{1}{2\pi\hbar} \int ds e^{iqs/\hbar} t\left(s - \frac{x}{2}\right) t^*\left(s + \frac{x}{2}\right). \quad (4.161)$$

Using Formula (4.113) for the modified time evolution we arrive at the expression for the final state,

$$\chi_{T_1+T_2}(0, p) = \tilde{T}\left(-\frac{pT_2}{m}, p + p\frac{T_2}{T_1}\right) R_{T_2}(-p) R_{T_1}\left(p\frac{T_2}{T_1}\right). \quad (4.162)$$

A few more steps of substitution result in the signal formula (4.160), up to a normalization factor.

The macroscopicity of a concrete experiment is obtained by matching the computed signal (4.160) to the measured data as a function of the momentum spread, which yields the excluded time parameter curve $\tau_e(\sigma_q)$. However, there is a way to avoid an elaborate fitting procedure for every individual case and to estimate the macroscopicity by means of the approximation (4.151). Recall that the greatest excluded time parameter is always found at the largest possible values of σ_q in point-particle interference, where the associated length scale \hbar/σ_q is much smaller than any diffractive aperture used in practice. The reduction factor in (4.160) assumes its minimum $R(\infty)$ for all relevant values $|x_2 - x_1| \gg \hbar/\sigma_q$. We may thus approximate

$$S_{v_z}(x) \approx R(\infty) \left| \int dx_1 \psi(x_1; x) \right|^2 + \underbrace{\int dx_2 [R(x_2) - R(\infty)] \int dx_1 |t(x_1)|^2}_{\sim \text{few } \hbar/\sigma_q}, \quad (4.163)$$

³⁴ The kernel is similar to the diffraction kernels used in Chapter 3 to describe near-field interference in the Wigner function representation, except that the integration is over the center position here. See for instance page 72.

where the first summand represents the original interference pattern diminished by the factor $R(\infty)$ and the second term adds a small constant background to the signal. The latter is negligible when the fringe signal is only slightly reduced because the bracketed integral evaluates to merely a few times \hbar/σ_q .

I estimated the macroscopicity of a given diffraction experiment from the recorded fringe pattern as follows: First, I normalized the recorded signal by integrating over all data points and compared it to the theoretically expected interference pattern (4.159), which I computed using the same normalization (and standard numerical tools provided by MATLAB). The fraction f between the measured and the computed height of the first order diffraction peak then serves as a rough estimate for $R(\infty)$. Finally, I evaluated the macroscopicity by means of the approximation (4.151), using velocity-averaged times of flight T_1 and T_2 from the source to the detector. Table 4.1 lists the results and all necessary experimental parameters for a selection of diffraction experiments with neutrons [223, 224], atoms [225–227] and molecules [4].

Table 4.1. Estimated macroscopicities for a selection of diffraction experiments with neutrons, atoms and molecules. The first order diffraction peak value was compared in each cited interference plot to the theoretical prediction based on the experimental parameters; the ratio of both defines the fraction f . In the vertically aligned setup [226] atoms fall through a double slit and into the detector within 200 ms; the fraction f is determined as the ratio between the peak values in Figs. 3b (measured) and 3g (computed). The neutron interference at a biprism in [223] is modelled as a superposition of two virtual sources separated by d , at the distance $L_1 + L_2$ from the detector. I obtained f by comparing the data points (150 a.u. peak height) to the fitted curve (200 a.u. peak height) in Fig. 9, after subtracting a dark count rate of 60 a.u. In all other cases I computed the expected diffraction pattern of N -slit gratings of period d , which I averaged over the apertures of source and detector and over Gaussian velocity distributions of mean $\langle v_z \rangle$ and variance Δv_z^2 . (In [4] the C_{60} -molecules were detected by a Gaussian laser of waist D , and I used the velocity distribution provided in the article.) Macroscopicities are obtained from (4.151) with help of the average source-grating and grating-detector passage times $T_{1,2} = L_{1,2}/\langle v_z \rangle$.

Reference	[223]	[224]	[225]	[226]	[227]	[4]
Figure	9	7	2b	3b,g	1	2a
particle	n	n	^{23}Na	^{20}Ne	^{84}Kr	C_{60}
distance L_1	4 m	5 m	1 m	8 cm	45 cm	1.14 m
distance L_2	5.7 m	5 m	1.5 m	11 cm	52 cm	1.25 m
number of slits N	2	2	50	2	100	100
slit distance d	107 μm	126 μm	200 nm	6 μm	100 nm	100 nm
slit opening	n. a.	17%	50%	33%	43%	38%
source aperture S	10 μm	15 μm	10 μm	20 μm	10 μm	10 μm
detector aperture D	30 μm	30 μm	25 μm	20 μm	25 μm	8 μm
mean velocity $\langle v_z \rangle$	907 m/s	216 m/s	1 km/s	$\lesssim 1$ m/s	396 m/s	226 m/s
velocity width $\Delta v_z/\langle v_z \rangle$	—	0.05	0.12	—	0.1	0.6
estimated fraction f	0.6	0.9	0.5	0.8	0.8	0.6
macroscopicity μ	4.8	6.2	6.8	9.1	8.3	10.6

Talbot-Lau setup The TLI scheme was extensively studied in Section 3.2, page 83ff. The resulting interference signal in the detector forms a periodic fringe pattern $S(x) = \sum_{\ell} S_{\ell} \exp(2\pi i \ell x/d)$ as a function of the lateral position x of the third grating. The classicalization effect can be incorporated in the same way as standard decoherence processes with a similar master equation [40].

The explicit result follows from the above expression (4.160) describing the classicalized interference pattern generated by a generic diffraction element $t(x)$. In the TLI scheme the latter is given by the second grating, the first grating defines the source aperture, and the movable third grating represents the detection mask for the resulting interference signal $S(x)$, according to (4.159). A Fourier transformation reveals that the Fourier components S_{ℓ} are modified by the factors

$$S_{\ell} \mapsto S_{\ell} R\left(\ell \frac{h T_2}{m d}\right) = S_{\ell} R_{T_1}\left(\ell \frac{h}{d} \frac{T_2}{T_1}\right) R_{T_2}\left(\ell \frac{h}{d}\right). \quad (4.164)$$

They must be averaged over a longitudinal velocity distribution $F(v_z)$ in stationary TLIs where the times $T_{1,2}$ are determined by the fixed distances $L_{1,2} = v_z T_{1,2}$ between the gratings. We find that the sinusoidal visibility of Talbot-Lau interference is reduced by

$$\mathcal{V}_{\sin} \mapsto \mathcal{V}_{\sin} \exp \left\{ \left(\frac{m}{m_e} \right)^2 \left[\frac{\operatorname{erf}(\sqrt{2\pi} \sigma_q T / m d)}{\sqrt{2\pi} \sigma_q \tau_e / m d} \exp \left(-\frac{2\pi^2 m_e^2 \sigma_s^2}{m^2 d^2} \right) - \frac{2T}{\tau_e} \right] \right\} \quad (4.165)$$

in the standard configuration, $T_1 = T_2 = T$, and at fixed velocity. Apart from the negligible influence of the position width $\sigma_s \ll d$, the reduction factor resembles the expression (3.106) on page 125. It describes the effect of the particular macrorealistic model of continuous spontaneous localization [157] discussed in Section 3.4.3.

Unless the reduced visibility fluctuates significantly over the distribution of particle velocities we may dispense with a velocity averaging of the expression (4.165). The simplified formula (4.151) can be used to obtain the macroscopicities for most of the TLI experiments. Table 4.2 lists the μ values for a representative selection of the molecular TLI experiments conducted in Vienna. The two experiments [5, 228] employ three material gratings, whereas a standing laser wave is used as the second grating in the more recent KDTLI setup [7, 19].

Table 4.2. The greatest macroscopicity values achieved in Talbot-Lau interferometry with large molecules, according to Eq. (4.151). The passage time through the interferometer is approximated by the mean value $2L/\langle v_z \rangle$. I assumed a reasonable value for the ratio f between observed and predicted visibility by means of the theory results and the error bars of the measured data at high visibilities, as provided in the references.

Reference	[5]	[228]	[7]	[19]
molecule	C ₇₀	C ₆₀ F ₄₈	C ₆₀ F ₄₈	PFNS8
mass m	840 amu	1632 amu	1632 amu	5672 amu
grating distance L	22 cm	38 cm	10.5 cm	10.5 cm
mean velocity $\langle v_z \rangle$	115 m/s	105 m/s	116 m/s	75 m/s
observed fraction f	$\gtrsim 0.9$	0.75	$\gtrsim 0.9$	$\gtrsim 0.8$
macroscopicity μ	10.9	11.3	11.2	12.1

4.3.2.2. Center-of-mass interference of extended objects

The classicalization effect on interference experiments with point-like particles is always expressed in terms of reduction factors of the form (4.148). They saturate at large momentum widths σ_q where the classicalizing modification affects the coherence between the interfering paths at its full decay rate $1/\tau = m^2/m_e^2\tau_e$, as demonstrated by the solid curve in Figure 4.2.

The situation changes in the case of extended particles. The internal structure of the particle must be taken into account as soon as the critical classicalization length scale \hbar/σ_q becomes comparable to the particle size. According to the effective treatment of compound particles presented in Section 4.1.5, we find that at smaller length scales only a fraction of the particle's mass contributes to the classicalization-induced coherence decay in the center-of-mass motion. The effective classicalization time and phase-space distribution of the object thus depend on its size. The explicit dependence is derived in Appendix C.2 for spherical, cuboidal and cylindrical bodies.

To give a practical example, let us describe the classicalization effect on small homogeneous spheres of mass M and radius R . For instance, double-slit interference with silica nanospheres is proposed in [25], and Talbot-Lau interference with gold nanoclusters in [11] (see Section 3.4 on page 114ff.).

We can adopt all the results for the treatment of point particle interference if we simply replace the coherence time parameter and the distribution function for a point mass m by the effective classicalization parameters for a sphere, as given in Appendix C.2.1. The visibility reduction factor (4.148) of a point particle changes into

$$R_t(p) = \exp \left[\frac{M^2}{m_e^2\tau_e} e^{-(m_e\sigma_s p/M\hbar)^2/2} \int_0^\infty dq \frac{9\sqrt{2}M\hbar^3}{\sqrt{\pi}pq\sigma_q^3 R^2} \text{Si} \left(\frac{qpt}{M\hbar} \right) e^{-q^2/2\sigma_q^2} j_1^2 \left(\frac{qR}{\hbar} \right) - \frac{M^2 t}{m_e^2\tau_e} \gamma_{\text{sph}} \left(\frac{\sigma_q R}{\hbar} \right) \right]. \quad (4.166)$$

It differs significantly for $\sigma_q R/\hbar \gtrsim 1$, as demonstrated by the dashed line in Figure 4.2. The curve determines the time parameters τ_e , which would be excluded by successfully interfering gold clusters of $M = 10^7$ amu in the Talbot-Lau setup [11]. It corresponds to the condition $R_T^2(h/d) = 1/2$, that is, it assumes that at least 50% of the expected interference contrast are detected using fluorine laser gratings with period $d = 80$ nm and delay time $T = 2T_T = 32$ ms. We can estimate a radius of $R \approx 6$ nm for the gold cluster ($\rho = 19320$ kg/m³), which roughly equals the length scale \hbar/σ_q below which the dashed line declines again. The curve assumes its maximum in a small window of length scales between the mean interference path separation and the cluster size yielding the macroscopicity $\mu = 20.4$. The same experiment with smaller clusters of 10^5 amu would yield $\mu = 14.5$, whereas the feasible upper limit of 10^8 amu ($R \approx 13$ nm) corresponds to $\mu = 23.3$. If we approximated the clusters as point particles, we would obtain $\mu = 14.5$, 20.5 and 23.5, respectively. At even higher masses the particle size becomes comparable to the path separation and the point-particle approximation ceases to be valid.

The macroscopicity of the proposed double-slit experiment [25] with silica nanospheres ($\rho = 2200$ kg/m³) of up to 20 nm radius can be assessed in a similar manner. As discussed in the point-particle case, the Fourier amplitude associated to the interference fringe oscillation behind the double slit is reduced by the factor $R(D) = R_{T_1}(MD/T_1) R_{T_2}(MD/T_2)$. Here, $D = 52$ nm denotes the slit distance, and the times of flight between source, double slit and detector are set to be $T_1 = 3.3$ ms

and $T_2 = 125$ ms. Assuming a measured fringe amplitude of more than 50% of the predicted value, $R(D) \geq 1/2$, we find the macroscopicity $\mu = 20.5$. If the nanospheres were treated as point particles, we would obtain the overestimated value 21.1.

4.3.2.3. Superpositions of micromechanical oscillations

A rather novel class of macroscopic quantum phenomena seems to be coming into reach in the rapidly developing field of quantum optomechanics. Improved methods of nanofabrication and optical control have led to the cooling of micrometer-sized mechanical oscillators down to the quantum limit of motion (see e.g. [229–231]), and could make it possible to observe nonclassical states of motion with such systems in the near future. These would test the laws of quantum mechanics on a much larger mass scale than ever before, but having said that, they would also operate on length scales much smaller than any of the arm separations realized in matter-wave interferometry. In fact, they operate in the opposite domain where the dimensions of the system exceed by far the spatial extension of its quantum state of motion.

A first concrete proposal to test the quantum coherence of micromechanical oscillators was presented in [170]. The authors suggest to use a vibrating micromirror in an optical cavity placed in one arm of a Michelson interferometer. The mirror shall be initially cooled close to its ground state of motion. When a photon enters the interferometer it splits between the two arms and coherently drives a small oscillation of the micromirror in one arm, which entangles both systems with one another. A photon escaping the cavity after one full period of oscillation fully retrieves its coherence, and it is expected to interfere in the output channel with 100% contrast.

In the presence of classicalization, however, the interference visibility of the photon would be reduced due to the loss of quantum coherence in the mirror system. The explicit visibility loss,

$$\mathcal{V}\left(\frac{2\pi}{\omega}\right) \approx \exp\left[-\frac{3\pi}{\omega\tau_e}\left(\frac{Mgx_0}{m_e\omega b}\right)^2\gamma_1^2\left(\frac{\sigma_q b}{\hbar}\right)\left(1 - e^{-\sigma_q^2 b^2/2\hbar^2}\right)\right] \quad (4.167)$$

follows from a tedious calculation carried out in detail in Appendix C.3.2. The mirror is modelled as a homogeneous silica cube (see Appendix C.2.2) of edge length $b = 10 \mu\text{m}$ and mass $M = 2.3$ ng. The values for the mirror frequency $\omega/2\pi = 500$ Hz, the coupling time $t = 2\pi/\omega$, the ground state amplitude $x_0 = \sqrt{2\hbar/M\omega} = 170$ fm, and the photon-mirror coupling strength $g/\omega = 1.63$ are taken from the reference. If we assume that the experiment were actually performed and 50% visibility were observed after one mirror cycle, $\mathcal{V}(2\pi/\omega) = 0.5$, this would rule out all classicalization time parameters τ_e below the dash-dotted curve in Figure 4.2. It would give rise to a macroscopicity of $\mu \approx 19.0$.

Present-day experiments are still far away from the proposed size and time scale. In the last years the oscillator design has evolved towards smaller, more sophisticated geometries with an increased optomechanical coupling, which improved the ability to cool and control such systems. For instance, the authors of [230] demonstrated the ground-state cooling of the flexural mode of a $M = 48$ pg heavy aluminium micromembrane vibrating at $\omega/2\pi = 10.56$ MHz—a constitutive step ahead, but the quantum nature of the membrane motion remains yet to be proven.

Would the membrane system in [230] test quantum physics at an unprecedented level? Suppose that the membrane of [230] could be brought into a superposition of its ground and its first excited state for a sufficiently long time, say 1000 oscillation cycles. To give a good upper estimate of the

resulting macroscopicity, let us approximate the membrane motion by the axial vibration of a rigid homogeneous cylinder (see Appendix C.2.3) of radius $R = 7.5 \mu\text{m}$ and thickness $b = 100 \text{ nm}$. A lengthy calculation presented in Appendix C.3.1 then results in the classicalization-induced decay of coherence

$$\frac{\langle 1|\rho_{2\pi n/\omega}|0\rangle}{\langle 1|\rho_0|0\rangle} \approx \left[1 + \frac{n\pi}{\omega\tau_e} \left(\frac{Mx_0}{m_e b} \right)^2 \gamma_{\perp} \left(\frac{\sigma_q R}{\hbar} \right) \left(1 - e^{-\sigma_q^2 b^2 / 2\hbar^2} \right) \right]^{-2}. \quad (4.168)$$

Assuming that this matrix element does not decay by more than 50% in $n = 1000$ cycles gives rise to the macroscopicity $\mu \approx 11.5$ —a value that was already topped with matter-wave interferometry, as shown in Figure 4.4.

4.3.2.4. Superpositions of persistent loop currents

The theoretical prediction and the experimental verification of many-body quantum superpositions in superconducting systems has initiated much of the discussion on how to measure macroscopicity, and it is still regarded as a prime example of macroscopic quantum phenomena. The first experiments to verify the existence of superposition states between counter-rotating currents of notable magnitude in superconducting loop geometries were carried out in 2000 [1, 2]. They were used as the key reference in many attempts to assess the degree of macroscopicity in pair-condensed electron systems over the years [3, 171, 172, 174, 175, 213, 214]. In later experiments, the general interest shifted towards applications in quantum information processing, which resulted in smaller, more compact loop designs at the expense of higher macroscopicity. Despite the small coherence time observed, the original SUNY experiment [1] still provides a benchmark for the magnitude of macroscopicities reached in superconducting systems, as for instance in the 6-year-later Berkeley experiment [168].

I evaluated the macroscopicity of the three cited experiments based on the approximation discussed in Section 4.2.4 and Appendix C.1: I estimated the classicalization-induced decay rate Γ of a given current superposition state by its initial value (4.134) and compared it to the measured coherence times T_2 . The experimentally falsified classicalization parameters are then obtained from the condition $\Gamma \geq 1/T_2$, which can be assessed numerically from the simplified expressions provided in Appendix C.1. Table 4.3 lists all parameters entering the computation and the resulting μ -values for the three experiments [1, 2, 168]. It includes, in addition, a hypothetical future experiment beyond the current level of feasibility, based on extrapolated values for the loop size and the coherence time. The current differences ΔI between the two arms of the superposition are taken from [213]. However, they do not influence the macroscopicity values in the end since the coherence decay is dominated by momentum diffusion in all cases, which does not depend on the value of the supercurrents.

The combined effect of diffusion and dephasing due to classicalization is illustrated by the dotted curve in Figure 4.2, which represents the time parameters τ_e excluded by the SUNY experiment [1]. It saturates at its global maximum NT_2 for large momentum widths σ_q of the order of the Fermi momentum $\hbar k_F$ in the superconducting material, where all N conductance electrons in the Fermi sphere would be exposed to momentum diffusion in the presence of classicalization. Cooper pairs would be broken, and even the electrons deep in the Fermi sea would be displaced in momentum space at the rate $1/\tau_e$. The coherence time of the current superposition state is then limited in proportion to the number of conductance electrons, $\Gamma \approx N/\tau_e$. This explains the maximum of the

dotted curve, $\tau_{\max} \sim 10^5$ s, which corresponds to a macroscopicity of $\mu = 5.2$. The described diffusion effect weakens at larger length scales where the average momentum transfer σ_q is not sufficient to overcome the energy gap Δ for breaking a Cooper pair. This explains the decline of the curve starting from about $\hbar/\sigma_q \gtrsim 1/k_\Delta = \hbar\sqrt{2m_e\Delta} = 5$ nm. The diffusion effect eventually breaks down at roughly $\hbar/\sigma_q \sim V^{1/3} = 14$ μm where the average momentum transfer does not even reach the elementary momentum unit of electrons in a discrete lattice of volume V . What remains at this point is the coherence decay due to a dephasing between the two branches of the superposition, as represented by the constant value on the right hand side of the diagram. The dephasing in momentum space is induced by the average position transfer exerted by the classicalizing modification, and it depends merely on the classicalization parameter $\sigma_s = 20$ pm. In the absence of dephasing, $\sigma_s = 0$, the dotted curve in Figure 4.2 would drop exponentially with growing \hbar/σ_q .

4.3.2.5. Survey of past and future experiments

I conclude this chapter with an overview of the macroscopicities attained in various matter-wave experiments so far, and with an outlook comparing several proposals for future experiments on the basis of the macroscopicity measure. The following data unites all the numerical values evaluated in the preceding subsections.

The historical diagram in Figure 4.4 shows the rising trend in macroscopicities achieved in a representative selection of mechanical superposition experiments. Atomic and molecular interferometry have reached the highest values with the advent of pulsed optical atom experiments [166, 167] and the molecular Talbot-Lau experiments in Vienna. The highest macroscopicity amounts to not less than 10^{12} seconds lifetime of an isolated electron in a nonclassical state if it were subject to classicalization.

Table 4.3. Setup parameters and macroscopicities of superposition experiments in superconducting loops, as given in the references. Additional material parameters are taken from [209, 213]. For the two experiments [1, 168] the coherence time T_2 is estimated by the smallest frequency splitting observed in the spectroscopical analysis of the superposition states. The third value is given by the authors of [2], which is also used as the basis of the hypothetical experiment on a much larger loop.

Experiment	Delft [2]	SUNY [1]	Berkeley [168]	hypothetical
superconducting material	Al	Nb	Al	Al
Fermi wave number k_F	1.74 \AA^{-1}	1.18 \AA^{-1}	1.74 \AA^{-1}	1.74 \AA^{-1}
energy gap Δ	0.17 meV	1.44 meV	0.17 meV	0.17 meV
Debye energy $\hbar\omega_D$	36.9 meV	23.7 meV	36.9 meV	36.9 meV
loop length L	20 μm	560 μm	180 μm	20 mm
material cross-section A	36000 nm ²	5 μm^2	1 μm^2	100 μm^2
current difference ΔI	900 nA	3 μA	292 nA	—
coherence time T_2	15 ns	$\gtrsim 1$ ns	$\gtrsim 10$ ns	1 ms
number of electrons N	1.28×10^{11}	1.55×10^{14}	3.20×10^{13}	3.56×10^{17}
macroscopicity μ	3.3	5.2	5.5	14.5

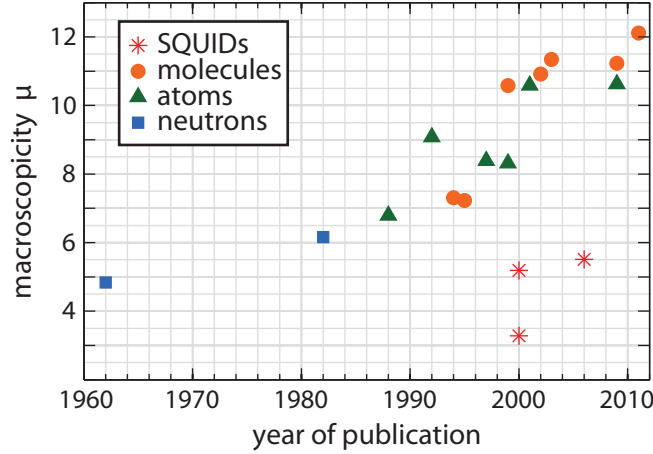


Figure 4.4. Macroscopicities of a representative selection of quantum superposition experiments with mechanical systems plotted against their publication date. I distinguish matter-wave interferometry with neutrons [223, 224] (squares), atoms [166, 167, 169, 225–227] (triangles), or molecules [4, 5, 7, 19, 125, 222, 228] (dots), and the superposition experiments [1, 2, 168] with persistent supercurrents (stars). The numerical μ -values of the data points are given in the calculations presented in this section.

Note that the first BEC interference experiment [169] is included among the atom interferometers in the timeline. I estimated its macroscopicity by means of the single-particle expression (4.151): $f = 75\%$ out of a maximum 100% contrast were measured after 40 ms time of flight of the coherently split sodium BEC, which yields $\mu \approx 8.4$. The interference fringes were recorded by measuring the single-particle density distribution in single runs of the experiment³⁵. Following the argumentation presented in Section 4.2.3 there is no reason to assume an enhancement of the macroscopicity beyond the level of a single atom, despite the macroscopic occupation of the interfering BEC state.

On the other hand, persistent-current experiments in superconducting loops seem to promise a large macroscopicity due to the sheer number of Cooper-paired electrons contributing to the superposition state. However, they clearly lag behind because of the short coherence times observed so far. This deficit could only be overcome by increasing both the loop size and the coherence time significantly: The hypothetical large setup introduced in the previous section yields the value $\mu \approx 14.5$, assuming 1 ms coherence time in a 20 mm long aluminium loop of $100 \mu\text{m}^2$ wire cross-section—challenging parameters to implement in the experiment, to say the least.

Other proposed quantum superposition experiments promise a comparable or even larger degree of macroscopicity, as estimated in the previous subsections. Their values are listed in Table 4.4. We find that the hypothetical Cooper-pair superposition experiment compares well with the space-based cesium interferometer proposed in [219], which is supposed to realize much larger coherence times of the order of 1000 s. This makes up for the huge overall mass difference between one cesium atom and the entire 10^{17} conductance electrons of the superconductor. The same degree of macroscopicity, however, should also be achievable in more easily feasible experiments, such as the next-generation matter-wave interferometers based on the Talbot-Lau scheme studied in Sec-

³⁵ The phase sensitivity and the coherence time of the BEC interferometer were increased in a later experiment [203]. However, I estimated a smaller macroscopicity in this case, $\mu \approx 8.3$, since only $f = 15\%$ visibility was found after 200 ms time of flight.

tion 3.4, and involving masses of 10^5 amu. This is due to the favorable scaling of the macroscopicity of de Broglie interference experiments with the mass of the particles. Since the latter could be increased by another three orders of magnitude, the proposed Talbot-Lau setup [11] turns out to be the most promising vehicle to test the quantum-to-classical transition. Quite remarkably, it offers the greatest degree of macroscopicity among the listed proposals, which is only rivalled by a comparable double-slit experiment with silica spheres of 10^7 amu [25], and by the superposition of a 10^{15} amu-heavy micromirror first proposed in [170]. Despite the large mass, the latter is limited in its macroscopicity because of the femtometer-sized oscillation amplitude of the mirror, as follows from the assessment in Section 4.3.2.3. The same problem applies even more severely to other nanomechanical oscillators with larger eigenfrequencies and smaller ground-state amplitudes. The vibrational superposition of an exemplary 48 pg-heavy micromembrane, which was recently cooled to its ground state in [230], would yield a considerably lower μ -value of 11.5 under similar experimental conditions. It represents the lowest entry in Table 4.4.

Nevertheless, none of the listed suggestions comes anywhere near the ‘classical’ everyday world. A simple gedankenexperiment illustrates this fact: If we could keep an idealized cat (i.e. a homogeneous 4 kg sphere of water) in a superposition of 10 cm distance for about 1 s then we would roughly obtain the macroscopicity $\mu \sim 57$, as follows from the treatment of spherical particle interference in Section 4.3.2.2. This value is the equivalent of a single isolated electron staying in a superposition state for 10^{57} seconds or 10^{40} times the age of the universe.

4.3.3. Concluding remarks and future directions

The proposed matter-wave experiments listed in Table 4.4 will take on the rising trend in the macroscopicity of fundamental quantum experiments, which originates from the breakthroughs in atomic and molecular matter-wave interferometry over the last two decades. Increasing effort is put into the field today, and even space-based experiment designs are being considered. The macroscopicity measure introduced in this chapter offers an objective and unbiased way to compare these different experimental ideas, and it may guide future research in probing the quantum-to-classical transition.

Table 4.4. Macroscopicities for a variety of hypothetical quantum superposition experiments, as conceived here or proposed by various research groups in the field of matter-wave interferometry. The listed values are collected from the detailed macroscopicity assessments presented throughout this section.

Hypothetical & proposed experiments	Macroscopicity μ
Oscillating micromembrane	11.5
Large superconducting loop	14.5
Talbot-Lau interference [11] at $M = 10^5$ amu	14.5
Cesium interferometer on a satellite [219]	14.5
Oscillating micromirror [170]	19.0
Double-slit interference of nanospheres [25]	20.5
Talbot-Lau interference [11] at $M = 10^8$ amu	23.3
Superposition of a 4 kg house cat	~ 57

Yet some questions remain to be answered about the notion of macroscopicity in general. The present work provides a physical interpretation of this notion exclusively for mechanical systems with a direct correspondence in classical Newtonian physics. In fact, the symmetries and consistent scaling principles underlying both quantum and classical mechanics are the essential ingredients of the minimally invasive, classicalizing modification the present approach builds upon. It is clear from this standpoint that genuinely quantum degrees of freedom, most prominently spin systems, cannot classicalize as they do not have a classical counterpart. Spin superposition experiments thus cannot be assigned a macroscopicity if mechanical superpositions are absent, irrespective of the great number of entangled spins achieved nowadays [232]. There is simply no reasonable alternative to quantum theory available in spin systems, hence there is also no classical ‘boundary’ of the theory that could be probed in experiments and exploited to define a notion of macroscopicity for spins.

We encounter a similar problem in modern BEC interferometers [205–207], where nonlinear interactions and superpositions of *internal* atomic states are employed to beat the classical precision limit in phase sensitivity by means of number squeezing. As in the case of spin ensembles, the superposition is made of many atoms entangled in their internal degrees of freedom, which are not directly subject to classicalization. A macroscopicity value can be assigned only to the motional part of such an entangled many-body state.

One may think accordingly that photonic systems, which are not prone to the classicalization effect developed here, are simply not accessible by this notion of macroscopicity either. At the same time, we find that current attempts to create nonclassical states of light involve an increasing number of photons entangled or superimposed in various degrees of freedom [233–236]. It should be noted that electromagnetic degrees of freedom do have a classical counterpart described by the Maxwell equations. The derivation of a minimally invasive classicalization effect from first principles, and the definition of a macroscopicity measure for quantum states of light, should be of priority in subsequent studies.

Other attempts to define a macroscopicity measure [3, 165, 171–176] have circumvented the mentioned restrictions by referring to specific many-body representations or classes of measurement operations, which serve to characterize a given quantum state. The first systematic assessment of macroscopicity was provided by Leggett [3, 165]. He identified two aspects of macroscopic superposition states: A large difference in the expectation values of an appropriate observable between the two branches of the superposition (so-called *extensive difference*, measured in atomic reference units), and a large degree of entanglement between all the constituent atomic particles taking part in the superposition (so-called *disconnectivity*)³⁶. While these two aspects appear to be reasonable and intuitively clear characteristics for the size of typical quantum phenomena, they are not objectively defined and therefore leave room for bias and interpretation³⁷. Nevertheless, various measures of macroscopicity have been proposed that are related to one or the other aspect.

³⁶ This aspect prevents many-body product states of the form $|\psi_N\rangle \propto (|A\rangle + |B\rangle)^{\otimes N}$ from being considered more macroscopic than the single-particle state $|\psi_1\rangle \propto |A\rangle + |B\rangle$. On the other hand, the disconnectivity of a GHZ-type state, $|\psi\rangle \propto |A\rangle^{\otimes N} + |B\rangle^{\otimes N}$, would increase with the number of particles N .

³⁷ This triggered an interesting and illustrative debate on the macroscopicity of many-body quantum phenomena. Leggett’s prime example of a macroscopic quantum effect was the superposition of persistent currents in a superconducting Josephson loop, first observed in [1, 2]. He claimed that the *disconnectivity* of the measured state was given by the total number of Cooper-paired electrons, more than a billion to be precise, flowing either clockwise or anticlockwise through the loop. A proper many-body analysis, however, reveals that the state is given by a superposition of two slightly displaced but largely overlapping Fermi spheres, as found by Korsbakken et al. [213, 214]. Hence, the vast majority of indistinguishable electrons occupies the same momentum space region in both branches of the superposition, and only a few hundred to thousand are actually *disconnected*, i.e. found in different states.

Several proposals were derived from information-theoretic considerations and emphasize the high degree of many-body correlations in a given representation of macroscopic quantum states [171, 173, 174, 176], whereas others measure the sensitivity of such states to decoherence and dephasing in a preferred basis of eigenstates [172, 175]. However, the decomposition of many-body quantum states into correlated constituent degrees of freedom is not unique, nor is the choice of a relevant basis to represent the state. Hence, there is a priori no unique standard of macroscopicity that one could refer to.

In this chapter, I have presented such a standard by referring to classical physics and by adhering to the consistent mass scaling properties of composite mechanical systems, which makes it applicable to arbitrary such systems without bias. It exploits Leggett's hypothesis of macrorealism, according to which the only way to reconcile the quantum description of the atomic world and the classical description of the everyday world is to introduce a modification of quantum mechanics that carries out the quantum-classical transition somewhere in between. In principle, such a classicalizing modification could be of almost any kind, as long as it assuredly turns quantum superpositions into classical mixtures and conserves the well-established classical equations of motions on large scales.

Leggett proposed to test his hypothesis in the lab by trying to observe quantum phenomena as macroscopic as possible; in this way one would exclude the possibility that those modifications would have kicked in too early and induced a breakdown of the observed effect. Here, we have arrived at a universal macroscopicity benchmark by turning this statement upside down: We can *call* an observed quantum phenomenon more macroscopic than another one if it leaves less room for the objective quantum-classical transition to occur.

In order to derive a quantitative measure out of this, I have restricted the analysis in Section 4.1 to 'minimal' modifications. They are just intrusive enough to do the job and avert quantum superpositions in the macroworld without doing harm to fundamental symmetry and consistency principles that are sacrosanct for both quantum and classical theory. By keeping other, more severe modifications out of the game we could develop the logarithmic quantity μ in Section 4.3, which naturally meets the requirements for a sound measure of macroscopicity.

Chapter 5.

Conclusion and outlook

“People who have visions should go see a doctor.”
— Helmut Schmidt

Let me close by reviewing the three main parts of this work, Chapter Two, Three and Four, from a broader perspective. In the first two of these we were driven by concrete practical considerations in the context of de Broglie wave interferometry, as pursued in Vienna: how to steer and interfere the center-of-mass motion of heavy nanoparticles. In summary, we developed a number of answers and predictions that have proven useful, or will become important, for current and future experiments:

- ★ **Feasibility of cavity-mediated cooling of molecules and nanoparticles** Slow and cold ensembles of molecules and nanoparticles are an essential prerequisite for high-mass matter-wave interferometry. However, unlike atoms, large molecules do not exhibit distinct internal resonances that could be coherently addressed by conventional laser cooling techniques. Thus efficient methods of motional cooling and control are lacking. I discussed in Chapter Two how and to what extent Sisyphus-type cooling can still be achieved for polarizable particles with help of a strongly driven optical high-finesse cavity. Using the right parameters, the delayed reaction of the cavity field to the moving particle is able to cause a velocity-dependent friction force as the particle modulates the cavity resonance while travelling across the field mode. We saw that this effect is small in realistic settings, but it could be enhanced by employing spherical resonator geometries with a large degenerate mode spectrum. There, each mode would contribute an additional velocity damping channel that increases the overall friction effect. The effect was studied in a weak-coupling master equation model. Yet, a practical implementation with single molecules remains challenging, and it would be interesting to combine it with ion-trapping techniques, or to study also collective self-organization effects [84] in the case of many molecules.
- ★ **Cavity cooling and trapping of large nanospheres** The growing mass and polarizability of large nanoparticles alleviates the problem of weak coupling and thus facilitates an efficient cavity-induced slowing under realistic conditions. This goal is pursued by several groups at the moment [23, 24, 137, 237, 238], mainly using silica nanospheres and infrared cavities. We saw with the help of Mie scattering theory in Chapter Two that not only the coupling of large nanospheres increases, but also the behaviour changes when their diameter gets comparable to the wavelength of the standing-wave cavity field. Their absorption and scattering properties get insensitive to the standing-wave field modulation, the radiation pressure may turn

them into effective low-field seekers at certain size regimes, and their overall field extinction power increases to an extent that facilitates a position-sensitive detection via the scattered light. Moreover, I also assessed the transverse forces in a Gaussian light mode and showed for a realistic setting that they can be employed to capture nanospheres in the center of the mode. Practical simulations and the application in experiments of the Vienna group are a matter of ongoing research.

- ★ **Optical gratings for matter waves** From the detailed assessment of the light-matter interaction between nanoparticles and standing waves, we could understand how the latter can be employed as diffractive elements for matter waves. Not only do they serve as phase gratings, as conventionally implemented in molecule interferometry, but they can also act as amplitude gratings by optical depletion—a convenient alternative to material grating masks. This requires the particles to be altered by photo-absorption such that they can be sorted out or distinguished from the others in a reliable fashion. In the simplest case, a single photon suffices to ionize the particle, which can then be removed by an electric field; this way the standing-wave acts as an absorptive masks with the nodes playing the role of the grating slits. Such single-photon ionization gratings have been proven to work [13], demonstrating the interplay between absorptive and diffractive effects on the most elementary level. Other possible depletion methods involving more than a single photon and internal conversion processes are being considered and should be assessed next.
- ★ **Poisson's spot with large molecules** In Chapter Three I turned to matter-wave interferometry techniques with molecules and nanoparticles, and I started by analyzing a peculiar near-field phenomenon that had been conceived almost two centuries ago to verify the wave nature of light: Poisson's spot, also known as Arago's spot. Although the appearance of a bright intensity maximum in the shadow center behind an opaque disc seems to be a decisive proof of wave interference, I showed that this ceases to be the case for large nanoparticles. The reason is that a classical ballistic model may lead to a similar prediction due to the strong van der Waals interaction between the particles and the walls of the obstacle. This makes it hard to distinguish quantum interference from classical deflection above a certain particle size. However, my analysis was based on a simplified treatment of the interaction potential, and more refined predictions should be based more sophisticated models [116].
- ★ **Talbot-Lau interferometry with optical gratings** Apart from Poisson's spot, Chapter Three was mostly about the Talbot-Lau near-field scheme, which is most suited to interfere large masses. I provided a full-fledged phase-space model for Talbot-Lau interferometry with optical gratings, and the main result was the detailed description of a time-domain Talbot-Lau interferometer with optical ionization gratings for heavy nanoclusters. The Vienna group has implemented the scheme in the lab by now, and the first interference was observed with anthracene clusters [13].
- ★ **Interferometric metrology techniques** The nanometer-sized and periodic interference fringes produced in a Talbot-Lau setup are highly sensitive to random or controlled phase shifts that may occur while the matter waves pass the three gratings of the interferometer. This can be utilized in precision metrology of the internal properties of the particle, such as the static polarizability or the optical absorption cross-section. The absolute value of the latter

can be measured at benchmark precision in the interferometric scheme discussed in Chapter Three. By shining in an additional laser between the gratings we can make use of the photon recoil upon absorption to extract the absorption cross section and fluorescence yield from the subsequent reduction of interference contrast as a function of laser power. The idea was originally proposed in [6] and awaits its first implementation.

★ **Mass limitations of matter-wave interferometry** Finally, I took all relevant limitations in Talbot-Lau interferometry into consideration and gave an accurate estimation of the highest possible masses that could be interfered in the time-domain Talbot-Lau scheme with vacuum-ultraviolet laser gratings, as conceived and developed in my group. We found on the one hand that the combined influence of gravity, environmental decoherence, and the finite cluster size limits the attainable mass to below a billion atomic mass units. On the other hand, we saw that hypothetical new physics at the macroscale may become testable already at about a million amu. The famous model of continuous spontaneous localization (CSL) [155, 157] is expected to kick in at this scale, inducing an effective loss of coherence which would be reflected in a mass-dependent drop of interference contrast.

The question of macroscopicity The long-term analysis of future mass limitations in macroscopic cluster interferometry, as conceived and implemented in Vienna, led us away from practical problems and to the deeper theoretical question of what it means to be macroscopic. In Chapter Four, this forced us to look at the bigger picture, where center-of-mass interferometry is only one example of a macroscopic quantum phenomenon, and where the mass is only one aspect of macroscopicity. As much as my colleagues and me are intuitively biased towards this aspect, so may physicists working on atom interference, many-body quantum phenomena, and nanomechanical oscillators be biased towards other aspects. This is why we felt it is necessary to part from our prejudice and conceive a general methodology to tackle the question of macroscopicity in arbitrary settings.

In Chapter Four I presented a universal way to measure macroscopicity in mechanical systems by referring to the hypothesis of macroscopic realism and by quantifying the extent to which this hypothesis is ruled out by the observation of a quantum phenomenon. Macroscopicity is thus defined by means of *empirical facts* rather than the theoretical representation of the given phenomenon. Hence, the quality and nature of the experiment matters as much as the formal complexity of the underlying quantum state. It will be worthwhile to study this connection further and explore the common features and interfaces between the formal size measures proposed by others [171–176] and the present empirical measure of macroscopicity.

Finally, let me remark that the macroscopicity standard defined here can be applied only to systems with a direct counterpart in classical physics. Quantum spin states, however large and complex, are therefore excluded because they do not possess such a classical reference. This does not mean that one cannot go further than this. The discussion in Chapter Four was restricted to nonrelativistic mechanical systems having their counterpart in Newtonian mechanics, and it is clear what to do next: One should try to extend the analysis also to relativistic and electromagnetic systems. This would eventually allow one to access the vast field of photonic quantum experiments by means of the presented method.

Appendix A.

Light-matter interaction

A.1. Complex field amplitude and quantization

The macroscopic Maxwell equations for electromagnetic fields refer to real-valued quantities. In case of a source-free medium, they read as $\nabla \cdot \mathbf{D} = \nabla \cdot \mathbf{B} = 0$, $\nabla \times \mathbf{H} = \partial_t \mathbf{D}$, $\nabla \times \mathbf{E} = -\partial_t \mathbf{B}$. It is, however, convenient to use a complexified version when dealing with time-harmonic electromagnetic waves, that is, fields oscillating at a fixed (optical) frequency ω . The time dependence of all fields is then of the form $\mathbf{E}(\mathbf{r}, t) = \mathbf{E}(\mathbf{r}) \exp(-i\omega t)$, and the time derivative can be replaced by $\partial_t \mapsto -i\omega$.

I will always presuppose homogeneous, isotropic, linear and non-magnetic media characterized by a relative dielectric permeability $\varepsilon = \varepsilon(\omega)$ and a magnetic permeability $\mu = 1$. Note that ε can take complex values in the case of absorbing media. The electric field \mathbf{E} and the magnetic field \mathbf{B} are related to the electric displacement field \mathbf{D} and to the magnetizing field \mathbf{H} via $\mathbf{D} = \varepsilon \varepsilon_0 \mathbf{E}$ and $\mathbf{B} = \mu_0 \mathbf{H}$. The Maxwell equations become

$$\mathbf{H}(\mathbf{r}) = \frac{1}{i\mu_0\omega} \nabla \times \mathbf{E}(\mathbf{r}), \quad \mathbf{E}(\mathbf{r}) = \frac{i}{\varepsilon \varepsilon_0 \omega} \nabla \times \mathbf{H}(\mathbf{r}), \quad (\text{A.1})$$

interrelating the complex electric and magnetic fields, with $\nabla \cdot \mathbf{H} = \nabla \cdot \varepsilon \mathbf{E} = 0$. Hence, this reduces to a single vector wave equation, or *Helmholtz equation*, for both fields,

$$\nabla \times \left[\nabla \times \begin{Bmatrix} \mathbf{E}(\mathbf{r}) \\ \mathbf{H}(\mathbf{r}) \end{Bmatrix} \right] = -\nabla^2 \begin{Bmatrix} \mathbf{E}(\mathbf{r}) \\ \mathbf{H}(\mathbf{r}) \end{Bmatrix} = \varepsilon k^2 \begin{Bmatrix} \mathbf{E}(\mathbf{r}) \\ \mathbf{H}(\mathbf{r}) \end{Bmatrix}, \quad (\text{A.2})$$

where $k = \omega/c$ denotes the *vacuum* wavenumber throughout this thesis. I will only describe waves in vacuum ($\varepsilon = 1$) or in piecewise homogeneous media, where the dielectric function ε does not depend on position except on boundary surfaces.

The physical fields are obtained from the complexified expressions by taking the real part, $\Re\{\mathbf{E}\}$ and $\Re\{\mathbf{H}\}$. In the case of a derived expression involving products of fields, this rule must be applied to each factor [33]. For an arbitrary product ‘ \circ ’ between two complexified vector fields \mathbf{a} and \mathbf{b} , we arrive at the physical expression by

$$\mathbf{a}(\mathbf{r}, t) \circ \mathbf{b}(\mathbf{r}, t) \rightarrow \Re\left[\mathbf{a}(\mathbf{r}) e^{-i\omega t}\right] \circ \Re\left[\mathbf{b}(\mathbf{r}) e^{-i\omega t}\right]. \quad (\text{A.3})$$

Doing a time-average $\langle \cdot \rangle_t$ over the fast optical oscillation then yields the simple form

$$\langle \mathbf{a}(\mathbf{r}, t) \circ \mathbf{b}(\mathbf{r}, t) \rangle_t \rightarrow \frac{1}{2} \Re\left[\mathbf{a}(\mathbf{r}) \circ \mathbf{b}^*(\mathbf{r})\right]. \quad (\text{A.4})$$

A standard way to describe both the coupling between distinguished wave components and to quantize wave fields lies in the separation of amplitude and mode. The mode defines the spatial structure and polarization of the field, whereas the complex amplitude encodes the stored energy and phase evolving in time. One first chooses an orthogonal basis set of eigenfunctions $\{\mathbf{u}_n(\mathbf{r})\}$ that solve the above Helmholtz equation (A.2) and fulfill the electric field boundary conditions of the physical system in question. The complementary set of solutions $\{k^{-1}\nabla \times \mathbf{u}_n(\mathbf{r})\}$ must fulfill the boundary conditions of the magnetic field, respectively. For example, the vector-valued functions can be plane waves with a fixed polarization, $\mathbf{u}_k(\mathbf{r}) = \boldsymbol{\epsilon} \exp(i\sqrt{\epsilon}\mathbf{k} \cdot \mathbf{r})$, or standing waves in a Fabry-Pérot configuration. They are called mode-polarization functions, or *mode functions* in the case of a fixed polarization vector $\boldsymbol{\epsilon}$. I adhere to the convention [239] of defining them as dimensionless functions and introducing their *mode volume* V_n through the orthogonality conditions

$$\int d^3r \mathbf{u}_n^*(\mathbf{r}) \cdot \mathbf{u}_m(\mathbf{r}) = \frac{1}{k^2} \int d^3r [\nabla \times \mathbf{u}_n^*(\mathbf{r})] \cdot [\nabla \times \mathbf{u}_m(\mathbf{r})] = \delta_{nm} V_n. \quad (\text{A.5})$$

With this mode picture at hand, and allowing for different frequency components, we can expand any electric field in vacuum as

$$\mathbf{E}(\mathbf{r}, t) = \sum_n E_n(t) \mathbf{u}_n(\mathbf{r}) = \sum_n \sqrt{\frac{2\hbar\omega_n}{\epsilon_0 V_n}} \alpha_n(t) \mathbf{u}_n(\mathbf{r}), \quad (\text{A.6})$$

where the expansion coefficients $E_n(t)$ determine the amplitude of the field. The expansion of \mathbf{H} follows from (A.1) accordingly. The time evolution of the wave field is now reduced to a (possibly coupled) time evolution of the individual complex amplitudes $\alpha_n(t) = \sqrt{\epsilon_0 V_n / 2\hbar\omega_n} E_n(t)$, keeping the spatial mode structure fixed¹.

In the canonical quantization procedure one simply replaces the complex amplitudes α_n and α_n^* by bosonic annihilation and creation operators, \mathbf{a}_n and \mathbf{a}_n^\dagger . The expression for the energy H_f stored in the vacuum field translates into the standard Hamiltonian of multiple harmonic oscillators,

$$\begin{aligned} H_f &= \frac{1}{2} \int d^3r [\epsilon_0 \Re \{ \mathbf{E}(\mathbf{r}, t) \}^2 + \mu_0 \Re \{ \mathbf{H}(\mathbf{r}, t) \}^2] = \sum_n \frac{\hbar\omega_n}{2} (\alpha_n^* \alpha_n + \alpha_n \alpha_n^*) \\ &\rightarrow H_f = \sum_n \hbar\omega_n \left(\mathbf{a}_n^\dagger \mathbf{a}_n + \frac{1}{2} \right). \end{aligned} \quad (\text{A.7})$$

The Heisenberg time evolution of the bosonic operators under the field Hamiltonian H_f remains harmonic, $\mathbf{a}_n(t) = \mathbf{a}_n \exp(-i\omega t)$.

A.2. Gaussian modes

Gaussian light modes are encountered in many experimental situations. The most common examples are fundamental standing-wave cavity modes with spherical mirrors and running laser waves. They are described by TEM₀₀-modes with a symmetric Gaussian mode profile of waist w [81, 82, 240]. The simple expression $\mathbf{E}(\mathbf{r}) \propto \boldsymbol{\epsilon} \exp(-r^2/w^2 + ikz)$ represents only a rough approximation for a linearly polarized Gaussian running wave directed towards the positive z -axis. It

¹ A spatial motion of the wave field would be described by a redistribution of amplitudes between different modes in this picture.

solves the Helmholtz equation (A.2) only to zeroth order in the expansion parameter $s = 1/kw$. Taking the rotation of this function yields also correction terms as compared to the linear polarization of the corresponding magnetic field.

A rigorous formulation of Gaussian modes treating (on equal footing) electric and magnetic field components involves vector potentials of a fixed polarization along the x - or y -axis [240]. As a consequence, the linear field polarization, say, along x , is appended by a longitudinal z -component and a y -component of higher order in s . A Gaussian running wave directed towards the positive (+) or negative (−) z -direction, and centered at $\mathbf{r} = 0$, is approximately described by the fields²

$$\mathbf{E}_{\pm}(\mathbf{r}) = E_0 q_{\pm} e^{-q_{\pm} \rho^2 \pm i k z} \begin{pmatrix} 1 + s^2 (\rho^2 q_{\pm}^2 + 2q_{\pm}^2 x^2/w^2 - \rho^4 q_{\pm}^3) + \mathcal{O}(s^4) \\ 2s^2 q_{\pm}^2 x y/w^2 + \mathcal{O}(s^4) \\ \mp 2is q_{\pm} x/w + \mathcal{O}(s^3) \end{pmatrix}, \quad (\text{A.8})$$

$$\mathbf{H}_{\pm}(\mathbf{r}) = \pm c \varepsilon_0 E_0 q_{\pm} e^{-q_{\pm} \rho^2 \pm i k z} \begin{pmatrix} 2s^2 q_{\pm}^2 x y/w^2 + \mathcal{O}(s^4) \\ 1 + s^2 (\rho^2 q_{\pm}^2 + 2q_{\pm}^2 y^2/w^2 - \rho^4 q_{\pm}^3) + \mathcal{O}(s^4) \\ \mp 2is q_{\pm} y/w + \mathcal{O}(s^3) \end{pmatrix}, \quad (\text{A.9})$$

with $\rho^2 = (x^2 + y^2)/w^2$ and $q_{\pm} = 1/(1 \pm 2iz/kw^2)$. I chose the parameters such that the electric field is mainly x -polarized. The lowest order addition to both the electric and the magnetic field is a longitudinal polarization component. The strict orthogonality between the direction of propagation and of polarization holds only for pure plane- or standing-wave modes. A cosine-type standing electric-field wave is obtained by combining $\mathbf{E}_{\text{sw}} = (\mathbf{E}_+ + \mathbf{E}_-)/2$. The corresponding magnetization field $\mathbf{H}_{\text{sw}} = (\mathbf{H}_+ + \mathbf{H}_-)/2$ is then of sine type.

If we look at the Gaussian wave from a coordinate system, which is shifted to the new origin \mathbf{r}_0 , we must simply replace \mathbf{r} by $\mathbf{r} + \mathbf{r}_0$ in the above field expressions. This will be of use when considering scattering situations at spherically symmetric geometries. If in addition the size of the scattering object in question is small compared to the waist of the field, we should consider expanding the translated field expressions in $r/w \ll 1$ as well. Let me introduce the abbreviations

$$\rho_0^2 = \frac{x_0^2 + y_0^2}{w^2}, \quad \rho_1^2 = \frac{2xx_0 + 2yy_0}{w^2}, \quad (\text{A.10})$$

$$A = \rho_0^2 - \rho_0^4 - 2\frac{z_0^2}{w^2}(\rho_0^2 - 2)^2, \quad B = \rho_0^2 - 1 + (2 - \rho_0^2)\rho_1^2, \quad C = \frac{\rho_1^4}{2} - \rho_1^2 - \frac{x^2 + y^2}{w^2}. \quad (\text{A.11})$$

The following field expressions are valid up to second order in both s and r/w (i.e. terms of the form $s^n (r/w)^m$ are dropped if $n + m \geq 3$).

$$\mathbf{E}_{\pm}(\mathbf{r} + \mathbf{r}_0) \approx E_0 e^{-\rho_0^2 \pm i k(z+z_0)} \begin{pmatrix} 1 + C \pm 2is [Bz_0 + (\rho_0^2 - 1)z]/w + s^2 (A + 2x_0^2/w^2) \\ 2s^2 x_0 y_0/w^2 \\ \mp 2is [(1 - \rho_1^2)x_0 + x]/w + 4s^2 (\rho_0^2 - 2)x_0 z_0/w^2 \end{pmatrix} \quad (\text{A.12})$$

$$\mathbf{H}_{\pm}(\mathbf{r} + \mathbf{r}_0) \approx \pm c \varepsilon_0 E_0 e^{-\rho_0^2 \pm i k(z+z_0)} \begin{pmatrix} 2s^2 x_0 y_0/w^2 \\ 1 + C \pm 2is [Bz_0 + (\rho_0^2 - 1)z]/w + s^2 (A + 2y_0^2/w^2) \\ \mp 2is [(1 - \rho_1^2)y_0 + y]/w + 4s^2 (\rho_0^2 - 2)y_0 z_0/w^2 \end{pmatrix} \quad (\text{A.13})$$

² Note that I use a harmonic time dependence of the form $\exp(-i\omega t)$, as opposed to [240]. The present field expressions are thus given by the complex conjugates of the ones from the reference.

A.3. Phase space representation of states and observables

Bound operators on the Hilbert space $L^2(\mathbb{R})$ of a one-dimensional motional degree of freedom can be represented by means of an arbitrary complete set of orthogonal operators (with respect to the Hilbert-Schmidt scalar product $(A, B) = \text{tr}(A^\dagger B)$). The Wigner-Weyl formulation of quantum mechanics is obtained by using the basis of reflection operators

$$R_{z,p} = \frac{1}{2} \int ds e^{ips/\hbar} |z + \frac{s}{2}\rangle \langle z - \frac{s}{2}|, \quad \text{tr}(R_{z,p}^\dagger R_{z',p'}) = \pi\hbar \delta(z - z') \delta(p - p'). \quad (\text{A.14})$$

One defines the *Weyl symbol* of an operator A as the expansion coefficient

$$A(z, p) = 2\text{tr}(R_{z,p} A) = \int ds e^{ips/\hbar} \langle z - \frac{s}{2} | A | z + \frac{s}{2} \rangle. \quad (\text{A.15})$$

The operator can be fully reconstructed from its Weyl symbol by $A = \int dz dp A(z, p) R_{z,p} / \pi\hbar$. The Wigner function of a given quantum state ρ is defined as the normalized Weyl symbol

$$w(z, p) = \frac{1}{2\pi\hbar} \int ds e^{ips/\hbar} \langle z - \frac{s}{2} | \rho | z + \frac{s}{2} \rangle \in \mathbb{R}, \quad \int dz dp w(z, p) = 1. \quad (\text{A.16})$$

We can interpret it as the quantum generalization of the phase space density distribution, $f(z, p) \geq 0$, of a classical state of motion:

- ★ The Wigner function reproduces the same marginals as its classical counterpart. We obtain the spatial density distribution by integrating over the momentum variable, $\int dp w(z, p) = \langle z | \rho | z \rangle$, and the momentum distribution by integrating over position.
- ★ Classically mixed states with vanishing quantum coherence can be described by a positive Wigner function that is identical to the according phase-space distribution function in a classical description.
- ★ Quantum expectation values of observables A can be expressed as a Wigner function average of the corresponding Weyl symbol, $\langle A \rangle = \int dz dp A(z, p) w(z, p)$. The same is true for phase-space observables in a classical model.
- ★ Given that the quantum state evolves coherently under the influence of the Hamiltonian $H = p^2/2m_p + V(z)$, its Wigner function solves the quantum-Liouville equation [77]

$$\left[\partial_t + \frac{p}{m_p} \partial_z - V'(z) \partial_p \right] w(z, p) = \sum_{\ell=1}^{\infty} \frac{(-\hbar^2/4)^\ell}{(2\ell+1)!} V^{(2\ell+1)}(z) \partial_p^{2\ell+1} w(z, p). \quad (\text{A.17})$$

It is identical to the classical Liouville equation in a semiclassical approximation to second order in \hbar^2 , where all higher-than-second-order derivatives are omitted. More generally, if Lindblad-type master equations are translated into phase space the same semiclassical approximation will yield a Fokker-Planck type equation (2.89) which has a clear classical correspondence.

The Weyl symbols of the position and the momentum observable are the respective phase-space coordinates. However, due to the noncommutative nature of quantum observables, there is no such simple correspondence most other cases. Given two non-commuting operators A and B we find that the Weyl symbols for their products read as [77]

$$(AB)(z, p) = A\left(z - \frac{\hbar}{2i}\partial_p, p + \frac{\hbar}{2i}\partial_z\right)B(z, p), \quad (\text{A.18})$$

$$(BA)(z, p) = \left[A^*\left(z - \frac{\hbar}{2i}\partial_p, p + \frac{\hbar}{2i}\partial_z\right)B^*(z, p)\right]^*. \quad (\text{A.19})$$

The differential operators in the arguments are to be understood by means of the Taylor expansion

$$A\left(z - \frac{\hbar}{2i}\partial_p, p + \frac{\hbar}{2i}\partial_z\right) = \sum_{n,m=0}^{\infty} \frac{1}{m!n!} A^{(m,n)}(z, p) \left(-\frac{\hbar}{2i}\partial_p\right)^m \left(\frac{\hbar}{2i}\partial_z\right)^n. \quad (\text{A.20})$$

Any master equation can be translated to a phase-space partial differential equation by subsequent applications of the above translation rules.

A.4. Weak-coupling dynamics of N particles in M modes

Here I generalize the weak-coupling master equation (2.81) for a single particle in the presence of a single driven and M empty cavity modes to a more general configuration of N (identical) particles in M driven or empty modes. Each mode shall be either empty, $\alpha_n = 0$, or pumped to a large steady-state amplitude, $|\alpha_n| \gg 1$. I restrict my considerations to the simple yet relevant case where the driving is realized by a single laser of frequency ω_p . Coupling it into the cavity thus singles out one or a few degenerate pump modes.

If we apply the first weak coupling assumption of Section 2.2.2.1, $|U_{mn}| \ll \kappa_n$, to each individual particle, we arrive at the following light-matter master equation in the ω_p -rotating and displaced frame,

$$\partial_t \rho = -\frac{i}{\hbar} [H_p + H_I, \rho] + \mathcal{L}_C(\rho) + \mathcal{L}_{\text{abs}}(\rho) + \mathcal{L}_{\text{sca}}(\rho), \quad (\text{A.21})$$

$$\mathcal{L}_C(\rho) = -i \left[\sum_{n=1}^M \Delta_n \mathbf{a}_n^\dagger \mathbf{a}_n, \rho \right] + \sum_{n=1}^M \kappa_n (2\mathbf{a}_n \rho \mathbf{a}_n^\dagger - \{\mathbf{a}_n^\dagger \mathbf{a}_n, \rho\}), \quad (\text{A.22})$$

$$H_p = \sum_{j=1}^N \left[\frac{\mathbf{p}_j^2}{2m_p} + \sum_{m,n=1}^M \hbar U_{mn} \alpha_m^* \alpha_n u_m^*(\mathbf{r}_j) u_n(\mathbf{r}_j) \right], \quad (\text{A.23})$$

$$H_I = \sum_{j=1}^N \sum_{m,n=1}^M \hbar U_{mn} \alpha_m^* \mathbf{a}_n u_m^*(\mathbf{r}_j) u_n(\mathbf{r}_j) + h.c. \quad (\text{A.24})$$

The absorption and scattering terms are given by sums over all driven modes,

$$\mathcal{L}_{\text{abs}}(\rho) = \gamma_{\text{abs}}^{(n)} |\alpha_n|^2 \sum_{j=1}^N \left[u_n(\mathbf{r}_j) \rho u_n^*(\mathbf{r}_j) - \frac{1}{2} \{ |u_n(\mathbf{r}_j)|^2, \rho \} \right], \quad (\text{A.25})$$

$$\mathcal{L}_{\text{sca}}(\rho) = \gamma_{\text{sca}}^{(n)} |\alpha_n|^2 \left[\sum_{j=1}^N \int d^2n R(\mathbf{n}) u_n(\mathbf{r}_j) e^{-ik\mathbf{n}\cdot\mathbf{r}_j} \rho e^{ik\mathbf{n}\cdot\mathbf{r}_j} u_n^*(\mathbf{r}_j) - \frac{1}{2} \{ |u_n(\mathbf{r}_j)|^2, \rho \} \right], \quad (\text{A.26})$$

with the respective extinction rates $\gamma_{\text{abs,sca}}^{(n)} = c\sigma_{\text{abs,sca}}/V_n$ and the mode volumes V_n . In the next step of the weak-coupling approximation I assume that all cavity modes remain empty (relative to the steady-state amplitude) at almost all times. This requires the effective rate of field fluctuations induced by the entirety of particles to be small compared to the cavity decay rate. That is to say, the second weak coupling condition becomes $|NU_{mn}\alpha_n| \ll \kappa_m \forall m, n$, which places a quite rigid bound on the allowed particle number in practical situations.

In full analogy to the line of arguments in Sections 2.2.2.2 and 2.2.2.3 we arrive at the effective N -particle master equation

$$\partial_t \rho_P = \mathcal{L}_P \rho_P - \sum_{j=1}^N \sum_{n,\ell,m=1}^M U_{\ell m} U_{mn} (\alpha_\ell^* \alpha_n [u_\ell^*(\mathbf{r}_j) u_m(\mathbf{r}_j), \mathbf{g}_{mn} \rho_P] + h.c.), \quad (\text{A.27})$$

$$\mathbf{g}_{mn} \approx \int_0^\infty d\tau e^{-(\kappa_m + i\Delta_m)\tau} \sum_{k=1}^N u_m^* \left(\mathbf{r}_k - \frac{\mathbf{p}_k \tau}{m_P} \right) u_n \left(\mathbf{r}_k - \frac{\mathbf{p}_k \tau}{m_P} \right). \quad (\text{A.28})$$

Note that, as a result of the second weak coupling condition, the non-retarded part of the time evolution, $\mathcal{L}_P \rho_P = -i[H_P, \rho_P]/\hbar + \mathcal{L}_{\text{abs}} \rho_P + \mathcal{L}_{\text{sca}} \rho_P$, reduces to a sum of uncoupled single-particle terms. The inter-particle coupling is mediated by the delayed cavity reaction, as represented by the memory operators \mathbf{g}_{mn} .

With the effective N -particle master equation at hand we can identify the cavity-induced friction and diffusion effect in phase space. For this let me again restrict our view to the one-dimensional motion along the z -axis of the cavity. Introducing the N -particle Wigner function

$$w(z_1, p_1, \dots, z_N, p_N) = \frac{1}{(2\pi\hbar)^N} \int ds_1 \dots ds_N \exp\left(\frac{i}{\hbar} \sum_j p_j s_j\right) \langle z_1 - \frac{s_1}{2}, \dots | \rho | z_1 + \frac{s_1}{2}, \dots \rangle \quad (\text{A.29})$$

we can convert the above master equation into a semiclassical Fokker-Planck-type equation for the $2N$ -dimensional Wigner function. The phase-space translation rules from Appendix A.3 generalize naturally to N particles. I once again define the memory integrals per particle as the phase-space counterparts of the memory operators,

$$G_{mn}(z, p) = \int_0^\infty e^{-(\kappa_m + i\Delta_m)\tau} u_m^* \left(z - \frac{p\tau}{m_P} \right) u_n \left(z - \frac{p\tau}{m_P} \right). \quad (\text{A.30})$$

A tedious but straightforward calculation reveals the dissipative force term

$$\begin{aligned} g_{p_j}^{(\text{dis})}(z_1, p_1, \dots) = & \sum_{n,\ell,m=1}^M \hbar \tilde{U}_{\ell m} \tilde{U}_{mn} \Re \left\{ 2i \alpha_\ell^* \alpha_n [\partial_{z_j} u_\ell^*(z_j) u_m(z_j)] \sum_{k=1}^N G_{mn}(z_k, p_k) \right. \\ & \left. - \hbar \alpha_\ell^* \alpha_n [\partial_{z_j}^2 u_\ell^*(z_j) u_m(z_j)] \partial_{p_j} G_{mn}(z_j, p_j) \right\} \end{aligned} \quad (\text{A.31})$$

as well as the diffusion coefficients

$$D_{p_j p_k}^{(\text{dis})}(z_1, p_1, \dots) = \sum_{n,\ell,m=1}^M 2\hbar^2 \tilde{U}_{\ell m} \tilde{U}_{mn} \Re \left\{ \alpha_\ell^* \alpha_n [\partial_{z_j} u_\ell^*(z_j) u_m(z_j)] \partial_{z_k} G_{mn}(z_j, p_j) \right\}, \quad (\text{A.32})$$

$$D_{z_j p_k}^{(\text{dis})}(z_1, p_1, \dots) = - \sum_{n,\ell,m=1}^M \hbar^2 \tilde{U}_{\ell m} \tilde{U}_{mn} \Re \left\{ \alpha_\ell^* \alpha_n [\partial_{z_k} u_\ell^*(z_k) u_m(z_k)] \partial_{p_j} G_{mn}(z_j, p_j) \right\}. \quad (\text{A.33})$$

The first order friction force term (first line) for the j th particle is affected by the accumulated trajectory of all other particles. That is, the particles couple through the cavity-mediated friction force. The second-order force terms for each particle are independent. The diffusion coefficients correlate all particles uniformly. A particle couples to the first-order field fluctuations caused by itself or by any other particle via the same memory integral expression. We should expect that this would lead to a strongly correlated interacting many-body system beyond the weak coupling regime. As a consequence, collective self-organization effects are expected to occur [84, 85].

A.5. Spherical wave expansion

The spherical wave expansion is an essential method to work with fields under spherically symmetric boundary conditions. Here, I use it to solve the Mie scattering problem of electromagnetic waves at spherical dielectrics [28, 29]. The idea is to expand the electric and magnetic fields in a given setup in the basis of spherical vector harmonics [34]. Given a harmonic field component of frequency $\omega = ck$ in a dielectric medium of (complex) refractive index $n = \sqrt{\epsilon}$, we may expand the electric and the magnetization field as

$$\mathbf{E}(\mathbf{r}) = \sum_{\ell=1}^{\infty} \sum_{m=-\ell}^{\ell} \left[C_{\ell,m}^{(M)} f_{\ell}(nkr) \mathbf{X}_{\ell,m}(\theta, \phi) + \frac{1}{k} C_{\ell,m}^{(E)} \nabla \times g_{\ell}(nkr) \mathbf{X}_{\ell,m}(\theta, \phi) \right], \quad (\text{A.34})$$

$$\mathbf{H}(\mathbf{r}) = \frac{c\epsilon_0}{i} \sum_{\ell=1}^{\infty} \sum_{m=-\ell}^{\ell} \left[n^2 C_{\ell,m}^{(E)} g_{\ell}(nkr) \mathbf{X}_{\ell,m}(\theta, \phi) + \frac{1}{k} C_{\ell,m}^{(M)} \nabla \times f_{\ell}(nkr) \mathbf{X}_{\ell,m}(\theta, \phi) \right]. \quad (\text{A.35})$$

The radial functions f_{ℓ} and g_{ℓ} must be linear combinations of spherical Bessel functions of the first and second kind, j_{ℓ} and y_{ℓ} . In practice, two possibilities matter: *Regular wave* solutions, which are finite and differentiable everywhere, must be given in terms of the Bessel functions $f_{\ell} = g_{\ell} = j_{\ell}$. *Outgoing scattered wave* solutions are given by the spherical Hankel functions $h_{\ell} := j_{\ell} + iy_{\ell}$. They diverge at $r = 0$, and they become spherical waves in the far field, $h_{\ell}(kr) \approx i^{-\ell-1} e^{ikr}/kr$ for $kr \gg 1$.

The spherical vector harmonics are defined by [34]

$$\begin{aligned} \mathbf{X}_{\ell,m}(\theta, \phi) &= \frac{\mathbf{r} \times \nabla}{i\sqrt{\ell(\ell+1)}} Y_{\ell,m}(\theta, \phi) = (-)^{m+1} \mathbf{X}_{\ell,-m}^*(\theta, \phi) \\ &= \frac{1}{2\sqrt{\ell(\ell+1)}} \begin{pmatrix} \sqrt{(\ell-m)(\ell+m+1)} Y_{\ell,m+1} + \sqrt{(\ell+m)(\ell-m+1)} Y_{\ell,m-1} \\ i\sqrt{(\ell+m)(\ell-m+1)} Y_{\ell,m-1} - i\sqrt{(\ell-m)(\ell+m+1)} Y_{\ell,m+1} \\ 2m Y_{\ell,m} \end{pmatrix}, \end{aligned} \quad (\text{A.36})$$

for $\ell > 0$. They are tangential to the unit sphere, $\mathbf{r} \cdot \mathbf{X}_{\ell,m} = 0$, and they form an orthonormal set of vector-valued functions on the unit sphere, just like the well-known spherical harmonics $Y_{\ell,m}(\theta, \phi)$ do for scalar functions. The latter are defined in terms of associated Legendre polynomials [63],

$$\begin{aligned} Y_{\ell,m}(\theta, \phi) &= \sqrt{\frac{2\ell+1}{4\pi} \frac{(\ell-m)!}{(\ell+m)!}} e^{im\phi} P_{\ell}^m(\cos \theta), \quad Y_{\ell,-m} = (-)^m Y_{\ell,m}^*, \\ P_{\ell}^m(x) &= \frac{(-\sqrt{1-x^2})^m}{2^{\ell} \ell!} \partial_x^{\ell+m} (x^2-1)^{\ell} \quad \forall m \geq 0. \end{aligned} \quad (\text{A.37})$$

The orthogonality relations read as

$$\int d\Omega \mathbf{X}_{\ell',m'}^* \cdot \mathbf{X}_{\ell,m} = \int d\Omega [\mathbf{n} \times \mathbf{X}_{\ell',m'}^*] \cdot [\mathbf{n} \times \mathbf{X}_{\ell,m}] = \int d\Omega Y_{\ell',m'}^* Y_{\ell,m} = \delta_{\ell\ell'} \delta_{mm'}, \quad (\text{A.38})$$

with $\mathbf{n} = \mathbf{r}/r$ the unit vector pointing in the direction Ω . The terms $\{\mathbf{n} \times \mathbf{X}_{\ell,m}\}$ form an independent and complementary set of basis functions, $\int d\Omega \mathbf{X}_{\ell',m'}^* \cdot [\mathbf{n} \times \mathbf{X}_{\ell,m}] = 0$. Combining the vector harmonics with the spherical Bessel functions leads to basis solutions of the vector wave equation,

$$\nabla \times [\nabla \times f_\ell(nkr) \mathbf{X}_{\ell,m}(\theta, \phi)] = \epsilon k^2 f_\ell(nkr) \mathbf{X}_{\ell,m}(\theta, \phi). \quad (\text{A.39})$$

This can be checked using the identity [34]

$$\nabla \times f(r) \mathbf{X}_{\ell,m}(\theta, \phi) = \frac{1}{r} \partial_r [r f(r)] \mathbf{n} \times \mathbf{X}_{\ell,m}(\theta, \phi) + \frac{i\sqrt{\ell(\ell+1)}}{r} f(r) \mathbf{n} Y_{\ell,m}(\theta, \phi). \quad (\text{A.40})$$

The differential equation underlying the Bessel-type functions and a few addition theorems [113] are also required,

$$\ell(\ell+1) f_\ell(x) = x^2 f_\ell''(x) + 2x f_\ell'(x) + x^2 f_\ell(x), \quad (\text{A.41})$$

$$f_\ell'(x) = f_{\ell-1}(x) - \frac{\ell+1}{x} f_\ell(x) = \frac{\ell}{x} f_\ell(x) - f_{\ell+1}(x), \quad (\text{A.42})$$

$$\frac{1}{x^2} = j_\ell y_\ell' - j_\ell' y_\ell = -i [j_\ell h_\ell' - j_\ell' h_\ell]. \quad (\text{A.43})$$

In a concrete physical situation, one is often left with specific electromagnetic field distributions, such as standing-wave modes or Gaussian modes, which must be expanded in the above partial-wave basis. The expansion coefficients can be obtained by means of the integrals

$$C_{\ell,m}^{(\text{E})} g_\ell(nkr) = \frac{-ik}{\sqrt{\ell(\ell+1)}} \int d\Omega Y_{\ell,m}^*(\theta, \phi) [\mathbf{r} \cdot \mathbf{E}(r, \theta, \phi)], \quad (\text{A.44})$$

$$C_{\ell,m}^{(\text{M})} f_\ell(nkr) = \frac{k}{c\epsilon_0 \sqrt{\ell(\ell+1)}} \int d\Omega Y_{\ell,m}^*(\theta, \phi) [\mathbf{r} \cdot \mathbf{H}(r, \theta, \phi)]. \quad (\text{A.45})$$

Whether the integrals on the right hand side evaluate to the Bessel-type dependence on the radial coordinate imposed by the left hand side, depends very much on the (approximate) functional form of a given field mode. One may be forced to invoke complicated numerical methods to extract the partial-wave expansion coefficients from the above relations [241].

A direct evaluation of the integrals is possible for the most elementary cases. An x -polarized vacuum plane-wave mode running along the positive or negative z -axis, $\mathbf{E}^{(\pm)} = E_0 \mathbf{e}_x \exp(\pm ikz)$, gets expanded as [34]

$$\mathbf{E}^{(\pm)}(\mathbf{r}) = \frac{E_0}{2} \sum_{\ell=1}^{\infty} (\pm)^\ell \iota_\ell \sum_{m=\pm 1} \left[j_\ell(kr) \mathbf{X}_{\ell,m} \pm \frac{m}{k} \nabla \times j_\ell(kr) \mathbf{X}_{\ell,m} \right], \quad (\text{A.46})$$

$$\mathbf{H}^{(\pm)}(\mathbf{r}) = \frac{c\epsilon_0 E_0}{2i} \sum_{\ell=1}^{\infty} (\pm)^\ell \iota_\ell \sum_{m=\pm 1} \left[\pm m j_\ell(kr) \mathbf{X}_{\ell,m} + \frac{1}{k} \nabla \times j_\ell(kr) \mathbf{X}_{\ell,m} \right]. \quad (\text{A.47})$$

Here I have introduced the abbreviation $\iota_\ell = i^\ell \sqrt{4\pi(2\ell+1)}$. We notice that the plane wave only supports partial waves with 'helicity numbers' $m = \pm 1$. (Each component represents one of the two circular polarizations.)

The same holds for standing waves. Let us consider a symmetric standing-wave field from a coordinate system where the origin is shifted from zero to z_0 , $\mathbf{E}_{\text{sw}} = E_0 \mathbf{e}_x \cos k(z + z_0)$. From a linear combination of the above expressions we obtain

$$\mathbf{E}_{\text{sw}}(\mathbf{r}) = \frac{E_0}{2} \sum_{\ell=1}^{\infty} \iota_\ell \sum_{m=\pm 1} \left[\zeta_\ell j_\ell(kr) \mathbf{X}_{\ell,m} + \zeta_{\ell+1} \frac{m}{k} \nabla \times j_\ell(kr) \mathbf{X}_{\ell,m} \right], \quad (\text{A.48})$$

$$\mathbf{H}_{\text{sw}}(\mathbf{r}) = \frac{c\varepsilon_0 E_0}{2i} \sum_{\ell=1}^{\infty} \iota_\ell \sum_{m=\pm 1} \left[\zeta_{\ell+1} m j_\ell(kr) \mathbf{X}_{\ell,m} + \zeta_\ell \frac{1}{k} \nabla \times j_\ell(kr) \mathbf{X}_{\ell,m} \right], \quad (\text{A.49})$$

with $\zeta_\ell = \cos kz_0$ for even ℓ , and $\zeta_\ell = i \sin kz_0$ for odd ℓ .

Things get messier in the case of Gaussian modes. We can expand the approximate expressions (A.12) and (A.13) for Gaussian running-wave fields in positive or negative z -direction explicitly. A terribly tedious and dull calculation leaves us with seven ℓ -dependent expansion coefficients corresponding to $|m| = 0, 1, 2, 3$:

$$\begin{aligned} C_{\ell,0}^{(\text{E},\pm)} &= E_0^\pm \frac{i(\pm)^\ell \iota_\ell \sqrt{\ell(\ell+1)} x_0}{k w^2} \left[1 \mp \frac{2iz_0}{k w^2} (2 - \rho_0^2) \right], \\ C_{\ell,0}^{(\text{M},\pm)} &= E_0^\pm \frac{\mp(\pm)^\ell \iota_\ell \sqrt{\ell(\ell+1)} y_0}{k w^2} \left[1 \mp \frac{2iz_0}{k w^2} (2 - \rho_0^2) \right] \end{aligned} \quad (\text{A.50})$$

$$\begin{aligned} C_{\ell,|m|=1}^{(\text{E},\pm)} &= (\pm)^{\ell+1} \iota_\ell E_0^\pm \left\{ \frac{m}{2} \left[1 \pm \frac{2iz_0}{k w^2} (\rho_0^2 - 1) \right] - \frac{i\ell(\ell+1)x_0 y_0}{2k^2 w^4} \right. \\ &\quad \left. + \frac{m}{2k^2 w^2} \left[A + \frac{\ell(\ell+1)x_0^2}{w^2} + \frac{(\ell-1)(\ell+2)}{2} (\rho_0^2 - 2) \right] \right\}, \\ C_{\ell,|m|=1}^{(\text{M},\pm)} &= (\pm)^\ell \iota_\ell E_0^\pm \left\{ \frac{1}{2} \left[1 \pm \frac{2iz_0}{k w^2} (\rho_0^2 - 1) \right] + \frac{m\ell(\ell+1)x_0 y_0}{2k^2 w^4} \right. \\ &\quad \left. + \frac{1}{2k^2 w^2} \left[A + \frac{\ell(\ell+1)y_0^2}{w^2} + \frac{(\ell-1)(\ell+2)}{2} (\rho_0^2 - 2) \right] \right\} \end{aligned} \quad (\text{A.51})$$

$$\begin{aligned} C_{\ell,|m|=2}^{(\text{E},\pm)} &= (\pm)^\ell \iota_\ell E_0^\pm \frac{i\sqrt{(\ell-1)(\ell+2)}}{2k w^2} \left(i \frac{m y_0}{|m|} - x_0 \right) \left[1 \pm \frac{2iz_0}{k w^2} (\rho_0^2 - 2) \right], \\ C_{\ell,|m|=2}^{(\text{M},\pm)} &= (\pm)^\ell \iota_\ell E_0^\pm \frac{\mp\sqrt{(\ell-1)(\ell+2)}}{2k w^2} \left(i \frac{m x_0}{|m|} + y_0 \right) \left[1 \pm \frac{2iz_0}{k w^2} (\rho_0^2 - 2) \right] \end{aligned} \quad (\text{A.52})$$

$$\begin{aligned} C_{\ell,|m|=3}^{(\text{E},\pm)} &= (\pm)^\ell \iota_\ell E_0^\pm \frac{\mp m \sqrt{(\ell-2)(\ell-1)(\ell+2)(\ell+3)}}{4|m| k^2 w^4} \left(i \frac{m y_0}{|m|} - x_0 \right)^2, \\ C_{\ell,|m|=3}^{(\text{M},\pm)} &= (\pm)^\ell \iota_\ell E_0^\pm \frac{-\sqrt{(\ell-2)(\ell-1)(\ell+2)(\ell+3)}}{4k^2 w^4} \left(i \frac{m y_0}{|m|} - x_0 \right)^2 \end{aligned} \quad (\text{A.53})$$

I use the notation of Appendix A.2, plus $E_0^\pm = E_0 \exp(-\rho_0^2 \pm ikz_0)$. No other m -components are involved. The expansion coefficients of the corresponding Gaussian *standing-wave* field $\mathbf{E}_{\text{sw}} =$

$(\mathbf{E}_+ + \mathbf{E}_-)/2$ read as

$$\begin{aligned} C_{\ell,0}^{(E)} &= \iota_\ell E_0 e^{-\rho_0^2} \frac{\sqrt{\ell(\ell+1)} x_0}{k w^2} \left[i \zeta_\ell + \zeta_{\ell+1} \frac{2z_0}{k w^2} (2 - \rho_0^2) \right], \\ C_{\ell,0}^{(M)} &= \iota_\ell E_0 e^{-\rho_0^2} \frac{\sqrt{\ell(\ell+1)} y_0}{k w^2} \left[-\zeta_{\ell+1} + i \zeta_\ell \frac{2z_0}{k w^2} (2 - \rho_0^2) \right], \end{aligned} \quad (\text{A.54})$$

$$\begin{aligned} C_{\ell,|m|=1}^{(E)} &= \iota_\ell E_0 e^{-\rho_0^2} \left\{ \frac{m}{2} \left[\zeta_{\ell+1} + i \zeta_\ell \frac{2z_0}{k w^2} (\rho_0^2 - 1) \right] - i \zeta_{\ell+1} \frac{\ell(\ell+1) x_0 y_0}{2 k^2 w^4} \right. \\ &\quad \left. + \frac{m \zeta_{\ell+1}}{2 k^2 w^2} \left[A + \frac{\ell(\ell+1) x_0^2}{w^2} + \frac{(\ell-1)(\ell+2)}{2} (\rho_0^2 - 2) \right] \right\}, \\ C_{\ell,|m|=1}^{(M)} &= \iota_\ell E_0 e^{-\rho_0^2} \left\{ \frac{1}{2} \left[\zeta_\ell + i \zeta_{\ell+1} \frac{2z_0}{k w^2} (\rho_0^2 - 1) \right] + i \zeta_\ell \frac{m \ell(\ell+1) x_0 y_0}{2 k^2 w^4} \right. \\ &\quad \left. + \frac{\zeta_\ell}{2 k^2 w^2} \left[A + \frac{\ell(\ell+1) y_0^2}{w^2} + \frac{(\ell-1)(\ell+2)}{2} (\rho_0^2 - 2) \right] \right\}, \end{aligned} \quad (\text{A.55})$$

$$\begin{aligned} C_{\ell,|m|=2}^{(E)} &= -\iota_\ell E_0 e^{-\rho_0^2} \frac{\sqrt{(\ell-1)(\ell+2)}}{2 k w^2} \left(\frac{m y_0}{|m|} + i x_0 \right) \left[\zeta_\ell + i \zeta_{\ell+1} \frac{2z_0}{k w^2} (\rho_0^2 - 2) \right], \\ C_{\ell,|m|=2}^{(M)} &= -\iota_\ell E_0 e^{-\rho_0^2} \frac{\sqrt{(\ell-1)(\ell+2)}}{2 k w^2} \left(i \frac{m x_0}{|m|} + y_0 \right) \left[\zeta_{\ell+1} + i \zeta_\ell \frac{2z_0}{k w^2} (\rho_0^2 - 2) \right], \end{aligned} \quad (\text{A.56})$$

$$\begin{aligned} C_{\ell,|m|=3}^{(E)} &= -\iota_\ell E_0 e^{-\rho_0^2} \frac{m \sqrt{(\ell-2)(\ell-1)(\ell+2)(\ell+3)}}{4 |m| k^2 w^4} \zeta_{\ell+1} \left(i \frac{m y_0}{|m|} - x_0 \right)^2, \\ C_{\ell,|m|=3}^{(M)} &= -\iota_\ell E_0 e^{-\rho_0^2} \frac{\sqrt{(\ell-2)(\ell-1)(\ell+2)(\ell+3)}}{4 k^2 w^4} \zeta_\ell \left(i \frac{m y_0}{|m|} - x_0 \right)^2. \end{aligned} \quad (\text{A.57})$$

A.6. Mie scattering at spherical dielectrics

The Mie problem of electromagnetic wave scattering at spherical dielectrics has been assessed in its many facets since the beginning of the 20th century [28, 29, 34, 90]. In many cases the situation of a plane running wave impinging on a spherical dielectric has been studied, whereas here, I will consider spherical particles brought into a Gaussian standing-wave mode.

In the simplest case of a homogeneous dielectric sphere of relative permittivity ϵ , exposed to an electromagnetic wave in vacuum, the Mie scattering problem is solved as follows: First the original fields $\{\mathbf{E}_0, \mathbf{H}_0\}$ in the absence of the sphere are expanded in spherical harmonics, see Appendix A.5, Equations (A.34) and (A.35). As a regular wave solution with no divergencies, the expansion reads as

$$\begin{pmatrix} \mathbf{E}_0 \\ i \mathbf{H}_0 / c \epsilon_0 \end{pmatrix} = \sum_{\ell, m} \left[\begin{pmatrix} C_{\ell, m}^{(M)} \\ C_{\ell, m}^{(E)} \end{pmatrix} j_\ell(kr) \mathbf{X}_{\ell, m} + \frac{1}{k} \begin{pmatrix} C_{\ell, m}^{(E)} \\ C_{\ell, m}^{(M)} \end{pmatrix} \nabla \times j_\ell(kr) \mathbf{X}_{\ell, m} \right]. \quad (\text{A.58})$$

Note that I chose the origin of the coordinate system to be the sphere center. In the presence of the sphere we can make the ansatz $\mathbf{E}_{\text{ext}} = \mathbf{E}_0 + \mathbf{E}_{\text{sca}}$ for the field outside of the sphere, with yet

undetermined outgoing scattered-wave fields

$$\begin{Bmatrix} \mathbf{E}_{\text{sca}} \\ i\mathbf{H}_{\text{sca}}/c\epsilon_0 \end{Bmatrix} = \sum_{\ell,m} \left[\begin{Bmatrix} \alpha_\ell C_{\ell,m}^{(M)} \\ \beta_\ell C_{\ell,m}^{(E)} \end{Bmatrix} h_\ell(kr) \mathbf{X}_{\ell,m} + \frac{1}{k} \begin{Bmatrix} \beta_\ell C_{\ell,m}^{(E)} \\ \alpha_\ell C_{\ell,m}^{(M)} \end{Bmatrix} \nabla \times h_\ell(kr) \mathbf{X}_{\ell,m} \right]. \quad (\text{A.59})$$

Due to the symmetry we expect the same angular field distribution, and that the unknown scattering coefficients α_ℓ and β_ℓ depend only on the index ℓ of the radial part. A similar ansatz is used for the fields inside the dielectric sphere, which must be regular and finite at $r = 0$,

$$\begin{Bmatrix} \mathbf{E}_{\text{int}} \\ i\mathbf{H}_{\text{int}}/c\epsilon_0 \end{Bmatrix} = \sum_{\ell,m} \left[\begin{Bmatrix} a_\ell C_{\ell,m}^{(M)} \\ nb_\ell C_{\ell,m}^{(E)} \end{Bmatrix} j_\ell(nkr) \mathbf{X}_{\ell,m} + \frac{1}{k} \begin{Bmatrix} b_\ell C_{\ell,m}^{(E)}/n \\ a_\ell C_{\ell,m}^{(M)} \end{Bmatrix} \nabla \times j_\ell(nkr) \mathbf{X}_{\ell,m} \right], \quad (\text{A.60})$$

with $n = \sqrt{\epsilon}$ the (complex) refractive index. The unknown coefficients are obtained from the boundary condition that the tangential components of the fields must be continuous everywhere. We thus have $\mathbf{n} \times \mathbf{E}_{\text{int}}(R\mathbf{n}) = \mathbf{n} \times [\mathbf{E}_0(R\mathbf{n}) + \mathbf{E}_{\text{sca}}(R\mathbf{n})]$ on the surface of the sphere with radius R . The same holds for the magnetization fields. The tangential component of each summand in the expansion is easily obtained with help of (A.40),

$$\mathbf{n} \times [\nabla \times f(r) \mathbf{X}_{\ell,m}] = -\partial_r [rf(r)] \mathbf{X}_{\ell,m}. \quad (\text{A.61})$$

Recall that $\{\mathbf{X}_{\ell,m}\}$ and $\{\mathbf{n} \times \mathbf{X}_{\ell,m}\}$ form two independent orthonormal sets of functions on the unit sphere. The two boundary conditions for \mathbf{E} and \mathbf{H} thus yield four independent equations for each ℓ to determine the unknown parameters by comparing the expansion coefficients. We obtain the well-known expressions for the scattering coefficients [29],

$$\alpha_\ell = \frac{j_\ell(nkR) \partial_R [Rj_\ell(kR)] - j_\ell(kR) \partial_R [Rj_\ell(nkR)]}{h_\ell(kR) \partial_R [Rj_\ell(nkR)] - j_\ell(nkR) \partial_R [Rh_\ell(kR)]} =: \frac{A_\ell}{F_\ell}, \quad (\text{A.62})$$

$$\beta_\ell = \frac{n^2 j_\ell(nkR) \partial_R [Rj_\ell(kR)] - j_\ell(kR) \partial_R [Rj_\ell(nkR)]}{h_\ell(kR) \partial_R [Rj_\ell(nkR)] - n^2 j_\ell(nkR) \partial_R [Rh_\ell(kR)]} =: \frac{B_\ell}{G_\ell}, \quad (\text{A.63})$$

and $a_\ell = 1/ikRF_\ell$, $b_\ell = n/ikRG_\ell$. These radial coefficients for a homogeneous sphere are used throughout this thesis to describe the light force, absorption and scattering at spherical particles.

Finally I briefly mention the slightly more involved example of a hollow dielectric sphere of outer radius R and inner radius $R_0 < R$. It hints at how to solve generic situations of spherically symmetric dielectrics with arbitrary interfaces. In this case we have three regions and two interfaces: The fields in the outer region, $r > R$, are given by $\{\mathbf{E}_{\text{ext}}, \mathbf{H}_{\text{ext}}\}$ like above. For the fields in the inner vacuum region, $r < R_0$, we start with an undetermined expression similar to (A.59), where α_ℓ, β_ℓ are replaced by two different coefficients c_ℓ, d_ℓ , and where the Hankel function h_ℓ is replaced by the regular Bessel function j_ℓ . The latter guarantees that the field is finite at the origin. This condition does not have to be fulfilled inside the dielectric, $R_0 < r < R$, anymore. That is to say, we replace the terms $a_\ell j_\ell$ and $b_\ell j_\ell$ in (A.60) by the general linear combinations of Bessel functions, $a_\ell j_\ell + i\tilde{a}_\ell y_\ell$ and $b_\ell j_\ell + i\tilde{b}_\ell y_\ell$. We are left with eight unknown ℓ -coefficients, which are determined by the boundary conditions at the two interfaces. Using a short-hand notation without arguments for $h_\ell = h_\ell(kR)$, $j_\ell = j_\ell(kR)$, $y_\ell^{(n)} = y_\ell(nkR)$, $y_\ell^{(n,0)} = y_\ell(nkR_0)$, $j_\ell^{(n)} = j_\ell(nkR)$, $j_\ell^{(n,0)} = j_\ell(nkR_0)$, and $j_\ell^{(0)} =$

$j_\ell(kR_0)$, we find

$$\alpha_\ell = \frac{1}{C_\ell} \left\{ \left[j_\ell \left(R j_\ell^{(n)} \right)' - j_\ell^{(n)} \left(R j_\ell \right)' \right] \left[j_\ell^{(0)} \left(R_0 y_\ell^{(n,0)} \right)' - y_\ell^{(n,0)} \left(R_0 j_\ell^{(0)} \right)' \right] \right. \\ \left. - \left[j_\ell \left(R y_\ell^{(n)} \right)' - y_\ell^{(n)} \left(R j_\ell \right)' \right] \left[j_\ell^{(0)} \left(R_0 j_\ell^{(n,0)} \right)' - j_\ell^{(n,0)} \left(R_0 j_\ell^{(0)} \right)' \right] \right\}, \quad (\text{A.64})$$

$$\beta_\ell = \frac{1}{D_\ell} \left\{ \left[j_\ell \left(R j_\ell^{(n)} \right)' - n^2 j_\ell^{(n)} \left(R j_\ell \right)' \right] \left[j_\ell^{(0)} \left(R_0 y_\ell^{(n,0)} \right)' - n^2 y_\ell^{(n,0)} \left(R_0 j_\ell^{(0)} \right)' \right] \right. \\ \left. - \left[j_\ell \left(R y_\ell^{(n)} \right)' - n^2 y_\ell^{(n)} \left(R j_\ell \right)' \right] \left[j_\ell^{(0)} \left(R_0 j_\ell^{(n,0)} \right)' - n^2 j_\ell^{(n,0)} \left(R_0 j_\ell^{(0)} \right)' \right] \right\}, \quad (\text{A.65})$$

$$a_\ell = \frac{y_\ell^{(n,0)} \left(R_0 j_\ell^{(0)} \right)' - j_\ell^{(0)} \left(R_0 y_\ell^{(n,0)} \right)'}{ikRC_\ell}, \quad \tilde{a}_\ell = \frac{j_\ell^{(n,0)} \left(R_0 j_\ell^{(0)} \right)' - j_\ell^{(0)} \left(R_0 j_\ell^{(n,0)} \right)'}{kRC_\ell}, \quad (\text{A.66})$$

$$b_\ell = \frac{n^2 y_\ell^{(n,0)} \left(R_0 j_\ell^{(0)} \right)' - j_\ell^{(0)} \left(R_0 y_\ell^{(n,0)} \right)'}{ikRD_\ell/n}, \quad \tilde{b}_\ell = \frac{n^2 j_\ell^{(n,0)} \left(R_0 j_\ell^{(0)} \right)' - j_\ell^{(0)} \left(R_0 j_\ell^{(n,0)} \right)'}{kRD_\ell/n}, \quad (\text{A.67})$$

$$c_\ell = \frac{i}{nk^2RR_0C_\ell}, \quad d_\ell = \frac{in}{k^2RR_0D_\ell}. \quad (\text{A.68})$$

The denominators are

$$C_\ell = \left[h_\ell \left(R y_\ell^{(n)} \right)' - y_\ell^{(n)} \left(R h_\ell \right)' \right] \left[j_\ell^{(0)} \left(R_0 j_\ell^{(n,0)} \right)' - j_\ell^{(n,0)} \left(R_0 j_\ell^{(0)} \right)' \right] \\ - \left[h_\ell \left(R j_\ell^{(n)} \right)' - j_\ell^{(n)} \left(R h_\ell \right)' \right] \left[j_\ell^{(0)} \left(R_0 y_\ell^{(n,0)} \right)' - y_\ell^{(n,0)} \left(R_0 j_\ell^{(0)} \right)' \right], \quad (\text{A.69})$$

$$D_\ell = \left[h_\ell \left(R y_\ell^{(n)} \right)' - n^2 y_\ell^{(n)} \left(R h_\ell \right)' \right] \left[j_\ell^{(0)} \left(R_0 j_\ell^{(n,0)} \right)' - n^2 j_\ell^{(n,0)} \left(R_0 j_\ell^{(0)} \right)' \right] \\ - \left[h_\ell \left(R j_\ell^{(n)} \right)' - n^2 j_\ell^{(n)} \left(R h_\ell \right)' \right] \left[j_\ell^{(0)} \left(R_0 y_\ell^{(n,0)} \right)' - n^2 y_\ell^{(n,0)} \left(R_0 j_\ell^{(0)} \right)' \right]. \quad (\text{A.70})$$

Appendix B.

Matter-wave interferometry

B.1. Ideal Poisson spot diffraction

The Poisson spot diffraction pattern behind an ideal disc of radius R is determined by the amplitude function (3.10) and the transmission function of the disc, $t(\mathbf{r}) = \Theta(r - R)$,

$$\psi(\mathbf{r}) = k\ell \int_{u>1} d^2u \exp \left[i\pi k\ell u^2 - 2\pi i k \frac{\mathbf{u} \cdot \mathbf{r}}{R} \right]. \quad (\text{B.1})$$

The function is isotropic, $\psi(\mathbf{r}) = \psi(r)$, which can be made explicit by switching to polar coordinates and by employing the integral representation of the Bessel function [113], $2\pi J_0(x) = \int_0^{2\pi} d\phi \exp(ix \cos \phi)$.

$$\psi(r) = 2\pi k\ell \int_1^\infty du u \exp(i\pi k\ell u^2) J_0\left(2\pi k u \frac{r}{R}\right) \quad (\text{B.2})$$

A direct evaluation of this integral is problematic because of the asymptotic $x^{-1/2}$ -scaling of the Bessel function which impedes the numerical convergence of the integral. On the other hand, the unrestricted integral over \mathbb{R}^2 ,

$$\psi_0(r) = k\ell \int d^2u \exp \left[i\pi k\ell u^2 - 2\pi i k \frac{\mathbf{u} \cdot \mathbf{r}}{R} \right], \quad (\text{B.3})$$

must exist since it determines the unmodulated matter-wave density that would be observed in the absence of the diffracting obstacle. The integral represents the Fourier transform of a complex Gaussian, which results in another complex Gaussian, as obtained from the formula [63]

$$\int_0^\infty dx x e^{\pm i a x^2} J_0(bx) = \pm \frac{i}{2a} e^{\mp i b^2/4a}. \quad (\text{B.4})$$

We are left with a phase term of unit modulus,

$$\psi_0(r) = 2\pi k\ell \int_0^\infty du u \exp(i\pi k\ell u^2) J_0\left(2\pi k u \frac{r}{R}\right) = i \exp\left(-i\pi \frac{kr^2}{\ell R^2}\right). \quad (\text{B.5})$$

Plugging this into the expression (3.11) yields the constant density $\mathcal{I}_0 = m^2 D(0) / (T_1 + T_2)^2$ of an uncollimated matter-wave beam that emerges from the source and hits the screen with no obstacle in between. The exact geometric projection of a beam with a finite collimation angle is obtained from (3.9),

$$w_0(r) = \left[\frac{m}{(T_1 + T_2)} \right]^2 \int d^2r_0 S(r_0) D\left(\frac{m}{T_1 + T_2} \left| \mathbf{r} + \frac{T_2}{T_1} \mathbf{r}_0 \right| \right). \quad (\text{B.6})$$

The trick now is to apply Babinet's principle and split the diffraction amplitude into $\psi(\mathbf{r}) = \psi_0(\mathbf{r}) - \psi_1(\mathbf{r})$. The difference term,

$$\psi_1(\mathbf{r}) = 2\pi k\ell \int_0^1 du u \exp(i\pi k\ell u^2) J_0\left(2\pi k u \frac{r}{R}\right), \quad (\text{B.7})$$

is a bound integral which can be easily computed using standard numerics software, such as MATLAB. It represents the diffraction amplitude of a circular aperture of radius R .

A simple calculation reveals the amplitudes at the center of the screen, $\mathbf{r} = 0$,

$$\psi_1(0) = i(1 - e^{i\pi k\ell}), \quad \psi(0) = i e^{i\pi k\ell}. \quad (\text{B.8})$$

The amplitude can also be given explicitly in the limit of large screen coordinates, $r \gg R/k$. For this I insert the lowest-order asymptotic expansion of the Bessel function [113], $J_0(x) \approx \sqrt{2/\pi x} \cos(x - \pi/4)$, into the integral (B.7). Its magnitude is then asymptotically bounded from above by

$$\begin{aligned} |\psi_1(\mathbf{r})| &\approx \sqrt{\frac{4k\ell^2 R}{r}} \left| \int_0^1 du \sqrt{u} \exp(i\pi k\ell u^2) \cos\left(2\pi k u \frac{r}{R} - \frac{\pi}{4}\right) \right| \\ &\leq \sqrt{\frac{4k\ell^2 R}{r}} \int_0^1 du \sqrt{u} = \frac{4k\ell}{3} \sqrt{\frac{R}{kr}}, \end{aligned} \quad (\text{B.9})$$

which vanishes in the limit $kr/R \rightarrow \infty$.

B.2. Classical Poisson spot of a point source

In the limit of a perfect point source, $R_0 \rightarrow 0$, the modified classical density distribution (3.25) on the screen behind the obstacle becomes

$$\begin{aligned} f(\mathbf{r}) &= \mathcal{I}_0 \int d^2 r_0 \delta\left[\mathbf{r}_0 - \frac{T_1}{T_2} \mathbf{r} + \mathbf{q}\left(\frac{T_2 \mathbf{r}_0}{\ell T_1}\right) \frac{T_1}{m}\right] \Theta\left[r_0 - \frac{\ell T_1}{T_2} (1 + \eta) R\right] \\ &= \mathcal{I}_0 \ell^2 \int_{r_0 \geq (1+\eta)R} d^2 r_0 \delta\left[\ell \mathbf{r}_0 - \mathbf{r} + \frac{\mathbf{q}(\mathbf{r}_0) T_2}{m}\right]. \end{aligned} \quad (\text{B.10})$$

We can split the δ -function into its x - and y -component, using polar coordinates and noting that the momentum kick $\mathbf{q}(\mathbf{r}_0)$ points into the inward radial direction,

$$\delta\left[\ell \mathbf{r}_0 - \mathbf{r} + \frac{\mathbf{q}(\mathbf{r}_0) T_2}{m}\right] = \delta\{[\ell r_0 - RQ(r_0)] \cos \theta - r\} \delta\{[\ell r_0 - RQ(r_0)] \sin \theta\}. \quad (\text{B.11})$$

The polar angle θ is defined with respect to the screen coordinate $\mathbf{r} = (r, 0)$. The second term can be evaluated in the angular coordinate with help of the identity $\delta[g(x)] = \sum_n \delta(x - x_n) / |g'(x_n)|$, where $\{x_n\}$ denote the simple zeros of the function $g(x)$. Here, they are $\theta = 0, \pi$, which leads to

$$\begin{aligned} \delta\left[\ell \mathbf{r}_0 - \mathbf{r} + \frac{\mathbf{q}(\mathbf{r}_0) T_2}{m}\right] &= \frac{\delta[\ell r_0 - RQ(r_0) - r] \delta(\theta) + \delta[\ell r_0 - RQ(r_0) + r] \delta(\theta - \pi)}{|\ell r_0 - RQ(r_0)|} \\ &= \frac{\delta[\ell r_0 - RQ(r_0) - r] \delta(\theta) + \delta[\ell r_0 - RQ(r_0) + r] \delta(\theta - \pi)}{r}. \end{aligned} \quad (\text{B.12})$$

Plugging this into the above expression (B.10) leaves us with the result

$$\begin{aligned} f(r) &= \frac{\mathcal{I}_0 \ell^2}{r} \int_{(1+\eta)R}^{\infty} dr_0 r_0 \{ \delta[\ell r_0 - RQ(r_0) - r] + \delta[\ell r_0 - RQ(r_0) + r] \} \\ &= \frac{\mathcal{I}_0 \ell^2}{r} \left\{ \frac{r_+}{|\ell - RQ'(r_+)|} + \frac{r_-}{|\ell - RQ'(r_-)|} \right\} \quad \text{if } r_{\pm} \geq (1+\eta)R. \end{aligned} \quad (\text{B.13})$$

The radii r_{\pm} in the obstacle plane are the solutions of the transcendental equations $\ell r_{\pm} - RQ(r_{\pm}) \mp r = 0$, and they constitute the two contributions to the density distribution. Each contribution is present only if the respective solution is larger than the effective radius of the obstacle, $r_{\pm} \geq (1+\eta)R$.

B.3. Capture range of a spherical obstacle

Consider the three-dimensional scattering of a particle at a sphere of radius R , which is located at $\mathbf{r} = 0$. It shall attract the particle by means of the radial potential $V(\mathbf{r}) = -C_4/(|\mathbf{r}| - R)^4$. The particle shall approach the sphere from $z = -\infty$ with an asymptotic velocity $v_z > 0$ and an impact parameter $r_0 > R$. The goal is to find the greatest value $r_0 = \eta R$ at which the incoming particle is captured and ultimately collides with the sphere.

Trajectories with a greater impact parameter are merely deflected and leave the vicinity of the sphere afterwards, that is, they are characterized by a perihelion $|\mathbf{r}| = r_{\min} > R$. At this point, the radial velocity vanishes, $\partial_t |\mathbf{r}| = 0$, and the particle velocity v_{\min} is purely tangential to the sphere. Angular momentum conservation relates the perihelion to the initial values, $r_0 v_z = r_{\min} v_{\min}$. The initial kinetic energy, $E = mv_z^2/2$, is also conserved, $E = mv_{\min}^2/2 + V(r_{\min})$. Combining both equations leads to a relation between the impact parameter and the turning point,

$$\frac{r_0}{R} = \frac{r_{\min}}{R} \sqrt{1 + \frac{C_4}{E(r_{\min} - R)^4}} = (v+1) \sqrt{1 + \frac{C_4}{ER^4 v^4}}, \quad (\text{B.14})$$

where I have expressed $r_{\min} = R(v+1)$. Given that there exists a turning point $v > 0$, the formula yields the corresponding impact parameter $r_0 = r_0(v)$. It turns out that this function has a unique minimum, $r_0 = \eta R$, which is easily found by setting the derivative to zero, $\partial_v r_0(v) = 0$, and plugging the solution v back into the above form. This leads to the result (3.32) given in the main text.

B.4. General form of the Talbot-Lau fringe pattern

I repeat the derivation of the Talbot-Lau fringe pattern for the more general case of different pulse separation times, $T_1 \neq T_2$, and a different periods of the first two gratings, $d_1 \neq d$. I start from (3.43), plug in the Fourier expansions of the kernels with different periods and perform all possible Dirac- δ integrations to obtain

$$\begin{aligned} w_3(x) &= \frac{1}{\Delta x} \sum_{n,k} \tilde{D} \left\{ d \frac{T_2}{T_1} \left[k \frac{d}{d_1} \left(1 + \frac{T_1}{T_2} \right) + n \right] \right\} B_k^{(1)} \left(\frac{dT_2}{d_1 T_1} \left[k \frac{d}{d_1} \left(1 + \frac{T_1}{T_2} \right) + n \right] \right) \\ &\quad \times B_n^{(2)} \left[\left(n + k \frac{d}{d_1} \right) \frac{T_2}{T_1} \right] \exp \left\{ 2\pi i \left(\frac{n}{d} + \frac{k}{d_1} \right) \left[x - \frac{a}{2} (T_1 + T_2)^2 \right] + \frac{i\pi n a}{d} T_1^2 \right\}. \end{aligned} \quad (\text{B.15})$$

Once again, we are only interested in the cases where the separation times are at least of the order of the Talbot time, $T_{1,2} \gtrsim T_T$, and where the grating constants d, d_1 do not differ by orders of magnitude. (In practical implementations, the latter differ at most by a small integer factor.) Then the incoherent initial illumination, $P_0 \gg h/d$, implies that the only non-vanishing contributions to (B.15) are those summands which fulfill

$$\left| n + k \frac{d}{d_1} \left(1 + \frac{T_1}{T_2} \right) \right| \ll 1. \quad (\text{B.16})$$

This is because the width of the Fourier transform \tilde{D} of the initial momentum distribution is bound by about $h/P_0 \ll d$. Note that n and k are integers. In the limit of no coherence, $P_0 \rightarrow \infty$, the relation can only be fulfilled if the ratios of grating constants, $v = d_1/d$, and separation times, $\eta = T_2/T_1$, are rational numbers [60], $(\eta + 1)/\eta v = r/s$. The coprime integers $r, s \in \mathbb{N}$ constitute the completely reduced representation of this *resonance condition*, and they restrict the double sum in (B.15) to index pairs (n, k) with $sn = -rk$. In principle, almost any chosen set of pulse separation times and grating periods will constitute a rational fraction r/s in the above sense. In practice, however, a pronounced fringe visibility can only be expected for small values of r and s , which include low-order Talbot coefficients in the Fourier sum.

We can relax the formal resonance condition in realistic situations with limited momentum spread by introducing the small deviations, $|\delta| \ll d$ and $|\tau| \ll T$, from the resonance configuration, $T_1 = T$, $T_2 = \eta T + \tau$, $d_1 = vd + \delta$. We may then approximate

$$\begin{aligned} \tilde{D} \left\{ d \frac{T_2}{T_T} \left[k \frac{d}{d_1} \left(1 + \frac{T_1}{T_2} \right) + n \right] \right\} &= \tilde{D} \left\{ d \frac{\eta T + \tau}{T_T} \left[\frac{k}{v + \delta/d} \left(1 + \frac{1}{\eta + \tau/T} \right) + n \right] \right\} \\ &\approx \tilde{D} \left\{ d \frac{\eta T + \tau}{T_T} \left[k \frac{r}{s} \left(1 - \frac{\delta}{vd} - \frac{\tau}{\eta(\eta + 1)T} \right) + n \right] \right\} \\ &\approx \delta_{sn, -rk} \tilde{D} \left[-\frac{kr}{sT_T} \left(\frac{\eta}{v} T\delta + \frac{d\tau}{\eta + 1} \right) \right]. \end{aligned} \quad (\text{B.17})$$

The remaining argument determines the loss of fringe visibility due to small deviations from resonance. It can be used to estimate the required precision in the adjustment of the TLI setup [60].

Introducing a new summation index, $s\ell = -k$, we find

$$\begin{aligned} w_3(x) &= \frac{1}{\Delta x} \sum_{\ell} \tilde{D} \left[\frac{r\ell}{T_T} \left(\frac{\eta}{v} T\delta + \frac{d\tau}{\eta + 1} \right) \right] B_{-s\ell}^{(1)} \left[\frac{r\ell}{vT_T} \left(\frac{\eta}{v} T\delta + \frac{d\tau}{\eta + 1} \right) \right] \\ &\quad \times B_{r\ell}^{(2)} \left[\frac{s\ell T}{vT_T} \left(1 + \frac{\tau}{\eta T} + \frac{\eta\delta}{vd} \right) \right] \exp \left[\frac{2\pi i s\ell x}{\eta vd} \left(1 + \frac{\eta\delta}{vd} \right) \right] \\ &\quad \times \exp \left\{ -\frac{i\pi ar\ell T^2}{d} \left[\eta + \frac{\eta\delta}{vd} (\eta + 1) + \frac{2\tau}{T} \right] \right\}, \end{aligned} \quad (\text{B.18})$$

to first order in the deviations. The recorded signal behind the third grating, and its visibility, are obtained by a convolution with the third grating mask, as given in the main text. Notice, however, that the period of the fringe pattern is here given by

$$d_3 = \frac{\eta vd}{s} \left(1 + \frac{\eta\delta}{vd} \right)^{-1}, \quad (\text{B.19})$$

and the period of G_3 must be adapted accordingly. If we set d_3 as the period of G_3 then the Fourier components of the detection signal $S(x_s)$ are obtained by multiplying the Fourier components in (B.18) with the mask coefficients $B_{-\ell}^{(3)}(0)$. The exponent in the third line of (B.18) represents the effective shift of the fringe pattern due to the acceleration a .

B.5. Decoherence events in the general TLI scheme

Here I study how the general Talbot-Lau fringe pattern is modified due to a single decoherence event $\mathcal{R}(x' - x)$ occurring at the time $t \in [-T_1, T_2]$ before or after the second grating. The event corresponds to a momentum averaging transformation in (quantum and classical) phase space, $w(x, p) \mapsto \int dq \tilde{\mathcal{R}}(q) w(x, p - q)$, with $\tilde{\mathcal{R}}(q)$ the Fourier transform of the decoherence function \mathcal{R} , as defined in (3.55). We obtain the modified Wigner function at G_3 by inserting this transformation as an additional step into the phase-space derivation of the unmodified result (3.43). We distinguish two cases: If the event occurs before G_2 , $t \in [-T_1, 0]$, we arrive at

$$\begin{aligned} \tilde{w}_3(x, p) = & \frac{1}{\Delta x} \int dp_0 dp_1 dq \tilde{\mathcal{R}}(q) D(p_0) T^{(2)} \left(x - \frac{pT_2}{m} + \frac{a}{2} T_2^2, p - p_1 - maT_2 \right) \\ & \times T^{(1)} \left(x - \frac{pT_2}{m} - \frac{p_1 T_1}{m} + \frac{q}{m} (T_1 + t) + \frac{a}{2} (T_1^2 + T_2^2), p_1 - p_0 - q - maT_1 \right). \end{aligned} \quad (\text{B.20})$$

If it occurs later, $t \in [0, T_2]$, the Wigner function reads as

$$\begin{aligned} \tilde{w}_3(x, p) = & \frac{1}{\Delta x} \int dp_0 dp_1 dq \tilde{\mathcal{R}}(q) D(p_0) T^{(2)} \left(x - \frac{pT_2}{m} + \frac{qt}{m} + \frac{a}{2} T_2^2, p - p_1 - q - maT_2 \right) \\ & \times T^{(1)} \left(x - \frac{pT_2}{m} - \frac{p_1 T_1}{m} + \frac{qt}{m} + \frac{a}{2} (T_1^2 + T_2^2), p_1 - p_0 - maT_1 \right). \end{aligned} \quad (\text{B.21})$$

The modified fringe pattern is given by the momentum-integrated Wigner function. In the latter case we immediately obtain a simple result,

$$\tilde{w}_3(x) = \int dq \tilde{\mathcal{R}}(q) w_3 \left(x + q \frac{t - T_2}{m} \right), \quad \forall t \in [0, T_2], \quad (\text{B.22})$$

with $w_3(x)$ the unmodified pattern. The fringe pattern is effectively smeared out over the momentum distribution. Expectedly, the effect on the fringe pattern is the strongest when the event happens close to the second grating, $t = 0$, and it vanishes when the event happens in the end, $t = T_2$.

The effect is more complicated in the case of $t \in [-T_1, 0]$ due to the interplay between the coherent grating kernels of G_1 and G_2 ,

$$\begin{aligned} \tilde{w}_3(x) = & \frac{1}{\Delta x} \int dp dp_0 dp_1 dq \tilde{\mathcal{R}}(q) D \left(p_0 + q \frac{t}{T_1} \right) \\ & \times T^{(1)} \left(x - \frac{qT_2}{m} \left(\frac{t}{T_1} + 1 \right) - \frac{pT_2}{m} - \frac{p_1 T_1}{m} + \frac{a}{2} (T_1^2 + T_2^2), p_1 - p_0 - maT_1 \right) \\ & \times T^{(2)} \left(x - \frac{qT_2}{m} \left(\frac{t}{T_1} + 1 \right) - \frac{pT_2}{m} + \frac{a}{2} T_2^2, p - p_1 - maT_2 \right). \end{aligned} \quad (\text{B.23})$$

However, the result can be simplified if we restrict our view to the incoherent limit, where the initial momentum distribution $D(p_0)$ is much broader than the kick distribution $\tilde{\mathcal{R}}(q)$. In this case we may approximate $D(p_0 + qt/T_1) \approx D(p_0)$ in the above integral, and we obtain a similar result as in the other case. By introducing the relative event time,

$$\vartheta = \begin{cases} 1 - t/T_2 & \text{for } t \in [0, T_2] \\ 1 + t/T_1 & \text{for } t \in [-T_1, 0] \end{cases} \in [0, 1], \quad (\text{B.24})$$

the modified fringe pattern can be expressed in a unified form,

$$\tilde{w}_3(x) \approx \int dq \tilde{\mathcal{R}}(q) w_3\left(x - \frac{qT_2}{m} \vartheta\right). \quad (\text{B.25})$$

Inserting the Fourier expansion (B.18) of the unmodified fringe pattern in the resonance approximation, $w_3(x) = \sum_{\ell} W_{\ell} \exp(2\pi i \ell x/d_3)$, we find that each of its Fourier components is modulated by a reduction factor,

$$\tilde{w}_3(x) = \sum_{\ell} \mathcal{R}\left(\frac{h\ell T_2 \vartheta}{md_3}\right) W_{\ell} \exp\left(\frac{2\pi i \ell x}{d_3}\right), \quad (\text{B.26})$$

with d_3 the fringe period (B.19).

Appendix C.

Classicalization and Macroscopicity

C.1. Decay of persistent current superpositions

The coherence decay rates (4.141) and (4.142) of current superposition states in superconducting loops, as defined in Section 4.2.4, become numerically accessible in the continuum approximation (4.72), where the sums over discrete wave vectors are replaced by integrals. We arrive at the expressions

$$\Gamma_{\text{deph}} = \frac{4V^2}{(2\pi)^6 \tau} \int d^3s \int_{(2\pi\hbar)^3/V} d^3q g(s, q) (1 - e^{i\Delta k \cdot s}) \left| \int d^3k v_k^2 e^{ik \cdot s} \right|^2, \quad (\text{C.1})$$

$$\Gamma_{\text{diff}} = \frac{2V}{(2\pi)^3 \tau} \int d^3s \int_{|\mathbf{k}_1 - \mathbf{k}_2| \geq 2\pi/V^{1/3}} d^3k_1 d^3k_2 g(s, \hbar |\mathbf{k}_1 - \mathbf{k}_2|) u_{\mathbf{k}_1} v_{\mathbf{k}_2} \times (u_{\mathbf{k}_1} v_{\mathbf{k}_2} + u_{\mathbf{k}_2} v_{\mathbf{k}_1} e^{i(\mathbf{k}_1 + \mathbf{k}_2) \cdot s}). \quad (\text{C.2})$$

It is assumed that the superconductor volume V is sufficiently large to extend the s -integration to infinity, and that both the distribution function g and the occupation amplitude $v_k = v_k$ are isotropic. Recall that the latter takes the complicated form (4.128) only within a small shell $k \in [k_-, k_+]$ around the Fermi surface $k = k_F$ which is determined by the phononic Debye cutoff frequency, $k_{\pm} = \sqrt{k_F^2 \pm 2m_e \omega_D / \hbar}$. The occupation amplitude outside the shell is given by the simple Fermi expression $v_k = \Theta(k_F - k) = v_k^2$. With this we are able to compute the term

$$\begin{aligned} \int d^3k v_k^2 e^{ik \cdot s} &= \int_{k \leq k_F} d^3k e^{ik \cdot s} + \int_{k \in [k_-, k_+]} d^3k [v_k^2 - \Theta(k_F - k)] e^{ik \cdot s} \\ &= \frac{4\pi k_F^2}{s} j_1(k_F s) + 4\pi \int_{k_-}^{k_+} dk \frac{k}{s} \sin(ks) [v_k^2 - \Theta(k_F - k)] \\ &= \frac{4\pi k_F^2}{s} j_1(k_F s) - 4\pi \int_{k_-}^{k_+} dk \frac{k}{s} \sin(ks) \left[\frac{k^2 - k_F^2}{2\sqrt{(k^2 - k_F^2)^2 + k_{\Delta}^4}} - \frac{\text{sgn}(k - k_F)}{2} \right] \\ &= \frac{4\pi k_F^2}{s} j_1(k_F s) - \frac{\pi}{s} \int_{-k_D^2}^{k_D^2} d\xi \sin\left(\sqrt{\xi + k_F^2} s\right) \left[\frac{\xi}{\sqrt{\xi^2 + k_{\Delta}^4}} - \text{sgn}(\xi) \right], \end{aligned} \quad (\text{C.3})$$

where j_1 denotes a spherical Bessel function [113], $k_D = \sqrt{2m_e \omega_D / \hbar}$ and $k_{\Delta} = \sqrt{2m_e \Delta / \hbar}$. In the last step the integrand k is substituted by $\xi = k^2 - k_F^2$. After expanding $\sin(\sqrt{\xi + k_F^2} s) \approx \sin(k_F s) +$

$\xi s \cos(k_F s)/2k_F$ we obtain the fully analytical expression

$$\int d^3k v_k^2 e^{ik \cdot s} \approx 4\pi k_F^3 \left\{ \frac{j_1(k_F s)}{k_F s} + \frac{k_D^4}{4k_F^4} \cos(k_F s) \left[1 - \sqrt{1 + \frac{k_\Delta^4}{k_D^4}} - \frac{k_\Delta^2}{k_D^2} \ln \left(\frac{k_D^2 + \sqrt{k_D^4 + k_\Delta^4}}{k_\Delta^2} \right) \right] \right\}. \quad (\text{C.4})$$

This approximation builds upon the fact that typical Debye energies $\hbar\omega_D$ are roughly two orders of magnitude smaller than typical Fermi energies $E_F = \hbar^2 k_F^2/2m_e$. We infer from the expression that we can also safely neglect the Cooper pairing term since $k_D^4 \ll k_F^4$. This yields

$$\begin{aligned} \Gamma_{\text{deph}} &\approx \frac{36\pi N^2}{k_F^2 \tau} \int_0^\infty ds j_1^2(k_F s) [1 - \text{sinc}(\Delta k s)] \int_{(2\pi\hbar)^3/V} d^3q g(s, q), \\ &\approx \frac{6\pi}{\tau} \left(N \frac{\Delta k}{k_F} \right)^2 \int_0^\infty ds \int_{(2\pi\hbar)^3/V} d^3q s^2 j_1^2(k_F s) g(s, q), \end{aligned} \quad (\text{C.5})$$

where the total number $N = 2N_s$ of electrons in the superconductor enters through the relation $k_F^3 = 3\pi^2 N/V$. In the second line I assume that the distribution $g(s, \cdot)$ covers only microscopic positions, $|s| \ll 1/\Delta k$, and that the displacement of the Fermi spheres is small compared to their extension, $\Delta k \ll k_F$, which is typically the case. In this limit the dephasing term is quadratically enhanced by the number of electrons found in the non-overlapping volume of the two displaced Fermi spheres, $\Gamma_{\text{deph}} \propto (N\Delta k/k_F)^2$. The result can be used to compute realistic values for the dephasing term Γ_{deph} .

The diffusion part (C.2) can be divided into two parts, $\Gamma_{\text{diff}} = 2V(I_1 + I_2)/(2\pi)^3 \tau$. The dominant first part represents the contribution of the integrals outside the pairing shell $[k_-, k_+]$,

$$I_1 = \int_{k_1 \geq k_+} d^3k_1 \int_{k_2 \leq k_-} d^3k_2 \int d^3s g(s, \hbar|\mathbf{k}_1 - \mathbf{k}_2|). \quad (\text{C.6})$$

The smaller second part I_2 contains the rest of the integral with $k_1, k_2 \in [k_-, k_+]$ (assuming that the shell contains more than one elementary unit $q_V = 2\pi\hbar/V^{1/3}$ of momentum). An estimated upper bound can be obtained in the limit of a broad distribution function $g(\cdot, q)$, $I_1 \lesssim 4\pi k_-^3/3$. If we neglect all corrections due to Cooper pairing, $I_2 \approx 0$ and $k_- \approx k_+ \approx k_F$, we arrive at $\Gamma_{\text{diff}} \lesssim N/\tau$.

We are now able to evaluate the decay rates in order to estimate the macroscopicity of concrete experiments, as done in Section (4.3.2.4). For this I set $\tau = \tau_e$, and I use the Gaussian reference distribution $g(s, q) = g_e(s, q)$ with the width parameters σ_s, σ_q . After a few steps of integration [63] we find that the approximated dephasing part (C.5) becomes

$$\begin{aligned} \Gamma_{\text{deph}} &= \frac{3}{4\tau_e} \left(N \frac{\Delta k}{k_F} \right)^2 \left[\text{erf} \left(\frac{q_V}{\sqrt{2}\sigma_q} \right) - \frac{\sqrt{2}q_V}{\sqrt{\pi}\sigma_q} \exp \left(-\frac{q_V^2}{2\sigma_q^2} \right) \right] \\ &\quad \times \frac{(k_F\sigma_s)^2 - 1 + [(k_F\sigma_s)^2 + 1] \exp(-2k_F^2\sigma_s^2)}{(k_F\sigma_s)^4}. \end{aligned} \quad (\text{C.7})$$

An analytical, but rather cumbersome, expression can also be given for the dominant contribution I_1 to the diffusion part,

$$\begin{aligned}
I_1 = & \frac{2\pi}{3} \left\{ k_-^3 - (k_+^3 + k_-^3) \operatorname{erf} \left[\frac{\hbar (k_+ + k_-)}{\sqrt{2}\sigma_q} \right] + (k_+^3 - k_-^3) \operatorname{erf} \left[\frac{\hbar (k_+ - k_-)}{\sqrt{2}\sigma_q} \right] \right\} \\
& + \sqrt{\frac{2}{\pi}} \frac{2\pi\sigma_q}{3\hbar} \exp \left[-\frac{\hbar^2 (k_+ + k_-)^2}{2\sigma_q^2} \right] \left(k_+ k_- - k_+^2 - k_-^2 + \frac{\sigma_q^2}{\hbar^2} \right) \\
& + \sqrt{\frac{2}{\pi}} \frac{2\pi\sigma_q}{3\hbar} \exp \left[-\frac{\hbar^2 (k_+ - k_-)^2}{2\sigma_q^2} \right] \left(k_+ k_- + k_+^2 + k_-^2 - \frac{\sigma_q^2}{\hbar^2} \right). \quad (\text{C.8})
\end{aligned}$$

The remaining part I_2 must be evaluated by means of numerical quadrature methods,

$$I_2 = \int_K d^3 k_1 d^3 k_2 \exp \left(-\frac{\hbar^2 |\mathbf{k}_1 - \mathbf{k}_2|^2}{2\sigma_q^2} \right) u_{k_1} v_{k_2} \left[u_{k_1} v_{k_2} + v_{k_1} u_{k_2} \exp \left(-\frac{\sigma_s^2 |\mathbf{k}_1 + \mathbf{k}_2|^2}{2} \right) \right], \quad (\text{C.9})$$

where the integration volume K contains all $\mathbf{k}_{1,2}$ in the Debye shell, $k_- \leq k_{1,2} \leq k_+$, that fulfill $\hbar |\mathbf{k}_1 - \mathbf{k}_2| \geq q_V$.

C.2. Geometry factors of spheres, cuboids and cylinders

The classicalization of the center-of-mass degree of freedom of rigid compound objects with mass M generally depends on their geometrical shape and consistence, as studied in Section 4.1.5. The effective classicalization times τ_{eff} and phase-space distributions g_{eff} must be used in cases where the spatial extension of the center-of-mass state is smaller than (or comparable to) the object size; they differ from the point-particle expressions $\tau = (m_e/M)^2 \tau_e$ and $g(s, q) = (M/m_e)^3 g_e(Ms/m_e, q)$ as a function of the particle size and the momentum width σ_q of the Gaussian reference distribution g_e , defined in (4.143).

Here the effective parameters are listed for the center-of-mass classicalization of elementary bodies: homogeneous spheres, cuboids and cylinders. Their functional dependence is determined by two factors: The Fourier transform (4.86) of the homogeneous mass density $\varrho(\mathbf{r})$ of the body, and the effective mass expression (4.85). The latter describes the reduction of the effective rate $1/\tau_{\text{eff}}$ with respect to the point-particle value, which will be denoted in the following by the *geometry factors*

$$\gamma = \frac{\tau}{\tau_{\text{eff}}} = \left(\frac{m_{\text{eff}}}{M} \right)^2 = \int d^3 q \frac{\exp(-q^2/2\sigma_q^2)}{(2\pi\sigma_q^2)^{3/2}} \left| \frac{\tilde{\varrho}(\mathbf{q})}{M} \right|^2. \quad (\text{C.10})$$

C.2.1. Homogeneous spheres

Homogeneous spheres of mass M and radius R are described by the isotropic mass density $\varrho(\mathbf{r}) = 3M\Theta(R - r)/4\pi R^3$. Its Fourier transform reads as

$$\tilde{\varrho}(\mathbf{q}) = \frac{3M\hbar^3}{q^3 R^3} \left[\sin\left(\frac{qR}{\hbar}\right) - \frac{qR}{\hbar} \cos\left(\frac{qR}{\hbar}\right) \right] = \frac{3M\hbar}{qR} j_1\left(\frac{qR}{\hbar}\right), \quad (\text{C.11})$$

with j_1 a spherical Bessel function [113]. Several steps of integration yield the explicit form of the spherical geometry factor,

$$\gamma_s(\xi) = \frac{3}{2\xi^6} \left[1 - 3\xi^2 + (1 - \xi^2) \exp(-2\xi^2) + \sqrt{2\pi}\xi^3 \operatorname{erf}(\sqrt{2}\xi) \right], \quad (\text{C.12})$$

as well as the resulting effective parameters,

$$\begin{aligned} \frac{1}{\tau_{\text{eff}}} &= \left(\frac{M}{m_e} \right)^2 \gamma_s \left(\frac{\sigma_q R}{\hbar} \right) \frac{1}{\tau_e}, \\ g_{\text{eff}}(s, q) &= \left(\frac{M}{2\pi m_e \sigma_s \sigma_q} \right)^3 \gamma_s^{-1} \left(\frac{\sigma_q R}{\hbar} \right) \exp \left(-\frac{M^2 s^2}{2m_e^2 \sigma_s^2} - \frac{q^2}{2\sigma_q^2} \right) \left[\frac{3\hbar}{qR} j_1 \left(\frac{qR}{\hbar} \right) \right]^2. \end{aligned} \quad (\text{C.13})$$

One can easily verify the point-particle limit $\gamma_s(\xi \rightarrow 0) = 1$. The characteristic momentum width of the effective phase-space distribution is either governed by the σ_q -parameter, or by the inverse sphere size $\sim \hbar/R$, depending on what quantity is smaller.

This leads to the Fourier transform of the effective phase-space distribution,

$$\tilde{g}_{\text{eff}}(\mathbf{r}, \mathbf{p}) = \exp \left(-\frac{m_e^2 \sigma_s^2 p^2}{2M^2 \hbar^2} \right) \gamma_s^{-1} \left(\frac{\sigma_q R}{\hbar} \right) \int_0^\infty \frac{\sqrt{2} dq}{\sqrt{\pi} \sigma_q} \exp \left(-\frac{q^2}{2\sigma_q^2} \right) \operatorname{sinc} \left(\frac{qr}{\hbar} \right) \left[\frac{3\hbar}{\sigma_q R} j_1 \left(\frac{qR}{\hbar} \right) \right]^2. \quad (\text{C.14})$$

which is necessary to compute the classicalized time evolution of the sphere.

The σ_s -term is safely negligible in the limit of macroscopic masses $M \gg m_e$. Moreover, we may expand the sinc-function in the integrand, $\operatorname{sinc}(x) \approx 1 - x^2/6$, in the diffusive regime where path separations are small, $|\mathbf{r}| \ll R$, \hbar/σ_q . The integration can then be carried out, yielding

$$\tilde{g}_{\text{eff}}(\mathbf{r}, \mathbf{p}) \approx \tilde{g}_{\text{eff}}(r) = 1 - \frac{3r^2}{4R^2} \frac{e^{-2(\sigma_q R/\hbar)^2} \left[1 + (\sigma_q R/\hbar)^2 \right] + (\sigma_q R/\hbar)^2 - 1}{(\sigma_q R/\hbar)^4 \gamma_s(\sigma_q R/\hbar)}. \quad (\text{C.15})$$

C.2.2. Homogeneous cuboids

A cuboid of constant mass density and side lengths $b_{x,y,z}$ corresponds to

$$\begin{aligned} Q(\mathbf{r}) &= \frac{M}{b_x b_y b_z} \Theta \left(\frac{b_x}{2} - |x| \right) \Theta \left(\frac{b_y}{2} - |y| \right) \Theta \left(\frac{b_z}{2} - |z| \right), \\ \tilde{Q}(\mathbf{q}) &= M \operatorname{sinc} \left(\frac{q_x b_x}{2\hbar} \right) \operatorname{sinc} \left(\frac{q_y b_y}{2\hbar} \right) \operatorname{sinc} \left(\frac{q_z b_z}{2\hbar} \right). \end{aligned} \quad (\text{C.16})$$

The resulting geometry factor is written, accordingly, as a product of three cartesian components,

$$\begin{aligned} \gamma_1(\xi) &= \frac{2}{\xi^2} \left[\exp \left(-\frac{\xi^2}{2} \right) - 1 + \sqrt{\frac{\pi}{2}} \xi \operatorname{erf} \left(\frac{\xi}{\sqrt{2}} \right) \right], \\ \frac{1}{\tau_{\text{eff}}} &= \left(\frac{M}{m_e} \right)^2 \gamma_1 \left(\frac{\sigma_q b_x}{\hbar} \right) \gamma_1 \left(\frac{\sigma_q b_y}{\hbar} \right) \gamma_1 \left(\frac{\sigma_q b_z}{\hbar} \right) \frac{1}{\tau_e}. \end{aligned} \quad (\text{C.17})$$

If we restrict our considerations to the one-dimensional motion of the cuboid along, say, the x -axis, we are left with the effective distribution function

$$g_{\text{1D}}(s, q) = \frac{M}{2\pi m_e \sigma_s \sigma_q} \gamma_1^{-1} \left(\frac{\sigma_q b_x}{\hbar} \right) \exp \left(-\frac{M^2 s^2}{2m_e^2 \sigma_s^2} - \frac{q^2}{2\sigma_q^2} \right) \text{sinc}^2 \left(\frac{q b_x}{2\hbar} \right) \quad (\text{C.18})$$

Once again we can omit the s -distribution for the large masses M that are usually considered, $g_{\text{1D}}(s, q) \approx g_{\text{1D}}(q) \delta(s)$. The momentum width is given by the smaller quantity among the reference width σ_q and the inverse dimension \hbar/b_x of the cuboid.

The diffusion approximation of the Fourier transform $\tilde{g}_{\text{1D}}(x) = \int dq g_{\text{1D}}(q) \exp(-iqx/\hbar)$ in the limit of small arguments $|x| \ll \hbar/\sigma_q$, b_x is obtained by expanding the integrand up to second order,

$$\tilde{g}_{\text{1D}}(x) \approx 1 - 2\gamma_1^{-1} \left(\frac{\sigma_q b_x}{\hbar} \right) \frac{x^2}{b_x^2} \int \frac{dq}{\sqrt{2\pi}\sigma_q} e^{-q^2/2\sigma_q^2} \sin^2 \left(\frac{q b_x}{2\hbar} \right) = 1 - \frac{x^2}{b_x^2} \frac{1 - \exp(-\sigma_q^2 b_x^2 / 2\hbar^2)}{\gamma_1(\sigma_q b_x / \hbar)}. \quad (\text{C.19})$$

C.2.3. Homogeneous cylinders

A homogeneous cylinder of height b and radius R is best described in cylindrical coordinates $\mathbf{r} = (r_\perp, \phi, z)$,

$$\varrho(\mathbf{r}) = \frac{M}{\pi R^2 b} \Theta \left(\frac{b}{2} - |z| \right) \Theta(R - r_\perp), \quad \tilde{\varrho}(\mathbf{q}) = \frac{2M\hbar}{q_\perp R} J_1 \left(\frac{q_\perp R}{\hbar} \right) \text{sinc} \left(\frac{q_z b}{2\hbar} \right). \quad (\text{C.20})$$

The Bessel function J_1 is obtained using standard integral formulae from [63]. The resulting geometry factor splits into a cartesian factor γ_\perp and the circular part

$$\gamma_\perp = \int d^2 q_\perp \frac{\exp(-q_\perp^2 / 2\sigma_q^2)}{2\pi\sigma_q^2} \left[\frac{2\sigma_q}{\xi q_\perp} J_1 \left(\frac{\xi q_\perp}{\sigma_q} \right) \right]^2 = \frac{2}{\xi^2} - \frac{2 \exp(-\xi^2)}{\xi^2} [I_0(\xi^2) + I_1(\xi^2)], \quad (\text{C.21})$$

which follows once again from nontrivial integral formulae [63]. This results in the effective time parameter

$$\frac{1}{\tau_{\text{eff}}} = \left(\frac{M}{m_e} \right)^2 \gamma_1 \left(\frac{\sigma_q b}{\hbar} \right) \gamma_\perp \left(\frac{\sigma_q R}{\hbar} \right) \frac{1}{\tau_e}. \quad (\text{C.22})$$

The one-dimensional distribution function of the cuboid, Equations (C.18) and (C.19), can be applied also here (after replacing the term b_x by b) if we are only interested in the classicalized motion of the cylinder along its z -axis.

C.3. Superpositions of harmonic oscillator states

Here the dynamical influence of the classicalizing modification on two different superposition states in harmonically oscillating mechanical systems is evaluated in one dimension. See Section 4.2.2.4 for the explicit form of the modified time evolution of harmonic systems, given the effective time parameter and the one-dimensional phase-space distribution.

C.3.1. Superposition of the oscillatory ground and excited state

Suppose that a harmonic oscillator ($H = \hbar\omega a^\dagger a$) of mass M is initially brought into the balanced superposition of ground and first excited state, $|\psi_0\rangle = (|0\rangle + |1\rangle)/\sqrt{2}$. In the ideal unmodified case the coherence between both states would be maintained, that is, the magnitude of the nondiagonal matrix element $\langle 1|\rho_t|0\rangle$ would remain constant over time. This changes in the presence of classicalization, which heats up the system and thus depletes the low-energy state occupation and coherence.

The matrix element can be expressed in terms of the characteristic function with help of the spatial representation of the energy eigenstates [164]

$$\psi_n(x) = \langle x|n\rangle = \frac{1}{\sqrt{2^n n!}} \left(\frac{M\omega}{\pi\hbar}\right)^{1/4} H_n\left(\sqrt{\frac{M\omega}{\hbar}}x\right) e^{-M\omega x^2/2\hbar}, \quad (\text{C.23})$$

where the two lowest order Hermite polynomials read as $H_0(x) = 1$ and $H_1(x) = 2x$. A straightforward calculation yields

$$\begin{aligned} \langle 1|\rho_t|0\rangle &= \int dx_1 dx_2 \psi_1^*(x_1) \psi_0(x_2) \langle x_1|\rho_t|x_2\rangle \\ &= \int dx dx_0 dp \psi_1^*(x_0) \psi_0(x+x_0) \chi_t(x, p) \exp\left[-\frac{i}{\hbar}p\left(x_0 + \frac{x}{2}\right)\right] \\ &= -\sqrt{\frac{M\omega}{2\hbar}} \int \frac{dx dp}{2\pi\hbar} \left(x + i\frac{p}{M\omega}\right) \exp\left[-\frac{E(x, p)}{2\hbar\omega}\right] \chi_t(x, p), \end{aligned} \quad (\text{C.24})$$

with the energy function $E(x, p) = (p^2 + M^2\omega^2 x^2)/2M$. The modified time evolution of the characteristic function is given by Equation (4.116),

$$\begin{aligned} \chi_t(x, p) &= R_t(x, p) \chi_0\left(x \cos \omega t - \frac{p}{M\omega} \sin \omega t, p \cos \omega t + M\omega x \sin \omega t\right), \\ R_t(x, p) &= \exp\left[\int_0^t \frac{dt'}{\tau_{\text{eff}}} \tilde{g}_{\text{ID}}\left(x \cos \omega t' - \frac{p}{M\omega} \sin \omega t', p \cos \omega t' + M\omega x \sin \omega t'\right) - \frac{t}{\tau_{\text{eff}}}\right], \end{aligned} \quad (\text{C.25})$$

and it remains to specify the characteristic function of the initial state. For this we note that the characteristic function can also be understood as the quantum expectation value of the displacement operator $D(\alpha) = \exp(\alpha a^\dagger - \alpha^* a)$, with $\alpha = \sqrt{M\omega/2\hbar}(x + ip/M\omega)$. The energy state representation of the displacement operator is given by [242]

$$\langle m|D(\alpha)|n\rangle = \sqrt{\frac{n!}{m!}} \alpha^{m-n} e^{-|\alpha|^2/2} \sum_{k=0}^n (-)^k \binom{n+m}{n-k} \frac{|\alpha|^{2k}}{k!} \quad (\text{C.26})$$

which yields

$$\chi_0(x, p) = \text{tr}\left[D\left[\sqrt{\frac{M\omega}{2\hbar}}\left(x + i\frac{p}{M\omega}\right)\right]\rho_0\right] = e^{-E(x, p)/2\hbar\omega} \left[1 - \frac{E(x, p)}{2\hbar\omega} + i\frac{p}{\sqrt{2\hbar M\omega}}\right]. \quad (\text{C.27})$$

Switching into dimensionless integration variables we finally arrive at

$$\begin{aligned} \langle 1|\rho_t|0\rangle &= \int \frac{dQdP}{\pi} (Q + iP) e^{-Q^2 - P^2} R_t \left(\sqrt{\frac{2\hbar}{M\omega}} Q, \sqrt{2\hbar M\omega} P \right) \\ &\times \left(\frac{Q^2 + P^2}{2} - 1 - iP \cos \omega t - iQ \sin \omega t \right). \end{aligned} \quad (\text{C.28})$$

The expression simplifies considerably in the macroscopic diffusion limit of large masses $M \gg m_e$ and small ground state oscillation amplitudes, $\sqrt{M\omega/2\hbar} \ll 1 \text{ \AA}$, which admits the approximation $\tilde{g}_{\text{ID}}(x, p) \approx \tilde{g}_{\text{ID}}(x) \approx 1 - Ax^2$. Explicit values for the term A are given in Appendix C.2 for oscillating spheres, cuboids and cylinders. If we consider only full oscillation cycles, $t = 2\pi n/\omega$, we obtain the simplified reduction factor

$$R_{2\pi n/\omega}(x, p) \approx \exp \left[-\frac{2\pi n A}{\omega \tau_{\text{eff}}} \left(\frac{x^2}{2} + \frac{p^2}{2M^2\omega^2} \right) \right] = \exp \left(-\frac{At}{\tau_{\text{eff}}} \frac{E(x, p)}{M\omega^2} \right). \quad (\text{C.29})$$

It is an even function in both x and p . So the odd terms in the integral (C.28) cancel,

$$\langle 1|\rho_{2\pi n/\omega}|0\rangle = \int \frac{dQdP}{\pi} P^2 \exp \left[-\left(Q^2 + P^2 \right) \left(1 + \frac{2\pi\hbar A n}{M\omega^2 \tau_{\text{eff}}} \right) \right] = \frac{1}{2} \left(1 + \frac{2\pi\hbar A n}{M\omega^2 \tau_{\text{eff}}} \right)^{-2}. \quad (\text{C.30})$$

C.3.2. Coherent state superposition by photon entanglement

Reference [170] describes a method to entangle an oscillating cubic mirror of mass M with a single photon and thereby test the quantum coherence between its oscillatory ground state $|0\rangle$ and a displaced coherent state $|\alpha(t)\rangle$ driven by the interaction with the photon. This is achieved by placing the oscillator as a cavity mirror in one arm of a Michelson interferometer and coupling in a single photon. A beam splitter brings the latter into a superposition of being either in arm A or B, which coherently displaces the mirror in arm A and results in the entangled state $|\psi(t)\rangle = c_A|A\rangle|\alpha(t)\rangle + c_B|B\rangle|0\rangle$.

Both arms are brought to interference when the outgoing photon hits the beam splitter once again after a time t and is detected in one of the output ports. The visibility depends on the degree of photon-mirror entanglement, and it is therefore also sensitive to the amount of coherence that could be lost in the mirror system.

The vibrating mirror shall be modeled as a single harmonic oscillator with frequency ω and free Hamiltonian $H_0 = \hbar\omega a^\dagger a = (\mathbf{p}^2 + M^2\omega^2\mathbf{x}^2)/2M$, which is initially cooled to its ground state $|0\rangle$. If the photon enters the corresponding cavity in arm A, the radiation pressure term $H_1 = -\hbar g (a + a^\dagger) = -\sqrt{2\hbar M\omega} g \mathbf{x}$ is added to H_0 , which drives the mirror into a displaced state with amplitude $\alpha(t) = (g/\omega) [1 - \exp(-i\omega t)]$. We find that at each full oscillation cycle, $t_n = 2\pi n/\omega$, the displacement vanishes and the photon disentangles from the mirror. Any reduction of interference visibility at this point must be due to coherence loss in the mirror.

Following the theoretical treatment in [243] the visibility can be given in terms of the off-diagonal matrix element of the reduced photon state, $\mathcal{V}(t) = |\langle A|\text{tr}(\rho)|B\rangle| = |\text{tr}(\rho_{AB})|$. The term ρ denotes the combined state of photon and mirror system, whereas $\rho_{AB} = \langle A|\rho|B\rangle$ represents a quasi-state operator on the mirror system. The latter evolves according to the non-hermitian equation

$$\partial_t \rho_{AB}(t) = -i\omega [a^\dagger a, \rho_{AB}(t)] + ig \sqrt{\frac{2M\omega}{\hbar}} \mathbf{x} \rho_{AB}(t) + \mathcal{L}_1[\rho_{AB}(t)], \quad (\text{C.31})$$

in the presence of the classicalizing modification \mathcal{L}_1 . The initial value is given by the ground state, $\rho_{AB}(0) = |0\rangle\langle 0|$. The solution to this differential equation will be developed in the following.

First the free harmonic evolution must be separated from the other terms by switching to the interaction frame with respect to H_0 . The transformed state $\rho_{AB}^{(I)} = \exp(iH_0 t/\hbar) \rho_{AB} \exp(-iH_0 t/\hbar)$ fulfills

$$\partial_t \rho_{AB}^{(I)}(t) = ig\sqrt{\frac{2M\omega}{\hbar}} x_t(\mathbf{x}, \mathbf{p}) \rho_{AB}^{(I)}(t) + \mathcal{L}_1^{(I)}[\rho_{AB}^{(I)}(t)], \quad (C.32)$$

with the same initial condition. The harmonic trajectories are abbreviated by

$$x_t(x, p) = x \cos \omega t + \frac{p}{M\omega} \sin \omega t, \quad p_t(x, p) = p \cos \omega t - M\omega x \sin \omega t. \quad (C.33)$$

Noting that the one-dimensional Weyl operators (4.9) transform as

$$\exp\left(\frac{i}{\hbar} H_0 t\right) W_1\left(s, \frac{q}{M}\right) \exp\left(-\frac{i}{\hbar} H_0 t\right) = W_1\left(x_{-t}(s, q), \frac{1}{M} p_{-t}(s, q)\right), \quad (C.34)$$

the classicalizing modification $\mathcal{L}_1^{(I)}$ in the interaction frame is obtained by mapping the phase-space distribution function $g_{1D}(s, q)$ to the time-dependent expression $g_{1D}^{(I)}(s, q; t) = g_{1D}(x_t(s, q), p_t(s, q))$.

The non-hermitian term in the time evolution can be eliminated by introducing the unitary operator

$$\begin{aligned} V_t &= e^{ig^2(\omega t - \sin \omega t)/\omega^2} \exp\left[-ig\sqrt{\frac{2M\omega}{\hbar}} \int_0^t dt' x_{t'}(\mathbf{x}, \mathbf{p})\right] \\ &= e^{ig^2(\omega t - \sin \omega t)/\omega^2} \exp\left\{i\frac{g}{\omega}\sqrt{\frac{2M\omega}{\hbar}} \left[\frac{\mathbf{p}}{M\omega}(\cos \omega t - 1) - \mathbf{x} \sin \omega t\right]\right\} \\ &= e^{ig^2(\omega t - \sin \omega t)/\omega^2} W_1\left(\frac{g}{\omega}\sqrt{\frac{2\hbar}{M\omega}}(\cos \omega t - 1), \frac{g}{\omega}\sqrt{\frac{2\hbar\omega}{M}} \sin \omega t\right), \end{aligned} \quad (C.35)$$

the time derivative of which yields $\partial_t V_t = -ig\sqrt{2M\omega/\hbar} x_t(\mathbf{x}, \mathbf{p}) V_t$. Note that the phase factor in V_t accounts for the fact that the time derivative of the operator-valued exponent does not commute with the exponent itself. Hence, another transformation of the state operator, $\rho_{AB}^{(V)} := V_t \rho_{AB}^{(I)}$, cancels the non-hermitian term and yields the simplified equation

$$\partial_t \rho_{AB}^{(V)}(t) = \mathcal{L}_1^{(V)}[\rho_{AB}^{(V)}(t)] = V_t \mathcal{L}_1^{(I)}[V_t^\dagger \rho_{AB}^{(V)}(t)], \quad (C.36)$$

with the initial value $\rho_{AB}^{(V)}(0) = |0\rangle\langle 0|$. The commutation rule for the Weyl operators (4.13) gives

$$V_t W_1\left(s, \frac{q}{M}\right) V_t^\dagger = W_1\left(s, \frac{q}{M}\right) \underbrace{\exp\left\{i\frac{g}{\omega}\sqrt{\frac{2M\omega}{\hbar}} \left[s \sin \omega t - \frac{q}{M\omega}(\cos \omega t - 1)\right]\right\}}_{=: C_t(s, q)}. \quad (C.37)$$

So the classicalizing modification in the (V) -picture is obtained by replacing the original distribution function with

$$g_{\text{ID}}^{(V)}(s, q; t) = g_{\text{ID}}(x_t(s, q), p_t(s, q)) C_t(s, q). \quad (\text{C.38})$$

This renders the differential equation (C.36) formally equivalent to the modified time evolution of a single particle in the interaction picture, as studied in Section 4.2.2. It can be solved in the characteristic function representation of $\rho_{AB}^{(V)}(t)$,

$$\chi_t^{(V)}(x, p) = \text{tr} \left(\rho_{AB}^{(V)}(t) W_1^\dagger \left(x, \frac{p}{M} \right) \right) = \exp \left[\int_0^t \frac{dt'}{\tau_{\text{eff}}} \bar{g}_{\text{ID}}^{(V)}(x, p; t') - \frac{t}{\tau_{\text{eff}}} \right] \chi_0^{(V)}(x, p), \quad (\text{C.39})$$

with the initial value

$$\begin{aligned} \chi_0^{(V)}(x, p) &= \langle 0 | W_1^\dagger \left(x, \frac{p}{M} \right) | 0 \rangle \stackrel{(\text{C.27})}{=} \langle 0 | D \left[\sqrt{\frac{M\omega}{2\hbar}} \left(x + i \frac{p}{M\omega} \right) \right] | 0 \rangle \\ &\stackrel{(\text{C.26})}{=} \exp \left(-\frac{M\omega}{4\hbar} \left| x + i \frac{p}{M\omega} \right|^2 \right), \end{aligned} \quad (\text{C.40})$$

and the time-dependent function

$$\begin{aligned} \bar{g}_{\text{ID}}^{(V)}(x, p; t) &= \int ds dq g_{\text{ID}}(x_t(s, q), p_t(s, q)) C_t(s, q) e^{i(qx - ps)/\hbar} \\ &= \int ds dq g_{\text{ID}}(s, q) \exp \left\{ i \frac{p_{-t}(s, q) x - p x_{-t}(s, q)}{\hbar} \right\} \\ &\quad \times \exp \left\{ i \frac{g}{\omega} \sqrt{\frac{2M\omega}{\hbar}} \left[x_{-t}(s, q) \sin \omega t - \frac{p_{-t}(s, q)}{M\omega} (\cos \omega t - 1) \right] \right\} \\ &= \tilde{g}_{\text{ID}}(x_g(1 - \cos \omega t) - x_t(x, p), p_t(x, p) - M\omega x_g \sin \omega t). \end{aligned} \quad (\text{C.41})$$

Here, I have introduced the mean position displacement $x_g = (g/\omega) \sqrt{2\hbar/M\omega}$. All this eventually leads to the final form of the visibility

$$\begin{aligned} \mathcal{V}(t) &= \left| \text{tr} \left(\rho_{AB}^{(I)}(t) \right) \right| = \left| \text{tr} \left(V_t^\dagger \rho_{AB}^{(V)}(t) \right) \right| = \chi_t^{(V)}(x_g(\cos \omega t - 1), M\omega x_g \sin \omega t) \\ &= \exp \left[\frac{g^2(\cos \omega t - 1)}{\omega^2} - \frac{t}{\tau_{\text{eff}}} + \int_0^t \frac{dt'}{\tau_{\text{eff}}} \bar{g}_{\text{ID}}^{(V)}(x_g(\cos \omega t - 1), M\omega x_g \sin \omega t; t') \right] \\ &= \exp \left\{ \frac{g^2(\cos \omega t - 1)}{\omega^2} + \int_0^t \frac{dt'}{\tau_{\text{eff}}} \left[\tilde{g}_{\text{ID}}(x_g(1 - \cos \omega t'), M\omega x_g \sin \omega t') - 1 \right] \right\}. \end{aligned} \quad (\text{C.42})$$

The argument of \tilde{g}_{ID} represents the path difference in phase space between the ground state and the dynamically displaced state of the mirror. The large mass of $M \sim 10^{18} m_e$ and the subatomic displacement $x_g \sim 10^{-13}$ m proposed in [170] admit the diffusive approximation $\tilde{g}_{\text{ID}}(x, p) \approx \tilde{g}_{\text{ID}}(x) \approx 1 - Ax^2$,

$$\mathcal{V}(t) \approx \exp \left\{ \frac{g^2}{\omega^2} \left[\cos \omega t - 1 - \frac{\hbar A}{M\omega\tau_{\text{eff}}} \left(3t - \frac{4}{\omega} \sin \omega t + \frac{1}{2\omega} \sin 2\omega t \right) \right] \right\}. \quad (\text{C.43})$$

Any reduction of the visibility at full oscillation cycles $t_n = 2\pi n/\omega$ can then be attributed to the classicalization effect, $\mathcal{V}(t_n) = \exp(-3\pi n A x_g^2 / \omega \tau_{\text{eff}})$.

Acknowledgements

Over at last! Here ends my thesis, and with it an essential chapter of my life. It took me longer than I had planned, but it was a great time and it even held a few pleasurable surprises in store for me towards the end. In other words, it could have been much worse! I was lucky to work with a cohesive team of warm and supportive colleagues, who always appreciated my ‘optimism’. In particular, I am grateful to those who have become dear friends of mine; you know who you are. Some of them have left already, others had to bear my presence even beyond working hours. I owe you! Very special thanks go out to my family for their support, to my two beloved flatmates for literally spicing up my life, and also to my fellow gourmands and movie addicts for sharing the passion for great food and cinema with me.

Coming back to science, let me thank my main supervisors Markus Arndt, Klaus Hornberger and Klemens Hammerer, as well as my collaborators, who put a lot of trust in me and made sure that I could do something useful as a theorist in an experimental group (besides being the local MATLAB help desk). I have learned a lot and I am happy to continue working with you. I also acknowledge the support by the FWF project DK-W1210 (CoQuS).

Finally, I feel that I should say something about that great old city of Vienna, splendorous and yet rotten to the core. In retrospect, after having spent more than five years of my life as a Piefke guest worker among her grumpy dwellers, I must thank Vienna for teaching me the lesson that there is only so much between courtesy and perfidy, indulgence and indolence, and affection and disgust.

Bibliography

- [1] J. R. FRIEDMAN, V. PATEL, W. CHEN, S. K. TOLPYGO, and J. E. LUKENS, *Quantum superposition of distinct macroscopic states*, Nature **406**, 43 (2000).
- [2] C. H. VAN DER WAL, A. C. J. TER HAAR, F. K. WILHELM, R. N. SCHOUTEN, C. J. P. M. HARMANS, T. P. ORLANDO, S. LLOYD, and J. E. MOOIJ, *Quantum Superposition of Macroscopic Persistent-Current States*, Science **290**, 773 (2000).
- [3] A. J. LEGGETT, *Testing the Limits of Quantum Mechanics: Motivation, State of Play, Prospects*, Journal of Physics: Condensed Matter **14**, R415 (2002).
- [4] M. ARNDT, O. NAIRZ, J. VOS-ANDREAE, C. KELLER, G. VAN DER ZOUW, and A. ZEILINGER, *Wave-particle duality of C60 molecules*, Nature **401**, 680 (1999).
- [5] B. BREZGER, L. HACKERMÜLLER, S. UTTENTHALER, J. PETSCHINKA, M. ARNDT, and A. ZEILINGER, *Matter-Wave Interferometer for Large Molecules*, Physical Review Letters **88**, 100404 (2002).
- [6] S. NIMMRICHTER, K. HORNBERGER, H. ULBRICHT, and M. ARNDT, *Absolute absorption spectroscopy based on molecule interferometry*, Physical Review A **78**, 063607 (2008).
- [7] K. HORNBERGER, S. GERLICH, H. ULBRICHT, L. HACKERMÜLLER, S. NIMMRICHTER, I. V. GOLDT, O. BOLTALINA, and M. ARNDT, *Theory and experimental verification of Kapitza-Dirac-Talbot-Lau interferometry*, New Journal of Physics **11**, 43032 (2009).
- [8] S. NIMMRICHTER, K. HAMMERER, P. ASENBAUM, H. RITSCH, and M. ARNDT, *Master equation for the motion of a polarizable particle in a multimode cavity*, New Journal of Physics **12**, 083003 (2010).
- [9] T. JUFFMANN, S. NIMMRICHTER, M. ARNDT, H. GLEITER, and K. HORNBERGER, *New Prospects for de Broglie Interferometry*, Foundations of Physics **42**, 98 (2010).
- [10] S. NIMMRICHTER, P. HASLINGER, K. HORNBERGER, and M. ARNDT, *Concept of an ionizing time-domain matter-wave interferometer*, New Journal of Physics **13**, 075002 (2011).
- [11] S. NIMMRICHTER, K. HORNBERGER, P. HASLINGER, and M. ARNDT, *Testing spontaneous localization theories with matter-wave interferometry*, Physical Review A **83**, 43621 (2011).
- [12] K. HORNBERGER, S. GERLICH, P. HASLINGER, S. NIMMRICHTER, and M. ARNDT, *Colloquium: Quantum interference of clusters and molecules*, Reviews of Modern Physics **84**, 157 (2012).
- [13] P. HASLINGER, N. DÖRRE, P. GEYER, J. RODEWALD, S. NIMMRICHTER, and M. ARNDT, *A universal matter-wave interferometer with optical ionization gratings in the time domain*, Nature Physics **9**, 144 (2013).
- [14] S. NIMMRICHTER and K. HORNBERGER, *Macroscopicity of Mechanical Quantum Superposition States*, Physical Review Letters **110**, 160403 (2013).
- [15] P. HORAK, G. HECHENBLAIKNER, K. GHERI, H. STECHER, and H. RITSCH, *Cavity-Induced Atom Cooling in the Strong Coupling Regime*, Physical Review Letters **79**, 4974 (1997).
- [16] C. WIEMAN, D. PRITCHARD, and D. WINELAND, *Atom cooling, trapping, and quantum manipulation*, Reviews of Modern Physics **71**, S253 (1999).
- [17] P. DOMOKOS and H. RITSCH, *Mechanical effects of light in optical resonators*, Journal of the Optical Society of America B **20**, 1098 (2003).

- [18] A. D. CRONIN and D. E. PRITCHARD, *Optics and interferometry with atoms and molecules*, Reviews of Modern Physics **81**, 1051 (2009).
- [19] S. GERLICH, S. EIBENBERGER, M. TOMANDL, S. NIMMRICHTER, K. HORNBERGER, P. J. FAGAN, J. TÜXEN, M. MAYOR, and M. ARNDT, *Quantum interference of large organic molecules*, Nature Communications **2**, 263 (2011).
- [20] T. JUFFMANN, A. MILIC, M. MÜLLNERITSCH, P. ASENBAUM, A. TSUKERNIK, J. TÜXEN, M. MAYOR, O. CHESHNOVSKY, and M. ARNDT, *Real-time single-molecule imaging of quantum interference*, Nature nanotechnology **7**, 297 (2012).
- [21] T. REISINGER, A. PATEL, H. REINGRUBER, K. FLADISCHER, W. ERNST, G. BRACCO, H. SMITH, and B. HOLST, *Poisson's spot with molecules*, Physical Review A **79**, 053823 (2009).
- [22] T. REISINGER, G. BRACCO, and B. HOLST, *Particle-wave discrimination in Poisson spot experiments*, New Journal of Physics **13**, 065016 (2011).
- [23] D. E. CHANG, C. A. REGAL, S. B. PAPP, D. J. WILSON, J. YE, O. PAINTER, H. J. KIMBLE, and P. ZOLLER, *Cavity opto-mechanics using an optically levitated nanosphere*, Proceedings of the National Academy of Science **107**, 1005 (2010).
- [24] O. ROMERO-ISART, M. L. JUAN, R. QUIDANT, and J. I. CIRAC, *Toward quantum superposition of living organisms*, New Journal of Physics **12**, 33015 (2010).
- [25] O. ROMERO-ISART, A. C. PFLANZER, F. BLASER, R. KALTENBAEK, N. KIESEL, M. ASPELMEYER, and J. I. CIRAC, *Large Quantum Superpositions and Interference of Massive Nanometer-Sized Objects*, Physical Review Letters **107**, 20405 (2011).
- [26] M. POOT and H. S. VAN DER ZANT, *Mechanical systems in the quantum regime*, Physics Reports **511**, 273 (2012).
- [27] M. ASPELMEYER, T. J. KIPPENBERG, and F. MARQUARDT, *Cavity Optomechanics*, arXiv:1303.0733 [cond-mat.mes-hall] (2013).
- [28] H. C. VAN DE HULST, *Light scattering by small particles*, Dover, 1981.
- [29] C. F. BOHREN and D. R. HUFFMAN, *Absorption and Scattering of Light by Small Particles*, Wiley-VCH, 1998.
- [30] A. P. KAZANTSEV, G. I. SURDUTOVICH, and V. P. YAKOVLEV, *Mechanical action of light on atoms*, World Scientific, Singapore, 1990.
- [31] S. HAROCHE and J.-M. RAIMOND, *Exploring the Quantum: Atoms, Cavities, and Photons (Oxford Graduate Texts)*, Oxford University Press, 2006.
- [32] S. M. BARNETT and R. LOUDON, *On the electromagnetic force on a dielectric medium*, Journal of Physics B: Atomic, Molecular and Optical Physics **39**, S671 (2006).
- [33] B. THIDÉ, *Electromagnetic Field Theory (Online Version)*, Dover, 2011.
- [34] J. D. JACKSON, *Classical Electrodynamics, 3rd Edition*, Wiley, 1999.
- [35] H.-P. BREUER and F. PETRUCCIONE, *The Theory of Open Quantum Systems*, Oxford University Press, 2002.
- [36] H. M. WISEMAN and G. J. MILBURN, *Quantum measurement and control*, Cambridge University Press, 2010.
- [37] M. GALLIS and G. FLEMING, *Environmental and spontaneous localization*, Physical Review A **42**, 38 (1990).
- [38] H. DU, R.-C. A. FUH, J. LI, L. A. CORKAN, and J. S. LINDSEY, *PhotochemCAD: A Computer-Aided Design and Research Tool in Photochemistry*, Photochemistry and Photobiology **68**, 141 (1998).

- [39] J. M. DIXON, M. TANIGUCHI, and J. S. LINDSEY, *PhotochemCAD 2: A Refined Program with Accompanying Spectral Databases for Photochemical Calculations*, *Photochemistry and Photobiology* **81**, 212 (2007).
- [40] K. HORNBERGER, J. E. SIPE, and M. ARNDT, *Theory of Decoherence in a Matter Wave Talbot-Lau Interferometer*, *Physical Review A* **70**, 53608 (2004).
- [41] K. HANSEN and E. CAMPBELL, *Thermal radiation from small particles*, *Physical Review E* **58**, 5477 (1998).
- [42] M. GANGL and H. RITSCH, *Collective dynamical cooling of neutral particles in a high-Q optical cavity*, *Physical Review A* **61**, 011402 (1999).
- [43] V. VULETIĆ and S. CHU, *Laser Cooling of Atoms, Ions, or Molecules by Coherent Scattering*, *Physical Review Letters* **84**, 3787 (2000).
- [44] H. CHAN, A. BLACK, and V. VULETIĆ, *Observation of Collective-Emission-Induced Cooling of Atoms in an Optical Cavity*, *Physical Review Letters* **90**, 063003 (2003).
- [45] P. MAUNZ, T. PUPPE, I. SCHUSTER, N. SYASSEN, P. W. H. PINKSE, and G. REMPE, *Cavity cooling of a single atom*, *Nature* **428**, 50 (2004).
- [46] S. NUSSMANN, K. MURR, M. HIJLKEMA, B. WEBER, A. KUHN, and G. REMPE, *Vacuum-stimulated cooling of single atoms in three dimensions*, *Nature Physics* **1**, 122 (2005).
- [47] M. WOLKE, J. KLINNER, H. KESSLER, and A. HEMMERICH, *Cavity cooling below the recoil limit*, *Science* **337**, 75 (2012).
- [48] B. LEV, A. VUKICS, E. HUDSON, B. SAWYER, P. DOMOKOS, H. RITSCH, and J. YE, *Prospects for the cavity-assisted laser cooling of molecules*, *Physical Review A* **77**, 023402 (2008).
- [49] C. GARDINER and P. ZOLLER, *Quantum Noise: A Handbook of Markovian and Non-Markovian Quantum Stochastic Methods with Applications to Quantum Optics (Springer Series in Synergetics)*, Springer, 2010.
- [50] E. D. PALIK and G. GHOSH, *Handbook of optical constants of solids*, Academic press, 1985.
- [51] M. L. GORODETSKY, A. D. PRYAMIKOV, and V. S. ILCHENKO, *Rayleigh scattering in high-Q microspheres*, *Journal of the Optical Society of America B* **17**, 1051 (2000).
- [52] U. KREIBIG and M. VOLLMER, *Optical Properties of Metal Clusters (Springer Series in Materials Science)*, Springer, 1995.
- [53] M. S. DRESSELHAUS, G. DRESSELHAUS, and P. C. EKLUND, *Science of Fullerenes and Carbon Nanotubes: Their Properties and Applications*, Academic Press, 1996.
- [54] G. LACH, B. JEZIORSKI, and K. SZALEWICZ, *Radiative Corrections to the Polarizability of Helium*, *Physical Review Letters* **92**, 233001 (2004).
- [55] A. MIFFRE, M. JACQUEY, M. BÜCHNER, G. TRÉNEC, and J. VIGUÉ, *Measurement of the electric polarizability of lithium by atom interferometry*, *Physical Review A* **73**, 011603 (2006).
- [56] P. ASENBAUM, *Private Communication*, 2012.
- [57] B. E. A. SALEH and M. C. TEICH, *Fundamentals of Photonics*, Wiley-Interscience, 2nd edition, 2007.
- [58] R. J. GLAUBER, *High-energy collision theory*, in *Lectures in theoretical physics: lectures delivered at the Summer Institute for Theoretical Physics, University of Colorado, Boulder*, page 315, Wiley-Interscience, 1959.
- [59] S. NIMMRICHTER, *Matter wave Talbot-Lau interferometry beyond the eikonal approximation*, Diploma thesis, Technische Universität München, 2007.

- [60] S. NIMMRICHTER and K. HORNBERGER, *Theory of near-field matter-wave interference beyond the eikonal approximation*, Physical Review A **78**, 023612 (2008).
- [61] P. R. BERMAN, *Atom Interferometry*, Academic Press, 1996.
- [62] A. TURLAPOV, A. TONYUSHKIN, and T. SLEATOR, *Talbot-Lau effect for atomic de Broglie waves manipulated with light*, Physical Review A **71**, 043612 (2005).
- [63] I. S. GRADSHTEYN, I. M. RYZHIK, A. JEFFREY, and D. ZWILLINGER, *Table of Integrals, Series, and Products*, Academic Press, 2007.
- [64] S. M. DUTRA, *Cavity Quantum Electrodynamics: The Strange Theory of Light in a Box*, Wiley-Interscience, 2005.
- [65] R. J. GLAUBER, *Quantum Theory of Optical Coherence*, Wiley-VCH, 2006.
- [66] D. WALLS and G. J. MILBURN, *Quantum Optics*, Springer, 2nd edition, 2007.
- [67] G. J. MILBURN, *Lorentz invariant intrinsic decoherence*, New Journal of Physics **8**, 96 (2006).
- [68] G. HECHENBLAIKNER, M. GANGL, P. HORAK, and H. RITSCH, *Cooling an atom in a weakly driven high-Q cavity*, Physical Review A **58**, 3030 (1998).
- [69] F. MARQUARDT, A. CLERK, and S. GIRVIN, *Quantum theory of optomechanical cooling*, Journal of Modern Optics **55**, 3329 (2008).
- [70] S. GRÖBLACHER, K. HAMMERER, M. R. VANNER, and M. ASPELMEYER, *Observation of strong coupling between a micromechanical resonator and an optical cavity field*, Nature **460**, 724 (2009).
- [71] M. ASPELMEYER, S. GRÖBLACHER, K. HAMMERER, and N. KIESEL, *Quantum optomechanics—throwing a glance*, Journal of the Optical Society of America B **27**, A189 (2010).
- [72] S. STENHOLM, *The semiclassical theory of laser cooling*, Reviews of Modern Physics **58**, 699 (1986).
- [73] J. CIRAC, R. BLATT, P. ZOLLER, and W. PHILLIPS, *Laser cooling of trapped ions in a standing wave*, Physical Review A **46**, 2668 (1992).
- [74] K. JAEHNE, K. HAMMERER, and M. WALLQUIST, *Ground-state cooling of a nanomechanical resonator via a Cooper-pair box qubit*, New Journal of Physics **10**, 095019 (2008).
- [75] P. DOMOKOS, P. HORAK, and H. RITSCH, *Semiclassical theory of cavity-assisted atom cooling*, Journal of Physics B: Atomic, Molecular and Optical Physics **34**, 187 (2001).
- [76] H. RISKEN and T. FRANK, *The Fokker-Planck Equation: Methods of Solution and Applications (Springer Series in Synergetics)*, Springer, 2008.
- [77] W. P. SCHLEICH, *Quantum Optics in Phase Space*, Wiley-VCH, 2001.
- [78] S. BARNETT and S. STENHOLM, *Hazards of reservoir memory*, Physical Review A **64**, 033808 (2001).
- [79] J. SALO, S. M. BARNETT, and S. STENHOLM, *Non-Markovian thermalisation of a two-level atom*, Optics Communications **259**, 772 (2006).
- [80] J. PIILO, K. HÄRKÖNEN, S. MANISCALCO, and K.-A. SUOMINEN, *Open system dynamics with non-Markovian quantum jumps*, Physical Review A **79**, 062112 (2009).
- [81] G. D. BOYD and J. P. GORDON, *Confocal multimode resonator for millimeter through optical wavelength masers*, Bell Syst. Tech. J **40**, 489 (1961).
- [82] N. HODGSON and H. WEBER, *Optical Resonators: Fundamentals, Advanced Concepts, Applications (Springer Series in Optical Sciences)*, Springer, 2005.
- [83] P. ASENBAUM, *Towards Cavity Cooling of a Molecular Beam*, Diploma thesis, Universität Wien, 2009.
- [84] P. DOMOKOS and H. RITSCH, *Collective Cooling and Self-Organization of Atoms in a Cavity*, Physical

Review Letters **89**, 253003 (2002).

- [85] A. BLACK, H. CHAN, and V. VULETIĆ, *Observation of Collective Friction Forces due to Spatial Self-Organization of Atoms: From Rayleigh to Bragg Scattering*, Physical Review Letters **91**, 203001 (2003).
- [86] A. PFLANZER, O. ROMERO-ISART, and J. I. CIRAC, *Master-equation approach to optomechanics with arbitrary dielectrics*, Physical Review A **86**, 013802 (2012).
- [87] B. DALTON, E. GUERRA, and P. KNIGHT, *Field quantization in dielectric media and the generalized multipolar Hamiltonian*, Physical review A **54**, 2292 (1996).
- [88] S. M. BARNETT and R. LOUDON, *The enigma of optical momentum in a medium*, Philosophical Transactions A **368**, 927 (2010).
- [89] L. D. LANDAU, L. P. PITAEVSKII, and E. LIFSHITZ, *Electrodynamics of Continuous Media, Second Edition: Volume 8 (Course of Theoretical Physics)*, Butterworth-Heinemann, 1984.
- [90] L. TSANG, J. A. KONG, and K.-H. DING, *Scattering of Electromagnetic Waves: Theories and Applications*, Wiley-Interscience, 2000.
- [91] J. A. STRATTON, *Electromagnetic Theory*, John Wiley & Sons, 2007.
- [92] D. M. POZAR, *Microwave Engineering*, Wiley, 4th edition, 2011.
- [93] H. MÜLLER, A. PETERS, and S. CHU, *A precision measurement of the gravitational redshift by the interference of matter waves*, Nature **463**, 926 (2010).
- [94] S.-W. CHIOU, T. KOVACHY, H.-C. CHIEN, and M. A. KASEVICH, *$10^2 \hbar k$ Large Area Atom Interferometers*, Physical Review Letters **107**, 130403 (2011).
- [95] J. SCHMIEDMAYER and M. ARNDT, *Embracing Quantum Metrology with Wide Arms*, Physics **4**, 74 (2011).
- [96] S. EIBENBERGER et al., *Molecular libraries for testing the quantum superposition principle beyond 10 000 amu*, Physical Chemistry Chemical Physics (in press) (2013).
- [97] J. CLAUSER and S. LI, *Talbot-vonLau atom interferometry with cold slow potassium*, Physical Review A **49**, 2213 (1994).
- [98] J. CLAUSER, *de Broglie-wave Interference of Small Rocks and Live Viruses*, in *Experimental Metaphysics*, edited by R. S. COHEN, M. HORNE, and J. STACHEL, chapter 1, pages 1–11, Kluwer Academic Publishers, 1997.
- [99] M. BORN and E. WOLF, *Principles of Optics: Electromagnetic Theory of Propagation, Interference and Diffraction of Light*, Cambridge University Press, 7th edition, 1999.
- [100] J. KOMRSKA, *Scalar Diffraction Theory in Electron Optics*, in *Advances in Electronics and Electron Physics Vol. 30*, edited by L. MARTON, chapter 4, page 139, Academic Press, 1st edition, 1971.
- [101] G. MATTEUCCI, *Electron wavelike behavior: A historical and experimental introduction*, American Journal of Physics **58**, 1143 (1990).
- [102] B. BREZGER, M. ARNDT, and A. ZEILINGER, *Concepts for near-field interferometers with large molecules*, Journal of Optics B: Quantum and Semiclassical Optics **5**, S82 (2003).
- [103] S. GERLICH, L. H. ULLER, K. HORNBERGER, A. STIBOR, H. ULBRICHT, M. GRING, F. GOLDFARB, T. SAVAS, M. M. URI, M. MAYOR, and M. ARNDT, *A Kapitza-Dirac-Talbot-Lau interferometer for highly polarizable molecules*, Nature Physics **3**, 711 (2007).
- [104] E. REIGER, L. HACKERMÜLLER, M. BERNINGER, and M. ARNDT, *Exploration of gold nanoparticle beams for matter wave interferometry*, Optics Communications **264**, 326 (2006).
- [105] M. GRING, S. GERLICH, S. EIBENBERGER, S. NIMMRICHTER, T. BERRADA, M. ARNDT, H. ULBRICHT,

- K. HORNBERGER, M. MÜRI, M. MAYOR, M. BÖCKMANN, and N. L. DOLTSINIS, *Influence of conformational molecular dynamics on matter wave interferometry*, Physical Review A **81**, 031604 (2010).
- [106] S. EIBENBERGER, S. GERLICH, M. ARNDT, J. TÜXEN, and M. MAYOR, *Electric moments in molecule interferometry*, New Journal of Physics **13**, 043033 (2011).
- [107] P. D. KEARNEY, A. G. KLEIN, G. I. OPAT, and R. GÄHLER, *Imaging and focusing of neutrons by a zone plate*, Nature **287**, 313 (1980).
- [108] R. GÄHLER and A. ZEILINGER, *Wave-optical experiments with very cold neutrons*, American Journal of Physics **59**, 316 (1991).
- [109] S. NOWAK, N. STUHLER, T. PFAU, and J. MLYNEK, *Charged Wire Interferometer for Atoms*, Physical Review Letters **81**, 5792 (1998).
- [110] R. DOAK, R. GRIENTI, S. REHBEIN, G. SCHMAHL, J. TOENNIES, and C. WÖLL, *Towards Realization of an Atomic de Broglie Microscope: Helium Atom Focusing Using Fresnel Zone Plates*, Physical Review Letters **83**, 4229 (1999).
- [111] J. E. HARVEY and J. L. FORGHAM, *The spot of Arago: New relevance for an old phenomenon*, American Journal of Physics **52**, 243 (1984).
- [112] R. L. LUCKE, *Rayleigh-Sommerfeld diffraction and Poisson's spot*, European Journal of Physics **27**, 193 (2006).
- [113] M. ABRAMOWITZ and I. A. STEGUN, editors, *Handbook of Mathematical Functions: With Formulas, Graphs, and Mathematical Tables*, Courier Dover Publications, 1965.
- [114] H. B. G. CASIMIR and D. POLDER, *The Influence of Retardation on the London-van der Waals Forces*, Physical Review **73**, 360 (1948).
- [115] S. ZAHEER, S. J. RAHI, T. EMIG, and R. L. JAFFE, *Casimir interactions of an object inside a spherical metal shell*, Physical Review A **81**, 030502 (2010).
- [116] C. EBERLEIN and R. ZIETAL, *Exact dispersion-force potentials: Interaction of an atom with a conductor-patched dielectric surface*, Physical Review A **86**, 052522 (2012).
- [117] M. BERNINGER, A. STEFANOV, S. DEACHAPUNYA, and M. ARNDT, *Polarizability measurements of a molecule via a near-field matter-wave interferometer*, Physical Review A **76**, 013607 (2007).
- [118] H. HABERLAND, M. KARRAIS, and M. MALL, *A new type of cluster and cluster ion source*, Zeitschrift für Physik D: Atoms, Molecules and Clusters **20**, 413 (1991).
- [119] T. JUFFMANN, S. TRUPPE, P. GEYER, A. G. MAJOR, S. DEACHAPUNYA, H. ULBRICHT, and M. ARNDT, *Wave and Particle in Molecular Interference Lithography*, Physical Review Letters **103**, 263601 (2009).
- [120] H. TALBOT, *LXXVI. Facts relating to optical science. No. IV*, Philosophical Magazine Series 3 **9**, 401 (1836).
- [121] L. RAYLEIGH, *XXV. On copying diffraction-gratings, and on some phenomena connected therewith*, Philosophical Magazine Series 5 **11**, 196 (1881).
- [122] K. PATORSKI, *The Self-Imaging Phenomenon and its Applications*, in *Progress in Optics XXVII*, edited by E. WOLF, volume 27 of *Progress in Optics*, chapter 1, pages 1–108, Elsevier, 1989.
- [123] W. B. CASE, M. TOMANDL, S. DEACHAPUNYA, and M. ARNDT, *Realization of optical carpets in the Talbot and Talbot-Lau configurations*, Optics Express **17**, 20966 (2009).
- [124] E. LAU, *Beugungserscheinungen an Doppelrastern*, Annalen der Physik **437**, 417 (1948).
- [125] M. CHAPMAN, C. EKSTROM, T. HAMMOND, R. RUBENSTEIN, J. SCHMIEDMAYER, S. WEHINGER, and D. E. PRITCHARD, *Optics and Interferometry with Na₂ Molecules*, Physical Review Letters **74**, 4783 (1995).

- [126] S. CAHN, A. KUMARAKRISHNAN, U. SHIM, T. SLEATOR, P. BERMAN, and B. DUBETSKY, *Time-Domain de Broglie Wave Interferometry*, Physical Review Letters **79**, 784 (1997).
- [127] A. STEFANOV, M. BERNINGER, and M. ARNDT, *A novel design for electric field deflectometry on extended molecular beams*, Measurement Science and Technology **19**, 055801 (2008).
- [128] H. ULBRICHT, M. BERNINGER, S. DEACHAPUNYA, A. STEFANOV, and M. ARNDT, *Gas phase sorting of fullerenes, polypeptides and carbon nanotubes*, Nanotechnology **19**, 045502 (2008).
- [129] G. SCOLES, *Atomic and Molecular Beam Methods, Vol. 1*, Oxford University Press, 1988.
- [130] J. BERKOWITZ, *Atomic and molecular photoabsorption: absolute total cross sections*, Academic Press, 2002.
- [131] J. E. WRAY, K. C. LIU, C. H. CHEN, W. R. GARRETT, M. G. PAYNE, R. GOEDERT, and D. TEMPLETON, *Optical power limiting of fullerenes*, Applied Physics Letters **64**, 2785 (1994).
- [132] S. DEACHAPUNYA, A. STEFANOV, M. BERNINGER, H. ULBRICHT, E. REIGER, N. L. DOLTSINIS, and M. ARNDT, *Thermal and electrical properties of porphyrin derivatives and their relevance for molecule interferometry*, Journal of Chemical Physics **126**, 164304 (2007).
- [133] D. PATTERSON, J. RASMUSSEN, and J. M. DOYLE, *Intense atomic and molecular beams via neon buffer-gas cooling*, New Journal of Physics **11**, 055018 (2009).
- [134] U. EVEN, J. JORTNER, D. NOY, N. LAVIE, and C. COSSART-MAGOS, *Cooling of large molecules below 1 K and He clusters formation*, Journal of Chemical Physics **112**, 8068 (2000).
- [135] T. GELDHAUSER, F. ZIESE, F. MERKT, A. ERBE, J. BONEBERG, and P. LEIDERER, *Acoustic laser cleaning of silicon surfaces*, Applied Physics A **89**, 109 (2007).
- [136] O. ROMERO-ISART, A. PFLANZER, M. JUAN, R. QUIDANT, N. KIESEL, M. ASPELMEYER, and J. CIRAC, *Optically levitating dielectrics in the quantum regime: Theory and protocols*, Physical Review A **83**, 013803 (2011).
- [137] G. A. T. PENDER, P. F. BARKER, F. MARQUARDT, J. MILLEN, and T. S. MONTEIRO, *Optomechanical cooling of levitated spheres with doubly resonant fields*, Physical Review A **85**, 021802 (2012).
- [138] N. DÖRRE, *Private Communication*, 2013.
- [139] M. SCHIFFER, M. RAUNER, S. KUPPENS, M. ZINNER, K. SENGSTOCK, and W. ERTMER, *Guiding, Focusing, and Cooling of Atoms in a Strong Dipole Potential*, Applied Physics A **67**, 705 (1998).
- [140] R. FULTON, A. BISHOP, and P. BARKER, *Optical Stark Decelerator for Molecules*, Physical Review Letters **93**, 243004 (2004).
- [141] A. E. COHEN, *Control of Nanoparticles with Arbitrary Two-Dimensional Force Fields*, Physical Review Letters **94**, 118102 (2005).
- [142] S. Y. T. VAN DE MEERAKKER, H. L. BETHLEM, and G. MEIJER, *Taming molecular beams*, Nature Physics **4**, 595 (2008).
- [143] H. SELIG, H. DITTUS, and C. LÄMMERZAHN, *Drop Tower Microgravity Improvement Towards the Nano-Level for the MICROSCOPE Payload Tests*, Microgravity Science and Technology **22**, 539 (2010).
- [144] L. HACKERMÜLLER, K. HORNBERGER, B. BREZGER, A. ZEILINGER, and M. ARNDT, *Decoherence in a Talbot Lau Interferometer: The Influence of Molecular Scattering*, Applied Physics A **77**, 781 (2003).
- [145] L. HACKERMÜLLER, K. HORNBERGER, B. BREZGER, A. ZEILINGER, and M. ARNDT, *Decoherence of Matter Waves by Thermal Emission of Radiation*, Nature **427**, 711 (2004).
- [146] K. HORNBERGER, S. UTTENTHALER, B. BREZGER, L. HACKERMÜLLER, M. ARNDT, and A. ZEILINGER, *Collisional Decoherence Observed in Matter Wave Interferometry*, Physical Review Letters **90**, 160401 (2003).

- [147] F. LONDON, *Zur Theorie und Systematik der Molekularkräfte*, Zeitschrift für Physik **63**, 245 (1930).
- [148] D. R. LIDE, editor, *CRC Handbook of Chemistry and Physics*, Taylor & Francis Group, 91st edition, 2010.
- [149] L. B. SCAFFARDI and J. O. TOCHO, *Size dependence of refractive index of gold nanoparticles*, Nanotechnology **17**, 1309 (2006).
- [150] L. DIÓSI, *A universal master equation for the gravitational violation of quantum mechanics*, Physics Letters A **120**, 377 (1987).
- [151] R. PENROSE, *On gravity's role in quantum state reduction*, General Relativity and Gravitation **28**, 581 (1996).
- [152] S. CARLIP, *Is quantum gravity necessary?*, Classical and Quantum Gravity **25**, 154010 (2008).
- [153] G. C. GHIRARDI, A. RIMINI, and T. WEBER, *Unified Dynamics for Microscopic and Macroscopic Systems*, Physical Review D **34**, 470 (1986).
- [154] P. PEARLE, *Combining Stochastic Dynamical State-Vector Reduction with Spontaneous Localization*, Physical Review A **39**, 2277 (1989).
- [155] G. C. GHIRARDI, P. PEARLE, and A. RIMINI, *Markov processes in Hilbert space and continuous spontaneous localization of systems of identical particles*, Physical Review A **42**, 78 (1990).
- [156] P. BONIFACIO, C. WANG, J. MENDONÇA, and R. BINGHAM, *Dephasing of a non-relativistic quantum particle due to a conformally fluctuating spacetime*, Classical and Quantum Gravity **26**, 145013 (2009).
- [157] A. BASSI and G. GHIRARDI, *Dynamical Reduction Models*, Physics Reports **379**, 257 (2003).
- [158] G. GHIRARDI, R. GRASSI, and F. BENATTI, *Describing the macroscopic world: closing the circle within the dynamical reduction program*, Foundations of Physics **25**, 5 (1995).
- [159] S. L. ADLER, *Lower and upper bounds on CSL parameters from latent image formation and IGM heating*, Journal of Physics A: Mathematical and Theoretical **40**, 2935 (2007).
- [160] W. FELDMANN and R. TUMULKA, *Parameter diagrams of the GRW and CSL theories of wavefunction collapse*, Journal of Physics A: Mathematical and Theoretical **45**, 065304 (2012).
- [161] S. L. ADLER and A. BASSI, *Is Quantum Theory Exact?*, Science **325**, 275 (2009).
- [162] A. BASSI, D.-A. DECKERT, and L. FERIALDI, *Breaking quantum linearity: Constraints from human perception and cosmological implications*, Europhysics Letters **92**, 50006 (2010).
- [163] B. VACCHINI, *On the precise connection between the GRW master equation and master equations for the description of decoherence*, Journal of Physics A: Mathematical and Theoretical **40**, 2463 (2007).
- [164] A. MESSIAH, *Quantum Mechanics*, Dover Publications, 1999.
- [165] A. J. LEGGETT, *Macroscopic quantum systems and the quantum theory of measurement*, Progress of Theoretical Physics Supplement **69**, 80 (1980).
- [166] A. PETERS, K. CHUNG, and S. CHU, *High-precision gravity measurements using atom interferometry*, Metrologia **38**, 25 (2001).
- [167] K.-Y. CHUNG, S.-W. CHIOU, S. HERRMANN, S. CHU, and H. MÜLLER, *Atom interferometry tests of local Lorentz invariance in gravity and electrodynamics*, Physical Review D **80**, 16002 (2009).
- [168] T. HIME, P. A. REICHARDT, B. L. T. PLOURDE, T. L. ROBERTSON, C.-E. WU, A. V. USTINOV, and J. CLARKE, *Solid-State Qubits with Current-Controlled Coupling*, Science **314**, 1427 (2006).
- [169] M. R. ANDREWS, C. G. TOWNSEND, H.-J. MIESNER, D. S. DURFEE, D. M. KURN, and W. KETTERLE, *Observation of Interference Between Two Bose Condensates*, Science **275**, 637 (1997).
- [170] W. MARSHALL, C. SIMON, R. PENROSE, and D. BOUWMEESTER, *Towards Quantum Superpositions of a*

- Mirror*, Physical Review Letters **91**, 130401 (2003).
- [171] W. DÜR, C. SIMON, and J. I. CIRAC, *Effective Size of Certain Macroscopic Quantum Superpositions*, Physical Review Letters **89**, 210402 (2002).
 - [172] G. BJÖRK and P. G. L. MANA, *A size criterion for macroscopic superposition states*, Journal of Optics B: Quantum and Semiclassical Optics **6**, 429 (2004).
 - [173] J. I. KORSBAKKEN and OTHERS, *Measurement-based measure of the size of macroscopic quantum superpositions*, Physical Review A **75**, 42106 (2007).
 - [174] F. MARQUARDT, B. ABEL, and J. VON DELFT, *Measuring the size of a quantum superposition of many-body states*, Physical Review A **78**, 12109 (2008).
 - [175] C.-W. LEE and H. JEONG, *Quantification of Macroscopic Quantum Superpositions within Phase Space*, Physical Review Letters **106**, 220401 (2011).
 - [176] F. FRÖWIS and W. DÜR, *Measures of macroscopicity for quantum spin systems*, New Journal of Physics **14**, 093039 (2012).
 - [177] L. DIÓSI, *Models for universal reduction of macroscopic quantum fluctuations*, Physical Review A **40**, 1165 (1989).
 - [178] K. KRAUS, *States, Effects, and Operations*, in *Lecture Notes in Physics*, volume 190, Springer, 1983.
 - [179] L. DIÓSI, *A Short Course in Quantum Information Theory: An Approach from Theoretical Physics*, Springer Berlin / Heidelberg, 2nd edition, 2010.
 - [180] R. ALICKI and K. LENDI, *Quantum Dynamical Semigroups and Applications*, Springer, 2007.
 - [181] G. LINDBLAD, *On the generators of quantum dynamical semigroups*, Communications in Mathematical Physics **48**, 119 (1976).
 - [182] V. GORINI, A. KOSSAKOWSKI, and E. C. G. SUDARSHAN, *Completely positive dynamical semigroups of N -level systems*, Journal of Mathematical Physics **17**, 821 (1976).
 - [183] J. M. LEVY-LEBLOND, *Galilei group and nonrelativistic quantum mechanics*, Journal of Mathematical Physics **4**, 776 (1963).
 - [184] G. W. MACKEY, *Induced representations of groups and quantum mechanics (Lectures given at Scuola Normale, Posa, Italy, 1967)*, W. A. Benjamin, 1968.
 - [185] V. BARGMANN, *On Unitary Ray Representations of Continuous Groups*, Annals of Mathematics **59**, 1 (1954).
 - [186] M. REED and B. SIMON, *Functional Analysis, Volume 1 (Methods of Modern Mathematical Physics)*, Academic Press, 1981.
 - [187] A. BARCHIELLI and L. LANZ, *Quantum mechanics with only positive-time evolution for an isolated system*, Il Nuovo Cimento B **44**, 241 (1978).
 - [188] A. S. HOLEVO, *Covariant quantum dynamical semigroups: unbounded generators*, Irreversibility and Causality Semigroups and Rigged Hilbert Spaces **504**, 67 (1998).
 - [189] A. S. HOLEVO, *A note on covariant dynamical semigroups*, Reports on Mathematical Physics **32**, 211 (1993).
 - [190] A. S. HOLEVO, *On conservativity of covariant dynamical semigroups*, Reports on Mathematical Physics **33**, 95 (1993).
 - [191] J. B. CONWAY, *A Course in Functional Analysis (Graduate Texts in Mathematics)*, Springer, 2nd edition, 1990.
 - [192] A. S. HOLEVO, *On the structure of covariant dynamical semigroups*, Journal of Functional Analysis

131, 255 (1995).

- [193] A. CALDEIRA and A. LEGGETT, *Path integral approach to quantum Brownian motion*, Physica A: Statistical Mechanics and its Applications **121**, 587 (1983).
- [194] B. VACCHINI and K. HORNBERGER, *Quantum linear Boltzmann equation*, Physics Reports **478**, 71 (2009).
- [195] E. JOOS and H. D. ZEH, *The emergence of classical properties through interaction with the environment*, Zeitschrift für Physik B: Condensed Matter **59**, 223 (1985).
- [196] G. C. GHIRARDI, O. NICROSINI, A. RIMINI, and T. WEBER, *Spontaneous localization of a system of identical particles*, Il Nuovo Cimento B **102**, 383 (1988).
- [197] B. ROBERTSON, *Introduction to Field Operators in Quantum Mechanics*, American Journal of Physics **41**, 678 (1973).
- [198] F. SCHWABL, *Advanced Quantum Mechanics*, Springer, 2008.
- [199] J. J. SAKURAI, *Modern Quantum Mechanics (Revised Edition)*, Addison-Wesley, 1994.
- [200] M. BUSSE and K. HORNBERGER, *Pointer basis induced by collisional decoherence*, Journal of Physics A: Mathematical and Theoretical **43**, 15303 (2010).
- [201] O. MORSCH and M. OBERTHALER, *Dynamics of Bose-Einstein condensates in optical lattices*, Reviews of Modern Physics **78**, 179 (2006).
- [202] A. J. LEGGETT, *Quantum liquids: Bose condensation and Cooper pairing in condensed-matter systems*, Oxford University Press, 2006.
- [203] G.-B. JO, Y. SHIN, S. WILL, T. PASQUINI, M. SABA, W. KETTERLE, D. PRITCHARD, M. VENGALATTORE, and M. PRENTISS, *Long Phase Coherence Time and Number Squeezing of Two Bose-Einstein Condensates on an Atom Chip*, Physical Review Letters **98**, 030407 (2007).
- [204] H. WALLIS, A. RÖHRL, M. NARASCHEWSKI, and A. SCHENZLE, *Phase-space dynamics of Bose condensates: Interference versus interaction*, Physical Review A **55**, 2109 (1997).
- [205] M. F. RIEDEL, P. BÖHI, Y. LI, T. W. HÄNSCH, A. SINATRA, and P. TREUTLEIN, *Atom-chip-based generation of entanglement for quantum metrology*, Nature **464**, 1170 (2010).
- [206] C. GROSS, T. ZIBOLD, E. NICKLAS, J. ESTÈVE, and M. K. OBERTHALER, *Nonlinear atom interferometer surpasses classical precision limit*, Nature **464**, 1165 (2010).
- [207] M. EGOROV, R. ANDERSON, V. IVANNIKOV, B. OPANCHUK, P. DRUMMOND, B. HALL, and A. SIDOROV, *Long-lived periodic revivals of coherence in an interacting Bose-Einstein condensate*, Physical Review A **84**, R021605 (2011).
- [208] M. NARASCHEWSKI, H. WALLIS, A. SCHENZLE, J. CIRAC, and P. ZOLLER, *Interference of Bose condensates*, Physical Review A **54**, 2185 (1996).
- [209] C. KITTEL, *Introduction to solid state physics*, Wiley, 1996.
- [210] K. KOPITZKI and P. HERZOG, *Einführung in die Festkörperphysik*, Vieweg+Teubner Verlag, 2007.
- [211] A. LEGGETT, *Probing quantum mechanics towards the everyday world: Where do we stand?*, Physica Scripta **T102**, 69 (2002).
- [212] S. E. SHAFRANJUK and J. B. KETTERSON, *Principles of Josephson-Junction-Based Quantum Computation*, in *Superconductivity, Vol. 1*, edited by K. H. BENNEMANN and J. KETTERSON, page 315, Springer, 2008.
- [213] J. I. KORSBAKKEN, F. K. WILHELM, and K. B. WHALEY, *Electronic structure of superposition states in flux qubits*, Physica Scripta **T137**, 014022 (2009).

- [214] J. I. KORSBAKKEN, F. K. WILHELM, and K. B. WHALEY, *The size of macroscopic superposition states in flux qubits*, Europhysics Letters **89**, 30003 (2010).
- [215] T. ORLANDO, J. MOOIJ, L. TIAN, C. VAN DER WAL, L. LEVITOV, S. LLOYD, and J. MAZO, *Superconducting persistent-current qubit*, Physical Review B **60**, 15398 (1999).
- [216] J. BARDEEN, L. N. COOPER, and J. R. SCHRIEFFER, *Theory of superconductivity*, Physical Review **108**, 1175 (1957).
- [217] M. BUFFA, O. NICROSINI, and A. RIMINI, *Dissipation and reduction effects of spontaneous localization on superconducting states*, Foundations of Physics Letters **8**, 105 (1995).
- [218] K. HORNBERGER, L. HACKERMÜLLER, and M. ARNDT, *Influence of molecular temperature on the coherence of fullerenes in a near-field interferometer*, Physical Review A **71**, 023601 (2005).
- [219] S. DIMOPOULOS, P. W. GRAHAM, J. M. HOGAN, M. A. KASEVICH, and S. RAJENDRAN, *Gravitational wave detection with atom interferometry*, Physics Letters A **678**, 37 (2009).
- [220] M. CHAPMAN, C. EKSTROM, T. HAMMOND, J. SCHMIEDMAYER, B. TANNIAN, S. WEHINGER, and D. PRITCHARD, *Near-field imaging of atom diffraction gratings: The atomic Talbot effect*, Physical Review A **51**, R14 (1995).
- [221] C. J. BORDÉ, C. SALOMON, S. AVRILLIER, A. VAN LERBERGHE, C. BRÉANT, D. BASSI, and G. SCOLES, *Optical Ramsey fringes with traveling waves*, Physical Review A **30**, 1836 (1984).
- [222] C. J. BORDÉ, N. COURTIER, F. DU BURCK, A. N. GONCHAROV, and M. GORLICKI, *Molecular interferometry experiments*, Physics Letters A **188**, 187 (1994).
- [223] H. MAIER-LEIBNITZ and T. SPRINGER, *Ein Interferometer für langsame Neutronen*, Zeitschrift für Physik **167**, 386 (1962).
- [224] A. ZEILINGER, R. GAEHLER, C. G. SHULL, and W. TREIMER, *Experimental status and recent results of neutron interference optics*, AIP Conference Proceedings **89**, 93 (1982).
- [225] D. KEITH, M. SCHATTEBURG, H. SMITH, and D. PRITCHARD, *Diffraction of Atoms by a Transmission Grating*, Physical Review Letters **61**, 1580 (1988).
- [226] F. SHIMIZU, K. SHIMIZU, and H. TAKUMA, *Double-slit interference with ultracold metastable neon atoms*, Physical Review A **46**, R17 (1992).
- [227] R. GRISENTI, W. SCHÖLLKOPF, J. TOENNIES, G. HEGERFELDT, and T. KÖHLER, *Determination of Atom-Surface van der Waals Potentials from Transmission-Grating Diffraction Intensities*, Physical Review Letters **83**, 1755 (1999).
- [228] L. HACKERMÜLLER, S. UTTENTHALER, K. HORNBERGER, E. REIGER, B. BREZGER, A. ZEILINGER, and M. ARNDT, *Wave Nature of Biomolecules and Fluorofullerenes*, Physical Review Letters **91**, 90408 (2003).
- [229] A. D. O'CONNELL, M. HOFHEINZ, M. ANSMANN, R. C. BIALCZAK, M. LENANDER, E. LUCERO, M. NEELEY, D. SANK, H. WANG, M. WEIDES, J. WENNER, J. M. MARTINIS, and A. N. CLELAND, *Quantum ground state and single-phonon control of a mechanical resonator*, Nature **464**, 697 (2010).
- [230] J. D. TEUFEL, T. DONNER, D. LI, J. W. HARLOW, M. S. ALLMAN, K. CİCAK, A. J. SIROIS, J. D. WHITTAKER, K. W. LEHNERT, and R. W. SIMMONDS, *Sideband cooling of micromechanical motion to the quantum ground state*, Nature **475**, 359 (2011).
- [231] J. CHAN, T. P. M. ALEGRE, A. H. SAFAVI-NAEINI, J. T. HILL, A. KRAUSE, S. GRÖBLACHER, M. ASPELMEYER, and O. PAINTER, *Laser cooling of a nanomechanical oscillator into its quantum ground state*, Nature **478**, 89 (2011).
- [232] K. HAMMERER, A. S. SÖRENSEN, and E. S. POLZIK, *Quantum interface between light and atomic ensembles*, Reviews of Modern Physics **82**, 1041 (2010).

- [233] A. OURJOUNTSEV, H. JEONG, R. TUALLE-BROURI, P. GRANGIER, and OTHERS, *Generation of optical 'Schrödinger cats' from photon number states*, *Nature* **448**, 784 (2007).
- [234] S. DELÉGLISE, I. DOTSENKO, C. SAYRIN, J. BERNU, M. BRUNE, J. M. RAIMOND, and S. HAROCHE, *Reconstruction of non-classical cavity field states with snapshots of their decoherence*, *Nature* **455**, 510 (2008).
- [235] T. GERRITS, S. GLANCY, T. S. CLEMENT, B. CALKINS, A. E. LITA, A. J. MILLER, A. L. MIGDALL, S. W. NAM, R. P. MIRIN, and E. KNILL, *Generation of optical coherent-state superpositions by number-resolved photon subtraction from the squeezed vacuum*, *Physical Review A* **82**, 31802 (2010).
- [236] W. B. GAO, C. Y. LU, X. C. YAO, P. XU, O. GÜHNE, A. GOEBEL, Y. A. CHEN, C. Z. PENG, Z. B. CHEN, and J. W. PAN, *Experimental demonstration of a hyper-entangled ten-qubit Schrödinger cat state*, *Nature Physics* **6**, 331 (2010).
- [237] P. F. BARKER and M. N. SHNEIDER, *Cavity cooling of an optically trapped nanoparticle*, *Physical Review A* **81**, 023826 (2010).
- [238] N. KIESEL, F. BLASER, U. DELIC, D. GRASS, R. KALTENBAEK, and M. ASPELMEYER, *Cavity cooling of an optically levitated nanoparticle*, *arXiv:1304.6679 [quant-ph]* (2013).
- [239] C. C. GERRY and P. L. KNIGHT, *Introductory Quantum Optics*, Cambridge University Press, 2005.
- [240] J. P. BARTON and D. R. ALEXANDER, *Fifth-order corrected electromagnetic field components for a fundamental Gaussian beam*, *Journal of Applied Physics* **66**, 2800 (1989).
- [241] A. A. R. NEVES, A. FONTES, L. A. PADILHA, E. RODRIGUEZ, C. H. D. B. CRUZ, L. C. BARBOSA, and C. L. CESAR, *Exact partial wave expansion of optical beams with respect to an arbitrary origin*, *Optics Letters* **31**, 2477 (2006).
- [242] K. CAHILL and R. GLAUBER, *Ordered Expansions in Boson Amplitude Operators*, *Physical Review* **177**, 1857 (1969).
- [243] A. BASSI, E. IPPOLITI, and S. ADLER, *Towards Quantum Superpositions of a Mirror: An Exact Open Systems Analysis*, *Physical Review Letters* **94**, 30401 (2005).

Lebenslauf – Stefan Nimmrichter

Persönliche Angaben

Geburtsdatum: 03.04.1984

Geburtsort: Riga

Staatsangehörigkeit: deutsch

Akademische Laufbahn

Mai 2002: Abitur am Schyren-Gymnasium Pfaffenhofen

Oktober 2002 – Dezember 2007: Studium der allgemeinen Physik mit Diplomabschluss an der TU München

Dezember 2006 – Dezember 2007: Diplomarbeit in theoretischer Quantenoptik („Matter wave Talbot-Lau interferometry beyond the eikonal approximation“) bei Dr. Klaus Hornberger, LMU München

Dezember 2007 – Juli 2013: Doktorarbeit in theoretischer Physik über molekulare Quantenoptik und Quantennanophysik („Macroscopic Matter-wave Interferometry“) in der Forschungsgruppe von Prof. Markus Arndt an der Universität Wien

Wissenschaftliche Aktivitäten

2007-2013: Mitglied im CoQuS-Doktoratskolleg an der Universität Wien

2008-2012: 5 Vorträge an internationalen Konferenzen (DPG-Frühjahrstagungen 2008-2010, 2012; APS spring meeting 2011)

September 2009: Gastvortrag auf Einladung in der Quantum-2-Cosmos-4-Konferenz in Bremen

September 2010: Organisation der CoQuS-Sommerschule „Frontiers of Modern Quantum Physics“ mit internationalen Gastprofessoren an der Universität Wien

2010 und 2012: Übungsleitung bei der Vorlesung „Theoretische Physik 1: Klassische Mechanik“

Mai 2013: Gastvorlesung in der WE-Heraeus-Sommerschule „Exploring the limits of the quantum superposition principle“ in Bad Honnef

Öffentlichkeitsarbeit

Januar 2013: Öffentlicher Vortrag für Schüler bei der „Wiener Science Lecture 2013“

März 2013: Öffentlicher Vortrag bei der VÖGB-Veranstaltung „Jazz und Quantenphysik“

Auszeichnungen

Preis für den besten Diplomabschluss in theoretischer Physik der TU München (2008)

- Publikationen als Erstautor** SN, K. Hornberger; Phys. Rev. A **78**, 023612 (2008)
Theory of near-field matter wave interference beyond the eikonal approximation
- SN, K. Hornberger, H. Ulbricht, M. Arndt; Phys. Rev. A **78**, 063607 (2008)
Absolute absorption spectroscopy based on molecule interferometry
- SN, K. Hammerer, P. Asenbaum, H. Ritsch, M. Arndt;
 New J. Phys. **12**, 083003 (2010)
Master equation for the motion of a polarizable particle in a multimode cavity
- SN, P. Haslinger, K. Hornberger, M. Arndt;
 New J. Phys. **13**, 075002 (2011)
Concept of an ionizing time-domain matter-wave interferometer
- SN, K. Hornberger, P. Haslinger, M. Arndt;
 Phys. Rev. A **83**, 043621 (2011)
Testing spontaneous localization theories with matter-wave interferometry
- SN, K. Hornberger; Phys. Rev. Lett. **110**, 160403 (2013)
Macroscopicity of Mechanical Quantum Superposition States
- Publikationen als Mitautor** K.Hornberger et al.; New J. Phys. **11**, 043032 (2009)
Theory and experimental verification of Kapitza-Dirac-Talbot-Lau interferometry
- M. Gring et al.; Phys. Rev. A **81**, 031604(R) (2010)
Influence of conformational molecular dynamics on matter wave interferometry
- T. Juffmann, SN, M. Arndt, H. Gleiter, K. Hornberger;
 Found. Phys. **42**, 98 (2012)
New prospects for de Broglie interferometry
- S. Gerlich et al.; Nature Comm. **2**, 263 (2011)
Quantum interference of large organic molecules
- K. Hornberger, S. Gerlich, P. Haslinger, SN, M. Arndt;
 Rev. Mod. Phys. **84**, 157 (2012)
Colloquium: Quantum interference of clusters and molecules
- P. Haslinger, N. Dörre, P. Geyer, J. Rodewald, SN, M. Arndt;
 Nature Phys. **9**, 144 (2013)
A universal matter-wave interferometer with optical ionization gratings in the time domain
- P. Asenbaum, S. Kuhn, SN, U. Sezer, M. Arndt;
 preprint arXiv:**1306.4617** [quant-ph]
Cavity cooling of free silicon nanoparticles in high-vacuum